Fakultät für Physik
Institut für Theorie der Kondensierten Materie

Mechanism, symmetry and topology of ordered phases in correlated systems

PhD thesis
by
Mathias Sebastian Scheurer

06.05.2016

Instructor: Prof. Dr. Jörg Schmalian

Mechanismus, Symmetrie und Topologie geordneter Phasen in korrelierten Systemen

Zur Erlangung des akademischen Grades eines

DOKTORS DER NATURWISSENSCHAFTEN

von der Fakultät für Physik
des Karlsruher Instituts für Technologie

genehmigte

DISSERTATION

von

Dipl. Phys. Mathias Sebastian Scheurer
aus Heilbronn

Tag der mündlichen Prüfung: 06.05.2016
Referent: Prof. Dr. J. Schmalian
Korreferent: Prof. Dr. Alexander D. Mirlin

To my fiancée.
For her immeasurable support and patience.

To my parents.
For believing in me, for giving me advice and for everything else.

Introduction

The theoretical classification and sharp experimental distinction of different phases of matter is one of the most important fundamental aspects of condensed matter physics. The first systematic approach was provided by Landau's theory of phase transitions [1] where different phases are characterized according to the *symmetries* that are broken at the phase transition. Many phase transitions fit well into Landau's paradigm including liquid-solid transitions, structural phase transitions, paramagnet-ferromagnet transitions and superconductivity. Similarly, quantum phase transitions, which occur at zero temperature by varying a non-thermal parameter, can be characterized by the symmetry changes of the ground state of the system. Landau's approach was challenged by the discovery of the quantum Hall effect in 1980 [2]. The observation of changes in the quantized value of the Hall conductance upon variation of the magnetic field signals the presence of quantum phase transitions, although no additional symmetries are broken. The seminal work of Thouless, Kohmoto, Nightingale, and den Nijs [3] clarified that the distinction between quantum Hall phases with different values of the Hall conductance is not a matter of symmetry but a matter of *topology*.

During the last years, it has been understood that the "topological order" of the quantum Hall effect is just an example of many different systems that can be classified topologically, which spurred enormous theoretical and experimental research interests in condensed matter physics [4–7]. Consider a many-body system which in its noninteracting limit can be described by a filled Fermi sea. Generally speaking, two phases with a gap in the vicinity of the Fermi level are topologically distinct with respect to a given set of symmetries if there is no continuous deformation between the two that keeps the gap intact and respects the symmetries. A state that is topologically distinct from the vacuum is referred to as topologically nontrivial and characterized by gapless modes localized at its boundary. In case of the quantum Hall effect, these edge channels can be intuitively seen as the cyclotron orbits of electrons bouncing off the edge of the system. A crucial property of the edge modes of topological phases of matter is their protection against Anderson localization [8] by disorder that respects the set of symmetries defining the nontrivial topology. Since disorder breaks all lattice symmetries, one usually focuses on more general symmetries such as time-reversal symmetry (TRS), i.e., the invariance under the reversal of the time direction, for defining topological states of matter [9, 10]. The gap around the Fermi level, which is a crucial ingredient of the definition of topological states of matter, occurs in the simplest case between the valence and conduction in a band insulator. In this sense, the advent of topology in condensed matter physics has revolutionized one of its longstanding cornerstones, the band theory of solids [11]. While the topological classification of noninteracting states of matter is fully understood theoretically [9, 10], the study of the stability of the classification towards interactions as well as the emergence of exotic topological phases that only occur due to the presence of significant correlations is an active area of current research [5, 7]. An example of the latter is provided by the fractional quantum Hall effect [12, 13].

As a second step, after having established a definition of different phases of matter, one has to analyze transitions between distinct phases with the ultimate goal of gaining detailed microscopic understanding of the *mechanism* driving the transition. What are the dominant interactions for the phase transition to occur? Can the phase emerge in a perfectly pure crystal or is it crucially stabilized by the presence of

disorder? These questions are in general very difficult to answer since they pose significant challenges both on the theoretical and experimental side.

A theorist has to face the problem that a microscopic calculation is required that focuses on the set of relevant degrees of freedom of the system and its crucial mutual interactions while being solvable in a controlled way at the same time. A famous example of an instability that has long been lacking a microscopic understanding is provided by superconductivity. Although phenomenological theories [14, 15] had been developed since the discovery of this phenomenon in 1911 [16], it took until 1957 that a successful microscopic theory, the Bardeen-Cooper-Schrieffer (BCS) theory, had been developed [17, 18]. Within BCS theory, the superconducting instability is driven by the attractive electron-electron interaction resulting from the coupling to phonons.

On the experimental side, approaches have to be developed that allow for testing different possible theories in order to pinpoint the microscopic mechanism of instabilities. For instance, in case of the BCS mechanism of superconductivity, the measurement of the isotope effect on the superconducting transition temperature [19, 20] has convincingly demonstrated the crucial relevance of the electron-phonon coupling for the superconducting instability. The properties of the superconducting states observed in heavy-fermion systems [21–23] and later in other material classes such as the cuprates [24] disagreed with predictions of BCS theory and, hence, indicated that also other "unconventional" mechanisms can lead to superconducting phase transitions [25, 26]. In case of the cuprates, two celebrated phase sensitive experiments, the corner-junction [27] and tricrystal-magnetometry [28] experiment, have convincingly demonstrated after many years of intense research [29] that the superconducting state also breaks rotational symmetries (d-wave superconductivity) in additional to the broken global U(1) phase rotation symmetry of BCS theory. This strongly supports a predominantly electronic pairing mechanism where spin-fluctuations provide the pairing glue for superconductivity [30–32].

This thesis will be concerned with all three different aspects of phase transitions outlined above – symmetry, topology and mechanism – as well as with their mutual interplay. We will to a large extent focus on superconducting transitions in noncentrosymmetric materials, i.e., systems without a center of inversion. In combination with atomic spin-orbit coupling (SOC), this lifts the spin-degeneracy of the Fermi surfaces which is the well-known Dresselhaus-Rashba effect [33, 34] and has crucial energetic consequences for the phase competition in the system. We will both study concrete physical systems of current interest and present general arguments and calculations that are only based on generic properties of the system such as symmetries and Fermi-surface topologies. As will be seen repeatedly in this thesis, the three central aspects of phase transitions mentioned above are particularly strongly related in case of noncentrosymmetric superconductors.

Firstly, in analogy to the connection between the symmetry of the paring state and the mechanism driving the instability, which has been proven to be a useful detective tool for the cuprates [27, 28], we will show that there is also a very direct *correspondence between the mechanism and the topology of superconductivity*. In addition to its importance from a pure theoretical point of view, this correspondence might also be used in experiment in order to determine the microscopic mechanism of a superconducting state. Investigation of topological properties of the condensate, i.e., the presence of gapless edge modes, yields information on whether it mainly arises from electron-phonon or from Coulomb interactions. A physical system where this approach might be relevant is given by the electron liquid that forms [35] at the interface between the two insulating perovskite oxides $LaAlO_3$ (LAO) and $SrTiO_3$ (STO). The complex reconstruction mechanism and the rich electronic behavior in this system has triggered enormous research efforts in recent years [36–38]. It represents a prime example of a superconducting system [39, 40] with strongly spin-orbit-split Fermi surfaces [41–43]. The two

candidate superconducting states, that are predicted in this work for an electron-phonon- and Coulomb-interaction-dominated pairing mechanism, have the same point symmetry but differ in their topology. The unknown mechanism of superconductivity might thus be detected via topological signatures.

Secondly, we will see that the point symmetries of the normal state in combination with the energetic constraints resulting from the spin splitting of the Fermi surfaces have strong general implications for the possible pairing states, in particular, concerning the time-reversal properties of the condensate. This is important as the determination of the superconducting order parameter is typically a very complicated and long-standing endeavor. For instance, it required many years of theoretical and experimental work for the experimental proof [27, 28] of d-wave pairing in the cuprates [29]. From this point of view, general selection rules for possible pairing states in noncentrosymmetric systems might be very helpful in order to pinpoint the microscopic order parameter in the numerous different systems belonging to this broad class of superconducting materials [38, 44–46].

The behavior under time-reversal is a pivotal property of a superconductor. It crucially influences its thermal and electromagnetic response since, e.g., only a superconducting condensate with broken TRS can exhibit the polar Kerr effect (PKE) [47–49]. In addition, inhomogeneities lead to the formation of local moments [50, 51] and an exotic thermoelectric effect has been proposed to occur in TRS-breaking condensates [52]. As there are only a few superconductors with strong indications of broken TRS, most notably Sr_2RuO_4 [47, 51, 53], UPt_3 [48, 54], URu_2Si_2 [49] as well as $LaNiC_2$ [55] and Re_6Zr [56], the general conditions for TRS-breaking Cooper instabilities discussed in this thesis might prove useful as design principles in the search for exotic superconducting states with broken TRS. Furthermore, as mentioned above, the topological classification of states of matter is determined by the presence or absence of TRS. Consequently, our constraints on the time-reversal properties of the superconductor formulated in terms of the point group of the normal state also reveal a connection between the *spatial symmetries* of the normal state and the *topological classification* of the possible resulting superconducting instabilities.

Taken together, the correspondence between the crystal symmetries of the normal state and the topological classification of the superconductor as well as between the mechanism and the topology of superconductivity can also be used as guiding principles in the search for materials hosting topologically nontrivial superconductors. Finding candidate materials for the realization of nontrivial topologies is important both from a fundamental physics point of view as well as for potential future applications.

The fundamental scientific interest directly follows from the properties outlined above. Topological states of matter do not fall into Landau's paradigm with a locally defined order parameter, they realize a holographic principle in the sense that the presence of edge modes is determined by bulk properties, known as the bulk-boundary correspondence, and the edge modes are robust against Anderson localization [8]. Additionally, in case of topological superconductors, the edge modes satisfy a reality constraint and thus represent a condensed matter realization [6] of Majorana's vision [57] of a particle that is its own antiparticle. Isolated "Majorana modes" that emerge, e.g., in vortices of two-dimensional (2D) topological superconductors, can be shown to obey exotic non-Abelian statistics which means that the outcome of a sequence of particle interchanges depends on the order in which they are carried out [58]. The latter property is also at the heart of the central long-term application of topological superconductors – topological quantum computing [59]. The basic idea of topological quantum computing is to store information in qubits formed out of spatially separated Majorana modes rendering them inherently protected against local perturbations which avoids decoherence at the "hardware level". Quantum computations are performed by adiabatically winding Majorana modes around each other.

While several materials hosting both 2D as well as three-dimensional (3D) topological band insulator phases have been identified experimentally (see Refs. [4, 5] and references therein), the main experi-

mental progress in case of topological superconductors has been achieved in "extrinsic" superconductors [60, 61], where superconductivity is not an inherent property of the material but externally induced via the proximity effect. Not only from a material science point of view but also because of its potential merits in applications, "intrinsic" topological superconductors are of great interest, i.e., systems where both superconductivity as well as the nontrivial topology arise spontaneously by virtue of the internal dynamics of the material. Especially in the search for "intrinsic" topological superconductors, general guiding principles are needed that are not based on model calculations but only depend on very few and experimentally accessible properties of the material such as the symmetries and the Fermi-surface topologies in the normal state. In this context, it is furthermore important to analyze whether topologically nontrivial condensates are stable against the inevitable presence of disorder in the material or whether disorder might even be intentionally used in order to stabilize a topological phase. These issues will be addressed in the work at hand.

More specifically, the following analysis is presented in the remainder of the thesis: After two introductory chapters (Chaps. 1 and 2) that provide more details and background information on the aspects mentioned above, we start in Chap. 3 with a discussion of interaction effects in topological band insulators. As outlined in the beginning, the impact of interactions both concerning the stability of a topological phase as well as its potential to induce new phases without noninteracting analogue represent important questions of current research. As a result of the excellent controllability, cold-atom experiments [62, 63] might shed light on the open questions of the field of strongly interacting topological insulators. For this reason, we propose in Chap. 3 a cold-atom setup to simulate various 2D and 3D topological insulator phases and discuss how a transition to a topological Mott insulator (TMI) [64] can be induced by interactions. Similarly to the fractional quantum Hall effect [12, 13] mentioned above, a TMI only occurs in the presence of interactions. It is a spin-liquid-like phase where the charge degrees of freedom are frozen in a Mott state, while the electron spin is characterized by a topologically nontrivial band structure. Phase diagrams are calculated within slave-rotor mean-field theory [65–67].

In Chap. 4, we study general selection rules for possible superconducting instabilities in 2D and 3D systems with nondegenerate Fermi surfaces that result from the combination of the point symmetries of the hight-temperature phase and energetic arguments based on the spin-orbit splitting E_{so} of the Fermi surfaces. The selection rules are valid as long as the superconducting gap at zero temperature is smaller than E_{so}. In particular, the constraints on the possibility of spontaneous TRS breaking are discussed. The general results are applied to several different materials. Interesting consequences arise for thin layers of compounds, such as Sr_2RuO_4 [47, 51, 53], UPt_3 [48, 54] and URu_2Si_2 [49], that harbor TRS-breaking superconductivity in their 3D bulk. Note that thin films of Sr_2RuO_4 and UPt_3 have been fabricated and shown to be superconducting [68, 69]. We will see that the superconducting state of thin layers of Sr_2RuO_4 is a promising candidate for time-reversal symmetric topological superconductivity. In addition, we illustrate how the selection rules can be employed to gain information about the order parameter of 2D systems with no 3D counterpart and serve as a design principle in the search for TRS-breaking superconductivity mainly using the different orientations of the LAO/STO heterostructures as examples.

The LAO/STO heterostructures are also the central topic of Chap. 5. While the general selection rules in combination with experiments [70] fully determines the symmetry properties of the condensate, the topology of the superconductor remains unresolved. For this purpose, we perform a microscopic calculation focusing on the most frequently studied (001)-oriented interface. We derive an interacting effective low-energy model of the system and analyze the phase competition using a renormalization group (RG) approach. In addition to competing density wave instabilities with interesting spatial

textures, we identify two distinct candidate pairing states and establish a one-to-one correspondence between the mechanism of superconductivity and its topology for the heterostructure. We discuss how this might be used in order to pinpoint both the superconducting order parameter as well as the unknown microscopic mechanism of superconductivity.

Chap. 6 will be devoted to extending the correspondence between the mechanism and topology derived for LAO/STO heterostructures to more general noncentrosymmetric systems. The analysis is mainly based on exact relations following from the symmetries of the normal state, most notably TRS, and independent of many microscopic details such as the number and character of relevant orbitals. As opposed to the previous chapters, the topological classification is performed on the level of Green's functions and an Eliashberg-theory [71, 72] approach is used such that the results for the electron-phonon coupling are also valid in the strong coupling regime. The findings of this chapter also complement the discussion of TRS in Chap. 4 by relating the behavior of the resulting condensate under time-reversal to the mechanism driving the instability. Furthermore, we formulate guiding principles for the search of "intrinsic" topological superconductors in noncentrosymmetric systems.

Finally, Chap. 7 is concerned with generalizing different aspects of superconductivity discussed in the previous chapters to weakly disordered systems. Here, "weakly" means that the mean-free path l is much larger than the inverse Fermi momentum k_F and that localization [8] can be neglected. Firstly, we study the sensitivity of different superconducting states against nonmagnetic as well as magnetic impurities. After a general analysis yielding an algebraic criterion for the protection of the mean-field transition temperature against disorder, we study specific superconductors, in particular, the two candidate pairing states of LAO/STO heterostructures deduced in Chap. 5. Secondly, we discuss how magnetic disorder can be used to stabilize time-reversal invariant topological superconductivity.

For convenience of the reader a list of acronyms and a summary of the notation as well as conventions used in this thesis is given on page 215f. and pages 217–220, respectively.

Contents

Chapter 1

1 Fundamentals: Spontaneous symmetry breaking

The title of the thesis contains the three key words “mechanism”, “symmetry” and “topology”. We will, not only for historical but also for pedagogical reasons, focus on the first two aspects in this chapter while the last one will be the topic of Chap. 2.

The purpose of this chapter is threefold: Firstly, the general concept of spontaneous symmetry breaking and possible mechanisms thereof, i.e., microscopic physical processes leading to it, are discussed. Secondly, the notation and conventions that will also be used later on are introduced. Finally, we also provide a short introduction to several different materials that are of interest for this thesis. Naturally, all of our discussions will be far from complete but rather adjusted to the work presented in the thesis. For readers interested in more details we refer to the literature in the corresponding sections.

More specifically, we begin in Sec. 1.1 with a general discussion of spontaneous symmetry breaking on the level of a phenomenological free energy expansion. As we are mainly interested in superconductivity in this work, the notation used refers to superconductors, however, the discussion also applies, *mutatis mutandis*, to other, e.g. magnetic, transitions. We then present (see Sec. 1.1.2) how the superconducting instability can be understood microscopically and introduce the notion of conventional and unconventional pairing. Sec. 1.2 will be devoted to the implications of fluctuations. In Sec. 1.3 we focus on the peculiarities of superconducting systems with broken inversion symmetry and discuss several materials. Finally, in Sec. 1.4, a brief introduction into impurity scattering, again with a focus on symmetries and superconductivity, is provided.

1.1 Free energy expansion

A very efficient phenomenological way to understand the spontaneous symmetry breaking occurring at phase transitions proceeds by expanding the free energy of the system in terms of the order parameter of the phase transition. This approach goes back to L. D. Landau who originally applied it in the early 1930’s [73] in order to explain the phenomenon of superconductivity which at that time was still lacking a microscopic theoretical explanation. Although he had chosen the wrong order parameter for describing the superconducting state [74], this work paved the way for the development of the celebrated Landau theory of phase transitions [1] in 1937, which was later successfully applied to superconductivity [15]. The latter became known as the Ginzburg-Landau theory of superconductivity after the duo that developed it.

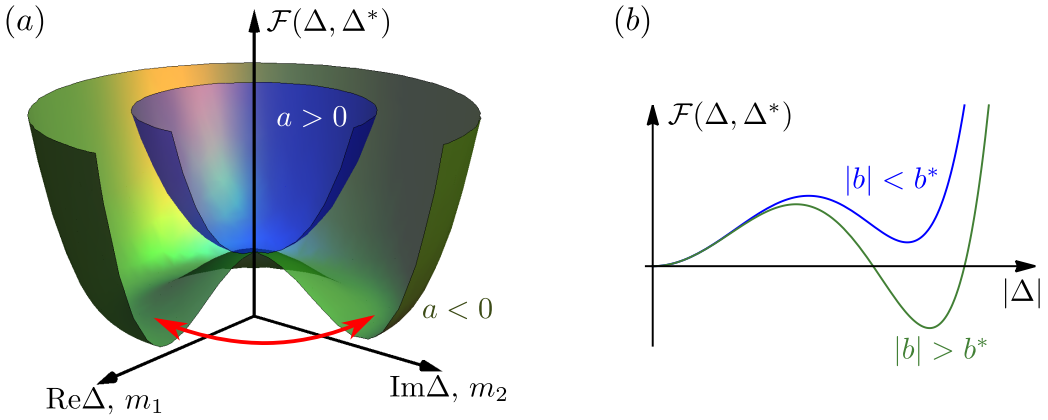

Figure 1.1: ***Free energy expansion.*** *In (a), the high-temperature (blue) and low-temperature (green) phase of the free energy (1.1) is shown. Goldstone modes, discussed in Sec. 1.2, are indicated in red. The behavior of the free energy in case of a first order phase transition is illustrated in (b).*

Landau's free energy expansion is based on two assumptions: (i) The phase transition is second order, i.e., the order parameter, which is, by design, finite in the "ordered" low-temperature and zero in the "disordered" high-temperature phase, varies continuously at the transition. (ii) The free energy $\mathcal{F}$ is an analytic function of the order parameter near the origin. This allows to expand $\mathcal{F}$ in order to describe the behavior of the system near the transition temperature T_c.

Ginzburg and Landau [15] postulated that the superconducting order parameter is a complex number which we will denote by $\Delta \in \mathbb{C}$. While its modulus squared measures the density of superconducting electrons, the time- and space-independent part of its phase is in case of an isolated superconductor of no physical significance. This means that the free energy should be invariant under the global U(1) phase rotation $\Delta \to \Delta e^{i\varphi}$, $\varphi \in \mathbb{R}$. First focusing on homogeneous superconductivity, this forces the expansion of $\mathcal{F}$ with respect to Δ and Δ^* to be of the form

$$\mathcal{F}(\Delta, \Delta^*) = \mathcal{F}(0) + a(T)|\Delta|^2 + \frac{b}{2}|\Delta|^4 + \mathcal{O}(|\Delta|^6). \tag{1.1}$$

Here a and b are expansion coefficients that are *a priori* unknown, which distinguishes the phenomenological Ginzburg-Landau approach from microscopic theories that can make predictions in terms of microscopic parameters (see Sec. 1.1.2). We will assume that $b > 0$ to ensure stability for $\Delta \to \infty$ and that b does not significantly vary with temperature. For $a(T) > 0$ the minimum of $\mathcal{F}$ occurs at $\Delta = 0$ which defines the normal phase. If $a(T) < 0$, the free energy will assume minimal values for any Δ with $|\Delta| = \sqrt{|a(T)|/b} \neq 0$ as can be seen in Fig. 1.1(a). In the ground state of the system, Δ will have some fixed phase which we can chose such that $\Delta \in \mathbb{R}$ without loss of generality. This means that the free energy $\mathcal{F}$ or, more fundamentally, the Hamiltonian of the system has some symmetry which is not shared by its ground state. This is known as *spontaneous symmetry breaking*. In the present case, the system spontaneously breaks global U(1) phase rotation symmetry at the transition. In Sec. 1.1.1, we will discuss more complicated symmetry groups. Before we do this, a few general remarks about free energy expansions are in order.

Firstly, as already mentioned in the historical introduction above, the same procedure can also be used to describe other types of phase transitions such as structural or magnetic phase transitions [1, 75].

E.g., in case of a ferromagnet, the order parameter would be the magnetization $\boldsymbol{m} = (m_1, \ldots, m_{d_m})$. In the isotropic case, $\mathcal{F}$ does not depend upon the direction of $\boldsymbol{m}$. This $\mathrm{SO}(d_m)$ rotation symmetry will be broken below the ordering temperature (down to a residual $\mathrm{SO}(d_m - 1)$ symmetry). The case $d_m = 2$, i.e., an XY-magnet, is special as SO(2) and U(1) are isomorphic (denoted by $\mathrm{SO}(2) \cong \mathrm{U}(1)$ in the following) which means that (in the absence of external fields) the mathematical description of symmetry breaking is identical in these two systems. The real and imaginary part of Δ can be associated with the two components m_1 and m_2 as indicated in Fig. 1.1(a).

Secondly, from the discussion above it is clear that $a(T)$ has to change sign at the transition temperature T_c. Assuming that $a(T)$ is also analytic around T_c, one can expand $a(T) \sim \alpha(T - T_c)$ in the vicinity of T_c which leads to the prediction that the order parameter behaves according to $\Delta \propto \sqrt{T_c - T}$ slightly below T_c. Inserting this back into the free energy expression (1.1) and differentiating twice with respect to T one finds that the heat capacity has a jump[1] at T_c which agrees with experiment [76].

In addition, free energy expansions also allow for studying inhomogeneous superconductors. In this case, the order parameter becomes spatially dependent $\Delta \to \Delta(\boldsymbol{x})$ and, focusing on leading order gradients of Δ, an additional term $\propto (\boldsymbol{\nabla}\Delta^*) \cdot \boldsymbol{\nabla}\Delta$ is added to the free energy (1.1) to penalize spatial variations of $\Delta(\boldsymbol{x})$. The coupling to magnetic fields is described by means of minimal substitution. As these aspects are not central to the thesis at hand, we refer to the literature (see, e.g., the textbook [77]) for a detailed discussion and just mention that these two modifications add two length scales to the free energy expansion (1.1): The superconducting coherence length ξ which is the length scale for the variation of Δ and the penetration depth λ determining how deep an external magnetic field can enter the superconductor.

Note that although free energy expansions are tailor-made to analyzing second order phase transitions they can be used to describe weak first order phase transitions as well: If $a > 0$, $b < 0$ and we have added a term $c|\Delta|^6$ in Eq. (1.1) with $c > 0$ to ensure stability, the position of the minimum of $\mathcal{F}$ jumps from $\Delta = 0$ to a finite $\Delta \neq 0$ upon increasing the magnitude of b through some critical value b^* as illustrated in Fig. 1.1(b). However, note that we cannot conclude that a first order phase transition takes place without knowing all coefficients of the expansion as higher order terms can always push minima at $\Delta \neq 0$ to positive values. Furthermore, in order to exclude a first order phase transition we even have to resum the power series to obtain a representation of $\mathcal{F}$ that is valid for arbitrary Δ as the order parameter could in principle jump to an arbitrarily large value beyond the radius of convergence of the free energy expansion. We will come back to this aspect in Sec. 4.3.1.

Notwithstanding these difficulties associated with first order phase transitions, the free energy expansion is very useful for analyzing the general symmetry breaking taking place at second order phase transitions and conveniently reveals its connection to group theory. This will be the focus of the next subsection.

1.1.1 Multicomponent order parameter

We now consider a system with a density matrix that is invariant under symmetries forming the group $\mathcal{G}$ for temperatures T slightly above the critical temperature T_c of the transition we are interested in. For concreteness we will entirely focus on superconducting transitions here. At T_c, some of these symmetries are spontaneously broken such that the density matrix is only invariant under the subgroup $\mathcal{H} < \mathcal{G}$. Since both the result itself as well as the required group theoretical methods and notation will be used

[1] Since this is a purely thermodynamic statement it holds irrespective of the order parameter chosen. This is why it was already predicted in Landau's original work [73] where the equilibrium current j was used as order parameter instead of Δ. Note that $j \propto \sqrt{T_c - T}$ disagrees with experiment.

repeatedly throughout the thesis, we will next discuss how the possible order parameters in case of the transition being continuous can be related to the symmetry group $\mathcal{G}$ of the high temperature phase. This relation which is originally due to Landau [1] has been extensively used to gain information about the superconducting phase transition in many different systems such as superfluid ^{3}He, heavy-fermion as well as cuprate superconductors and others [50, 78–84].

Order parameter. Following the current understanding of the microscopic theory of superconductivity (see Sec. 1.1.2), the superconducting order parameter is a (complex-valued) fermionic two-particle wavefunction $\Delta_{\alpha\beta}(\boldsymbol{k})$, which means that it transforms in the same way as the bilinear $\psi_{\boldsymbol{k}\alpha}\psi_{-\boldsymbol{k}\beta}$ of fermionic spinors $\psi_{\boldsymbol{k}\alpha}$. Here $\boldsymbol{k}$ denotes crystal momentum and α, β refer to all additional electronic degrees of freedom within the unit cell of the system which are relevant for describing superconductivity. This might include the spin[2] degree of freedom of the electrons, the relevant orbitals of the different atoms in the unit cell and, in case of systems with reduced dimension, additional subbands resulting from the confinement along one or two spatial directions.

Since $\Delta_{\alpha\beta}(\boldsymbol{k})$ is a fermionic two-particle wavefunction, it must be totally antisymmetric under exchange of the particles and, hence, satisfy the antisymmetry constraint

$$\Delta_{\alpha\beta}(\boldsymbol{k}) = -\Delta_{\beta\alpha}(-\boldsymbol{k}). \tag{1.2}$$

As anticipated by the notation used for the order parameter, we will assume that the total momentum of the two electrons vanishes which means in terms of symmetries that no translational symmetries are broken at the phase transition. This is a very natural assumption since superconducting transitions at which translation symmetry is spontaneously broken are quite rare as will become clear in Sec. 1.1.2. Furthermore, we will mainly focus on translation-symmetry-preserving superconducting states in the remainder of the thesis such that it is convenient to use the notation already in this section which will be best suited for describing this situation.[3]

Symmetry constraints. The symmetry group has the form $\mathcal{G} = \mathcal{G}_0 \otimes \mathrm{U}(1)$, where U(1) is the group of global phase rotations, $\Delta_{\alpha\beta}(\boldsymbol{k}) \to \Delta_{\alpha\beta}(\boldsymbol{k})e^{i\varphi}$, already encountered in context of Eq. (1.1) and $\mathcal{G}_0$ the group of symmetry operations in spin and real space. As we do not consider spontaneous translation symmetry breaking, it is sufficient to restrict ourselves to the symmetry operations that leave at least a single lattice point invariant. Note that the normal state of many superconducting systems also has TRS, i.e., is invariant under the inversion of the time-direction. The mathematics of this type of symmetry is quite different from the symmetries of $\mathcal{G}_0$ as it is described by an antiunitary operator[4]. For this reason, the discussion of the implications of TRS will be postponed to Sec. 4.1.

Denoting the spinor and coordinate representation[5] of $g \in \mathcal{G}_0$ by $\mathcal{R}_\Psi(g)$ and $\mathcal{R}_v(g)$, respectively, and recalling that $\Delta(\boldsymbol{k})$ transforms as $\psi_{\boldsymbol{k}}\,\psi^T_{-\boldsymbol{k}}$, the transformation behavior of the order parameter is given

[2] Note that, although the electrons in crystals are always spin-1/2 particles, the effective low-energy theory in the presence of strong Zeeman splittings might involve spinless fermions (see Sec. 4.7).

[3] We note that, for the current purpose, allowing for spontaneous breaking of translation symmetries is straightforward: The analysis of general space group symmetry breaking would most closely parallel the present discussion when using $\Delta_{xx'}$ as order parameter where x and x' are multi-indices combining both the Bravais lattice index as well as all relevant electronic degrees of freedom within the unit cell.

[4] An operator O is said to be antiunitary if and only if it is antilinear, i.e., $cO = Oc^*$ for any $c \in \mathbb{C}$, and satisfies $OO^\dagger = O^\dagger O = \mathbb{1}$.

[5] A representation of a group $\mathcal{G}$ is a group homomorphism from $\mathcal{G}$ to the general linear group, i.e., a map ρ assigning every $g \in \mathcal{G}$ a nonsingular square matrix $\rho(g)$ such that $\rho(g_1)\rho(g_2) = \rho(g_1 g_2)\ \forall g_1, g_2 \in \mathcal{G}$.

by

$$\Delta(\boldsymbol{k}) \xrightarrow{g} \mathcal{R}_\Psi(g)\Delta(\mathcal{R}_v^{-1}(g)\boldsymbol{k})\mathcal{R}_\Psi^T(g). \tag{1.3}$$

To analyze the consequences of the invariance of the free energy $\mathcal{F}$ under Eq. (1.3), it is very convenient [1] to expand the order parameter in terms of (matrix-valued) basis functions χ_μ^n transforming under the irreducible representations (IRs) of $\mathcal{G}_0$,

$$\Delta(\boldsymbol{k}) = \sum_n \sum_{\mu=1}^{d_n} \eta_\mu^n \chi_\mu^n(\boldsymbol{k}), \qquad \eta_\mu^n \in \mathbb{C}. \tag{1.4}$$

Here n labels the different IRs with dimension d_n and $\{\chi_\mu^n(\boldsymbol{k}), \mu = 1, \dots d_n\}$ are the associated partner functions, i.e.

$$\mathcal{R}_\Psi(g)\chi_\mu^n(\mathcal{R}_v^{-1}(g)\boldsymbol{k})\mathcal{R}_\Psi^T(g) = \left(\mathcal{R}_\chi^n(g)\right)_{\mu\nu} \chi_\nu^n(\boldsymbol{k}), \tag{1.5}$$

where $\mathcal{R}_\chi^n(g)$ cannot be brought into the same block-diagonal form for all $g \in \mathcal{G}_0$, which is the defining property for the representation $\mathcal{R}_\chi^n(g)$ to be irreducible. In Eq. (1.5) and in the remainder of the thesis, we use the convention that, unless stated otherwise, indices appearing twice are assumed to be summed over. It is well-known from group theory that $\mathcal{R}_\chi^n(g)$ can be taken to be unitary without loss of generality and that the expansion in Eq. (1.4) is always possible [85].

Most importantly, Eq. (1.4) allows us to represent the transformation of $\Delta(\boldsymbol{k})$ in terms of the expansion coefficients $\{\eta_\mu^n\}$,

$$\eta_\mu^n \xrightarrow{g} \eta_\nu^n \left(\mathcal{R}_\chi^n(g)\right)_{\nu\mu}. \tag{1.6}$$

Similarly, we can regard the free energy as a function $\mathcal{F}(\eta_\mu^n, (\eta_\mu^n)^*)$ of the complex variables $\{\eta_\mu^n\}$ (and their complex conjugates) instead of being a function*al* in $\Delta_{\alpha\beta}(\boldsymbol{k})$. Invariance under $\mathcal{G}$ then forces

$$\mathcal{F}\left(\eta_\mu^n, (\eta_\mu^n)^*\right) = \mathcal{F}\left(\eta_\mu^n e^{i\varphi}, (\eta_\mu^n)^* e^{-i\varphi}\right), \qquad \forall \varphi \in \mathbb{R}. \tag{1.7a}$$

$$\mathcal{F}\left(\eta_\mu^n, (\eta_\mu^n)^*\right) = \mathcal{F}\left(\eta_\nu^n \left(\mathcal{R}_\chi^n(g)\right)_{\nu\mu}, (\eta_\nu^n)^* \left(\mathcal{R}_\chi^n(g)\right)_{\nu\mu}^*\right), \qquad \forall g \in \mathcal{G}_0, \tag{1.7b}$$

Assuming again that (i) the transition is of second order and that (ii) the free energy is an analytic function in $\{\eta_\mu^n\}$ (and their complex conjugate), we can expand the free energy to describe the phase transition in the vicinity of T_c. Due to Eq. (1.7a), the leading contribution reads

$$\mathcal{F}\left(\eta_\mu^n, (\eta_\mu^n)^*\right) = \mathcal{F}(0,0) + \sum_{n,n'} \sum_{\mu=1}^{d_n} \sum_{\mu'=1}^{d_{n'}} \left(\eta_\mu^n\right)^* \mathcal{M}_{\mu\mu'}^{nn'}(T)\, \eta_{\mu'}^{n'} + \mathcal{O}\left(|\eta|^4\right). \tag{1.8}$$

To satisfy Eq. (1.7b), it must hold

$$\mathcal{M}^{nn'} = \left(\mathcal{R}_\chi^n(g)\right)^* \mathcal{M}^{nn'} \left(\mathcal{R}_\chi^{n'}(g)\right)^T \tag{1.9}$$

for all IRs n, n' and all group elements g. Summing this equation over all $g \in \mathcal{G}_0$ and applying the "grand orthogonalilty theorem" of group theory, [85]

$$\sum_{g\in\mathcal{G}_0} \left(\mathcal{R}_\chi^n(g)\right)_{\mu\nu}^* \left(\mathcal{R}_\chi^{n'}(g)\right)_{\mu'\nu'} = \frac{|\mathcal{G}_0|}{d_n} \delta_{n,n'}\delta_{\mu,\mu'}\delta_{\nu,\nu'}, \tag{1.10}$$

where $|\mathcal{G}_0|$ is the order of $\mathcal{G}_0$, one finds that $\mathcal{M}$ must have the form $\mathcal{M}^{nn'}_{\mu\mu'}(T) = \delta_{\mu\mu'}\delta_{nn'}a_n(T)$. Consequently, the expansion (1.8) simply becomes

$$\mathcal{F}\left(\eta^n_\mu, (\eta^n_\mu)^*\right) = \mathcal{F}(0,0) + \sum_n \sum_{\mu=1}^{d_n} a_n(T) \left|\eta^n_\mu\right|^2 + \mathcal{O}\left(|\eta|^4\right), \tag{1.11}$$

which constitutes the generalization of Eq. (1.1) to multiple components ($\Delta \to \{\eta^n_\mu\}$). For $T > T_c$, in the normal phase, all a_n must be positive for the free energy being minimal at $\eta^n_\mu = 0$. At T_c, one of the prefactors, say $a_{n_0}(T)$, changes sign such that the minimum occurs at $\eta^n_\mu = 0$ for all $n \neq n_0$ and $\eta^{n_0}_\mu \neq 0$. This leads to the well-known [1] result that, *for a second order phase transition, the order parameter must transform according to one of the IRs of the symmetry group $\mathcal{G}_0$ of the high-temperature phase.*

Note that it could in principle happen that two (or more) of the coefficients $a_n(T)$ change sign at the same temperature. This, however, would constitute an "accidental degeneracy" in the sense that the simultaneous change of sign is not imposed by any symmetry and, hence, can be removed by small changes in the system that do not affect its symmetry. In other words, it requires fine-tuning of parameters, e.g., pressure or doping etc., to make the transition temperatures of the competing phases degenerate. Unless stated otherwise, we will therefore neglect accidental degeneracies in the following.

If the IR with the highest T_c, again denoted by n_0, is one-dimensional, $d_{n_0} = 1$, the transformation behavior of the order parameter under $\mathcal{G}_0$ is completely determined. Of course, the detailed form of the associated basis function $\chi^{n_0}_1(\boldsymbol{k})$ depends on microscopic details of the system and, thus, cannot be inferred from pure symmetry arguments. However, if $d_{n_0} > 1$, we have to determine the orientation of the vector $(\eta^{n_0}_1, \ldots, \eta^{n_0}_{d_{n_0}})$. It follows from higher order terms in the expansion of the free energy which are again constructed by taking into account the symmetry constraints (1.7): To begin with the quartic term, its general form as allowed by the U(1)-symmetry (1.7a) reads

$$\mathcal{F}\left(\eta^n_\mu, (\eta^n_\mu)^*\right) = \mathcal{F}(0,0) + \sum_{\mu=1}^{d_{n_0}} a_{n_0}(T) \left|\eta^{n_0}_\mu\right|^2 + \sum_{\mu_1,\mu_2,\mu_3,\mu_4=1}^{d_{n_0}} b_{\mu_1\mu_2\mu_3\mu_4} \left(\eta^{n_0}_{\mu_1}\right)^* \left(\eta^{n_0}_{\mu_2}\right)^* \eta^{n_0}_{\mu_3}\eta^{n_0}_{\mu_4} + \mathcal{O}\left(|\eta|^6\right) \tag{1.12}$$

upon setting $\eta^n_\mu = 0$ for $n \neq n_0$. In order to find the most general form of the tensor b from a group theoretical point of view, we just have to search for all trivial representations contained in

$$(n_0)^* \otimes (n_0)^* \otimes n_0 \otimes n_0, \tag{1.13}$$

where $(n_0)^*$ denotes the complex conjugate representation of n_0. Minimizing the free energy then yields the allowed vectors $(\eta^{n_0}_1, \ldots, \eta^{n_0}_{d_{n_0}})$. If physically distinct states are still degenerate, one has to proceed by analyzing higher orders in the expansion. In Chap. 4.3.2, this method of determining the possible order parameter vectors is illustrated for the case of the two-dimensional IR E of the group C_{4v}. We finally mention that it is also possible to construct the order parameter vectors from purely group-theoretical considerations (see [83] and references therein): For many symmetry groups, the possible residual groups $\mathcal{H}$ must be maximal subgroups of $\mathcal{G}$, i.e., there is no phase with more symmetries than $\mathcal{H}$ apart from the normal state.

Symmetry group. We will next discuss basic aspects concerning the symmetry group $\mathcal{G}_0$. One central question to be asked when analyzing the possible superconducting instabilities in a system is whether SOC is relevant for describing the transition or not [50, 78, 83, 84]. SOC describes the coupling of the

motion of the electron to its spin degree of freedom. Intuitively, this can be understood by recalling from classical electrodynamics [86] that an electric field $\boldsymbol{E} = -\boldsymbol{\nabla} V$ (V is the electric potential) becomes a magnetic field in the rest frame of a moving electron which, in turn, couples to the magnetic moment associated with the electron's spin. It is a relativistic effect which is described by the Dirac equation. Expanding the latter up to order $(v/c)^2$, where c is the speed of light and v the velocity scale of electronic motion, one finds (among other terms) the microscopic SOC Hamiltonian [87]

$$h_{\mathrm{SO}} = \frac{e}{4m_e^2c^2}\boldsymbol{p}(\boldsymbol{\sigma} \times \boldsymbol{\nabla} V). \tag{1.14}$$

Here m_e, e and $\boldsymbol{p}$ denote the electron mass, charge and momentum, respectively. Furthermore, $\boldsymbol{\sigma} = (\sigma_1, \sigma_2, \sigma_3)$ are Pauli matrices describing the spin of the electron. We refer to the literature (see, e.g., the textbook [87]) for an introduction to the plethora of effects of SOC in solid state systems. For the general purpose of the present discussion, we are only interested the impact of SOC on the symmetry group $\mathcal{G}_0$.

If SOC can be neglecting for describing the superconducting transition, there are no terms in the Hamiltonian that couple the spin and real-space degrees of freedom of the electrons. This means that spin and real space coordinates can be transformed independently and the group $\mathcal{G}_0$ assumes the form[6]

$$\mathcal{G}_0 = \mathrm{SO}(3) \times \mathcal{G}_c, \tag{1.15}$$

where SO(3) represents spin rotations and $\mathcal{G}_c$ is the group of crystal symmetries. As already mentioned above, although $\mathcal{G}_c$ should in general be taken to be the full space group, we will neglect translation symmetry breaking such that we can focus on the point group[7] $\mathcal{G}_p$ of the system and set $\mathcal{G}_c = \mathcal{G}_p$. It is clear that this crucially reduces the complexity as the 230 possible space groups of 3D systems decay into only 32 different point groups [85]. In case of $\mathcal{G}_0$ given by Eq. (1.15), its IRs can be labeled by the composite index $n = (n_c, n_s)$ where n_c and n_s denote all IRs of $\mathcal{G}_c$ and SO(3), respectively. As the superconducting order parameter $\Delta_{\alpha\beta}(\boldsymbol{k})$ is a wavefunction of two electrons (see Sec. 1.1.2) which are spin-1/2 particles, only the one-dimensional *singlet*, $n_s = s$, and the three-dimensional *triplet*, $n_t = t$, representations of SO(3) have to be considered. The order parameter must transform according to one of the IRs of $\mathcal{G}_0$ and we can thus conclude that, in the absence of SOC, only either singlet,

$$\Delta(\boldsymbol{k}) = \sum_{\mu_c=1}^{d_{n_c}} \eta_{\mu_c}^{(n_c,s)} \chi_{\mu_c}^{(n_c)}(\boldsymbol{k}) i\sigma_2, \tag{1.16a}$$

or triplet,

$$\Delta(\boldsymbol{k}) = \sum_{\mu_c=1}^{d_{n_c}} \sum_{\mu_s=1,2,3} \eta_{(\mu_c,\mu_s)}^{(n_c,t)} \chi_{\mu_c}^{(n_c)}(\boldsymbol{k}) \sigma_{\mu_s} i\sigma_2, \tag{1.16b}$$

superconductivity is possible at a single superconducting phase transition. In Eq. (1.16), $\chi_{\mu_c}^{(n_c)}$ denote basis functions with respect to all degrees of freedom other than spin transforming under the IR n_c of $\mathcal{G}_c$ (in the sense of Eq. (1.5)). Furthermore, we have already used that $i\sigma_2$ and $\boldsymbol{\sigma} i\sigma_2$ represent possible choices for the partner functions of the singlet and triplet representation of SO(3), respectively.

[6] Spin rotation symmetry can also be broken by magnetic fields. We will come back to this in Sec. 4.7 but not consider it here.

[7] Any space group operation g can be decomposed in an operation r that leaves at least one point invariant and a translation $\boldsymbol{t}$ which we write as $g = [r|\boldsymbol{t}]$. The set of all $[r|0]$ with $[r|\boldsymbol{t}]$ belonging to the space group is called the point group $\mathcal{G}_p$ of the system. Note that, in general, $\mathcal{G}_p$ does not have to be a subgroup of the space group.

The situation changes completely when SOC is relevant for the phase transition: As can be seen in Eq. (1.14), the spin and spatial degrees of freedom cannot be transformed independently anymore such that the symmetry group is reduced from Eq. (1.15) to $\mathcal{G}_0 = \mathcal{G}_c$. Now the representation $\mathcal{R}_\Psi(g)$ of $g \in \mathcal{G}_0$ has to be understood as a simultaneous operation both on the spatial degrees of freedom (crystal momentum, orbitals, ...) and on the spin of the electrons. In other words, the generator of rotation is given by the sum of orbital angular momentum and spin. As spin and spatial coordinates are entangled in the presence of SOC, the distinction between pure singlet and triplet order parameters as in Eq. (1.16) is in general not possible any more.

To proceed further with the discussion of spin-orbit-coupled systems, let us next assume that, for the purpose of describing superconductivity, it is sufficient to regard the order parameter $\Delta(\boldsymbol{k})$ as a matrix in spin-space only. This is less restrictive than it might seem, since it does not necessarily imply that there is, e.g., only one relevant orbital in the system. The reason is that one can introduce a pseudospin basis, represented by the Pauli matrices s_j, $j = 0, 1, 2, 3$, that behaves effectively like a the microscopic spin. The details of this pseudospin approach, which is frequently used in the literature (see, e.g., Refs. [88, 89]), is described in Appendix A.1. To connect to the discussion presented above, it is very convenient to expand the 2×2 matrix Δ in terms of Pauli matrices according to

$$\Delta(\boldsymbol{k}) = \left(\Delta^S_{\boldsymbol{k}} + \boldsymbol{d}_{\boldsymbol{k}} \cdot \boldsymbol{s}\right) i s_2. \tag{1.17}$$

Here $\Delta^S_{\boldsymbol{k}} \in \mathbb{C}$ and $\boldsymbol{d}_{\boldsymbol{k}} \in \mathbb{C}^3$ are the *singlet component* and *triplet vector* of the order parameter corresponding to Eqs. (1.16a) and (1.16b), respectively. Due to the fermionic antisymmetry constraint (1.2), $\Delta^S_{\boldsymbol{k}}$ and $\boldsymbol{d}_{\boldsymbol{k}}$ have to be symmetric and antisymmetric functions of $\boldsymbol{k}$,

$$\Delta^S_{\boldsymbol{k}} = \Delta^S_{-\boldsymbol{k}} \qquad \boldsymbol{d}_{\boldsymbol{k}} = -\boldsymbol{d}_{-\boldsymbol{k}}. \tag{1.18}$$

This has important consequences for systems where the high-temperature phase is invariant under spatial inversion I. In these so-called *centrosymmetric* systems, it holds $I \in \mathcal{G}_0$ which commutes with all operations of the symmetry group $\mathcal{G}_0$ such that all IRs can be classified into "gerade" (even parity), $\mathcal{R}_\chi(I) = 1$, and "ungerade" (odd parity), $\mathcal{R}_\chi(I) = -1$ (see Appendix A.2). Recalling that the spin is invariant under I (it is a pseudovector), Eq. (1.18) forces the pairing state to be a pure singlet ($\boldsymbol{d}_{\boldsymbol{k}} = 0$) or a pure triplet ($\Delta^S_{\boldsymbol{k}} = 0$) in case of a gerade or ungerade IR, respectively. Taken together, we have seen that both significant SOC as well as the absence of inversion symmetry in the normal state ($I \notin \mathcal{G}_0$) are required to allow for the mixing of singlet and triplet pairing at a single superconducting phase transition [84, 90]. In Chap. 6.2.4, we will show that, under certain circumstances, one can still group all possible superconducting states into two basic classes in direct analogy to the singlet and triplet states of centrosymmetric systems. Systems with $I \notin \mathcal{G}_0$, which are called *noncentrosymmetric*, are in particular focus of the thesis at hand and will therefore be discussed in more detail in Sec. 1.3.

Finally, we mention that, if we take $\mathcal{G}_0 = \mathcal{G}_c$ in a spin-orbit-coupled system with $\mathcal{G}_c$ being the group of symmetry operations in real space, the matrices $\mathcal{R}_\Psi(g)$ transforming the wavefunctions will not form a representation. The reason is that, e.g., $\mathcal{R}_\Psi(C_2C_2) = -\mathbb{1}$ for half-integer spin particles, where C_2 denotes a rotation by π around some given axis, although $C_2C_2 = E$ (E is the identity element of the group). This subtlety can be circumvented by replacing $\mathcal{G}_c$ by its double group[8] $\mathcal{G}'_c$. However, as

[8] The basic construction of a double group consists of first introducing an additional element $\overline{E}$ which will have the same representation on spatial coordinates as E but changes the sign of spinors. The set of all $g \in \mathcal{G}$ and associated elements $\overline{g} := \overline{E}g$ forms the double group $\mathcal{G}'$. The name comes from the fact that $|\mathcal{G}'| = 2|\mathcal{G}|$. Upon choosing proper multiplication laws, $\mathcal{R}_\Psi(g)$, $g \in \mathcal{G}'$, will then indeed form a representation. For an introduction to double groups and their IRs we refer to Ref. [91].

we will be mainly interested in the transformation properties of the superconducting order parameter, this difference is of no relevance: As can be seen in Eq. (1.3), the representation of g on the order parameter involves the product of two $\mathcal{R}_\Psi(g)$ such that Δ will always transform under the single-group representations. Physically, this is due to the fact that Δ is a two-particle wavefunction with integer spin. Therefore, we will in the remainder of the thesis not distinguish between $\mathcal{G}_c$ and $\mathcal{G}_c'$ always keeping in mind that spin-wavefunctions transform under the double group $\mathcal{G}_c'$. For the same reason, we have used SO(3) in Eq. (1.15) instead of SU(2), which covers SO(3) twice ($\mathrm{SO}(3) = \mathrm{SU}(2)/\mathbb{Z}_2$).

1.1.2 Microscopic mechanism of superconductivity

Although the Ginzburg-Landau approach [15] and the earlier phenomenological theory of Heinz and Fritz London [14] yield the correct physical behavior, no understanding about the microscopic origin of superconductivity is provided. Despite being of considerable interest for many theorists [74] ever since the discovery of superconductivity in 1911 [16], it took until 1957 that a consistent microscopic theory of superconductivity was eventually formulated [17, 18] which became known as the BCS theory after its three developers – Bardeen, Cooper and Schrieffer.

One of the central theoretical groundworks for the BCS theory was provided by Cooper who showed [92] that a Fermi surface is unstable towards the formation of bound states consisting of two electrons with opposite spin, $\uparrow$ and $\downarrow$, and crystal momentum, $\boldsymbol{k}$ and $-\boldsymbol{k}$, now known as *Cooper pairs*, in the presence of an attractive interaction in the vicinity of the Fermi energy. It is a weak-coupling instability in the sense that it already occurs at an infinitesimal strength of the attraction. Physically, this is due to the fact that if a state $(\boldsymbol{k}, \uparrow)$ is on the Fermi surface the same will hold for $(-\boldsymbol{k}, \downarrow)$ as long as the normal state is time-reversal symmetric [93], i.e., in the absence of (external or internal) magnetic fields.

The many-body formulation of the *Cooper instability* is provided by the BCS theory [17, 18]. A pedagogical introduction to this subject can be found in any textbook on theoretical condensed matter physics, e.g., in Refs. [77, 94]. We just mention that it is a mean-field theory where the attractive interaction is decoupled in the particle-particle channel leading to the celebrated BCS Hamiltonian

$$\hat{H}_{\mathrm{BCS}} = \sum_{\boldsymbol{k},\,\sigma} \epsilon_{\boldsymbol{k}} \hat{c}^\dagger_{\boldsymbol{k}\sigma} \hat{c}_{\boldsymbol{k}\sigma} + \sum_{\boldsymbol{k}} \left(\Delta\, \hat{c}^\dagger_{\boldsymbol{k}\uparrow} \hat{c}^\dagger_{-\boldsymbol{k}\downarrow} + \mathrm{H.c.} \right). \tag{1.19}$$

Here $\epsilon_{\boldsymbol{k}}$ denotes the normal state dispersion and $\hat{c}^\dagger_{\boldsymbol{k}\sigma}$ ($\hat{c}_{\boldsymbol{k}\sigma}$) is the creation (annihilation) operator of electrons with momentum $\boldsymbol{k}$ and spin σ. From Eq. (1.19), the Ginzburg-Landau expansion (1.1) with explicit expressions for the coefficients can be regained as has first been shown by L. P. Gorkov [95]. In Appendix C.2 we will perform such a calculation explicitly. This establishes that the order parameter in the Ginzburg-Landau expansion should be seen as a two-electron wavefunction. In the BCS Hamiltonian (1.19) the order parameter is just a single complex number Δ as it is restricted to singlet pairing. In the general case (see also Sec. 4.1.1) with singlet, triplet, several orbitals etc. the order parameter $\Delta_{\alpha\beta}(\boldsymbol{k})$ introduced in Sec. 1.1.1 is to be identified with $\langle \hat{c}_{-\boldsymbol{k}\beta} \hat{c}_{\boldsymbol{k}\alpha} \rangle$ immediately leading to the antisymmetry constraint (1.2) and transformation behavior (1.3).

The possibility of attractive interactions between electrons with energies close to the Fermi surface as a consequence of the electron-phonon coupling goes back to Fröhlich [96]. Intuitively, the electronic attraction results from the much larger time scales of ionic motion ($\propto \omega_D^{-1}$) as compared to those of electrons ($\propto E_F^{-1}$) with ω_D and E_F denoting the Debye and Fermi energy, respectively. When an electron polarizes the lattice locally, this polarization can still attract other electrons after the first electron has left which leads to an attractive effective force between the electrons. It has later been

shown [97] that this effect is in the vicinity of the Fermi surface not generically overcompensated by the Coulomb repulsion as one might naively expect. This is most easily understood in an RG calculation [98, 99] yielding that repulsive interactions with bare dimensionless coupling constant μ_0^* are at energies of the order of ω_D reduced to

$$\mu^* = \frac{\mu_0^*}{1 + \mu_0^* \ln(E_F/\omega_D)}. \tag{1.20}$$

As E_F/ω_D is typically large and not strongly material dependent, it holds $\mu^* \simeq 0.1$ for many materials [98, 100]. This is the reason why the Coulomb interaction can in many cases be neglected for understanding the superconducting properties. A direct experimental demonstration of the importance of the electron-phonon coupling for the emergence of superconductivity is provided by the *isotope effect* on T_c, i.e., its change upon substituting atoms of the superconductor by different isotopes [19, 20].

Unconventional mechanism. The discovery of superconductivity in heavy-fermion systems, first in $CeCu_2Si_2$ [21] and soon in others such as UBe_{13} [22] and UPt_3 [23], indicated that the electron-phonon/BCS mechanism outlined above does not always apply: Firstly, the tendency of these materials towards magnetism contradicted the fact that BCS superconductors are suppressed by magnetic scattering [101]. Furthermore, the observed scaling $\propto T^3$ of the specific heat in UBe_{13} [102] disagreed with the exponential behavior $\propto \exp(-\Delta/T)$ predicted from BCS theory which was the first indication of nodes on the Fermi surface and the nontrivial transformation behavior of the order parameter [50]. Other material classes showing "unconventional" superconductivity with strong deviations from BCS behavior [25, 26], the organic [103], the cuprate [24] and, most recently, the iron-based [104] superconductors, have been discovered.

There is no generally accepted definition of unconventional. Some authors [50] just refer to unconventional pairing if and only if the order parameter breaks point symmetries which, however, leads to the conclusion that orthorhombic cuprates [29] or iron-based superconductors [26] are conventional. In this thesis we will use the term *conventional* in the context of a superconducting mechanism to refer to systems where the same pairing state arises when hypothetically switching off the Coulomb interaction. Otherwise the superconductor will be referred to as *unconventional*.

Due to the plethora of different physical systems showing unconventional superconducting behavior, which are typically also strongly correlated, there is not *the* single theory of unconventional superconductivity. One broadly applicable effective low-energy approach is provided by the spin-fermion model [30–32] which will be discussed in Chap. 6.2.1.

Translation symmetry breaking. As already mentioned in Sec. 1.1.1, we have so far been making the assumption in this section that the translational symmetries are the same above and below the superconducting transition as we have been focusing on Cooper pairs with zero total momentum or, equivalently, a spatially homogeneous order parameter. It has first been pointed out independently by P. Fulde and R. A. Ferrell [105] and A. Larkin and Y. Ovchinnikov [106] that spatially inhomogeneous superconducting states are excepted at low temperatures for sufficiently large magnetic fields $H > H_c$. The occurrence of these so-called Fulde-Ferrell-Larkin-Ovchinnikov (FFLO) states is most easily understood by focusing on spin-singlet pairing in systems with spin-rotation symmetry (at $H = 0$) and neglecting orbital-pair breaking[9] (imagine, e.g, a 2D system with an in-plane magnetic field): The Zeeman splitting associated with H breaks the degeneracy of the states $(\boldsymbol{k}, \uparrow)$ and $(-\boldsymbol{k}, \downarrow)$ which is important for the Cooper instability as discussed above. For $H > H_c$, it becomes energetically

[9] The orbital effect leads in type-II superconductors to the emergence of the Abrikosov vortex phase and is thus detrimental to FFLO states [107].

favorable to form Cooper pairs out of states on different Fermi surfaces and, hence, with non-vanishing center-of-mass momentum.

This discussion shows that translation-symmetry-breaking superconducting states are expected to occur only in the presence of magnetic fields or, more generally, if TRS is broken in the normal state. This expectation is confirmed by various calculations that also take into account the possibility of SOC [108–112]. Candidate materials for the realization of this exotic state of matter are heavy-fermion superconductors, in particular, $CeCoIn_5$, and layered organic superconductors [107, 113].

As this thesis will be mainly concerned with systems with TRS in the normal state, we will, for most of the time, neglect the possibility of FFLO states in the following.

1.2 Impact of fluctuations

The existence of a nontrivial minimum ($\Delta_0 \neq 0$) of the free energy functional or, equivalently of the mean-field equations is a necessary condition for a phase transition to occur, however, it is in general not sufficient. The reason is that thermal or quantum fluctuations, if sufficiently strong, can destabilize the phase which can be analyzed formally by expanding the action[10] $S[\Delta]$ in small deviations $\delta\Delta$ from its stationary point Δ_0. Furthermore, fluctuations can also change the properties of the phase transition such as its order and critical exponents. Fortunately, there exist general criteria formulated in terms of the symmetry breaking at the phase transition and the dimensionality of the system to estimate the importance of fluctuations which will be discussed in this section.

The key players in fluctuations physics are the massless modes associated with the breaking of a continuous symmetry which are known as *Nambu-Goldstone modes* in honor of the authors of the two seminal papers [116, 117]. The existence of these modes is readily understood by considering $\delta\Delta = \sum_a \phi_a T_a \Delta_0$, where T_a, $a = 1, ..., \dim_c(\mathcal{G})$, are the generators of the continuous subgroup (Lie group) of the symmetry group $\mathcal{G}$ of the high-temperature phase. By design, the $\dim_c(\mathcal{H})$ generators of $\mathcal{H}$ satisfy $T_a\Delta_0 = 0$, whereas all remaining $N_{\mathrm{NG}} = \dim_c(\mathcal{G}) - \dim_c(\mathcal{H})$ generators necessarily define massless Nambu-Goldstone modes [116–118]. The low-energy action of the system is thus of the form

$$S_{\mathrm{NG}} = \sum_{a=1}^{N_{\mathrm{NG}}} \int \mathrm{d}^d x \, c_a^i \, (\partial_i \phi_a)^2 \tag{1.21}$$

with c_a^i being unknown real constants. Here the d-dimensional vector x and similarly the associated derivatives ∂_i refer to spatial coordinates in case of thermal fluctuations while comprising both space and time for describing quantum fluctuations.

In case, e.g., of a superconductor where the global $U(1)$ symmetry is fully broken in the sense that there is no residual continuous symmetry, one Nambu-Goldstone mode is expected which corresponds to long-wavelength phase rotations as indicated by the red arrow in Fig. 1.1(a). For the isotropic d_m-dimensional ferromagnet, $O(d_m)$ is broken down to $O(d_m - 1)$ leading to $d_m - 1$ Nambu-Goldstone modes (magnons).

From this perspective one might wonder how spontaneous symmetry breaking can occur at all given that all configurations of the Goldstone manifold should enter the partition function with equal weight. To see this consider, e.g., a ferromagnet. Physically, there might be some small imperfection in the

[10] For an introduction to field-integrals we refer the reader to the literature. E.g., a discussion of field-integral methods with strong focus on application to modern condensed matter theory can be found in the textbook of Altland and Simons [114], whereas technical aspects are covered in Ref. [115].

system or in its environment that leads to a preferred direction for the magnetization. Since a macroscopic number of degrees of freedom order at the phase transition, the probability of tunneling to one of the degenerate states is vanishingly small. Theoretically, this is implemented by adding a symmetry-breaking term $\propto \eta$ (e.g. a magnetic field in case of the ferromagnet) to the Hamiltonian. The phase transition can then be described by first taking the thermodynamic limit *before* setting $\eta \to 0$ [114, 115].

Whether the fluctuations associated with the Goldstone modes in Eq. (1.21) allow for long-range order crucially depends on d. The Mermin-Wagner-Hohenberg theorem [119–121] states that compact continuous symmetries cannot be broken for $d \leq 2$. A simple and insightful, albeit by far not rigorous, derivation proceeds [114] by first assuming long range order and then calculating fluctuation corrections to the expectation value of the order parameter governed by the low-energy action (1.21). These corrections are proportional to the integral $\int_q \mathrm{d}^d q/q^2$ of the Goldstone propagator $1/q^2$ which is divergent in the infra-red for $d \leq 2$ illustrating the dominant role played by fluctuations in low-dimensions. A more careful treatment shows that the expectation value of the order parameter vanishes for $d \leq 2$ [119–121].

From this follows that no proper long-range superconducting order can occur at finite temperatures in a 2D system. However, one can still have a superconducting phase transition between a disordered high-temperature phase with exponential superconducting correlations and a low-temperature state with *quasi-long-range* order defined by algebraically decaying ($\sim 1/|\boldsymbol{x}|^\alpha$, $\alpha > 0$) correlations. As every Gaussian theory, i.e., of the form of Eq. (1.21), will yield algebraic decay [114] the question arises about the mechanism driving the phase transition.

The answer was provided by Berezinskii, Kosterlitz and Thouless [122, 123]. The key aspect is that the symmetry group $U(1)$ of phase rotations allows for *topological excitations* in 2D that are proliferated at high-temperatures and lead to the transition to a phase with exponential correlations. This effect cannot be captured in the Gaussian approximation (as in Eq. (1.21)) where the nontrivial geometry of the symmetry group is neglected. In other words, we have to restore the periodicity of the action under a shift of the superconducting phases by 2π. The simplest model satisfying these requirements is given by the XY-model,

$$S_{XY} = -J \sum_{\langle ij \rangle} \cos(\varphi_i - \varphi_j), \tag{1.22}$$

where $\sum_{\langle ij \rangle}$ denotes the sum over nearest neighbors and φ_i are the local phase degrees of freedom. This model has, in addition to spin-wave excitations around the ordered state already captured on the Gaussian level, also vortex excitations where the phase winds around $n \in \mathbb{N}$ times upon traversing a closed path around the vortex core. Vortices are topological in the sense that they cannot be continuously "unwinded" on the enclosing path which is also directly related to the discrete nature of the topological charge n. In the next chapter we will discuss the importance of topology for condensed matter physics from a different physical point of view.

The existence of a phase transition can be easily understood thermodynamically [123]: The energy of an isolated vortex in a system of linear size L is given by[11] $\pi J n^2 \ln(L/a)$. It scales logarithmically exactly as the associated change of entropy $\sim 2T \ln(L/a)$. Consequently, for $T > T_{\mathrm{BKT}} \simeq \pi J/2$ the free energy is reduced by producing isolated vortices. This indicates the existence of a finite transition temperature T_{BKT} separating a low-temperature "gas" of tightly-bound vortex-antivortex pairs from a high-temperature "plasma" of unbound vortices. A convenient more rigorous formulation of this so-called Berezinskii-Kosterlitz-Thouless (BKT) transition, that also takes into account the logarithmic vortex-vortex interaction, is provided by the RG approach of Ref. [124].

[11] We ignore the non-universal contribution from the vortex core here as it does not grow with L.

In a superconductor the situation is more complicated since it is, as opposed to, e.g., superfluid Helium [78], charged and, hence, couples to the electromagnetic field. By virtue of the Higgs mechanism, the electromagnetic gauge field becomes a massive vector field in the superconductor leading to the peculiar electromagnetic response of a superconductor including the Meissner effect [125]. The coupling to the electromagnetic field also directly affects the vortex-vortex interaction in a 2D superconducting film: Due to stray fields, the interaction is only logarithmic for separations $r \ll \Lambda_P$ with $\Lambda_P = 2\lambda_L^2/D$ denoting the Pearl length [126] where λ_L is the London penetration depth and D the film thickness. At large distances, $r \gg \Lambda_P$, the vortex-interaction decays algebraically $\propto 1/r$ such that a BKT transition is expected to be observable only for samples of linear size $L < \Lambda_P$. However, more recently, it has been shown that the interaction is also not logarithmic in small samples on an insulating substrate but rather exponential due to boundary effects at the sample edges [127].

Finally, we note that, also in 3D, the coupling to the fluctuating electromagnetic field affects the phase transition. As has been shown in Ref. [128], integrating out the electromagnetic field produces a non-analytic term $\propto |\Delta|^3$ in the Ginzburg-Landau expansion that will render the transition first order for a type-I superconductor[12]. This effect is, however, numerically very small and, hence, extremely difficult to resolve experimentally in a superconductor [128].

1.3 Noncentrosymmetric superconductors

In Sec. 1.1.1, we have seen from pure symmetry considerations that, in the presence of SOC [84], point groups without a center of inversion, i.e. *noncentrosymmetric* point groups, play a special role in the context of superconductivity as they lead to the mixing of singlet and triplet pairing [90]. E.g., the admixture of a triplet component to a singlet state is not only of purely theoretical interest but also has direct consequences for the physical properties of the superconductor as it renders the spin susceptibility anisotropic and finite at $T = 0$ which is directly measurable via Knight shift experiments [90]. In this section, we provide an overview of noncentrosymmetric superconductors that is tailor made for the studies presented in the subsequent chapters of this thesis and, hence, very selective. For a broader introduction to the rich field, we refer to the literature [38, 44–46].

The presence or absence of a center of inversion also has crucial consequences for the band structure in the normal state: Consider an eigenstate at some crystal momentum $\boldsymbol{k}$ with spin polarization $\boldsymbol{s}$. Applying inversion (I) transforms $\boldsymbol{k}$ to $-\boldsymbol{k}$ but leaves the $\boldsymbol{s}$ invariant as it is an axial vector like orbital angular momentum [93]. Subsequent application of time-reversal (Θ), sends $-\boldsymbol{k}$ back to $\boldsymbol{k}$ but inverts the direction of $\boldsymbol{s}$ as required for any angular momentum such that this state and the state we started with are linearly independent. If both I and Θ are symmetries, there must be (at least) two spin-degenerate states for any crystal momentum. This degeneracy can be removed either by breaking TRS, e.g., by applying a magnetic field, or by breaking inversion symmetry. We will focus here on the latter possibility and just mention that we will come back to the former in Chap. 4.7.1.

In the simplest case of just a single band $\epsilon_{\boldsymbol{k}}$ that is spin-degenerate in the presence of inversion and TRS, the spin-splitting can be described by the Hamiltonian

$$h_{\boldsymbol{k}}^A = \boldsymbol{g}_{\boldsymbol{k}} \cdot \boldsymbol{\sigma}, \qquad \boldsymbol{g}_{\boldsymbol{k}}^* = \boldsymbol{g}_{\boldsymbol{k}}, \quad \boldsymbol{g}_{-\boldsymbol{k}} = -\boldsymbol{g}_{\boldsymbol{k}} \tag{1.23}$$

where $\boldsymbol{\sigma} = (\sigma_1, \sigma_2, \sigma_3)$ denote Pauli matrices describing spin. The two properties of $\boldsymbol{g}_{\boldsymbol{k}}$, which will be referred to as *spin-orbit vector* in the following, result form Hermiticity and TRS of the Hamiltonian,

[12] The reason is that fluctuations of Δ can be neglected in a type-I superconductor while this is not the case for type-II superconductivity. It has been shown [129] that this makes the transition second order again in the latter case.

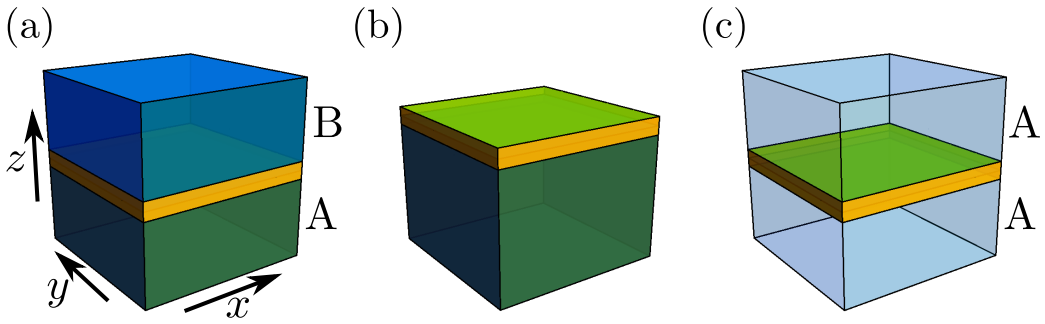

Figure 1.2: ***Experimental realizations of 2D systems.*** *(Quasi-)2D conducting systems (yellow) can be realized (a) at interfaces between two different materials $A \neq B$, (b) in a thin layer on a substrate or at the surface of a bulk material and (c) in a thin film in a symmetric environment (A might be vacuum). Only in the latter case, inversion symmetry can be preserved.*

respectively. The second property of $\boldsymbol{g_k}$ also means that $h^A_{\boldsymbol{k}}$ is odd under I and thus breaks I maximally. Adding $h^A_{\boldsymbol{k}}$ to the centrosymmetric part $\sigma_0\epsilon_{\boldsymbol{k}}$ of the Hamiltonian yields the spectrum $\epsilon_{\boldsymbol{k}} \pm |\boldsymbol{g_k}|$. The splitting of the bands, known as the *Dresselhaus-Rashba effect* [33, 34], is thus given by the magnitude of the spin-orbit vector. The most frequently encountered form is the Rashba spin-orbit coupling where $\boldsymbol{g_k} = \alpha(-\sin k_2, \sin k_1, 0)^T$. To deduce the structure of the spin-orbit vector, again the point symmetries of the system can give useful constraints [87]. It can, alternatively, also be explicitly calculated by starting from a multi-band model with microscopic SOC and hopping matrix elements that are only allowed in the absence of inversion symmetry. Integrating out [130] all bands except for those in the vicinity of the Fermi surface yields an effective low-energy Hamiltonian explicitly containing the Dresselhaus-Rashba effect. In Chap. 5.1.1, both the symmetry as well as the microscopic approach will be applied to a multi-orbital system.

Concerning the material realization of noncentrosymmetric superconductors or electron liquids in general, one can distinguish the following four different cases:

1. 3D systems with noncentrosymmetric crystal structures.
2. Conducting interfaces between two different materials A and B as shown in Fig. 1.2(a).
3. Atomically thin conducting films either in an asymmetric environment, e.g., on an insulating substrate only on one side as shown in Fig. 1.2(b), or in a symmetric environment, see Fig. 1.2(c), but with a noncentrosymmetric crystal structure in the thin layer itself.
4. Locally any surface of a bulk material (see Fig. 1.2(b)).

To begin with 1., we first note that 21 out of the 32 possible point groups of 3D crystalline systems are noncentrosymmetric.[13] A famous example is the noncentrosymmetric heavy-fermion superconductor $CePt_3Si$ discovered in 2004 [131]. The upper critical field reported in Ref. [131] represents a milestone for noncentrosymmetric superconductivity as it showed the presence of triplet pairing in this system – in contrast to common belief [132] at that time that the broken inversion symmetry acts as pair breaking

[13] For a discussion of all point groups in 3D and 2D systems with respect to the aspects relevant for this thesis, we refer to Appendix A.3.

for triplet states. It was subsequently clarified theoretically that triplet pairing is indeed possible in noncentrosymmetric systems [133]. Today several different noncentrosymmetric superconductors in strongly as well as weakly coupled systems have been found and analyzed. We refer to the literature for a systematic introduction to this broad field [44, 45] and just mention two noncentrosymmetric superconductors that have attracted recent attention: Both in $LaNiC_2$ [55] as well as in Re_6Zr [56] muon spectroscopy has provided convincing evidence for broken TRS in the superconducting state. As we will see repeatedly throughout this thesis, spontaneous TRS breaking at a superconducting phase transition represents an exciting and exotic phenomenon.

The superconductors of the type 2. and 3. in the list presented above are (quasi-)2D, i.e., only one (a few) subband(s) resulting from the quantum-well confinement along the z direction is (are) relevant for describing superconductivity. Unless stated otherwise, we will for simplicity not distinguish between 2D and quasi-2D in the following. Only thin films can have point-symmetry operations relating z to $-z$ and, hence, allow for the largest number of possible point groups among the 2D systems.

Finally, 4. represents a special case as it refers to both 2D as well as 3D superconductors: It includes 2D superconductivity arising, as originally suggested by Ginzburg [134], in a surface band of a material that is insulating in its bulk or at the surface layers of a metallic system due to modified interactions at the surface (e.g., due to surface phonons). An interesting but controversial [46] example is provided by the possible observation [135] of superconductivity at Na-doped surfaces of WO_3. In addition, at surfaces of any 3D bulk superconductor inversion symmetry is locally broken. As we will discuss in Chap. 4.8, this can force the local suppression of the bulk superconducting order parameter and might even lead to the emergence of a competing superconducting phase at the surface with different symmetries.

From our present considerations it becomes clear that the noncentrosymmetric point groups are particularly relevant for 2D systems as inversion symmetry is automatically broken in the experimental realization of 2D electron liquids at heterostructures, in atomic sheets on a substrate and at surfaces. Only for thin sheets in a symmetric environment (see Fig. 1.2(c)), which is, e.g., the case for suspended graphene [136], inversion symmetry can be preserved. Naturally, whether the broken inversion symmetry significantly affects superconductivity (or any other aspect for that matter) crucially depends on the material considered and the property of interest.

In the following, we will discuss a few examples of 2D superconductors that are realized at interfaces of heterostructures and in thin films. For a broader overview we refer to Ref. [46].

1.3.1 Interfaces between oxides

Besides the study of superconductivity in various heterostructures consisting of copper oxide materials [137, 138], in particular the observation of superconductivity in 2007 [39] at the interface between the two insulating perovskite oxides LAO and STO has sparked considerable interest of researchers in the last years [36–38]. This resulted not only from the complex reconstruction mechanism [139, 140] that leads to the paradox situation of metallic behavior when bringing band insulators in contact but also from the novel properties of this system that are interesting both from a fundamental physics point of view as well as for potential applications.

The formation of a conducting sheet [35] at the interface between LAO and STO beautifully shows that heterostructures can be designed in order to make charge configurations possible that are unavailable in the bulk. In the absence of vacancies and charge transfer, the oxygen is in a -2 state which, together with the $+2$ charge of Sr, leads to a Ti^{4+} configuration. This means that the two $3d^2$ and $4s^2$ states of Ti are empty explaining the insulating behavior of undoped bulk STO. Furthermore, it implies

that STO consists of neutral layers as can be seen in Fig. 1.3(a) while LAO is built from alternatingly charged layers as a consequence of the 3+ state of Al. Recalling from electrostatics [86] that surface charges lead to a jump in the electric potential, this polar discontinuity produces a voltage built-up as illustrated in the left panel of Fig. 1.3(b) that diverges with the thickness of the LAO crystal. This is known as the "polar catastrophe". It can be circumvented by transferring half an electron per unit cell to the interface (right panel in Fig. 1.3(b)) corresponding to electron-doping into the Ti $3d$ shell and, hence, leading to metallic behavior in the interface [139, 140].

On the one hand, this picture is consistent with local charge measurements [139] and the existence of a critical thickness (four unit cells) of the LAO layer for conductivity [141]. On the other hand, the observation of a metallic interface also in the (110)-oriented interface and even in case of amorphous LAO [142] where there is no polar discontinuity shows that other mechanisms must be at work. Indeed, more recent experiments [143] show that oxygen vacancies are the dominant source of mobile carriers in the amorphous interface and also contribute to conductivity in the crystalline (001) interface.

The superconducting transition with critical temperature $T_c \simeq 100 - 200\,\mathrm{mK}$ (depending on sample) has been shown to be consistent with the expected behavior of a BKT transition [39] including the current voltage relation $V \propto I^3$ at the transition and the scaling of resistance with temperature. The 2D character of superconductivity is further confirmed by the estimated upper limit of the thickness of the superconducting layer (10 nm) being much shorter than the superconducting coherence length $\xi \simeq 100\,\mathrm{nm}$.

The superconducting properties, such as its transition temperature and superfluid density, can be tuned via the electrostatic field effect [144, 145]. Most importantly, this allows for a gate-tuned quantum phase transition between an insulator and a superconducting state [144]. Another property of the system that can be tuned via gating is the strength of the Dresselhaus-Rashba effect outlined above. In addition to its gate-dependence, magnetotransport studies [41, 42] have revealed that the associated spin-splitting is also a very strong effect: It is of the order of 10 meV and, hence, much larger than the maximal superconducting gap ($\simeq 0.04\,\mathrm{meV}$) and even comparable to the Fermi energy ($E_F \simeq 20\,\mathrm{meV}$).

More recently, tunnel spectroscopy measurements [70] have been performed that indicate the absence of nodes on the Fermi surface. Furthermore, the transport transition temperature T_c does not follow the gap opening temperature T_{gap} in the tunnel spectra. This "pseudogap" behavior in the density of states bears strong resemblance to the cuprate superconductors, however, on very different energy scales and carrier concentrations as can be seen in Fig. 1.3(c).

A property of the heterostructure that might be important for future applications is that the electron gas can be pattered spatially with unit cell resolution: Making use of the critical thickness of four unit cells for conductivity, a profile in the LAO thickness realized via microlithography determines the spatial structure of the buried electron gas [146]. Furthermore, it has been shown that at an interface with three unit cells of LAO, i.e., slightly below the critical thickness, conducting behavior can be reversibly switched on and off via gating [141]. In Ref. [147], this has been exploited to write and erase conducting textures with voltage-biased atomic fore microscope tips.

Another interesting aspect is the observation of magnetism at the interface [148] although both LAO as well as STO are nonmagnetic in the bulk. Magnetism was later shown to even coexist with superconductivity in the same sample [149, 150]. Scanning superconducting quantum interference devise (SQUID) magnetometry [149] revealed a spatially inhomogeneous magnetic landscape consisting of magnetic patches of the size of a few micrometer in a uniform paramagnetic background. Surprisingly, the susceptometry data showed no spatial correlation between superconductivity and magnetism. Both intrinsic, interaction-induced, mechanisms have been suggested [111, 151, 152] for magnetism as well as oxygen vacancies are discussed as the dominant origin of the magnetic ordering [153–155].

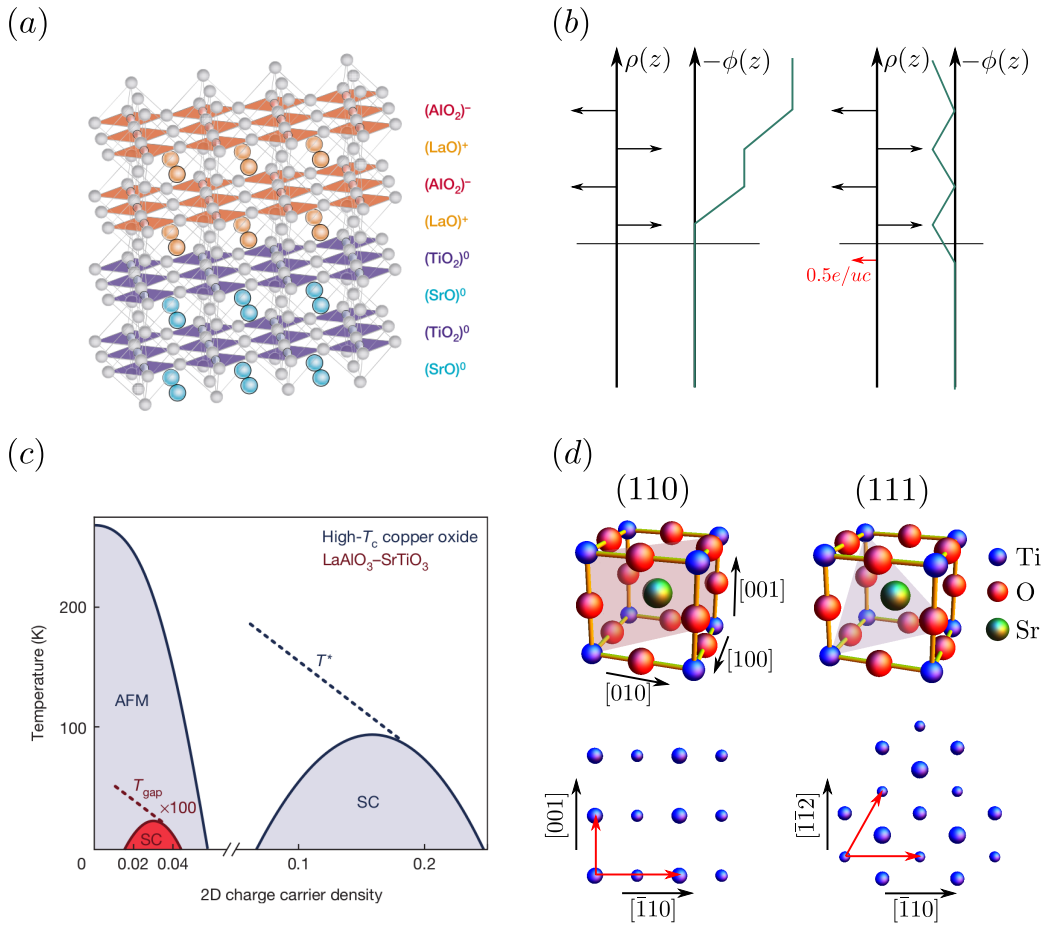

Figure 1.3: ***Oxide heterostructures.*** *In (a), the crystal structure of the LAO/STO heterostructure is illustrated (Reprinted by permission from Macmillan Publishers Ltd: Nature [35], copyright 2004). The corresponding (idealized) charge distribution $\rho(z)$ and resulting electric potential $\phi(z)$ before (left) and after (right) transferring half an electron per unit cell (uc) to the interface are shown in (b). In (c) the superconducting phase diagram (Reprinted by permission from Macmillan Publishers Ltd: Nature [70], copyright 2013) of the LAO/STO system (red) is compared with that of the cuprates (blue). Part (d) illustrates the crystal structure of the two alternative orientations of the heterostructures.*

Finally, the physics at LAO/STO heterostructures was broadened further by the demonstration that not only for (001)-oriented interfaces but also for the (110) and (111) orientations, conducting behavior with mobilities similar to those of the (001) interface can be obtained [142, 156]. As can be seen in the schematic illustration in Fig. 1.3(d) of the crystal structure, these additional orientations have point groups C_{2v} and C_{3v} differing from that of the (001) interface (C_{4v}). As will be discussed in Chap. 4.6.3, this has crucial consequences for the properties of possible superconducting phases. The (110) and (111) interfaces are far less studied, although gate-tunable strong spin-orbit splitting [43] as well as 2D superconductivity [40] have already been demonstrated for the (110)-oriented interface.

In particular concerning superconductivity, there are many open questions [37, 38]: How can the superconducting state coexist with magnetism in the same sample? What is the superconducting order parameter? Is a conventional or an unconventional mechanism responsible for the emergence of superconductivity? Is unconventional superconductivity possible given the inevitable presence of impurities such as oxygen vacancies (cf. Sec. 1.4.2)? Are there crucial differences to be expected for the different orientations of the interface? In the remainder of the thesis, in Chaps. 4.6.3, 5, 6.3.1 and 7.3, we will come back to these questions from different perspectives.

1.3.2 Thin films

Here we will discuss four different physical systems: We begin with single-layer FeSe on STO which has been successfully grown for the first time very recently [157] yielding surprisingly large superconducting transition temperatures [158, 159]. Then we will turn our attention to two materials, Sr_2RuO_4 and UPt_3, that are mainly known for their exotic superconducting bulk properties [160–164], in particular, spontaneous TRS-breaking in the superconducting state [47–49, 51, 53, 54], but have also been shown to harbor superconductivity in the thin film limit [68, 69]. Although the choice of the latter two materials seems to be surprising, we will see in Chap. 4.6 that the broken TRS in the bulk phase leads to interesting consequences for superconductivity in the thin layer system. For the very same reason, we also briefly discuss URu_2Si_2 [165].

Single-layer FeSe. In 2012, scanning tunneling microscope (STM) measurements [157] have revealed an anomalously large superconducting gap in one unit cell of FeSe epitaxially grown on (001) STO. Being nearly an order of magnitude larger than its value in bulk FeSe, this triggered enormous research interest as it promised the possibility of very large transport transition temperatures [158, 159].

This expectation was soon underpinned by ARPES studies [167, 168] observing the opening of a particle-hole symmetric gap around the Fermi surface at temperatures between 55 K and 70 K. However, at that time, *ex situ* transport measurements only showed zero resistance at significantly lower temperatures [157]. Recently, *in situ* transport measurements have been carried out indicating a superconducting transition above 100 K [169] which is remarkable as this transition temperature would not only be more than 10 times larger than its bulk value of 9.4 K [170] but also by far break the record of 56 K for all known bulk iron-based superconductors [171]. One has to note, however, that these measurements are still considered to be controversial and thus need further confirmation [158, 159].

From the crystal structure shown in Fig. 1.4(a) it is easily seen that the point group of the system is C_{4v}. Note that inversion symmetry is automatically broken due to the STO substrate rendering the space group symmorphic as opposed to the nonsymmorphic[14] symmetry group of bulk FeSe and other iron-based superconductors [172].

Another interesting property of single-layer FeSe is that there are no hole pockets surrounding the Γ-point, a characteristic feature of iron-based superconductors, as can be clearly seen in the ARPES data shown in Fig. 1.4(b) [167]. There are only electron pockets around the M point. Although not visible in the data, these consist of four singly degenerate Fermi surfaces – two, associated with the "folding" of the Brillouin zone [167, 173], times two, due to the spin splitting resulting from the broken inversion symmetry [174]. The absence of hole pockets implies that the FeSe layer is effectively electron doped,

[14] A space group is called *symmorphic* if an origin can be chosen such that it contains its point group as a subgroup. Otherwise, a space group is *nonsymmorphic* [85]. This can occur in the presence of fractal translations. In bulk FeSe, there is a glide-plane symmetry involving a fractal translation that is broken due to the substrate in the single-layer system.

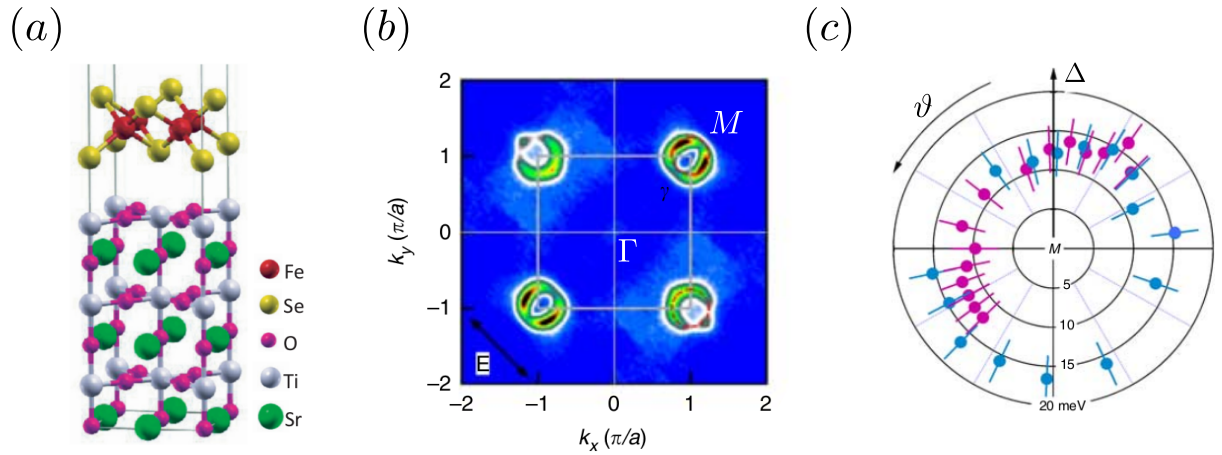

Figure 1.4: ***Single-layer FeSe.*** *Part (a) is a ball-and-stick model of the crystal structure of FeSe on STO. Reprinted figure with permission from Liu, Lu, and Xiang, PRB 85, 235123 (2012) [166]. Copyright 2012 by the American Physical Society. In (b), ARPES data of Ref. [167] on Fermi surfaces in the "folded" Brillouin zone, i.e., associated with a real space unit cell containing two Fe atoms, have been reprinted. As discussed in the main text, there are four singly degenerate Fermi surfaces enclosing the M point. (c) Gap of two different samples (pink and blue) as a function of the polar angle ϑ with respect to the M point (Part (b) and (c) are reprinted by permission from Macmillan Publishers Ltd: Nat. Commun. [167], copyright 2016).*

which is commonly attributed to oxygen vacancies in the STO substrate but not yet fully understood [158, 159]. Remarkably, the Fermi surface topology is different already for two and more unit cells of FeSe: Both electron and hole pockets are present [175] and superconductivity disappears which remains a puzzle at present time [159].

Furthermore, it has been controversial [159] whether the large gap seen by STM and ARPES is entirely due to superconductivity and not a consequence of some magnetic order. Although first principle calculation have indicated magnetic ordering [176], ARPES experiments [177] show that the superconductivity is rather associated with the suppression of spin-density wave (SDW) order, which is present in thin films of FeSe, but seems to be absent in the single-layer system. Very recently [178] the absence of magnetic order has been demonstrated via muon spin rotation/relaxation measurements.

The superconducting behavior in single-layer FeSe leaves many more open questions [158, 159]. The central issue concerns the unknown mechanism leading to the tremendously enhanced superconducting transition temperature. First indications come from the clear observation of replica bands [175] most likely resulting from the shaking off of bosonic excitations which have been interpreted [159, 175] as oxygen optical phonons of STO. Another important question concerns the form of the order parameter. Here the main hint comes from ARPES experiments that clearly indicate the absence of nodes on the Fermi surfaces as can be seen in Fig. 1.4(c).

In Chaps. 4.6.3 and 6.3.2, we will come back to these two questions with a particular focus on the broken inversion symmetry in the normal state as well as on the time-reversal properties, the spatial symmetries and the topology of the superconductor.

Sr_2RuO_4. The next material we will discuss is Sr_2RuO_4 which has been the focus of immense research interest (see Refs. [160–162] and references therein) since the discovery of superconductivity ($T_c \simeq 1.5\,\mathrm{K}$) in its bulk state in 1994 [179]. Although the main focus of this thesis is on thin layers of this material, let us first briefly discuss the aspects of the normal and superconducting state in bulk Sr_2RuO_4 which will be helpful when analyzing the possible pairing states in the thin layer limit.

Sr_2RuO_4 has, exactly as the cuprates, a centrosymmetric layered perovskite structure as shown in Fig. 1.5(a). As opposed to most systems with this structure, no structural phase transitions occur down to 100 mK that could reduce the point group D_{4h} [160]. The relevant low-energy degrees of freedom are the t_{2g} orbitals, $4d_{xy}$, $4d_{xz}$ and $4d_{yz}$, of the Ru atom [180]. Very soon after the discovery of superconductivity, the observation of quantum oscillations [181] illustrating the high purity of the samples revealed that the low-temperature metallic phase of Sr_2RuO_4 is a well-behaved Fermi liquid. As expected from the layered crystal structure, the electronic dispersion is quasi 2D in the sense that the Fermi surfaces only very weakly depend on the momentum along the c direction [181, 182].

Today, there is very strong experimental evidence for odd-parity triplet pairing as was originally conjectured in Ref. [183, 184]: This includes the absence of a change in the spin susceptibility at the superconducting transition measured via Knight shift [185] and spin-polarized neutron scattering [186], phase-sensitive SQUID measurements [187] as well as the study of magnetic field modulation of the critical current in Josephson junctions [53].

The most promising candidate pairing state is a chiral p-wave state characterized by a triplet vector $\boldsymbol{d_k} = (k_1 \pm ik_2)\boldsymbol{e}_3$ in accordance with many experiments [47, 51, 53, 188, 189]. Most importantly for the work at hand, this state breaks the TRS (see Chap. 4.1 for detailed discussion of TRS in the context of superconductivity) of the normal state. While this will not lead to a finite magnetization in a homogeneous sample, surfaces and defects can induce local magnetic moments [50] the appearance of which at the superconducting transition has been observed in muon spin relaxation studies [51]. Furthermore, the existence of several domain structures ($k_1 \pm ik_2$, $k_2 \pm ik_1$) has been detected in Josephson junction experiments [53]. The most direct experimental evidence of the broken TRS is provided by the observation [47] of the PKE below T_c, i.e., the rotation of the polarization direction of the reflected light. It can be shown that the PKE does not exist in a time-reversal symmetric state [47] and, hence, constitutes a decisive tool for analyzing TRS breaking.

Another exciting consequence of the chiral order parameter is the presence of edge currents of topological origin [190] (see also Chap. 2.2.2). However, the associated magnetic moments have not yet been seen in experiment despite enormous efforts [191, 192].

Furthermore, there is no consensus on which bands are most relevant for understanding superconductivity: As originally conjectured based on specific heat measurements [193], the rather isotropic γ band derived from the $4d_{xy}$ orbitals, which is close to a Van Hove singularity, has been widely expected to play the central role for the superconducting instability [194, 195]. The comparatively weak [196] pair hopping to the remaining Fermi surfaces only induces a small gap on the latter. More recently, it has been suggested in Ref. [197] that the quasi-one-dimensional (1D) α and β bands (due to the $4d_{xz}$ and $4d_{yz}$ orbitals) are more important. A very recent work [198], treating all bands on equal footing found that the superconducting gap is rather of the same order on all bands.

As already mentioned, we are mainly interested in the physics of thin layers of Sr_2RuO_4 deposited on substrate which will break inversion symmetry and reduce the point group (at least) to C_{4v}. Studying the impact of the reduced dimensionality and the broken inversion symmetry on superconductivity is interesting on its own right and might, on top of that, also give important insights concerning the unresolved aspects of its bulk behavior outlined above. The experimental realization of thin layers of Sr_2RuO_4 is still in its infancy as defects and impurities in most cases lead to large values of the residual

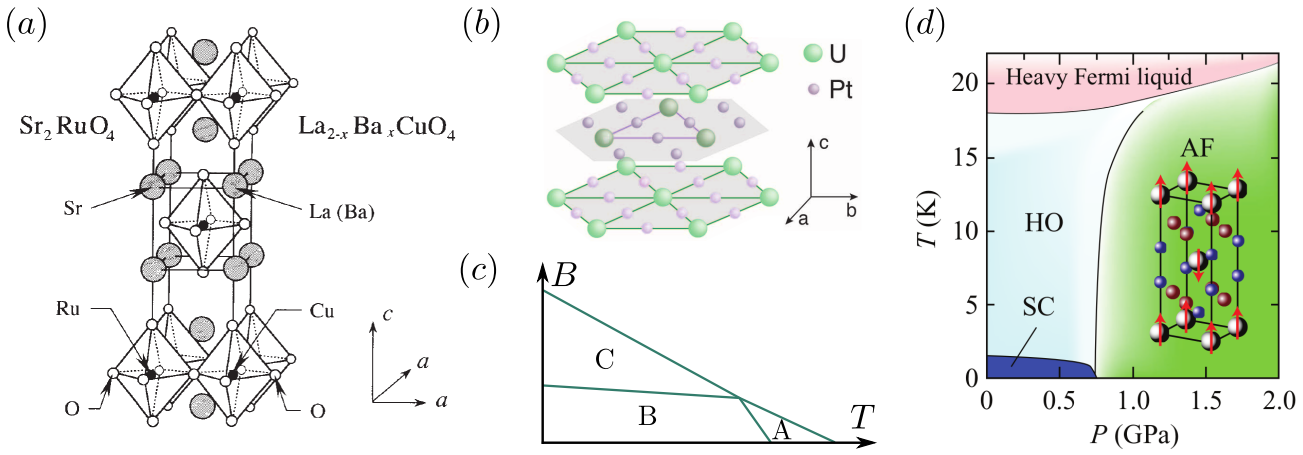

Figure 1.5: ***Selective properties of three TRS-breaking bulk superconductors.*** *(a) Crystal structure of Sr_2RuO_4 in comparison with that of a cuprate superconductor (Reprinted by permission from Macmillan Publishers Ltd: Nature [179], copyright 1994). (b) Crystal structure of UPt_3 (From Schemm et al., Science 345, 6193 (2014) [48]. Reprinted with permission from AAAS.). (c) Schematic magnetic field B/temperature T phase diagram of UPt_3 based on data of Ref. [201]. (d) Phase diagram of URu_2Si_2 as a function of pressure P and temperature T (Reprinted from Ref. [202], copyright 2009 by IOP Publishing Ltd).*

resistivity suppressing the emergence of superconductivity [199, 200]. In Ref. [68], however, the successful growth of a superconducting thin film has been reported. Using $(LaAlO_3)_{0.3}(SrAl_{0.5}Ta_{0.5}O_3)_{0.7}$ as substrate, a c axis-oriented epitaxial film has been grown by means of pulsed laser deposition (PLD). The resulting thin film (thickness $\simeq 96\,\mathrm{nm}$) showed a high residual resistivity ratio (> 80) and superconductivity with onset temperature of $\simeq 0.9\,\mathrm{K}$, i.e., comparable to the T_c of bulk Sr_2RuO_4. In Chap. 4.6.1, we will analyze the possible pairing states in thin layers of Sr_2RuO_4 with broken inversion symmetry on theoretical grounds.

UPt_3. Ever since the discovery [23] of superconductivity in the heavy-fermion compound UPt_3, it was expected to have an unconventional origin. Still today there are many controversies concerning both its superconducting as well as normal state properties [163, 164]. We will proceed analogously to our discussion of Sr_2RuO_4 and first summarize the most important aspects of bulk UPt_3. At the end we will comment on thin films of this material which will be investigated further in Chap. 4.6.2.

The crystal structure of UPt_3, shown in Fig. 1.5(b), consists of U atoms forming a closed-packed hexagonal structure with Pt in the middle of the planar bonds. The associated point groups is D_{6h} [163]. Qualitatively, the normal state is a Fermi liquid but with much higher effective mass which is directly visible, e.g., in the specific heat [23]. The band structure results from the strong hybridization between the $5f$ and $5d$ orbitals of U and Pt. There are five bands with strong f character crossing the Fermi level leading to a richly structured Fermi surface [163, 203].

One of the most stimulating aspects of UPt_3 is the presence of three distinct superconducting phases as can be seen in the schematic magnetic field-temperature phase diagram shown in Fig. 1.5(c) which was originally resolved by specific heat [204, 205] and later mapped out, e.g., by ultrasonic velocity

measurements [201]. This clearly bares resemblance to the (temperature-pressure-field) phase diagram of ^{3}He that also contains three phases [78]. We will here focus on zero magnetic field, i.e., on the A and B phase with transition temperatures $T_c^A \simeq 550\,\mathrm{mK}$ and $T_c^B \simeq 480\,\mathrm{mK}$, respectively [163].

Although still controversial (see Ref. [163, 164] and references therein), the most widely accepted candidate order parameter structure is $\boldsymbol{d_k} = (\delta_1(k_1^2 - k_2^2)k_3 + 2i\delta_2 k_1 k_2 k_3)\boldsymbol{e}_3$, i.e., a triplet state transforming under E_{2u} of the point group D_{6h}. In the A phase, only one of the prefactors is finite while at T_c^B the other one sets in breaking TRS. Note that there are also triplet components perpendicular to $\boldsymbol{e}_3$ transforming under the same IR such that, from a pure symmetry point of view, the triplet vector does not have to fully polarized along the z direction.

There are several experimental observations in favor of the triplet state outlined above: Firstly, the broken TRS has been demonstrated by muon spin relaxation [54] and PKE [48] experiments. The anisotropy of the thermal conductivity [206] and phase sensitive Josephson interferometry experiments [207] point towards the E_{2u} representation. The main indication for the triplet vector being polarized along the z direction is provided by the anisotropy of the upper critical field [208].

Another important aspect of superconductivity in UPt_3 is that it coexists with antiferromagnetic order: As was first noticed by muon spin relaxation experiments [209] and mapped out by neutron scattering [210], at $T_N \simeq 5\,\mathrm{K}$ antiferromagnetic order with very small magnetic moments of order of $\simeq 0.01\mu_B$ per U atom (μ_B denotes the Bohr magneton) sets in. Despite extensive studies its origin has still remained a puzzle [163]. A direct experimental indication of the correlation between superconductivity and antiferromagnetism was provided by the combination of specific heat [211] and neutron scattering [212] measurements under hydrostatic pressure: It is found that the difference $T_c^A - T_c^B$ is proportional to the square of the magnetic moment both vanishing at $\simeq 3 - 4\,\mathrm{kbar}$. This is very naturally understood [213, 214] by a superconducting order parameter transforming under a two-dimensional IR with the antiferromagnetic order acting as a weak symmetry-breaking perturbation slightly breaking the point symmetry down to D_{2h}.

Also in case of UPt_3, thin films have been successfully grown: As reported in Ref. [69], UPt_3 has been sputter deposited on various different substrates using several different orientations. Superconducting behavior has been found on (111) STO, however, with significantly reduced transition temperature ($\simeq 130\,\mathrm{mK}$) as compared to the bulk. In Chap. 4.6.2, we will see how energetic arguments can dramatically reduce the possible superconducting order parameters in the thin layer superconductor.

URu_2Si_2. Finally, let us introduce URu_2Si_2 [165, 215] as a second example of a heavy-fermion superconductor [216–218]. Although, in this case, no successful thin layer experiment has been reported to the best of our knowledge, we will see in Chap. 4.6.2 that there are strong general theoretical constraints on the superconducting order parameter in the quasi-2D limit. We will therefore give a brief introduction to this material here.

The mystery about URu_2Si_2 began with the observation [216–218] of two phase transitions: A superconducting transition at $T_c \simeq 1.5\,\mathrm{K}$ and a transition at $T_h \simeq 17.5\,\mathrm{K}$ into what is now commonly referred to as "hidden order" phase [165, 215]. The small magnetic moments ($\simeq 0.03\mu_B$ per U atom) [219] appearing below T_h clearly cannot account for the amount of entropy change [216–218] at the transition. As indicated by its name, the order parameter of the "hidden order" phase turned out to be elusive to any of the condensed matter probing tools such as neutrons, X-rays and muons. Despite enormous efforts [165], it has not yet been fully resolved today although promising progress has been made very recently [215].

At T_h most of the mobile carriers disappear [220] leading to a semimetallic phase out of which superconductivity emerges: As can be seen in the temperature-pressure phase diagram shown in

Fig. 1.5(d), the superconducting state is fully embedded in the hidden order phase (the same holds in the temperature-magnetic field diagram as well [165]) both being suppressed at $T = 0$ at the onset of antiferromagnetism. This shows that, as opposed to other heavy-fermion superconductors such as UPt_3 discussed above, superconductivity cannot coexist with antiferromagnetism and indicates its close relation to the hidden order phase. Therefore, analyzing superconductivity is important for a full understanding of the hidden order phase.

At present time, the superconducting phase is believed to be the chiral d-wave state $\Delta^S_{\boldsymbol{k}} = (k_1+ik_2)k_3$, i.e., a spin-singlet superconducting order parameter transforming under E_g of D_{4h} and breaking TRS. The latter property has again been convincingly demonstrated by the PKE [49]. Strong support of the order parameter structure comes from thermal transport measurement in magnetic fields [202, 221–223].

In Chap. 4.6.2, the impact of inversion symmetry breaking in a quasi-2D layer of this material will be analyzed.

1.4 Impact of disorder

So far, our theoretical considerations of phase transitions were crucially based on the crystal symmetries of the system. Given that any realistic crystal structure will inevitably have imperfections, it is an important question to ask how this can be taken into account in a way that only depends on a minimal number of parameters and whether there are implications for the properties of the impurities resulting from the crystalline symmetries of the idealized clean system.

The remainder of this section should be read as a tailor-made introduction to the basic concepts required for and the notation used in our analysis of disorder effects in superconductors of Chap. 7. For a pedagogical introduction to impurity effects in condensed-matter systems in general, we refer to the textbooks [94, 114, 224]. A broader discussion of disorder in superconducting systems can be found in the review articles [225–227].

1.4.1 How to describe disorder

Assuming that all relevant time scales are much smaller than the time it takes for the local distortion of the system to equilibrate, we can describe disorder as a static ("quenched") additional contribution $\hat{H}_{\text{dis}}$ to the Hamiltonian. Focusing for simplicity on quadratic terms, we can write

$$\hat{H}_{\text{dis}} = \int_{\boldsymbol{x},\boldsymbol{x}'} \hat{c}^\dagger_\alpha(\boldsymbol{x}) W_{\alpha\alpha'}(\boldsymbol{x},\boldsymbol{x}') \hat{c}_{\alpha'}(\boldsymbol{x}'), \qquad W^*_{\alpha'\alpha}(\boldsymbol{x}',\boldsymbol{x}) = W_{\alpha\alpha'}(\boldsymbol{x},\boldsymbol{x}'), \tag{1.24}$$

where $\hat{c}^\dagger_\alpha(\boldsymbol{x})$ creates a fermionic quasiparticle in state α at space point $\boldsymbol{x}$ (either discrete on a lattice or in a continuum description). To obtain a description that only depends on a few characteristic parameters, a statistical description is applied where W is treated as a random field that will be averaged over to calculate physical quantities. This can be done as long as the physical quantity of interest is *self-averaging* which is expected to be the case when the phase coherence length is much smaller than the system size. The disorder ensemble can either be described as a set of identical local perturbations at random positions [94, 224] or W can be taken as a random matrix field distributed according to some probability measure $p[W]$ [114]. We will focus on the latter choice as it is most easily implemented in the field-integral approach and allows for a convenient discussion of point symmetries (see below). For simplicity taking W to be Gaussian distributed, the entire information of $p[W]$ is

contained in the correlator

$$\Gamma_{\alpha_1\alpha_1',\alpha_2\alpha_2'}(\boldsymbol{x}_1,\boldsymbol{x}_1',\boldsymbol{x}_2,\boldsymbol{x}_2') := \langle W_{\alpha_1\alpha_1'}(\boldsymbol{x}_1,\boldsymbol{x}_1')W_{\alpha_2\alpha_2'}(\boldsymbol{x}_2,\boldsymbol{x}_2')\rangle_{\text{dis}} \tag{1.25}$$

where $\langle\ldots\rangle_{\text{dis}}$ denotes the disorder average. When performing the disorder average in the calculation of physical quantities, one encounters the technical problem that also the normalization of the path integral depends on the disorder configuration. One way to circumvent this problem is provided by the *replica approach* [228] which is based on the identity $\ln(\mathcal{Z}) = \lim_{R\to 0}(\mathcal{Z}^R - 1)/R$ where $\mathcal{Z}$ denotes the partition function. Physically, $\mathcal{Z}^R$ can be seen as the partition function of R identical copies of the original system which can be conveniently described by adding an additional replica index $r = 1,\ldots,R$ to the Grassmann analogues c_α^r, $\overline{c}_\alpha^r$ of $\hat{c}_\alpha$, $\hat{c}_\alpha^\dagger$ in Eq. (1.24). At the end of the calculation of physical quantities, the limit $R \to 0$ has to be taken. Averaging over disorder leads to the effective four-fermion interaction with action [114]

$$S_{\text{R}} = -\frac{1}{2}\sum_{r,r'=1}^{R}\int_{\tau,\tau'}\int_{\boldsymbol{x}_1,\boldsymbol{x}_1',\boldsymbol{x}_2,\boldsymbol{x}_2'} \overline{c}_{\alpha_1}^r(\boldsymbol{x}_1,\tau)c_{\alpha_1'}^r(\boldsymbol{x}_1',\tau)\overline{c}_{\alpha_2}^{r'}(\boldsymbol{x}_2,\tau')c_{\alpha_2'}^{r'}(\boldsymbol{x}_2',\tau')\Gamma_{\alpha_1\alpha_1',\alpha_2\alpha_2'}(\boldsymbol{x}_1,\boldsymbol{x}_1',\boldsymbol{x}_2,\boldsymbol{x}_2'), \tag{1.26}$$

where τ denotes imaginary time. This shows that the correlator introduced in Eq. (1.25) plays the role of the bare vertex function in the replica approach. For completeness, we note that the impurity vertex in the disorder-averaging technique of Refs. [94, 224] is proportional to the concentration of impurities and the modulus squared of the single impurity potential.

Crystal symmetries. Although any given disorder realization will generally break all symmetries of the system, on average the symmetries of the clean system must be restored. E.g., a spin-magnetic impurity might locally break the fourfold rotation symmetry of a tetragonal crystal, however, it will be oriented along the two equivalent crystal axes with equal probability. Mathematically, it means that the disorder correlator (1.25) must be invariant under the full symmetry group of the idealized clean system. To be more specific and for future reference, let us focus on spatially local and δ-correlated disorder such that the correlator assumes the simpler form

$$\langle W_{\alpha_1\alpha_1'}(\boldsymbol{x}_1,\boldsymbol{x}_1')W_{\alpha_2\alpha_2'}(\boldsymbol{x}_2,\boldsymbol{x}_2')\rangle_{\text{dis}} = \delta(\boldsymbol{x}_1-\boldsymbol{x}_1')\delta(\boldsymbol{x}_2-\boldsymbol{x}_2')\delta(\boldsymbol{x}_1-\boldsymbol{x}_2)\Gamma_{\alpha_1\alpha_1',\alpha_2\alpha_2'}(\boldsymbol{x}). \tag{1.27}$$

In order to restore (lattice) translation symmetry on average, it must hold $\Gamma_{\alpha_1\alpha_1',\alpha_2\alpha_2'}(\boldsymbol{x}) = \Gamma_{\alpha_1\alpha_1',\alpha_2\alpha_2'}$ making the distribution and, hence, the disorder-induced effective electron-electron interaction (1.26) homogeneous. Demanding that all point symmetries $g \in \mathcal{G}_p$ be satisfied on average is equivalent to

$$\Gamma_{\alpha_1\alpha_1',\alpha_2\alpha_2'} = \big(\mathcal{R}_\Psi(g)\big)_{\alpha_1\widetilde{\alpha}_1}\big(\mathcal{R}_\Psi(g)\big)_{\alpha_2\widetilde{\alpha}_2}\,\Gamma_{\widetilde{\alpha}_1\widetilde{\alpha}_1',\widetilde{\alpha}_2\widetilde{\alpha}_2'}\Big(\mathcal{R}_\Psi^\dagger(g)\Big)_{\widetilde{\alpha}_2'\alpha_2'}\Big(\mathcal{R}_\Psi^\dagger(g)\Big)_{\widetilde{\alpha}_1'\alpha_1'}, \tag{1.28}$$

where (exactly as in Sec. 1.1.1) $\mathcal{R}_\Psi(g)$ denotes the wavefunction representation of g. In Chap. 7.3.1, the most general symmetry-allowed form of Γ will be discussed for a system with C_{4v} point group and spin as well as two distinct orbital degrees of freedom.

Perturbation around the good metal. Within replica theory, the analysis of disorder effects becomes tantamount to studying an interacting problem with the highly τ-nonlocal interaction in Eq. (1.26). As usual, the exact treatment of this interaction is generally beyond reach and a small parameter has to be identified in order to organize a resummation of diagrams. To this end, let us

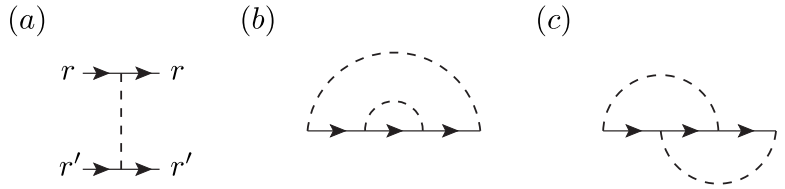

Figure 1.6: ***SCBA.*** *(a) Diagrammatic representation of the impurity vertex in Eq. (1.26). The two second order contributions to the self-energy that are finite in the replica limit $R \to 0$ are shown in (b) and (c). Solid lines with arrows represent bare quasiparticle propagators.*

consider the quasiparticle self-energy as a test quantity. Using a dashed line to represent the disorder vertex Γ as shown in Fig. 1.6(a), there are two second order diagrams that do not vanish in the replica limit $R \to 0$ which are given in Fig. 1.6(b) and (c). Anticipating that the Green's function will only assume sizable values in a shell of thickness $\propto 1/l$ around the Fermi surface, where l denotes the mean-free path, it readily follows (see, e.g., Ref. [114]) from phase space constraints that the second diagram in Fig. 1.6(c) will be suppressed by a relative factor of $1/(k_F l)$. Here k_F denotes the Fermi momentum. More generally, only taking the asymptotically leading contributions in the weak-disorder limit $k_F l \gg 1$ is equivalent to only keeping the diagrams without crossed impurity which is also known as the self-consistent Born approximation (SCBA).

1.4.2 Disorder in superconductors and the Anderson theorem

As the main focus of this thesis is on the phase competition in superconducting systems, let us close this section with a brief discussion of the influence of impurity scattering on the transition temperature T_c of superconductors as a measure for the stability of the condensate against the presence of disorder in the system.

Only a few years after the formulation of the BCS theory (see Sec. 1.1.2) it has been realized [229–231] that the transition temperature of a BCS superconductor, i.e., an s-wave, spin-singlet pairing state, is only very weakly affected by the presence of nonmagnetic impurities which became known as the *Anderson theorem*. The physical reason [229] is that nonmagnetic impurities preserve the TRS of the normal state. Although crystal momentum is not a good quantum number for a given disorder realization, a state and its time-reversed partner are still guaranteed to be degenerate and can hence form Cooper pairs. As long as the density of states remains unaffected by disorder, T_c stays constant. A more precise formulation has been provided by Abrikosov and Gorkov [230, 231]: Summing up the leading diagrams in the weak disorder limit $k_F l \gg 1$ (see Sec. 1.4.1 above), one can show that T_c is not affected by nonmagnetic disorder.

As expected from Anderson's argument, the behavior changes completely in case of magnetic impurities. As has been first demonstrated in Ref. [101], the transition temperature of a BCS superconductor is suppressed already in the limit $k_F l \gg 1$ and vanishes when the mean-free path l becomes of the order of the superconducting coherence length ξ.

Note that the Anderson theorem does not take into account Anderson localization [8] and its interplay with Coulomb interaction [226, 232]. As is intuitively clear, localization is a natural opponent of superconductivity and can lead to superconductor-insulator transitions in 2D systems. In the remainder of this thesis, in particular in Chap. 7, we will assume that localization effects can be neglected. This

corresponds to the limit of sufficiently large localization lengths [227, 233]

$$R_l \gg (T_c\,\rho_F)^{-\frac{1}{d}}, \tag{1.29}$$

where d is the dimensionality of the system and ρ_F the density of states at the Fermi level. In 3D, $k_F l \gg 1$ already ensures the absence of localization.

Various studies [160, 225, 234–240] of the stability of unconventional superconductors have revealed that already nonmagnetic impurities act as pair breaking in these systems – similarly to magnetic disorder in BCS superconductors. For this reason, it has become common wisdom that unconventional superconductivity is only possible in comparatively clean systems. By the same token, analyzing the sensitivity of T_c to nonmagnetic disorder can be used to gain information about the pairing mechanism in superconductors (see, e.g., Ref. [241]). In Chap. 7, we will examine critically the validity of the latter two statements with a particular focus on LAO/STO heterostructures.

Chapter 2

2 Fundamentals: Topological states of matter

In addition to classifying phases in terms of symmetries, which has been the central topic of the preceding chapter, topology can be used to discriminate between different states of matter, as we will see here.

In the first section, an introduction to the topological classification of phases on the mean-field level is provided and the physical consequences of the associated topological invariants are discussed. In Sec. 2.2, an overview of the physical systems and models relevant for this thesis is given. A brief description of the fascinating properties of the isolated zero-energy modes bound to defects in topological superconductors can be found in Sec. 2.3. Finally, Sec. 2.4 is concerned with the extension of the topological classification to interacting systems.

2.1 Definition of topological insulators and superconductors

A topologically nontrivial state of matter of a given symmetry class is, within the conventions used in this thesis, a gapped fermionic system which cannot be *adiabatically* deformed into the vacuum. In this context, "adiabatically" means continuously (in Hamiltonian space) without closing the gap or breaking the symmetries characterizing the corresponding symmetry class. In the language of topology [242], the adiabatic deformation corresponds to a homotopy and a state being topologically nontrivial is equivalent to saying that it is not homotopic to the vacuum. In general, the gap of the system can have several different physical origins. It can, e.g, arise in a band insulator, i.e., as the gap between occupied valence and unoccupied conduction bands, in a superconductor by a Cooper instability (see Chap. 1.1.2), as a spinon gap in a Mott insulator (Sec. 2.4.2) or as a consequence of localization (see, e.g., Refs. [243, 244]). In this thesis we will be exclusively concerned with the former three possibilities which will be referred to as *topological insulator*, *topological superconductor* and *topological Mott insulator* in the following.

The nontrivial topology leads to the emergence of gapless *edge modes* localized at the boundary of the system to a topologically trivial phase such as the vacuum. A hallmark of these edge modes is the protection against disorder that respects the symmetries of the associated symmetry class [9, 10] which is intuitively understood by regarding a given disorder configuration as an adiabatic deformation of the Hamiltonian that might change the detailed wavefunction of the edge modes but, according to the definition of the nontrivial topology of the bulk system, not their presence.

In the remainder of this section, we will define more precisely what topologically nontrivial means,

discuss the relation to edge modes and illustrate the general statements with the help of a simple working example.

2.1.1 Antiunitary symmetries and Cartan-Altland-Zirnbauer symmetry classes

From the introduction given above, we see that symmetries are key to define topological phases. It is well-known [93] that all physical symmetries are represented either by unitary or antiunitary operators (see footnote 4 on p. 4). To reduce the number of cases to consider, one can take advantage of the fact that unitary symmetries allow for block diagonalization of the Hamiltonian [85]. Each irreducible block without any unitary symmetries can then be classified separately[1] according to the presence or absence of antiunitary symmetries. The latter which cannot be removed by block diagonalization and are for this reason also referred to as "extremely generic symmetries" [247] include of TRS and particle-hole symmetry (PHS).

A Hamiltonian $\hat{H}$ is said have TRS if it commutes with an antiunitary operator $\hat{\Theta}$,

$$[\hat{H}, \hat{\Theta}] = 0 \quad \Leftrightarrow \quad \hat{T}\hat{H}^T\hat{T}^\dagger = \hat{H}, \tag{2.1}$$

where we have, in the second equality, taken advantage of the fact that $\hat{H}$ is Hermitian and that any antiunitary operator can always be written as the product of complex conjugation, $\mathcal{K}$ in the following, and a unitary operator $\hat{T}$ [93]. For a more physical discussion of TRS we refer to Chap. 4.1.

Similarly, PHS means that the Hamiltonian anticommutes with an antiunitary operator $\hat{\Xi}$, i.e.,

$$\{\hat{H}, \hat{\Xi}\} = 0 \quad \Leftrightarrow \quad \hat{C}\hat{H}^T\hat{C}^\dagger = -\hat{H} \tag{2.2}$$

where $\hat{\Xi} = \hat{C}\mathcal{K}$ has been inserted to obtain the second, equivalent, relation.

Since any of $\hat{\Theta}$ and $\hat{\Xi}$ can either be present, squaring to $+1$ or -1 [93], or absent, this yields $3 \times 3 = 9$ distinct possibilities. For all but one of these cases, the behavior of the Hamiltonian under the combined (unitary) operation $\hat{\Pi} := \hat{\Theta}\hat{\Xi}$, is determined. The sole exception is the absence of both TRS and PHS in which case, the Hamiltonian can either satisfy the *chiral symmetry* relation

$$\{\hat{H}, \hat{\Pi}\} = 0 \tag{2.3}$$

or not. Taken together, this yields 10 different possibilities which are referred to as *Cartan-Altland-Zirnbauer symmetry classes*. Altland and Zirnbauer [248, 249], extending the classic work of Wigner and Dyson on random matrix theory [250], have established these symmetry classes together with the one-to-one correspondence[2] to the 10 symmetric spaces classified by Cartan [251].

These classes, using Cartan's notation, together with the associated symmetries are summarized in the first four columns if Table 2.1. Here 0 denotes the absence of the symmetry, ± 1 the square of the operator in case of TRS and PHS and 1 the presence of a chiral symmetry. The fact that this exhausts all possibilities is most easily seen by noting that the presence of a second TRS, PHS or chiral symmetry is tantamount to having a unitary symmetry which can be removed by block diagonalization as discussed above.

[1] We will not discuss the more recent development of "topological crystalline insulators" where also crystal symmetries are taken into account [245, 246].

[2] For every symmetry class, the associated time-evolution operator $\exp(-i\hat{H}t)$ belongs to a different symmetric space. The same symmetric spaces also occur (though in different order) as target manifolds of diffusive non-linear sigma models and as classifying spaces discussed in Sec. 2.1.2 below. A pedagogical discussion can be found, e.g., in Ref. [247].

2.1.2 Mean-field definition of topological indices

There are several different approaches to characterize the topology of Hamiltonians belonging to one of the 10 symmetry classes outlined above. Among others, this includes (1) analyzing whether the associated non-linear sigma model manifold allows for the presence of a topological term which is physically based on the requirement of having edge states that are protected from Anderson localization [9, 10]. (2) Topological band theory, i.e., studying the topology of the mapping from the Brillouin zone or a sphere to a clean, noninteracting mean-field Hamiltonian [9, 247, 252–255] and (3) topological field theory of electromagnetic gauge fields [5, 256]. As it will be most important for the work at hand, we focus on (2) here and will briefly comment on (3) in Sec. 2.4 when discussing topological aspects beyond the noninteracting level.

To introduce topological band theory, let us consider a general mean-field Hamiltonian $H_{\boldsymbol{k}}$, $\boldsymbol{k} \in \mathcal{M}$, of a d-dimensional system which is a matrix with respect to all relevant microscopic degrees of freedom (spin, orbitals etc.) and, in case of a Bogoliubov-de Gennes (BdG) Hamiltonian of a superconductor, also with respect to particle-hole space. It depends on $\boldsymbol{k}$ which is, in case of a lattice, the crystal momentum vector and, hence, belongs to the Brillouin zone, i.e., a d-dimensional torus, $\mathcal{M} \cong \mathbb{T}_d$. In case of a continuum theory, $\boldsymbol{k}$ is just Fourier-conjugate to the real space coordinates and, after compactification[3], can be taken to belong to the d-dimensional sphere, $\mathcal{M} \cong \mathbb{S}_d$. The TRS , PHS and chiral symmetry introduced in the previous subsection on a more general (and basis-independent) level now assume the form

$$\Theta H_{-\boldsymbol{k}} \Theta^\dagger = H_{\boldsymbol{k}}, \qquad \Xi H_{-\boldsymbol{k}} \Xi^\dagger = -H_{\boldsymbol{k}}, \qquad \Pi H_{\boldsymbol{k}} \Pi^\dagger = -H_{\boldsymbol{k}}. \tag{2.4}$$

According to our definition stated at the beginning of the section, the topology of the system does not change under adiabatic deformation of the Hamiltonian, so we can equally well just study the "flat-band Hamiltonian" [9]

$$Q_{\boldsymbol{k}} = \sum_s \operatorname{sign}(E_{\boldsymbol{k}s}) \left|\Psi_{\boldsymbol{k}s}\right\rangle \left\langle\Psi_{\boldsymbol{k}s}\right|, \tag{2.5}$$

where $|\Psi_{\boldsymbol{k}s}\rangle$ denote the eigenstates of $H_{\boldsymbol{k}}$ with corresponding eigenvalues $E_{\boldsymbol{k}s}$. For every $\boldsymbol{k} \in \mathcal{M}$, $Q_{\boldsymbol{k}}$ can be diagonalized by a unitary transformation, $Q_{\boldsymbol{k}} = U_{\boldsymbol{k}} \Lambda U_{\boldsymbol{k}}^\dagger$ with $\Lambda = \operatorname{diag}(\mathbb{1}_m, -\mathbb{1}_n)$, where n (m) denotes the number of occupied (empty) bands. Noting the $\mathrm{U}(n)$ and $\mathrm{U}(m)$ "gauge freedom" among the empty and filled bands, we see that $Q_{\boldsymbol{k}}$ defines the mapping

$$Q : \mathcal{M} \longrightarrow G_{m,n+m}(\mathbb{C}) = \frac{\mathrm{U}(n+m)}{\mathrm{U}(n) \times \mathrm{U}(m)}. \tag{2.6}$$

If there are no additional symmetries, i.e., we consider a system of class A, the set of different topological phases corresponds to the set of homotopically distinct maps (2.6) which is the d-th homotopy group $\pi_d(G_{m,n+m}(\mathbb{C}))$. For example, it holds[4] [9] $\pi_2(G_{m,n+m}(\mathbb{C})) = \mathbb{Z}$ and $\pi_3(G_{m,n+m}(\mathbb{C})) = \{E\}$ which means that the 2D system is characterized by an integer-valued topological index[5] $\nu_{\mathbb{Z}}$ while no topologically nontrivial phase is possible in 3D. As the homotopy group π_d refers to $\mathbb{S}_d$ as base manifold, this only exhausts the possible topological invariants in the continuum theory. On the lattice the

[3] Compactification means that we associate $|\boldsymbol{k}| \to \infty$ with a single point which is physically motivated by the fact that $h(\boldsymbol{k})$ is only a low-energy theory such that it can be taken to be constant at large momenta.

[4] All homotopy groups listed in the following and in Table 2.1 have to be understood in the sense that the size (here the value of n and m) has to be taken sufficiently large such that the homotopy groups have "stabilized" (to their value at $n, m \to \infty$). E.g., although $\pi_3(G_{1,2}(\mathbb{C})) = \mathbb{Z}$ it holds $\pi_3(G_{m,n+m}(\mathbb{C})) = \{E\}$ for n, m sufficiently large [9].

[5] It plays the role of the dimensionless Hall conductivity in the quantum Hall [2] effect, see Sec. 2.2.1.

different geometry of $\mathcal{M} = \mathbb{T}_d$ allows for additional indices [247, 257], the so-called *weak topological indices* to be discussed below in Sec. 2.1.4.

In all other symmetry classes there are additional symmetries that constrain $Q_{\boldsymbol{k}}$ which might either force the mapping to be generically trivial, i.e., prohibit the presence of a topological phase, or by constraining the possible adiabatic deformations render configurations topological that would be homotopic to the trivial insulator without any symmetries. If there is a chiral symmetry, the Hamiltonian and, hence, also its associated flat-band version $Q_{\boldsymbol{k}}$ can be brought in block off-diagonal form [9]

$$Q_{\boldsymbol{k}} = \begin{pmatrix} 0 & q_{\boldsymbol{k}} \\ q_{\boldsymbol{k}}^\dagger & 0 \end{pmatrix} \tag{2.7}$$

with $q_{\boldsymbol{k}} q_{\boldsymbol{k}}^\dagger = \mathbb{1}_n$ with $2n$ denoting the number of bands. Consequently, the chiral symmetry has changed the target manifold to $U(n)$. Without any additional antiunitary symmetries (class AIII) the different different topological phases correspond to $\pi_d(\mathrm{U}(n))$. From $\pi_d(\mathrm{U}(n)) = \{E\}$ for d even and $\pi_d(\mathrm{U}(n)) = \mathbb{Z}$ for d odd [9], we have, in combination with our discussion of class A, already understood the alternating pattern of the presence of a $\mathbb{Z}$ invariant and no topological insulator (denoted by 0) in the first two rows of Table 2.1.

In all other classes, there are additional antiunitary symmetries that relate $Q_{\boldsymbol{k}}$ and $Q_{-\boldsymbol{k}}$ which can effectively change the topology of $\mathcal{M}$ by "orbifolding", i.e., identifying $\boldsymbol{k}$ and $-\boldsymbol{k}$. E.g., the antiunitary symmetries in the two classes BDI and DIII, both of which have a chiral symmetry, lead to $q_{\boldsymbol{k}}^* = q_{-\boldsymbol{k}}$ and $q_{\boldsymbol{k}}^T = -q_{-\boldsymbol{k}}$ in Eq. (2.7), respectively [9]. At this point, the classification of mean-field Hamiltonians in arbitrary d and for arbitrary symmetry classes has become a mathematically well-defined problem that can be elegantly solved using the K-theory approach of Ref. [257]. We will not discuss this method and just refer to the review [7] for an introduction. The result can be found in Table 2.1 which shows that, in addition to the $\mathbb{Z}$ topological invariants, there are also $\mathbb{Z}_2 = \{-1, 1\}$ (which forms a group with respect to multiplication) invariants $\nu_{\mathbb{Z}_2}$. This means that systems can only be either trivial $\nu_{\mathbb{Z}_2} = 1$ or topological $\nu_{\mathbb{Z}_2} = -1$ and all topological phases are homotopically equivalent.

In the following we will discuss how the topological invariants can be calculated for a given model $H_{\boldsymbol{k}}$ which will, as a byproduct, also provide us with understanding of some additional entries in Table 2.1. To motivate and illustrate the expressions for the invariants, let us first introduce an explicit model that will also guide our intuition for the subsequent considerations.

1D toy model. To present a simple, yet nontrivial, example we take a two-band model in 1D and expand the Hamiltonian in Pauli matrices τ_μ according to $h_k = \sum_{\mu=0}^3 g_\mu(k)\tau_\mu$. Assume that this model belongs to class BDI and, hence, obeys a TRS and PHS with $\Theta^2 = \mathbb{1}$ and $\Xi^2 = \mathbb{1}$. Taking, e.g., $\Theta = \mathcal{K}$ and $\Xi = \tau_1\mathcal{K}$ the Hamiltonian must have the form

$$h_k = g_2(k)\tau_2 + g_3(k)\tau_3, \qquad g_2(k) = -g_2(-k), \quad g_3(k) = g_3(-k). \tag{2.8}$$

A concrete model with this structure is provided by the Kitaev chain [258] which describes spinless fermions on a 1D lattice with p-wave superconducting pairing. Using $\hat{c}_j$ and $\hat{c}_j^\dagger$ to denote the fermionic annihilation and creation operator on site j, the Hamiltonian reads

$$\hat{H} = -\frac{1}{2}\sum_{j=1}^{N-1}\left(t\hat{c}_j^\dagger\hat{c}_{j+1} - \Delta\hat{c}_j\hat{c}_{j+1} + \mathrm{H.c.}\right) - \mu\sum_{j=1}^{N}\hat{c}_j^\dagger\hat{c}_j, \tag{2.9}$$

Table 2.1: *Periodic table of topological states of matter. The notation for symmetries and invariants is explained in the main text. The parent states of the dimensional reduction procedure are indicated in bold type. The entire table is periodic as a function of d with periodicity 8 ("Bott periodicity" [7]).*

Cartan	Θ	Ξ	Π	$d=1$	$d=2$	$d=3$	$d=4$	$d=5$	$d=6$	$d=7$	$d=8$
A	0	0	0	0	$\mathbb{Z}$	0	$\mathbb{Z}$	0	$\mathbb{Z}$	0	$\mathbb{Z}$
AIII	0	0	1	$\mathbb{Z}$	0	$\mathbb{Z}$	0	$\mathbb{Z}$	0	$\mathbb{Z}$	0
AI	+1	0	0	0	0	0	$\mathbb{Z}$	0	$\mathbb{Z}_2$	$\mathbb{Z}_2$	$\mathbf{\mathbb{Z}}$
BDI	+1	+1	1	$\mathbf{\mathbb{Z}}$	0	0	0	$\mathbb{Z}$	0	$\mathbb{Z}_2$	$\mathbb{Z}_2$
D	0	+1	0	$\mathbb{Z}_2$	$\mathbf{\mathbb{Z}}$	0	0	0	$\mathbb{Z}$	0	$\mathbb{Z}_2$
DIII	−1	+1	1	$\mathbb{Z}_2$	$\mathbb{Z}_2$	$\mathbf{\mathbb{Z}}$	0	0	0	$\mathbb{Z}$	0
AII	−1	0	0	0	$\mathbb{Z}_2$	$\mathbb{Z}_2$	$\mathbf{\mathbb{Z}}$	0	0	0	$\mathbb{Z}$
CII	−1	−1	1	$\mathbb{Z}$	0	$\mathbb{Z}_2$	$\mathbb{Z}_2$	$\mathbf{\mathbb{Z}}$	0	0	0
C	0	−1	0	0	$\mathbb{Z}$	0	$\mathbb{Z}_2$	$\mathbb{Z}_2$	$\mathbf{\mathbb{Z}}$	0	0
CI	+1	−1	1	0	0	$\mathbb{Z}$	0	$\mathbb{Z}_2$	$\mathbb{Z}_2$	$\mathbf{\mathbb{Z}}$	0

where the real constants t, Δ and μ are the hopping amplitude, superconducting pairing strength and chemical potential, respectively. Although this model looks quite artificial, we will see in Sec. 2.2.2 that it can be effectively realized in a condensed matter setup. Let us first study the system on a ring, i.e., with periodic boundary conditions, and in the limit $N \to \infty$. Transforming to momentum space, $j \to k \in \mathcal{M} \cong \mathbb{S}_1$, and introducing Nambu spinors $\hat{\Psi}_k^\dagger = (\hat{c}_k^\dagger, \hat{c}_{-k})$ the Hamiltonian can be cast in quadratic form $\hat{H} = \sum_k \hat{\Psi}_k^\dagger h_k \hat{\Psi}_k$. The BdG Hamiltonian h_k has the form of Eq. (2.8) with $g_2(k) = \Delta \sin(k)$ and $g_3(k) = -t\cos(k) - \mu$ which proves that the system belongs to class BDI.

In the basis where the chiral symmetry operator $\Pi = \Theta\Xi = \tau_1$ is diagonal, any h_k in Eq. (2.8) and its flat-band Hamiltonian Q_k become off-diagonal as in Eq. (2.7) and $q_k = -e^{i\theta(k)}$ where $e^{i\theta(k)} = (g_3(k) + ig_2(k))/E_{k+}$ with $E_{k\pm} = \pm\sqrt{g_3^2(k) + g_2^2(k)}$ denoting the spectrum of h_k. We now see explicitly that $q_k^* = q_{-k}$ as anticipated above.

In this simple model, $q_k = -e^{i\theta(k)}$ just defines a mapping $\mathbb{S}_1 \to \mathbb{S}_1$ which can be classified by an integer since $\pi_1(\mathbb{S}_1) = \mathbb{Z}$. This integer is a winding number $\nu_{\mathbb{Z}}$ measuring the number of times $\theta(k)$ winds around upon k traversing the Brillouin zone once. Algebraically, the winding number can be written as

$$\nu_{\mathbb{Z}} = \frac{1}{2\pi}\int_{-\pi}^{\pi} \mathrm{d}\theta(k) = \frac{1}{2\pi i}\int_{-\pi}^{\pi} \mathrm{d}k\, q^{-1}\partial_k q. \tag{2.10}$$

In case of the Kitaev model, the winding number is either 0 or ± 1 depending on whether $|\mu| > t$ or $|\mu| < t$ as can be seen in Fig. 2.1(a) and (b), respectively. As is directly clear geometrically, the winding number cannot be modified upon adiabatic deformations of the Hamiltonian. Only when the gap closes such that $E_{k+} = 0$ for some k, the phase $\theta(k)$ is not well defined at this point allowing for a change in $\nu_{\mathbb{Z}}$. Consequently, $\nu_{\mathbb{Z}}$ is a topological index. Furthermore, it holds $\nu_{\mathbb{Z}} = 0$ for $t = \Delta = 0$ which identifies $\nu_{\mathbb{Z}} = 0$ and $\nu_{\mathbb{Z}} \neq 0$ as topologically trivial and nontrivial, respectively.

Generalization. Having established the form (2.10) of the winding number, the generalization to systems with more than two orbitals, where q_k is a matrix, proceeds naturally by taking the trace

of the integrand [247]. More generally, the winding number associated with the nontrivial homotopy groups $\pi_{2N+1}(U(n)) = \mathbb{Z}$, $N \in \mathbb{N}$, of $U(n)$ relevant for systems with chiral symmetry as discussed above, is given by [247]

$$\nu_{2N+1} = \frac{(-1)^N N!}{(2N+1)!}\left(\frac{1}{2\pi i}\right)^{N+1}\int_{\mathcal{M}} \mathrm{d}^{2N+1}k\, w_{2N+1}[q], \quad w_d[q] = \epsilon_{\mu_1\ldots\mu_d}\mathrm{tr}\left[(q^{-1}\partial_{k_{\mu_1}}q)\cdots(q^{-1}\partial_{k_{\mu_d}}q)\right], \tag{2.11}$$

where $\epsilon_{\mu_1\ldots\mu_d}$ denotes the d-dimensional totally antisymmetric tensor. Eq. (2.11) can be seen as the antisymmetrized and properly normalized generalization of Eq. (2.10).

Whether this invariant is forced to be zero by additional antiunitary symmetries depends on the dimensionality $d = 2N+1$ and on the symmetry class. E.g., the constraint $q_{\boldsymbol{k}}^T = -q_{-\boldsymbol{k}}$ in class DIII leads to the symmetry $w_{2N+1}[q_{\boldsymbol{k}}] = (-1)^{N+1}w_{2N+1}[q_{-\boldsymbol{k}}]$ of the winding density [247]. Consequently, Eq. (2.11) can have nonzero values only for odd N, i.e., for $d = 3, 7, \ldots$ in accordance with Table 2.1. Note that this does not automatically imply that there are no topologically nontrivial DIII states possible in other dimensions since antiunitary symmetries can also protect the deformation into the vaccum state. Indeed, inspection of Table 2.1 shows that $\mathbb{Z}_2$ invariants exist in $d = 1, 2$. A very convenient way to understand this and to derive expressions for the invariants proceeds by a Kaluza-Klein-like [259, 260] dimensional reduction approach as has first been suggested in this context in Ref. [256]. The $\mathbb{Z}_2$ phases can then be understood as lower-dimensional symmetry-protected descendants of the parent $\mathbb{Z}$ states (indicated in bold type in Table 2.1) in the same symmetry class. In Sec. 2.2.3, we will illustrate this procedure for class DIII.

For an extension of our current analysis to all symmetry classes we refer to Ref. [247] and continue with discussing the physics at the boundary between topologically distinct phases.

2.1.3 Bulk boundary correspondence

We start again with the Kitaev chain model (2.9) which we now study with open boundary conditions, i.e., surrounded by vacuum. This can be done very conveniently [258] by decomposing every fermionic operator into its hermitian and antihermitian part, $\hat{c}_j = (\hat{\gamma}_{2j-1} + i\hat{\gamma}_{2j})/\sqrt{2}$ where $\hat{\gamma}_j$ satisfy

$$\hat{\gamma}_j^\dagger = \hat{\gamma}_j, \qquad \{\hat{\gamma}_j, \hat{\gamma}_{j'}\} = \delta_{jj'} \tag{2.12}$$

to preserve the fermionic commutation relations. Eq. (2.9) then becomes

$$\hat{H} = \frac{i}{2}\sum_{j=1}^{N-1}\Big((t-\Delta)\hat{\gamma}_{2j}\hat{\gamma}_{2j+1} - (t+\Delta)\hat{\gamma}_{2j-1}\hat{\gamma}_{2j+2}\Big) - \mu\sum_{j=1}^{N}\left(\frac{1}{2} + i\hat{\gamma}_{2j-1}\hat{\gamma}_{2j}\right). \tag{2.13}$$

Let us now consider two isolated parameter configurations. Firstly, for $\Delta = t = 0$ and $\mu < 0$, which belongs to the topologically trivial phase according to our discussion above (see Fig. 2.1(a)), we see that only $\hat{\gamma}_j$ associated with the same original fermionic operator are coupled as illustrated in Fig. 2.1(c). The system has a unique ground state given by the vaccum of the $\hat{c}_j$ operators.

Secondly, for the topological configuration $\Delta = -t$ and $\mu = 0$ with a nontrivial winding as in Fig. 2.1(b), only operators $\hat{\gamma}_j$ belonging to neighboring sites are coupled in Eq. (2.13) as shown in Fig. 2.1(d). Most importantly, the outermost operators $\hat{\gamma}_1$ and $\hat{\gamma}_{2N}$ do not enter the Hamiltonian. They describe localized zero energy modes and satisfy the reality constraint and commutation relations in Eq. (2.12) which are the defining properties of *Majorana bound states* (MBSs). The name refers to E. Majorana who showed in 1937 that the Dirac equation also allows for real solutions [57] and, hence,

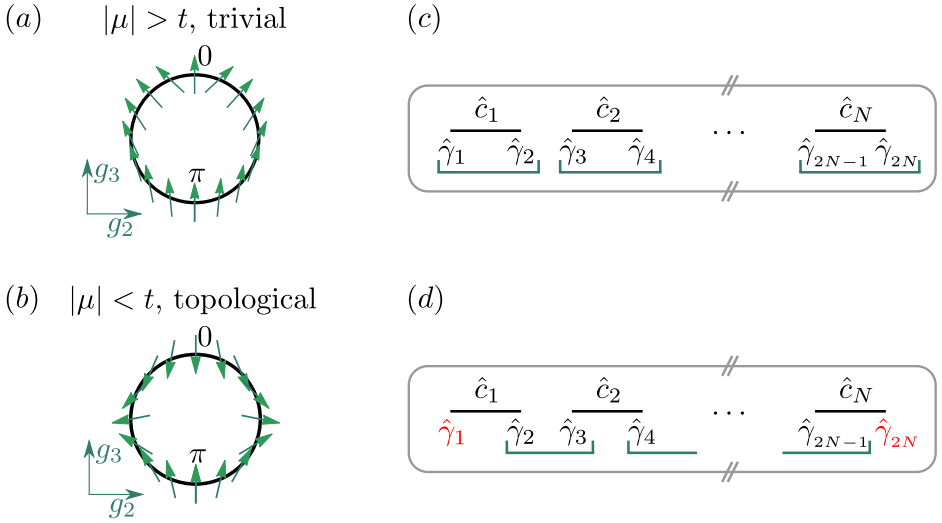

Figure 2.1: ***Kitaev chain.*** *Depending on the parameters of the Hamiltonian, the vector* $(g_2(k), g_3(k))$ *is characterized by a trivial (a) or a nontrivial (b) winding number. As explained in the main text, this leads, respectively, to the absence (c) or presence (d) of MBSs (shown in red) at the ends of the wire.*

for free fermionic particles that are their own antiparticles. The presence of these modes leads to a twofold degeneracy of the ground state of the system which is most easily seen by combining $\hat{\gamma}_1$ and $\hat{\gamma}_{2N}$ into an ordinary complex fermion $\hat{a} = (\hat{\gamma}_1 + i\hat{\gamma}_{2N})/\sqrt{2}$ which can be occupied without changing the total energy. It is crucial that, as opposed to our original decomposition of the fermion operators $\hat{c}_j$ to arrive at Eq. (2.12), the two constituents of $\hat{a}$ are spatially separated making $\hat{a}$ are thermodynamically nonlocal object. This has fascinating consequences as will be discussed in Sec. 2.3. For other parameter configurations within the topological phase ($|\mu| < t$, $\Delta \neq 0$) the MBSs will generically not be localized at a single site but rather decay exponentially [258] into to the bulk. For finite distances between different MBSs this leads to an exponentially small energetic splitting.[6]

The presence of zero-energy modes at the interface between two topologically distinct phases not only holds for the Kitaev model but is a general phenomenon known as *bulk-boundary correspondence* [4, 262]. Whether the edge modes are real Majorana modes or complex, i.e., of Dirac type, depends on whether the symmetry class has a PHS (naturally occurring in the BdG formalism of superconductivity) or not (e.g., in a topological insulator, see Sec. 2.2.1).

The bulk-boundary correspondence can be intuitively understood in the limit where the length-scales of the bulk system (e.g., the Fermi wavelength) are much smaller than the length scales on which the parameters $X = X(x_\perp)$ of the Hamiltonian vary along the coordinate $x_\perp$ perpendicular to the boundary to describe the interface between the topologically distinct phases. Then the variation of X across the boundary can be understood as a continuous deformation of the associated bulk Hamiltonian $h_{\boldsymbol{k}}[X(x_\perp)]$. By definition, the gap of $h_{\boldsymbol{k}}[X(x_\perp)]$ must close at the configuration $X(0)$ at the interface $x_\perp = 0$ which corresponds to the presence of localized zero energy modes. In case of a symmetry

[6] Typically, the decay length of the wavefunctions will be of order of the superconducting coherence length ξ and, hence, the splitting will be proportional to $\propto \exp(-L/\xi)$ where L is the distance between the MBSs (see, e.g., Ref. [261] for a demonstration of the overlap-induced splitting in a more complicated model).

class with PHS (see Eq. (2.2)), the positive energy ($E > 0$) eigenstates ψ_E can be related to those with negative energy via $\psi_{-E} = \Xi\psi_E$. If there is a single isolated zero-energy mode ψ_0, it must hold $\Xi\psi_0 = \psi_0$ which is the defining property of a MBS.

The validity of the bulk-boundary correspondence can be checked either by explicit calculation of the edge modes in a given model[7] or by proving the associated "index theorems" (see, e.g., Refs. [263–267]).

2.1.4 Weak invariants

As already mentioned above, the torus $\mathbb{T}_d$, which is the base manifold $\mathcal{M}$ of the mapping defined by $Q_{\boldsymbol{k}}$ for a d-dimensional system with lattice translation symmetry, generally allows for more topological indices than determined by the d-th homotopy group π_d which refers to $\mathbb{S}_d$ as base manifold. Additional invariants are possible if one of the lower dimensional homotopy groups π_{d-1}, π_{d-2}, ... π_1 are nontrivial [247, 257]. By design these additional invariants are only defined if the system is translation invariant which shows that the associated topological features such as edge states are not protected against local perturbations that preserve the "extremely generic symmetries" of the symmetry class. For this reason they are referred to as *weak invariants* as opposed to the *strong invariants* associated with π_d which are still well-defined if translation symmetry is absent ($\mathcal{M} = \mathbb{S}_d$) and lead to boundary modes that are protected against disorder [9, 10].

Generally, weak indices of "codimension" k can be seen as strong invariants defined in $d-k$ dimensional submanifolds of $\mathbb{T}_d$ and, hence, their existence is directly read off from Table 2.1 [247]. We will illustrate this for two examples that will be important later.

3D topological insulators. Let us start with a 3D model of class AII, i.e., with TRS and $\Theta^2 = -\mathbb{1}$, which is usually referred to as 3D topological insulator (see Sec. 2.2.1 below). From Table 2.1, we see that there is a $\mathbb{Z}_2$ strong invariant, denoted by ν_0 in the following, and weak $\mathbb{Z}_2$ invariants of codimension 1. The latter can be defined as the 2D strong invariants ν_j, $j = 1, 2, 3$, of symmetry class AII of the Hamiltonian restricted to the time-reversal invariant planes $k_j = \pi$ with $\nu_j = 0$ ($\nu_j = 1$) referring to trivial (topological). Taken together, an insulating 3D system of class AII is on the lattice classified by the four $\mathbb{Z}_2$ invariants $(\nu_0; \nu_1, \nu_2, \nu_3)$ [253–255]. The weak topological insulator (WTI) is characterized by $\boldsymbol{\nu} = (\nu_1, \nu_2, \nu_3) \neq 0$ and $\nu_0 = 0$ while it holds $\nu_0 = 1$ for a strong topological insulator (STI). Intuitively, the WTI can be thought of as a stack of weakly coupled nontrivial 2D AII insulators where (ν_1, ν_2, ν_3) are the Miller indices of the orientation of the layers.

At the edge of the system, say perpendicular to the z direction, e.g., $\nu_1 = 1$ implies the presence of an odd number of time-reversed partners (also known as *Kramers partners*) of edge modes crossing the Fermi level at $k_1 = \pi$. In Chap. 3 we will see this explicitly.

Another, more surprising, consequence of nonzero weak invariants $\boldsymbol{\nu} \neq 0$ is the emergence of 1D counter-propagating Kramers partners of zero-energy modes at dislocation lines given that $\boldsymbol{\nu} \cdot \boldsymbol{b}$ is odd [268]. Here $\boldsymbol{b}$ denotes the Burgers vector of the dislocation in the basis of the primitive vectors of the lattice. The presence of these modes bound to the 1D defect can be understood from a generalized form of the bulk boundary correspondence outlined above [247, 269]: An r dimensional topological defect of a given symmetry class is capable of binding zero modes if there is a nontrivial invariant in Table 2.1 of the same symmetry class in $d = r + 1$ dimensions. For the boundary of a system it holds $r = d - 1$ which reduces to the case discussed in Sec. 2.1.3. For the dislocation line we have $r = 1$ and, hence,

[7] We refer to the textbook [262] for the analysis of edge modes in many different models of topological insulators and superconductors.

the presence or absence of modes is determined by the ($d = 2$) $\mathbb{Z}_2$ index in class AII which corresponds to the weak indices of a 3D topological insulator.

Time-reversal invariant superconductors. As an example with weak invariants in 2D, let us consider a class DIII system which will later be relevant realized as a time-reversal symmetric superconductor (see also Sec. 2.2.3). As can be read off from Table 2.1, this system is in 2D characterized by a strong $\mathbb{Z}_2$ invariant $\nu_{\mathbb{Z}_2}$ and two weak invariants $\boldsymbol{\nu} = (\nu_1, \nu_2)$ that are defined as 1D strong DIII invariants in the time-reversal invariant lines $k_j = \pi$ [247, 270]. Similarly as above, Kramers pairs of isolated MBSs occur at dislocations with Burgers vector $\boldsymbol{b}$ if $\boldsymbol{\nu} \cdot \boldsymbol{b}$ is odd [247, 269, 270].

2.2 Experimental realization of topological phases and further models

The purpose of this section is to provide a brief overview of different physical realizations of topological states of matter that will help the reader understand the context of the models and systems we will encounter in the subsequent chapters. For a more complete discussion we refer to the textbook [262], the review articles [4, 6] and the references of the different subsections below.

2.2.1 Topological insulators

The first solid-state example of a topological state of matter in the sense introduced above is given by the quantum Hall effect discovered in 1980 [2]. The quantum Hall effects occurs when electrons are confined to 2D and subjected to a strong magnetic field perpendicular to the plane of the system. It is characterized by plateaus in the Hall conductivity σ_{xy} at quantized values $\sigma_{xy} = \nu_{\mathbb{Z}} e^2/h$ with $\nu_{\mathbb{Z}} \in \mathbb{Z}$. Using linear response theory, it has been shown [3] that $\nu_{\mathbb{Z}}$ is given by a topological invariant (first Chern number) of the bands below the chemical potential, which naturally explains the robust quantization of σ_{xy}. This invariant, often referred to as TKNN invariant after the authors of Ref. [3], mathematically classifies the mapping in Eq. (2.6) (for $d = 2$) and corresponds to the $\mathbb{Z}$ invariant of class A in 2D (see Table 2.1). The bulk-boundary correspondence guarantees the presence of $\nu_{\mathbb{Z}}$ chiral edge modes at the boundary of the system[8] which can be, in the context of the quantum Hall effect, understood as skipping cyclotron orbits [4].

In 2005, C. Kane and G. Mele pointed out, initially considering graphene as an example [271, 272], that the quantum Hall effect has a natural time-reversal symmetric analogue which is known as the quantum spin Hall (QSH) effect. Most intuitively, it can be seen as two time-reversed copies of the quantum Hall effect and is, thus, characterized by a vanishing charge Hall conductance but has a quantized spin Hall conductance defined as the difference of the Hall conductance of the two time-reversed blocks of the Hamiltonian. As can be seen in Table 2.1 (class AII, $d = 2$), the system is classified by a $\mathbb{Z}_2$ index ν distinguishing between the topologically trivial ($\nu = 0$) state and the topological QSH ($\nu = 1$) phase which are characterized by an even and odd number of Kramers partners of edge modes, respectively. The QSH state has been predicted [252] to occur in HgTe quantum wells and subsequently discovered experimentally in these systems [273].

For future reference, let us briefly discuss the model introduced in Ref. [252] for describing the topological phase transition in HgTe quantum wells, which became known as the Bernevig-Hughes-Zhang (BHZ) model in honor of the authors of the seminal paper. Using symmetry arguments, they

[8] More precisely, $\nu_{\mathbb{Z}}$ only determines the difference in the number of left and right movers [4].

deduced the effective low-energy Hamiltonian of the system

$$h_{\boldsymbol{k}} = \begin{pmatrix} h_0(\boldsymbol{k}) & 0 \\ 0 & h_0^*(-\boldsymbol{k}) \end{pmatrix}, \qquad h_0(\boldsymbol{k}) = \sum_{\mu=0}^{3} g_\mu(\boldsymbol{k})\tau_\mu, \qquad \boldsymbol{g} = (g_1, g_2, g_3) = (Ak_1, Ak_2, m) + \mathcal{O}(k^2), \tag{2.14}$$

valid in the vicinity of the Γ point. The different components in Eq. (2.14) refer to different quantum well eigenstates which are not of importance for the present discussion. The relation between the upper and lower 2×2 block results from TRS. Note that $g_0(\boldsymbol{k})$ has not been specified in Eq. (2.14) as it does not enter the expression for the topological invariant. BHZ argued that the topological invariant ν changes, i.e., that a topological phase transition occurs, when the mass m changes sign. This can be understood geometrically by considering the winding of the normalized vector $\boldsymbol{g}/|\boldsymbol{g}|$ on the Brillouin zone similarly to our discussion of the Kitaev model in Fig. 2.1(a) and (b).

In 2007, the topological classification of insulators has been extended to 3D in Refs. [253–255]. As we have already discussed in Sec. 2.1.4, a 3D topological insulator of class AII is characterized by four $\mathbb{Z}_2$ invariants $(\nu_0; \nu_1, \nu_2, \nu_3)$ where ν_0 is the strong and ν_j, $j = 1, 2, 3$, are the weak invariants. Since then, several materials have been experimentally identified as 3D topological insulators (see Ref. [4] and references therein).

2.2.2 TRS-breaking topological superconductors

In Sec. 2.1.2 we have already introduced the Kitaev chain model as a minimal model of a topological superconductor. Given that electrons carry spin and that there only very few p-wave superconductors, it is not obvious how it can be realized experimentally. As a consequence of the enormous interest in topological superconductivity and the related MBSs, several proposal have been published recently (see [6] and references therein). In one of the most promising proposals [274, 275], a semiconducting nanowire with strong SOC and a large g-factor, such as InSb or InAs, is brought into a magnetic field that breaks physical spin-1/2 TRS[9] effectively rendering the system spinless at low-energies. The proximity to an s-wave superconductor induces superconductivity in the wire which is transformed in p-wave pairing by virtue of the SOC. A transition between topologically trivial and nontrivial can be induced, e.g., by changing the magnetic field.

Promising experimental progress has been recently achieved along these lines [60] and in related setups [61] where zero bias peaks in spectroscopic measurements indicate the presence of MBSs.

The prototype model of a TRS-breaking 2D topological superconductor is the spinless chiral p-wave superconductor with Hamiltonian [6, 262]

$$\hat{H} = \int \mathrm{d}\boldsymbol{x} \left[\hat{c}^\dagger \left(-\frac{\boldsymbol{\nabla}^2}{2m} - \mu \right) \hat{c} - \left(\frac{\Delta}{2} \hat{c}^\dagger (\partial_{x_1} + i\partial_{x_2}) \hat{c}^\dagger + \mathrm{h.c.} \right) \right], \tag{2.15}$$

where we used a continuum description. It belongs to class D and is, hence, characterized by a $\mathbb{Z}$ invariant $\nu_{\mathbb{Z}}$ (see Table 2.1) which can, similarly as in case of the Kitaev model, be seen as the number of times the unit vector associated with its 2×2 BdG Hamiltonian covers $\mathbb{S}_{d=2}$ [6, 262]. For the explicit form of the model given in Eq. (2.15), one finds $\nu_{\mathbb{Z}} = 0$ for $\mu < 0$ and $\nu_{\mathbb{Z}} = 1$ for $\mu > 0$ corresponding to

[9] There is an emergent TRS with $\Theta^2 = \mathbb{1}$ as long as we consider a single-channel wire [276]. In Chap. 4.7.1, we will see how this also naturally emerges in a 2D system in the presence of a strong (in-plane) magnetic field.

the trivial and topological phase, respectively. The topological phase is characterized by the presence of gapless chiral Majorana modes [190, 262]. In addition, isolated zero-energy MBSs are localized in vortices with odd winding number n [277], i.e., spatially dependent order parameter configurations $\Delta(r,\varphi) = |\Delta|(r)e^{in\varphi}$, $n \in \mathbb{Z}$, with r, φ denoting polar coordinates with respect to the center (vortex core) of the defect where the order parameter vanishes.

As already discussed in Chap. 1.3.2, the bulk superconducting phase of Sr_2RuO_4 is believed to be a chiral p-wave state. However, the finite current associated with the resulting chiral modes localized at the boundary of the system [190] seems to be absent in experiment [191, 192]. The observation of MBSs at vortex cores is more complicated as Sr_2RuO_4 is a spinfull system, i.e., effectively consists of two copies of Eq. (2.15). Therefore, a vortex binds a pair of MBSs that will eventually hybridize and move to finite energies[10]. For this reason one should rather investigate half-quantum vortices which can be shown to be equivalent to an $n = 1$ vortex for only one of the spin-components [58] and, hence, binding just a single Majorana zero mode. Many more systems have been proposed to effectively realize a chiral p-wave state (see Ref. [6] and references therein).

2.2.3 Time-reversal invariant topological superconductors

Instead of taking two copies of Eq. (2.15) with the same chirality, one can combine two time-reversed copies of Eq. (2.15) which defines the simplest model of a *time-reversal symmetric* or *helical* topological superconductor [262, 278, 279]. This theoretical construction obviously closely parallels the construction of the QSH effect from the quantum Hall system discussed in Sec. 2.2.1. Time-reversal symmetric superconductors belong to class DIII and are characterized by a $\mathbb{Z}$ invariant $\nu_{\mathbb{Z}}$ in 3D and a $\mathbb{Z}_2$ invariant $\nu_{\mathbb{Z}_2}$ in 2D and 1D as can be read off in Table 2.1. The hallmark of the topological phase ($\nu_{\mathbb{Z}} \neq 0$, $\nu_{\mathbb{Z}_2} = -1$) is the presence of Kramers partners of Majorana modes at the boundary of the system to a trivial phase ($\nu_{\mathbb{Z}} = 0$, $\nu_{\mathbb{Z}_2} = 1$).

Simplified mean-field invariants. Being frequently used in the subsequent chapters, we next discuss the simplified expressions for these topological invariants derived in Ref. [280] and, as a byproduct, illustrate the method of dimensional reduction [256].

As we have argued in Sec. 2.1.2, the $\mathbb{Z}$ topological invariant of a 3D DIII system is given by Eq. (2.11) (with $N = 1$) where $q_{\boldsymbol{k}}$ is the off-diagonal component of the flat-band Hamiltonian in Eq. (2.7). Using the eigenstates $\{|\psi_{\boldsymbol{k}s}\rangle\}$ of the normal state mean-field Hamiltonian $h_{\boldsymbol{k}}$ with corresponding energies $\epsilon_{\boldsymbol{k}s}$ as basis, one can write [280]

$$q_{\boldsymbol{k}} \sim \sum_s e^{i\theta_s(\boldsymbol{k})} |\psi_{\boldsymbol{k}s}\rangle \langle\psi_{\boldsymbol{k}s}|, \qquad e^{i\theta_s(\boldsymbol{k})} = \frac{\epsilon_{\boldsymbol{k}s} + i\widetilde{\Delta}_s(\boldsymbol{k})}{|\epsilon_{\boldsymbol{k}s} + i\widetilde{\Delta}_s(\boldsymbol{k})|}, \qquad \widetilde{\Delta}_s(\boldsymbol{k}) \equiv \langle\psi_{\boldsymbol{k}s}|\Delta(\boldsymbol{k})T^\dagger|\psi_{\boldsymbol{k}s}\rangle, \qquad (2.16)$$

where T is the unitary part of the (normal state) time-reversal operator, i.e., normal state TRS is equivalent to $Th^*_{-\boldsymbol{k}}T^\dagger = h_{\boldsymbol{k}}$, and all matrix elements of the superconducting order parameter $\Delta(\boldsymbol{k})$ between different Fermi surfaces have been neglected. This is always justified in a system with singly degenerate Fermi surfaces (see Chap. 1.3) in the vicinity of T_c where $\Delta(\boldsymbol{k})$ is small. The denominator in the middle expression in Eq. (2.16) simply stems from the deformation of the BdG Hamiltonian into a flat-band model.

[10] Note that a vortex is a defect of dimension $r = 0$ and is, hence, characterized by a $\mathbb{Z}_2$ index in class D (see Table 2.1 and Refs. [247, 267, 269]).

Using this in Eq. (2.11) and assuming a fully gapped superconductor, one can show that

$$\nu_{\mathbb{Z}} = \frac{1}{2}\sum_s \operatorname{sign}\left(\widetilde{\Delta}_s(\boldsymbol{k}_s)\right) C_{1s}, \tag{2.17}$$

where the summation involves all disconnected Fermi surfaces and $\boldsymbol{k}_s$ is an arbitrary point on Fermi surface s. Furthermore, C_{1s} is its first Chern number,

$$C_{1s} := \frac{i}{2\pi}\int_s \mathrm{d}\omega^{jj'}\left(\langle\partial_{k_{j'}}\psi_{\boldsymbol{k}s}|\partial_{k_j}\psi_{\boldsymbol{k}s}\rangle - (j\leftrightarrow j')\right), \tag{2.18}$$

where $\mathrm{d}\omega^{jj'}$ are the surface element two forms [280]. The dependence of $\nu_{\mathbb{Z}}$ on the sign of $\widetilde{\Delta}_s$ mathematically results from the fact that it determines the direction of rotation of the phase $\theta_s(\boldsymbol{k})$ upon passing through the Fermi surface.

The analogous expressions for the $\mathbb{Z}_2$ invariant in 2D readily follow from Eq. (2.17) by dimensional reduction [256]: The very same fact, $\pi_2(\mathrm{U}(n)) = \{E\}$, that does not allow for a winding number in chiral systems in even dimensions, also guarantees the existence of a continuous interpolation $q_{\boldsymbol{k},u}$ from a trivial configuration $\mathbb{1}_n = q_{\boldsymbol{k},0}$ to the off-diagonal block of the flat-band Hamiltonian $q_{\boldsymbol{k}} = q_{\boldsymbol{k},\pi}$ we want to analyze. Properly extending the map to $u \in [-\pi,\pi]$ to satisfy TRS, $q_{\boldsymbol{k},u}$ can be regarded as a fictitious 3D system with momentum $(\boldsymbol{k},u)$ of class DIII and invariant given by Eq. (2.17). Due to the freedom in choosing the extension $q_{\boldsymbol{k},u}$, the invariant of the 2D system is only related to the parity $\nu_{\mathbb{Z}_2} = (-1)^{\nu_{\mathbb{Z}}}$ of the fictitious 3D invariant [256]. We thus get

$$\nu_{\mathbb{Z}_2} = (-1)^{\nu_{\mathbb{Z}}} = \prod_s \left[i\operatorname{sign}\left(\widetilde{\Delta}_s(\boldsymbol{k}_s)\right)\right]^{C_{1s}} = \prod_s \left[\operatorname{sign}\left(\widetilde{\Delta}_s(\boldsymbol{k}_s)\right)\right]^{m_s}, \tag{2.19}$$

where, in the last equality, use has been made of $\sum_s C_{1s} = 0$ and $(-1)^{C_{1s}} = (-1)^{m_s}$ with m_s denoting the number of time-reversal invariant momenta (TRIM) enclosed by Fermi surface s [280]. TRIM are defined as the discrete set of points in Brillouin zone with $\boldsymbol{k} \equiv -\boldsymbol{k}$. E.g., in 2D, there four nonequivalent TRIM, $(0,0)$, $(\pi,0)$, $(0,\pi)$ and (π,π).

Upon further reducing to 1D, one again finds Eq. (2.19) with $m_s \to 1$ [280] as one might have expected given that every Fermi "surface" encloses the Γ-point in a 1D system.

Candidate systems. An example of a topological super*fluid* of class DIII is provided by the Balian-Werthamer [234] state ($\boldsymbol{d}_{\boldsymbol{k}} \propto \boldsymbol{k}$ in Eq. (1.17)) that is believed to be realized in the B phase of ^{3}He [78]. The corresponding topological invariant $\nu_{\mathbb{Z}} = 1$ is readily evaluated using Eq. (2.17) as demonstrated in Ref. [280]. Recently, convincing experimental evidence for Majorana edge modes in superfluid ^{3}He has been reported [281].

However, there are no conclusive signatures of time-reversal symmetric topological super*conductivity* [246] so far. In Refs. [282, 283] it has been shown that, in a centrosymmetric system, odd parity states are good candidates for the realization of nontrivial DIII topology. However, the established p-wave superconductors, Sr_2RuO_4 and UPt_3, break TRS (see Chap. 1.3.1). One of most promising candidates [282] for topological odd parity pairing is the doped topological insulator $Cu_xBi_2Se_3$ that becomes superconducting below $\simeq 4\,\mathrm{K}$ [284]. Experiments probing the topological signatures in this system are still controversial [246].

In this thesis, we will use different approaches to study topological properties in various noncentrosymmetric systems. As we will see, the broken inversion symmetry strongly restricts the possibilities

of breaking TRS and, hence, the superconductor will quite naturally belong to class DIII. To calculate the associated topological invariants, the simplified expressions, Eqs. (2.17) and (2.19), will be very useful.

2.2.4 Cold atoms

In recent years, topological states of matter have also spurred considerable research interests in the cold-atom community [285–290]. Cold atoms [62, 63] offer an experimental platform for simulating complex many-body systems. System parameters can be tuned over wide ranges, such as the interaction strength via the phenomenon of Feshbach resonance, and various detection methods, that are not possible in the solid-state context, have been successfully applied. Naturally, an exhaustive introduction to this broad field of research is beyond the scope of this subsection. We refer instead to the review articles [62, 63] and briefly discuss the experimental realization of *artificial gauge potentials* [291] which represents an important cornerstone for the implementation of nontrivial topology in cold-atom systems.

As we have seen above, magnetic fields and SOC are crucial building blocks of topologically nontrivial states of matter. In case of neutral atoms, these effects have to be implemented in form of artificial gauge potentials [291]. This can be achieved by designing a state-dependent lattice where different internal states of the atom are spatially shifted. In the simplest case, one uses two sufficiently long-lived states of the atom and tunes the laser creating the lattice potential to the "anti-magic" wavelength where the polarizabilities of the two states are identical in magnitude but opposite in sign. Consequently, the lattice potential is shifted by half a lattice constant between the two internal states. While direct tunneling between different sites is suppressed by choosing the lattice constant sufficiently large, laser-assisted tunneling is induced by applying an additional laser that is resonant with the transition between the two internal states. Due to the spatial variation of the phase of the additional laser beam, it imprints different phases on the hopping matrix elements between different nearest neighbors. This can be used to emulate the Peierls phase associated with a magnetic field. Incorporating more internal states, it can also give rise to non-Abelian gauge potentials that mimic SOC.

In Chap. 3, we will introduce and discuss in detail a model which contains non-Abelian Peierls phases that can be realized in cold atoms and give rise to various 2D and 3D topological phases.

2.3 Majorana fermions and quantum computation

As the analysis presented in this thesis is to a large extent concerned with topological properties of superconductors, we will briefly discuss one of the most fascinating aspects of MBSs, the non-Abelian statistics they obey, and their related potential application in quantum computation. For a more in depth discussion we refer to the review [59]. This section is mainly based on the Diploma thesis [292].

2.3.1 Non-Abelian statistics

One of the most important cornerstones of many-body quantum mechanics is the underlying quantum statistics, i.e. how the wavefunction transforms when particles are interchanged. In 3D, there are only two possibilities: The many-body wavefunction has to be symmetric or antisymmetric under transposition of any two particles for a system of identical bosons or fermions, respectively. The fundamental restriction is a consequence of the fact that winding one particle around another in 3D is topologically equivalent to not performing any operation. The wavefunction must transform under a representation of the symmetric group. However, when a 2D system is considered windings are

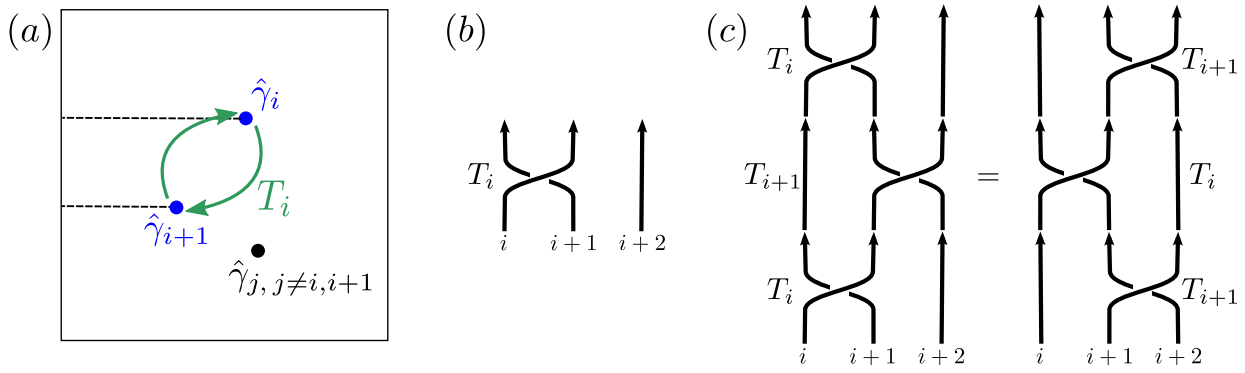

Figure 2.2: ***Non-Abelian statistics.*** *(a) Clockwise interchange of two vortices. Graphical representation of (b) the generator T_i and (c) the defining property in Eq. (2.24).*

obviously nontrivial operations such that the underlying group, the braid group to be defined below, is not finite any more which leads to a much richer spectrum of possible quantum statistics [59]. Particles with statistics other than bosonic or fermionic are called *any*ons.

The emergence of anyonic statistics and its application for quantum computing will first be discussed in the conceptually simplest case of a chiral p-wave superconductor with Hamiltonian as given in Eq. (2.15). At the end of the section, we comment on the modifications in case of time-reversal symmetric superconductors.

Suppose that $2M$ vortices (each with winding number $n = 1$ for simplicity) located at positions $\boldsymbol{R}_j$, $j = 1, 2, \ldots, 2M$ have been prepared. As already mentioned in Sec. 2.2.2, each vortex hosts a single Majorana zero mode provided that all vortices are sufficiently separated. Therefore, the local order parameter "seen" by a MBS localized at vortex j is approximately

$$\Delta(\boldsymbol{x}) \simeq |\Delta(\boldsymbol{x})| \exp(\varphi_j(\boldsymbol{x}) + \Omega_j), \quad \varphi_j(\boldsymbol{x}) = \arg(\boldsymbol{x} - \boldsymbol{R}_j), \quad \Omega_j = \sum_{k\neq j}^{2M} \arg(\boldsymbol{R}_j - \boldsymbol{R}_k), \tag{2.20}$$

i.e. a single vortex with a constant phase shift determined by the positions of all other vortices.

To derive the behavior of the many-body wavefunction under transposition of MBSs, we follow D. A. Ivanov [58] and analyze the transformation of the Majorana operators $\hat{\gamma}_j$. The localized Majorana wavefunction for a single vortex is found as the zero energy eigenstate of the BdG Hamiltonian of Eq. (2.15) with a vortex profile order parameter. According to Eq. (2.20), the presence of other vortices effectively generates a constant phase shift. Using the Nambu spinor $\hat{\Psi} = (\hat{c}, \hat{c}^\dagger)^T$ the transformation behavior of an eigenstate reads

$$\psi = (u, v)^T \to (ue^{i\Omega/2}, ve^{-i\Omega/2})^T \quad \text{for} \quad \Delta(\boldsymbol{x}) \to \Delta(\boldsymbol{x})e^{i\Omega}. \tag{2.21}$$

The global phase has been chosen such that the pseudo reality constraint $\Xi\phi_{\gamma_j} = \phi_{\gamma_j}$ with $\Xi = \tau_1\mathcal{K}$ of the Majorana solutions is preserved. This ensures that the second quantized operators $\hat{\gamma}_j$ satisfy Eq. (2.12), i.e. their defining property as Majorana operators. Furthermore, this convention makes all non-Abelian parts of the Berry phase vanish [293, 294] such that any nontrivial evolution under cyclic adiabatic manipulation of vortex positions is due to the explicit monodromy of the BdG wavefunction in Eq. (2.21).

To illustrate the consequences assume that two neighbouring vortices i and $i+1$ are clockwise interchanged without encircling another one as shown in Fig. 2.2(a). To have a single-valued superconducting phase, one needs to introduce branch cuts (black dashed lines). As can be seen from the figure, one of the vortices (here vortex $i+1$) crosses the branch cut. The corresponding jump by 2π in the superconducting phase generates an additional minus sign in $\hat{\gamma}_i$ according to Eq. (2.21). For all other vortices $j \neq i, i+1$ the process is only seen as a trivial – back and forth – phase fluctuation and hence has no net effect on the corresponding quasiparticle operators. In summary, we have found that the vortex transposition denoted by T_i leads to

$$T_i : \begin{cases} \hat{\gamma}_i & \longrightarrow \hat{\gamma}_{i+1}, \\ \hat{\gamma}_{i+1} & \longrightarrow -\hat{\gamma}_i, \\ \hat{\gamma}_j & \longrightarrow \hat{\gamma}_j, \qquad \forall\, j \neq i, i+1. \end{cases} \tag{2.22}$$

It is straight-forward to check that the transposition operations satisfy the defining relations

$$T_i T_j = T_j T_i, \qquad |i-j| > 1, \tag{2.23}$$

$$T_i T_j T_i = T_j T_i T_j, \quad |i-j| = 1. \tag{2.24}$$

of the generators of the braid group $\mathcal{B}_{2M}$ – replacing the more familiar symmetric group of quantum statistics in $(3+1)$ dimensions. The braid group can be visualized by strands wrapping around each other. An element of $\mathcal{B}_{2M}$ is defined as the equivalence class of configurations of these strands which can be smoothly deformed into one another. As an example, the elementary braiding operation T_i is shown in Fig. 2.2(b). Obviously, the group is non-Abelian since $T_i T_{i+1} \neq T_{i+1} T_i$. However, braiding operations which do not involve a common strand commute as expressed by Eq. (2.23). The nontrivial defining relation (2.24) is illustrated in Fig. 2.2(c).

To derive the quantum statistics we need to find the representation $\hat{\rho}$ of the braid group on the set of degenerate ground states. This is provided by $\hat{\rho}(T_i) = \exp(\pi \hat{\gamma}_{i+1} \hat{\gamma}_i / 2)$ since $\hat{\rho}(T_i) \hat{\gamma}_j [\hat{\rho}(T_i)]^{-1} = T_i(\hat{\gamma}_j)$. It reveals the much more complicated structure of vortex statistics compared to that of 3D bosons and fermions. Most remarkably, the operators $\hat{\rho}(T_i)$ and $\hat{\rho}(T_{i+1})$ do not commute. This means that the outcome of a sequence of transpositions depends in general on the order of the operations, i.e. vortices in a chiral p-wave superconductor obey non-Abelian statistics.

2.3.2 Topological quantum computation

In ordinary computers information is stored in a finite number of bits which can only be prepared in one of two states usually denoted by 0 and 1. The basic idea of quantum computing [295] is to use the laws of quantum mechanics for information processing. The fundamental building blocks of a quantum computer are called qubits and constitute two-level systems. A classical computer with N bits can only be in 2^N different configurations, whereas the state of its quantum mechanical analogue is generally any linear combination of all 2^N basis states and hence described by $2^N - 1$ complex numbers. Therefore, quantum entanglement provides enormous capacity compared to classical setups.

A quantum computation can be viewed as a sequence of unitary transformations on the system's Hilbert space. These transformations are called quantum gates and realized by switching on certain terms in the Hamiltonian, e.g. by applying a magnetic field. Unfortunately, at present the realization of quantum computers highly suffers from decoherence due to unintended interactions with the environment. Finite precision in the realization of quantum gates gives rise to additional errors.

These two problems can be circumvented at the "hardware level" using the concept of topological quantum computation [59]. Consider a system exhibiting quasiparticles with non-Abelian statistics such as the vortices of the chiral p-wave superconductor. The ground state manifold is chosen as the computational space, i.e. the state of the computer is given by the set of occupation numbers of the M complex fermions that can be constructed out of the $2M$ MBSs present in the system. Since the vortices can in principle be brought arbitrarily far away from each other, the information is encoded in a highly non-local way. Consequently, the system is immune to local perturbations.

To perform a proper quantum computation, gate operations are applied by adiabatically winding vortices around each other. Fortunately, the outcome of a braiding process only depends on the topology of the trajectories and not on their precise shape and dynamics as long as adiabaticity is sufficiently satisfied [292, 296–300]. Therefore, systematic gate errors are fundamentally avoided. Finally, the outcome of the computation has to be measured. This can be done, for example, by bringing vortices together. Depending on the occupation of the fermion associated with the two MBSs, a finite energy quasiparticle may or may not be left behind after the fusion process.

In addition to the plethora of open questions concerning the practical implementation of these manipulations, there are also fundamental limitations to topological quantum computations: Firstly, the lower limit on the time scales on which braiding operations can be performed resulting from the adiabaticity requirement have been analyzed [292, 296–300] and estimated to be comparable to the lower bound associated with single-electron tunneling [301]. The parameter window within which reliable topological quantum computations can be performed might thus be quite small.

Secondly, topological quantum computing using MBSs is not universal, i.e. braiding operations alone are not sufficient to realize any unitary gate transformation. In particular a $(\pi/8)$ phase gate is missing as is straightforwardly shown using the representation $\hat{\rho}(T_i)$ derived above. Apart from more elaborate schemes where the topology of the system is changed [59], this gate has to be implemented by a non-topological operation. The most evident way is to bring the MBSs close together such that the resulting energy splitting generates the required phase shift [302]. More elaborate schemes have been suggested to realize the required phase gate (see, e.g., [299, 303]).

In case of a helical superconductor (see Sec. 2.2.3), the situation is more complicated: In a time-reversal symmetric vortex, there is always a Kramers pair of MBSs [262, 266, 269, 278, 279] such that the statistics of the entire vortex becomes Abelian [278] and the vortex braiding cannot be used to perform topological quantum computations as outline above [262]. At least in the idealized case where the superconductor can be seen as two time-reversed copies of the chiral p-wave superconductor, a TRS-breaking vortex, where just one of the copies experiences a winding of the superconducting phase, hosts an isolated MBS. These vortices have non-Abelian statistics exactly as in case of a chiral p-wave superconductor [269, 278] and might thus be employed for topological quantum computation.

2.4 Beyond mean-field

The classification of topological phases presented in Sec. 2.1.2 was limited to the noninteracting case. Naturally, the question arises whether the notion of topological phases is still meaningful in the presence of interactions. By means of case studies, it has been shown that the classification stated in Table 2.1 is not stable against arbitrary interactions: In Ref. [304], an adiabatic deformation of an interacting 1D model of class BDI has been used to proof that the $\mathbb{Z}$ classification (winding number) discussed in Sec. 2.1.2 is reduced to $\mathbb{Z}_8$.

Note that our previous definition of topological invariants in terms of mean-field Hamiltonians does

not even allow for four-fermion terms of infinitesimal strength and, hence, an adiabatic extension to interacting systems constitutes a first important step. This will be the topic of Sec. 2.4.1. In this context, "adiabatic extension" means that the gapped ground state of the many-body system is singly degenerate and can be continuously deformed into a noninteracting system without closing the gap [5, 7, 305]. In Sec. 2.4.2, we will discuss an example of an interacting topological state of matter, the topological Mott insulator proposed by D. Pesin and L. Balents [64].

2.4.1 Adiabatic interactions and topological Hamiltonian approach

As one might have expected, the mean-field Hamiltonian will be replaced by the full Green's function $G(k)$, with $k \equiv (i\omega, \boldsymbol{k})$ comprising both Matsubara frequency[11] ω and (crystal) momentum $\boldsymbol{k}$, to define a mapping that can be classified topologically. Topological invariants expressed in terms of Green's function naturally occur as coefficients in *topological field theories* [256] which represent an alternative way to define topological states of matter. Topological field theories describe the low-energy response of a topological system to external perturbations such as the electromagnetic potential A_μ [5]. E.g., in even spatial dimensions d one can show by integrating out noninteracting fermions coupled to a U(1) gauge field A_μ that the perturbative expansion in A_μ contains a Chern-Simons term with prefactor [256, 306]

$$\nu[G] = C_n \int \mathrm{d}^{d+1}k\, \epsilon_{\mu_1 \ldots \mu_{d+1}} \operatorname{tr}\left[(G\partial_{k_{\mu_1}} G^{-1}) \ldots (G\partial_{k_{\mu_{d+1}}} G^{-1}) \right], \tag{2.25}$$

where C_n denotes a normalization constant. Leaving the discussion of the physical consequences of topological terms in the electromagnetic response to [5, 256, 262], we just mention that Eq. (2.25) defines a topological invariant associated with the map from $d+1$ dimensional frequency momentum space to the space of non-singular Green's functions in analogy to the winding number in Eq. (2.11). It can be shown that Eq. (2.25) still determines the electromagnetic response and, hence, constitutes a physically meaningful topological invariant in the presence of arbitrarily strong interactions as longs as the adiabaticity constraint discussed above is satisfied [305]. In addition to the 1D counterexample [304] mentioned above, adiabaticity is also not fulfilled, e.g., in the fractional quantum Hall states where interactions induce a gap in a hugely degenerate partially populated Landau level [12, 13].

Similar expressions in terms of Green's functions for classes with chiral symmetry [307] have been obtained and the symmetry protected descendants have been analyzed by means of dimensional reduction [256]. On the mean-field level, it holds $G^{-1}(k) = i\omega - H_{\boldsymbol{k}}$ and this approach reduces [5, 256, 307] to topological band theory discussed in Sec. 2.1.2. However, the Green's function method also contains effects beyond mean field [307, 308]: As directly follows from the symmetry of Eq. (2.25) under $G \leftrightarrow G^{-1}$, the topological invariant can not only change due to gap closing, i.e., poles of G, but also as a consequence of zeros of the Green's function resulting from poles in the ω-dependence of the self-energy $\Sigma(i\omega, \boldsymbol{k})$. The latter cannot be captured in a static mean-field description.

We mention that, in addition to the requirement of adiabaticity, the Green's function approach does also not take into account the potentially significantly enhanced role of interactions at the edge of the system. The protecting symmetries might be broken at the surface of the system thereby destroying the validity of the bulk boundary correspondence (see Sec. 2.1.3) in the presence of interactions.

The fact that the Green's function approach requires a frequency integration as in Eq. (2.25) to be performed, makes the evaluation of topological invariants more cumbersome and less intuitive than the mean-field approach of topological band theory. As has been shown in Refs. [309, 310], this drawback

[11] The entire discussion will be limited to $T = 0$, where Matsubara frequencies become continuous variables.

can be circumvented by constructing an effective noninteracting problem with the same topological invariants. The crucial step is to introduce an adiabatic deformation

$$G_\lambda(i\omega, \boldsymbol{k}) = (1-\lambda)G(i\omega, \boldsymbol{k}) + \lambda \left[i\omega + G^{-1}(0, \boldsymbol{k})\right]^{-1}, \qquad \lambda \in [0,1], \tag{2.26}$$

of the full Green's function $G(k) = G_{\lambda=0}(k)$ into an effective mean-field Green's function $G_{\lambda=1}(k)$ which does not change the value of topological invariants such as that of Eq. (2.25) as it does not incorporate singularities or gap closings [309, 310]. Due to the equivalence to topological band theory in the noninteracting limit [5, 256, 307], the evaluation of Green's function invariants is thus tantamount to calculating the invariant of the fictitious mean-field Hamiltonian

$$H^t_{\boldsymbol{k}} := -G^{-1}(i\omega = 0, \boldsymbol{k}), \tag{2.27}$$

also known as *topological Hamiltonian* [311], using the procedure of Sec. 2.1.2.

The counterintuitive result that the entire information about the topology of the full Green's function is contained in its $\omega = 0$ component can be qualitatively understood from the point of view of the bulk boundary correspondence [311]: The quasiparticle energies (and lifetimes) are obtained by solving for ω such that $G^{-1}(\omega)$ has an eigenvalue zero. The boundary modes, if present, are at zero energy and, hence, their existence is fully determined by $G^{-1}(\omega = 0)$. While $H^t_{\boldsymbol{k}}$ cannot be used to reliably calculate the spectrum of the system at finite energies, it can exactly determine whether the boundary of the system hosts zero modes or not.

2.4.2 Topological Mott insulator

An example of a topological phase that results from the interplay of topological band structures and significant electronic correlations is provided by the TMI[12] proposed by D. Pesin and L. Balents [64]. It is a spin-liquid state [313] in which the electron is effectively separated in its charge and spin degree of freedom. The charges undergo a Mott transition, i.e., are localized by sufficiently large electron-electron interaction, while the spin degrees of freedom of the electrons, the so-called *spinons*, are deconfined. The band structure of the spinon excitations can be classified topologically exactly as discussed in Chap. 2.1 on the noninteracting level. By definition, a TMI has a spinon Hamiltonian with a nontrivial topological invariant and, hence, is characterized by the presence of spin-only edge modes at the boundary to a topologically trivial phase such as the vacuum. If the dimensionality and symmetry class of the system allows also for weak invariants (see Sec. 2.1.4), one can further distinguish between strong topological Mott insulator (STMI) and weak topological Mott insulator (WTMI) phases. Note that although the spinon band structure can be classified using the methods of noninteracting topological phases, the TMI does not have a noninteracting analogue due to its fractionalized nature.

In Chap. 3.2.2 and Appendix B.2, we will introduce an approach, the slave-rotor mean-field theory [65–67], that conveniently allows for the description of TMI phases [64, 314]. This will place the phenomenological discussion of this subsection on quantitative grounds. While, in 2D, fluctuations are detrimental to the stability of a TMI found at the mean-field level, it is known to be stable in 3D [64, 314–316].

A TMI phase has been originally proposed to occur in Ir-based pyrochlore materials [64], but has not yet been experimentally observed. In the next chapter (see in particular Chap. 3.2), we will present a way how 3D STMI and WTMI phases can be controllably realized in a cold-atom setup.

[12] Note that the definition of TMI we use in this thesis (discussed here and in Chap. 3) crucially differs from the notion of TMI of Raghu *et al.* [312]. The definition of TMI of Ref. [312] refers to a topological insulator phase that is reached by spontaneous symmetry breaking.

Chapter 3

3 Dimensional crossover and topological Mott insulators in cold atoms

Before focusing on solid-state materials in the subsequent chapters, let us start with cold-atom systems which, from a condensed matter perspective, offer the following two possibilities: Firstly, cold atoms allow for simulating solid-state problems in a highly controllable way and, secondly, provide the opportunity to realize exotic phases that have not been found in condensed-matter systems so far [62, 63]. In this chapter, we will take advantage of both of these achievements of cold atoms and, on top of that, illustrate the basic concepts of topological invariants, the bulk-boundary correspondence and the interplay of topology and interactions discussed in the previous chapter.

In the first part, Sec. 3.1, of this chapter, we will present a minimal and experimentally feasible model of a time-reversal invariant topological insulator (class AII [249, 251]) that effectively represents a 3D generalization of an experimental cold-atom setup [285, 286, 288] for the study of 2D topological phases. By varying a single hopping parameter in the Hamiltonian, it allows to simulate the dimensional crossover from 2D QSH and topologically trivial insulating phases to 3D WTI, STI and trivial phases (see Chap. 2.1.4). The phase diagram contains a single point where all distinct phases meet.

In the second part, Sec. 3.2, we study the impact of interactions within slave-rotor theory [65–67]. While conventional on-site Hubbard terms will not lead to TMI phases (see Chap. 2.4.2), we show how the Hubbard interaction can be effectively modified in cold-atom experiments in order to make the realization of both WTMI and STMI states possible. The setup we propose thus allows for the controlled experimental analysis of these exotic spin-liquid-like phases which have not yet been seen in solid-state systems.

This chapter is based on Ref. [317].

3.1 Dimensional crossover from 2D to 3D topological phases

The starting point of our analysis is the "time-reversal invariant Hofstadter model" on the square lattice defined by the Hamiltonian [285–288]

$$\hat{H}_{\mathrm{2D}} = -\sum_{\boldsymbol{j}} \left(t\, \hat{c}^{\dagger}_{\boldsymbol{j}+\boldsymbol{e}_x} e^{2\pi i \gamma \sigma_1} \hat{c}_{\boldsymbol{j}} + t\, \hat{c}^{\dagger}_{\boldsymbol{j}+\boldsymbol{e}_y} e^{2\pi i \alpha j_x \sigma_3} \hat{c}_{\boldsymbol{j}} + \mathrm{H.c.} \right) + \lambda \sum_{\boldsymbol{j}} (-1)^{j_x} \hat{c}^{\dagger}_{\boldsymbol{j}} \hat{c}_{\boldsymbol{j}} \,, \tag{3.1}$$

where $\hat{c}_{\boldsymbol{j}} = (\hat{c}_{\boldsymbol{j}\uparrow}, \hat{c}_{\boldsymbol{j}\downarrow})$ are two-component fermionic creation operators referring to lattice site $\boldsymbol{j}$. Below we discuss both the 2D and 3D case corresponding to $\boldsymbol{j} \in \mathbb{Z}^2$ and $\boldsymbol{j} \in \mathbb{Z}^3$, respectively. The parameter

α describes the flux per plaquette of an artificial magnetic field perpendicular to the xy plane, which due to the Pauli matrix σ_3 points in opposite directions for opposite spins. It can thus be seen as two time-reversed copies of the original Hofstadter problem [318]. For $\gamma = 0$, the two spin-orientations $\uparrow$ and $\downarrow$ are decoupled while these components are mixed by the hopping term along the x direction as long as $2\gamma \notin \mathbb{Z}$. The λ term describes a staggering of the optical lattice potential along the x direction. All three terms can be experimentally implemented in cold-atom systems [285, 286, 288]. Note that the internal on-site degrees of freedom $\uparrow$ and $\downarrow$ are not realized as physical spin eigenstates of electrons but rather as suitably chosen states of the atoms used in the cold-atom experiment (see also Chap. 2.2.4).

Due to the preserved spin-1/2 TRS, the model belongs to the symmetry class AII [249, 251] (see also Chap. 2.1.1). In 2D, its phase diagram hosts topological QSH and topologically trivial normal insulator (NI) states as well as (semi)-metallic phases [285, 287]. As we have discussed in Chap. 2.2.1, the QSH phase is characterized by an odd number of helical edge states per edge, while the NI features an even number (including zero). The topological $\mathbb{Z}_2$ invariant ν (see Table 2.1) distinguishes between QSH ($\nu = 1$) and NI ($\nu = 0$) phase [271, 272]. We will focus on half filling and fixed values of $\alpha = 1/6$ and $\gamma = 1/4$, as the phase diagram as a function of the staggered potential λ already contains both gapped phases as well as semi-metallic points. As shown in Fig. 3.1(a) the 2D system is a QSH insulator for $|\lambda| < \lambda_c = 2^{1/3}t$ and becomes normal insulating for $|\lambda| > \lambda_c$ [285, 287]. The system is semi-metallic at $\lambda = 0$ hosting two doubly degenerate Dirac cones and at $\lambda = \lambda_c$ with one doubly degenerate Dirac cone.

We are interested in studying the dimensional crossover from 2D to 3D by continuously turning on a hopping parameter t_z in the third direction that couples the different 2D layers. The simplest interlayer coupling term that makes STI phases possible is of the form

$$\hat{H}_z = -t_z \sum_{\boldsymbol{j}} \left(\hat{c}^\dagger_{\boldsymbol{j}+\boldsymbol{e}_z} e^{2\pi i \alpha j_x \sigma_2} \hat{c}_{\boldsymbol{j}} + \text{H.c.} \right). \tag{3.2}$$

It contains a synthetic gauge field that represents an artificial magnetic field along the y direction, which points in opposite directions for spins aligned parallel and anti-parallel to the y axis. Such a term can be most easily implemented in an all optical realization of the lattice potential [286, 288]. Note that Eq. (3.2) respects TRS and, hence, the resulting 3D Hamiltonian $\hat{H}_{2\text{D}} + \hat{H}_z$ still belongs to class AII. As we have seen in Chap. 2.1.4, the system is characterized by four $\mathbb{Z}_2$ invariants – the three weak invariants ν_j, $j = 1, 2, 3$, and the strong invariant ν_0, which will be calculated below.

We emphasize that the dimensional crossover we investigate here is slightly different from what one would normally consider in the solid state context: In the latter case, the crossover would be realized by increasing the thickness of the material in the z direction, while we consider a geometrically fully 3D system ($\boldsymbol{j} \in \mathbb{Z}^3$) where the coupling t_z in Eq. (3.2) is continuously turned on. This is more realistic in cold-atom systems and, in addition, also eliminates the spurious oscillations of topological invariants that occur when varying the thickness in the third direction [319].

3.1.1 Effective four band model

As we have to deal with a 12-band model in 3D, some intuitive understanding is desirable. For this reason, we derive an effective theory valid in the vicinity of the point $(t_z, \lambda) = (0, \lambda_c)$ in the phase diagram of Fig. 3.1(a), where all the distinct phases meet: QSH and NI (for $t_z = 0$ and $\boldsymbol{j} \in \mathbb{Z}^2$) as well as STI, WTI, and NI (when $t_z > 0$ and $\boldsymbol{j} \in \mathbb{Z}^3$). The doubly degenerate Dirac cone at this multi-critical point is formed out of four bands, the other eight bands are well-separated from the Fermi level.

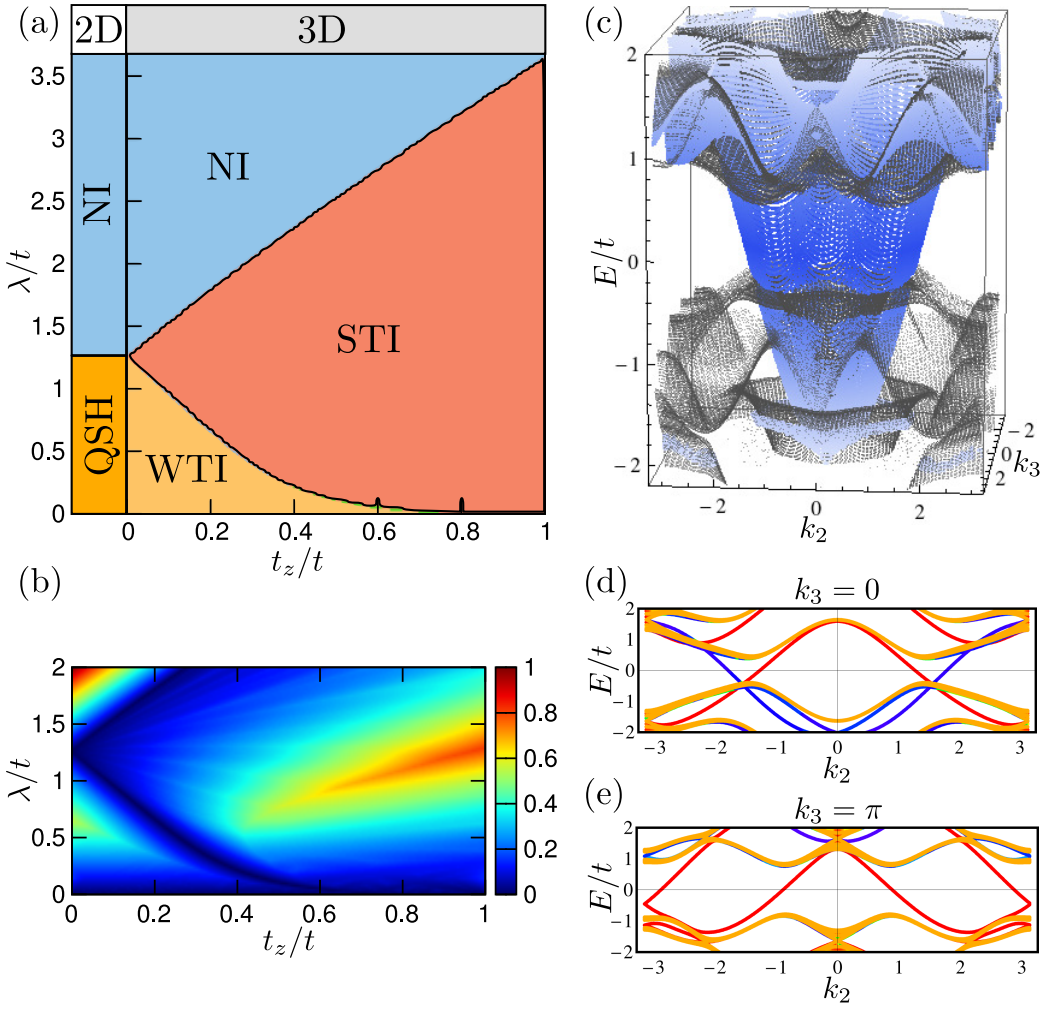

Figure 3.1: ***Phase diagram and spectra of the noninteracting model.*** *(a) 2D-3D crossover phase diagram as a function of layer coupling t_z and staggered lattice potential λ. (b) Bulk gap as a function of t_z and λ. (c) Surface state spectrum (blue) of the isotropic 3D system $t_z = t$, $\lambda = \lambda_c$ at the $x = 0$ surface as a function of momenta k_2 and k_3. Bulk states are shown as gray dots. We use open (periodic) boundary conditions along the x (y, z) direction. (d-e) One-dimensional cuts of the spectrum for fixed values of k_3. Gapless edge states localized at the $x = 0$ $(x = L)$ edge are shown in blue (red) yielding $z_0 = 1$ and $z_\pi = 0$ and thus $\nu_0 = z_0 + z_\pi = 1$.*

Neglecting corrections quadratic in t_z/t, $(\lambda-\lambda_c)/t$, and k_1, k_2, quasi-degenerate perturbation theory [87] yields the effective four-band Hamiltonian

$$h^{\text{eff}}_{i,j}(\boldsymbol{k}) = \langle\psi_{0i}|h_{\boldsymbol{k}}|\psi_{0j}\rangle\,, \quad i,j=1,\ldots,4, \tag{3.3}$$

where $h_{\boldsymbol{k}}$ denotes the full 12-component Bloch-Hamiltonian associated with the terms in Eqs. (3.1) and (3.2), $|\psi_{0j}\rangle$ are the four zero-energy eigenfunctions of $h_{\boldsymbol{k}=\boldsymbol{0}}$ at the multi-critical point. Retaining only the relevant terms linear in k_1 and k_2, Eq. (3.3) assumes the form

$$h^{\text{eff}}(\boldsymbol{k}) = \begin{pmatrix} h_0(\boldsymbol{k}) & -ic\,\tau_1 t_z \sin(k_3) \\ ic\,\tau_1 t_z \sin(k_3) & h_0^*(-\boldsymbol{k}) \end{pmatrix}, \tag{3.4a}$$

where the upper left 2×2 block is given by

$$h_0(\boldsymbol{k}) = g_i(\boldsymbol{k})\tau_i, \quad \boldsymbol{g}(\boldsymbol{k}) = \Big(-at\,k_2, bt\,k_1, m(k_3)\Big) \tag{3.4b}$$

with mass $m(k_3) = d\,[(\lambda_c/t + \lambda_c^2/t^2)t_z\cos(k_3) - \delta\lambda]$ and $\delta\lambda = \lambda - \lambda_c$. The Pauli matrices τ_i act within the 2×2 blocks in Eq. (3.4a) and a, b, c, d are positive constants. For convenience, we have chosen the basis functions such that the time-reversal operator is given by $is_2\mathcal{K}$, where the Pauli matrices s_i act between the different 2×2 blocks and $\mathcal{K}$ denotes complex conjugation. The relation between the lower and the upper diagonal blocks in Eq. (3.4a) can thus be seen as a consequence of TRS. In addition, this convention directly reveals the connection of the 2D system ($t_z = 0$) to the BHZ model [252], the paradigmatic model of a QSH state introduced in Chap. 2.2.1. We see that Eq. (3.4) with $t_z = 0$ is of the form of Eq. (2.14) which directly allows us to identify $\delta\lambda = 0$ as the boundary between QSH and NI phases. As the regime $\delta\lambda > 0$ is adiabatically connected to the topologically trivial limit $\lambda \to \infty$, the effective model reproduces the 2D phase diagram.

To continue with the 3D system, let us first emphasize that the effective Hamiltonian (3.4) is valid for the entire range $-\pi < k_3 \leq \pi$, since t_z (and not k_3) has been taken as expansion parameter. As discussed in Chap. 2.1.4, the four $\mathbb{Z}_2$ invariants ν_j, with $j = 0,1,2,3$, are defined by invariants of 2D cuts of the 3D Brillouin zone [253–255]. To determine the strong invariant $\nu_0 \equiv (z_0 + z_\pi) \bmod 2$, we need to calculate the $\mathbb{Z}_2$ invariants z_0 and z_π associated with the time-reversal invariant planes $k_3 = 0$ and $k_3 = \pi$. As Eq. (3.4) again assumes the form of the BHZ model for fixed $k_3 = 0$ and $k_3 = \pi$, we can directly conclude that the two QSH invariants z_0 and z_π differ when $m(0)m(\pi) < 0$. Therefore, the system is in the STI phase if and only if

$$|\delta\lambda| < (\lambda_c/t + \lambda_c^2/t^2)t_z \simeq 2.85\,t_z. \tag{3.5}$$

Note that, despite the fact that the mass $m(k_3)$ has to vanish somewhere between $k_3 = 0$ and $k_3 = \pi$, the Hamiltonian is still fully gapped. This is a consequence of the block-off-diagonal terms in Eq. (3.4a) that are finite for $k_3 \neq 0, \pi$. Interestingly, for $\lambda = \lambda_c$, this model allows for a transition into an STI, a phase that has no 2D analog, already for infinitesimal coupling t_z.

Being adiabatically connected to $t_z = 0$, the other two phases ($|\delta\lambda| > 2.85\,t_z$) can be easily identified from the knowledge about the 2D system. For $\delta\lambda > 2.85\,t_z$, we find an NI, whereas, in case of $\delta\lambda < -2.85\,t_z$, the system resides in a WTI phase characterized by $(\nu_0;\nu_1,\nu_2,\nu_3) = (0;0,0,1)$ [253–255].

Finally, the effective Hamiltonian also allows understanding why a spin- and position-independent hopping term along the z direction cannot result in an STI phase. Such a term would simply lead to a contribution proportional to the identity matrix in the 12-band Bloch-Hamiltonian $h_{\boldsymbol{k}}$ and thus to a term $\mathbb{1}_{4\times 4} f(k_3)$ in the effective low-energy theory (3.3). Consequently, $\boldsymbol{g}$ in Eq. (3.4b) would be independent of k_3 and hence $z_0 = z_\pi$, excluding the appearance of an STI.

3.1.2 Numerical validation

We verified our analysis of the effective model by numerically computing the $\mathbb{Z}_2$ invariant in all insulating phases of the full 12-band model using the approach of Ref. [320]. The corresponding phase diagram is illustrated in Fig. 3.1(a) and is in perfect agreement with our previous discussion. The 2D gapped QSH (NI) phase turns into a WTI (NI), but most importantly the STI phase emerges from the 2D quantum critical point. This is the only possibility for an STI to appear at infinitesimal coupling t_z as this phase is not adiabatically connected to the NI and QSH.

The bulk gap, which closes at the phase transitions, is shown in Fig. 3.1(b). It reaches its maximal value of the order of t for isotropic hopping. Computing the spectrum with open (periodic) boundary conditions along the x (y, z) direction, we clearly observe in Fig. 3.1(c) (shown for $t_z = t$) a single gapless Dirac-like surface state (in blue) localized at the $x = 0$ surface, which crosses the bulk gap (bulk bands in gray). The Dirac point is located inside the bulk bands (which is not unusual). The surface Fermi circle encloses an odd number of TRIM reflecting the non-trivial strong invariant $\nu_0 = 1$. 1D cuts of the spectrum for $k_3 = 0$ and $k_3 = \pi$ are shown in Fig. 3.1(d) and (e), respectively. We see explicitly that $m(0)$ and $m(\pi)$ have opposite signs since the parity of the number of Kramers partners of surface states on a given boundary changes from odd (QSH) to even (NI) when k_3 is tuned from $k_3 = 0$ to $k_3 = \pi$.

3.2 Interaction effects and topological Mott phases

In the second part of this chapter, we will include interactions and study whether the model introduced above can be tuned into a TMI phase. As discussed in more detail in Chap. 2.4.2, a TMI is characterized by a fractionalization into an internal and a number degree of freedom. In the TMI phase the atoms are localized, but their internal degree of freedom remains deconfined and inherits the nontrivial band topology of the original fermions.

So far, in explicit calculations, mainly the consequences of Hubbard on-site interactions

$$\hat{H}_U = U \sum_{\boldsymbol{j}} \hat{n}_{\boldsymbol{j}\uparrow} \hat{n}_{\boldsymbol{j}\downarrow}, \qquad \hat{n}_{\boldsymbol{j}\sigma} = \hat{c}^\dagger_{\boldsymbol{j}\sigma} \hat{c}_{\boldsymbol{j}\sigma}, \tag{3.6}$$

have been investigated in order to address interaction effects in topological band structures [64, 314, 321]. While this is very natural for solid state systems, the achievement of ultracold quantum gases and optical lattices allows considering interactions which cannot be realized in real materials. In the present context, this is essential since the interaction (3.6) does not lead to the sought after TMI phase within slave-rotor theory. The reason will become clear in Sec. 3.2.2 below.

3.2.1 Twisting the Hubbard interaction

As illustrated in Fig. 3.2(a), the key idea for effectively realizing an exotic interaction term is to encode the spin degree of freedom $\sigma = \uparrow, \downarrow$ spatially and use the internal atomic hyperfine states to represent the even/odd site information along x: $\mu = +$ for $j_x = 2n$ and $\mu = -$ for $j_x = 2n + 1$ with integer n. We denote the fermionic operators of the new lattice by $\hat{d}_{\boldsymbol{j}\mu}$.

As one can readily understand from Fig. 3.2(a), a local Hubbard interaction realized on the new

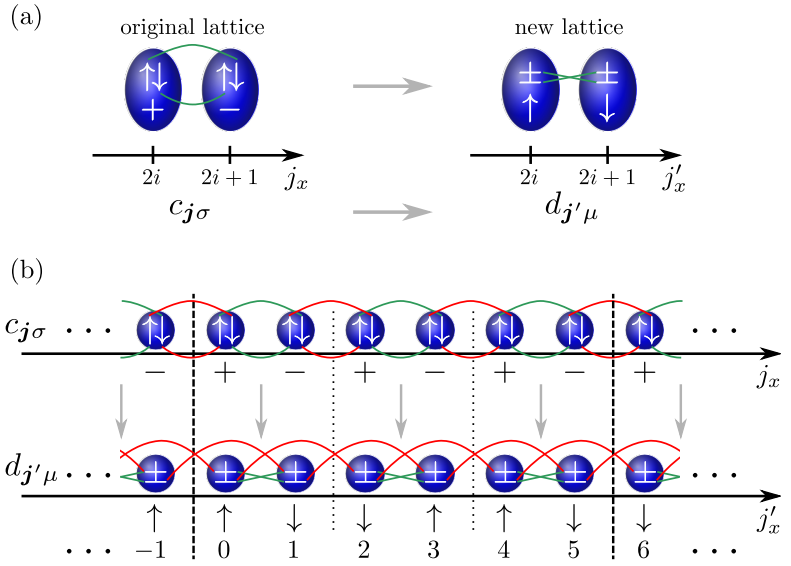

Figure 3.2: ***Twisting the Hubbard interaction.*** *Part (a) shows the relabeling of the spin σ and spatial even/odd site degree of freedom μ. To obtain an identical Hamiltonian $\hat{H}_{2D}+\hat{H}_z$ one must realize different hopping elements between nearest and next-nearest neighbor sites as illustrated in (b) for the x direction. The required hoppings along the y and z direction are described in detail in Appendix B.1.*

lattice, $\hat{H}'_U = U\sum_{\boldsymbol{j}} \hat{n}^d_{\boldsymbol{j}+}\hat{n}^d_{\boldsymbol{j}-}$, where $\hat{n}^d_{\boldsymbol{j}\mu} = \hat{d}^\dagger_{\boldsymbol{j}\mu}\hat{d}_{\boldsymbol{j}\mu}$, reads, at half filling, as

$$\hat{H}'_U = \frac{U}{2}\sum_{\boldsymbol{j},\sigma=\uparrow,\downarrow} (\hat{n}_{2j_xj_yj_z\sigma} + \hat{n}_{(2j_x+1)j_yj_z\sigma} - 1)^2 \tag{3.7}$$

in terms of the occupation numbers of the original $\hat{c}_{\boldsymbol{j}\sigma}$ fermions. Consequently, $\hat{H}'_U$ does not couple $\uparrow$-spin and $\downarrow$-spin on a given site but instead pairs of neighboring sites having the same spin orientation; the Hubbard term is twisted. As shown below, it will generate TMI phases [64] if we keep the same noninteracting Hamiltonian $\hat{H}_{2D}+\hat{H}_z$ as before. To achieve this, one needs to experimentally implement different laser induced hopping elements for the $\hat{d}_{\boldsymbol{j}\mu}$ fermions as illustrated in Fig. 3.2(b) for the x direction. Only nearest neighbor and next-nearest neighbor terms along the three spatial directions are required.

3.2.2 Interacting phase diagram within slave-rotor mean-field theory

We approach the TMI using slave-rotor theory [65–67] which starts by writing the fermion operator $\hat{d}_{\boldsymbol{j}\mu}$ as a product of number and internal degree of freedom according to

$$\hat{d}_{\boldsymbol{j}\mu} = e^{i\theta_{\boldsymbol{j}}}\hat{s}_{\boldsymbol{j}\mu}. \tag{3.8}$$

Here, $\theta_{\boldsymbol{j}}$ denote phases conjugate to the total particle number (of $\hat{d}_{\boldsymbol{j}\mu}$ fermions) on site $\boldsymbol{j}$ and $\hat{s}_{\boldsymbol{j}\mu}$ is a spinon fermion operator that carries the internal index. The system is then described by two coupled mean-field Hamiltonians: a quantum XY rotor model, which captures the number degrees of freedom,

and a renormalized noninteracting spinon Hamiltonian. As the strength of the quantum fluctuations in the rotor model is determined by the interaction U, the rotor undergoes a transition from a ferro- to a paramagnetic state as U is increased beyond a critical value U_c. This transition corresponds to the Mott transition. The spinons, on the other hand, are characterized by a band structure with renormalized parameters (set by the correlations between the rotors), that can be topologically nontrivial and carry gapless surface excitations. This means that the topological classification has again been effectively reduced to the analysis of noninteracting mean-field Hamiltonians despite the presence of strong interactions that lead to fractionalized excitations. The slave-rotor saddle-point equations can be shown to be controlled in a large-N limit [65]. In the following, we focus on the 3D limit of the system where the spin-liquid phases found on the mean-field level are known to be stable against fluctuations [64]. We leave the technical aspects of the slave-rotor approach to Appendix B.2 and proceed with the results and physical implications of the calculation.

We find that the interaction only renormalizes the hopping elements t, t_z but leaves λ unchanged. Physically, this is due to the fact that H'_U is, at half filling, not sensitive to an imbalance between $\mu = +$ and $\mu = -$. This is the reason why the Hubbard interaction had to be twisted: The usual on-site term in Eq. (3.6) would penalize the staggered density patterns induced by the λ term in Eq. (3.1). We have shown that this renormalizes λ to zero at the Mott transition within slave-rotor theory rendering the spinon spectrum gapless and, hence, excludes the possibility of a TMI state.

On top of renormalizing t and t_z, the twisted interaction (3.7) induces slight spatial anisotropies between the hopping elements as well as inhomogeneities in the six-atom unit cell. In Fig. 3.3(a) we show the interacting phase diagram as a function of U/t and t_z/t in the region of the dimensional crossover for $\lambda/t = 0.25$. The hoppings of the $\hat{d}_{\boldsymbol{j}\mu}$ fermions on the new lattice have been chosen such that their Bloch Hamiltonian is unitarily equivalent to the Bloch Hamiltonian of the $\hat{c}_{\boldsymbol{j}\sigma}$ fermions and, consequently, the $U = 0$ line reproduces a cut of the phase diagram in Fig. 3.1(a). The noninteracting phases remain stable for small interactions $U/t \lesssim 2$, but the anisotropies lead to the emergence of a correlated semi-metallic phase at intermediate $U/t \simeq 2$, where interactions induce a formation of Dirac cones.

Stronger interactions drive the system across a quantum phase transition to various Mott phases at a critical interaction strength U_c. In the Mott state, the fermionic degrees of freedom are fractionalized with charge (or number) and internal hyperfine degrees of freedom being split. While the number degrees of freedom are localized, the internal hyperfine degrees of freedom are deconfined. The resulting spinon band structure can remain topological across the Mott transition, which defines the sought after STMI and WTMI phases. The dashed lines in Fig. 3.3(a) are only a guide for the eye indicating that the different Mott phases persist for $U \gtrsim U_c$. At even larger interaction strength magnetically ordered phases are likely to emerge (not shown). Note that the various complex hopping terms lead to a rather frustrated spin exchange and we expect the onset of magnetism for $U \gg U_c$.

In Fig. 3.3(b) we present the interacting phase diagram at the critical interaction strength U_c as a function of λ/t and t_z/t to show that WTMI and STMI occupy a large part of it. These phases exhibit a bulk gap of the order of 10% of the renormalized bandwidth (see Fig. 3.3(c)). Due to the topological nature of the spinon band structure, they feature gapless spinon surface states shown in Fig. 3.3(d) and (e) which is the defining property of the TMI phases.

Note that time-reversal is in our proposal a nonlocal operation interchanging sites with even and odd j_x in the new basis of $\hat{d}_{\boldsymbol{j}\mu}$ fermions defining the experimental lattice. Clearly, this is a consequence of the fact that the transformation $\hat{c}_{\boldsymbol{j}\sigma} \to \hat{d}_{\boldsymbol{j}'\mu}$ depicted in Fig. 3.2 is nonlocal. However, on the scale of the system size, time-reversal and the mapping to the new lattice can be regarded as quasi-local

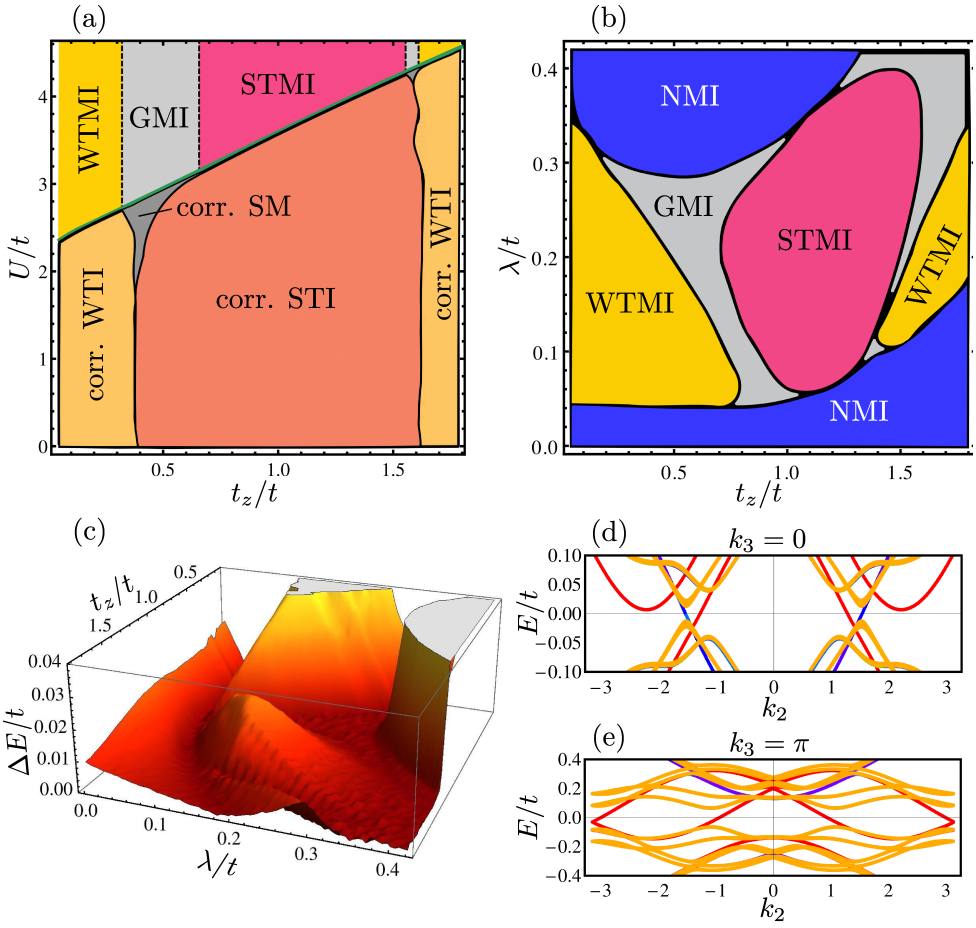

Figure 3.3: ***Properties of the interacting system according to slave-rotor theory.*** *(a) Interacting phase diagram as a function of interaction U and hopping t_z for fixed $\lambda/t = 0.25$. Upon increasing U the phases found at $U = 0$ remain mostly intact with renormalized parameters. For $t_z/t \simeq 0.4$ an extended correlated semi-metallic (SM) phase appears at $U/t \simeq 2$. At a critical value U_c/t (green line) the system enters a Mott insulating state with WTMI and STMI as well as gapless Mott insulator (GMI) phases. The GMI phase exhibits a semi-metallic spinon spectrum. Dashed lines are a guide to the eye showing that Mott phases persist for $U > U_c$. (b) Interacting phase diagram (with NMI referring to a Mott phase with trivially gapped spinon structure) and (c) bulk gap at U_c as a function of staggering λ and hopping t_z. The STMI phase occupies a large part of the phase diagram and features a significant bulk gap. (d-e) 1D cut through the spinon band structure in the STMI phase for the isotropic system $t_z = t$ and $\lambda/t = 0.15$. We use open (periodic) boundary conditions along the x (y, z) direction. Bulk states are shown in yellow, gapless spinon edge states at the $x = 0$ ($x = L$) edge are shown in blue (red).*

operations and, in particular, do not interchange surface states at distinct surfaces. Thus any quasi-local perturbation of the $\hat{d}_{\boldsymbol{j}'\mu}$ fermions is also quasi-local in the basis of $\hat{c}_{\boldsymbol{j}\sigma}$ and the surface states in the new lattice localized on a given boundary form a time-reversal symmetric electronic system. This shows that the protection [9, 10] of the surface states against localization by time-reversal symmetric disorder also holds in the present case.

3.2.3 Detection

Finally, let us also briefly discuss how the TMI phases are reflected in observable quantities. The atoms are frozen in a Mott insulating state which can be detected via standard time-of-flight measurements. The most straightforward way to detect the spinon surface states is to measure the spin-dependent spectral function. Alternatively, one might consider transport or thermodynamic quantities [322, 323]. In contrast to noninteracting topological insulators, the TMIs do not exhibit a finite "charge" (or number) response at low frequencies due to the Mott gap. The gapless spinon surface states, however, carry entropy resulting in a thermal conductivity that is linear in temperature [64] and a heat capacity that scales as $T\ln(1/T)$ [324]. Distinguishing between WTMI and STMI is possible as they feature a different number of surface states. The specific heat and thermal conductivity will thus be quantitatively different in the two phases.

3.3 Summary of Chapter 3

In summary, we have proposed a minimal model given by the Hamiltonian $\hat{H}_{\mathrm{2D}}+\hat{H}_z$ defined in Eqs. (3.1) and (3.2) with the following properties: All of its terms can be implemented in cold-atom experiments [285, 286, 288] and it allows for simulating the dimensional crossover within class AII [249, 251] from topologically trivial (NI) and nontrivial (QSH) 2D insulating phases to WTI, STI and trivial phases in 3D. The crossover is tuned by varying the hopping strength t_z in the z direction and summarized in the phase diagram given in Fig. 3.1(a). In accordance with our discussion in Chap. 2.1.4, turning on t_z adiabatically in the QSH phase can only lead to a WTI. However, right at the transition in the 2D limit between the QSH and the trivial phase, the model enters the STI phase already at infinitesimal t_z. We have seen how the topological invariants are conveniently calculated by comparison of the effective low-energy model (3.4) of the system, which is valid in the vicinity of the point in Fig. 3.1(a) where all different phases meet, with the BHZ Hamiltonian introduced in Chap. 2.2.1.

The impact of electronic repulsion on the model in the 3D limit has been studied within slave-rotor mean-field theory [65–67]. We have discussed why the most widely studied local Hubbard interaction (3.6) cannot lead to a TMI phase within our model. Instead, an interaction term involving nearest neighbors as given by Eq. (3.7) has to be considered. We have shown how an interaction of this form can be effectively realized as summarized graphically in Fig. 3.2. As can be seen in the phase diagram in Fig. 3.3(a) and (b), this term yields both WTMI and STMI as well as trivial (NMI) and gapless Mott phases (GMI). The central property of nontrivial Mott insulating states, the emergence of spin-only edge modes, can be used to detect this exotic state of matter (see Sec. 3.2.3).

Chapter 4

4 Selection rules for pairing states in noncentrosymmetric superconductors

In Chap. 1.3 we have seen that determining the detailed microscopic structure of the order parameter of a superconductor is in general a very nontrivial task. In many systems, such as Sr_2RuO_4, UPt_3 and URu_2Si_2, it took several years of intense theoretical and experiment work to collect convincing evidence for a single candidate pairing state, while controversies still remain [160–165]. In the case of superconductivity, e.g., in oxide heterostructures and FeSe on STO, which has a much shorter history [39, 40, 157], no prime candidate state has been established yet [37, 38, 159]. To pinpoint the order parameter structure, group theoretical methods have turned out to be very useful [50, 78–84] which is a consequence of the fact [1] that, at a second order phase transition, the order parameter has to transform under one of the IRs of the symmetry group of the high-temperature phase (see Chap. 1.1.1).

In this chapter, we will combine these symmetry-based constraints on pairing states with energetic arguments valid for systems with singly-degenerate Fermi surfaces. The latter property naturally holds in the presence of strong SOC and broken inversion symmetry. While the absence of a center of inversion constitutes a special case for 3D systems, it is rather the typical situation in the experimental realization of 2D systems as mentioned in Chap. 1.3. The selection rules we will derive yield strong additional constraints on possible pairing states, in particular, for spontaneous TRS breaking at a single superconducting phase transition. They are general in the sense that they are formulated only in terms of the point symmetry and time-reversal properties of the high-temperature phase and hold in the absence of additional translation symmetry breaking as long as the splitting E_{so} of the Fermi surfaces is larger than the superconducting energy scales.

These selection rules can be used to gain information about the time-reversal properties of a superconductor with unknown microscopic order parameter and, in addition, be read as a design principle in the experimental search for superconductors that spontaneously break TRS. The presence or absence of TRS is a crucial property of a superconductor because it not only determines its topological classification (see Chap. 2.1) but also its thermal and electromagnetic response: Broken TRS in a superconductor leads, e.g., to the formation of magnetic moments at inhomogeneities [50, 51], to a small but measurable [47–49] rotation of the polarization direction of reflected light (PKE) and has recently been predicted to induce an unconventional giant thermoelectric effect [52].

This chapter is organized as follows: In Sec. 4.1, we will discuss in detail what TRS means and requires to be broken in the context of superconductivity. The weak-pairing description, which is central for the analysis of this chapter, will be introduced in Sec. 4.2. These first two sections are

mainly intended to introduce the notation and to deduce the basic properties that will then be used to derive selection rules for pairing states in the remainder of the chapter. In Sec. 4.3, higher order terms of the Ginzburg-Landau expansion are analyzed with respect to the mean-field order of the phase transition and TRS breaking in multidimensional or complex IRs. Sec. 4.4 will be devoted to the particularly restrictive constraints for 2D systems, for simplicity focusing on the physically most relevant case of spinfull, as opposed to spin-polarized, fermions. The discussion of the latter will be postponed to Sec. 4.7. In Sec. 4.5, we will analyze under which physical conditions the weak-pairing description and, hence, the selection rules can be used. The results will be applied to several different materials in Sec. 4.6. Finally, in Sec. 4.8, we will discuss the consequences of our analysis for surfaces of 3D materials.

This chapter is based on unpublished work [325, 326]. The discussion of oxide heterostructures is partially also presented in Ref. [38].

4.1 TRS in superconductors

In Chap. 2.1.1, we have introduced TRS on a very formal level: A Hamiltonian $\hat{H}$ is said to be time-reversal symmetric if it commutes with an anitunitary operator $\hat{\Theta}$. More physically, this means that the microscopic dynamics of the system is invariant under the reflection of the time-direction in the following sense: If the system is initially prepared in the state $|\Psi_i\rangle$, it will evolve into $|\Psi_f\rangle = \exp(-i\Delta t\hat{H})|\Psi_i\rangle$ during time Δt. The "backward evolution" from $\hat{\Theta}|\Psi_f\rangle$ to $\hat{\Theta}|\Psi_i\rangle$ is now governed by the time-reversed Hamiltonian $\hat{H}_\theta = \hat{\Theta}\hat{H}\hat{\Theta}^\dagger$, i.e.,

$$\hat{\Theta}|\Psi_i\rangle = \exp(-i\Delta t\hat{H}_\theta)\hat{\Theta}|\Psi_f\rangle\,. \tag{4.1}$$

In case of TRS it holds $\hat{H}_\theta = \hat{H}$ and the backward evolution is generated by the exact same Hamiltonian. Note that the Hamiltonian $\hat{H}$ can both be seen as a single-particle, mean-field, Hamiltonian (as, e.g., in Chap. 2.1.2) as well as the full many-body Fock-space Hamiltonian.

As we will discuss in this section, TRS plays a special role in superconductivity: Firstly, the Cooper pairs (see Chap. 1.1.2) are built from time-reversed partners of states (so-called *Kramers partners*) such that the presence of TRS in the high-temperature phase is crucial for the superconducting instability itself. Secondly, the U(1) gauge symmetry leads to strong requirements for spontaneous TRS-breaking [81]. In Sec. 4.1.1, we will mainly introduce the notation used in this chapter and then (see Sec. 4.1.2) analyze what TRS breaking requires in the context of a general superconducting multicomponent Ginzburg-Landau expansion that only takes into account the symmetries of the high-temperature phase.

4.1.1 The general mean-field Hamiltonian

In this chapter, we will analyze the general superconducting mean-field Hamiltonian

$$\hat{H}_{\mathrm{MF}} = \sum_{\boldsymbol{k}} \hat{c}^\dagger_{\boldsymbol{k}\alpha}\left(h_{\boldsymbol{k}}\right)_{\alpha\beta}\hat{c}_{\boldsymbol{k}\beta} + \frac{1}{2}\sum_{\boldsymbol{k}}\left(\hat{c}^\dagger_{\boldsymbol{k}\alpha}\Delta_{\alpha\beta}(\boldsymbol{k})\hat{c}^\dagger_{-\boldsymbol{k}\beta} + \mathrm{H.c.}\right) \tag{4.2}$$

where $\hat{c}^\dagger_{\boldsymbol{k}\alpha}$ and $\hat{c}_{\boldsymbol{k}\alpha}$ describe the creation and annihilation of quasiparticles in a state characterized by the quantum numbers $(\boldsymbol{k},\alpha)$, respectively. Here $\boldsymbol{k}$ is the d-dimensional crystal momentum and the indices $\alpha,\beta = 1,2,\ldots N$ represent all relevant microscopic degrees of freedom, e.g., spin, orbitals and, in case of a 2D system, also subbands. The normal state properties are described by $h_{\boldsymbol{k}}$ which contains the entire information on the band structure and Bloch wavefunctions. To conveniently distinguish between first and second quantized operators we will use hats to denote the latter.

Eq. (4.2) is a generalized form of the original BCS Hamiltonian introduced in Sec. 1.1.2 which allows for all possible two-particle pairing states that do not break translation symmetry. The order parameter matrix Δ is exactly the same as in the general Ginzburg-Landau expansion of Sec. 1.1.1.

Using the fermionic anticommutation relations in Eq. (4.2), it follows that

$$\Delta(\boldsymbol{k}) = -\Delta^T(-\boldsymbol{k}) \tag{4.3}$$

recovering the antisymmetry constraint (1.2).

Furthermore, the transformation of the order parameter under operations g of the symmetry group $\mathcal{G}_0$ of the high temperature phase follows from the representation on the field operators

$$\hat{c}^\dagger_{\boldsymbol{k}\alpha} \xrightarrow{g} \hat{c}^\dagger_{\mathcal{R}_v(g)\boldsymbol{k}\beta} \left(\mathcal{R}_\Psi(g)\right)_{\beta\alpha} \tag{4.4}$$

where $\mathcal{R}_\Psi(g)$ and $\mathcal{R}_v(g)$ are the spinor and vector representation of g. As already discussed in Sec. 1.1.1, $\mathcal{G}_0$ will either be equal to the point group $\mathcal{G}_p$ or $\mathrm{SO}(3)\times\mathcal{G}_p$ with $\mathrm{SO}(3)$ describing spin-rotations depending on whether independent spin-rotation symmetry is broken or preserved in the normal state. Due to the assumed form of the mean-field Hamiltonian (4.2) the translation symmetries will be unaltered in the superconducting phase such that we do not have to investigate the full space group of the system.

By design, the high-temperature Hamiltonian h is invariant under all $g \in \mathcal{G}_0$ and, hence,

$$\mathcal{R}_\Psi(g) h_{\mathcal{R}_v^{-1}(g)\boldsymbol{k}} \mathcal{R}_\Psi^\dagger(g) = h_{\boldsymbol{k}} \tag{4.5}$$

as follows from applying Eq. (4.4) to the first term in the mean-field Hamiltonian (4.2). Similarly, we get the transformation behavior of the order parameter,

$$\Delta(\boldsymbol{k}) \xrightarrow{g} \mathcal{R}_\Psi(g)\Delta(\mathcal{R}_v^{-1}(g)\boldsymbol{k})\mathcal{R}_\Psi^T(g), \tag{4.6}$$

in accordance with Eq. (1.3).

In the following, time-reversal will be represented by the antiunitary operators $\hat{\Theta}$ and Θ in Fock and single-particle space, respectively. We define the action of $\hat{\Theta}$ via

$$\hat{\Theta}\hat{c}^\dagger_{\boldsymbol{k}\alpha}\hat{\Theta}^\dagger = \hat{c}^\dagger_{-\boldsymbol{k}\beta} T_{\beta\alpha}, \qquad T^\dagger T = \mathbb{1}, \tag{4.7}$$

such that demanding that the first term in Eq. (4.2) commutes with $\hat{\Theta}$ is equivalent to

$$\Theta h_{-\boldsymbol{k}} \Theta^\dagger = h_{\boldsymbol{k}} \tag{4.8}$$

with $\Theta = T\mathcal{K}$ where $\mathcal{K}$ denotes complex conjugation. For the sake of generality we will not further specify T. It will only be important that

$$\Theta^2 = (-1)^{2S}\mathbb{1}, \tag{4.9}$$

where $S = 0$ and $S = 1/2$ for spinless and spinfull electrons. The connection (4.9) between the spin S (holds for all $S \in \mathbb{N}/2$) and the square of the time-reversal operator readily follows by demanding that Θ inverts the direction of the spin [93]. Although our main interest is on spinfull fermions, $S = 1/2$, we will also discuss the spinless case ($S = 0$). The latter is relevant when fermionic TRS is broken but the effective low-energy theory has an emergent TRS with $\Theta^2 = \mathbb{1}$. This occurs quite generically in the presence of strong Zeeman splittings as we will see in Sec. 4.7.1.

Applying Eq. (4.7) in the pairing term of the mean-field Hamiltonian (4.2) shows that the order parameter transforms as

$$\Delta_{\boldsymbol{k}} \longrightarrow T\Delta^*_{-\boldsymbol{k}}T^T \tag{4.10}$$

under time-reversal.

The key step in multicomponent Ginzburg-Landau expansions as discussed in Sec. 1.1.1 is the expansion of the order parameter

$$\Delta(\boldsymbol{k}) = \sum_n \sum_{\mu=1}^{d_n} \eta^n_\mu \chi^n_\mu(\boldsymbol{k}), \qquad \eta^n_\mu \in \mathbb{C}, \tag{4.11}$$

in terms of the basis functions $\{\chi^n_\mu\}$ transforming under the different IRs n of $\mathcal{G}_0$ as defined in Eq. (1.5). This allows to represent all unitary symmetries in terms of the expansion coefficients $\{\eta^n_\mu\}$. However, in case of time-reversal we face the problem that the unitary symmetries of $\mathcal{G}_0$ do not determine the behavior of the basis functions under Eq. (4.10). In the next subsection we will analyze how the TRS of the high-temperature phase makes it possible to express Eq. (4.10) solely in terms of the expansion coefficients $\{\eta^n_\mu\}$.

4.1.2 Consequences for the basis functions

To study the implications of the TRS of the high-temperature phase on the basis functions $\{\chi^n_\mu\}$, it is very convenient to introduce $\{\widetilde{\chi}^n_\mu(\boldsymbol{k})\}$ via

$$\chi^n_\mu(\boldsymbol{k}) = \widetilde{\chi}^n_\mu(\boldsymbol{k})T. \tag{4.12}$$

Since the unitary part of the time-reversal operator appears explicitly, this notation will also turn out to be very useful when studying the superconductor in the eigenbasis of the normal state Hamiltonian $h_{\boldsymbol{k}}$ in the subsequent sections of this chapter.

To proceed, we take advantage of the fact that time-reversal is not a spatial symmetry and must, hence, commute with all operations of the symmetry group $\mathcal{G}_0$,

$$[\Theta, \mathcal{R}_\Psi(g)] = 0 \quad \forall g \in \mathcal{G}_0. \tag{4.13}$$

To illustrate this statement, consider, e.g., rotations which are generated by the angular momentum operators $\boldsymbol{J}$. Depending on the system, $\boldsymbol{J}$ can be just spin or orbital angular momentum or the sum of both. In all cases, it holds $\{\Theta, \boldsymbol{J}\} = 0$ by construction and, hence, $\mathcal{R}_\Psi = \exp(-i\boldsymbol{\alpha}\cdot\boldsymbol{J})$ with $\boldsymbol{\alpha}$ describing the axis and angle of rotation commutes with Θ.

Using Eq. (4.13), it readily follows that the new basis functions $\{\widetilde{\chi}^n_\mu(\boldsymbol{k})\}$ transform according to

$$\mathcal{R}_\Psi(g)\widetilde{\chi}^n_\mu(\mathcal{R}_v^{-1}(g)\boldsymbol{k})\mathcal{R}^\dagger_\Psi(g) = \left(\mathcal{R}^n_\chi(g)\right)_{\mu\nu}\widetilde{\chi}^n_\nu(\boldsymbol{k}) \tag{4.14}$$

which is more convenient as the behavior (1.5) of $\{\chi^n_\mu\}$ as it transforms like a sesquilinear form such as $h_{\boldsymbol{k}}$ in Eq. (4.5).

Since the point groups of crystalline systems allow for both real and complex IRs [91], we have to discuss both cases here. We denote the complex conjugate representation of n by $\bar{n}$ which is defined by

$$\mathcal{R}^{\bar{n}}_\chi(g) = \left(\mathcal{R}^n_\chi(g)\right)^*. \tag{4.15}$$

Note that if n is an IR, the same also holds for $\bar{n}$ as is easily shown. If $n = \bar{n}$, the representation is said to be real.

The central statement of this subsection is that the TRS of the high-temperature phase implies that the basis functions $\widetilde{\chi}^n_\mu(\boldsymbol{k}) = \chi^n_\mu(\boldsymbol{k})T^\dagger$ can always be chosen so as to satisfy

$$\left(\widetilde{\chi}^n_\mu(\boldsymbol{k})\right)^\dagger = \widetilde{\chi}^{\bar{n}}_\mu(\boldsymbol{k}). \tag{4.16}$$

In particular, for a real representation ($n = \bar{n}$) the basis functions are Hermitian. In Ref. [81], this statement has been shown for the special case of real IRs and just a single pseudospin degree of freedom. In Appendix C.1 we present a generalized proof that works also when $n \neq \bar{n}$ and for an arbitrary number N of relevant microscopic degrees of freedom within the unit cell. It is additionally shown that Eq. (4.16) still holds when the normal state is antiferromagnetically ordered or more generally in the case of SDW order. It even applies in the presence of magnetic impurities as long as TRS is restored on average (no net magnetic moment), the system is self-averaging (see Chap. 1.4) and the superconducting order parameter can be assumed to be homogeneous.

Before discussing the consequences of Eq. (4.16) for the representation of TRS on the expansion coefficients $\{\eta^n_\mu\}$, we give a simple, though less general, argument for why Eq. (4.16) holds. For this purpose, consider the quartic interaction term in the Cooper channel

$$\hat{H}^C_{\text{int}} = -\sum_{n,n'}\sum_{\mu,\mu'} C^{nn'}_{\mu\mu'} \left[\sum_{\boldsymbol{k}} \hat{c}^\dagger_{\boldsymbol{k}} \widetilde{\chi}^n_\mu(\boldsymbol{k}) T \left(\hat{c}^\dagger_{-\boldsymbol{k}}\right)^T\right] \left[\sum_{\boldsymbol{k}'} \hat{c}^T_{-\boldsymbol{k}'} \left(\widetilde{\chi}^{n'}_{\mu'}(\boldsymbol{k}')T\right)^\dagger \hat{c}_{\boldsymbol{k}'}\right] \tag{4.17}$$

expanded in terms of the basis functions $\{\chi^n_\mu\}$. Demanding that $\hat{H}_{\text{int}}$ be invariant under Eq. (4.4) for all $g \in \mathcal{G}_0$ and using the grand orthogonalilty theorem (1.10), it follows that C, exactly as $\mathcal{M}$ in Eq. (1.8), must be fully diagonal, $C^{nn'}_{\mu\mu'} = \delta_{nn'}\delta_{\mu\mu'}g_n$.

Focusing on time-reversal symmetric normal state Hamiltonians the interaction has to satisfy $\hat{H}^C_{\text{int}} = \hat{\Theta}\hat{H}^C_{\text{int}}\hat{\Theta}^\dagger$ which is equivalent to invariance of Eq. (4.17) under replacing all basis functions $\widetilde{\chi}^n_\mu$ by their Hermitian conjugate $(\widetilde{\chi}^n_\mu)^\dagger$. As directly follows from Eq. (4.14), $(\widetilde{\chi}^n_\mu)^\dagger$ transforms exactly as $\widetilde{\chi}^{\bar{n}}_\mu$, such that TRS requires

$$\widetilde{\chi}^n_\mu(\boldsymbol{k}) = e^{i\zeta^n_\mu}\left(\widetilde{\chi}^{\bar{n}}_\mu(\boldsymbol{k})\right)^\dagger, \qquad g_n = g_{\bar{n}}. \tag{4.18}$$

As the phase factors $e^{i\zeta^n_\mu}$ do not play any role, we can set them to 1 leading to Eq. (4.16).

Real representation. Let us first discuss real representations where the constraints on the coupling constants in Eq. (4.18) are trivial and the basis functions are Hermitian. Applying Eq. (4.10) in the expansion (4.11) of the order parameter then shows that time-reversal simply amounts to replacing

$$\eta^n_\mu \longrightarrow (-1)^{2S+1}\left(\eta^n_\mu\right)^*, \tag{4.19}$$

where we have used the antisymmetry property (4.3). Note that the additional minus sign in case of spinless fermions is of no significance as it can be removed by a U(1) gauge transformation[1]. For the very same reason, a global phase of all $\{\eta^n_\mu\}$ can always be absorbed leading to the well-known [81] result that a superconducting order parameter can only break TRS if it transforms under a multidimensional representation.

[1] We could have chosen $e^{i\zeta^n_\mu} = (-1)^{2S+1}$ in Eq. (4.18) to remove the additional factor in Eq. (4.19).

Complex representation. In case of a complex IR, time-reversal is tantamount to replacing all η_μ^n by $(\eta_\mu^{\bar{n}})^*$. This forces the prefactors $a_n(T)$ and $a_{\bar{n}}(T)$ in the Ginzburg-Landau expansion (1.11) to be identical which embodies the degeneracy of coupling constants in Eq. (4.18). Therefore, when analyzing the possible superconducting phases associated with a complex representation n one always has to consider its conjugate partner $\overline{n}$ as well. In fact, it is very convenient to think of this pair as a reducible real representation of dimension $2d_n$. To make this more explicit, let us write

$$\Delta_{\boldsymbol{k}} = \cdots + \sum_{\mu=1}^{d_n} \left(\eta_\mu^n \widetilde{\chi}_\mu^n(\boldsymbol{k}) + \eta_\mu^{\overline{n}} \widetilde{\chi}_\mu^{\overline{n}}(\boldsymbol{k}) \right) T + \cdots = \cdots + \sum_{\mu=1}^{2d_n} \eta_\mu^{\widetilde{n}} \widetilde{\chi}_\mu^{\widetilde{n}}(\boldsymbol{k}) T + \ldots, \tag{4.20}$$

where we have introduced basis functions ($\mu = 1, \ldots, d_n$)

$$\widetilde{\chi}_\mu^{\widetilde{n}}(\boldsymbol{k}) = \frac{1}{\sqrt{2}} \left(\widetilde{\chi}_\mu^n(\boldsymbol{k}) + \widetilde{\chi}_\mu^{\overline{n}}(\boldsymbol{k}) \right), \qquad \widetilde{\chi}_{\mu+d_n}^{\widetilde{n}}(\boldsymbol{k}) = \frac{1}{\sqrt{2}\, i} \left(\widetilde{\chi}_\mu^n(\boldsymbol{k}) - \widetilde{\chi}_\mu^{\overline{n}}(\boldsymbol{k}) \right) \tag{4.21}$$

which are obviously Hermitian due to Eq. (4.16) and

$$\eta_\mu^{\widetilde{n}} = \frac{1}{\sqrt{2}} \left(\eta_\mu^n + \eta_\mu^{\overline{n}} \right), \qquad \eta_{\mu+d_n}^{\widetilde{n}} = \frac{i}{\sqrt{2}} \left(\eta_\mu^n - \eta_\mu^{\overline{n}} \right). \tag{4.22}$$

Since $\{\eta_\mu^n, \eta_\mu^{\overline{n}}\} \leftrightarrow \{\eta_\mu^{\widetilde{n}}\}$ just defines a unitary transformation, the quadratic contribution to the free energy preserves its diagonal form (1.11). Due to Hermiticity of the basis functions, time-reversal has the same representation as in Eq. (4.19) with n replaced by $\widetilde{n}$. Also all symmetry operations $g \in \mathcal{G}_0$ are represented by real matrices in the new basis as is straightforwardly shown.

Taken together, we have seen that the order parameter must necessarily transform either under a real multidimensional or a complex IR to obtain a TRS-breaking condensate. In the remainder of this chapter, we will supplement these purely symmetry-based considerations with energetic arguments for systems with singly-degenerate Fermi surfaces in order to gain refined criteria for the time-reversal properties of the possible superconducting states.

4.2 Weak-pairing limit

In order to apply energetic arguments, the most natural basis is not provided by the microscopic degrees of freedom, like spin, orbitals etc., as referred to by the Greek indices α, β in Eq. (4.2), but rather by the eigenstates $\psi_{\boldsymbol{k}s}$ of the high-temperature Hamiltonian $h_{\boldsymbol{k}}$ satisfying $h_{\boldsymbol{k}} \psi_{\boldsymbol{k}s} = \epsilon_{\boldsymbol{k}s} \psi_{\boldsymbol{k}s}$. For this reason, we introduce new field operators according to

$$\hat{c}_{\boldsymbol{k}\alpha} = \sum_s \left(\psi_{\boldsymbol{k}s} \right)_\alpha \hat{f}_{\boldsymbol{k}s}, \qquad \hat{c}_{\boldsymbol{k}\alpha}^\dagger = \sum_s \hat{f}_{\boldsymbol{k}s}^\dagger \left(\psi_{\boldsymbol{k}s}^* \right)_\alpha. \tag{4.23}$$

If we used all N eigenstates at every $\boldsymbol{k}$, this would just constitute an exact unitary transformation. We will, however, apply the following low-energy approach: Only the bands leading to Fermi surfaces are taken into account and we will focus on states with energies $\epsilon_{\boldsymbol{k}s}$ close to the Fermi level with associated energetic cutoff denoted by Λ, i.e., $|\epsilon_{\boldsymbol{k}s}| < \Lambda$. We use the freedom in labeling the states such that the set $\{\boldsymbol{k} | \epsilon_{\boldsymbol{k}s} = 0\}$ of crystal momenta, which will be referred to as Fermi surface s, is connected. In this way, the description of topological properties follows most easily as the meaning of the label s used here and in the expression for the topological invariants of Sec. 2.2.3 coincides. Furthermore, the nodal

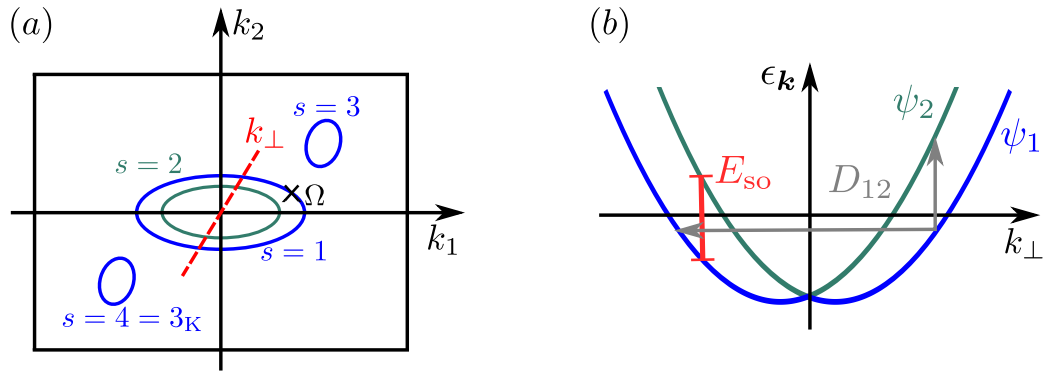

Figure 4.1: ***Parameterization and energetics of Fermi surfaces.*** *In (a), the basic notation which is used in this chapter to label the Fermi surfaces is illustrated for the special case of a 2D system. The angle Ω will be used to refer to a single state on a given Fermi surface in Sec. 4.3 below. A 1D cut of the spectrum along the red dashed line is shown schematically in (b) together with the inter-Fermi-surface matrix element D_{12} coupling single particle states separated energetically by E_{so}.*

structure of the superconductor can be compactly expressed (see below). In addition, we introduce the notation that the Kramers partner of the state $(s, \boldsymbol{k})$ is denoted by $(s_{\mathrm{K}}, \boldsymbol{k})$. Taken together, these conventions imply that a Fermi surface s and its Kramers partner s_{K} can both be identical or distinct: In the example shown in Fig. 4.1(a), it holds $s = s_{\mathrm{K}}$ for $s = 1, 2$, while $s = 3 = 4_{\mathrm{K}}$.

In the remainder of this chapter, we will focus on systems with singly-degenerate Fermi surfaces. As discussed in Chap. 1.3, this requires both the presence of SOC and broken inversion symmetry if spin-1/2 TRS is preserved, i.e., if Eq. (4.8) with $\Theta^2 = -\mathbb{1}$ holds. We emphasize that our analysis also allows for the situation that fermionic TRS is broken but an effective spin-0 TRS emerges (see Sec. 4.7.1). In that case Θ in Eq. (4.8) satisfies $\Theta^2 = +\mathbb{1}$ and the Fermi surfaces can also be nondegenerate for centrosymmetric point groups. In both cases, independent spin-rotation symmetry is broken such that $\mathcal{G}_0$ is equal to the point group of the system.

The absence of degeneracy allows for uniquely relating wavefunctions of the low-energy theory according to

$$\psi_{\boldsymbol{k}s} = e^{i\varphi^s_{\boldsymbol{k}}} \Theta \psi_{-\boldsymbol{k}s_{\mathrm{K}}}, \tag{4.24}$$

where $\varphi^s_{\boldsymbol{k}} \in \mathbb{R}$ are phases that depend on the phases of the eigenstates $\psi_{\boldsymbol{k}s}$. The importance of these phases for properly describing the noncentrosymmetric superconductors has first been emphasized in Ref. [327]. The reason is that, for $S = 1/2$, they cannot be set to 1 and, hence, removed from the theory by adjusting the phases of the eigenstates. This follows from the property

$$e^{i\varphi^{s_{\mathrm{K}}}_{-\boldsymbol{k}}} = (-1)^{2S} e^{i\varphi^s_{\boldsymbol{k}}} \tag{4.25}$$

which is enforced by $\Theta^2 = (-1)^{2S}$. In more physical terms, the minus sign on the right-hand side of Eq. (4.25) in the case of $S = 1/2$ just expresses the fact that, despite being singly degenerate, the bands of the normal state Hamiltonian are formed by spin-1/2 particles. This is an essential physical property of the system which must be reflected in its theoretical description.

Applying Eq. (4.23) to the general mean-field Hamiltonian (4.2), the latter can be restated as

$$\hat{H}_{\mathrm{MF}} = \sum_{\boldsymbol{k}} \hat{f}^{\dagger}_{\boldsymbol{k}s} \epsilon_{\boldsymbol{k}s} \hat{f}_{\boldsymbol{k}s} + \frac{1}{2} \sum_{\boldsymbol{k}} \left(\hat{f}^{\dagger}_{\boldsymbol{k}s} D_{ss'}(\boldsymbol{k}) e^{-i\varphi^{s'}_{\boldsymbol{k}}} \hat{f}^{\dagger}_{-\boldsymbol{k}s'_{\mathrm{K}}} + \mathrm{H.c.} \right), \tag{4.26}$$

where we have introduced the matrix elements

$$D_{ss'}(\boldsymbol{k}) = \langle \psi_{\boldsymbol{k}s} | \Delta(\boldsymbol{k}) T^{\dagger} | \psi_{\boldsymbol{k}s'} \rangle \tag{4.27}$$

of the order parameter with respect to the wavefunctions of the high-temperature Hamiltonian and taken advantage of the relation (4.24) to write D as a scalar product. To cast the $\hat{H}_{\mathrm{MF}}$ in quadratic form, $\hat{H}_{\mathrm{MF}} = \frac{1}{2} \sum_{\boldsymbol{k}} \hat{\Psi}^{\dagger}_{\boldsymbol{k}} h^{\mathrm{BdG}}_{\boldsymbol{k}} \hat{\Psi}_{\boldsymbol{k}}$, we introduce the Nambu spinor $\Psi_{\boldsymbol{k}s} = (f_{\boldsymbol{k}s}, f^{\dagger}_{-\boldsymbol{k}s_{\mathrm{K}}} e^{-i\varphi^{s}_{\boldsymbol{k}}})^{T}$. The associated BdG Hamiltonian reads

$$\left(h^{\mathrm{BdG}}_{\boldsymbol{k}} \right)_{ss'} = \begin{pmatrix} \epsilon_{\boldsymbol{k}s} \delta_{s,s'} & D_{ss'}(\boldsymbol{k}) \\ D^{*}_{s's}(\boldsymbol{k}) & -\epsilon_{\boldsymbol{k}s} \delta_{s,s'} \end{pmatrix}. \tag{4.28}$$

We now consider the *weak-pairing limit*, where matrix elements of the order parameter between states at different Fermi surfaces, such as D_{12} in Fig. 4.1(b), can be neglected. Formally, this corresponds to replacing

$$D_{ss'}(\boldsymbol{k}) \longrightarrow \delta_{s,s'} \widetilde{\Delta}_{s}(\boldsymbol{k}). \tag{4.29}$$

Note that this only refers to the order parameter and not to the interaction driving the superconducting instability. Fermi-surface-off-diagonal matrix elements of the latter are even required to ensure the superconducting order parameter to be unique. The reason is that, otherwise, changing the relative phase of $\widetilde{\Delta}_s$ between different s would be a symmetry of the free energy. In more physical terms, Eq. (4.29) means that anomalous averages are made of the same quantum numbers as the normal state.

Applying Eq. (4.29) in the BdG Hamiltonian (4.28) immediately yields the excitation spectrum

$$E_{\boldsymbol{k}s} = \sqrt{\epsilon^{2}_{\boldsymbol{k}s} + \left| \widetilde{\Delta}_{\boldsymbol{k}s} \right|^{2}} \tag{4.30}$$

in the weak-pairing limit. Recalling that the Fermi surfaces have been defined to be connected, we see that the Fermi surface s of the superconductor is fully gapped if and only if $\widetilde{\Delta}_{\boldsymbol{k}s} \neq 0$ for all $\boldsymbol{k}$ on s. Note that this criterion for the presence or absence of a node is much simpler than its analogue in case of doubly-degenerate Fermi surfaces [50].

As can be seen in Fig. 4.1(b), the Fermi-surface-off-diagonal matrix elements, $D_{ss'}$ with $s \neq s'$, couple states which are energetically separated. Denoting the associated energy scale by E_{so}, it is natural to expect the weak-pairing limit (4.29) to be applicable as long as E_{so} is much larger than the energy scales of superconductivity. As we will see explicitly in Sec. 4.5, using the weak-pairing limit to derive selection rules for pairing states merely requires E_{so} to be larger than the gap at $T = 0$ or, equivalently, larger than T_c (times some prefactor of order 1).

For the moment, let us assume that Eq. (4.29) is applicable and analyze the consequences for the possible superconducting states. As a first step we reconsider the fermionic antisymmetry constraint (4.3) and then investigate the representation of the elements of the symmetry group $\mathcal{G}_0$ and TRS in the weak-pairing limit.

4.2.1 Fermi-Dirac statistics

The relation analogous to Eq. (4.3) formulated in the eigenbasis of the high-temperature Hamiltonian is most easily found by shifting $(s, s', \boldsymbol{k}) \to (s_{\rm K}, s'_{\rm K}, -\boldsymbol{k})$ in the summation in the second term in Eq. (4.26) and using the property (4.25) of the phase factors. One finds

$$D_{ss'}(\boldsymbol{k}) = (-1)^{2S+1} D_{s'_{\rm K} s_{\rm K}}(-\boldsymbol{k}) e^{i(\varphi^{s'}_{\boldsymbol{k}} - \varphi^{s}_{\boldsymbol{k}})}, \tag{4.31}$$

which can, alternatively, also be obtained by using Eq. (4.3) in the definition (4.27) of D. Most importantly, in the weak-pairing limit (4.29) the phase factors cancel and Eq. (4.31) becomes

$$\widetilde{\Delta}_s(\boldsymbol{k}) = (-1)^{2S+1} \widetilde{\Delta}_{s_{\rm K}}(-\boldsymbol{k}), \tag{4.32}$$

i.e., the order parameter has to be necessarily even (odd) under $(s, \boldsymbol{k}) \to (s_{\rm K}, -\boldsymbol{k})$ for spinfull, $S = 1/2$, (spinless, $S = 0$) fermions.

This shows that Fermi-Dirac statistics is much more restrictive in the weak-pairing limit as compared to the situation of doubly-degenerate Fermi surfaces: In the latter case, where we can still use[2] the description (4.26) of the mean-field Hamiltonian in the eigenbasis of $h_{\boldsymbol{k}}$, there are 3 independent functions, $D_{11}(\boldsymbol{k})$, $D_{22}(\boldsymbol{k})$ and $D_{12}(\boldsymbol{k})$, per Fermi surface doublet. The main difference is that $D_{12}(\boldsymbol{k})$, which is in general by no means less important than the diagonal terms of D as our distinction between the outer and inner Fermi surface is artificial, is not restricted at all by the fermionic anticommutation relations as opposed to the Fermi surface diagonal terms.

Although (the $S = 1/2$ case of) the property (4.32) of the diagonal matrix elements of the order parameter had already been known for more than 10 years [327], to the best of our knowledge, its strong implications for the possible pairing states of 2D systems, to be discussed in Sec. 4.4 below, had not been pointed out until recently [325].

4.2.2 Symmetry properties in the weak pairing description

Let us next discuss the transformation behavior of $\widetilde{\Delta}_s(\boldsymbol{k})$ under the action of symmetry operations of the high-temperature phase.

Unitary symmetries. For the description of the unitary symmetries $g \in \mathcal{G}_0$ it is most convenient to apply the expansion (4.11) in order to obtain the representation

$$\widetilde{\Delta}_s(\boldsymbol{k}) \equiv \langle \psi_{\boldsymbol{k}s} | \Delta(\boldsymbol{k}) T^\dagger | \psi_{\boldsymbol{k}s} \rangle = \sum_n \sum_{\mu=1}^{d_n} \eta^n_\mu \varphi^n_\mu(\boldsymbol{k}, s), \qquad \eta^n_\mu \in \mathbb{C}, \tag{4.33}$$

where the new basis functions $\varphi^n_\mu(\boldsymbol{k})$ are defined by

$$\varphi^n_\mu(\boldsymbol{k}, s) := \langle \psi_{\boldsymbol{k}s} | \widetilde{\chi}^n_\mu(\boldsymbol{k}) | \psi_{\boldsymbol{k}s} \rangle \,. \tag{4.34}$$

Comparing Eqs. (4.11) and (4.33) shows that the weak-pairing approximation (4.29) allowed us to reduce the complexity of the description: While $\{\chi^n_\mu(\boldsymbol{k})\}$ are matrix fields satisfying $\left(\chi^n_\mu(\boldsymbol{k})\right)^T = -\chi^n_\mu(-\boldsymbol{k})$ due to Fermi-Dirac statistics and $\left(\widetilde{\chi}^n_\mu(\boldsymbol{k})\right)^\dagger = \widetilde{\chi}^{\bar{n}}_\mu(\boldsymbol{k})$ as a consequence of the TRS of the

[2] Can be formally seen by artificially introducing an infinitesimal amount of spin-orbit splitting that makes it possible to identify two singly-degenerate Fermi surfaces but does not affect any physical property of the system.

high-temperature phase, the new basis $\{\varphi_\mu^n(\boldsymbol{k},s)\}$ just consists of scalar functions for each Fermi surface with the corresponding properties

$$\varphi_\mu^n(\boldsymbol{k},s) = (-1)^{2S+1}\varphi_\mu^n(-\boldsymbol{k},s_\mathrm{K}), \qquad \varphi_\mu^n(\boldsymbol{k},s) = \left(\varphi_\mu^{\bar{n}}(\boldsymbol{k},s)\right)^*, \tag{4.35}$$

respectively.

To investigate how the basis functions $\{\varphi_\mu^n(\boldsymbol{k},s)\}$ transform, recall that the Fermi surfaces are assumed to be non-degenerate and, hence, it must hold

$$\psi_{\boldsymbol{k}s} = e^{i\rho_{\boldsymbol{k}}^s(g)}\mathcal{R}_\Psi^\dagger(g)\psi_{\mathcal{R}_v(g)\boldsymbol{k}\mathcal{R}_s(g)s} \tag{4.36}$$

as a consequence of Eq. (4.5). Here $\rho_{\boldsymbol{k}}^s(g) \in \mathbb{R}$ are some irrelevant phases and $\mathcal{R}_s(g)$ denotes the representation of g on the Fermi surface index s which depends on the Fermi surface topology. Using Eq. (4.36), one readily finds from the definition (4.34) that the basis functions $\{\varphi_\mu^n(\boldsymbol{k},s)\}$ transform under the same, s-independent, IRs as the matrix fields $\{\chi_\mu^n(\boldsymbol{k})\}$, i.e.,

$$\varphi_\mu^n(\mathcal{R}_v(g)^{-1}\boldsymbol{k},\mathcal{R}_s(g)^{-1}s) = \left(\mathcal{R}_\chi^n(g)\right)_{\mu\nu}\varphi_\nu^n(\boldsymbol{k},s). \tag{4.37}$$

This means that, once we have found the IR n_0 under which the order parameter $\Delta(\boldsymbol{k})$ transforms, together with the associated orientation of the vector $(\eta_1^{n_0},\dots\eta_{d_{n_0}}^{n_0})$, we also know the symmetry properties of the order parameter

$$\widetilde{\Delta}_s(\boldsymbol{k}) = \sum_{\mu=1}^{d_{n_0}}\eta_\mu^{n_0}\varphi_\mu^{n_0}(\boldsymbol{k},s) \tag{4.38}$$

as it transforms exactly the same way.

Time-reversal. Finally, let us discuss the representation of TRS on in the eigenbasis of the normal state Hamiltonian. Applying the time-reversal transformation (4.10) in the definition (4.27) of D, one finds that the order parameter matrix behaves as

$$D(\boldsymbol{k}) \longrightarrow (-1)^{2S+1}D^\dagger(\boldsymbol{k}) \tag{4.39}$$

under time-reversal, where we have taken advantage of Eqs. (4.3) and (4.9). As the additional prefactor $(-1)^{2S+1}$ can always be absorbed by properly adjusting the global phase of the order parameter, time-reversal amounts to Hermitian conjugation of D.

In particular, it implies that, in the weak-pairing limit, the superconducting state preserves TRS if $\widetilde{\Delta}_s(\boldsymbol{k})$ can be chosen to be real. Alternatively, this could have been obtained from Eq. (4.19) and recalling that the basis functions $\{\varphi_\nu^n(\boldsymbol{k},s)\}$ are real valued. From the expression (4.30) of the spectrum of the superconducting state we see that a time-reversal symmetric superconductor will have a nodal point on the Fermi surface s if $\widetilde{\Delta}_{\boldsymbol{k}s}$ changes sign on s.

4.3 Ginzburg-Landau expansion in noncentrosymmetric systems

After introducing the notation and analyzing the symmetry properties in the previous two sections, we have now set the stage for the derivation of selection rules for possible pairing states in the weak-pairing limit. As already mentioned in the introduction of this chapter, the constraints we will deduce

result from the synergy of *sym*metry as well as en*ergetic* considerations, which will be referred to as *symergetics* in the following, since the interplay of the symmetry group $\mathcal{G}_0$ and the weak-pairing limit are key in the derivation.

Postponing the analysis of the competition between superconducting order parameters transforming under different IRs of $\mathcal{G}_0$ to the subsequent sections, we will for the moment focus on one given IR n_0. Then it is sufficient to restrict the interaction (4.17) in the Cooper channel to $n = n_0$ and, hence, analyze the interacting Hamiltonian

$$\hat{H}_{n_0} = \sum_{\boldsymbol{k}} \hat{c}^\dagger_{\boldsymbol{k}} h_{\boldsymbol{k}} \hat{c}_{\boldsymbol{k}} - g_{n_0} \sum_{\mu} \left[\sum_{\boldsymbol{k}} \hat{c}^\dagger_{\boldsymbol{k}} \widetilde{\chi}^{n_0}_\mu(\boldsymbol{k}) T \left(\hat{c}^\dagger_{-\boldsymbol{k}} \right)^T \right] \left[\sum_{\boldsymbol{k}'} \hat{c}^T_{-\boldsymbol{k}'} \left(\widetilde{\chi}^{n_0}_\mu(\boldsymbol{k}') T \right)^\dagger \hat{c}_{\boldsymbol{k}'} \right], \tag{4.40}$$

where $g_{n_0} > 0$ is assumed to have a positive transition temperature T_c. As shown in Appendix C.2.1, the full Ginzburg-Landau expansion can be very compactly written as

$$\mathcal{F}(\eta^{n_0}_\mu) = \mathcal{F}(0) + \frac{1}{g_{n_0}} \sum_{\mu=1}^{d_{n_0}} |\eta^{n_0}_\mu|^2 + \sum_{l=1}^{\infty} \frac{2^{2l-1}}{l} (-1)^l \sum_s \left\langle \left| \sum_{\mu=1}^{d_{n_0}} \eta^{n_0}_\mu \varphi^{n_0}_\mu(\Omega, s) \right|^{2l} \right\rangle_s I_l(\Lambda, T), \tag{4.41}$$

where we have introduced the manifestly positive integrals/Matsubara sums

$$I_l(\Lambda, T) := \rho_F \int_{-\Lambda}^{\Lambda} \mathrm{d}\epsilon \, T \sum_{\omega_n} \frac{1}{(\omega_n^2 + \epsilon^2)^l} > 0, \quad \omega_n = \pi T(2n+1), \quad n \in \mathbb{Z}, \tag{4.42}$$

with ρ_F denoting the total density of states at the Fermi level. Furthermore, $\langle \ldots \rangle_s$ denotes the average over Fermi surface s formally defined by

$$\langle F(\Omega) \rangle_s := \rho_F^{-1} \int_s \mathrm{d}\Omega \, \rho_s(\Omega) F(\Omega) \tag{4.43}$$

for any function F that only depends on the position Ω on the Fermi surface and, within the cutoff Λ, not on the coordinate perpendicular to it. Note that, in 2D, Ω can be seen, e.g., as the polar angle parameterizing the two central Fermi surfaces illustrated in Fig. 4.1(a) while, in 3D, Ω comprises two angles. For the general purpose of the considerations here, no explicit parameterization will have to be specified. We will only take advantage of the fact that the angle-resolved density of states $\rho_s(\Omega)$ – defined via the separation of the summation over the low-energy degrees of freedom in the vicinity of Fermi surface s,

$$\sum_{\boldsymbol{k}}^{s;\Lambda} \ldots \sim \int_s \mathrm{d}\Omega \, \rho_s(\Omega) \int_{-\Lambda}^{\Lambda} \mathrm{d}\epsilon \ldots, \tag{4.44}$$

into an integration over Ω and energy ϵ – is always positive, $\rho_s(\Omega) > 0$.

To obtain Eq. (4.41), we have made the common assumption that the basis functions $\varphi^{n_0}_\mu$ do not depend on energy ($\varphi^{n_0}_\mu(\boldsymbol{k}, s) \to \varphi^{n_0}_\mu(\Omega, s)$). Formally, this can be seen as the zeroth order term in an expansion in ϵ. This terms is expected to be dominant as long as the quasiparticle picture holds since all corrections have weight zero at the Fermi surface ($\epsilon = 0$).

In the remainder of this section, we will analyze the implications of Eq. (4.41) concerning both the allowed order parameter vectors of real multidimensional and complex one-dimensional representations as well as the order of the phase transition on the mean-field level.

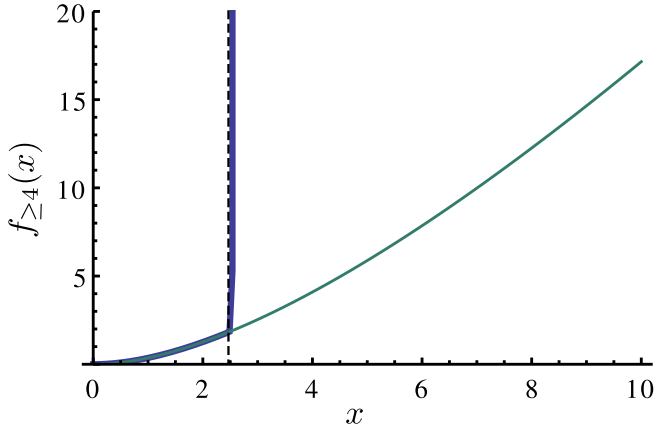

Figure 4.2: ***Higher order terms in the Ginzburg-Landau expansion.*** *The different representations of the dimensionless function $f_{\geq 4}(x)$ determining the terms in the free energy of fourth and higher order with respect to the order parameter are shown: Power series representation, convergent for $x < \pi^2/4$ as indicated by the black dashed line, shown in blue (keeping terms up to 300th order in x) and its analytical continuation (4.47) as solid green line.*

4.3.1 Order of the phase transition

To see whether the Ginzburg-Landau expansion (4.41) allows for a first-order mean-field transition we have to analyze the terms of fourth and higher orders in the superconducting order parameter,

$$\mathcal{F}_{\geq 4}(\eta_\mu^{n_0}) = \sum_{l=2}^{\infty} \frac{2^{2l-1}}{l}(-1)^l \sum_s \left\langle \left| \sum_{\mu=1}^{d_{n_0}} \eta_\mu^{n_0} \varphi_\mu^{n_0}(\Omega, s) \right|^{2l} \right\rangle_s I_l(\Lambda, T). \tag{4.45}$$

The transition can only be of first order if $\mathcal{F}_{\geq 4}(\eta_\mu^{n_0})$ becomes negative for some value of $\eta_\mu^{n_0}$.

Setting $\Lambda \to \infty$ in the integrals $I_l(\Lambda, T)$, one straightforwardly finds

$$\mathcal{F}_{\geq 4}(\eta_\mu^{n_0}) = T^2 \sum_s \int_s \mathrm{d}\Omega\, \rho_s(\Omega)\, f_{\geq 4}\left(\left| \sum_{\mu=1}^{d_{n_0}} \eta_\mu^{n_0} \varphi_\mu^{n_0}(\Omega, s) \right|^2 / T^2 \right), \tag{4.46}$$

where $f_{\geq 4}$ has a power series representation of the form $f_{\geq 4}(x) = \sum_{l=2}^{\infty}(-1)^l c_l x^l$ with the coefficients c_l given in Appendix C.3. It is easy to show analytically and can also be inferred from the plot in Fig. 4.2 that, at least within the radius of convergence $\pi^2/4$ of the power series, $f_{\geq 4}(x)$ is positive. Due to $\rho_s(\Omega) > 0$, we conclude that $\mathcal{F}_{\geq 4}(\eta_\mu^{n_0}) > 0$ and, hence, no first order transition is possible as long as $|\sum_{\mu=1}^{d_{n_0}} \eta_\mu^{n_0} \varphi_\mu^{n_0}(\Omega, s)|/T < \pi/2$.

To go beyond the radius of convergence we have to resum the power series: As show in Appendix C.3 one finds by means of analytic continuation the alternative series representation

$$f_{\geq 4}(x) = \sum_{n=0}^{\infty} \left[\frac{4x}{2n+1} + 2\pi \left(\pi(2n+1) - \sqrt{4x + \pi^2(2n+1)^2} \right) \right], \tag{4.47}$$

which converges for any $x \in \mathbb{R}^+$. It also allows to identify the branch cut of the root at $x < -\pi^2/4$ as the mathematical reason for the radius of convergence of the power series being $\pi^2/4$. As can be seen from the plot of Eq. (4.47) in Fig. 4.2, the analytic continuation of the power series is a positive function. Positivity can also be shown for finite Λ (see Appendix C.3).

Assuming that the exact free energy is an analytic function in $|\sum_{\mu=1}^{d_{n_0}} \eta_\mu^{n_0} \varphi_\mu^{n_0}(\Omega, s)|^2$, this proofs that *the superconducting phase transition is, on the mean-field level, always continuous in the weak-pairing limit.* Note that this holds not only when temperature is varied to drive the phase transition but actually for any parameter such as pressure or doping concentration as long as the TRS of the normal phase is preserved. This is very similar to the situation in centrosymmetric superconductors with intraband pairing where the thermal phase transition is continuous and only the transition in a magnetic field is of first order (for a type-I superconductor) as is commonly known [328]. However, it has recently been shown that, in case of interband pairing, the thermal transition can also become first order [329].

Naturally, fluctuations will eventually change the situation: As discussed in Chap. 1.2, in 2D already the Goldstone modes will make the transition of BKT type [122–124]. Furthermore, one has to take into account the fact that the superconductor is a condensed state of charged particles which inevitably couple to the electromagnetic field. E.g, in 3D, this will render the transition weakly first order in a type-I superconductor [128].

However, despite these fluctuation corrections that eventually change the character of the phase transition, the result of this subsection tells us that we can safely neglect the possibility of a first order transition and, hence, focus on the first few orders in the Ginzburg-Landau expansion for deriving general selection rules for pairing states in the following. We emphasize that it is perfectly legitimate to deduce the latter on the mean-field level: As we have seen in Sec. 1.2, as a first step, before analyzing fluctuations, one has to determine the form and, in particular, the symmetry properties, of the order parameter which is the central theme of the analysis of this chapter. Including fluctuations will modify the behavior of physical quantities in the vicinity of the phase transition which is, however, beyond the scope of the present discussion.

4.3.2 Possible order parameter vectors

Let us next analyze the consequences of the constrained form (4.41) of the Ginzburg-Landau expansion for the possible order parameter vectors $(\eta_1^{n_0}, \dots \eta_{d_{n_0}}^{n_0})$. Naturally, only real multidimensional and complex IRs are of interest here. As already mentioned above, since our analysis is performed in the weak-pairing limit which requires the Fermi surfaces to be singly degenerate, we can set the symmetry group $\mathcal{G}_0$ equal to the point group of the system without loss of generality.

Case study C_{4v}. For pedagogical reasons we will first focus on $\mathcal{G}_0 = C_{4v}$, which will be our working example for the entire chapter, and then generalize the result to all possible point groups of 2D and 3D crystalline systems (see Appendix A.3 for an overview).

From the character table given in Table 4.1, we see that C_{4v} only has one IR of interest for the current discussion: The real two-dimensional IR E where the two components η_1 and η_2 transform as x and y under all symmetry operations.

Using the approach outlined in Chap. 1.1.1, the most general Ginzburg-Landau expansion up to fourth order in η_μ is easily constructed: As a first step, one decomposes the quadratic forms $\eta_\mu A_{\mu\mu'} \eta_{\mu'}$ into IRs leading to $E \otimes E = A_1 \oplus A_2 \oplus B_1 \oplus B_2$. This, in turn, shows that a fourth order term contains

Table 4.1: *Character table of C_{4v}.*

	E	$2C_4$	C_2	$2\sigma_v$	$2\sigma_d$	Basis functions
A_1	1	1	1	1	1	x^2+y^2
A_2	1	1	1	-1	-1	$xy(x^2-y^2)$
B_1	1	-1	1	1	-1	x^2-y^2
B_2	1	-1	1	-1	1	xy
E	2	0	-2	0	0	(x,y)

the trivial representation four times corresponding to the four invariant terms

$$\left|\eta_1^2+\eta_2^2\right|^2, \quad \left|\eta_1\eta_2\right|^2, \quad \left|i\eta_1\eta_2 - i\eta_2\eta_1\right|^2, \quad \left|\eta_1^2-\eta_2^2\right|^2. \tag{4.48}$$

As the third one is identically zero, there are three independent coupling constants in the fourth order contribution to the Ginzburg-Landau expansion. Following the notation of Ref. [79], we thus have

$$\begin{aligned}\mathcal{F}(\eta_1,\eta_2) = \mathcal{F}(0) + a_E(T)\left(\left|\eta_1\right|^2+\left|\eta_2\right|^2\right) + \beta_1\left(\left|\eta_1\right|^2+\left|\eta_2\right|^2\right)^2 \\ + \beta_2\left|\eta_1^2+\eta_2^2\right|^2 + \beta_3\left(\left|\eta_1\right|^4+\left|\eta_2\right|^4\right) + \mathcal{O}\left(|\eta|^6\right).\end{aligned} \tag{4.49}$$

It is straightforward to minimize this expression (see, e.g., Ref. [79]) with respect to (η_1,η_2). Except for accidental degeneracies and assuming a second order phase transition, this shows that only three distinct order parameter configurations,

$$(\eta_1,\eta_2)=(1,0), \qquad (\eta_1,\eta_2)=(1,1), \qquad (\eta_1,\eta_2)=(1,i), \tag{4.50}$$

are possible. The associated phase diagram that shows the dependence on the phenomenological parameters β_j is given in Fig. 4.3.

Noting that only the third state in Eq. (4.50) is not invariant under time-reversal (4.19), we conclude that TRS breaking is possible at a phase transition to a superconducting state transforming under E, but it does not have to occur. As Eq. (4.49) is the most general free energy as allowed by symmetry, this is as good as it gets if we only take into account the symmetry group $\mathcal{G}_0$ of the system. To proceed, we now also apply energetic arguments: Assuming that the splitting E_{so} of the Fermi surfaces is sufficiently large for the weak-pairing limit (4.29) to be applicable, we can use the expression in Eq. (4.41) for the free energy. Expanding the latter up to fourth order in η_μ must yield an expression of the form of Eq. (4.49). As we will see in the following, this expansion will, on top of that, also yield constraints on the coefficients β_j that crucially affect the possible order parameter vectors (η_1,η_2).

To this end, let us consider the fourth order term

$$\mathcal{F}_4(\eta_1,\eta_2) = 4\sum_s \left\langle \left| \sum_{\mu=1}^{2} \eta_\mu \varphi_\mu^E(\Omega,s) \right|^4 \right\rangle_s I_2(\Lambda,T), \tag{4.51}$$

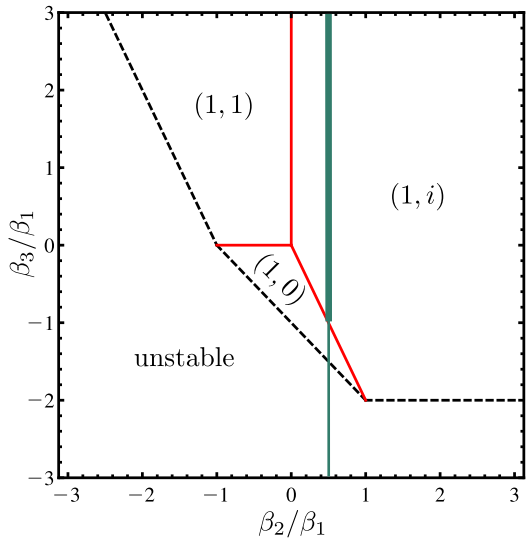

Figure 4.3: ***Phase diagram for order parameter transforming under E of C_{4v}.*** *It follows from minimizing the free energy (4.49). For concreteness, $\beta_1 > 0$ has been assumed. Unstable means that higher order terms in the free energy have to be taken into account to get a minimum at finite η_μ^E. In the weak-pairing limit only configurations on the thick part of the green line are possible leaving $(1, i)$ as the only allowed configuration.*

of Eq. (4.41). We expand the absolute value making use of $\varphi_\mu^E(\boldsymbol{k}, s) \in \mathbb{R}$ and the linearity of $\langle \ldots \rangle_s$ to obtain

$$\begin{aligned}\mathcal{F}_4(\eta_1, \eta_2) =& 4I_2(\Lambda, T)\Big[\alpha_1|\eta_1|^4 + \alpha_2|\eta_2|^4 + 4\beta|\eta_1|^2|\eta_2|^2 + \beta\left(\eta_1^2\eta_2^{*2} + \eta_1^{*2}\eta_2^2\right) \\ &+ 2\left(\gamma_{12}|\eta_1|^2 + \gamma_{21}|\eta_2|^2\right)\left(\eta_1\eta_2^* + \eta_1^*\eta_2\right)\Big],\end{aligned} \tag{4.52}$$

where we have defined

$$\alpha_\mu := \sum_s \left\langle \left(\varphi_\mu^E(\Omega, s)\right)^4 \right\rangle_s , \qquad \beta := \sum_s \left\langle \left(\varphi_1^E(\Omega, s)\varphi_2^E(\Omega, s)\right)^2 \right\rangle_s \tag{4.53a}$$

as well as

$$\gamma_{\mu\mu'} := \sum_s \left\langle \left(\varphi_\mu^E(\Omega, s)\right)^3 \varphi_{\mu'}^E(\Omega, s) \right\rangle_s . \tag{4.53b}$$

These coefficients must satisfy certain relations that result from the symmetries of the system. As the point group C_{4v} is generated by the reflection σ_{xz} at the xz plane and the fourfold rotation C_4^z along the z axis it is sufficient to focus on these two symmetry operations which are represented by

$$\sigma_{xz}: \quad (\eta_1, \eta_2) \longrightarrow (\eta_1, -\eta_2), \tag{4.54a}$$

$$C_4^z: \quad (\eta_1, \eta_2) \longrightarrow (\eta_2, -\eta_1) \tag{4.54b}$$

on the order parameter vector (η_1, η_2). Demanding invariance of the free energy contribution (4.52) under Eqs. (4.54a) and (4.54b) leads to $\gamma_{12} = \gamma_{21} = 0$ and $\alpha_1 = \alpha_2 \equiv \alpha$, respectively. It is readily seen

that, as required, Eq. (4.52) then assumes the form of Eq. (4.49) with

$$\beta_1 = 8\beta I_2(\Lambda, T) = 2\beta_2 > 0, \qquad \beta_3 = 4(\alpha - 3\beta) I_2(\Lambda, T). \tag{4.55}$$

The first relation fixes the ratio $\beta_2/\beta_1 = 1/2$ such that only the configurations on the green line in Fig. 4.3 are possible which already excludes the order parameter configuration $(\eta_1, \eta_2) = (1, 1)$.

Furthermore, as $\rho_s(\Omega) > 0$, we know that

$$\sum_s \left\langle \left[\left(\varphi_1^E(\Omega, s)\right)^2 - \left(\varphi_2^E(\Omega, s)\right)^2 \right]^2 \right\rangle_s \geq 0 \quad \Leftrightarrow \quad \alpha \geq \beta. \tag{4.56}$$

Using this in Eq. (4.55), one finds $\beta_3/\beta_1 \geq -1$ such that only coupling constants on the thick part of the green line can be realized. We have thus shown that the resulting superconducting state must break TRS when transforming under the two-dimensional representation E of C_{4v}. We emphasize that this has been obtained only taking into account the symmetry C_{4v} of the system and making the energetic assumption that the weak-pairing approximation can be applied. Further microscopic details such as the number of relevant orbitals, Fermi surface structure, coupling constants etc. are irrelevant.

General proof by contradiction. In order to generalize these considerations to all possible point groups of crystalline systems, it is much more convenient and insightful to investigate the problem from a more general point of view instead of approaching the laborious task of performing the very same analysis for all possible multidimensional or complex IRs that are relevant for 2D and 3D systems.

For this purpose, let us consider a general real representation n_0 of arbitrary dimension $d_{n_0} > 1$. It might be either an IR of the symmetry group $\mathcal{G}_0$ of the system or the real reducible representation constructed from a complex IR of $\mathcal{G}_0$ as discussed in Sec. 4.1.2. In both cases, the basis functions $\{\varphi_\mu^{n_0}\}$ can be chosen to be real (see Eq. (4.21)). We assume that the symmetries of the system guarantee that the free energy is invariant under

$$\eta_\mu \to \begin{cases} -\eta_\mu, & \mu = \mu_0 \\ \eta_\mu, & \mu \neq \mu_0 \end{cases} \tag{4.57}$$

for all $\mu_0 \in \{1, 2, \ldots, d_{n_0}\}$, i.e., the free energy must be even in all coefficients separately, and that

$$\alpha_\mu = \sum_s \left\langle \left(\varphi_\mu^{n_0}(\Omega, s)\right)^4 \right\rangle_s \equiv \alpha \tag{4.58}$$

for all $\mu = 1, 2, \ldots d_{n_0}$. E.g., for the IR E of C_{4v}, these two properties are satisfied which directly follows from Eq. (4.54) as we have seen above.

The order parameter vector $(\eta_1, \eta_2, \ldots, \eta_{d_{n_0}})$ associated with the representation n_0 is determined by minimizing the free energy $\mathcal{F}(\eta_\mu)$ which, taking into account only the terms up to fourth order in η_μ, reads as

$$\mathcal{F}(\boldsymbol{\eta}) = \mathcal{F}(0) + a(T)\lambda^2 + 4I_2(\Lambda, T)\beta(\boldsymbol{z})\lambda^4 + \mathcal{O}(\lambda^6), \qquad \beta(\boldsymbol{z}) = \sum_s \left\langle \left| \sum_{\mu=1}^{d_{n_0}} z_\mu \varphi_\mu^{n_0}(\Omega, s) \right|^4 \right\rangle_s > 0, \tag{4.59}$$

where we have used the convenient parameterization

$$\eta_\mu = \lambda z_\mu, \qquad \lambda \in \mathbb{R}^+, \quad z_\mu \in \mathbb{C} : \sum_\mu |z_\mu|^2 = 1. \tag{4.60}$$

Minimizing with respect to λ, one finds, infinitesimally below the phase transition, where $a(T) < 0$ with infinitesimal modulus, the nontrivial minimum at

$$\lambda = \lambda_0 = \sqrt{\frac{-a(T)}{8I_2(\Lambda, T)\beta(\boldsymbol{z})}} \tag{4.61}$$

with value

$$\mathcal{F}(\lambda_0 \boldsymbol{z}) = \mathcal{F}(0) - \frac{a^2(T)}{16I_2(\Lambda, T)\beta(\boldsymbol{z})} + \mathcal{O}(\lambda^6). \tag{4.62}$$

Therefore, minimizing the Ginzburg-Landau expansion up to fourth order is tantamount to minimizing $\beta(\boldsymbol{z})$ on the $(2d_{n_0} - 1)$-dimensional hypersphere $\boldsymbol{z}^\dagger \boldsymbol{z} = 1$.

Note that, it is not always possible to determine the order parameter uniquely from the fourth order expansion since the set $\mathcal{Z}$ of unit vectors $\boldsymbol{z}$ minimizing $\beta(\boldsymbol{z})$ might contain physically inequivalent states that are degenerate in fourth order[3]. This degeneracy will be removed by including higher-order terms in the Ginzburg-Landau expansion. Recalling that first order transitions have been ruled out in Sec. 4.3.1, focusing on the expansion up to fourth order, however, already rigorously excludes all states with $\boldsymbol{z} \notin \mathcal{Z}$ as candidate pairing states. In the following we use this to show that a purely real order parameter vector cannot be realized in systems with free energy expansion (4.41).

We apply a proof by contradiction assuming that there is a purely real $x_\mu \in \mathbb{R}$ with $\boldsymbol{x} \in \mathcal{Z}$. Now choose μ_0 such that $x_{\mu_0} \neq 0$ and consider

$$\boldsymbol{z}_\xi = (x_1, \ldots, e^{i\xi} x_{\mu_0}, \ldots, x_{d_{n_0}}), \tag{4.63}$$

where we introduced relative complexity between coefficient μ_0 and all others parameterized by $\xi \in \mathbb{R}$. It holds

$$\beta(\boldsymbol{z}_\xi) = \sum_s \left\langle \left| x_{\mu_0} e^{i\xi} \varphi_{\mu_0}^{n_0}(\Omega, s) + \sum_{\mu \neq \mu_0} x_\mu \varphi_\mu^{n_0}(\Omega, s) \right|^4 \right\rangle_s \tag{4.64}$$

$$\sim \beta(\boldsymbol{x}) - 2\xi^2 \sum_s \left\langle x_{\mu_0} \varphi_{\mu_0}^{n_0}(\Omega, s) \Big(\sum_{\mu \neq \mu_0} x_\mu \varphi_\mu^{n_0}(\Omega, s) \Big) \Big(\sum_\mu x_\mu \varphi_\mu^{n_0}(\Omega, s) \Big)^2 \right\rangle_s \tag{4.65}$$

for $\xi \ll 1$ taking advantage of the reality of the basis functions. Due to the symmetry (4.57), all terms containing an odd power of any of the x_μ must vanish and we can write

$$\beta(\boldsymbol{z}_\xi) \sim \beta(\boldsymbol{x}) - C(\boldsymbol{x})\xi^2, \qquad C(\boldsymbol{x}) = 4 \sum_{\mu \neq \mu_0} x_{\mu_0}^2 x_\mu^2 \sum_s \left\langle \Big(\varphi_{\mu_0}^{n_0}(\Omega, s) \varphi_\mu^{n_0}(\Omega, s) \Big)^2 \right\rangle_s . \tag{4.66}$$

Recalling the positivity of the angle-resolved density of states $\rho_s(\Omega)$, we have

$$\sum_s \left\langle \Big(\varphi_{\mu_0}^{n_0}(\Omega, s) \varphi_\mu^{n_0}(\Omega, s) \Big)^2 \right\rangle_s \geq 0, \tag{4.67}$$

where equality only holds if one of the basis functions vanishes identically, $\varphi_\mu^{n_0} = 0$ or $\varphi_{\mu_0}^{n_0} = 0$. Due to assumption (4.58) this can only be the case when all basis functions vanish. Although this sounds like a physically irrelevant, purely mathematical comment at first glance, the exact vanishing of the

[3] E.g., this is the case for the two-dimensional IR of the cubic group O [79].

basis functions can be enforced by symmetry in 2D systems as will be important in Sec. 4.4. For the present discussion, we have to assume that $\varphi_\mu^{n_0} \neq 0$ as, otherwise, the superconducting order cannot occur within the weak-pairing approximation since Eq. (4.41) then becomes

$$\mathcal{F}(\eta_\mu) = \mathcal{F}(0) + \frac{1}{g_{n_0}} \sum_{\mu=1}^{d_{n_0}} |\eta_\mu|^2 \tag{4.68}$$

which is minimized by $\eta_\mu = 0$. Without loss of generality, we can thus take Eq. (4.67) to be valid with $\geq$ replaced by $>$.

Then, $C(\boldsymbol{x}) > 0$ for all $\boldsymbol{x} \neq \boldsymbol{e}_{\mu_0}$[4]. Consequently, Eq. (4.66) implies that $\exists \xi : \beta(\boldsymbol{z}_\xi) < \beta(\boldsymbol{x})$ and, hence, contradicts our assumption that β can be minimized by a real vector, unless $\boldsymbol{x}$ is fully polarized along one axes ($\boldsymbol{x} = \boldsymbol{e}_{\mu_0}$).

To rule out that β assumes its minimal value at $\boldsymbol{x} = \boldsymbol{e}_{\mu_0}$, we define

$$\boldsymbol{z}'_\xi = \frac{1}{\sqrt{1+\xi^2}} \left(\boldsymbol{e}_{\mu_0} + i\xi \boldsymbol{e}_{\mu_1} \right) \tag{4.69}$$

with some $\mu_1 \neq \mu_0$ and consider

$$\beta(\boldsymbol{z}'_\xi) = \frac{1}{(1+\xi^2)^2} \sum_s \left\langle \left| \varphi_{\mu_0}^{n_0}(\Omega, s) + i\xi \varphi_{\mu_1}^{n_0}(\Omega, s) \right|^4 \right\rangle_s \tag{4.70}$$

$$\sim \beta(\boldsymbol{e}_{\mu_0}) - 2\xi^2 \left(\sum_s \left\langle \left(\varphi_{\mu_0}^{n_0}(\Omega, s) \right)^4 \right\rangle_s - \sum_s \left\langle \left(\varphi_{\mu_0}^{n_0}(\Omega, s) \varphi_{\mu_1}^{n_0}(\Omega, s) \right)^2 \right\rangle_s \right) \tag{4.71}$$

The term in brackets is positive which readily follows from

$$\sum_s \left\langle \left[\left(\varphi_{\mu_0}^{n_0}(\Omega, s) \right)^2 - \left(\varphi_{\mu_1}^{n_0}(\Omega, s) \right)^2 \right]^2 \right\rangle_s > 0 \tag{4.72}$$

in combination with assumption (4.58). Here and similarly in the Eq. (4.56), equality is excluded since this would only be the case if

$$\varphi_{\mu_0}^{n_0}(\Omega, s) = \pm \varphi_{\mu_1}^{n_0}(\Omega, s), \tag{4.73}$$

i.e., if the basis functions were linearly dependent. This in turn would imply that

$$\int_s \mathrm{d}\Omega \left(\varphi_{\mu_0}^{n_0}(\Omega, s) \right)^2 = \pm \int_s \mathrm{d}\Omega \, \varphi_{\mu_0}^{n_0}(\Omega, s) \varphi_{\mu_1}^{n_0}(\Omega, s) = 0 \tag{4.74}$$

forcing $\varphi_{\mu_0}^{n_0} = 0$ which is ruled out as discussed above. The last equality in Eq. (4.74) follows from the orthogonality of basis functions transforming as different components of an IR or, more generally, from

$$\int_s \mathrm{d}\Omega \, \varphi_\mu^n(\Omega, s) \varphi_{\mu'}^{n'}(\Omega, s) \propto \delta_{n,n'} \delta_{\mu,\mu'} \tag{4.75}$$

which directly follows from the grand orthogonality theorem (1.10).

[4] The reason for this is clear: If all x_μ vanish except for one (by design x_{μ_0}), the phase factor in Eq. (4.64) cancels out as required by gauge symmetry.

Having established the strict positivity of the term in brackets in Eq. (4.71), we see that we can always find a configuration with lower value of β than that of $\boldsymbol{x} = \boldsymbol{e}_{\mu_0}$. Taken together, $\beta(\boldsymbol{z})$ does not assume its minimal value at a purely real $\boldsymbol{z}$. Physically, this means that the resulting superconductor necessarily breaks TRS.

With this general proof at hand, we only have to show that the symmetries require invariance of the free energy under (4.57) and lead to Eq. (4.58) to proof that only relatively complex, i.e., TRS-breaking, order parameter vectors are possible for a given point group.

As shown in Appendix C.4, these prerequisites are indeed fulfilled for all multidimensional real IRs of all possible point groups of 2D and 3D crystalline systems. For the real representations constructed from the complex IRs of the crystalline point groups, the situation is different which is a consequence of the symmetries being less restrictive since n_0 is reducible in this case: For the one-dimensional complex IRs of $C_4 \cong S_4$ and of C_{4h}, we still have $\alpha_1 = \alpha_2 \equiv \alpha$, however, the invariance under Eq. (4.57) is not enforced by symmetry any more.

This implies that $\gamma_{12} = -\gamma_{21} \equiv \gamma$ is generally nonzero in the fourth order term (4.52) in the free energy expansion and has crucial consequences since $C(\boldsymbol{x})$ in Eq. (4.66) is not guaranteed to be positive any more,

$$C(\boldsymbol{x}) = 4x_1^2x_2^2\beta + 2\gamma\left(x_1^3x_2 - x_1x_2^3\right) = \beta\, f_1(\phi, \gamma/\beta), \tag{4.76}$$

where we have, in the second equality, inserted the parameterization $(x_1, x_2) = (\cos(\phi), \sin(\phi))$ and introduced the function

$$f_1(\phi, g_1) = \sin(2\phi)\left(\sin(2\phi) + g_1\cos(2\phi)\right) \tag{4.77}$$

for later reference. For any $g_1 \in \mathbb{R} \setminus \{0\}$ there is a $\phi \in \mathbb{R}$ such that the function becomes negative. Consequently, our former proof by contradiction does not apply in its current form.

To generalize it, for the specific case of $d_{n_0} = 2$, we consider

$$\boldsymbol{z}_{\boldsymbol{\xi}} = U(\boldsymbol{\xi})\boldsymbol{x} \tag{4.78}$$

instead of Eq. (4.63) with unitary $U(\boldsymbol{\xi})$ to ensure $\boldsymbol{z}_{\boldsymbol{\xi}}^\dagger \boldsymbol{z}_{\boldsymbol{\xi}} = 1$. Due to gauge invariance it is sufficient to consider $U(\boldsymbol{\xi}) \in \mathrm{SU}(2)$ which we parameterize according to

$$U(\boldsymbol{\xi}) = e^{i\frac{\boldsymbol{\xi}\cdot\boldsymbol{\tau}}{2}}, \qquad \boldsymbol{\xi} \in \mathbb{R}^3, \tag{4.79}$$

with $\boldsymbol{\tau}$ denoting Pauli matrices. Taking $\boldsymbol{\xi} = \xi\boldsymbol{e}_3$ corresponds to Eq. (4.63) with $d_{n_0} = 2$ which rules out all real-valued states with $f_1(\phi, \gamma/\beta) > 0$ as discussed above. To obtain a second constraint, consider $\boldsymbol{\xi} = \xi\boldsymbol{e}_1$ which yields

$$\beta(\boldsymbol{z}_{\xi\boldsymbol{e}_1}) \sim \beta(\boldsymbol{x}) - \widetilde{C}(\boldsymbol{x})\xi^2, \qquad \widetilde{C}(\boldsymbol{x}) = \frac{1}{2}(x_1^2 - x_2^2)^2(\alpha - \beta) + 2\gamma x_1x_2\left(x_1^2 - x_2^2\right). \tag{4.80}$$

Again inserting $(x_1, x_2) = (\cos(\phi), \sin(\phi))$, we find

$$\widetilde{C}(\boldsymbol{x}) = \frac{\alpha - \beta}{2} f_2\left(\phi, 2\gamma/(\alpha - \beta)\right), \qquad f_2(\phi, g_2) = \cos(2\phi)\left(\cos(2\phi) + g_2\sin(2\phi)\right). \tag{4.81}$$

As $\alpha > \beta$ (see Eq. (4.72)), this excludes all real-valued states with $f_2(\phi, 2\gamma/(\alpha - \beta)) > 0$. Exactly as in case of f_1, there are, for any nonzero real g_2, $\phi \in \mathbb{R}$ such that $f_2(\phi, g_2) < 0$.

However, we can actually exclude all real states with one out of $f_1(\phi, \gamma/\beta)$ and $f_2(\phi, 2\gamma/(\alpha-\beta))$ positive. It is straightforward to show that there is $\phi \in \mathbb{R}$ with $f_1(\phi, g_1), f_2(\phi, g_2) \leq 0$ only if $g_1 g_2 \geq 1$. Therefore, we can exclude all real states unless

$$\frac{\gamma}{\beta}\frac{2\gamma}{\alpha-\beta} \geq 1 \quad \Leftrightarrow \quad \gamma^2 \geq \frac{1}{2}\beta(\alpha-\beta). \tag{4.82}$$

To proof that this can never be satisfied, we first note that

$$\langle \varphi_\mu | \varphi_{\mu'} \rangle := \rho_F^{-1} \sum_s \int_s \mathrm{d}\Omega\, \rho_s(\Omega) \varphi_\mu^*(\Omega, s) \varphi_{\mu'}(\Omega, s) \tag{4.83}$$

defines an inner product since $\rho_s(\Omega) > 0$ and, hence, satisfies the Cauchy-Schwarz inequality

$$|\, \langle \varphi_\mu | \varphi_{\mu'} \rangle\, |^2 \leq \langle \varphi_\mu | \varphi_\mu \rangle \cdot \langle \varphi_{\mu'} | \varphi_{\mu'} \rangle\,. \tag{4.84}$$

This, together with $\alpha_1 = \alpha_2$ and $\gamma_1 = -\gamma_2$, can be used to conclude that

$$\gamma^2 = \frac{1}{4}\left(\gamma_1 - \gamma_2\right)^2 = \frac{1}{4}\left|\langle \varphi_1\varphi_2 | \varphi_1^2 - \varphi_2^2 \rangle\right|^2 \leq \frac{1}{4}\langle \varphi_1\varphi_2 | \varphi_1\varphi_2 \rangle \cdot \langle \varphi_1^2 - \varphi_2^2 | \varphi_1^2 - \varphi_2^2 \rangle = \frac{1}{2}\beta(\alpha-\beta). \tag{4.85}$$

Equality is only possible when $\varphi_1\varphi_2$ and $\varphi_1^2 - \varphi_2^2$ are linearly dependent which is in principle possible (both transform under B of $C_4 \simeq S_4$) but requires fine tuning. Consequently, Eq. (4.82) cannot be satisfied such that the free energy cannot be minimized by a purely real order parameter vector and the state must break TRS.

Taken together, we have shown in this subsection that, for any 2D and 3D crystalline system both with spin-0 or spin-1/2 TRS in the normal state, *a superconductor with an order parameter transforming under a complex or multidimensional IR must necessarily break TRS if the weak-pairing approximation applies.*

The experimental observation of a splitting of the transition into two upon reducing the point symmetry in such a way that the components of the multidimensional representation transform under different IRs of the reduced symmetry group (see, e.g., Refs. [213, 214]) indicates that the order parameter transforms under a multidimensional IR. If the weak-pairing limit applies, the observation of a splitting will strongly indicate that TRS is broken. This shows how the statement derived above can be used as a tool to determine the TRS properties of a superconductor.

Importance of symmetries. Before closing, we want to emphasize that despite the generality of our proofs by contradiction, point symmetries are essential ingredients. To see this, consider

$$\beta(\boldsymbol{z}) = \sum_s \left\langle \left| \sum_{\mu=1}^{d_{n_0}} z_\mu \varphi_\mu^{n_0}(\Omega, s) \right|^4 \right\rangle_s \equiv \rho_F^{-1} \sum_s \int_s \mathrm{d}\Omega\, \rho_s(\Omega) \left| \sum_{\mu=1}^{d_{n_0}} z_\mu \varphi_\mu^{n_0}(\Omega, s) \right|^4 \tag{4.86}$$

determining the fourth-order term of the Ginzburg-Landau expansion according to Eq. (4.59). If it was possible to proof that its minimum (subject to $\boldsymbol{z}^\dagger \boldsymbol{z} = 1$) cannot occur at a purely real $\boldsymbol{z}$ without further symmetry requirements, it would also hold for the trial density of states $\rho_s(\Omega) = \rho_0 \delta_{s,s_0} \delta(\Omega - \Omega_0)$. Inserting this in Eq. (4.86) and, for simplicity, focusing on $d_{n_0} = 2$, we get

$$\beta(\boldsymbol{z}) = \rho_0 \left| z_1 \varphi_1^{n_0}(\Omega_0, s_0) + z_2 \varphi_2^{n_0}(\Omega_0, s_0) \right|^2, \tag{4.87}$$

which is clearly minimized by a real-valued $\boldsymbol{z}$ with $z_1/z_2 = -\varphi_2^{n_0}(\Omega_0, s_0)/\varphi_1^{n_0}(\Omega_0, s_0)$.

4.4 Further consequences for 2D systems

In this section, we will focus on 2D systems and discuss the constraints for possible pairing states coming from the fermionic anticommutation relations (4.32) in the weak-pairing limit. For simplicity of the presentation, let us for the moment restrict the analysis to the physically more relevant case of spinfull fermions ($S = 1/2$) and postpone the discussion of $S = 0$ to Sec. 4.7. Since $\Theta^2 = -1$, we will now have to focus on noncentrosymmetric systems in order to have singly-degenerate Fermi surfaces as required for the weak-pairing limit to be applicable. Note, however, that inversion symmetry is quite naturally broken in the practical realization of 2D superconductors as we have discussed in Chap. 1.3.

Even more importantly for the present purpose, 2D is also special concerning the Fermi-Dirac constraint (4.32), which forces $\widetilde{\Delta}_s(\boldsymbol{k})$ to be even under $(s, \boldsymbol{k}) \to (s_\mathrm{K}, -\boldsymbol{k})$, since the latter transformation can be realized as a twofold rotation C_2^z perpendicular to the plane of the system (the xy plane in the following). If C_2^z is element of the point group $\mathcal{G}_p$ of the system, all IRs of $\mathcal{G}_p$ will be either even or odd under this rotation (see Appendix A.2). In this case, the Fermi-Dirac constraint (4.32) forces all basis functions $\varphi_n(\boldsymbol{k}, s)$ transforming under an IR that is odd under C_2^z to vanish identically, i.e.,

$$\mathcal{R}^n_\chi(C_2^z) = -\mathbb{1}_{d_n} \quad \Rightarrow \quad \varphi^n_\mu(\boldsymbol{k}, s) = 0, \tag{4.88}$$

which directly follows from combining Eqs. (4.35) and (4.37). It means that a superconducting state transforming under an IR with $\mathcal{R}^n_\chi(C_2^z) = -\mathbb{1}$ is not possible in the weak-pairing limit. In Sec. 4.5.1, we will analyze in detail under which energetic conditions the weak-pairing limit can be used in order to exclude these pairing states.

Let us illustrate Eq. (4.88) in a minimal example: Consider a single-orbital system with normal state Hamiltonian

$$h_{\boldsymbol{k}} = \frac{\boldsymbol{k}^2}{2m_e}\sigma_0 + \boldsymbol{g}_{\boldsymbol{k}} \cdot \boldsymbol{\sigma} \tag{4.89}$$

with Pauli matrices σ_j describing the spin of the electrons and m_e the effective mass. Suppose the model has C_2^z as well as TRS leading to $(g_{\boldsymbol{k}1}, g_{\boldsymbol{k}2}, g_{\boldsymbol{k}3}) = (-g_{-\boldsymbol{k}1}, -g_{-\boldsymbol{k}2}, g_{-\boldsymbol{k}3})$ and $\boldsymbol{g}_{\boldsymbol{k}} = -\boldsymbol{g}_{-\boldsymbol{k}}$ which implies $g_3 = 0$. The associated eigenstates are then given by $\psi_{\boldsymbol{k}s} = (1, p_s e^{i\alpha^g_{\boldsymbol{k}}})^T/\sqrt{2}$, where $p_1 = -p_2 = 1$ and $\alpha^g_{\boldsymbol{k}}$ denotes the angle of $\boldsymbol{g}_{\boldsymbol{k}}$ relative to the g_1 axis. We decompose the superconducting order parameter into singlet and triplet, $\Delta(\boldsymbol{k}) = \left(\Delta^S_{\boldsymbol{k}} + \boldsymbol{d}_{\boldsymbol{k}} \cdot \boldsymbol{\sigma}\right) i\sigma_2$, and demand it to be odd under C_2^z which is equivalent to $i\sigma_3\Delta(-\boldsymbol{k})i\sigma_3 = -\Delta(\boldsymbol{k})$ (see Eq. (4.6)). As $\Delta^S_{\boldsymbol{k}} = \Delta^S_{-\boldsymbol{k}}$ and $\boldsymbol{d}_{\boldsymbol{k}} = -\boldsymbol{d}_{-\boldsymbol{k}}$ this forces the order parameter to be a pure triplet state with the $\boldsymbol{d}$ vector aligned along the z axis. It then directly follows that the matrix elements

$$\psi^\dagger_{\boldsymbol{k}s}\Delta_{\boldsymbol{k}}\psi^*_{-\boldsymbol{k}s'} = -\frac{1}{2}d_{\boldsymbol{k}3}\left(p_s - p_{s'}\right)e^{-i\alpha^g_{\boldsymbol{k}}} \tag{4.90}$$

of the order parameter with respect to the eigenfunctions of $h_{\boldsymbol{k}}$ vanish for $s = s'$ as expected from our general symmetry discussion. We mention that the vanishing (4.88) of basis functions has very recently also been pointed out in Ref. [330].

Before proceeding with the discussion of the consequences of these "symergetic" constraints on the possibility of TRS breaking at a superconducting phase transition (Sec. 4.4.1) and on the orientation of the triplet vector (Sec. 4.4.2), we want to clarify the meaning of 2D in this section: Clearly, the system does not have to be strictly 2D and the presence of a finite number of subbands – formally included in the Greek indices α, β in Eq. (4.2) – is possible as long as the energetic splitting between the different Fermi surfaces is sufficiently large for the weak-pairing approximation to be applicable. Our notion

of 2D does, however, not include highly anisotropic 3D materials consisting of weakly coupled stacked conducting sheets.

4.4.1 Design principle for spontaneous TRS-breaking superconductivity

Let us begin our discussion of TRS by first reexamining our working example of C_{4v} and then generalize our observation to all possible noncentrosymmetric point groups of 2D systems.

Case study C_{4v}. From the character table of C_{4v} in Table 4.1, we see that this point group only allows for real IRs. Consequently, TRS can only be broken in the two-dimensional IR E. However, the basis functions of E are forced to be odd under C_2^z and, hence, must vanish according to Eq. (4.90). Consequently, a superconducting state transforming under E, i.e., transforming as any of the three possible configurations x, $x+y$ and $x+iy$ (see Eq. (4.50)), can be excluded. In particular, no spontaneous TRS breaking can occur at a single superconducting phase transition in the weak-pairing limit.

This shows that our considerations of the higher-order terms in the Ginzburg-Landau expansion in Sec. 4.3.2 for a system with C_{4v} symmetry are irrelevant in 2D as the combination of point-symmetry and Fermi-Dirac constraints do not allow for finite pairing in the E representation to begin with. Note that the latter does not hold for 3D systems where $(s, \boldsymbol{k}) \to (s_\mathrm{K}, -\boldsymbol{k})$ cannot be realized as a rotation and, hence, order parameters transforming under E are not excluded but necessarily have to break TRS as shown in Sec. 4.3.2.

Arbitrary point group. It is straightforward to generalize this analysis to all possible point groups of 2D systems embedded in 3D space which are summarized in Appendix A.3. As mentioned above, we can restrict the discussion to the noncentrosymmetric point groups as the absence of a center of inversion is required for the Fermi surfaces to be nondegenerate. As a first step, we note that TRS breaking is also not possible for C_4 which only has one-dimensional IRs and its complex IRs are all odd under C_2^z. The very same must hold for the isomorphic groups D_4, D_{2d} and S_4. For all other groups containing only a twofold (such as C_{2v}) or without any (like, e.g., for C_1) rotation symmetry along the z axis, all IRs are real and one-dimensional excluding TRS-breaking superconductivity. For the remaining possible point groups, all of which contain a threefold rotation, one cannot exclude spontaneous TRS breaking on the general level of the present discussion.

Taken together, this leads to the following necessary condition or design principle for spontaneous TRS breaking at a single superconducting phase transition in any crystalline 2D system where the pairing approximation applies [325, 326]: *The superconducting condensate can only break TRS if a threefold rotation symmetry is element of the point group of the high-temperature phase.*

As we will see in Sec. 4.6, this result can be used both to gain information about the time-reversal properties of superconducting states that have been found experimentally but not yet fully microscopically identified and as a design principle in the search for TRS-breaking superconductors.

4.4.2 Orientation of the triplet vector

Let us next discuss the consequences of the exclusion of IRs that are odd under C_2^z for the spin-structure of the possible order parameters.

Multiple orbitals. For the sake of generality, we will consider the general situation where the order parameter $\Delta(\boldsymbol{k})$ is a matrix not only in spin, but also in orbital and/or subband space. Then the decomposition into spin singlet (antisymmetric spin wavefunction) and triplet (symmetric spin wavefunction)

takes the more general form

$$\Delta(\boldsymbol{k}) = \Delta^S_{\boldsymbol{k}}\, T + \sum_{j=1}^{3} D^j_{\boldsymbol{k}}\, \sigma_j T, \tag{4.91}$$

where, as opposed to Eq. (1.17), $\Delta^S_{\boldsymbol{k}}$ and $D^j_{\boldsymbol{k}}$ are generally matrices in orbital and/or subband space. The correct spin-symmetry of the singlet and triplet terms follows from $T^T = -T$ and $(\boldsymbol{\sigma} T)^T = -T\boldsymbol{\sigma}^* = \boldsymbol{\sigma} T$, respectively.

In the following it will be convenient to choose a real orbital/subband basis such that the representation of time-reversal $T\mathcal{K}$ becomes trivial ($\propto \mathbb{1}_o$) in orbital space, $T = i\sigma_2 \otimes \mathbb{1}_o$. Within these conventions, the Fermi-Dirac constraint (4.3) leads to

$$\left(\Delta^S_{-\boldsymbol{k}}\right)^T = \Delta^S_{\boldsymbol{k}} \qquad \left(D^j_{-\boldsymbol{k}}\right)^T = -D^j_{\boldsymbol{k}}. \tag{4.92}$$

Focusing on point groups $\mathcal{G}_p$ that contain a twofold rotation C_2^z, the superconducting order parameter must be even under this rotation in the weak-pairing limit as discussed above. Splitting the representation $\mathcal{R}_\Psi(C_2^z)$ of C_2^z into its spin $\mathcal{R}_{\Psi_s}(C_2^z)$ and orbital/layer part $\mathcal{R}_{\Psi_o}(C_2^z)$, it follows

$$\mathcal{R}_{\Psi_o}(C_2^z)\Delta^S_{-\boldsymbol{k}}\mathcal{R}^\dagger_{\Psi_o}(C_2^z) = \Delta^S_{\boldsymbol{k}}, \quad \mathcal{R}_{\Psi_o}(C_2^z)D^{1,2}_{-\boldsymbol{k}}\mathcal{R}^\dagger_{\Psi_o}(C_2^z) = -D^{1,2}_{\boldsymbol{k}}, \quad \mathcal{R}_{\Psi_o}(C_2^z)D^{3}_{-\boldsymbol{k}}\mathcal{R}^\dagger_{\Psi_o}(C_2^z) = D^{3}_{\boldsymbol{k}}. \tag{4.93}$$

These conditions can be simplified by considering the symmetries of the unit cell Hamiltonian h_{uc}: It is invariant under $\mathcal{G}_p$ and, neglecting accidental degeneracies, all of its eigenspaces are spanned by basis functions of an IR of $\mathcal{G}_p$. Any IR[5] will be either even or odd under C_2^z (see, again, Appendix A.2) such that

$$\mathcal{R}_{\Psi_o} = \mathrm{diag}\left(c_1, c_2, \ldots, c_{N/2}\right), \qquad c_j \in \{+1, -1\}. \tag{4.94}$$

using an eigenbasis of h_{uc}. E.g., in LAO/STO heterostructures (see Sec. 1.3.1), the states at the Fermi surface result from the Ti $3d_{xy}$ (transforms under B_2 of C_{4v}) and $3d_{xz}$, $3d_{yz}$ (transforming under E of C_{4v}) orbitals. In this basis, we have $\mathcal{R}_{\Psi_o} = \mathrm{diag}(1, -1, -1)$.

If the splitting between the different degenerate subspaces is sufficiently large, we can neglect subspace-off-diagonal pairing matrix elements and Eq. (4.93) becomes

$$\left(\Delta^S_{\boldsymbol{k}}\right)^T = \Delta^S_{\boldsymbol{k}}, \qquad \left(D^{1,2}_{\boldsymbol{k}}\right)^T = D^{1,2}_{\boldsymbol{k}}, \qquad \left(D^{3}_{\boldsymbol{k}}\right)^T = -D^{3}_{\boldsymbol{k}}, \tag{4.95}$$

where we have already taken into account Eq. (4.92). It shows that the z component $D^3_{\boldsymbol{k}}$ of the triplet vector must have vanishing intraorbital matrix elements. This means that, as far as physical properties are concerned that are only sensitive to the orbital-diagonal components of the order parameter, the superconductor will behave as if its triplet vector was aligned in the xy plane. Due to the energetic separation between the different orbitals (except for high-symmetry points) it might in many cases be legitimate to neglect the interorbital pairing yielding $D^3_{\boldsymbol{k}} = 0$.

If this assumption indeed holds, we conclude that [326] *in any noncentrosymmetric 2D system with a two-fold rotation symmetry perpendicular to the plane as an element of the point group of the high-temperature phase, the triplet vector has to be aligned within the plane of the system as long as the weak-pairing limit applies.*

[5] Strictly speaking, h_{uc} we use to construct the basis is only the spin-independent part of the full unit cell Hamiltonian, i.e., without any SOC effects. This is important as we otherwise had to consider the IRs of the double group $\mathcal{G}'_p$.

Pseudospin basis. If a system has inversion (I) and TRS (Θ), one can always, despite the entanglement of orbital and spin degrees of freedom in the presence of SOC, introduce a $\boldsymbol{k}$-space-local pseudospin basis [88, 89] $\{|-,\boldsymbol{k}\rangle, |+,\boldsymbol{k}\rangle\}$ on the doubly-degenerate Fermi surfaces that has exactly the same transformation behavior as the physical spin-up and spin-down under these two symmetry operations (see Appendix A.1 for a constructive proof of this statement), $\mathcal{R}_\Psi(I)\,|\tau,\boldsymbol{k}\rangle = |\tau,-\boldsymbol{k}\rangle$ and $\Theta\,|\tau,\boldsymbol{k}\rangle = \tau\,|-\tau,-\boldsymbol{k}\rangle$ with $\tau = \pm$.

Within the pseudospin basis, the restrictions on the triplet vector discussed above assume a more generally valid form. To see this, one has to split the normal state Hamiltonian into a centrosymmetric and noncentrosymmetric part. Diagonalizing the former yields doubly-degenerate eigenvalues (band index j in the following) and allows for introducing a pseudospin basis as discussed above. Denoting the field operators in this basis by $\hat{a}_{\boldsymbol{k}\tau j}$, $\tau = \pm$, the pairing term of the general mean-field Hamiltonian (4.2) assumes the form

$$\hat{H}^{\Delta}_{\mathrm{MF}} = \frac{1}{2}\sum_{\boldsymbol{k}} \hat{a}^{\dagger}_{\boldsymbol{k}\tau j}\left(\widetilde{\Delta}_{\boldsymbol{k}}\right)_{\tau j,\tau' j'} \hat{a}^{\dagger}_{-\boldsymbol{k}\tau' j'} + \mathrm{H.c.}. \tag{4.96}$$

If the energetic separation between the different pairs of spin-orbit-split bands is sufficiently large, we can neglect all terms with $j \neq j'$ in the order parameter, and then expand the diagonal contributions in terms of pseudospin singlet and triplet (associated Pauli matrices denoted by s_i, $i = 0,1,2,3$),

$$\left(\widetilde{\Delta}_{\boldsymbol{k}}\right)_{\tau j,\tau' j'} = \delta_{jj'}\left(\widetilde{\Delta}^{S(j)}_{\boldsymbol{k}} i s_2 + \widetilde{\boldsymbol{d}}^{(j)}_{\boldsymbol{k}}\cdot \boldsymbol{s}\, i s_2\right)_{\tau\tau'}. \tag{4.97}$$

For every j, it looks like a problem with only spin-1/2 degrees of freedom despite the presence of several orbitals. Since the pseudospin also has the same transformation behavior under C_2^z, we immediately find that, irrespective of the potentially strong mixing of different orbitals on the Fermi surfaces due to SOC, the pseudospin triplet vector has to be aligned parallel to the plane of the system if $C_2^z \in \mathcal{G}_p$.

We emphasize, however, that as far as physical properties are concerned, it is the microscopic spin-basis that is relevant in general since the coupling to external perturbations (such as magnetic field or the nuclear angular momentum) is defined with respect to the physical spin and orbital degrees of freedom.

4.5 Beyond weak-pairing

Before applying these general results derived in the weak-pairing limit to several materials in the next section, we will first analyze in more quantitative terms under which physical conditions the weak-pairing approximation is applicable. For this purpose, we have to study the energetics of noncentrosymmetric superconductors also taking into account the matrix elements $D_{ss'}(\boldsymbol{k})$ of the order parameter with respect to different Fermi surfaces $s \neq s'$.

4.5.1 Necessary condition for purely off-diagonal pairing

Let us first consider the most favorable scenario for a superconducting phase with vanishing intra-Fermi-surface matrix elements $D_{ss}(\boldsymbol{k}) = 0$: Assume that the effective electron-electron interaction is, at low energies, dominated by the Cooper channel in Eq. (4.40) associated with an IR n_0 of the point group $\mathcal{G}_p$ of a 2D system that is odd under $C_2^z \in \mathcal{G}_p$. All other interaction channels and, hence, all competing instabilities are assumed to be negligible. The inclusion of the latter lead to even weaker criteria for the applicability of the weak-pairing limit as we will see in Sec. 4.5.2 below.

To analyze the superconducting instability, we perform a mean-field decoupling of the interaction term in Eq. (4.40) leading to

$$\hat{H}_{\text{int}}^{\text{MF}} = -g_{n_0} \sum_{\mu=1}^{d_{n_0}} \sum_{\boldsymbol{k}} \left(\eta_\mu^{n_0} \hat{c}_{\boldsymbol{k}}^\dagger \widetilde{\chi}_\mu^{n_0}(\boldsymbol{k}) T \left(\hat{c}_{-\boldsymbol{k}}^\dagger \right)^T + \text{H.c.} \right) + g_{n_0} \sum_{\mu=1}^{d_{n_0}} \left| \eta_\mu^{n_0} \right|^2 . \tag{4.98}$$

As follows from the central symmetry argument of Sec. 4.4, the mean-field pairing term will become fully Fermi surface off diagonal after transforming into the eigenbasis of the normal state Hamiltonian $h_{\boldsymbol{k}}$. Such a superconducting state can only be realized in a system if its zero temperature condensation energy (see Appendix C.5)

$$E_c(\Delta_0) = \frac{1}{2} \sum_s \sum_{\boldsymbol{k}} \left(\left| E_{\boldsymbol{k}s}(\Delta_0) \right| - \left| \epsilon_{\boldsymbol{k}s} \right| \right) - \frac{\Delta_0^2}{g_{n_0}} \tag{4.99}$$

is positive. In Eq. (4.99), $E_{\boldsymbol{k}s}$ denotes the excitation spectrum of the superconducting mean-field Hamiltonian and using $\Delta_0 := g_{n_0} \sqrt{\sum_\mu |\eta_\mu^{n_0}|^2}$ to describe the dependence on the superconducting order parameter indicates that we are not interested in the detailed structure of the complex order parameter vector $(\eta_1^{n_0}, \ldots, \eta_{d_{n_0}}^{n_0})$ but rather only in its magnitude.

To keep the discussion as simple as possible, let us assume that at a given crystal momentum $\boldsymbol{k}$ only two different bands have to be taken into account which means that bands come energetically close (on the energy scales of the superconductor) only in pairs. The near degeneracy of more bands typically only occurs at high-symmetry points of the Brillouin zone. Besides, it is not expected that the inclusion of more than two bands essentially changes the physics under discussion.

In Appendix C.5, an upper bound $E_c^{\max}(\Delta_0)$ on the condensation energy (4.99) is derived. The main step in this calculation consists of replacing the matrix element $|D_{12}(\boldsymbol{k})|/\Delta_0$ by its maximum value m on the Fermi surface. Physically, this corresponds to the situation of "optimal basis functions" with $|D_{12}(\boldsymbol{k})|$ being constant except for negligibly small regions where it has to vanish as dictated by symmetry. Mathematically, this replacement enhances the value of the condensation energy $E_c(\Delta_0)$ at given Δ_0. Evaluating the sum in Eq. (4.99) as an integral, which we cut off energetically at Λ, shows that the condensation energy can only be positive when the spin-orbit splitting E_{so} of the Fermi surface satisfies [325]

$$E_{\text{so}} < \frac{2\Lambda}{\sinh(1/\lambda)}, \tag{4.100}$$

where the dimensionless coupling constant is defined by $\lambda = 4\rho_F m^2 g$ with ρ_F denoting the density of states at the Fermi level.

Physically, Eq. (4.100) means that, in the weak-coupling limit, $\lambda \ll 1$, superconductivity can only emerge when the spin-orbit splitting is exponentially small. Put differently, in any system with E_{so} comparable to the energetic range of the attractive interaction (e.g., the Debye energy in case of a conventional mechanism), superconductivity with $D_{ss} = 0$ must be a genuine strong coupling phenomenon. The physical reason is that, as can be seen in Fig. 4.1(b), the superconducting order parameter only couples states with single-particle energies differing by E_{so}. This cuts off the Cooper logarithm that usually makes superconductivity a weak-coupling phenomenon.

Finally, one also finds that $\Delta_0 m > E_{\text{so}}/4$ at the positive maximum of $E_c^{\max}(\Delta_0)$ indicating that the weak-pairing limit and its selection rules for pairing states derived above can be used as long as the superconducting gap at $T = 0$ is smaller than the spin-orbit splitting of the Fermi surfaces.

4.5.2 Limit of weak inversion-symmetry breaking

Above we have focused on the situation that the superconducting phase with vanishing intra-Fermi-surface matrix elements has no competing instabilities by assuming that all other interaction channels are negligible. This yielded a generally valid sufficient condition for the applicability of the weak-pairing limit to rule out this type of pairing states. Here we will analyze the complementary limit where there are other superconducting instabilities with slightly smaller transition temperatures which will be relevant for our discussion of Sr_2RuO_4 in Sec. 4.6.1 below. We will see that, in this case, already in the limit of weak spin-orbit splitting, $E_{\mathrm{so}} \ll T_c$, the pairing state with $D_{ss}(\boldsymbol{k}) = 0$ are suppressed.

To this end, we have to take into account several terms transforming under different IRs n in the Cooper channel of the interaction and thus start from the interacting Hamiltonian

$$\hat{H} = \sum_{\boldsymbol{k}} \hat{c}^\dagger_{\boldsymbol{k}} h_{\boldsymbol{k}} \hat{c}_{\boldsymbol{k}} - \sum_n g_n \sum_\mu \left[\sum_{\boldsymbol{k}} \hat{c}^\dagger_{\boldsymbol{k}} \widetilde{\chi}^n_\mu(\boldsymbol{k}) T \left(\hat{c}^\dagger_{-\boldsymbol{k}} \right)^T \right] \left[\sum_{\boldsymbol{k}'} \hat{c}^T_{-\boldsymbol{k}'} \left(\widetilde{\chi}^n_{\mu'}(\boldsymbol{k}') T \right)^\dagger \hat{c}_{\boldsymbol{k}'} \right] . \tag{4.101}$$

Let us compare the superconducting state transforming under the IR $n = n_1$ which is odd under $C_2^z \in \mathcal{G}_p$ with any of the others transforming under $n = n_2$. Denoting the associated transition temperatures in the absence of spin-orbit splitting, $E_{\mathrm{so}} = 0$, by $T^{n_1}_{c,0}$ and $T^{n_2}_{c,0}$, respectively, we assume that $T^{n_1}_{c,0} > T^{n_2}_{c,0}$ with $T^{n_1}_{c,0} - T^{n_2}_{c,0} \ll T^{n_1}_{c,0}$. Furthermore, exactly as in Sec. 4.5.1, we simplify the situation by assuming that at every $\boldsymbol{k}$ only two different bands, separated by $E_{\mathrm{so}}(\boldsymbol{k})$, have to be taken into account which we label by $j = 1, 2$ in the entire Brillouin zone. As shown in Appendix C.2.2, the critical value $\langle E^2_{\mathrm{so}} \rangle^c$ of the Fermi surface average of $E^2_{\mathrm{so}}(\boldsymbol{k})$ for a transition to the state transforming under n_2 is given by

$$\sqrt{\langle E^2_{\mathrm{so}} \rangle^c} \sim \frac{4\pi}{\sqrt{7\zeta(3)}} \sqrt{\frac{C^o_{n_2} + C^d_{n_2}}{C^d_{n_2}}} T^{n_1}_{c,0} \sqrt{\frac{T^{n_1}_{c,0} - T^{n_2}_{c,0}}{T^{n_1}_{c,0}}} \tag{4.102}$$

as $(T^{n_1}_{c,0} - T^{n_2}_{c,0})/T^{n_1}_{c,0} \to 0$. Here

$$C^d_n := \sum_{j=1,2} \langle |m_{jj}(\Omega, n)|^2 \rangle , \qquad C^o_n := 2 \langle |m_{12}(\Omega, n)|^2 \rangle \tag{4.103}$$

are Fermi surface averages[6] of the order parameter matrix elements

$$|m_{jj'}(\boldsymbol{k}, n)| := \left| \sum_\mu \hat{\eta}^n_\mu \langle \psi_{\boldsymbol{k}j} | \widetilde{\chi}^n_\mu(\boldsymbol{k}) | \psi_{\boldsymbol{k}j'} \rangle \right| \tag{4.104}$$

with normalized $\hat{\eta}^n_\mu := \eta^n_\mu / \sqrt{\sum_\mu |\eta^{n_0}_\mu|^2}$. By construction, it holds $C^d_{n_1} = 0$.

Eq. (4.102) shows that a pairing state with vanishing Fermi-surface-diagonal matrix elements will be suppressed at a value of the spin-orbit splitting E_{so} that is, by a factor scaling as $\propto \sqrt{(T^{n_1}_{c,0} - T^{n_2}_{c,0})/T^{n_1}_{c,0}}$, smaller than its transition temperature $T^{n_1}_{c,0}$ for $E_{\mathrm{so}} = 0$. Consequently, in a system such as Sr_2RuO_4 where several superconducting states transforming under different IRs are known to be nearly degenerate (see Sec. 4.6.1), the weak-pairing limit can be applied even for $E_{\mathrm{so}} \ll T_c$.

To gain intuition for the prefactors in Eq. (4.102), let us calculate the matrix elements $m_{jj'}(\boldsymbol{k}, n_2)$ explicitly for the single-orbital model in Eq. (4.89) with TRS and $C_2^z \in \mathcal{G}_p$. If the competing state

[6] Defined in direct analogy to Eq. (4.43). Due to the limit $E_{\mathrm{so}} \ll T_c$ we consider here, the density of states can be assumed to be identical on the spin-orbit-split Fermi surfaces such that the average does not depend on j.

transforming under n_2 has purely singlet pairing, one will find that $m_{jj'}(\boldsymbol{k}, n_2) \propto \delta_{jj'}$ independent of $\boldsymbol{g_k}$ and, hence, $C^o_{n_2} = 0$. Then the prefactor in Eq. (4.102) becomes minimal which is just a consequence of the fact that the transition temperature of the singlet state is not affected at all by the energetic splitting $E_{\mathrm{so}} = 0$ as it only couples Kramers partners with the same energy. This is different in case of triplet pairing, $\sum_\mu \hat{\eta}^{n_2}_\mu \widetilde{\chi}^n_\mu(\boldsymbol{k}) = \boldsymbol{\sigma} \cdot \boldsymbol{d_k}$, where the matrix elements are given by

$$|m_{jj}(\boldsymbol{k}, n_2)| = |\hat{\boldsymbol{g}}_{\boldsymbol{k}} \cdot \boldsymbol{d_k}|, \qquad |m_{12}(\boldsymbol{k}, n_2)| = \left| \left(\hat{\boldsymbol{g}}_{\boldsymbol{k}} \times \boldsymbol{d_k} + \boldsymbol{d_k} \right)_3 \right|, \tag{4.105}$$

where we have introduced the normalized spin-orbit vector $\hat{\boldsymbol{g}}_{\boldsymbol{k}} := \boldsymbol{g_k}/|\boldsymbol{g_k}|$.

We first note that, in accordance with Sec. 4.4.2, the diagonal matrix elements vanish if the triplet vector is aligned along the z direction with the entire weight of the superconducting order parameter appearing in $|m_{12}(\boldsymbol{k}, n_2)| = |d_{\boldsymbol{k}z}|$.

For an order parameter transforming under a representation that is even under C_2^z, the triplet vector is fully aligned within the plane of the system and, hence, $|m_{12}(\boldsymbol{k}, n)| = |\hat{\boldsymbol{g}}(\boldsymbol{k}) \times \boldsymbol{d_k}|$. This form of the off-diagonal matrix elements, which basically describe the "pair-breaking" effect of the spin-orbit splitting, shows that increasing E_{so} favors states with $\boldsymbol{d_k}$ parallel to $\boldsymbol{g_k}$ ($\boldsymbol{d_k} \uparrow\uparrow \boldsymbol{g_k}$). We emphasize that this does not necessarily imply that the leading instability satisfies this property as the interaction might favor a pairing state where $\boldsymbol{d_k}$ is not parallel to $\boldsymbol{g_k}$ in the entire Brillouin zone. In Ref. [133], it has been shown that in the special case where the interaction kernel is spin-independent, we indeed get $\boldsymbol{d_k} \uparrow\uparrow \boldsymbol{g_k}$ for finite E_{so}.

4.6 Application to materials

Having derived various general selection rules for superconducting instabilities and their time-reversal properties, let us next apply these findings to several physical systems.

4.6.1 Consequences for Sr_2RuO_4

We start the discussion with the following gedankenexperiment: Consider a 3D superconductor with strong SOC that breaks TRS in its bulk and imagine putting it on a substrate and gradually reducing its thickness d normal to the substrate as illustrated in Fig. 4.4. If the point group $\mathcal{G}_p$ of the resulting thin film, which must be necessarily noncentrosymmetric by the presence of the substrate, does not allow for a threefold rotation symmetry, our analysis of Sec. 4.4 indicates that there are only two possibilities: At some point during the reduction of d, superconductivity either disappears entirely or a transition into a TRS-preserving superconducting phase occurs. If, in addition, $C_2^z \in \mathcal{G}_p$ we also know that the triplet vector will eventually be aligned in the plane of the thin layer system.

A natural candidate material for transforming this gedankenexperiment into a real experiment is provided by the layered perovskite Sr_2RuO_4: As discussed in more detail in Sec. 1.3.2, in bulk Sr_2RuO_4, there is a phase transition at $T_c \simeq 1.5\,\mathrm{K}$ from a Fermi-liquid phase [181] into a superconductor [179] that is most likely a chiral p-wave state with triplet vector $\boldsymbol{d_k} \propto (k_1 + ik_2)\boldsymbol{e}_3$ that breaks TRS [47, 51, 53, 185–189]. SOC is expected to be strong for Ru ($Z = 44$) which provides the mobile carriers that become superconducting. Together with the small transition temperature, this leads to the expectation that the weak-pairing description should be applicable in the thin-film limit. On top of that there are strong both theoretical [183, 195] as well as experimental [331, 332] indications that the chiral p-wave state is nearly degenerate with the four triplet states transforming under the ungerade one-dimensional IRs of its point group D_{4h}. This near degeneracy is naturally understood by noting that it is exact in case of

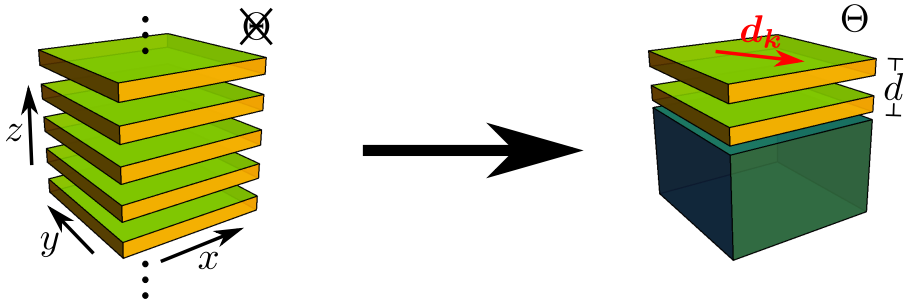

Figure 4.4: ***Gedankenexperiment.*** *Taking a TRS-breaking superconductor (left) on a substrate and reducing its thickness d (right) will force the condensate to either disappear or transform into a time-reversal symmetric state (if $C_3^z \notin \mathcal{G}_p$) with triplet vector $\boldsymbol{d_k}$ constrained to the plane of the system (if $C_2^z \in \mathcal{G}_p$).*

independent spin-rotation symmetry and, hence, only broken by the presence of SOC [183]. The relative difference of the transition temperatures $\Delta T_c/T_c$ has been estimated [195] to be smaller than 0.01 such that the weak-pairing description is expected to apply already for E_{so} being smaller than T_c as can be seen from Eq. (4.102). Furthermore, thin films of Sr_2RuO_4 have already been realized experimentally and shown to be superconducting [68]. Assuming that there are no additional distortions of the crystal structure due to the substrate, the point group D_{4h} of the bulk will be reduced to C_{4v} at the interface. We thus conclude that TRS must be restored and the triplet vector must rotate to be aligned in-plane in the thin-film limit.

This is fully consistent with the analysis of Refs. [333, 334] on the impact of the Dresselhaus-Rashba effect on the superconducting instabilities in Sr_2RuO_4 where the transition to a time-reversal symmetric state with in-plane $\boldsymbol{d}$ vector has been predicted by microscopic calculations focusing on the γ band. The symergetic arguments of this chapter show that this transition occurs irrespective of which band is relevant for describing superconductivity and independent of any further assumptions about the microscopic theory such as the structure of the interaction of the system.

Pairing states in thin layer. Let us next take a closer look at the possible order parameters in thin layer Sr_2RuO_4. In Table 4.2, the allowed pairing states are listed according to the IRs of C_{4v}. Due to SOC and the absence of inversion symmetry, singlet and triplet will automatically mix. However, the triplet component is expected to be much larger than singlet as the triplet interaction channel is dominant in bulk Sr_2RuO_4. Although the relevant low-energy degrees of freedom of Sr_2RuO_4 are derived from three different orbitals, the Ru $4d_{xy}$, $4d_{xz}$ and $4d_{yz}$ states, we have assumed that the order parameter is trivial ($\propto \mathbb{1}_o$) in orbital space in Table 4.2 to avoid lengthy expressions.

In accordance with Sec. 4.4, the Fermi-surface-diagonal matrix elements $\widetilde{\Delta}_s(\boldsymbol{k})$ of the order parameter vanish for the two-dimensional IR E and all energetically allowed triplet vectors are aligned in the plane of the system. We emphasize that the former statement also holds when order parameters with arbitrary orbital structure are taken into account, while the latter holds as long as only orbital diagonal components are relevant. Note that *diagonal* in orbital space is less restrictive than *trivial* in orbital space. This distinction might be particularly relevant for Sr_2RuO_4, where an order parameter that is diagonal but not trivial with respect to the different orbitals has been suggested [197] for bulk Sr_2RuO_4. From a pure symmetry point of view, the presence of several orbitals transforming

Table 4.2: *Singlet ($\Delta^S_{\boldsymbol{k}}$) and triplet ($\boldsymbol{d_k}\cdot\boldsymbol{\sigma}$) components as well as weak-pairing description ($\widetilde{\Delta}_s(\boldsymbol{k})$) of the possible superconducting phases of a system with C_{4v} point group assuming trivial behavior in orbital space. Here X and Y denote continuous, real-valued, momentum-dependent functions transforming as $\sin(k_1)$ and $\sin(k_2)$ under C_{4v}.*

Gr. th.	Pairing	TRS	$\Delta^S_{\boldsymbol{k}}$	$\boldsymbol{d_k}\cdot\boldsymbol{\sigma}$	$\widetilde{\Delta}_s(\boldsymbol{k})$
A_1	s-wave	y	$1, X^2+Y^2$	$Y\sigma_1 - X\sigma_2$	$1, X^2+Y^2$
A_2	g-wave	y	$XY(X^2-Y^2)$	$X\sigma_1 + Y\sigma_2$	$XY(X^2-Y^2)$
B_1	$d_{x^2-y^2}$	y	X^2-Y^2	$Y\sigma_1 + X\sigma_2$	X^2-Y^2
B_2	d_{xy}	y	XY	$X\sigma_1 - Y\sigma_2$	XY
$E(1,0)$	$e_{(1,0)}$	y	0	$\sigma_3 Y$	0
$E(1,1)$	$e_{(1,1)}$	y	0	$\sigma_3(Y-X)$	0
$E(1,i)$	$e_{(1,i)}$	n	0	$\sigma_3(X+iY)$	0

nontrivially enriches the structure of the allowed pairing states within a given representation: Using the basis $\{4d_{xy}, 4d_{xz}, 4d_{yz}\}$, the matrix $\mathrm{diag}(0,1,-1)$ transforms under B_1 of C_{4v}. Therefore, e.g., the order parameter $\mathrm{diag}(0,1,-1)(Y\sigma_1 + X\sigma_2)$, that is diagonal in orbital space, transforms under A_1 but is not included in Table 4.2. Similarly, there is actually one additional orbital-diagonal term in the singlet and triplet channel for every representation (except for the singlet component in case of E) in Table 4.2.

Topological properties. Our symergetic arguments strongly imply that the superconducting state of the thin layer of Sr_2RuO_4 preserves TRS and, hence, belongs to class DIII (see Chap. 2.1). In 2D, its topological properties are classified by a $\mathbb{Z}_2$ invariant $\nu_{\mathbb{Z}_2}$ that is, within the weak-pairing limit, given by Eq. (2.19),

$$\nu_{\mathbb{Z}_2} = \prod_s \left[\mathrm{sign}\left(\widetilde{\Delta}_s(\boldsymbol{k}_s) \right) \right]^{m_s}, \tag{4.106}$$

which we have reprinted for convenience of the reader [280]. In Eq. (4.106), m_s denotes the number of TRIM enclosed by Fermi surface s.

To analyze the topology of the four possible pairing states transforming under the one-dimensional IRs of C_{4v}, we assume that the Fermi surfaces of the thin layer are the same as in the bulk except for the splitting of the degeneracy induced by the inversion-symmetry-breaking terms. More specifically, using the orbital basis $\{4d_{xy}, 4d_{xz}, 4d_{yz}\}$ and σ_j to describe spin, the centrosymmetric part of the noninteracting Hamiltonian is taken to be

$$h^S_{\boldsymbol{k}} = \begin{pmatrix} \epsilon_{xy}(\boldsymbol{k}) - \mu - \delta\epsilon_{xy} & 0 & 0 \\ 0 & \epsilon_{xz}(\boldsymbol{k}) - \mu & t_\eta \sin(k_1)\sin(k_2) \\ 0 & t_\eta \sin(k_1)\sin(k_2) & \epsilon_{yz}(\boldsymbol{k}) - \mu \end{pmatrix} + \frac{\lambda}{2}\boldsymbol{L}\cdot\boldsymbol{\sigma} \tag{4.107}$$

with $\epsilon_{xy}(\boldsymbol{k}) = -2t_3\big(\cos(k_1)+\cos(k_2)\big) - 4t_4\cos(k_1)\cos(k_2)$, $\epsilon_{xz}(\boldsymbol{k}) = -2t_1\cos(k_1) - 2t_2\cos(k_2)$ and $\epsilon_{yz}(\boldsymbol{k}) = -2t_2\cos(k_1) - 2t_1\cos(k_2)$ as is commonly used to describe the Fermi-liquid of bulk Sr_2RuO_4

[198, 335, 336]. In Eq. (4.107), t_η describes the mixing of the $4d_{xz}$ and $4d_{yz}$ orbitals caused by next-nearest neighbor hopping and $\delta\epsilon_{xy}$ incorporates the energetic offset between the d_{xy} (B_2 of C_{4v}) and d_{xz}/d_{yz} (E of C_{4v}) orbitals at the Γ point. Furthermore, λ is the atomic SOC strength and $\boldsymbol{L} = (L_1, L_2, L_3)$ the vector of angular momentum operators projected onto the three d orbitals which can be expressed in terms of Gell-Mann matrices [337] as $L_1 = \lambda_2$, $L_2 = -\lambda_5$, $L_3 = \lambda_7$ (see also Appendix D.1.2).

As opposed to the bulk, inversion symmetry is broken in the thin layer due to the presence of the substrate deforming the atomic orbitals and making additional hopping processes possible. One can show (cf. Appendix D.1.2) that this leads to the additional contribution

$$h^A_{\boldsymbol{k}} = \delta \left(L_1 \sin(k_2) - L_2 \sin(k_1) \right) \tag{4.108}$$

to the Hamiltonian which can be described by a single parameter δ as dictated by the residual C_{4v} symmetry. The Fermi surfaces and the spectrum along high-symmetry lines of the full Bloch Hamiltonian $h_{\boldsymbol{k}} = h^S_{\boldsymbol{k}} + h^A_{\boldsymbol{k}}$ are shown in Fig. 4.5(a) and (b), respectively. The values of the parameters of $h^S_{\boldsymbol{k}}$ are given in the caption and have been determined in Ref. [198] for bulk Sr_2RuO_4 by comparison with experiment [160, 181]. The strength δ of the inversion-symmetry breaking is very hard to estimate and is also expected to depend on many details of the sample, in particular, on the substrate used and the thickness of the film. Here we take a rather large value of $\delta = 0.45t_1$ in order to make the spin-orbit splitting clearly visible in the spectra. Note, however, that the following discussion is independent of the value of δ as long as the topology of the Fermi surfaces with respect to the TRIM of the Brillouin zone (green dots in Fig. 4.5(a)) is the same as in bulk Sr_2RuO_4, i.e., as long as $\delta < 0.47t_1$.

As the topological invariant $\nu_{\mathbb{Z}_2}$ in Eq. (4.106) is only well defined when the superconducting state has a fully established gap, we will first focus on the pairing states without any nodes in the weak-pairing limit. Due to Eq. (4.37), $\widetilde{\Delta}_s(\boldsymbol{k})$ transforms as a scalar. Recalling Eq. (4.30) and the Fermi surface structure in Fig. 4.5(a), we conclude that only the state transforming under A_1 (the $e_{(1,i)}$ state is disfavored energetically) will be nodeless[7].

Using the general parameterization (4.91) of the superconducting order parameter in terms of singlet and triplet, the crucial diagonal matrix elements of the order parameter become

$$\widetilde{\Delta}_s(\boldsymbol{k}) = \langle \psi_{\boldsymbol{k}s} | \Delta^S_{\boldsymbol{k}} \sigma_0 | \psi_{\boldsymbol{k}s} \rangle + \sum_{j=1}^{3} \langle \psi_{\boldsymbol{k}s} | D^j_{\boldsymbol{k}} \sigma_j | \psi_{\boldsymbol{k}s} \rangle \,, \tag{4.109}$$

where $\Delta^S_{\boldsymbol{k}}$ and $D^j_{\boldsymbol{k}}$ are matrices in orbital space only. It is reasonable to assume (see also the more detailed discussion in Chap. 6.2.3) that the spin-orbit splitting of the Fermi surfaces is smaller than the scale on which the spin-texture $\boldsymbol{g}_{\boldsymbol{k}}$ of the Rashba-Dresselhaus effect and the orbital polarization of the wavefunctions change. In this limit, the singlet term (first term in Eq. (4.109)) is identical on the spin-orbit split Fermi surfaces, whereas the triplet contribution (second term) has identical magnitude but opposite sign.

From the expression (4.106) of the topological $\mathbb{Z}_2$ invariant, we can directly conclude that the superconductor is topologically trivial (nontrivial) if singlet (triplet) dominates. As already mentioned above, since triplet dominates in the bulk, it is natural to assume that this also holds for the thin layer. Naively, for a surface, e.g., along the x axis, we expect a single Kramers pair of Majorana modes at $k_1 = \pi$ and two pairs at $k_1 = 0$. This follows from calculating the DIII topological invariant of the fictitious 1D systems at fixed $k_1 = 0, \pi$ for all bands separately which is most easily done by noting that

[7] Naturally, there can always be accidental nodes which we will not consider here.

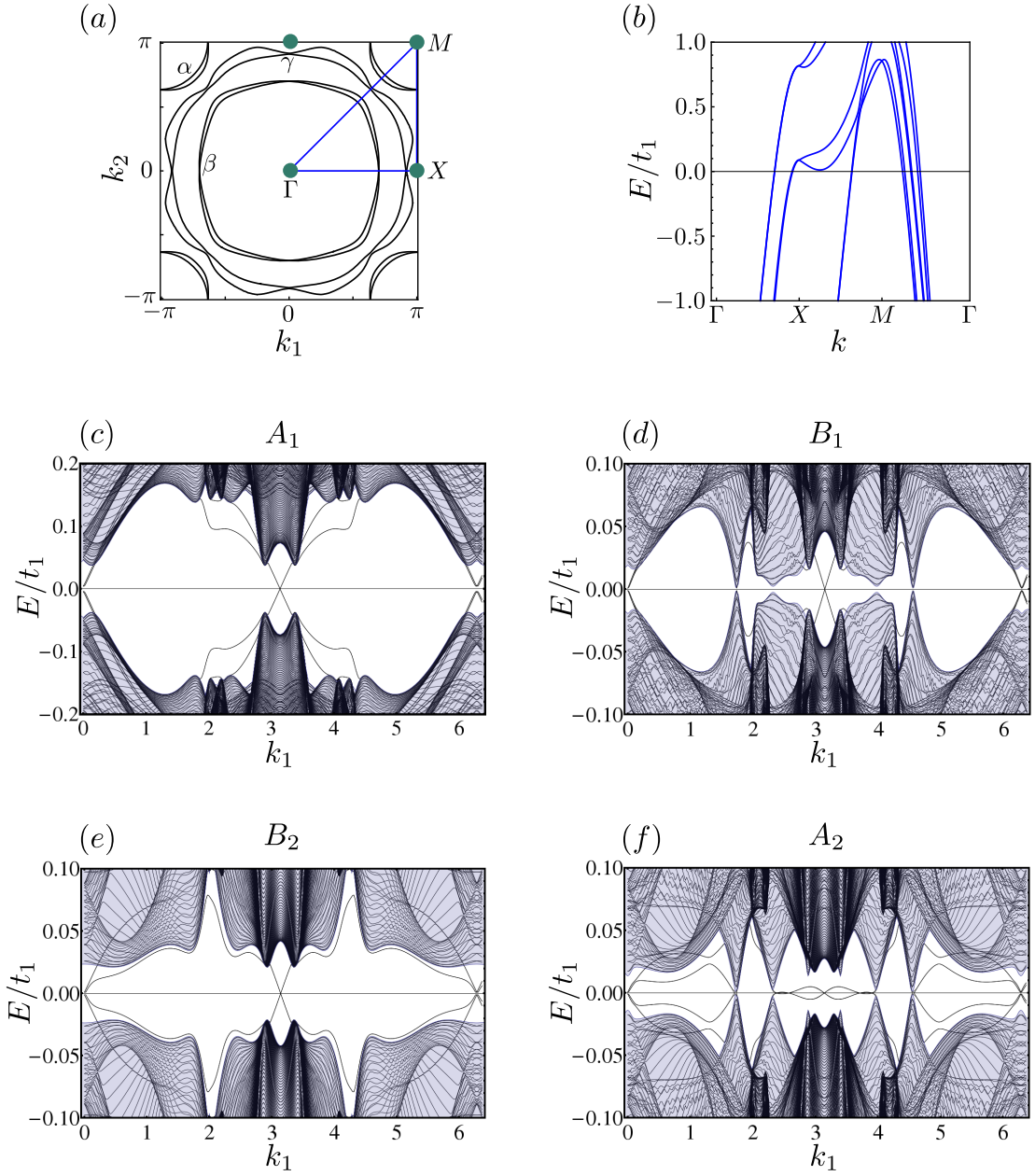

Figure 4.5: ***Bulk and edge bands of Sr_2RuO_4.*** *Fermi surfaces (a) and spectrum (b) along high-symmetry lines shown in green in part (a) following from the bulk Hamiltonian defined in the main text. TRIM are indicated as green dots in (a). In (c)-(f), the low-energy part of the spectra of the superconducting phases with triplet vector* $0.2t_1(\sin k_2, -\sin k_1, 0)$, $0.08t_1(\sin k_2, \sin k_1, 0)$, $0.12t_1(\sin k_1, -\sin k_2, 0)$ *and* $0.08t_1(\sin k_1, \sin k_2, 0)$ *are shown transforming under A_1, B_1, B_2 and A_2, respectively. Here we have used periodic along the x and open boundary conditions along the y axis (175 sites). The spectrum of the infinite bulk system is indicated in light blue. In all plots of the figure we have taken $t_2 = 0.1t_1$, $t_3 = 0.8t_1$, $t_4 = 0.3t_1$, $t_\eta = -0.04t_1$, $\lambda = 0.2t_1$, $\mu = t_1$ and $\delta\epsilon_{xy} = 0.1t_1$ [198] as well as $\delta = 0.45t_1$.*

Eq. (4.106) also holds in the 1D case where $m_s = 1$. Note, however, that the two pairs of Majorana modes at $k_1 = 0$ will in general be gapped out since already infinitesimal couplings of the β and γ bands that preserve TRS and PHS lead to a finite gap. Indeed, this is what we obtain by numerically diagonalizing the superconducting mean-field Hamiltonian: Using periodic along the x and open boundary conditions along the y direction, we observe a Kramers pair of MBSs at $k_1 = \pi$ and two additional subgap sates that are slightly gapped out[8] at $k_1 = 0$ in the spectrum shown in Fig. 4.5(c). In the plot, we have assumed that the order parameter is trivial in orbital space as in Table 4.2 which seems to be a natural approximation given that the recent RG calculation of Ref. [198] indicates that the superconducting gap has approximately the same size on all three bands. We emphasize that, apart from the plot, our discussion of the topological invariant $\nu_{\mathbb{Z}_2}$ is not based on this assumption.

From this reasoning, we also directly conclude that the system is characterized by the weak topological indices $(1, 1)$ introduced in Chap. 2.1.4. Consequently, a Kramers doublet of MBSs must occur at any dislocation characterized by a Burgers vector $\boldsymbol{b} = (b_1, b_2)$ (expressed in the basis of primitive vectors) with $b_1 + b_2$ odd [247, 269, 270].

Let us next discuss the remaining possible pairing states transforming under A_2, B_1 and B_2. As already mentioned above, in all three cases, there are necessarily nodes in the strict weak-pairing limit.

The triplet order parameter transforming under B_1 constitutes a special case: There are no (symmetry-imposed) nodes at $k_1 = \pi$ (or $k_2 = \pi$). Therefore, the DIII invariant of the fictitious 1D problem given by restricting the Hamiltonian on $\boldsymbol{k} = (\pi, k_2)$, $0 < k_2 \leq \pi$, is well defined and easily shown to be nontrivial with the help of Eq. (4.106). This means that, say for a surface along the x axis, there should still be a Kramers pair of MBSs at $k_1 = \pi$ despite the presence of low-energy excitations at $k_1 \neq \pi$. This is confirmed by the numerically determined spectrum shown in Fig. 4.5(d). The edge modes are topologically protected in the sense that they cannot be gapped out by continuous deformations of the quadratic Hamiltonian that do not move the nodal points all the way to $k_1 = \pi$ or close the gap, neither break TRS/PHS nor the translation symmetry along the x axis. In particular, the latter restriction to k_1-preserving perturbations is a limitation as compared to the usual notion of fully gapped (strong) topological phases (see Chap. 2.1) as it means that already nonmagnetic disorder can destroy the edge modes – very much like in case of gapped weak topological phases. Note, however, that due to sign changes between the spin-orbit-split Fermi surfaces the triplet state itself is already prone to nonmagnetic disorder (see Ref. [160] and Chaps. 1.4 and 7) and, hence, very clean samples are anyway required to stabilize the superconducting condensate. As Sr_2RuO_4 can be prepared in remarkably clean form [160], the lack of protection of the MBSs against time-reversal symmetric scatterers might be irrelevant in experiment.

It is worth noting that the spin-orbit splitting of the Fermi surfaces is extremely small at the high-symmetry lines $k_2 = 0, \pi$ (and, by symmetry, also at $k_1 = 0, \pi$) as can be easily seen in Fig. 4.5(a) and (b). This can be understood from the symmetry point of view: Consider, e.g., the splitting of the β and γ bands along the Γ-X-line. Since the low-energy states in the vicinity of the high-symmetry line are mainly due to the xy (γ band) and xz (β band) orbitals, the splitting is expected to arise predominantly from the hybridization of these orbitals. The associated matrix element must, however, transform as Y and, hence, vanishes at the Γ-X-line. The small splitting is due to the coupling to the energetically distant yz orbital. This has important consequences for the B_2 pairing state which has its nodes at exactly these high-symmetry lines in the weak-pairing description: There are values of the order parameter which are still smaller than the typical splitting of the Fermi surfaces (such that

[8] This gap survives in the limit of the system being infinitely large in the y direction as opposed to the gap of the Majorana modes at $k_1 = \pi$ that just results from the finite overlap of the edge modes at opposite edges.

Eq. (4.106) can be safely used) but comparable to or larger than the splitting at these high-symmetry points of the Fermi surface rendering the superconductor fully gapped. As long as triplet dominates, the state must be topologically nontrivial with MBSs at the boundary to a trivial phase as illustrated in Fig. 4.5(e).

For the very same reason, also the A_2 state has no nodes along $k_1 = 0$ and $k_2 = 0$ and, hence, harbors MBSs which are protected in the same sense as those of the B_1 state (see Fig. 4.5(f)).

Taken together, we have seen that for all four pairing states that are allowed by our symergetic selection rules, MBSs as signatures of nontrivial DIII topology are expected to occur at the boundary to a trivial phase. This makes thin films of Sr_2RuO_4 a promising physical system for the observation of Majorana physics. Due to the restored TRS in the thin layer, these edge modes always come in Kramers pairs and thus will not produce any current or magnetic field as opposed to the chiral p-wave state discussed for bulk Sr_2RuO_4.

4.6.2 Other TRS-breaking superconductors

As illustrated by the general gedankenexperiment outlined above, our symergetic constraints are particularly interesting for thin layers of superconductors that break TRS in their bulk. For this reason, we next discuss further examples of materials, URu_2Si_2 and UPt_3, which are strongly believed to harbor a superconducting state that is not invariant under time-reversal [48, 49, 54].

URu_2Si_2. We begin with URu_2Si_2 (see Chap. 1.3.2 for an introduction) as it is, from a pure symergetic point of view, very similar to Sr_2RuO_4: It has the same bulk point group, D_{4h}, [165] which will be lowered to C_{4v} in a thin layer on a substrate (again assuming no additional distortions). Note that there are reports of rotational symmetry breaking at the hidden order transition [338], however, this does not seem to have any observable impact on superconductivity[9] and will thus be neglected here. The tiny magnetic moments ($\simeq 0.03\mu_B$ per U atom) which are present in the hidden order phase [219] are today known to have an extrinsic origin (defects, stress) and not to coexist with superconductivity [165, 339]. It is therefore natural to expect them to be irrelevant for understanding the superconducting instability. Above the superconducting transition, the system can hence be approximated to be time-reversal symmetric. Furthermore, the small transition temperature $T_c \simeq 1.5\,\mathrm{K}$ [216–218] and the strong SOC following from the large $Z = 92$ of U indicate that the weak-pairing limit seems to be applicable in the thin layer limit. Therefore, Table 4.2 and the symergetic constraints discussed for Sr_2RuO_4 apply for URu_2Si_2 as well.

In the bulk, most likely a chiral d-wave state $\Delta^S_{\boldsymbol{k}} = (k_1 + ik_2)k_3$ transforming under E_g of D_{4h} is realized [49, 202, 221–223]. Without any symergetic arguments, it is clear that this state cannot survive the thin-film limit due its k_3 dependence. From a pure symmetry point of view, the most natural [340] pairing state in the quasi-2D limit would be $e_{(1,i)}$ transforming under the representation E subduced[10] from E_g of D_{4h}. In the present case, this is the TRS-breaking triplet order parameter with $\boldsymbol{d}_{\boldsymbol{k}} = (k_1 + ik_2)\boldsymbol{e}_3$, which, however, is suppressed in the weak-pairing limit due to being odd under C_2^z (see Sec. 4.4).

Exactly as in case of Sr_2RuO_4, we know that the superconducting state of the thin layer can only transform under one of four 1D IRs of C_{4v} with order parameter structures as summarized in Table 4.2.

[9] For example, no splitting of the features in the specific heat measurement of Ref. [222] can be seen.

[10] Consider a group $\mathcal{G}$ and a proper subgroup $\mathcal{H}$. Restricting an IR ρ of $\mathcal{G}$ to elements of $\mathcal{H}$ defines a representation of $\mathcal{H}$ which is called the representation subduced from ρ. For our purposes, the subgroup just lacks the inversion operation as generator as compared to $\mathcal{G}$ such that all subduced representations are automatically irreducible.

Table 4.3: *Character table of C_{6v}.*

	E	$2C_6$	$2C_3$	C_2	$3\sigma_v$	$3\sigma_d$	Basis functions
A_1	1	1	1	1	1	1	x^2+y^2
A_2	1	1	1	1	−1	−1	$xy(3x^2-y^2)(3y^2-x^2)$
B_1	1	−1	1	−1	1	−1	$x(3y^2-x^2)$
B_2	1	−1	1	−1	−1	1	$y(3x^2-y^2)$
E_1	2	1	−1	−2	0	0	(x,y)
E_2	2	−1	−1	2	0	0	$(x^2-y^2,2xy)$

TRS must be restored and the triplet vector must necessarily be oriented parallel to the plane of the system. Note that the generality of our symergetic arguments is particularly important for URu_2Si_2 where the microscopic details of the hidden order phase are still under debate [165, 215] rendering explicit calculations of the superconducting instability very difficult.

UPt_3. The heavy-fermion superconductor [23] UPt_3 will be our third example of a material where the breaking of TRS in its bulk superconducting state has been demonstrated experimentally [48, 54]. As discussed in more detail in Chap. 1.3.2, the order parameter is widely believed [48, 54, 206–208, 211–214] to be a triplet state with a $\boldsymbol{d}$ vector of the form $\boldsymbol{d_k} = (\delta_1(k_1^2-k_2^2)k_3+2i\delta_2 k_1 k_2 k_3)\boldsymbol{e}_z$, i.e., mainly polarized along the z direction and transforming under the two-dimensional IR E_{2u} of its bulk point group D_{6h}. The small magnetic moments (of order $0.01\mu_B$ per U atom) associated with the antiferromagnetic order [209, 210] are commonly regarded as a small perturbation for superconductivity [213, 214]. Therefore, we will first ignore them in the following and then later comment on the implications in case they are also present in the quasi-2D limit. The combination of SOC being very strong [163], as expected from the large proton numbers of Pt ($Z=78$) and U ($Z=92$), and the small transition temperatures ($T_c \simeq 0.5\,\mathrm{K}$ [23]) in this system makes it an ideal candidate for the application of a weak-pairing description to understand the superconducting properties in thin films on a substrate. Similarly to Sr_2RuO_4, thin films of UPt_3 have indeed been fabricated and also shown to host superconductivity [69].

Assuming that no further structural distortions take place in the thin layer system, the point group will be reduced to C_{6v}. As it contains a twofold rotation C_2^z perpendicular to the plane of the system, the triplet vector must rotate to be aligned parallel to the 2D layer according to Sec. 4.4.2. However, the presence of the threefold rotation symmetry C_3^z still allows for TRS to be broken. Note that the restriction on the $\boldsymbol{d}$ vector will in general only hold if the order parameter is diagonal in band space which is a very common [163, 207, 208, 214] assumption in the literature on UPt_3. Due to the complex structure of the Fermi surfaces [163, 203] arising from a hybridization of the U $5f$ and Pt $5d$ electrons it does not seem to be *a priori* clear whether this assumption holds. An analysis of the triplet vector in superconducting thin layers of UPt_3 might hence give insights into the orbital structure of the order parameter in the bulk system.

Let us now take a closer look at the possible pairing states of the thin-film limit: From the character table of C_{6v} given in Table 4.3, we see that there are in total 6 IRs out of which 3 can be discarded in the

Table 4.4: *Summary of the superconducting phases of a system with C_{6v} symmetry, such as UPt_3, that are allowed by the symergetic selection rules. As in Table 4.2, X, Y are basis functions transforming as $\sin(k_1)$ and $\sin(k_2)$ under the point group.*

Gr. th.	Pairing	TRS	$\Delta^S_{\boldsymbol{k}}$	$\boldsymbol{d_k}\cdot\boldsymbol{\sigma}$
A_1	s-wave	y	$1, X^2+Y^2$	$X\sigma_2 - Y\sigma_1$
A_2	i-wave	y	$XY(3X^2-Y^2)(3Y^2-X^2)$	$X\sigma_1 + Y\sigma_2$
$E_2(1,i)$	$e_{2(1,i)}$	n	$(X+iY)^2$	$\sigma_1(Y-iX)+\sigma_2(X+iY)$

weak-pairing limit as they are odd under C_2^z. Recalling the result of Sec. 4.3.2, we know that the order parameter must necessarily break TRS when transforming under a two-dimensional IR. Consequently, the order parameter vector configurations $(\eta_1^{E_2}, \eta_2^{E_2}) = (1,0)$ and $(\eta_1^{E_2}, \eta_2^{E_2}) = (0,1)$ are also ruled out. Consequently, out of the 10 order parameters that are possible by symmetry, only 3 remain as a consequence of the energetic selection rules derived in this chapter. In Table 4.4, these remaining options are summarized where we have again assumed the order parameter to be trivial in orbital space just to keep the expressions as simple as possible. The TRS-breaking state $e_{2(1,i)}$ corresponds to the order parameter believed to be realized in bulk UPt_3 as E_2 is the representation subduced from E_{2u} of D_{6h}. Note, however, that only the in-plane components of the triplet vector can be finite in the quasi-2D system which are empirically known to be negligibly small in the bulk superconductor [208]. This indicates that the pairing interactions leading to finite in-plane triplet vectors in the E_{2u} representation are very inefficient and, hence, it is not clear at all whether the $e_{2(1,i)}$ state is also realized in the thin film.

Finally, let us discuss the impact of the potential presence of antiferromagnetic order [209, 210]. If, similar to the bulk, there is a small amount of antiferromagnetism ($\boldsymbol{M} \neq 0$) that just slightly breaks the sixfold rotation symmetry down to a twofold rotation symmetry (C_{6v} reduced to C_{2v}), we can regard $\boldsymbol{M}$ as a weak symmetry-breaking field [213, 214]: In case of A_1 being favored in the limit $\boldsymbol{M} = 0$, the presence of antiferromagnetism does not split the transition, but only leads to a small admixing of $X^2 - Y^2$ and $X\sigma_2 + Y\sigma_1$. Similarly, for A_2, there will be no splitting of the transition but small additional XY and $X\sigma_1 - Y\sigma_2$ contributions. Only in case of the two-dimensional representation, the transition will be split into two. As time-reversal symmetric order parameter vector configurations are not possible for a two-dimensional IR in the weak-pairing limit, the observation of a splitting in experiment directly implies the breaking of TRS.

4.6.3 Superconductors with unknown microscopic structure

Finally, let us illustrate, using oxide heterostructures (see Chap. 1.3.1) and single-layer FeSe on STO (see Chap. 1.3.2) as examples, that our symergetic arguments can also be used to gain information about the time-reversal properties of superconductors that have not been microscopically identified [36–38, 158, 159] and to streamline the search for new superconductors that spontaneously break the TRS of the normal state.

Oxide heterostructures. We begin our discussion with LAO/STO heterostructures that can be grown [35, 142, 156] along three different orientations, [001], [110] and [111] with respective point

Table 4.5: *Pairing states of the* (110) *interface organized according to the IRs of its point group* C_{2v}*. Only* A_1 *and* A_2 *are possible in the weak-pairing limit.*

Gr. th.	Pairing	TRS	$\widetilde{\Delta}_s(\boldsymbol{k})$	# Nodes/FS
A_1	s-wave	y	1; X_1^2; X_2^2	0
A_2	d_{xy}	y	X_1X_2	4
B_1	p_x	y	0	ungapped
B_2	p_y	y	0	ungapped

groups C_{4v}, C_{3v} and C_{2v}. As has already been discussed in Chap. 1.3.1, superconductivity has so far only been observed [39, 40] in the former two orientations while there is no experimental report on superconductivity for the less studied (111) interface. At present date, neither the mechanism leading to superconductivity nor the detailed structure of its order parameter has been unambiguously identified. In the following we will discuss the implications of the symergetic selection rules derived in this chapter on the possible pairing states in these systems based on Ref. [325]. Parts of this discussion have also been summarized in Ref. [38].

Firstly, note that the oxide heterostructures constitute prime examples for the applicability of the weak-pairing description: The gap at optimal doping ($\simeq 0.04\,\mathrm{meV}$) is known to be much smaller than the spin splitting $E_{\mathrm{so}} \simeq 10\,\mathrm{meV}$ of the Fermi surfaces which is even comparable to the Fermi energy ($E_F \simeq 20\,\mathrm{meV}$) [41].

From our analysis of Sec. 4.4, we can directly conclude that the pairing states of the (001) and (110) interfaces must be necessarily time-reversal symmetric due to the absence of a threefold rotation symmetry while only the point group of the (111)-terminated heterostructure allows for spontaneous TRS breaking at the superconducting phase transition. This motivates a closer experimental inspection of the low-temperature behavior in the (111) system as it offers the possibility of an exotic TRS-breaking superconducting state. Furthermore, because of the absence of a twofold rotation symmetry perpendicular to the interface, it is also the only 2D system we have discussed so far in this chapter that allows for an (orbital diagonal) out-of-plane component of the triplet vector.

Let us now take a closer look at the possible pairing states for the three different orientations: For the (001) termination, again Table 4.2 holds. As all Fermi surfaces of the system enclose the Γ point [341–343] and experiment indicates a fully established gap [70], only the s-wave state remains as a candidate order parameter (see Eq. (4.30)). We emphasize that this only fully determines the symmetry of the pairing state, i.e., the (absence of) sign changes of the order parameter $\widetilde{\Delta}_s(\boldsymbol{k})$ *on* all Fermi surfaces, but not the topological DIII invariant $\nu_{\mathbb{Z}_2}$ in Eq. (4.106) or, put differently, the sign changes of $\widetilde{\Delta}_s(\boldsymbol{k})$ *between* different Fermi surfaces. The invariant depends on the relative sign of the basis functions φ_μ^n on the different Fermi surfaces and thus has to be determined in an explicit microscopic calculation which will be the topic of the next chapter. We will see that $\nu_{\mathbb{Z}_2}$, albeit insensitive to symmetries, will be intimately related to the mechanism of superconductivity.

The possible pairing states of the (110) interface are summarized in Table 4.5 for simplicity only showing the weak-pairing order parameter $\widetilde{\Delta}_s(\boldsymbol{k})$. Here, $X_1(\boldsymbol{k})$ and $X_2(\boldsymbol{k})$ are scalar basis functions transforming as the momenta along the $[\bar{1}10]$ and [001] direction, respectively (see also Fig. 1.3(d), left panels). As the point group C_{2v} only allows for one-dimensional IRs, TRS breaking is already forbidden

Table 4.6: *Superconducting phases of the* (111) *interface as allowed by the point group C_{3v} of the normal state. The two TRS-preserving states transforming under E are not possible in the weak-pairing limit as shown in Sec. 4.3.2.*

Gr. th.	Pairing	TRS	$\widetilde{\Delta}_s(\boldsymbol{k})$	# Nodes/FS
A_1	s-wave	y	$1;\ X_1^2+X_2^2$	0
A_2	f-wave	y	$X_1X_2(3X_1^2-X_2^2)(3X_2^2-X_1^2)$	12
$E(1,0)$	$e_{(1,0)}$	y	X_1X_2	4
$E(\sqrt{3},1)$	$e_{(\sqrt{3},1)}$	y	$2\sqrt{3}X_1X_2+(X_1^2-X_2^2)$	4
$E(1,i)$	$e_{(1,i)}$	n	$2X_1X_2+i(X_1^2-X_2^2)$	0

just as a consequence of the presence of SOC, i.e., also in case of doubly-degenerate Fermi surfaces. Out of the four states as allowed by symmetry, two are fully ungapped in the weak-pairing limit due to being odd under C_2^z and are, hence, energetically suppressed.

Finally, the pairing states of the (111)-oriented LAO/STO heterostructure can be found in Table 4.6, where $X_1(\boldsymbol{k})$ ($X_2(\boldsymbol{k})$) transforms as the crystal momentum along the $[\bar{1}10]$ ($[\bar{1}\bar{1}2]$) direction (see also Fig. 1.3(d), right panels). In accordance with the design principle of Sec. 4.4.1, there is a state, $e_{(1,i)}$, that breaks TRS which, in this case, is even fully gapped in the weak-pairing limit. Note that since the point group C_{3v} does not contain C_2^z, none of the IRs can be generally excluded. Only the two time-reversal symmetric symmetry-allowed states $e_{(1,0)}$ and $e_{(\sqrt{3},1)}$ are ruled out as a consequence of our analysis of higher-order terms of the Ginzburg-Landau expansion in Sec. 4.3.2.

Note that the leading basis function $X_1(3X_2^2-X_1^2)$ in case of A_2 happens to be odd under C_2^z. Consequently, it cannot open up a gap in the weak-pairing limit. As C_{3v} does not contain an operation with $(X_1,X_2)\to(-X_1,-X_2)$, the basis function of a given representation can have distinct parity. The leading contribution to $\widetilde{\Delta}_s(\boldsymbol{k})$ then reads $X_1X_2(3X_1^2-X_2^2)(3X_2^2-X_1^2)$ yielding 12 instead of 6 as the minimal number of nodes per Fermi surface.

Before closing, we will make the following two comments. Firstly, in our discussion of oxide heterostructures we have been tacitly assuming that the normal state can be approximated to be time-reversal symmetric which, at first sight, seems to contradict the observation of magnetic order [148–150] in these systems (see also Chap. 1.3.1). The crucial point is that superconductivity is mostly associated with the itinerant bands derived from the $3d_{xz}$ and $3d_{yz}$ orbitals [344, 345] while magnetism is predominantly due to the $3d_{xy}$ states that are closest to the interface and localized [111, 151, 152, 346, 347]. Within this physical picture that will be discussed in more detail in Chap. 5.1.1, the magnetic order can only affect the validity of our discussion if the resulting effective Zeeman splitting E_Z in the superconducting bands is comparable to or larger than the spin-orbit splitting E_{so} on the Fermi surface. The opposite limit $E_Z\ll E_{\mathrm{so}}$ seems to be realized as a consequence of the small orbital admixture of $3d_{xy}$ in the bands relevant for superconductivity [111]. This picture is further confirmed by the experimental observation [149] that there is no significant spatial correlation between the isolated ferromagnetic patches and the superconducting order parameter.

Secondly, the entire analysis of this chapter is based on the assumption (see Eq. (4.2)) that there is no translational symmetry breaking at the superconducting phase transition. This seems to be critical as Refs. [108, 110–112] point towards the possibility an FFLO-like state that is stabilized by

the combination of strong SOC and the exchange coupling to ferromagnetic moments. However, the aforementioned absence of correlation between magnetism and superconductivity [149], irrespective of the value of E_Z, is inconsistent with this expectation. In addition, we will see in the microscopic calculation of Chap. 5 that FFLO states only occur as subleading instabilities and for very exotic interaction parameters.

Single-layer FeSe. Although inversion symmetry is automatically broken by the asymmetric presence of the substrate, it is *a priori* not clear whether the weak-pairing description and all the subsequent constraints derived in this chapter are applicable to FeSe on STO due to its large transition temperature and gap [157]. If we assume that it does, exactly the same restrictions as in case of (001) oxide interfaces will apply because the two systems share the same point group (C_{4v}). The order parameter must transform under one of the one-dimensional IRs of C_{4v} (cf. Table 4.2) with triplet vector parallel to the layer and preserve TRS. In combination with experiment [167] showing a fully established gap on the Fermi surfaces enclosing the M point (see Fig. 1.4(c)), only the s-wave state remains as a possible pairing state in the weak-pairing limit. Note that, as discussed in Chap. 1.3.2, recent experiments [177, 178] clearly indicate the absence of magnetic order in the single-layer system such that the assumption of a time-reversal symmetric normal phase is justified.

As already mentioned above in the context of the (001) oxide interface, this does not fully determine the corresponding DIII invariant: Recalling from Fig. 1.4(b) and the corresponding discussion in Chap. 1.3.2 that there are two pairs of spin-orbit-split Fermi surfaces around the M point, three possibilities remain: The pairing field can have the same sign on all four electron pockets, the signs can be pairwise identical or only differ on one Fermi surface. Only the latter type of pairing state is topologically nontrivial as readily follows from Eq. (4.106). In Chap. 6.3.2 we will see that, under very general assumptions, the topological order parameter cannot be realized if superconductivity arises from the coupling to collective particle-hole modes, such as SDW fluctuations, or phonons.

4.7 Spinless fermions

For completeness, we will finally extend the analysis of Sec. 4.4 to spinless fermions, i.e., to $S = 0$ in Eq. (4.9). Following the discussion presented in the supplementary material of Ref. [325], we will first discuss how this situation can occur and then analyze the symergetic constraints on the possible pairing states for $S = 0$.

4.7.1 Strong magnetic fields

To see how an emergent spin-0 TRS can be realized in a broad class of solid state systems, let us consider spin-1/2 fermions which do not experience any SOC and are described by a Hamiltonian with physical TRS represented by the operator $\Theta_{1/2} = i\sigma_2 \otimes \mathbb{1}_o \mathcal{K}$. Here $\mathbb{1}_o$ is the unit matrix in orbital space and σ_j refers to the spin. Due to the absence of SOC, the Hamiltonian has the form $\sigma_0 \otimes h^o_{\boldsymbol{k}}$ and the full symmetry group is given by $\mathcal{G}_0 = \mathrm{SO}(3) \times \mathcal{G}_p$. Applying an in-plane magnetic field, say along the x direction, leads to an additional Zeeman term. The resulting Hamiltonian

$$h_{\boldsymbol{k}} = \sigma_0 \otimes h^o_{\boldsymbol{k}} + \sigma_1 \otimes \mathbb{1}_o E_Z \tag{4.110}$$

now only has $\mathcal{G}_B = \mathrm{SO}(2) \times \mathcal{G}_p$ symmetry. The physical spin-1/2 TRS $\Theta_{1/2}$ is broken, however, it still holds

$$\widetilde{\Theta} h_{-\boldsymbol{k}} \widetilde{\Theta}^\dagger = h_{\boldsymbol{k}}, \qquad \widetilde{\Theta} = \sigma_0 \otimes \mathbb{1}_o \mathcal{K}. \tag{4.111}$$

For the analysis of the symmetry properties of the superconducting order parameter, it is essential that the representation $\mathcal{R}_\Psi$ of the point group can be chosen to commute with $\widetilde{\Theta}$ (see Eq. (4.13)). More physically, it means that the associated generators, i.e. the angular momenta of the theory, have to anticommute with its time-reversal operator $\widetilde{\Theta}$.

For the SO(2) part of $\mathcal{G}_B$ this is not the case as $\widetilde{\Theta}$ does not anticommute with σ_1. Let us thus assume that the Zeeman energy E_Z is larger than the bandwidth of $h^o_{\boldsymbol{k}}$. Then, we can project onto one of the two Zeeman-split multiplets to obtain an effective low-energy theory. Without loss of generality, let us choose the multiplet that is energetically lower. The effective Hamiltonian then reads

$$h^{\text{eff}}_{\boldsymbol{k}} = h^o_{\boldsymbol{k}} - \mathbb{1}_o |E_Z|, \tag{4.112}$$

which now only has the point symmetry group $\mathcal{G}_p$. All point symmetry operations in the effective theory are generated by the orbital angular momentum $\boldsymbol{l}$ satisfying $\{\Theta, \boldsymbol{l}\} = 0$ with $\Theta = \mathbb{1}_o \mathcal{K}$. It is therefore always possible to choose the representation $\mathcal{R}_{\Psi_{\text{eff}}}$ of the symmetry group in the effective theory to commute with Θ.

We have thus seen that in a 2D electronic system without SOC subject to strong magnetic fields, the effective low-energy model naturally has an emergent TRS with $\Theta^2 = \mathbb{1}$. We will now discuss the symergetic restrictions on possible pairing states within such a theory.

4.7.2 Selection rules for spinless systems

As compared to the situation of spinfull electrons ($S = 1/2$), there are two crucial differences: Firstly, the Fermi-Dirac constraint (4.32) forces the weak-pairing order parameter to be odd under $(s, \boldsymbol{k}) \to (s_{\text{K}}, -\boldsymbol{k})$,

$$\widetilde{\Delta}_s(\boldsymbol{k}) = -\widetilde{\Delta}_{s_{\text{K}}}(-\boldsymbol{k}). \tag{4.113}$$

Secondly, $\Theta^2 = \mathbb{1}$ also allows for singly-degenerate Fermi surfaces in case of centrosymmetric point groups.

This already shows that, in the presence of inversion symmetry, Eq. (4.113) is particularly restrictive as it rules out all even IRs irrespective of the dimensionality of the system. To derive a design principle for spontaneous TRS breaking in 2D systems similar to that of Sec. 4.4.1, let us again first consider the point group C_{4v}. From its character table given in Table 4.1 we conclude that Eq. (4.113) forbids all IRs except for the multidimensional IR E. Recalling our analysis of higher-order terms of the Ginzburg-Landau expansion in Sec. 4.3.2, this implies that the spin-0 TRS must necessarily be broken at the superconducting phase transition in a 2D system with C_{4v} symmetry.

Systematically studying all possible point groups (see Appendix A.3), one finds the following sufficient condition for spontaneous TRS-breaking superconductivity in the weak-pairing limit [325, 326]: *If the point group of the high-temperature phase of a 2D system contains a fourfold proper or improper rotation symmetry, spin-*0 *TRS will be automatically broken in the superconducting state.*

4.8 Consequences for surfaces

At the surface of a crystal, inversion symmetry is locally broken. For this reason one might expect that our analysis, at least qualitatively, is also relevant for the behavior at the boundaries of a system. This will be discussed in more detail in this subsection.

The consequences are most easily and universally analyzed for systems that consist of weakly coupled quasi-2D layers. If the surface of interest is parallel to the planes, the superconducting texture near the

surface can be found by considering every layer as a separate quasi-2D system with inversion-symmetry-breaking terms increasing with decreasing distance to the surface. Therefore, the local behavior of the condensate should bear strong similarities to that of the superconductor in our gedankenexperiment introduced in Sec. 4.6.1 where the thickness d of the material is replaced by the distance to the surface. Once these noncentrosymmetric perturbations become sufficiently large, a bulk state which is odd under a twofold rotation perpendicular to the surface must be suppressed and a competing superconducting state can emerge near the surface. According to our analysis of Sec. 4.5, the critical value of the associated splitting E_{so} strongly depends on the coupling constants and energetics of the competing instabilities but should, in general, be smaller than T_c. If the residual point group at the surface contains no threefold rotation symmetry, TRS must be restored locally and the presence of a C_2^z symmetry will force the $\boldsymbol{d}$ vector to be aligned parallel to the surface. Note that adding small couplings between the layers, which are inevitably present in any material, will just spatially smear out the otherwise sharp transition between the bulk and surface superconducting phases.

Out of the materials we have discussed so far in this chapter, Sr_2RuO_4 represents an example of a system that consists of weakly-coupled quasi-2D layers (see Chap. 1.3.2) such that the present discussion can be applied. At its (001) surface, the point symmetry is reduced to C_{4v} which, according to the arguments presented above, forces the $\boldsymbol{d}$ vector to rotate to be parallel to the surface and TRS to be restored. In this system we expect the surface effect to be particularly important as the chiral p-wave state of the bulk is nearly degenerate [183, 195, 331, 332] with the triplet states transforming under the four ungerade one-dimensional IRs of D_{4h}. Therefore, one expects that already a small amount of inversion-symmetry breaking induces a transition to a TRS-preserving state, most likely with dominant triplet pairing. Note that this behavior of superconductivity at the surface of Sr_2RuO_4 has already been pointed out in Refs. [333, 334] on the basis of an explicit calculation in a single-band model for an isolated quasi-2D layer. It would be interesting to analyze whether the presence of a time-reversal symmetric superconducting layer near the surface of Sr_2RuO_4 could account for the absence of magnetic signals in experiments [191, 192] that are expected as a consequence of the chiral pairing state in the bulk [190].

In the general case of a material, where the coupling between layers perpendicular to the surface is not small, the discussion is more complicated. In particular, the bulk pairing state can depend on the momentum component $k_\perp$ perpendicular to the surface. Fortunately, the boundary conditions at specularly reflecting surfaces, derived originally by Ambegaokar *et al.* [348] (see also Ref. [50]), state that exactly these components will be suppressed at the surface. Our symergetic arguments are complementary and indicate that, among the remaining states, those that are odd under a twofold rotation perpendicular to the surface will be energetically disfavored locally. Whether this leads to a significant reduction of the bulk order parameter near the surface and the local emergence of a competing instability crucially depends on the microscopic details of the system considered.

The combination of the boundary conditions at specularly reflecting surfaces and our symergetic constraints imply that many superconducting bulk states, in particular those breaking TRS, are expected to be suppressed in the vicinity of surfaces. When a subleading bulk instability takes over locally, investigation of surface superconductivity might be used to gain information about the phase competition in the bulk.

4.9 Summary of Chapter 4

To summarize, we have considered general constraints on possible pairing states in systems with singly-degenerate Fermi surfaces that result from the combination of symmetry and energetic arguments. These selection rules hold under the following assumptions:

1. The superconducting state is reached by a single phase transition from the normal phase which is time-reversal symmetric. This TRS can both be of the usual spin-1/2 type, i.e., $\Theta^2 = -\mathbb{1}$, or an effective TRS with $\Theta^2 = \mathbb{1}$. The latter situation can arise, e.g., in the presence of strong Zeeman splittings that strips off the spin degree of freedom from the electrons (see Sec. 4.7.1).

2. No translation symmetry breaking, as known from FFLO [105, 106] pairing states, occurs at the superconducting phase transitions. Group theoretically this means that we can restrict ourselves to the IRs of the point group $\mathcal{G}_p$ as opposed to those of the full space group and, in more physical terms, the electrons forming Cooper pairs have zero total momentum. This assumption is not very restrictive as translation-symmetry-breaking superconducting states represent rather exotic phenomena that are mainly expected when TRS is broken (see Chap. 1.1.2).

3. Finally, the spin-orbit splitting E_{so} of the Fermi surfaces is sufficiently large for the weak-pairing description, formally defined by Eq. (4.29), to be applicable for determining the leading superconducting instability. In Sec. 4.5, we have seen that this is satisfied if E_{so} is larger than the zero temperature gap or the transition temperature of superconductivity (times some number of order 1). The presence of other competing instabilities can significantly reduce the critical value of E_{so} for the applicability of the weak-pairing description.

We have first shown (see Sec. 4.3.1) by resumming the full Ginzburg-Landau expansion that the superconducting transition must be continuous on the mean-field level. Although fluctuations will eventually change the behavior of the order parameter in the vicinity of the transition [122, 123, 126–128] (see also Chap. 1.2), this allowed us to use a finite order Ginzburg-Landau expansion to derive the possible pairing states. From this we have seen in Sec. 4.3.2 that, as a consequence of the reduced number of degrees of freedom in the weak-pairing description and the symmetry constraints of $\mathcal{G}_p$, a superconducting order parameter transforming under a multidimensional or complex IR of $\mathcal{G}_p$ will automatically break TRS. This means that the IR being multidimensional or complex is not only a necessary but also a sufficient condition for spontaneous TRS breaking. In this sense, the broken inversion symmetry facilitates the formation of a TRS-breaking superconductor in 3D. Maybe other 3D noncentrosymmetric superconductors with broken TRS will join $LaNiC_2$ [55] and Re_6Zr [56] soon.

The prerequisites for TRS-breaking Cooper instabilities are much more restrictive in 2D. Here, the Fermi-Dirac constraint (4.32) of the weak-pairing order parameter $\widetilde{\Delta}_s(\boldsymbol{k})$ has crucial consequences for the allowed IRs since inversion of the 2D momentum can be realized as a twofold rotation C_2^z perpendicular to the plane of the system. For spinfull fermions, $\Theta^2 = -\mathbb{1}$, it has been shown in Sec. 4.4 that a threefold rotation symmetry as element of the high-temperature point group $\mathcal{G}_p$ is a necessary condition for TRS-breaking Cooper instabilities. Furthermore, if $C_2^z \in \mathcal{G}_p$, the triplet vector has to be aligned parallel to the plane of the system as long as interband matrix elements of the order parameter are negligible.

Similarly, we have seen in Sec. 4.7.2 that a TRS with $\Theta^2 = \mathbb{1}$ will automatically be broken at a superconducting phase transition in a system with $\mathcal{G}_p$ containing a fourfold proper or improper rotation symmetry.

The strength of these statements is related to the fact that they only depend on very few and experimentally accessible properties of the system – the high-temperature time-reversal and point symmetries as well as the energetic separation of the Fermi surfaces. E.g., RG corrections of the coupling constants will not affect the results as the symmetries are not changed during the RG flow.

Finally, we have illustrated the predictive power of these general statements using several different materials, Sr_2RuO_4, UPt_3, URu_2Si_2, oxide heterostructures as well as FeSe on STO, as examples (see Sec. 4.6). Most importantly, we concluded that the pairing state of thin layers of Sr_2RuO_4 [68] must be, as opposed to its bulk behavior, necessarily TRS preserving as well as characterized by an in-plane triplet vector. By analyzing all remaining possible pairing states, we have seen that the thin layer system represents a promising platform for the observation of MBSs. Note that due to the preserved TRS, these edge modes must always come in counter-propagating pairs. As a consequence of the layered structure of Sr_2RuO_4, the rotation of the $\boldsymbol{d}$ vector as well as the restoration of TRS should also occur at a (001) surface of the crystal (see Sec. 4.8).

In thin layers of UPt_3 [69], TRS breaking cannot be excluded resulting from the presence of a threefold rotation symmetry. Nonetheless, the selection rules turned out to be highly restrictive reducing the 10 symmetry-allowed pairing states down to the 3 remaining candidates summarized in Table 4.4.

Among the three different orientations of oxide interfaces [35, 142, 156], only the (111)-terminated heterostructure allows for spontaneous TRS-breaking superconductivity. This motivates a more thorough experimental study of the low-temperature physics of this interface or, more generally, of any quasi-2D system with a threefold rotation symmetry in the search for exotic low-dimensional superconducting states that break TRS.

Chapter 5

5 Instabilities in oxide heterostructures

In the previous chapter, we have seen that very general energetic arguments valid for systems with large spin-orbit splitting of the Fermi surfaces can be used to gain information about the symmetry properties of the possible superconducting instabilities. E.g., in case of LAO/STO heterostructures, we could determine the relative phase of the superconducting order parameter on symmetry-related parts of the Fermi surface. However, this approach is neither sufficient to fully identify the microscopic pairing state, in particular its topological properties, nor does it in any way provide information on the microscopic driving force of superconductivity. To address the latter two issues, an explicit microscopic calculation is required that takes into account, e.g., the character of the relevant orbitals, the geometry of the Fermi surfaces of the system and the interaction terms leading to the superconducting instability.

In this chapter, we will perform such a microscopic calculation specifically for oxide heterostructures analyzing the phase competition between both superconducting and density wave instabilities. As the mechanism of superconductivity is still unknown (see [36–38] and Chap. 1.3.1), we take into account all symmetry-allowed interactions within our effective low-energy description. We find two candidate pairing states which have the same symmetry properties but differ in their topology. Assuming a conventional, i.e., electron-phonon-dominated, mechanism we obtain a topologically trivial superconductor whereas unconventional pairing, characterized by a microscopically repulsive interaction, leads to the topological state. While symmetry breaking at the superconducting phase transition has proven to be a powerful tool to provide evidence for an electronic pairing mechanism in cuprate superconductors [27, 28], the one-to-one correspondence between the mechanism and the topology of superconductivity derived in this chapter for LAO/STO heterostructures might be used to pinpoint the microscopic origin of superconductivity in the latter system. The observation of topological signatures, most notably, the emergence of Majorana modes at the edge of the system, would strongly point towards an unconventional pairing mechanism.

For simplicity, we will entirely focus on the most frequently studied (001)-oriented interface. The extension of the central results to the second orientation where superconductivity has been observed [40] will be discussed in the next chapter (see, in particular, Chap. 6.3.1).

This chapter consists of two parts: In the first part, Sec. 5.1, we will motivate in detail the effective interacting low-energy theory tailor-made to understand superconductivity and its competitors in (001) LAO/STO heterostructures. The derivation of the leading and subleading instabilities in this model, the analysis of the properties of the resulting phases and the discussion of experimental approaches to deduce the nature of the superconducting state can be found in Sec. 5.2.

This chapter is based on Ref. [349]. The results have been reviewed more recently in Ref. [38].

5.1 Model of the 2D electron liquid

The first step to gain theoretical understanding of the phase transitions in a system, is to find a minimal yet physically sensible model, i.e, a model that captures the essential physical features but does not depend on irrelevant microscopic details. Deriving such a model for (001) oriented oxide heterostructures with the main, but not exclusive, goal of describing superconductivity will be the topic of this section.

As discussed in Chap. 1.3.1, conductivity is induced in LAO/STO heterostructures by populating the Ti $3d$ shell. The relevant low-energy degrees of freedom are the states of the t_{2g} manifold, i.e., the $3d_{xy}$, $3d_{xz}$ and $3d_{yz}$ orbitals while the e_g states lie energetically higher [341–343]. As opposed to bulk STO, the bottom of the $3d_{xy}$ band is lower in energy than that of the band derived from the other two orbitals [343, 350]. The interface states of $3d_{xy}$ character are widely believed to be mainly localized and relevant for the observed magnetism [111, 151, 152, 346, 347]. This also naturally explains the highly reduced concentration of transport carriers [344] compared to the expectation of half an electron per unit cell from the polar catastrophe mechanism (see Chap. 1.3.1) or seen in local charge measurements [139]. Furthermore, it strongly indicates that the bands associated with the $3d_{xz}$ and $3d_{yz}$ orbitals are most likely the main host of superconductivity. This expectation is confirmed by carrier-concentration-dependent experiments [344, 345] demonstrating that the sweet spot of superconductivity is associated with the chemical potential entering the bands with $3d_{xz}$ and $3d_{yz}$ character.

For this reason, we will assume that it is sufficient to focus on these two orbitals to understand superconductivity and, in Sec. 5.1.1, derive the associated noninteracting Hamiltonian in the vicinity of the Γ-point. In this chapter, we will not take into account any coupling of the $3d_{xz}$ and $3d_{yz}$ states to magnetic moments that could possibly develop in the $3d_{xy}$ states. Irrespective of whether magnetism has an intrinsic [111, 151, 152] or an extrinsic [153–155] origin, the experimental observation [149] that there is no significant spatial correlation between superconductivity and magnetism clearly shows that the former does not have to be taken into account to understand the latter. The physical reason for this decoupling could be the spatial separation between the corresponding quantum well states as the $3d_{xy}$ bands are closer to the interface than the other bands [342] in combination with the small mixing of the $3d_{xy}$ and the $3d_{xz}/3d_{yz}$ orbitals [111].

Independent of the aforementioned magnetic textures with length scales [149] much larger than the superconducting coherence length ξ [39], one might wonder whether the strong tendency of the system towards the formation of magnetic moments could render also initially nonmagnetic impurities, such as oxygen vacancies, magnetic on atomic length scales by local spontaneous symmetry breaking. The impact of magnetic impurities on the stability of superconductivity in oxide heterostructures thus constitutes a very important aspect which will be postponed to Chap. 7.3.

5.1.1 Noninteracting two-orbital model

Using $\hat{c}_{\boldsymbol{k}\alpha}$ with α referring to the four combinations of the spin orientations and the two orbitals $\{3d_{xz}, 3d_{yz}\}$ to describe the annihilation of an electron of crystal momentum $\boldsymbol{k}$ in state α, the noninteracting two-orbital Hamiltonian can be written as

$$\hat{H}_0 = \sum_{\boldsymbol{k}} \hat{c}^\dagger_{\boldsymbol{k}\alpha} \left(h_{\boldsymbol{k}}\right)_{\alpha\beta} \hat{c}_{\boldsymbol{k}\beta}, \qquad h_{\boldsymbol{k}} = h^{\mathrm{m}}_{\boldsymbol{k}} + h^{\mathrm{so}}_{\boldsymbol{k}}, \tag{5.1}$$

where h has been split into two contributions h^{m} and h^{so} which are trivial and nontrivial in spin space, respectively. As shown in Appendix D.1.1, the most general form of h^{m} up to second order in

momentum that is consistent with the TRS and the C_{4v} symmetry of the system reads

$$h^{\mathrm{m}}_{\boldsymbol{k}} = \begin{pmatrix} \frac{k_1^2}{2m_{\mathrm{l}}} + \frac{k_2^2}{2m_{\mathrm{h}}} - \mu & \eta k_1 k_2 \\ \eta k_1 k_2 & \frac{k_1^2}{2m_{\mathrm{h}}} + \frac{k_2^2}{2m_{\mathrm{l}}} - \mu \end{pmatrix} \otimes \sigma_0, \tag{5.2}$$

where σ_0 is the unit matrix in orbital space and the upper (lower) component correspond of the matrix to the $3d_{xz}$ ($3d_{yz}$) orbital. Physically, the distinct masses m_{l} and m_{h} result from the different overlap of the orbitals along the coordinate axes. The mass anisotropy is known to be very strong, $m_{\mathrm{h}}/m_{\mathrm{l}} \simeq 15 - 30$ [341], which will play an important role in our analysis of instabilities below. Furthermore, η is an orbital mixing term caused by second-nearest neighbor hopping.

The spin-rotation symmetry is broken by h^{so} which contains the combined effect of SOC and broken inversion symmetry and, up to linear order in momentum, must be of the form

$$h^{\mathrm{so}}_{\boldsymbol{k}} = \frac{1}{2}\lambda\tau_2\sigma_3 + \alpha_0\tau_0\left(k_1\sigma_2 - k_2\sigma_1\right) + \alpha_1\tau_1\left(k_1\sigma_1 - k_2\sigma_2\right) + \alpha_3\tau_3\left(k_1\sigma_2 + k_2\sigma_1\right), \tag{5.3}$$

where λ, α_j are *a priori* unknown constants and τ_j (σ_j) represent Pauli matrices in orbital (spin) space. The first term is centrosymmetric and just corresponds to the atomic SOC of the $3d_{xz}$ and $3d_{yz}$ orbitals. The other three terms are odd under inversion and describe the Dresselhaus-Rashba effect [33, 34] introduced in Chap. 1.3. We see that the combination of two different orbitals allows, in addition to the usual Rashba term ($\propto \tau_0$), also for two terms with Dresselhaus spin-momentum structure that transform nontrivially in orbital space ($\propto \tau_1, \tau_3$).

To reduce the number of unknown parameters, let us derive Eq. (5.3) from the three-orbital model that also takes into account the $3d_{xy}$ states. Using the orbital basis $\{3d_{xy}, 3d_{xz}, 3d_{yz}\}$, the spin-independent part of the Hamiltonian reads

$$\widetilde{h}^{\mathrm{m}}_{\boldsymbol{k}} = \begin{pmatrix} \frac{\boldsymbol{k}^2}{2m_{xy}} - \mu - \delta\epsilon_{xy} & -i\delta k_2 & -i\delta k_1 \\ i\delta k_2 & \frac{k_1^2}{2\widetilde{m}_{\mathrm{l}}} + \frac{k_2^2}{2\widetilde{m}_{\mathrm{h}}} - \mu & \widetilde{\eta} k_1 k_2 \\ i\delta k_1 & \widetilde{\eta} k_1 k_2 & \frac{k_1^2}{2\widetilde{m}_{\mathrm{h}}} + \frac{k_2^2}{2\widetilde{m}_{\mathrm{l}}} - \mu \end{pmatrix} \otimes \sigma_0, \tag{5.4}$$

which is the most general symmetry-allowed expression up to second order in momentum (see Appendix D.1.2). The lower right 2×2 block contains the same terms as in Eq. (5.2) although with unrenormalized parameters. By symmetry, the $3d_{xy}$ band has an isotropic mass (m_{xy}) but is shifted energetically to lower energies ($\delta\epsilon_{xy} > 0$) as already mentioned above. The effect of the broken inversion symmetry is captured in the terms $\propto \delta$ (already encountered in the context of Sr_2RuO_4 in Eq. (4.108)) which can only be finite in vicinity of the interface. In the tight-binding language, one can think of δ as the matrix element

$$\delta \simeq aE_0 \left\langle d_{xy}, \boldsymbol{R}_i | z | d_{xz}, \boldsymbol{R}_i + a\boldsymbol{e}_2 \right\rangle, \tag{5.5}$$

where E_0 is the strength of the electric field resulting from the asymmetry under $z \to -z$, a denotes the lattice constant and $|d_l, \boldsymbol{R}_i\rangle$ refers to the Wannier wavefunctions of orbital character $l \in \{xy, xz, yz\}$ localized at Bravais lattice point $\boldsymbol{R}_i$.

Furthermore, we include the atomic SOC term $\widetilde{h}^{\mathrm{so}}_{\boldsymbol{k}} = \boldsymbol{L}\cdot\boldsymbol{\sigma}$ where $\boldsymbol{L} = (L_1, L_2, L_3)$ is the vector of 3×3 matrices of angular-momentum operators (see Appendix D.1.2) projected onto the subspace spanned by the three orbitals $\{3d_{xy}, 3d_{xz}, 3d_{yz}\}$. Its form follows from Eq. (1.14) upon assuming $V = V(|\boldsymbol{x}|)$ with approximately constant derivative.

Using the method of Ref. [130], we integrate out the $3d_{xy}$ orbital which is possible as a consequence of the energetic separation from the other two orbitals in the part of the Brillouin zone that will be of interest for our analysis of instabilities. We recover h^{m} (with renormalized parameters) and h^{so} with the simple relation $\alpha_0 = -\alpha_1 = -\alpha_3$ between the Rashba-Dresselhaus coefficients. Furthermore, the latter can be expressed as $\frac{1}{2}\delta\lambda/E_0$ where E_0 is the energetic splitting between the $3d_{xy}$ and $3d_{xz}/3d_{yz}$ bands showing that both the broken inversion symmetry as well as the atomic SOC are required for the Dresselhaus-Rashba effect.

As δ and E_0 are expected to crucially depend on the microscopic details at the interface, we take $\alpha_0 = 10\,\mathrm{meV\AA}$ estimated from magnetotransport data [41]. Using $\lambda = 20\,\mathrm{meV}$, $m_{\mathrm{h}}/m_{\mathrm{l}} = 30$, $m_{\mathrm{l}} = 0.7m_e$ with m_e denoting the free electron mass and $\eta = 0.28m_e^{-1}$ as has been deduced from Refs. [41, 341, 344, 350], the two-orbital Hamiltonian $h_{\boldsymbol{k}}$ yields the spectrum shown in Fig. 5.1(a). We see that the inversion antisymmetric Dresselhaus-Rashba terms render the Fermi surfaces nondegenerate and that the atomic SOC pushes two of the four bands to higher energies. As already discussed above, superconductivity is known to be associated [344, 345] with the Fermi energy entering the bottom of the $3d_{xz}$ and $3d_{yz}$ bands. For this reason we will focus on electron concentrations where the chemical potential lies below the upper two bands shown in gray in Fig. 5.1(a) which can thus be neglected[1] in the following. The form of the Fermi surfaces associated with the other two bands, along with the spin (arrows) and orbital (color code) polarization of the eigenstates, is shown in Fig. 5.1(b) and (c). It agrees well with the ARPES data on the buried LAO/STO interface electron liquid [343] and on the surface states of STO [341, 342]. In the regions, highlighted in green in Fig. 5.1(b) and (c), where the Fermi surfaces are nearly straight lines, the wavefunctions are characterized by strong orbital polarizations of either $3d_{xz}$ or $3d_{yz}$ character and a spin-orientation largely aligned parallel to one of the coordinate axis. This crucially enhances the stability of superconductivity against disorder as we will see in Chap. 7.3.

5.1.2 Interacting effective low-energy theory

As far as the energetics of instabilities is concerned, the most important aspect is the strong nesting in the nearly straight regions of the Fermi surface. It is a consequence of the mass anisotropy and becomes exact in the hypothetical limit $m_{\mathrm{h}}/m_{\mathrm{l}} \to \infty$. This observation makes it possible to use a simplified low-energy description, where only the degrees of freedom in the vicinity of these nested regions of the Fermi surface are taken into account. We see that there are four symmetry-related nested subspaces consisting of four patches each. Let us first focus on one of the subspaces, e.g., the four red patches in Fig. 5.1(a), and discuss the impact of scattering between different nested subspaces later.

Patch approximation. Exactly as in Chap. 4, it will be most convenient to perform the calculation in the eigenbasis of the noninteracting Hamiltonian (5.1). We thus introduce new fermionic operators $\hat{f}_{\boldsymbol{k}s}$ via $\hat{c}_{\boldsymbol{k}\alpha} = \sum_s \left(\psi_{\boldsymbol{k}s}\right)_\alpha \hat{f}_{\boldsymbol{k}s}$ with $\psi_{\boldsymbol{k}s}$ denoting an eigenstate of $h_{\boldsymbol{k}}$ with corresponding energy $\epsilon_{\boldsymbol{k}s}$. It will be convenient to label the four patches within one of the nested subspaces by $\sigma = \pm$ referring to sign of k_1 and $s = 1, 2$ where $s = 1$ ($s = 2$) represents the outer (inner) Fermi surface. Within a given patch, the single-particle states will be labeled by $k_\perp$ and $k_\parallel$ which are defined relative to the center of the patch in the direction perpendicular and parallel to the Fermi surface, respectively (see Fig. 5.1(a)). Upon passing to a field-integral description [114, 115] and linearizing the spectrum around the Fermi energy, $\epsilon_{\boldsymbol{k}s} \sim \sigma v_s k_\perp$, the noninteracting part of the low-energy theory is described by

$$S_0 = \int_k^{\Lambda_\perp, \Lambda_\parallel} \bar{f}_{k(\sigma,s)} \left(-i\omega_n + \sigma v_s k_\perp\right) f_{k(\sigma,s)}, \tag{5.6}$$

[1] As the splitting λ is much larger than the superconducting gap [70, 350], this is a natural assumption.

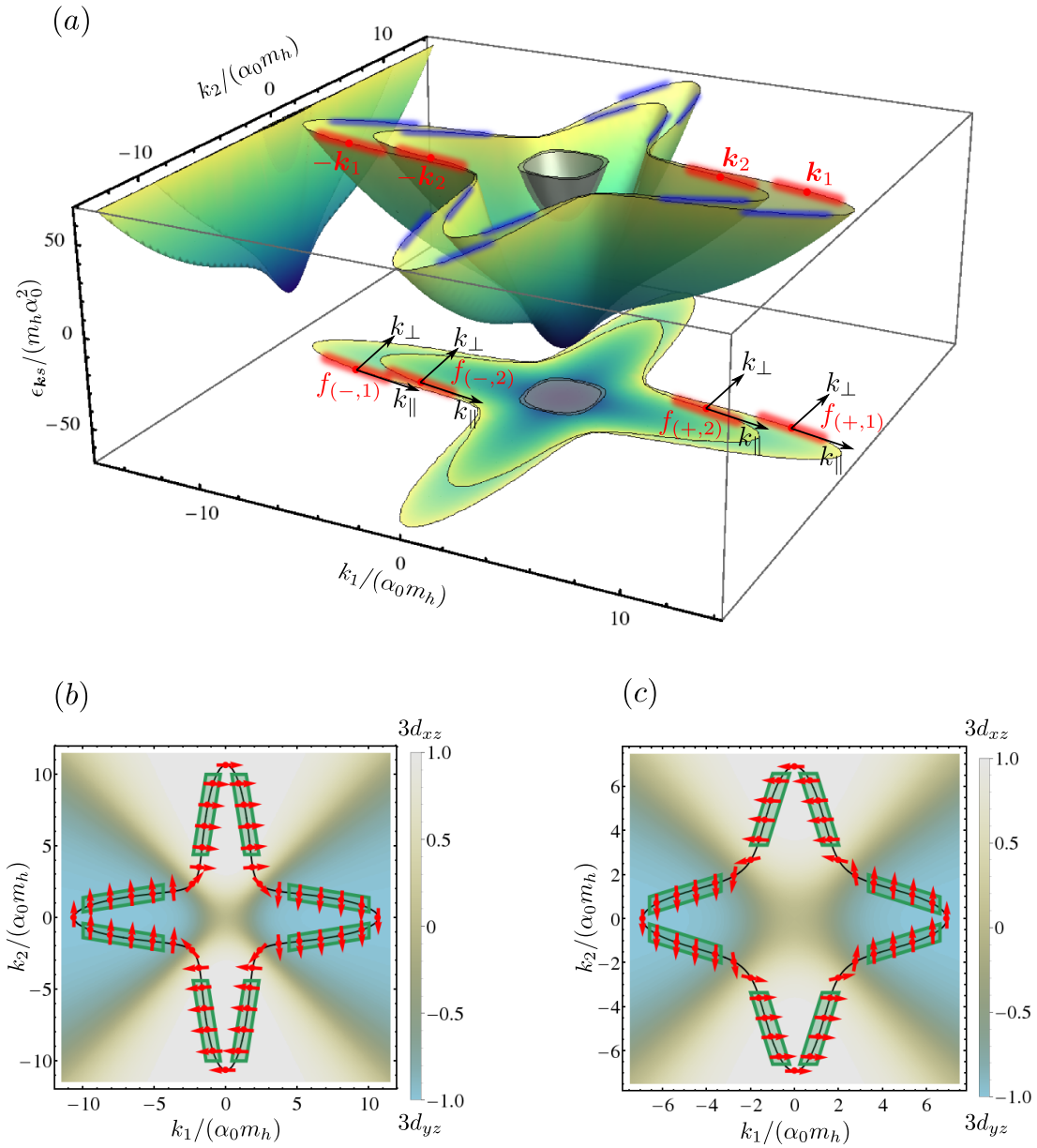

Figure 5.1: ***Spectrum and the wave functions of two-orbital model.*** *In (a), the spectrum of the Hamiltonian $h_{\boldsymbol{k}}$ defined in Eqs. (5.1)-(5.3) is shown using the parameters stated in the main text. In the effective low-energy approach we use, the analysis is restricted to the nested subspaces (highlighted in red and blue). The orbital weight (color) and orientation of the spin (red arrows) are illustrated in (b) and (c) for the outer and inner Fermi surface, respectively. Note that, as a consequence of TRS and C_2^z rotation symmetry, the spin has to lie in the xy plane. In the green regions of the Fermi surface, the wavefunctions are nearly constant and strongly polarized with respect to both its spin and orbital degree of freedom.*

where the Grassmann fields f and $\bar{f}$ correspond to the quasiparticle operators $\hat{f}$ and $\hat{f}^\dagger$ introduced above and Matsubara frequency ω_n and momentum $(k_\perp, k_\parallel)$ is comprised in one variable $k \equiv (\omega_n, k_\perp, k_\parallel)$. Furthermore, we use

$$\int_k^{\Lambda_\perp,\Lambda_\parallel} \dots = T\sum_{\omega_n} \int_{-\Lambda_\parallel}^{\Lambda_\parallel} \frac{\mathrm{d}k_\parallel}{2\pi} \int_{-\Lambda_\perp}^{\Lambda_\perp} \frac{\mathrm{d}k_\perp}{2\pi} \dots, \tag{5.7}$$

for notational convenience where $\Lambda_\perp$ and $\Lambda_\parallel$ are momentum cutoffs perpendicular and tangential to the Fermi surface. Although the finite curvature of the Fermi surface is neglected in Eq. (5.6), it will later enter the stage in form of a cutoff of the RG as will be discussed in Sec. 5.2.

For the analysis of this chapter, it will be very convenient to fix the phase convention of the eigenstates $\psi_{\boldsymbol{k}s}$ and consequently of the fields $f_{k(\sigma,s)}$. Instead of explicitly solving for the wavefunctions, we will, similarly to the construction of the pseudspin basis in Appendix A.1, take advantage of symmetries of the system. Exploiting the presence of a two-fold rotation symmetry C_2^z perpendicular to the plane, we can construct the eigenstate with $k_1 < 0$ from those with $k_1 > 0$ via

$$\psi_{-\boldsymbol{k}s} := \mathcal{R}_\Psi^\dagger(C_2^z)\psi_{\boldsymbol{k}s}, \qquad k_1 > 0, \qquad \mathcal{R}_\Psi(C_2^z) = i\tau_0\sigma_3, \tag{5.8}$$

where the explicit form of the representation $\mathcal{R}_\Psi(C_2^z)$ of C_2^z refers to the basis used in Eq. (5.3). To fix the phase of the states with $k_1 > 0$, we use that the Hamiltonian is also invariant under time-reversal with $\Theta = i\sigma_2\mathcal{K}$ where $\mathcal{K}$ denotes complex conjugation. Consecutive application of Θ and $\mathcal{R}_\Psi(C_2^z)$ leads to a $\boldsymbol{k}$-local symmetry of the Hamiltonian that makes it always possible to adjust the phase such that

$$\psi_{\boldsymbol{k}s} = \tau_0\sigma_1\psi^*_{\boldsymbol{k}s}, \qquad k_1 > 0. \tag{5.9}$$

In the following, we will impose the constraints in Eqs. (5.8) and (5.9), which fix the phases of the eigenstates (except for a trivial global minus sign) and, hence, also define the transformation behavior of the Grassmann fields under the symmetry operations.

Including interactions. To allow for an unbiased analysis of instabilities within the low-energy theory, we take into account all k-independent quartic interaction terms that respect the point group and TRS of the system. Introducing the multi-index notation $\tau \equiv (\sigma, s)$, we parameterize the interaction according to

$$S_{\mathrm{int}} = \int_{k_1,k_2,k_3,k_4}^{\Lambda_\perp,\Lambda_\parallel} \bar{f}_{k_4\tau_4}\bar{f}_{k_3\tau_3}f_{k_2\tau_2}f_{k_1\tau_1}\,\widetilde{\mathcal{W}}^{\tau_4\tau_3}_{\tau_2\tau_1}\,\delta(k_1+k_2-k_3-k_4), \tag{5.10}$$

where $\delta(\dots)$ is the delta function with respect to $\int_k^{\Lambda_\perp,\Lambda_\parallel}$ defined in Eq. (5.6). It will turn out that the dimensionless parameterization $\mathcal{W} = \frac{2\Lambda_\parallel}{\pi^2 v_1}\widetilde{\mathcal{W}}$ is most convenient as the results will not depend on the longitudinal cutoff $\Lambda_\parallel$ of the patches and the RG equations will assume a very compact form.

As it requires fine-tuning of the filling, we will not consider the possibility of Umklapp processes such that only two basic types of combinations of σ_j are possible: Firstly, there is forward scattering, where all four fermions in Eq. (5.10) have the same index σ which must be of the form

$$\mathcal{W}^{(\sigma,s_4)(\sigma,s_3)}_{(\sigma,s_2)(\sigma,s_1)} \equiv V^{s_4s_3}_{s_2s_1}(\sigma) = g_0(\sigma)\left[\delta_{s_4,s_1}\delta_{s_3,s_2} - \delta_{s_4,s_2}\delta_{s_3,s_1}\right], \tag{5.11}$$

due to Fermi-Dirac statistics. Secondly, the scattering of a pair of quasiparticles with $\sigma_1 \neq \sigma_2$ into a pair of electrons with $\sigma_3 \neq \sigma_4$, which we refer to as backscattering, will be parameterized according to

$$\mathcal{W}^{(-,s_4)(+,s_3)}_{(+,s_2)(-,s_1)} \equiv W^{s_4s_3}_{s_2s_1} = \sum_{j,j'=0}^{3} g_{jj'}\left(\tau_j\right)_{s_4s_1}\left(\tau_{j'}\right)_{s_3s_2}. \tag{5.12}$$

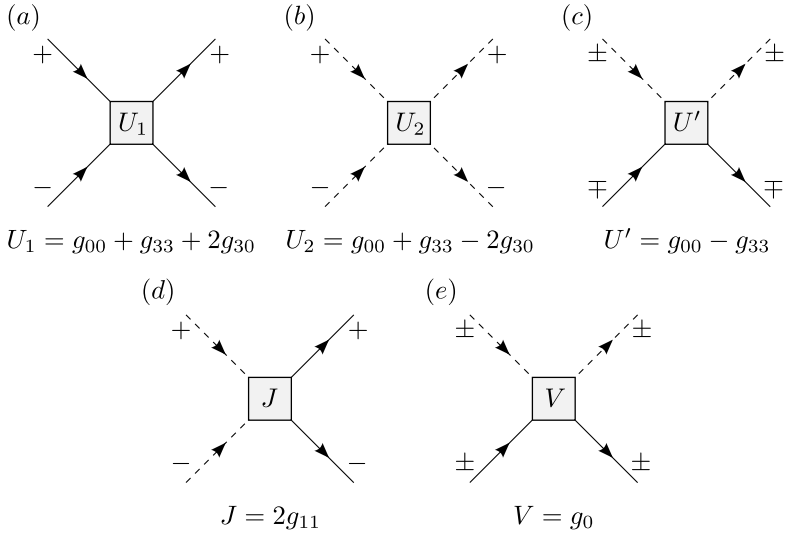

Figure 5.2: ***Diagrammatic representation of the scattering processes.*** *The combination of twofold rotation, TRS and momentum conservation only allows for four independent backscattering processes (a-d) and one forward scattering term (e). Solid and dashed lines refer to the outer and inner Fermi surface and $\pm$ indicates the sign of k_1 in the four nested patches highlighted in red in Fig. 5.1(a).*

Here τ_j are Pauli matrices acting the abstract, $\boldsymbol{k}$-nonlocal isospin space of patches with identical σ.

The number of coupling constants is reduced by the constraints of TRS and the C_2^z rotation symmetry. To begin with the latter, it directly follows from the phase conventions defined above that $f_{k(\pm,s)} \to \mp f_{k'(\mp,s)}$ with $k' = (\omega, -k_\perp, -k_\parallel)$ under C_2^z. Applying this to Eq. (5.10), implies $V(+) = V(-)$ and $W^{s_4 s_3}_{s_2 s_1} = W^{s_3 s_4}_{s_1 s_2}$ or, equivalently, $g_0(+) = g_0(-) \equiv g_0$ and $g^T = g$. Note that all other symmetry operations of C_{4v} act *between* different nested subspaces and, hence, do not have to be considered when analyzing a single subspace. These symmetries fully determine the interaction terms within the other nested subspaces. Similarly, TRS can be shown to imply $g_{ss'} = 0$ if either $s = 2$ and $s' \neq 2$ or $s' = 2$ and $s \neq 2$. Together, these constraints reduce the number 18 of possible coupling constants (2 in Eq. (5.11) and 16 in Eq. (5.12)) to only 8.

As already discussed in Chaps. 1.3.1 and 4.6.3, the spin-orbit splitting E_{so} of the Fermi surfaces is a very strong effect in LAO/STO heterostructures which even constitutes a significant fraction of the Fermi energy [41, 42] as is also visible in Fig. 5.1(a). For this reason, it seems very plausible that the energetic cutoff ($\simeq v_s \Lambda_\perp$) of the low-energy theory we use to deduce the instabilities can be chosen to smaller than E_{so} or, stated differently, that the patches in Fig. 5.1 do not overlap. Here we will focus on this scenario and just refer to Ref. [349] where also the opposite limit $E_{\mathrm{so}} \ll v_s \Lambda_\perp$ has been discussed. When the patches do not overlap, momentum conservation rules out further terms. As is straightforwardly shown, it forces $g_{10} = g_{31} = 0$ and $g_{22} = -g_{11}$ such that only five independent coupling constants remain. The notation we are currently using for the interaction terms is mathematically very convenient but physically less insightful. Therefore, we represent the five distinct scattering processes diagrammatically in Fig. 5.2 expressed with respect to the four different patches. We see that there are two generally different intraband Coulomb terms, U_1 and U_2, an interband Coulomb interaction U', pair hopping J as well as forward scattering V.

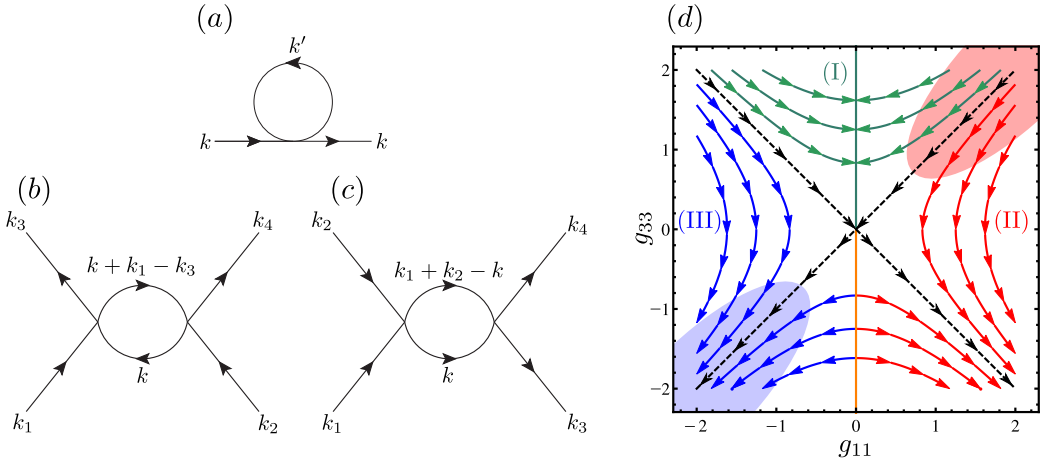

Figure 5.3: ***Diagrammatics of Wilson RG and flow diagram for our model.*** *The three diagrams of one-loop RG, the "tadpole" (a), the "ZS" (b) and the "BCS" diagram (c), are shown. The resulting flow (5.17) for our low-energy model in the simplified case of identical Fermi velocities is illustrated in (d). The red and blue shaded regions correspond to microscopically repulsive and attractive interactions, respectively.*

5.2 Instabilities of the system

Having derived an effective interacting low-energy theory, which is defined by the action $S = S_0 + S_{\text{int}}$, we are now in a position to analyze the instabilities of the system. For this purpose, we apply the well-established procedure, e.g., also used in Refs. [351, 352], of first deriving the RG flow of the coupling constants and identifying the instability associated with the divergence of a certain interaction channel via mean-field theory.

5.2.1 RG flow diagram and leading instability

In the Wilson RG approach, as discussed in detail for fermions with a finite Fermi surface in Ref. [99], "fast" modes with momenta $\Lambda_\perp e^{-\Delta l} < k_\perp < \Lambda_\perp$, $\Delta l > 0$, are integrated out yielding, after properly rescaling k and the field variables, an effective action with renormalized parameters. The noninteracting quadratic part S_0 of the action simply splits into the contributions from the "fast" and "slow" modes, whereas the interaction leads to nontrivial terms in the effective action that can in general only be treated perturbatively.

The corresponding one-loop contributions are shown diagrammatically in Fig. 5.3(a)-(c). The tadpole diagram, Fig. 5.3(a), represents the impact of the interactions on the bands of the system. Here and in the following, we will neglect this contribution to the RG flow, since, by definition, we assume that all possible interaction effects on the chemical potential and on the Dresselhaus-Rashba effect have already been effectively accounted for by S_0 [99].

The other two diagrams, Fig. 5.3(b) and (c), which are usually referred to as "ZS" and "BCS", respectively, lead to the corrections

$$\Delta_{\text{ZS}}\widetilde{\mathcal{W}}^{\tau_4\tau_3}_{\tau_2\tau_1} = -4\left(\widetilde{\mathcal{W}}^{\tau_4\tau'}_{\tau_2\tau}\widetilde{\mathcal{W}}^{\tau\tau_3}_{\tau'\tau_1} - \widetilde{\mathcal{W}}^{\tau_3\tau'}_{\tau_2\tau}\widetilde{\mathcal{W}}^{\tau\tau_4}_{\tau'\tau_1}\right)\int_k^{\Lambda_\perp,\Lambda_\parallel} G^{>}_{\tau}(k+k_1-k_3)G^{>}_{\tau'}(k) \tag{5.13}$$

and

$$\Delta_{\mathrm{BCS}}\widetilde{\mathcal{W}}^{\tau_4\tau_3}_{\tau_2\tau_1} = 2\widetilde{\mathcal{W}}^{\tau_4\tau_3}_{\tau\tau'}\widetilde{\mathcal{W}}^{\tau\tau'}_{\tau_2\tau_1}\int_k^{\Lambda_\perp,\Lambda_\parallel} G^>_\tau(k)G^>_{\tau'}(k_1+k_2-k) \tag{5.14}$$

of the interaction tensor $\widetilde{\mathcal{W}}$ in Eq. (5.10). In Eqs. (5.13) and (5.14), $G^>_{(\sigma,s)}(k) = (i\omega - \sigma v_s k_\perp)^{-1}\theta^{\Delta l}_{k_\perp}$ is the bare Green's function associated with the fast modes of S_0 where $\theta^{\Delta l}_{k_\perp} = 1$ as long as $\Lambda_\perp e^{-\Delta l} < k_\perp < \Lambda_\perp$ and $\theta^{\Delta l}_{k_\perp} = 0$ otherwise.

Evaluating the shell integrals asymptotically in the limit $\Delta l \to 0$ allows for reformulating the change of coupling constants in form of differential equations, the so called RG *flow equations*. Using the parameterization introduced above, one finds

$$\frac{\mathrm{d}\mathcal{W}^{(\sigma,s_4)(\sigma,s_3)}_{(\sigma,s_2)(\sigma,s_1)}}{\mathrm{d}l} \equiv \frac{\mathrm{d}V^{s_4s_3}_{s_2s_1}(\sigma)}{\mathrm{d}l} = 0 \tag{5.15}$$

i.e., the forward scattering terms are not renormalized at all at one loop order. This is different for the backscattering processes where the diagrams in Fig. 5.3(b) and (c) yield nontrivial contributions. The associated flow equations can be conveniently stated in the matrix form

$$\frac{\mathrm{d}W^{s_4s_3}_{s_2s_1}}{\mathrm{d}l} = \sum_{s,s'}\frac{1}{x_s+x_{s'}}\left(W^{s_4s'}_{s_2s}W^{ss_3}_{s's_1} - W^{s_4s_3}_{s's}W^{ss'}_{s_2s_1}\right), \qquad x_s := v_s/v_1, \tag{5.16}$$

where the contributions of the first and second term emanate from the ZS and BCS diagram, respectively.

We see that the flow equations (5.16) depend on the ratio v_2/v_1 of the Fermi velocities. Let us first focus on the simplest scenario where both Fermi velocities are identical, $x_s = 1$, which represents are good approximation as can be checked explicitly using the band structure shown in Fig. 5.1(a), and postpone the discussion of the general case $v_1 \neq v_2$ to Sec. 5.2.4. The RG equations assume the particularly simple form

$$\frac{\mathrm{d}g_{11}}{\mathrm{d}l} = -2g_{11}g_{33}, \qquad \frac{\mathrm{d}g_{33}}{\mathrm{d}l} = -2g_{11}^2, \qquad \frac{\mathrm{d}g_{00}}{\mathrm{d}l} = \frac{\mathrm{d}g_{30}}{\mathrm{d}l} = \frac{\mathrm{d}g_0}{\mathrm{d}l} = 0 \tag{5.17}$$

in the limit $v_1 = v_2$, where we have inserted the parameterization of Eq. (5.12). Consequently, only two out of the five allowed coupling constants flow with associated flow diagram presented in Fig. 5.3(d). We observe that there are three different regions: For any set of bare coupling constants in region (I), the couplings flow to the line of fixed points $g^*_{11} = 0$, $g^*_{33} > 0$ and, most importantly, do not diverge. This means that the system does not develop a weak-coupling instability for these interaction parameters and is thus expected to reside in the metallic phase. This is different in region (II) and (III) where the running coupling constants diverge and asymptotically approach a ratio of $g_{33}/g_{11} = -1$ and $g_{33}/g_{11} = +1$, respectively. In terms of the interaction processes shown in Fig. 5.2, these two strong-coupling fixed points correspond to $-U_1 \sim -U_2 \sim U' \sim \pm J/2 \gg |V|$ with $U' > 0$ where the upper $+$ sign refers to region (II) and the lower $-$ sign to (III).

In order to deduce the nature of the instabilities at these two strong-coupling fixed points, we follow Refs. [351, 352] and determine the order parameter with the highest transition temperature. For the sake of generality, we consider all possible particle-particle, $\overline{\Delta}^{\mathrm{SC}}_{\tau\tau'}$, as well as particle-hole order parameters, $\Delta^{\mathrm{DW}}_{\tau\tau'}$, which are formally defined as the expectation values

$$\overline{\Delta}^{\mathrm{SC}}_{\tau\tau'} = \int_k^{\Lambda_\perp,\Lambda_\parallel}\langle \bar{f}_{k\tau}\bar{f}_{-k\tau'}\rangle\,, \qquad \Delta^{\mathrm{DW}}_{\tau\tau'} = \int_k^{\Lambda_\perp,\Lambda_\parallel}\langle \bar{f}_{k\tau}f_{k\tau'}\rangle\,, \tag{5.18}$$

within the nested subspace. Note that this parameterization also includes translation-symmetry-breaking superconducting states, i.e., of FFLO type, where the Cooper pairs have finite center of mass momentum (see Chap. 1.1.2).

As shown in Appendix D.2, one finds that the leading instability at both strong-coupling fixed points is of superconducting type where the order parameter only couples time-reversed states, i.e., $\overline{\Delta}^{\mathrm{SC}}_{(\sigma,s)(\sigma',s')} = 0$ if $\sigma = \sigma'$ or $s \neq s'$. This affirms our assumption in Chap. 4.6.3 that no translation symmetry breaking takes place at the superconducting phase transition in oxide heterostructures. More specifically, we find $\overline{\Delta}^{\mathrm{SC}}_{(+,j)(-,j)} = (-1)^j \Delta_0$ and $\overline{\Delta}^{\mathrm{SC}}_{(+,j)(-,j)} = \Delta_0$ at the fixed point of region (II) and (III) which will be referred to as s^{+-} and s^{++} superconductivity, respectively.

5.2.2 Candidate pairing states

In this subsection, we will analyze further properties as well as possible microscopic origins of these two superconducting states and discuss how they can be distinguished experimentally.

Microscopic mechanism. We begin with the microscopic origin of the interactions leading to the superconducting instabilities described by the RG in Fig. 5.3(d). Let us first neglect any electron-phonon coupling and only take into account the repulsive Coulomb interaction. Using the microscopic basis with l referring to the Ti $3d_{xz}$ and $3d_{yz}$ orbitals as well as $\uparrow$, $\downarrow$ labeling spin-orientations, we consider an intra- and interorbital Hubbard interaction $\mathcal{U}$ and $\mathcal{U}'$ as well as the Hund's coupling $\mathcal{J}_H$ and the pair exchange $\mathcal{J}'$ described by the Hamiltonian

$$\begin{aligned}\hat{H}_{\mathrm{int}} = \mathcal{U} \sum_{i,l} \hat{n}_{il\uparrow}\hat{n}_{il\downarrow} + \frac{1}{2}\mathcal{U}' \sum_{i,l\neq l'} \hat{n}_{il}\hat{n}_{il'} - \frac{1}{2}\mathcal{J}_H \sum_{i,l\neq l'} \left(\hat{n}_{il\uparrow}\hat{n}_{il'\uparrow} + \hat{n}_{il\downarrow}\hat{n}_{il'\downarrow}\right) \\ + \mathcal{J}' \sum_{i,l\neq l'} \hat{c}^\dagger_{il\uparrow}\hat{c}^\dagger_{il\downarrow}\hat{c}_{il'\downarrow}\hat{c}_{il'\uparrow} + \mathcal{J}_H \sum_{l\neq l'} \hat{c}^\dagger_{il\uparrow}\hat{c}^\dagger_{il'\downarrow}\hat{c}_{il\downarrow}\hat{c}_{il'\uparrow}.\end{aligned} \tag{5.19}$$

Here i refers to the Bravais lattice site $\boldsymbol{R}_i$ and $\hat{n}_{il\uparrow} = \hat{c}^\dagger_{il\uparrow}\hat{c}_{il\uparrow}$, $\hat{n}_{il\downarrow} = \hat{c}^\dagger_{il\downarrow}\hat{c}_{il\downarrow}$ as well as $\hat{n}_{il} = \hat{n}_{il\uparrow} + \hat{n}_{il\downarrow}$ have been used for notational convenience. When writing the coupling constants in Eq. (5.19) as matrix elements of the Coulomb interaction kernel decaying as $1/r$ with r denoting the distance of the interacting particles, one finds $\mathcal{J}_H = \mathcal{J}' \equiv \mathcal{J}$ and $\mathcal{U} = \mathcal{U}' + 2\mathcal{J}$ as long as the atomic wavefunctions have approximately the angular dependence of the spherical harmonics. According to first principle calculations [353] for Ti in transition metals, it typically holds $\mathcal{J}/\mathcal{U} \simeq 1/8$. Projection the interaction (5.19) onto the effective low-energy theory with the phase conventions in Eqs. (5.8) and (5.9) yields

$$g_{00} \simeq g_{11} \simeq g_{33} > 0, \quad |g_{00}| \gg |g_{30}|. \tag{5.20}$$

We emphasize that Eq. (5.20) is remarkably stable against detuning the interaction parameters away from the three approximate relations between them mentioned above. It means that the bare couplings of the RG flow reside in the red region in Fig. 5.3(d) and, hence, implies that the s^{+-} superconductor is an *unconventional* superconductor (see Chap. 1.1.2) driven by the particle-hole fluctuations that eventually change the sign of g_{33} making the Cooper instability possible. No microscopically attractive interaction induced by the electron-phonon coupling is required to stabilize the s^{+-} state.

Correspondingly, if we only focus on the interaction induced by the electron-phonon coupling[2] and neglect Coulomb repulsion, the bare interaction will be attractive and the flow will start in the blue

[2] See also Chap. 6.1.1 for a detailed discussion of electron-phonon-induced electron-electron interaction in noncentrosymmetric systems.

region of Fig. 5.3(d) which identifies the s^{++} state as a *conventional* superconductor. Naturally, residual Coulomb repulsion and electron-phonon coupling are simultaneously present in the real system. Conventional (unconventional) pairing then refers to electron-phonon-induced attraction (Coulomb repulsion) being dominant and only slightly renormalized by the residual Coulomb repulsion (the electron-phonon-based electron-electron interaction) such that the flow still starts in region (III) (in region (II)) of Fig. 5.3(d) leading to the s^{++} (s^{+-}) pairing state.

Recently, inelastic tunneling spectroscopy measurements [354] have revealed clear evidence for electron-phonon coupling in LAO/STO heterostructures. Since a quantitative determination of the electron-phonon coupling constant is not possible with this approach and the shift of the phonon frequencies induced by changing the oxygen isotope did not lead to an observable shift of the critical temperature of superconductivity, this does not exclude the electronic pairing scenario. A detailed theoretical analysis [355] of the competition between the electron-phonon coupling and the screened Coulomb interaction indicates that the effective interaction might indeed be repulsive. This is a consequence of the comparatively weak screening of the Coulomb interaction due to the low carrier concentrations in the system.

Symmetry and topology. To connect to our discussion of symmetry and topology of superconductivity in the previous chapters, let us consider the mean-field Hamiltonian

$$\hat{H} = \hat{H}_0 + \sum_{s=1,2} \sum_{\boldsymbol{k}\in S_s} \left(\hat{f}^\dagger_{\boldsymbol{k}s} \widetilde{m}_{ss} \hat{f}^\dagger_{-\boldsymbol{k}s} + \text{H.c.} \right) + \dots . \tag{5.21}$$

associated with the two candidate pairing states. Here S_s denotes the patch in the vicinity of $\boldsymbol{k}_s$ in Fig. 5.1(a) and the ellipsis stands for the mean-field terms in the remainder of the Brillouin zone. As readily follows from performing a mean-field decoupling of the interaction terms in Eq. (5.10), we have $\widetilde{m} = 4(\gamma_0\tau_0+\gamma_3\tau_3)\Delta_0^*$ with $\gamma_0 = g_{00}+2g_{11}+g_{33}$, $\gamma_3 = 2g_{30}$ for the s^{++} and $\gamma_0 = 2g_{30}$, $\gamma_3 = g_{00}-2g_{11}+g_{33}$ for the s^{+-} state.

Comparison of Eqs. (4.26) and (5.21) shows that $D_{ss}(\boldsymbol{k}_s) \equiv \widetilde{\Delta}_s(\boldsymbol{k}_s) = \widetilde{m}_{ss} e^{i\varphi^s_{\boldsymbol{k}_s}}$. Since $e^{i\varphi^s_{\boldsymbol{k}_s}} = i\,\mathrm{sign}(k_1)$ as readily follows from the phase conventions in Eqs. (5.8) and (5.9), we can choose the global phase of Δ_0 such that $\widetilde{\Delta}_s(\boldsymbol{k}_s)$ is real. Recalling Chap. 4.2.2, this means that the superconductor does not break TRS *within* one of the strongly nested subspaces. Although this confirms our more generally valid "symergetic" arguments of Chap. 4.6.3, it is just a consequence of the fact that the effective point group of the model we are considering is $C_2 \equiv \{E, C_2^z\}$ which only has real one-dimensional IRs and, hence, does not allow for spontaneous TRS breaking at a single superconducting phase transition (see Chap. 4.1.2). The relative phase of the order parameter $\widetilde{\Delta}_s(\boldsymbol{k})$ *between* the four different nested subspaces is determined by the value of the (nonsingular) coupling constants that describe scattering events between different subspaces. Instead of taking into account these interactions in a microscopic calculation, we can resort to our analysis of Chap. 4.6.3 where it has been shown that the superconducting state cannot break TRS as a consequence of the strong spin-orbit splitting of the Fermi surfaces and the point group C_{4v}. Consequently, there is just a single IR, A_1 with $\widetilde{\Delta}_s(\boldsymbol{k})$ having no sign changes on a given Fermi surface, that is consistent with experiments [70] indicating the absence of nodes of the superconducting gap.

While the "symergetic" arguments of the previous chapter have uniquely determined the behavior of $\widetilde{\Delta}_s(\boldsymbol{k})$ within all Fermi surfaces, the microscopic calculation presented here yields the relative sign $\mathrm{sign}(\gamma_0+\gamma_3)\,\mathrm{sign}(\gamma_0-\gamma_3)$ between the two Fermi surfaces and relates it to the mechanism of superconductivity: For conventional pairing (region (III) in Fig. 5.3(d)), where the RG flow leads to the asymptotic behavior $g_{11} \sim g_{33} \to -\infty$ while g_{00}, g_{30} stay finite, we have $|\gamma_0| \gg |\gamma_3|$, i.e., there is no

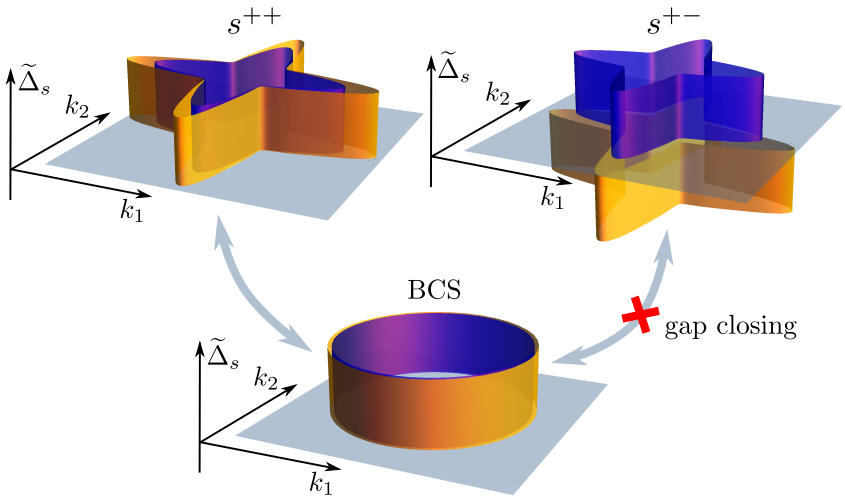

Figure 5.4: ***Adiabatic connection to BCS superconductor.*** *The value of the pairing field at the inner (blue) and outer (orange) Fermi surface is shown for the standard BCS superconductor as well as for the s^{++} and s^{+-} states of oxide heterostructures. The topologically trivial BCS superconductor is adiabatically connected to the s^{++} phase, whereas a TRS-preserving continuous deformation into the s^{+-} state requires closing the gap at some point along the path.*

sign change between the Fermi surfaces. For the unconventional state (region (II) in Fig. 5.3(d)) we find $|\gamma_3| \gg |\gamma_0|$ and, hence, opposite signs of $\widetilde{\Delta}_s(\boldsymbol{k})$ on the two Fermi surfaces.

As introduced in Chap. 2.2.3, a 2D superconductor with TRS is characterized by a $\mathbb{Z}_2$ topological invariant that can be conveniently evaluated via Eq. (2.19). As both Fermi surfaces $s = 1, 2$ enclose a single TRIM, it simply holds

$$\nu_{\mathbb{Z}_2} = \prod_{s=1,2} \operatorname{sign}\left(\widetilde{\Delta}_s(\boldsymbol{k}_s)\right) = \operatorname{sign}(\gamma_0 + \gamma_3)\operatorname{sign}(\gamma_0 - \gamma_3), \tag{5.22}$$

i.e., the topological invariant is determined by the relative sign on the two Fermi surfaces. This reveals a *one-to-one correspondence* between the mechanism and topology of superconductivity: While the conventional, i.e., mainly electron-phonon-induced, s^{++} superconductor is topologically trivial ($\nu_{\mathbb{Z}_2} = 1$ in Eq. (5.22)), the unconventional s^{+-} state which results from the Coulomb repulsion is topologically nontrivial ($\nu_{\mathbb{Z}_2} = -1$).

As it constitutes a central aspect of this chapter, let us gain intuitive understanding for the relation between the relative sign of $\widetilde{\Delta}_s(\boldsymbol{k}_s)$ on the two Fermi surfaces and the topological invariant $\nu_{\mathbb{Z}_2}$ expressed in Eq. (5.22). For this purpose, we compare the s^{++} and s^{+-} states with the standard BCS superconductor, i.e., an isotropic system with spin-degenerate Fermi surfaces and singlet s-wave pairing. As illustrated in Fig. 5.4, this phase can be continuously deformed into the s^{++} pairing state of the (001) oxide heterostructure without closing the gap[3] by turning on perturbations that break inversion and continuous rotation symmetry. For this reason, the s^{++} state is, exactly as the BCS

[3] To understand this more formally, add an infinitesimal amount of (TRS-preserving) spin-orbit splitting to the BCS state. As the BCS order parameter only couples Kramers partners, only its Fermi-surface-diagonal matrix elements, $s = s'$ in Eq. (4.27), are finite. Since $\Delta(\boldsymbol{k})T^\dagger = \sigma_0\Delta_0$, it follows $\widetilde{\Delta}_s(\boldsymbol{k}) = \Delta_0$ independent of s.

superconductor, topologically trivial. Note that the relative phase of the order parameter between the two Fermi surfaces cannot be continuously varied as this would break TRS. Consequently, the continuous TRS-preserving deformation of the BCS superconductor into the s^{+-} state must involve a gap closing at least on one of the Fermi surfaces, where, as follows from Eq. (5.22), a topological phase transition occurs.

We emphasize the difference of the topological s^{+-} state to recent theoretical work [356–358] that has pointed out the possibility of topological superconductivity in LAO/STO heterostructures stabilized by the interplay of magnetism and superconductivity. In that scenario, the spin-1/2 TRS is necessarily broken while the s^{+-} state proposed here is time-reversal symmetric.

Detection. The one-to-one correspondence between the mechanism and the topology of superconductivity derived above provides a tool to probe the unknown microscopic pairing mechanism in LAO/STO heterostructures: The observation of topological features of the superconducting state necessarily implies that the pairing mechanism must be unconventional. Conversely, the absence of topological signatures indicates that the electron-phonon coupling is the key driving force of superconductivity.

The hallmark of a 2D topological class-DIII superconductor is the presence of gapless counter-propagating Kramers partners of 1D Majorana modes localized on a length scale of the order of the superconducting coherence length ($\xi \simeq 100\,\mathrm{nm}$ [39]) at the boundary of the system to a trivial insulating phase [6, 262]. For studying MBSs in LAO/STO heterostructures it might be very useful that, as discussed in Chap. 1.3.1, boundaries between superconducting and insulating phases can be precisely engineered either by reducing the thickness of the LAO crystal locally [146] or via voltage-biased atomic force microscope tips [147]. We emphasize that the s^{+-} state, that emerges in case of a microscopically repulsive interaction in the heterostructure, is an "intrinsic" topological superconductor where both the pairing, the nontrivial topology and the MBSs result from the internal dynamics of the material. This has to be contrasted with "extrinsic" realizations of MBSs (e.g., the nanowire system [274, 275] discussed in Chap. 2.2.2) where superconductivity is induced via the proximity effect in a normal conductor and, potentially, external fields are applied.

The presence of MBSs localized at boundaries to trivial phases can be tested experimentally via tunneling spectroscopy where MBSs are expected to lead to conductance peaks at zero bias [60, 61]. Experiments of this type seem to be feasible as successful tunneling measurements of the superconducting bulk properties in LAO/STO heterostructures have been reported [70]. Naturally, electric transport measurements cannot be used to probe the presence of edge modes. However, the Majorana modes can carry heat current flowing along the edge of the system which is known as "thermal quantum Hall effect" [359, 360] in obvious terminological analogy to the electronic quantum Hall effect discussed in Chap. 2.2.1. The expected thermal conductance is given by $c\,G_0$ with $G_0 = \pi^2 k_B^2 T/(3h)$ denoting the thermal conductance quantum and $c = 1/2$ for a single noninteracting Majorana channel at the edge [360]. Although, interactions will generally modify the value of c as has been demonstrated in Ref. [361], thermal transport measurements can give important hints on the presence or absence of MBSs and, in turn, on the mechanism of superconductivity in LAO/STO heterostructures. In addition, the experimental analysis of Josephson junctions between the superconducting state in the heterostructure and a topologically trivial s-wave superconductor can be used to probe topological properties: As has been shown in Ref. [362], the presence of the Kramers pair of MBSs is expected to lead to a π-periodic current-phase relation and a half-period Fraunhofer effect. Furthermore, applying an in-plane Zeeman field, that gappes out the MBSs, will restore the ordinary Josephson effect. Given that Josephson junctions/SQUID devices have been successfully realized in superconducting LAO/STO heterostructures very recently [363], Josephson junction experiments designed to probe the topology of

the superconducting state do not seem to be beyond reach in the near future.

5.2.3 Competing instabilities

We have seen in Sec. 5.2.1 that superconductivity will eventually be favored at the strong-coupling fixed points. By successfully reducing the characteristic momentum or energy scale during the Wilson RG flow, our theory becomes more and more sensitive to low-energy details of the system such as the finite curvature of the Fermi surfaces. For any $m_\mathrm{l}/m_\mathrm{h} \neq 0$, the nesting is not perfect which will eventually force our RG to be cut off. If the flow stops before any subset of the coupling constants diverges, other *competing* phases will be possible as illustrated in Fig. 5.5(a) for repulsive (upper panel) and attractive (lower panel) bare interactions. If this is the case, all coupling constants can be of the same order in the mean-field equations (see Appendix D.2.1) such that the phase diagram of competing phases also depends on the couplings that do not flow. As can be seen in Fig. 5.5(b) and (c) showing the states competing with s^{+-} and s^{++}, respectively, one charge-density wave (CDW) instability (CDW^{12}), three distinct SDW phases (SDW^{11}, SDW^{22}, SDW^{12}) can emerge or the leading superconducting state dominates also for $m_\mathrm{l}/m_\mathrm{h} \neq 0$. Here we use the notation that the superscripts of $CDW^{ss'}$ and $SDW^{ss'}$ refer to the expectation values $\Delta^{\mathrm{DW}}_{(-,s)(+,s')}$ (and $\Delta^{\mathrm{DW}}_{(-,s')(+,s)}$ if $s \neq s'$) that are finite. The states SDW^{12} and CDW^{12} differ in the relative phase between $\Delta^{\mathrm{DW}}_{(-,1)(+,2)}$ and $\Delta^{\mathrm{DW}}_{(-,2)(+,1)}$ making the former and the latter state odd and even under time-reversal, respectively.

From Fig. 5.5(b) and (c) we see that the topological s^{+-} superconductor competes with time-reversal odd SDW phases, while the main competitor of the topologically trivial s^{++} superconductor is the time-reversal symmetric CDW^{12} state. Consequently, the experimental observation of a competing SDW or CDW phase residing in the Ti $3d_{xz}$ and $3d_{yz}$ orbitals might give additional hints on the microscopic origin of the superconducting state. In Chap. 6.2, we will see that there is a very general connection between the topology of the superconducting state and the time-reversal properties of the competing particle-hole instability.

Let us next discuss the spatial textures of the CDW and SDW phases which follow from the structure of the respective density wave order parameter $\Delta^{\mathrm{DW}}_{\tau\tau'}$ and the wavefunctions of the single-particle states on the Fermi surfaces graphically represented in Fig. 5.1(b) and (c). To begin with CDW^{12}, one finds that the local charge density has the form

$$\rho(\boldsymbol{x}) \propto \cos\left(\boldsymbol{Q}_{12} \cdot \boldsymbol{x}\right) + \ldots, \tag{5.23}$$

where $\boldsymbol{Q}_{12} = \boldsymbol{k}_1 + \boldsymbol{k}_2$ is the associated nesting vector. The first contribution stems solely from the nested subspace shown in red in Fig. 5.1(a) and the ellipsis stands for the terms emanating from the remaining three subspaces. Exactly as in case of superconductivity, also the relative sign of the density wave order parameter between the four different nested subspaces cannot be inferred from the current calculation without taking into account additional interactions mediating between the different subspaces. For concreteness, we will assume that also the density wave order parameters do not break any point symmetries although the generalization to arbitrary IRs is straightforward. This fully determines the contributions from the remaining three subspaces in Eq. (5.23) and leads to the charge profile in Fig. 5.6(a) as is explained in more detail in Appendix D.3. Note that the periodicity crucially depends on the ratio of the two components of the nesting vector $\boldsymbol{Q}_{12}$.

The spatial structure of the SDW states SDW^{12} and SDW^{11}, SDW^{22} can be calculated in a similar way yielding the textures shown in Fig. 5.6(b) and (c), respectively. To arrive at this result, we have taken the spins to be aligned parallel/antiparallel to the y axis within the red regions of Fig. 5.1(a) which

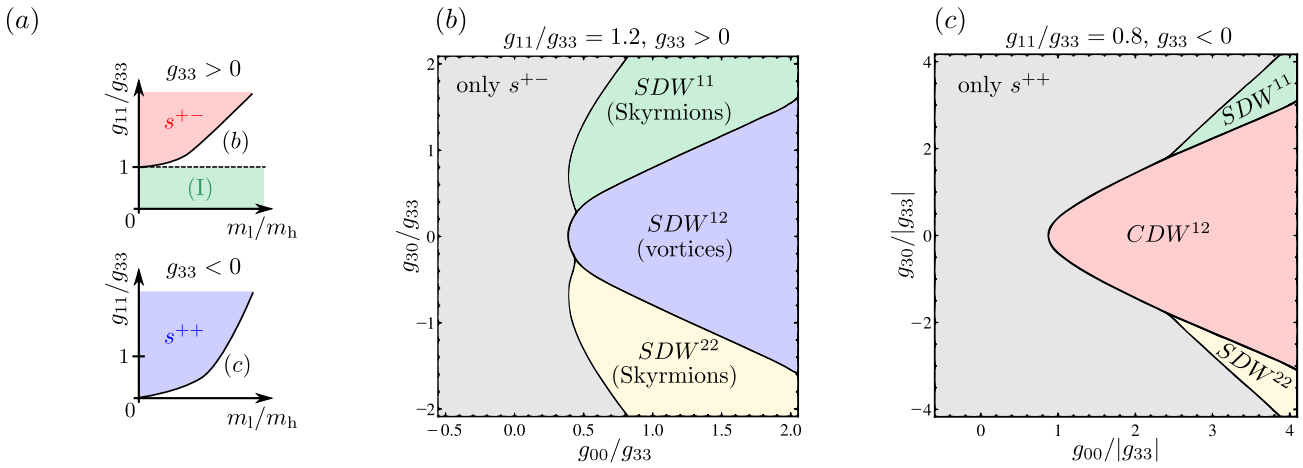

Figure 5.5: ***Phase diagrams of competing instabilities.*** *Schematic phase diagrams for finite mass anisotropies $m_l/m_h \neq 0$ are shown in (a) using the same color code as in Fig. 5.3(d). The phases competing with the s^{+-} and s^{++} superconductors are shown in (b) and (c) for different bare coupling constants. The notation of the phases is explained in the main text.*

constitutes a good approximation as can be seen in Fig. 5.1(b) and (c). Within this approximation, the spin expectation value lies in the plane of the system in case of the spin density phase SDW^{12}. The two-dimensional vector field is a lattice of vortices both with positive and negative winding numbers. Note that the orbital-diagonal matrix elements of the angular momentum operator vanishes (see Eq. (D.4)) such that the orbital polarization in the nested patches of the Fermi surfaces implies that the main contribution to the magnetic moments associated with the SDW phases comes from the electronic spin. In the other two SDW phases, SDW^{11} and SDW^{22}, the spin is not confined to the plane and rotates in 3D space. One finds a rich spin-texture consisting of isolated Skyrmions and Antiskyrmions as well as closely bound Skyrmion-Antiskyrmion pairs, one of which is shown in Fig. 5.6(d). The existence of a Skyrmion lattice phase is natural since these Skyrmions are known to occur as solutions of Ginzburg-Landau equations for systems with spin-orbit interaction [364, 365].

5.2.4 Different Fermi velocities

As already mentioned in Sec. 5.2.1, we have also performed the analysis presented above for the situation of different Fermi velocities $v_1 \neq v_2$. The RG equations following from Eq. (5.16) are more complicated in this case with all four backscattering coupling constants, g_{00}, g_{30}, g_{11} and g_{33}, flowing under RG. We leave a more detailed discussion of the instabilities to Appendix D.4 where the explicit form of the RG equations can be found (see Eq. (D.18)) and just state the main results.

A projection of the (four-dimensional) RG flow onto the $g_{11}g_{33}$ plane is shown in Fig. 5.7. In this way, the similarity to the flow in Fig. 5.3(d) is most apparent. In particular, one can still identify the three regions (I), (II) and (III). As before, none of the couplings diverges in region (I) and, hence, there is no weak-coupling instability. The strong-coupling fixed points of region (II) and (III) are, as in case of $v_1 = v_2$, associated with a superconducting instability with mean-field Hamiltonian of the form of Eq. (5.21) where $\widetilde{m}_{ss}$ have opposite (s^{+-} state) and equal sign (s^{++} state) on the two Fermi surfaces,

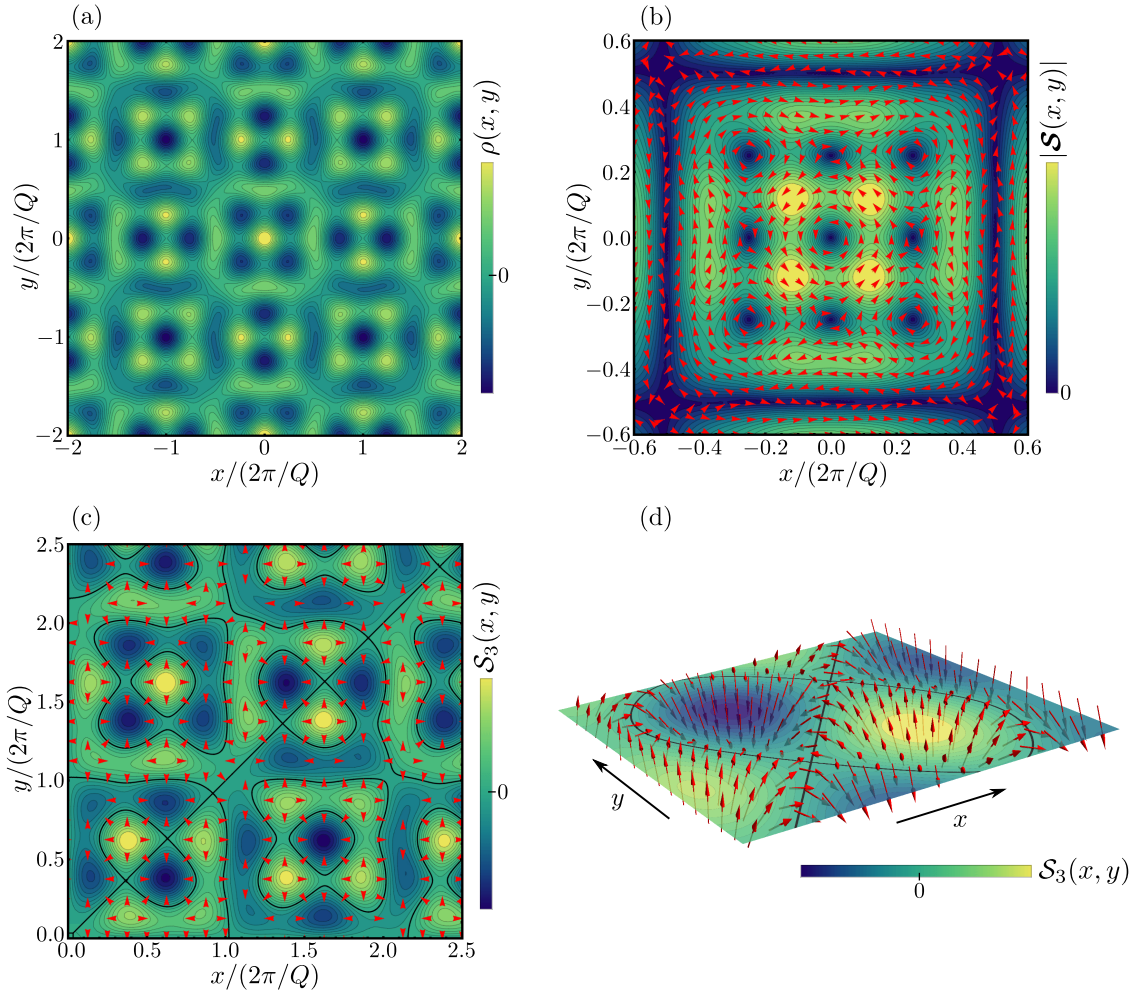

Figure 5.6: ***Spatial texture of the different density wave phases.*** *In (a), the charge density pattern of CDW^{12} is shown. In case of SDW^{12}, where the nesting vector is again given by $\boldsymbol{Q}_{12} = \boldsymbol{k}_1 + \boldsymbol{k}_2$, the spin $\boldsymbol{S}$ lies approximately in the plane of the system (the xy plane). As shown in (b) using red arrows to indicate the direction of the spin, one finds a lattice of vortices. In case of SDW^{11}, the nesting vector is $2\boldsymbol{k}_1$ and we observe a lattice of Skyrmions and Antiskyrmions as illustrated in (c), where the red arrows indicate the direction of the xy components of the spin and the black lines are the zeros of its z component $\mathcal{S}_3$. Part (d) illustrates one of the emerging closely bound Skyrmion-Antiskyrmion pairs. The texture of SDW^{22} with nesting vector $2\boldsymbol{k}_2$ is identical to SDW^{11} upon replacing $\mathcal{S}_3 \to -\mathcal{S}_3$. In all plots, a nesting vector of the form $(2, 0.48)Q$ has been assumed.*

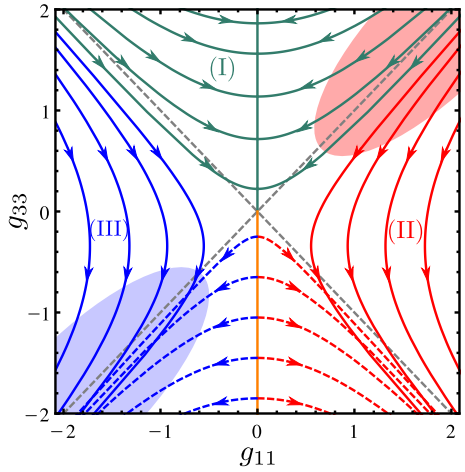

Figure 5.7: ***Flow for different velocities.*** *Projection of the flow onto the $g_{11}g_{33}$ plane for $v_2/v_1 = 0.4$ and the bare values $g_{00} = 1$ and $g_{30} = 0.1$. Gray dashed lines are the separatrices of the flow in Fig. 5.3(d).*

respectively. As a repulsive Coulomb (an attractive electron-phonon-induced) interaction corresponds to initial coupling constants in the red (blue) region, we again find that the unconventional superconductor is topologically nontrivial while the conventional superconductor is trivial. This generalizes the one-to-one correspondence between the mechanism and the topology of superconductivity established above to the case $v_1 \neq v_2$.

Note that translation-symmetry-breaking superconducting instabilities do not emerge as leading instabilities. An FFLO state only occurs as a competing phase and, in addition, only for bare coupling constants far away from the expected approximate relation (5.20). This confirms once again our assumption in Chap. 4.6.3 that the superconducting condensate of LAO/STO heterostructures preserves the lattice translation symmetry.

5.3 Summary of Chapter 5

In this chapter, we have studied the possible interaction-induced instabilities in (001)-oriented LAO/STO heterostructures from a microscopic point of view.

We have derived an effective model for the Ti $3d_{xz}$ and $3d_{yz}$ states which are expected to be most relevant for superconductivity [344, 345]. The simultaneous presence of magnetic moments in oxide heterostructures is understood as a phenomenon associated with the Ti $3d_{xy}$ states [111, 151, 152, 346, 347] that are both spatially as well as energetically separated from the relevant part of the $3d_{xz}/3d_{yz}$ bands [342, 343]. This might explain the independence of magnetism and superconductivity seen in experiment [149].

The spectrum and wavefunctions of the effective two-orbital model are summarized in Fig. 5.1. As superconductivity is associated with the chemical potential entering the bottom of the $3d_{xz}/3d_{yz}$ bands, we focused on the situation of just two singly degenerate Fermi surfaces surrounding the Γ point. The splitting of the bands and the spin textures are a consequence of the Rashba-Dresselhaus effect while the strong nesting in the highlighted patches of the Fermi surface results from the mass anisotropy

$m_\mathrm{h}/m_\mathrm{l} \gg 1$ of the orbitals [341–343].

Focusing on the degrees of freedom within the nested patches but, apart from that, taking into account all symmetry-allowed interaction terms, we have analyzed the phase competition using an RG approach. Independent of the value of the Fermi velocities, two strong-coupling fixed points can be identified which correspond to two superconducting instabilities: An s^{++} state where the sign of the mean-field order parameter is identical on the two spin-orbit-split Fermi surfaces and an s^{+-} phase where the sign is opposite. By considering a microscopically repulsive Coulomb and an attractive electron-phonon-induced interaction separately we find the corresponding bare couplings of the RG flow which allowed us to identify the s^{+-} and s^{++} states as unconventional and conventional superconductors, respectively.

We have seen how the microscopic analysis of this chapter and the general energetic argument of Chap. 4 complement one another. While the latter excludes spontaneous TRS breaking at the superconducting phase transition and thus, in conjunction with experiment [70], forces the relative phase of the order parameter *on* a given Fermi surface to be trivial, only the former yields information about the relative sign *between* the two Fermi surfaces and relates it to the mechanism of superconductivity. Using the expression for the associated topological invariant of class DIII discussed in Chap. 2.2.3, we have shown that the conventional s^{++} and the unconventional s^{+-} state are topologically trivial and nontrivial, respectively. This one-to-one correspondence between the mechanism driving the superconducting instability and the topology of the resulting condensate might be useful to probe the unknown superconducting mechanism in oxide heterostructures. In particular, the observation of MBSs at the edge of the system, which on its own would constitute a fascinating result, would on top of that also be a strong indication for an unconventional pairing mechanism in LAO/STO heterostructures. The presence of Majorana modes can be probed via tunneling spectroscopy [60, 61], thermal conductivity [359–361] or Josephson junction [362] measurements.

In addition, the competing particle-hole instabilities show very interesting spatial textures as can be seen in Fig. 5.6. As a consequence of the spin structure of the wavefunctions on the Fermi surfaces induced by the Dresselhaus-Rashba effect, the competing SDW phases are periodic arrangements of topological defects either of vortex or Skyrmion type. As the s^{++} state mainly competes with a CDW instability while the s^{+-} phase competes solely with SDW instabilities, the experimental study of competing particle-hole phases could also shed light on the microscopic mechanism of superconductivity. In the next chapter, we will see that there is a very general connection between the topology of the superconducting state and the time-reversal properties of the competing particle-hole phase.

Chapter 6

6 Correspondence between mechanism and topology in noncentrosymmetric systems

In the preceding chapter, it has been shown for a model of the 2D electron liquid at (001) oxide heterostructures that there is a one-to-one correspondence between the mechanism driving the superconducting phase transition and the topology of the resulting condensate: In case of a conventional mechanism, i.e., superconductivity based on electron-phonon coupling alone, the condensate is topologically trivial, whereas the unconventional pairing state, induced by the repulsive electron-electron interaction, turned out to be a topological superconductor. In this chapter, we analyze to which extent this one-to-one correspondence can be generalized to arbitrary noncentrosymmetric superconducting systems (see Chap. 1.3).

On top of that, the following considerations will also provide general guiding principles for the search of "intrinsic" topological superconductors, i.e., systems where both superconductivity as well as its nontrivial topology arise due to spontaneous symmetry breaking. These guiding principles are general in the sense that they are not based on explicit model studies and only depend on very few properties of the system such as symmetries and Fermi surface topologies of the normal conducting high-temperature phase which are also directly accessible experimentally (e.g., via photoemission experiments).

Furthermore, this chapter will also connect to and complement the analysis of Chap. 4: While conditions for spontaneous TRS breaking at superconducting phase transitions have been formulated in Chap. 4 in terms of the point symmetries of the normal state, we will here relate the time-reversal properties of the condensate to the mechanism driving the instability.

For this purpose, we will focus, exactly as in Chaps. 4 and 5, on noncentrosymmetric systems where the spin-orbit splitting E_{so} of the Fermi surfaces is larger than the transition temperature T_c of superconductivity such that the weak-pairing approximation (see Chap. 4.2) is applicable. Our results are mainly based on exact relations following from the symmetries, most importantly the TRS, of the high-temperature phase. As opposed to the previous two chapters, we will study the superconducting instability and analyze the topological properties of the resulting state beyond the mean-field approximation by calculating the Nambu Green's function self-consistently via Eliashberg theory [71, 72, 366] and applying the topological Hamiltonian approach (cf. Chap. 2.4.1). Throughout the chapter, we consider only clean systems and postpone the inclusion of disorder effects to Chap. 7.

The present chapter is organized in three parts: In the first part, Sec. 6.1, we analyze the time-reversal properties and the topology of electron-phonon-interaction-induced superconductors and also present a brief introduction to Eliashberg theory. Secondly, in Sec. 6.2, these considerations will be generalized

to unconventional pairing which we describe using an effective low-energy approach in the spirit of the spin-fermion model [30–32]. Finally, in the third part (Sec. 6.3), our results will be illustrated using oxide heterostructures and single-layer FeSe on STO as examples.

The analysis presented in this chapter has been published in Ref. [367].

6.1 Superconductivity due to electron-phonon coupling

In the first part of this chapter, we will focus on superconducting phases in noncentrosymmetric systems resulting from a purely conventional mechanism, i.e., induced by the electron-phonon coupling alone. It will be shown that all possible pairing states will be fully gapped, neither break any point group symmetry nor TRS and be necessarily topologically trivial. The proof provided holds on a very general level as no details about the microscopic model (number of relevant orbitals, bandstructure etc.) will have to be specified. It will only be assumed that the normal phase is time-reversal symmetric, the system is sufficiently clean for disorder effects to be negligible and that the spin-orbit splitting is sufficiently large for the weak-pairing approximation (see Chap. 4.2) to be applicable.

More specifically, let us consider fermions described by the general noninteracting Hamiltonian

$$\hat{H}_0 = \sum_{\boldsymbol{k}} \hat{c}^\dagger_{\boldsymbol{k}\alpha} \left(h_{\boldsymbol{k}}\right)_{\alpha\beta} \hat{c}_{\boldsymbol{k}\beta}, \tag{6.1}$$

where, exactly as in Chap. 4.1, $\boldsymbol{k}$ denotes d-dimensional crystal momentum and the indices $\alpha, \beta = 1, 2, \dots N$ represent all relevant microscopic degrees of freedom, e.g., spin, orbitals and potentially subbands. The creation (annihilation) of quasiparticles is described by the operator $\hat{c}^\dagger$ ($\hat{c}$). As already mentioned above, the only symmetry we assume in this section is TRS. Mathematically, this means that the normal state Hamiltonian in Eq. (6.1) has to satisfy $\Theta h_{-\boldsymbol{k}} \Theta^\dagger = h_{\boldsymbol{k}}$ with single-particle representation $\Theta = T\mathcal{K}$ of the time-reversal operator where $\mathcal{K}$ denotes complex conjugation and T is unitary. As opposed to Chap. 4, we will for concreteness entirely focus on spin-1/2 fermions here such that N will be even and $\Theta^2 = -\mathbb{1}$ leading to $T^T = -T$.

The electron-phonon coupling giving rise to superconductivity is taken to be of the general form

$$\hat{H}_{\text{el-ph}} = \sum_{\boldsymbol{k},\boldsymbol{k}',l} \hat{c}^\dagger_{\boldsymbol{k}\alpha} g^{(l)}_{\alpha\beta}(\boldsymbol{k},\boldsymbol{k}') \hat{c}_{\boldsymbol{k}'\beta} \left(\hat{b}^\dagger_{\boldsymbol{k}'-\boldsymbol{k}l} + \hat{b}_{\boldsymbol{k}-\boldsymbol{k}'l}\right). \tag{6.2}$$

For now, further interaction channels are assumed to be irrelevant. At the end of Sec. 6.1.3, we will comment on the impact of residual Coulomb repulsion on our results. In Eq. (6.2), $\hat{b}^\dagger_{\boldsymbol{q}l}$ and $\hat{b}_{\boldsymbol{q}l}$ are the creation and annihilation operators of phonons of branch l. The coupling $\hat{H}_{\text{el-ph}}$ can be seen as a generalized (relativistic) version of the well-known Fröhlich Hamiltonian [368] where the associated coupling matrix $g^{(l)}$ can, by virtue of spin-orbit interaction, couple states of different spin and might, on top of that, have nontrivial structure, e.g., in orbital or subband space. It will not be explicitly specified here – only the constraints resulting from Hermiticity and TRS will be taken into account. The former implies

$$g^{(l)}_{\alpha\beta}(\boldsymbol{k},\boldsymbol{k}') = \left(g^{(l)}_{\beta\alpha}(\boldsymbol{k}',\boldsymbol{k})\right)^*. \tag{6.3}$$

To analyze the consequences of the latter, first note that

$$\hat{\Theta} \hat{b}^{(\dagger)}_{\boldsymbol{q}l} \hat{\Theta}^\dagger = \hat{b}^{(\dagger)}_{-\boldsymbol{q}l} \tag{6.4}$$

since the deformation of the lattice $\hat{Q}_{\boldsymbol{q}} \sim \hat{b}^\dagger_{-\boldsymbol{q}} + \hat{b}_{\boldsymbol{q}}$ and the conjugate momentum $\hat{P}_{\boldsymbol{q}} \sim i(\hat{b}^\dagger_{\boldsymbol{q}} - \hat{b}_{-\boldsymbol{q}})$ must be even, $\hat{\Theta}\hat{Q}_{\boldsymbol{q}}\hat{\Theta}^\dagger = \hat{Q}_{-\boldsymbol{q}}$, and odd, $\hat{\Theta}\hat{P}_{\boldsymbol{q}}\hat{\Theta}^\dagger = -\hat{P}_{-\boldsymbol{q}}$, under time-reversal, respectively. Using this in Eq. (6.2), one immediately finds that TRS demands

$$g^{(l)}(\boldsymbol{k}, \boldsymbol{k}') = T \left(g^{(l)}(-\boldsymbol{k}, -\boldsymbol{k}') \right)^* T^\dagger. \tag{6.5}$$

Finally, the Hamiltonian of the phonons reads

$$\hat{H}_{\text{ph}} = \sum_{\boldsymbol{q},l} \hat{b}^\dagger_{\boldsymbol{q}l} \hat{b}_{\boldsymbol{q}l} \omega_{\boldsymbol{q}l}, \tag{6.6}$$

where the phonon dispersion $\omega_{\boldsymbol{q}l}$ satisfies $\omega_{\boldsymbol{q}l} > 0$ and $\omega_{\boldsymbol{q}l} = \omega_{-\boldsymbol{q}l}$ due to stability of the crystal and TRS, respectively.

6.1.1 Effective electron-electron interaction

Restating the Hamiltonian $\hat{H}_0 + \hat{H}_{\text{ph}} + \hat{H}_{\text{el-ph}}$ of the system in the action description [114, 115] and integrating out the phonon degrees of freedom yields the effective electron-electron interaction

$$S^{\text{eff}}_{\text{int}} = -\sum_l \int_{k_1,k_2,q} \frac{\omega_{\boldsymbol{q}l}}{\Omega_n^2 + \omega^2_{\boldsymbol{q}l}} g^{(l)}_{\alpha\beta}(\boldsymbol{k}_1 + \boldsymbol{q}, \boldsymbol{k}_1) g^{(l)}_{\alpha'\beta'}(\boldsymbol{k}_2 - \boldsymbol{q}, \boldsymbol{k}_2)\ \bar{c}_{k_1+q\alpha} \bar{c}_{k_2-q\alpha'} c_{k_2\beta'} c_{k_1\beta}. \tag{6.7}$$

Here $\bar{c}_\alpha$ and c_α are the Grassmann analogues corresponding to the fermionic creation and annihilation operators $\hat{c}^\dagger_\alpha$ and $\hat{c}_\alpha$. As before, we use $k \equiv (i\omega_n, \boldsymbol{k})$, $q \equiv (i\Omega_n, \boldsymbol{q})$ with $\int_k$ comprising both momentum ($\boldsymbol{k}$, $\boldsymbol{q}$) and Matsubara ($\omega_n = \pi T(2n+1)$, $\Omega_n = 2\pi T n$, $n \in \mathbb{Z}$) summation.

For describing superconducting instabilities, it is very convenient to work in the eigenbasis of the noninteracting part $h_{\boldsymbol{k}}$ of the high-temperature Hamiltonian. We thus write

$$c_{k\alpha} = \sum_s \left(\psi_{\boldsymbol{k}s}\right)_\alpha f_{ks}, \qquad \bar{c}_{k\alpha} = \sum_s \bar{f}_{ks} \left(\psi^*_{\boldsymbol{k}s}\right)_\alpha \tag{6.8}$$

where $\psi_{\boldsymbol{k}s}$ denote the eigenstates of $h_{\boldsymbol{k}}$, i.e. $h_{\boldsymbol{k}}\psi_{\boldsymbol{k}s} = \epsilon_{\boldsymbol{k}s}\psi_{\boldsymbol{k}s}$. Eq. (6.8) just constitutes the field-integral analogue of the transformation (4.23). In this chapter, we apply exactly the same low-energy approach as in Chap. 4: For given $\boldsymbol{k}$, the summation over s in Eq. (6.8) will restricted such that only bands leading to Fermi surfaces and states with energies $\epsilon_{\boldsymbol{k}s}$ in the vicinity of the chemical potential ($-\Lambda < \epsilon_{\boldsymbol{k}s} < \Lambda$) are taken into account. For phonons, the cutoff Λ is determined by the Debye frequency ω_D which sets the scale for the possible energy transfer in electron-phonon induced electron-electron scattering. Furthermore, the states will be labeled in such a way that any Fermi surface s, formally defined as the set of Fermi momenta $\{\boldsymbol{k}|\epsilon_{\boldsymbol{k}s} = 0\}$, is connected (see Fig. 6.1(a)).

Inserting the transformation (6.8) into Eq. (6.7) yields

$$S^{\text{eff}}_{\text{int}} = \int_{k_1,k_2,q} V^{s_1s_2}_{s_3s_4}(k_1, k_2, q)\ \bar{f}_{k_1+qs_1} \bar{f}_{k_2-qs_2} f_{k_2s_3} f_{k_1s_4} \tag{6.9}$$

with coupling tensor

$$V^{s_1s_2}_{s_3s_4}(k_1, k_2, q) = -\sum_l \frac{\omega_{\boldsymbol{q}l}}{\Omega_n^2 + \omega^2_{\boldsymbol{q}l}} G^{(l)}_{s_1s_4}(\boldsymbol{k}_1 + \boldsymbol{q}, \boldsymbol{k}_1) G^{(l)}_{s_2s_3}(\boldsymbol{k}_2 - \boldsymbol{q}, \boldsymbol{k}_2) \tag{6.10}$$

where we have introduced the fermion boson coupling

$$G^{(l)}_{ss'}(\boldsymbol{k},\boldsymbol{k}') = \psi^\dagger_{\boldsymbol{k}s}\, g^{(l)}(\boldsymbol{k},\boldsymbol{k}')\psi_{\boldsymbol{k}'s'} \tag{6.11}$$

in the eigenbasis representation. The Hermiticity constraint (6.3) now becomes

$$G^{(l)}_{ss'}(\boldsymbol{k},\boldsymbol{k}') = \left[G^{(l)}_{s's}(\boldsymbol{k}',\boldsymbol{k})\right]^* . \tag{6.12}$$

In this chapter we will focus on noncentrosymmetric systems, where the combination of SOC and hopping processes between orbitals that are only allowed in the absence of inversion symmetry will generically lift the spin-degeneracy of the Fermi surfaces (see also Chap. 1.3). As already discussed in detail in Chap. 4.2, the TRS of the normal phase then allows to uniquely express the wavefunction of the low-energy state at $\boldsymbol{k}$ in terms of the wavefunction at momentum $-\boldsymbol{k}$: Recalling the notation that s_K denotes the Fermi surface consisting of the Kramers partners of the momenta of s (cf. Fig. 6.1(a)), we have

$$\psi_{\boldsymbol{k}s} = e^{i\varphi^s_{\boldsymbol{k}}}\Theta\psi_{-\boldsymbol{k}s_\mathrm{K}} \tag{6.13}$$

with time-reversal phases $\varphi^s_{\boldsymbol{k}} \in \mathbb{R}$ that are determined by how the phases of the eigenstates $\psi_{\boldsymbol{k}s}$ are chosen. Although already introduced in Chap. 4.2, we have restated the relation (6.13) here for the convenience of the reader as it will be used repeatedly in the following analysis. Note that we will focus on $\Theta^2 = -\mathbb{1}$ such that the phases satisfy

$$e^{i\varphi^{s_\mathrm{K}}_{-\boldsymbol{k}}} = -e^{i\varphi^s_{\boldsymbol{k}}}. \tag{6.14}$$

Using Eqs. (6.5) and (6.13), i.e. the consequences of TRS for the electron-phonon coupling and the wavefunctions of the normal state Hamiltonian, it is straightforward to show that

$$G^{(l)}_{ss'}(\boldsymbol{k},\boldsymbol{k}') = e^{i(\varphi^{s'}_{\boldsymbol{k}'}-\varphi^s_{\boldsymbol{k}})}\left(G^{(l)}_{s_\mathrm{K}s'_\mathrm{K}}(-\boldsymbol{k},-\boldsymbol{k}')\right)^* . \tag{6.15}$$

This is a central relation for our analysis as it can be used to rewrite the Cooper channel of the interaction (6.9), i.e., the scattering process of a Kramers pair $\{s,k;s_\mathrm{K},-k\}$ of quasiparticles into another Kramers pair $\{s',k';s'_\mathrm{K},-k'\}$ as depicted in Fig. 6.2(a). Eq. (6.15) readily yields for this type of scattering event

$$V^{s's'_\mathrm{K}}_{s_\mathrm{K}s}(k,-k,k'-k) = e^{i(\varphi^s_{\boldsymbol{k}}-\varphi^{s'}_{\boldsymbol{k}'})}\mathcal{V}_{s's}(k';k) \tag{6.16}$$

where

$$\mathcal{V}_{s's}(k';k) = -\sum_l \frac{\omega_{\boldsymbol{k}'-\boldsymbol{k}l}}{(\omega_{n'}-\omega_n)^2+\omega^2_{\boldsymbol{k}'-\boldsymbol{k}l}}\left|G^{(l)}_{s's}(\boldsymbol{k}',\boldsymbol{k})\right|^2 < 0. \tag{6.17}$$

The very same matrix elements also govern the forward scattering processes shown in Fig. 6.2(b) with amplitude $\mathcal{F}_{s's}(k';k) := V^{s's}_{s's}(k,k',k'-k)$: Using the Hermiticity (6.3) of the electron-phonon interaction one finds $\mathcal{F} = \mathcal{V}$.

Consequently, the combination of TRS and the fact that the Fermi surfaces are singly degenerate highly constraints the Cooper channel of the interaction. As stated in Eq. (6.16), it can be written as the product of the time-reversal phases defined in Eq. (6.13) and the forward scattering matrix $\mathcal{V}_{s's}(k';k)$ which only has negative entries. We emphasize that this is a very general result since no additional model specific assumptions other than TRS and singly-degenerate Fermi surfaces (such as

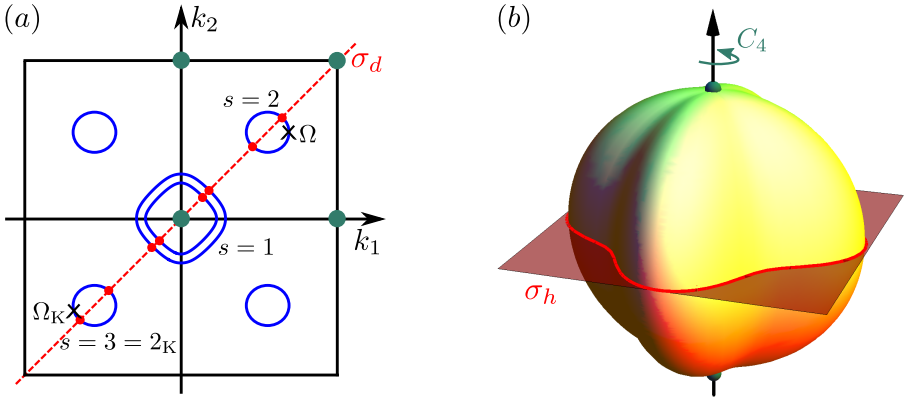

Figure 6.1: ***Parameterization of Fermi surfaces and fixed points of symmetries.*** *In (a), the notation used in this chapter is illustrated using a 2D example with C_{4v} symmetry. Fermi surfaces (blue) are chosen to be connected and the Kramers partner of (s, Ω) is denoted by (s_K, Ω_K). The four distinct TRIM are indicated as green dots and the fixed points (red) of the mirror operation σ_d (red dashed line) are shown. Part (b) illustrates the fixed point manifolds on the Fermi surface of a 3D system associated with a rotation symmetry C_4 (green dots) and a mirror operation (red line).*

number/character of relevant orbitals or dimensionality of the system) have been taken into account. In the next subsection, we will analyze the consequences for the resulting possible superconducting instabilities using Eliashberg theory [71, 72].

Before proceeding, a few remarks are in order: Naturally, the Cooper scattering amplitude (6.16) is a complex number that depends on the phases of the eigenstates $\psi_{\boldsymbol{k}s}$ whereas the forward scattering amplitude $\mathcal{V}$ is independent of the phases as it always involves a wavefunction and its complex conjugate in pairs (cf. Fig. 6.2(b)). Despite the gauge dependence of the Cooper scattering amplitude, the time-reversal and topological properties of the resulting superconducting state are, of course, independent of the time-reversal phases $\varphi^s_{\boldsymbol{k}}$ as we will see explicitly below.

Strictly speaking, the inequality sign in Eq. (6.17) has to be understood as smaller than zero except for configurations $\{s, \boldsymbol{k}; s', \boldsymbol{k}'\}$ where $\mathcal{V}$ is forced to vanish by symmetry. The Fermi momenta $\boldsymbol{k}$ where symmetries can impose zeros of $\mathcal{V}$ form a manifold that has dimension $d-2$ or smaller. To see this, first note that these zeros can only arise from zeros of G. The latter transforms according to

$$G^{(l)}_{ss'}(\boldsymbol{k}, \boldsymbol{k}') = e^{i(\rho^{s'}_{\boldsymbol{k}'}(g) - \rho^s_{\boldsymbol{k}}(g))} G^{(l)}_{\mathcal{R}_s(g)s\mathcal{R}_s(g)s'}(\mathcal{R}_v(g)\boldsymbol{k}, \mathcal{R}_v(g)\boldsymbol{k}') \tag{6.18}$$

under a symmetry operation g of the point group $\mathcal{G}_p$, where $\rho^s_{\boldsymbol{k}}(g)$ defined in Eq. (4.36) depend on the relative phases of the eigenstates $\psi_{\boldsymbol{k}s}$ at different $\boldsymbol{k}$. For general $\boldsymbol{k}$, it holds $\mathcal{R}_v(g)\boldsymbol{k} \neq \boldsymbol{k}$ such that Eq. (6.18) just relates G at different momenta. Zeros can thus only be imposed by symmetry at Fermi momenta $\boldsymbol{k}_j$ with $\mathcal{R}_v(g)\boldsymbol{k}_j = \boldsymbol{k}_j$ for some $g \in \mathcal{G}_p$. It is easily seen that the set of these "fixed points" forms a manifold with dimension smaller than the dimensionality $(d-1)$ of the Fermi surfaces of the system. Consider, e.g., the 2D system shown in Fig. 6.1(a) with C_{4v} symmetry. In the generic case (no Fermi surfaces going through high-symmetry points), only mirror planes, e.g., σ_d shown as red dashed line, have fixed points (red dots) which are just isolated points in the Brillouin zone. We note in passing that $G^{(l)}_{s_j s_{j'}}(\boldsymbol{k}_j, \boldsymbol{k}_{j'})$ is forced to vanish if the eigenvalues of $\psi_{\boldsymbol{k}_j s_j}$ and $\psi_{\boldsymbol{k}_{j'} s_{j'}}$ with respect to the mirror

operator are not complex conjugate to one another. In 3D, rotation and mirror symmetries can lead to fixed point manifolds of dimension zero (green dots) and one (red line), respectively, as illustrated in Fig. 6.1(b). Because of the reduced dimensionality, these zeros of $\mathcal{V}$ will not affect the superconducting properties as they will have measure zero in the continuum limit of the summation over the states on the Fermi surface. We will come back to this point below in more rigorous terms.

Finally, let us list three properties

$$\mathcal{V}_{s's}(k';k) = \mathcal{V}_{ss'}(k;k'), \tag{6.19a}$$

$$\mathcal{V}_{s's}(k';k) = \mathcal{V}_{s'_{\mathrm{K}}s_{\mathrm{K}}}(-k';-k), \tag{6.19b}$$

$$\mathcal{V}_{s's}\left(i\omega_{n'},\boldsymbol{k}';i\omega_n,\boldsymbol{k}\right) = \mathcal{V}_{s's}\left(-i\omega_{n'},\boldsymbol{k}';-i\omega_n,\boldsymbol{k}\right), \tag{6.19c}$$

which are readily read off from Eq. (6.17) and will be taken into account in the following[1].

6.1.2 Eliashberg theory in the weak-pairing limit

In this subsection, we will first provide a streamlined introduction to Eliashberg theory which focuses on the aspects relevant to the present analysis. For a broader discussion, in particular concerning its success in describing many different superconducting materials, we refer to textbooks (see, e.g., Ref. [368]) and the review article [369].

Eliashberg theory. Soon after the formulation of BCS theory, significant discrepancies between its predictions (e.g., ratio of zero temperature gap and transition temperature, critical field) and experiment have been observed for superconductors with strong electron-phonon coupling such as lead or mercury (see Ref. [370] and references therein). Around 1960, G. M. Eliashberg generalized [71, 72] the BCS theory beyond the weak-coupling limit based on the previous pioneering work of A. B. Migdal [366] on the electron-phonon coupling.

The aim of Eliashberg theory consists of calculating the Green's function in the superconducting phase self-consistently. Being the central building block of many body theory, the Green's function can then be used to calculate physical observables and, as we will discuss in detail below, analyze the symmetry and topological properties of the condensate. From BCS theory it is clear that we need to calculate the full Nambu Green's function with both the normal ($\Longrightarrow \leftrightarrow \langle\hat{c}^\dagger\hat{c}\rangle$) as well as anomalous ($\Longrightarrow\!\!\!\!\Longleftarrow \leftrightarrow \langle\hat{c}\hat{c}\rangle$, $\langle\hat{c}^\dagger\hat{c}^\dagger\rangle$) components in order to describe superconductivity.

Let us take a look, e.g., at the self-consistency equation of the anomalous propagator the first terms of which are represented diagrammatically in Fig. 6.2(c). There is an infinite number of missing diagrams with three and more phonon lines. It is hopelessly difficult to sum up all diagrams and solve the exact self-consistency equations such that some diagrammatic selection principle is required. The latter is provided by Migdal's theorem [366] which states that all vertex corrections of the electron-phonon coupling with n phonon lines are suppressed by a factor $(m/M)^{n/2}$ where m and M denote the mass of the electrons and the ions, respectively. Involving the adiabaticity ratio m/M of ionic motion as compared to electrons, it is the diagrammatic manifestation of the reasoning behind the celebrated Born-Oppenheimer approximation [371]. In the present context, it allows us to expand the self-consistency equations in terms of $\lambda\sqrt{m/M}$ instead of the dimensionless interaction parameter $\lambda = \rho_F\mathcal{V}$ of the BCS approach, where ρ_F denotes the density of states at the Fermi surface. Consequently, in Fig. 6.2(c), all

[1] Eq. (6.19b) is also enforced in the action description of the Cooper channel just by the fact that the Grassmann fields f, $\bar{f}$ anticommute and, hence, physically due to Fermi-Dirac statistics.

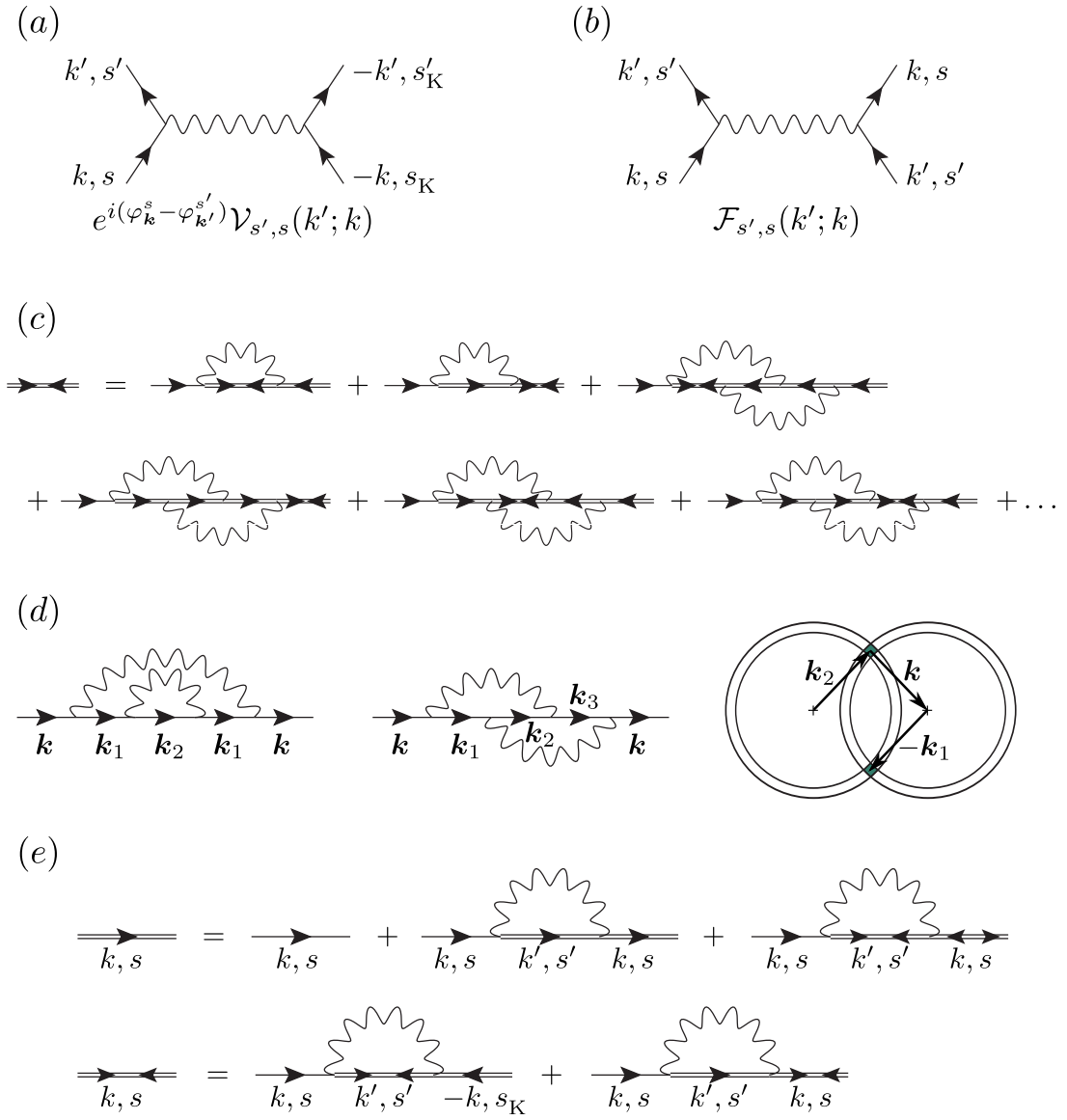

Figure 6.2: ***Diagrammatics of Eliashberg theory.*** *To calculate the superconducting properties only the Cooper (a) and forward scattering channel (b) of the electron-electron interaction are required. In part (c), the first few diagrams of the self-consistency equation for the anomalous Green's function are shown. All diagrams except for the first two contain vertex corrections and are thus suppressed by the smallness of the ratio m/M [366]. To understand this, we compare diagrams without and with vertex corrections in (d) that are of the same order in the coupling constant. In the latter case, the available phase space is reduced as compared to the former case as illustrated geometrically. In (e), the self-consistency equations for the normal and anomalous Green's functions within Eliashberg approximation are represented diagrammatically. Here the labels k, s take into account the weak-pairing approximation (6.21).*

diagrams with two or more phonon lines contain vertex corrections and are thus suppressed by a factor of $\lambda\sqrt{m/M}$ as compared to the first two diagrams.

Instead of reproducing the details of the analysis of Migdal [366], we present an intuitive argument that strongly resembles the motivation of the SCBA well-known from the analysis of impurity scattering (see Chap. 1.4.1) and shows that the factor $\sqrt{m/M}$ results from phase-space restrictions due to the mismatch of the typical phonon (ω_D) and electron (E_F) energies: Let us compare the first two diagrams in Fig. 6.2(d) which are of the same order in the electron-phonon coupling. Focusing for simplicity on a quadratic spectrum, setting the incoming momentum $\boldsymbol{k}$ on the Fermi surface and recalling that the maximal energy transfer due to electron-phonon scattering is set by the Debye frequency ω_D, we see that, in case of the first diagram, both internal momenta $\boldsymbol{k}_1$ and $\boldsymbol{k}_2$ are free to run independently over the shell $k_F - \Delta k < |\boldsymbol{k}_j| < k_F + \Delta k$. Here $\Delta k \propto \omega_D/v_F$ is the maximal momentum transfer due to phonons with v_F and k_F denoting the Fermi velocity and momentum, respectively. As for the second diagram, which contains a vertex correction, the momenta have to be additionally fine-tuned such that also $\boldsymbol{k}_3 = \boldsymbol{k} + \boldsymbol{k}_2 - \boldsymbol{k}_1$ belongs to a shell around the Fermi surface with thickness $2\Delta k$. It is easy to see that exactly the same applies for the analogous diagram containing an anomalous vertex correction. Consequently, for fixed $\boldsymbol{k}_2$, this constrains $\boldsymbol{k}_1$ to be part of the green intersection area of the two shells shown in Fig. 6.2(d). This implies that, for $d > 1$, the two diagrams with vertex corrections are suppressed by a phase space factor of $\Delta k/k_F$ relative to the first diagram in Fig. 6.2(d). As $\Delta k/k_F \propto \omega_D/E_F \propto \sqrt{m/M}$, we recover Migdal's result [366].

Typically $\sqrt{m/M} \simeq 10^{-2}$ and, hence, neglecting all diagrams with vertex corrections, as is done in Eliashberg theory [71, 72], is still expected to be valid in the strong-coupling regime $\lambda \simeq 1$ and, indeed, successfully describes many superconductors with strong electron-phonon coupling [369]. The resulting self-consistency equations both for the normal as well as for the anomalous propagator are represented diagrammatically in Fig. 6.2(e). In the following, we will study these self-consistency equations for noncentrosymmetric superconductors in order to gain information about the symmetry and topological properties of possible superconducting states.

Weak-pairing limit. As anticipated by the notation introduced in Sec. 6.1.1, it will be most convenient to perform this analysis in the eigenbasis of the normal state Hamiltonian $h_{\boldsymbol{k}}$. We thus introduce the Nambu Green's function as

$$\mathcal{G}_{ss'}(i\omega_n, \boldsymbol{k}) := -\frac{1}{\beta}\begin{pmatrix} \langle f_{ks}\bar{f}_{ks'}\rangle & \langle f_{ks}f_{-ks'_{\mathrm{K}}}\rangle \\ \langle \bar{f}_{-ks_{\mathrm{K}}}\bar{f}_{ks'}\rangle & \langle \bar{f}_{-ks_{\mathrm{K}}}f_{-ks'_{\mathrm{K}}}\rangle \end{pmatrix}. \tag{6.20}$$

According to this ansatz, all Cooper pairs carry zero total momentum excluding the formation of translation-symmetry breaking superconductivity, e.g., FFLO [105, 106] states.

In addition, we assume that, for determining the superconducting properties, the Green's function can be approximated to be diagonal in Fermi-surface space,

$$\mathcal{G}_{ss'}(i\omega_n, \boldsymbol{k}) = \delta_{s,s'}\mathcal{G}_s(i\omega_n, \boldsymbol{k}), \tag{6.21}$$

which is the Green's function description of the weak-pairing approximation introduced in Chap. 4.2 on the mean-field level. As already discussed in detail in Chaps. 4.2 and 4.5, this approximation is valid as long as the transition temperature T_c is smaller than the energetic splitting E_{so} of the Fermi surfaces. In short, the reason is that the matrix elements of the Green's function (6.20) with $s \neq s'$ couple single-particle states with energies differing by E_{so}. Loosely speaking, in the calculation of the leading

superconducting instability this will cut off the Cooper logarithms associated with these processes unless the integrals are first cut off by temperature. Therefore, the weak-pairing approximation is expected to be applicable for determining the superconducting properties as long as $E_{\mathrm{so}} \gtrsim T_c$.

On the level of the Eliashberg equations, the weak-pairing approximation means that the incoming and outgoing Fermi-surface index s is identical as already indicated in Fig. 6.2(e). Consequently, only the forward, Fig. 6.2(a), and the Cooper, Fig. 6.2(b), scattering amplitudes of the phonon-mediated interaction enter. We thus see how the presence of a strong spin splitting of the Fermi surfaces leads to more universal behavior as compared to centrosymmetric systems where additional index combinations $\{s_j\}$ of the electron-electron interaction (6.9) would be relevant in the self-consistency equations.

To write down the Eliashberg equations in algebraic form, we parameterize the Green's function according to

$$\mathcal{G}_s^{-1}(k) = i\omega_n Z_s(k)\tau_0 - \widetilde{\epsilon}_s(k)\tau_3 - \begin{pmatrix} 0 & \Phi_s(k) \\ \overline{\Phi}_s(k) & 0 \end{pmatrix} \tag{6.22}$$

with quasiparticle weight $Z_s(k)$, $\widetilde{\epsilon}_s(k) = \epsilon_{\boldsymbol{k}s} + \delta\epsilon_s(k)$, where $\delta\epsilon_s(k)$ is the band renormalization, and anomalous self-energies $\Phi_s(k)$ and $\overline{\Phi}_s(i\omega_n, \boldsymbol{k}) = \Phi_s^*(-i\omega_n, \boldsymbol{k})$. These quantities, which uniquely determine $\mathcal{G}$, follow from the self-consistency equations

$$Z_s(k) = 1 + \frac{2}{i\omega_n}\sum_{s'}\int_{k'} \mathcal{V}_{ss'}(k;k')\frac{i\omega_{n'} Z_{s'}(k')}{\mathcal{D}_{s'}(k')}, \tag{6.23a}$$

$$\widetilde{\Phi}_s(k) = 2\sum_{s'}\int_{k'} \mathcal{V}_{ss'}(k;k')\frac{\widetilde{\Phi}_{s'}(k')}{\mathcal{D}_{s'}(k')}, \tag{6.23b}$$

$$\delta\epsilon_s(k) = -2\sum_{s'}\int_{k'} \mathcal{V}_{ss'}(k;k')\frac{\widetilde{\epsilon}_{s'}(k')}{\mathcal{D}_{s'}(k')}, \tag{6.23c}$$

where we have introduced

$$\mathcal{D}_s(k) = \left[i\omega_n Z_s(k)\right]^2 - \left[\widetilde{\epsilon}_s^2(k) + \overline{\Phi}_s(k)\Phi_s(k)\right] \tag{6.24}$$

for notational convenience. Here Eqs. (6.19a) and (6.19b) have been taken into account to write the expressions in more compact form. The additional factor of 2 on the right-hand sides of Eq. (6.23) (as compared to the more frequently encountered form of the Eliashberg equations for spinfull fermions) arises since, in the band basis, the theory looks as if we were considering spinless particles making more contractions of the interaction vertex possible. The time-reversal phases $\varphi_{\boldsymbol{k}}^s$ of the Cooper amplitude in Eq. (6.16) that have been absorbed by defining $\widetilde{\Phi}_s(k) := \Phi_s(k)e^{i\varphi_{\boldsymbol{k}}^s}$ are reminiscent of the fact that we are considering not truly spinless particles, but spin-1/2 particles with singly-degenerate bands.

Here, we will focus on the vicinity of the critical temperature of the superconducting transition and, hence, linearize the Eliashberg equations (6.23) in Φ. To proceed further, let us rewrite the momentum summation as an angular integration over the Fermi surfaces and an energy integration (momentum perpendicular to the Fermi surface) subject to an energetic cutoff Λ (of order of ω_D). More explicitly, we replace

$$\sum_s \int_k \cdots \to \beta^{-1}\sum_{\omega_n}\sum_s \int_{-\Lambda}^{\Lambda} \mathrm{d}\epsilon \int_s \mathrm{d}\Omega\, \rho_s(\Omega)\ldots, \tag{6.25}$$

where $\rho_s(\Omega) > 0$ denotes the angle-resolved density of states that is taken to be independent of ϵ. The dimensionality of $\int_s \mathrm{d}\Omega$ is set by the dimensionality of the Fermi surface s. For the general purposes of this analysis, we do not have to specify any parameterization, we will, as illustrated in Fig. 6.1, only apply the convention that the Kramers partner of the state (s, Ω) is given by $(s_\mathrm{K}, \Omega_\mathrm{K})$.

In addition, we take the interaction $\mathcal{V}$, $\delta\epsilon$ and $\widetilde{\Phi}$ as well as the quasiparticle residue Z to be only weakly dependent on the momentum perpendicular to the Fermi surface and set

$$\begin{aligned} \mathcal{V}_{ss'}(i\omega_n, \boldsymbol{k}; i\omega_{n'}, \boldsymbol{k}') &\simeq \mathcal{V}_{ss'}(i\omega_n, \Omega; i\omega_{n'}, \Omega'), \\ \widetilde{\Phi}_s(i\omega_n, \boldsymbol{k}) &\simeq \widetilde{\Phi}_s(i\omega_n, \Omega) \end{aligned} \tag{6.26}$$

and similarly for $\delta\epsilon$ and Z. This is justified as the dependence of $\mathcal{V}$ on the momentum perpendicular to the Fermi surface is determined by the momentum dependence of the phononic spectrum $\omega_{\boldsymbol{q}l}$. It is, hence, by a factor of v_s/v_F, where v_s denotes the sound velocity, slower than the dependence of the quasiparticle spectrum ϵ. From Eq. (6.23), we see that the same then automatically holds for Z, $\widetilde{\Phi}$ and $\delta\epsilon$. As $v_s/v_F \propto \omega_D/E_F \propto \sqrt{m/M}$, Eq. (6.26) is valid in the adiabatic limit $m/M \ll 1$.

With these approximations, the Eliashberg equations (6.23) become (for $\Lambda \to \infty$)

$$Z_s(i\omega_n, \Omega) = 1 - \frac{2}{2n+1} \sum_{n'} \sum_{s'} \int_{s'} \mathrm{d}\Omega' \rho_{s'}(\Omega') \mathcal{V}_{ss'}(i\omega_n, \Omega; i\omega_{n'}, \Omega') \operatorname{sign}(2n'+1), \tag{6.27a}$$

$$\delta_s(i\omega_n, \Omega) = \sum_{n'} \sum_{s'} \int_{s'} \mathrm{d}\Omega' v_{ss'}(i\omega_n, \Omega; i\omega_{n'}, \Omega') \delta_{s'}(i\omega_{n'}, \Omega'), \tag{6.27b}$$

$$\delta\epsilon_s(k) = 0, \tag{6.27c}$$

i.e., there is no Fermi velocity correction. In Eq. (6.27), the normalized anomalous self-energy

$$\delta_s(i\omega_n, \Omega) := \Theta_{s,n}(\Omega)\, \widetilde{\Phi}_s(i\omega_n, \Omega) \tag{6.28}$$

with[2]

$$\Theta_{s,n}(\Omega) = \frac{\sqrt{\rho_s(\Omega)}}{\sqrt{|2n+1|}\sqrt{|Z_s(i\omega_n, \Omega)|}} \tag{6.29}$$

has been introduced in order to render the kernel

$$v_{ss'}(i\omega_n, \Omega; i\omega_{n'}, \Omega') := -2\Theta_{s,n}(\Omega) \mathcal{V}_{ss'}(i\omega_n, \Omega; i\omega_{n'}, \Omega') \Theta_{s',n'}(\Omega') \tag{6.30}$$

of the gap equation (6.27b) symmetric.

For completeness, we mention that Eq. (6.27b) assumes the form of the linearized BCS mean-field equations upon linearizing in $\mathcal{V}$ (tantamount to replacing $Z \to 1$) and neglecting the frequency dependence of $\mathcal{V}$ which then automatically renders $\widetilde{\Phi}$ independent of frequency. The weak-pairing BCS order parameter $\widetilde{\Delta}$, the central object in the analysis of Chap. 4.2, is then given by

$$\widetilde{\Delta}_s(\boldsymbol{k}) = \widetilde{\Phi}_s(i\omega_n, \boldsymbol{k}) \tag{6.31}$$

and the Cooper logarithm comes from the remaining frequency summation.

[2] In the expression for $\Theta_{s,n}(\Omega)$, we have, for simplicity, already taken into account that Z is real. In general, $|Z_s(i\omega_n, \Omega)|$ has to be replaced by $Z_s(i\omega_n, \Omega) \operatorname{sign}(\mathrm{Re}(Z_s(i\omega_n, \Omega)))$ such that δ and v will only be generically real if $Z \in \mathbb{R}$.

6.1.3 Symmetry and topology of the resulting condensate

We will next discuss the general implications of the linearized Eliashberg equations (6.27) for the unitary as well as antiunitary symmetries of the condensate and then analyze its topological properties.

As a first step, note that, after linearizing in $\widetilde{\Phi}$, Eq. (6.27a) explicitly determines $Z_s(i\omega_n, \Omega)$, i.e., it follows without solving a self-consistency equation. We directly see that $Z_s(i\omega_n, \Omega) \in \mathbb{R}$. In addition, it holds $Z_s(k) = Z_{s_\mathrm{K}}(-k)$ which is a consequence of its definition but can, alternatively, be explicitly seen in Eq. (6.27a) using Eq. (6.19b). Together with $Z_s(i\omega_n, \Omega) = Z_s^*(-i\omega_n, \Omega)$ following from Eq. (6.19c), we can summarize

$$Z_s(i\omega_n, \Omega) = Z_s(-i\omega_n, \Omega) = Z_{s_\mathrm{K}}(i\omega_n, \Omega_\mathrm{K}) \in \mathbb{R}. \tag{6.32}$$

The properties of the superconducting order parameter follow from the second Eliashberg equation (6.27b). As opposed to mean-field theory, the temperature dependence of Eq. (6.27b) is more complicated and hidden in the kernel v defined in Eq. (6.30). However, it can be shown (see Appendix E.2) that the leading superconducting instability is, as in the mean-field case, determined by the largest eigenvalue of the (symmetric and real) matrix v while the order parameter $\delta_s(i\omega_n, \Omega)$ belongs to the corresponding eigenspace.

Recalling Eq. (6.17), the kernel v only has positive elements (except for the fixed-point manifolds of symmetry operations), such that the Perron-Frobenius theorem [372–374] can be used. It states that the largest eigenvalue of a square matrix with strictly positive entries is positive and nondegenerate with associated eigenvector that can be chosen to have purely positive components as well. More generally, it holds for any irreducible[3] nonnegative matrix and, thus, still applies if we take into account the isolated zeros of v that can be imposed by symmetry (see Fig. 6.1). Therefore, the leading instability is characterized by $\delta_s(i\omega_n, \Omega) > 0$ and, hence, $\widetilde{\Phi}_s(i\omega_n, \Omega) > 0$, i.e., the superconductor is fully gapped with the sign of the gap being the same on all Fermi surfaces. Also as a function of Matsubara frequency, the anomalous self-energy does not change sign. Due to the absence of any sign change, the superconducting state cannot break any point-group symmetry and must, therefore, transform under the trivial representation of the point group. Recalling that the weak-pairing mean-field order parameter $\widetilde{\Delta}_s(\boldsymbol{k})$ transforms as a superposition of scalar basis functions of an irreducible representation (see Eq. (4.38)), this statement follows intuitively in case of one-dimensional representations. For a general proof, we refer to Appendix E.3.

Since $v_{ss'}(i\omega_n, \Omega; i\omega_{n'}, \Omega')$ is invariant under a simultaneous sign change of ω_n and $\omega_{n'}$, which follows from and Eqs. (6.19c) and (6.32), we know that $\delta_s(-i\omega_n, \Omega)$ is also a solution of Eq. (6.27b). Due to the absence of degeneracies, we conclude that $\delta_s(i\omega_n, \Omega) = \pm\delta_s(-i\omega_n, \Omega)$, i.e., we obtain either an even- or an odd-frequency pairing state. As $\delta_s(i\omega_n, \Omega) > 0$ odd-frequency pairing can be excluded. In combination with $\widetilde{\Phi}_{s_\mathrm{K}}(-k) = \widetilde{\Phi}_s(k)$ following from Fermi-Dirac statistics and the property (6.14) of the time-reversal phases, one has

$$\widetilde{\Phi}_s(i\omega_n, \Omega) = \widetilde{\Phi}_s(-i\omega_n, \Omega) = \widetilde{\Phi}_{s_\mathrm{K}}(i\omega_n, \Omega_\mathrm{K}) > 0. \tag{6.33}$$

Antiunitary symmetries. Let us now use the results of the previous analysis, Eqs. (6.32) and (6.33),

[3] A matrix M is *reducible* if there is a permutation matrix P such that $PMP^T = \begin{pmatrix} X & Y \\ 0 & Z \end{pmatrix}$, with X and Z both being square. Otherwise M is said to be *irreducible*. As is well-known from graph theory, a matrix is irreducible if and only if its adjacency graph is strongly connected [374]. From this it readily follows that $\mathcal{V}$ is irreducible: As is clear by inspection of Fig. 6.1, we can reach any (fixed) point from any other (fixed) point via an intermediate generic point on the Fermi surface.

to investigate the antiunitary symmetries of the condensate. As we do not want to restrict ourselves to the mean-field level here, we have to discuss these symmetries on the level of Green's functions.

To begin with PHS, it holds (we refer to Appendix E.1.2 for more details on the derivation of this and Eq. (6.35) below)

$$\Xi \mathcal{G}_{s_\mathrm{K}}(i\omega_n, -\boldsymbol{k})\Xi^{-1} = -\mathcal{G}_s(i\omega_n, \boldsymbol{k}), \quad \Xi = \tau_1 \mathcal{K}, \tag{6.34}$$

which is just a consequence of the inherent redundancy of the Nambu Green's function in Eq. (6.20). Therefore, the condensate satisfies this symmetry by design.

TRS is a much more interesting physical property of a superconductor in the sense that it can be spontaneously broken at the phase transition. Despite being relatively rare, there are several systems with strong experimental indications [47–49, 51, 53–56] of TRS-breaking superconductivity as we have seen in Chap. 1.3. Extending our mean-field analysis of TRS in the weak-pairing description in Chap. 4.2 to the level of Green's functions, the TRS constraint now reads

$$\widetilde{\Theta}_{\boldsymbol{k}s}\mathcal{G}_{s_\mathrm{K}}(-k)\widetilde{\Theta}_{\boldsymbol{k}s}^{-1} = \mathcal{G}_s(k), \quad \widetilde{\Theta}_{\boldsymbol{k}s} = \tau_3 e^{-i\varphi_{\boldsymbol{k}}^s \tau_3}\mathcal{K}, \tag{6.35}$$

when transformed into the eigenbasis according to Eq. (6.8). The phases $\varphi_{\boldsymbol{k}}^s$ enter because of the relation (6.13) between the wavefunctions of Kramers partners. Note that the expression for the time-reversal operator stated above yields $\widetilde{\Theta}_{\boldsymbol{k}s}^2 = \mathbb{1}$ which, at first sight, seems to disagree with $\mathcal{G}_s$ being a Green's function of spin-1/2 fermions. This can be reconciled by noting that the full time-reversal operator $\widetilde{\Theta}_{\boldsymbol{k}s}\mathcal{I}$ that also includes the inversion $\mathcal{I}$ of momentum[4] indeed satisfies $(\widetilde{\Theta}_{\boldsymbol{k}s}\mathcal{I})^2 = \widetilde{\Theta}_{\boldsymbol{k}s}\widetilde{\Theta}_{-\boldsymbol{k}s_\mathrm{K}} = -\mathbb{1}$ as a consequence of Eq. (6.14). Note that this subtlety usually does not play any role as the time-reversal operator in momentum space in many cases (e.g. in the microscopic basis as in Eq. (4.7)) does not depend on momentum. It shows once again that the property (6.14) of the phases $\varphi_{\boldsymbol{k}}^s$ carries the information that the nondegenerate bands of the system microscopically arise from spin-1/2 fermions.

In order to compare our Green's function approach with the mean-field description used in Chap. 4, which will be particularly useful when discussing the topological properties below, let us consider the generic superconducting mean-field Hamiltonian

$$\hat{H}_\mathrm{MF} = \sum_{\boldsymbol{k}} \hat{c}_{\boldsymbol{k}}^\dagger h_{\boldsymbol{k}} \hat{c}_{\boldsymbol{k}} + \frac{1}{2}\sum_{\boldsymbol{k}} \left(\hat{c}_{\boldsymbol{k}}^\dagger \Delta(\boldsymbol{k}) \left(\hat{c}_{-\boldsymbol{k}}^\dagger\right)^T + \mathrm{H.c.} \right). \tag{6.36}$$

Performing the transformation into the band basis according to Eq. (4.23), we get, within the weak-pairing approximation, $\hat{H}_\mathrm{MF} = \frac{1}{2}\sum_{\boldsymbol{k}} \hat{\Psi}_{\boldsymbol{k}s}^\dagger h_{\boldsymbol{k}s}^\mathrm{BdG} \hat{\Psi}_{\boldsymbol{k}s}$ with Nambu spinor $\hat{\Psi}_{\boldsymbol{k}s}^\dagger = \begin{pmatrix} \hat{f}_{\boldsymbol{k}s}^\dagger & \hat{f}_{-\boldsymbol{k}s_\mathrm{K}} \end{pmatrix}$ and BdG Hamiltonian

$$h_{\boldsymbol{k}s}^\mathrm{BdG} = \begin{pmatrix} \epsilon_{\boldsymbol{k}s} & \widetilde{\Delta}_s(\boldsymbol{k}) e^{-i\varphi_{\boldsymbol{k}}^s} \\ \widetilde{\Delta}_s^*(\boldsymbol{k}) e^{i\varphi_{\boldsymbol{k}}^s} & -\epsilon_{\boldsymbol{k}s} \end{pmatrix}. \tag{6.37}$$

Here, exactly as in Eq. (6.31), $\widetilde{\Delta}_s(\boldsymbol{k}) = \langle \psi_{\boldsymbol{k}s} | \Delta(\boldsymbol{k}) T^\dagger | \psi_{\boldsymbol{k}s} \rangle$ are the Fermi-surface-diagonal matrix elements of the order parameter which are directly related to the topology of the superconductor as we have seen in Chap. 2.2.3.

Demanding that Eq. (6.36) be time-reversal symmetric, $\hat{\Theta}\hat{H}_\mathrm{MF}\hat{\Theta}^{-1} = \hat{H}_\mathrm{MF}$ with $\hat{\Theta}$ as defined in Eq. (4.7), one finds that TRS is equivalent to $\widetilde{\Delta}_s(\boldsymbol{k}) \in \mathbb{R}$ (cf. Eq. (4.39)). Comparison with Eq. (6.37)

[4] Formally defined by $\left(\mathcal{I}y\right)_{\boldsymbol{k}s} = y_{-\boldsymbol{k}s_\mathrm{K}}$ when acting on a function $y_{\boldsymbol{k}s}$.

shows that TRS on the level of the BdG Hamiltonian reads $\widetilde{\Theta}_{\boldsymbol{k}s} h^{\mathrm{BdG}}_{-\boldsymbol{k}s_{\mathrm{K}}} \widetilde{\Theta}^{-1}_{\boldsymbol{k}s} = h^{\mathrm{BdG}}_{\boldsymbol{k}s}$ which is just a special case of Eq. (6.35) restricted to the mean-field level where

$$\mathcal{G}_s(i\omega_n, \boldsymbol{k}) = \left(i\omega_n - h^{\mathrm{BdG}}_{\boldsymbol{k}s}\right)^{-1}. \tag{6.38}$$

The relation (6.38) between the mean-field Green's function $\mathcal{G}$ and the weak-pairing representation of the general multiband mean-field Hamiltonian (6.36) will be relevant below when discussing topological properties of the superconducting phase beyond mean-field.

It is straightforward to check that Eq. (6.35) is satisfied as a consequence of $Z_s(k)$ and $\widetilde{\Phi}_s(k)$ being real valued and invariant under in $(s,k) \to (s_{\mathrm{K}}, -k)$ (cf. Eqs. (6.32) and (6.33)) together with $\epsilon_{\boldsymbol{k}s} = \epsilon_{-\boldsymbol{k}s_{\mathrm{K}}}$ resulting from the TRS of the high-temperature phase. Therefore, no spontaneous TRS breaking is possible in the weak-pairing limit if superconductivity is due to electron-phonon coupling.

Topological properties. The analysis above shows that the resulting system is invariant both under charge conjugation Ξ with $\Xi^2 = \mathbb{1}$ as well as under time-reversal $\widetilde{\Theta}_{\boldsymbol{k}s}\mathcal{I}$ satisfying $(\widetilde{\Theta}_{\boldsymbol{k}s}\mathcal{I})^2 = -\mathbb{1}$ and, thus, belongs to class DIII [249, 251]. As we have seen in Chap. 2.1.2, the superconductor is classified by a $\mathbb{Z}_2$ in 1D and 2D and by a $\mathbb{Z}$ topological invariant in 3D. To calculate these invariants, we will use the topological Hamiltonian approach (see Chap. 2.4.1 for an introduction to this method): For a system with a finite gap, the topological properties of the many-body system described by the full Green's function $\mathcal{G}$ are calculated from the effective mean-field Green's function

$$\mathcal{G}^t_s(i\omega_n, \boldsymbol{k}) = \left(i\omega_n - h^t_{\boldsymbol{k}s}\right)^{-1} \tag{6.39}$$

where the "topological Hamiltonian" is given by

$$h^t_{\boldsymbol{k}s} := -\mathcal{G}_s^{-1}(i\omega = 0, \boldsymbol{k}). \tag{6.40}$$

For the calculation of the topological invariant, we have to go to zero temperature. In Eq. (6.40), and similarly in the following expressions, $i\omega = 0$ has to be understood as the limit $T \to 0$ of the function evaluated at the Matsubara frequency $\omega_0 = \pi/\beta$ (or equally well $\omega_{-1} = -\pi/\beta$). For this purpose, we assume that no additional topological phase transition occurs in the temperature range between the onset of superconductivity and $T = 0$. In more mathematical terms, it means that, upon lowering T to zero, the structure of the solution of the (nonlinear) Eliashberg equations does not change in a way that affects the topological invariant. This is a quite natural assumption and, on top of that, can be directly verified experimentally as a topological phase transition requires an additional closing of the gap between T_c and $T = 0$. If it holds, the topological properties of the superconducting phase can be inferred from the solution of the linear Eliashberg equations (6.27).

Due to $\widetilde{\Phi}_s(0, \Omega) > 0$, the superconductor is fully gapped and the Green's function $\mathcal{G}_s(i\omega, \boldsymbol{k})$ must be an analytic function of ω in a finite domain containing the imaginary axis. Consequently, $i\omega Z_s(i\omega, \boldsymbol{k})\big|_{i\omega=0} = 0$ as $i\omega Z_s(i\omega, \boldsymbol{k})$ is an odd function of ω (cf. Eq. (6.32)). Therefore, the topological Hamiltonian becomes

$$h^t_{\boldsymbol{k}s} = \begin{pmatrix} \epsilon_{\boldsymbol{k}s} & \widetilde{\Phi}_s(i\omega = 0, \boldsymbol{k}) e^{-i\varphi^s_{\boldsymbol{k}}} \\ \widetilde{\Phi}_s(i\omega = 0, \boldsymbol{k}) e^{i\varphi^s_{\boldsymbol{k}}} & -\epsilon_{\boldsymbol{k}s} \end{pmatrix}, \tag{6.41}$$

which is manifestly Hermitian. Furthermore, it is readily checked to be particle-hole and time-reversal symmetric with Ξ and $\widetilde{\Theta}_{\boldsymbol{k}s}$ as given in Eqs. (6.34) and (6.35).

The resulting topological properties are most easily inferred by reading the approximation of the general mean-field Hamiltonian in Eq. (6.36) to the weak-pairing description (6.37) in reverse: Comparison of $\mathcal{G}^t$ in Eq. (6.39) and Eq. (6.38) shows that $h^t_{\boldsymbol{k}s}$ can be seen as the weak-pairing approximation of some mean-field Hamiltonian of the form of Eq. (6.36) with the property

$$\widetilde{\Delta}_s(\boldsymbol{k}) \equiv \langle \psi_{\boldsymbol{k}s} | \Delta(\boldsymbol{k}) T^\dagger | \psi_{\boldsymbol{k}s} \rangle = \widetilde{\Phi}_s(i\omega = 0, \boldsymbol{k}). \tag{6.42}$$

We emphasize that, although Eq. (6.42) looks deceptively similar to the BCS approximation (6.31), the topological Hamiltonian approach we use is equivalent [309, 310] to the expressions for the topological invariants involving frequency integrals of the full Green's functions probing all frequencies ω_n of the self-energy.

Recalling Chap. 2.2.3, the topological class-DIII invariant of a mean-field Hamiltonian of the form of Eq. (6.36) is, within the weak-pairing limit, determined by the sign of the order-parameter matrix elements $\widetilde{\Delta}_s(\boldsymbol{k})$ on the different Fermi surfaces of the system. More explicitly, in the 3D case, it holds

$$\nu_{\mathbb{Z}} = \frac{1}{2} \sum_s \operatorname{sign}\left(\widetilde{\Delta}_s(\boldsymbol{k}_s)\right) C_{1s}, \tag{6.43}$$

where $\boldsymbol{k}_s$ is an arbitrary point on and C_{1s} denotes the first Chern number (2.18) of Fermi surface s [280]. Due to Eqs. (6.33) and (6.42), we find

$$\nu_{\mathbb{Z}} = \frac{1}{2} \sum_s C_{1s} = 0, \tag{6.44}$$

i.e., a topologically trivial superconductor. In the second equality of Eq. (6.44), we have used that the total Chern number of all Fermi surfaces vanishes [280].

In lower dimensions, the expression (6.43) for the topological invariant assumes the form

$$\nu_{\mathbb{Z}_2} = \prod_s \left[\operatorname{sign}\left(\widetilde{\Delta}_s(\boldsymbol{k}_s)\right) \right]^{m_s} \tag{6.45}$$

as readily follows by means of dimensional reduction [280]. In Eq. (6.45), m_s denotes the number of TRIM (green dots in Fig. 6.1(a)) enclosed by Fermi surface s in case of a 2D system, whereas $m_s = 1$ for a 1D superconductor. Again, we find, in both dimensions, a trivial superconductor ($\nu_{\mathbb{Z}_2} = 1$) resulting from $\operatorname{sign}(\widetilde{\Delta}_s(\boldsymbol{k}_s)) = 1$.

Taken together, superconductivity in noncentrosymmetric systems that arises due to electron-phonon coupling alone can neither break TRS nor any point symmetry of the system and must necessarily be topologically trivial. This has been derived under very general assumptions: The inversion-symmetry breaking is assumed to be sufficiently strong for the weak-pairing approximation to be valid ($E_{\mathrm{so}} \gtrsim T_c$). We have used the Eliashberg approach which is controlled in the limit of adiabatic ionic motion ($m/M \ll 1$) and, in principle, allows for arbitrarily strong interactions $\mathcal{V}$. Also the analysis of topological invariants is performed beyond the mean-field level. Thus, also interaction effects without static mean-field counterpart are captured (see Chap. 2.4). This is important as dynamical fluctuations can indeed change the topological properties of the system as has been demonstrated, e.g., in Ref. [308].

Remarks. Note that these conclusions are not altered when electronic renormalization effects of the phononic dispersion are taken into account since $\omega_{\boldsymbol{q}l}$ in Eq. (6.6) can already be regarded as the fully

renormalized spectrum. In Sec. 6.2 below, we will show, using exact relations derived from the spectral representation, that the same holds even if frequency-dependent corrections to the phonon propagator are considered.

Furthermore, it is instructive to compare this result valid for noncentrosymmetric systems with the situation where inversion symmetry is preserved. In this case, all Fermi surfaces are doubly degenerate and the superconducting state can only be either singlet or triplet. In Ref. [282], it has been shown that in 2D and, for simplicity, focusing on a single Fermi surface enclosing the Γ point, any fully gapped, time-reversal symmetric odd parity state will be topological. In our case, there are two main differences: Firstly, the absence of inversion symmetry generally mixes singlet and triplet components. Secondly, for a Fermi surface around the Γ point, breaking point symmetries necessarily implies the presence of nodes. This is most easily seen by noting that the absence of TRS breaking forces $\widetilde{\Delta}_s$ to be real such that the spectrum $\pm\sqrt{\epsilon_{\boldsymbol{k}s}^2 + \widetilde{\Delta}_s^2(\boldsymbol{k})}$ of the BdG Hamiltonian (6.37) must have nodes when $\widetilde{\Delta}_s(\boldsymbol{k})$ changes sign on the Fermi surface. This is in stark contrast to centrosymmetric systems where the gap at momentum $\boldsymbol{k}$ is given by $|\boldsymbol{d}_{\boldsymbol{k}}|$ for a time-reversal symmetric triplet state [50] and, hence, is fully gapped unless the $\boldsymbol{d}$ vector (cf. Eq. (1.17) for its definition) vanishes on the Fermi surface.

An important question that arises is how a superconductor that is predominantly induced by electron-phonon coupling can end up being topological.

Firstly, one very natural mechanism that can lead to topologically nontrivial properties is finite residual Coulomb repulsion. As discussed in Chap. 1.1.2, RG corrections at energies between the Fermi energy and the Debye frequency make it small in the sense that its dimensionless coupling constant, the Coulomb pseudopotential μ^*, is typically of order 0.1 [97–100]. Nonetheless, it can induce to sign changes of the gap function as has been demonstrated, e.g., in Refs. [375–377]. In particular, it is expected that these sign changes occur *between* different Fermi surfaces if the electron-phonon interaction has the following favorable structure: Again focusing for simplicity on a model with two singly-degenerate Fermi surfaces enclosing the Γ point, the topologically trivial superconducting state with $\widetilde{\Delta}_s$ having the same sign on both Fermi surfaces (s^{++}) will be (nearly) degenerate with the nontrivial s^{+-} state (sign changes between the two Fermi surfaces) if the interband Cooper scattering is negligibly small. In this case, already a small residual repulsion can favor the topological s^{+-} state. The analogous discussion in centrosymmetric superconductors can be found in Ref. [89], where it is shown using mean-field theory that a topological [282] odd-parity state can be induced by residual repulsions in an otherwise trivial electron-phonon superconductor.

Secondly, one might ask whether disorder can induce a transition from an electron-phonon driven trivial superconductor to a topologically nontrivial state. In Chap. 7.2, we will show that this is indeed possible in case of magnetic scattering. Although TRS is locally broken for a given disorder realization, the edge modes of the resulting topological superconductor of class DIII can still be protected due to unitary symmetries.

6.2 Unconventional mechanism

In the second part of the chapter, we will extend the analysis to superconductors of unconventional origin, i.e., systems where superconductivity is not based on electron-phonon interaction but arises from a purely electronic mechanism. In Sec. 6.2.1, we will first introduce the effective low-energy approach we use for describing unconventional pairing and then study the resulting superconducting properties using Eliashberg theory (Sec. 6.2.2). An approximate symmetry expected to be valid as long as the spin-orbit splitting E_{so} is much smaller than the bandwidth Λ_t will be derived in Sec. 6.2.3 leading to

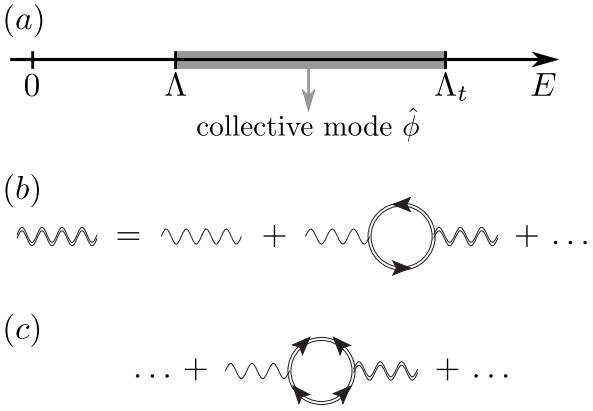

Figure 6.3: ***Energy scales and bosonic propagator.*** *Part (a) illustrates the energy scales of the effective low-energy approach we use for describing unconventional pairing. In (b) and (c), we show the self-energy corrections of the bosonic propagator due to normal conducting electrons and the superconducting order parameter, respectively. Note that the latter type of corrections are at least of quadratic order in the anomalous self-energy* Φ*.*

strong constraints on the possible pairing states (see Sec. 6.2.4). Sec. 6.2.5 is devoted to the analysis of more general models of unconventional pairing.

6.2.1 Effective fluctuation approach

Not only the electron-phonon coupling but also the Coulomb interaction can give rise to superconductivity. As we have seen in the explicit microscopic calculation of Chap. 5, instead of discussing the bare Coulomb interaction, i.e., defined on the energy scale of the bandwidth Λ_t, we should rather think in terms of the renormalized low-energy effective interaction for understanding the properties of the dominant instabilities in the system. Naturally, the associated RG corrections strongly depend on the microscopic details of the system such as the Fermi surface geometry. Therefore, this "microscopic" approach is definitely not suitable for the general purposes of this chapter. Instead, we will employ the following effective low-energy approach which is widely used for describing the properties of unconventional superconductors (see, e.g., Refs. [31, 32] for a detailed introduction): As mentioned, we are not interested in the behavior of the system at high energies (of the order of Λ_t), and, hence, focus only on the physics for energies smaller than some cutoff $\Lambda < \Lambda_t$. As shown schematically in Fig. 6.3(a), it is assumed that processes at energies between Λ and Λ_t drive the system close to some instability that we describe by the collective real ($\hat{\phi}^\dagger_{\boldsymbol{q}j} = \hat{\phi}_{-\boldsymbol{q}j}$) bosonic mode $\hat{\phi}_{\boldsymbol{q}j}$, $j = 1, 2, \ldots, N_B$. In case of the cuprates, these bosons embody the spin fluctuations associated with the closeness to antiferromagnetism [31, 32], whereas in case of the unconventional pairing state of LAO/STO heterostructures the competing instability is the incommensurate SDW[12] of Chap. 5.2.3. Although these bosons describe the collective fluctuations of the electrons, treating them as separate degrees of freedom just constitutes a very efficient way to separate the energy scales.

For simplicity, we will first assume that the associated order parameter is either even ($t = +$) or odd

$(t = -)$ under time-reversal, which means mathematically

$$\hat{\Theta}\hat{\phi}_{\boldsymbol{q}j}\hat{\Theta}^\dagger = t\,\hat{\phi}_{-\boldsymbol{q}j}. \tag{6.46}$$

The proximity to, e.g., (real) CDW or SDW order correspond to time-reversal even (TRE), $t = +1$, or time-reversal odd (TRO), $t = -1$, fluctuations, respectively.

Furthermore, we assume that the interaction processes at energies larger than Λ neither destroy the Fermi-liquid behavior of the fermions nor lead to TRS breaking. Consequently, the noninteracting part of the fermionic Hamiltonian is still of the form of Eq. (6.1) with $\hat{\Theta}\hat{H}_0\hat{\Theta}^\dagger = \hat{H}_0$. Assuming well-defined quasiparticles is a quite natural assumption as only processes above Λ have effectively been taken into account in the model. Note that this does not mean that the system is necessarily a Fermi liquid at all energy scales as infrared singularities can lead to non-Fermi liquid behavior *within* the effective model [31]. The fermions are coupled to the bosons via

$$\hat{H}_{\text{int}} = \sum_{\boldsymbol{k},\boldsymbol{q}} \hat{c}^\dagger_{\boldsymbol{k}+\boldsymbol{q}\alpha}\lambda^{(j)}_{\alpha\beta}\hat{c}_{\boldsymbol{k}\beta}\,\hat{\phi}_{\boldsymbol{q}j} \tag{6.47}$$

and all other residual electron-electron interactions as well as the electron-phonon coupling will be neglected, since, by assumption, the channel described by the collective mode $\hat{\phi}_{\boldsymbol{q}j}$ is dominant. In Eq. (6.47), the matrices $\{\lambda^{(j)}\}$ have to be Hermitian and satisfy

$$\Theta\lambda^{(j)}\Theta^\dagger = t\,\lambda^{(j)} \tag{6.48}$$

resulting from $\hat{\phi}$ being real and Eq. (6.46), respectively. In case of a model with only a single orbital where α just refers to the spin of the electrons, one could have $\{\lambda^{(j)}\} = \{\sigma_0\}$, $N_B = 1$, in case of $t = +$ and $\{\lambda^{(j)}\} = \{\sigma_1, \sigma_2, \sigma_3\}$, $N_B = 3$, for $t = -$. Here σ_j, $j = 0, 1, 2, 3$, denote the Pauli matrices in spin space. For simplicity of the presentation of the results, the discussion of more complex fermion-boson couplings will be postponed to Sec. 6.2.5.

Order parameter susceptibility. The dynamics of the bosons will be described by the action

$$S_{\text{col}} = \frac{1}{2}\int_q \phi_{qj}\left(\chi_0^{-1}(i\Omega_n, \boldsymbol{q})\right)_{jj'}\phi_{-qj'}, \tag{6.49}$$

where ϕ is the field variable corresponding to the operator $\hat{\phi}$ and $\chi_0(i\Omega_n, \boldsymbol{q})$ is the bare susceptibility with respect to the order parameter of the competing particle-hole instability the system is close to. The full susceptibility $\chi(i\Omega_n, \boldsymbol{q})$, renormalized by particle-hole fluctuations as shown in Fig. 6.3(b), is more important since it is experimentally accessible, e.g., via neutron scattering or nuclear magnetic resonance (NMR) relaxation rate measurements [31], and because it will enter the superconducting self-consistency equations discussed in Sec. 6.2.2 below.

Using the spectral representation, it is shown in Appendix E.1.1 that χ has to satisfy (the same holds for χ_0) the exact relations

$$\chi(i\Omega_n, \boldsymbol{q}) = \chi^T(-i\Omega_n, -\boldsymbol{q}), \tag{6.50a}$$

$$\chi(i\Omega_n, \boldsymbol{q}) = \chi^\dagger(-i\Omega_n, \boldsymbol{q}), \tag{6.50b}$$

$$\chi(i\Omega_n, \boldsymbol{q}) = \chi(-i\Omega_n, \boldsymbol{q}). \tag{6.50c}$$

The first identity is just a consequence of χ being a correlator of twice the same operator $\hat{\phi}$ evaluated at $\boldsymbol{q}$ and $-\boldsymbol{q}$, whereas the second line is based on Hermiticity, $\hat{\phi}^\dagger_{\boldsymbol{q}j} = \hat{\phi}_{-\boldsymbol{q}j}$. Finally, the third relation follows from TRS of the system.

Being Hermitian, $\chi(i\Omega_n, \boldsymbol{q})$ has real eigenvalues all of which have to be positive as required by stability: By assumption, the competing instability will not occur and, hence, the bosons have to have a finite mass.

Effective electron-electron interaction. In the following, we will proceed in a manner very similar to the analysis of the electron-phonon coupling in Sec. 6.1.1: Writing the entire model in the field integral representation and integrating out the bosons leads to an effective electron-electron interaction of the form of Eq. (6.9) with

$$V^{s_1 s_2}_{s_3 s_4}(k_1, k_2, q) = -\frac{1}{2}\boldsymbol{\Lambda}^T_{s_2 s_3}(\boldsymbol{k}_2 - \boldsymbol{q}, \boldsymbol{k}_2)\chi(q)\boldsymbol{\Lambda}_{s_1 s_4}(\boldsymbol{k}_1 + \boldsymbol{q}, \boldsymbol{k}_1), \tag{6.51}$$

where we have introduced the N_B-component vector of matrix elements

$$\boldsymbol{\Lambda}_{ss'}(\boldsymbol{k}, \boldsymbol{k}') = \psi^\dagger_{\boldsymbol{k}s}\boldsymbol{\lambda}\psi_{\boldsymbol{k}'s'} \tag{6.52}$$

in analogy to G in Eq. (6.11). Note that we use χ instead of the bare χ_0 such that the interaction vertex in Eq. (6.51) is already fully renormalized by particle-hole fluctuations. Due to Eqs. (6.13) and (6.48), TRS of the system implies

$$\boldsymbol{\Lambda}_{ss'}(\boldsymbol{k}, \boldsymbol{k}') = t\, e^{i(\varphi^{s'}_{\boldsymbol{k}'} - \varphi^{s}_{\boldsymbol{k}})} \left(\boldsymbol{\Lambda}_{s_\mathrm{K} s'_\mathrm{K}}(-\boldsymbol{k}, -\boldsymbol{k}')\right)^*, \tag{6.53}$$

which constitutes the obvious generalization of Eq. (6.15) including not only TRE (such as phonons) but also TRO fluctuations.

We have seen in Sec. 6.1.2 that, in the weak-pairing approximation, the superconducting properties are fully determined by the Cooper and the forward scattering channel shown in Fig. 6.2(a) and (b). As before, we still find that these two interaction channels are determined by the same matrix elements,

$$V^{s's'_\mathrm{K}}_{s_\mathrm{K} s}(k, -k, k' - k) = t\, e^{i(\varphi^{s}_{\boldsymbol{k}} - \varphi^{s'}_{\boldsymbol{k}'})}\mathcal{V}_{s's}(k'; k), \tag{6.54a}$$

$$\mathcal{F}_{s's}(k', k) = \mathcal{V}_{s's}(k'; k) \tag{6.54b}$$

with

$$\mathcal{V}_{s's}(k'; k) = -\frac{1}{2}\boldsymbol{\Lambda}^\dagger_{s's}(\boldsymbol{k}', \boldsymbol{k})\chi(k' - k)\boldsymbol{\Lambda}_{s's}(\boldsymbol{k}', \boldsymbol{k}). \tag{6.55}$$

To show this, TRS (6.53) and Hermiticity, $\boldsymbol{\lambda}^\dagger = \boldsymbol{\lambda}$, have been taken advantage of.

Recalling that stability forces $\chi(q)$ to be positive definite, we conclude that $\mathcal{V}_{s's} < 0$. We see that the forward scattering amplitude $\mathcal{F}$ is, exactly as in case of phonons, negative for all states on the Fermi surfaces, whereas the global sign of the Cooper channel is reversed in case of TRO fluctuations as compared to phonons (or TRE electronic fluctuations).

6.2.2 Predictions of Eliashberg theory

Let us next analyze the consequences for the possible superconducting phases. As before, we apply Eliashberg theory that is frequently used for studying superconductivity caused by collective bosonic modes other than phonons (see, e.g., Ref. [378] and references therein). As in this case, $m/M \ll 1$

will not hold in general, one expects this approach only to be applicable in the weak-coupling regime. However, in the limit of large numbers of fermion flavors (N_F), neglecting vertex corrections is also justified in the strong-coupling case: In Ref. [378], it has been shown that vertex corrections are suppressed by a factor $1/N_F$ and approach a finite value[5] in the strong coupling limit $\lambda \to \infty$ at fixed finite N_F. While there are complications with this large-N_F theory in 2D [379], some efforts have been made to develop controlled approaches for this case as well [380].

Using Hermiticity of $\boldsymbol{\lambda}$, Eqs. (6.53) and (6.50c), it is straightforward to check that the three properties (6.19) of the vertex function $\mathcal{V}$ are still satisfied. Consequently, the linearized Eliashberg equations are again of the form of Eq. (6.27) with $\mathcal{V}_{s's}(k';k)$ now given by Eq. (6.55) and an additional prefactor of t on the right-hand side of the gap equation (6.27b), i.e., v is replaced by tv. Note that the renormalized propagator χ is taken into account which, diagrammatically, corresponds to replacing the bare bosonic line in Fig. 6.2(e) by the full line (see Fig. 6.3(b)). We emphasize that, for the linearized Eliashberg equations, there are no anomalous propagators entering the full bosonic line: Any term in the bosonic self-energy involving the anomalous self-energy Φ, such as the one shown in Fig. 6.3(c), is at least of quadratic order in Φ and, hence, does not contribute. Therefore, we can safely use the TRS constraint (6.50c) near the transition without a priori knowledge about the time-reversal properties of the superconducting condensate.

Repeating the arguments presented in Sec. 6.1.3, we directly conclude that Eq. (6.32) is still valid. The kernel tv of the gap equation is symmetric (cf. Eq. (6.19a)), real and, hence, diagonalizable. As shown in Appendix E.2.2, the leading superconducting instability is again determined by its largest eigenvalue.

To begin with TRE fluctuations, $t = +$, the kernel has, exactly as $\mathcal{V}$ in Eq. (6.55), only positive components, such that the Perron-Frobenius theorem can be applied[6]. It follows that the resulting superconducting order parameter satisfies $\delta > 0$ and, thus, preserves TRS and has no sign changes, neither on a given Fermi surface nor between different Fermi surfaces. It must transform under the trivial representation of the point group. Again Eq. (6.33) is satisfied and, according to our analysis of Sec. 6.1.3, the associated state is topologically trivial – exactly as in the case of electron-phonon coupling.

For TRO fluctuations, we have $t = -$ such that δ now belongs to the eigenspace of v with the smallest eigenvalue. This has two crucial consequences. Firstly, we cannot generically exclude spontaneous TRS breaking since it is no longer guaranteed that this eigenspace is one-dimensional. Although all eigenvectors of the real matrix v can always be chosen to be real valued, the superconducting order parameter can be a complex superposition of the degenerate eigenvectors which makes TRS breaking possible. Note that, apart from accidental degeneracies which we will neglect here, these degeneracies can be enforced by symmetry if the point group of the system allows for multidimensional or complex irreducible representations as we have discussed in detail in Chap. 4.1. Secondly, the eigenvectors with minimal eigenvalue can have many sign changes which, depending on the form of the Fermi surfaces, can break any point symmetry of the system and lead to nodal points.

To proceed, we will assume that the resulting superconducting state preserves TRS and, thus, belongs to class DIII. This is not very restrictive, in particular for 2D: In Chap. 4, we have shown that spontaneous TRS breaking can only occur at a single superconducting phase transition in the weak-pairing limit if there is a threefold rotation symmetry perpendicular to the plane of the 2D system. Further-

[5] The reason is that the full bosonic propagator (see Fig. 6.3(b)) entering the vertex correction depends on λ. In the limit $\lambda \to \infty$, this cancels the prefactor λ of the vertex correction.

[6] Exactly as before, there can be symmetry-imposed zeros which, for the very same reasoning as in case of phonons, do not affect our results.

more, as we want to discuss topological properties of superconductors, we will focus on fully gapped systems, where the sign changes take place *between* different Fermi surfaces. Being fully gapped, we can apply the weak-pairing expressions in Eqs. (6.43) and (6.45) for the DIII invariant to the topological Hamiltonian (6.41).

To derive necessary conditions for the emergence of nontrivial topological invariants, we will next discuss an approximate symmetry that is expected to be applicable to many noncentrosymmetric systems. It will give rise to an asymptotic symmetry of the gap equation (6.27b) and, in turn, constrain the possible superconducting order parameters and associated topological properties.

6.2.3 Asymptotic symmetry

To deduce this approximate symmetry which relates the wavefunctions at different spin-orbit split Fermi surfaces and discuss the limit where it becomes exact, let us split the quadratic Hamiltonian (6.1) of the fermions according to

$$h_{\boldsymbol{k}} = h^{\mathrm{S}}_{\boldsymbol{k}} + h^{\mathrm{A}}_{\boldsymbol{k}} \tag{6.56}$$

with a term h^{S} that is symmetric and a term h^{A} that is antisymmetric under inversion. We first diagonalize the centrosymmetric part of the Hamiltonian. The corresponding eigenvalues $\epsilon^{\mathrm{S}}_{\boldsymbol{k}j}$, $j = 1, 2, ..., N$, must be doubly degenerate due to the combination of inversion and TRS. Note that h^{S} in general also includes SOC, which entangles the spin and orbital degrees of freedom of the electrons. Nonetheless, as is easily seen by construction (see Appendix A.1), one can still introduce a $\boldsymbol{k}$-space-local pseudospin basis $\{|\boldsymbol{k}, j, \sigma\rangle\}$ which has the same transformation properties under TRS and inversion as the physical spin. Denoting the Pauli matrices in this basis by s_i, $i = 0, 1, 2, 3$, we have

$$\langle \boldsymbol{k}, j, \sigma | h^{\mathrm{A}}_{\boldsymbol{k}} | \boldsymbol{k}, j', \sigma' \rangle = \delta_{j,j'}\, \boldsymbol{g}^{(j)}_{\boldsymbol{k}} \cdot \boldsymbol{s}_{\sigma\sigma'}, \tag{6.57}$$

where $\boldsymbol{g}^{(j)}_{\boldsymbol{k}} = -\boldsymbol{g}^{(j)}_{-\boldsymbol{k}}$ and no term $\propto s_0$ can be present as dictated by TRS and h^{A} being odd under inversion. In Eq. (6.57), we have neglected all matrix elements between different j which is justified as long as the energetic separation between the different bands $\epsilon^{\mathrm{S}}_{\boldsymbol{k}j}$ is much larger than $|\boldsymbol{g}|$. A finite $\boldsymbol{g}$ can only arise if inversion symmetry is broken. It will lift the degeneracy of the bands $\epsilon^{\mathrm{S}}_{\boldsymbol{k}j}$ as is illustrated by the 2D example shown in Fig. 6.4, where $N = 2$, $\epsilon^{\mathrm{S}}_{\boldsymbol{k}} = -t(\cos k_1 + \cos k_2) - \mu$ and the standard Rashba spin-orbit coupling, $\boldsymbol{g}_{\boldsymbol{k}} = \alpha(-\sin k_2, \sin k_1, 0)^T$, have been assumed: The doubly degenerate Fermi surface (dashed black line) associated with ϵ^{S} is split into two (solid green lines).

Due to the decomposition of $h_{\boldsymbol{k}}$ in Eq. (6.56), its eigenstates $\psi_{\boldsymbol{k}s}$ satisfying

$$\boldsymbol{g}^{(j)}_{\boldsymbol{k}} \cdot \boldsymbol{s}\ \psi_{\boldsymbol{k}s} = \nu \left| \boldsymbol{g}^{(j)}_{\boldsymbol{k}} \right| \psi_{\boldsymbol{k}s}, \quad \nu = \pm, \tag{6.58}$$

and eigenvalues $\epsilon_{\boldsymbol{k}s} = \epsilon^{\mathrm{S}}_{\boldsymbol{k}j} + \nu |\boldsymbol{g}^{(j)}_{\boldsymbol{k}}|$ can now be labeled by the composite index $s = (j, \nu)$. If $\boldsymbol{g}^{(j)}_{\boldsymbol{k}}$ varies slowly on the separation $|\boldsymbol{g}|/v_F$ of the Fermi surfaces $s = (j, \nu)$ and $s_{\mathrm{R}} \equiv (j, -\nu)$, we can approximate $\boldsymbol{g}^{(j)}_{\boldsymbol{k}} \simeq \boldsymbol{g}^{(j)}(\Omega)$ and, hence, $\psi_{\boldsymbol{k}s} \simeq \psi_{\Omega s}$ in Eq. (6.58). As $\Theta \boldsymbol{s} \Theta^\dagger = -\boldsymbol{s}$, we obtain the asymptotic symmetry

$$\psi_{\Omega s} \sim e^{i\gamma^s_\Omega} \Theta \psi_{\Omega s_{\mathrm{R}}} \tag{6.59}$$

that becomes exact in the limit $\boldsymbol{g}^{(j)} \to 0$. Here γ^s_Ω are phase factors that depend on the choice of the eigenstates. Note that this relation is structurally similar to that based on TRS in Eq. (6.13): Both are $\boldsymbol{k}$-nonlocal antiunitary symmetries. TRS connects a state at $\boldsymbol{k}$ and its Kramers partner at $-\boldsymbol{k}$,

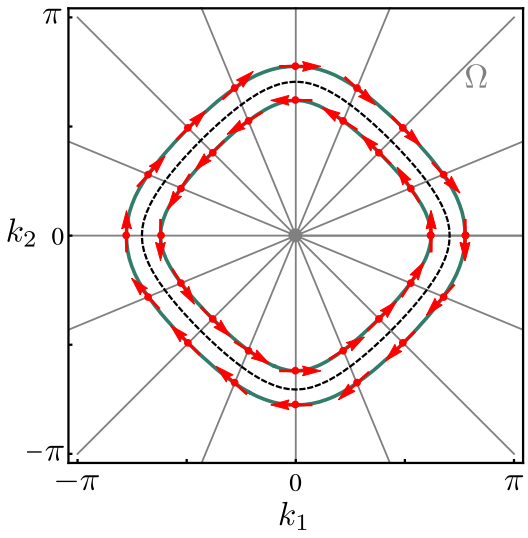

Figure 6.4: ***Approximate symmetry between Rashba partners.*** *The Fermi surfaces (green lines) and pseudospin orientation (red arrows) of the Rashba model defined in the main text are shown (using $\alpha = 0.25t$, $\mu = -0.4t$). The black dashed line is the doubly degenerate Fermi surface for $\alpha \to 0$. In agreement with Eq. (6.59), the pseudospin orientation is approximately antiparallel on the two Fermi surfaces for states with the same polar angle Ω.*

whereas Eq. (6.59) relates wavefunctions of necessarily different Fermi surfaces – the state (s, Ω) and its "Rashba partner" (s_{R}, Ω).

Physically, Eq. (6.59) means that, for given Ω, the pseudospin orientation of the wavefunctions on the "Rashba pair" of Fermi surfaces $\{s, s_{\mathrm{R}}\}$ is antiparallel. As can be seen in Fig. 6.4, where Ω is chosen to be the polar angle of $\boldsymbol{k}$, Eq. (6.59) represents a very good approximation even for the moderately large value of the spin-orbit coupling used in the plot. Naturally, the validity of Eq. (6.59) for discussing superconducting properties crucially depends on the bandstructure of the system. Typically, one expects $\boldsymbol{g}_{\boldsymbol{k}}$ to vary on momentum scales of order of the size the Brillouin zone, i.e., Eq. (6.59) to be valid for $E_{\mathrm{so}} \ll \Lambda_t$.

In the following, we will assume that Eq. (6.59) holds and analyze its consequences. Firstly, taking advantage of the aforementioned similarity to TRS, we obtain

$$\boldsymbol{\Lambda}_{ss'}(\Omega, \Omega') = t\, e^{i(\gamma^{s'}_{\Omega'} - \gamma^{s}_{\Omega})} \left(\boldsymbol{\Lambda}_{s_{\mathrm{R}} s'_{\mathrm{R}}}(\Omega, \Omega') \right)^{*}. \tag{6.60}$$

As a second step, this, together with Eq. (6.50), allows for rewriting the central interaction matrix element (6.55) as follows

$$\mathcal{V}_{s's}(i\omega_{n'}, \Omega'; i\omega_n, \Omega) = -\frac{1}{2} \boldsymbol{\Lambda}^{\dagger}_{s'_{\mathrm{R}} s_{\mathrm{R}}}(\Omega', \Omega) \chi(i\omega_{n'} - i\omega_n, \boldsymbol{k} - \boldsymbol{k}') \boldsymbol{\Lambda}_{s'_{\mathrm{R}} s_{\mathrm{R}}}(\Omega', \Omega) \tag{6.61}$$

already using the approximation and notation introduced in Eq. (6.26). The right-hand side of this equation only equals $\mathcal{V}_{s'_{\mathrm{R}} s_{\mathrm{R}}}(i\omega_{n'}, \Omega'; i\omega_n, \Omega)$ and leads to the symmetry

$$\mathcal{V}_{s's}(i\omega_{n'}, \Omega'; i\omega_n, \Omega) = \mathcal{V}_{s'_{\mathrm{R}} s_{\mathrm{R}}}(i\omega_{n'}, \Omega'; i\omega_n, \Omega) \tag{6.62}$$

under two assumptions: Firstly, similar to $\boldsymbol{g}$, the susceptibility $\chi(i\Omega_n, \boldsymbol{q})$ must be slowly varying in $\boldsymbol{q}$ on the scale $|\boldsymbol{g}|/v_F$. This is a very natural assumption as the description in terms of a collective mode will only be sensible if there are long-wavelength fluctuations. Secondly, and much more importantly, $\chi(i\Omega_n, \boldsymbol{q})$ must be an even function of momentum $\boldsymbol{q}$. We see from Eq. (6.50) that TRS alone does not determine the behavior under $(\Omega_n, \boldsymbol{q}) \to (\Omega_n, -\boldsymbol{q})$ such that further information about the system is required. For this purpose, let us assume that there is a symmetry relating the fermionic momenta $\boldsymbol{k}$ and $-\boldsymbol{k}$, i.e., the full Hamiltonian of the system commutes with the unitary operator $\hat{\mathcal{S}}$ defined via

$$\hat{\mathcal{S}}\hat{c}^\dagger_{\boldsymbol{k}\alpha}\hat{\mathcal{S}}^\dagger = \hat{c}^\dagger_{-\boldsymbol{k}\beta}S_{\beta\alpha}, \quad S^\dagger S = \mathbb{1}. \tag{6.63}$$

In a 2D system this symmetry can be realized as a two-fold rotation C_2^z perpendicular to the plane of the system. As we have already used in Chap. 4.4, C_2^z commutes with all other symmetry operations such that the irreducible representations of the point group must be either even or odd under this operation (see Appendix A.2 for the proof of this statement) and the same holds for the order parameter of the competing particle-hole instability. This means that

$$\hat{\mathcal{S}}\hat{\phi}_{\boldsymbol{q}j}\hat{\mathcal{S}}^\dagger = \pm\hat{\phi}_{-\boldsymbol{q}j} \tag{6.64}$$

leading to the required relation

$$\chi(i\Omega_n, \boldsymbol{q}) = \chi(i\Omega_n, -\boldsymbol{q}) \tag{6.65}$$

as shown in Appendix E.1.1. One might expect that, even in the absence of a two-fold rotation symmetry or in a 3D system, Eq. (6.65) still constitutes a valid approximation for $E_{\mathrm{so}} \ll \Lambda_t$: Although the superconducting instability, arising from infrared singularities, is essentially influenced by the splitting $|\boldsymbol{g}|$ of the Fermi surfaces due to the broken inversion symmetry, the susceptibility χ might not. As the tendency of the system towards the competing instability mainly results from processes at energies comparable to Λ_t (cf. Fig. 6.3(a)), the inversion-symmetry-breaking terms are expected to be negligible in the limit $E_{\mathrm{so}} \ll \Lambda_t$ for the calculation of χ. In that sense, Eq. (6.63) is realized as an approximate inversion symmetry again yielding Eq. (6.65).

6.2.4 Consequences for the possible pairing states

Let us now deduce the implications of the resulting asymptotic property (6.62) of the interaction matrix. Due to $\rho_s \sim \rho_{s_{\mathrm{R}}}$ in the limit $E_{\mathrm{so}} \ll \Lambda_t$, we have $Z_s \sim Z_{s_{\mathrm{R}}}$ as can be seen directly from Eq. (6.27a). Therefore, the kernel v of the gap equation (6.27b) has the same symmetry as $\mathcal{V}$ in Eq. (6.62). We conclude that the anomalous self-energy of any resulting superconducting state must be of the form

$$\widetilde{\Phi}_s(i\omega_n, \Omega) = p\,\widetilde{\Phi}_{s_{\mathrm{R}}}(i\omega_n, \Omega) \tag{6.66}$$

with either $p = +$ or $p = -$ for all s, ω_n and Ω. This is a central result of this section. It highly constraints the possible order parameters and allows them to be grouped into two basic classes: The relative sign of the order parameter at Rashba partners can only be either positive ($p = +$) or negative ($p = -$) for *all* Rashba pairs. In the following, the corresponding pairing states will be denoted by "Rashba even" and "Rashba odd", respectively.

This classification of possible pairing states can be seen as the analogue of the well-known decomposition into even (singlet) and odd (triplet) parity states in centrosymmetric systems discussed in Chap. 1.1.1. This connection becomes even more explicit by noting that, upon continuously turning on a spin-orbit term $(\boldsymbol{g}^{(j)}_{\boldsymbol{k}} \cdot \boldsymbol{\sigma})$ in a centrosymmetric Hamiltonian, a singlet state $(\Delta(\boldsymbol{k}) = \Delta^S_{\boldsymbol{k}} i\sigma_2)$ will

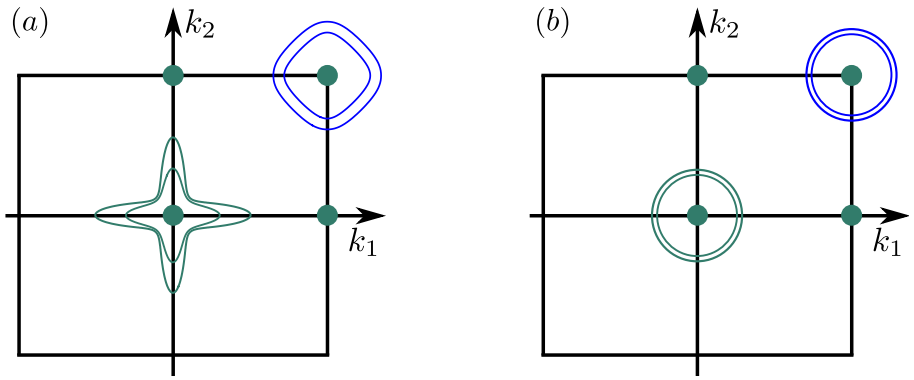

Figure 6.5: ***Basic nesting configurations for two Rashba pairs.*** *In (a), we expect χ to be peaked at momenta connecting states within the two Rashba pairs leading to Rashba odd pairing. The resulting state will nonetheless be topologically trivial as the number of TRIM enclosed by Rashba pairs is even. In case of (b), a Rashba even state is expected.*

turn into a Rashba even state $\widetilde{\Delta}_s(\boldsymbol{k}) = \Delta^S_{\boldsymbol{k}}$. This just constitutes a generalization of the adiabatic deformation of the BCS state ($\Delta^S_{\boldsymbol{k}} = \text{const.}$) into the s^{++} superconductor illustrated in Fig. 5.4. Similarly, turning on a spin-orbit term in a triplet superconductor ($\Delta(\boldsymbol{k}) = \boldsymbol{d}_{\boldsymbol{k}} \cdot \boldsymbol{\sigma} i\sigma_2$) and neglecting the Fermi surface off-diagonal matrix elements of the order parameter will yield a Rashba odd state ($\widetilde{\Delta}_{(j,\nu)}(\boldsymbol{k}) = \nu \boldsymbol{d}_{\boldsymbol{k}} \cdot \boldsymbol{g}^{(j)}_{\boldsymbol{k}}$).

Naturally, Eq. (6.66) has also crucial consequences for the possible topological properties of the superconductor. To discuss this, we will, as already mentioned above, have to assume in the following that the superconducting state is fully gapped and time-reversal symmetric.

Let us first focus on the 2D case where the topological invariant is determined by Eq. (6.45) with $\widetilde{\Delta}_s(\boldsymbol{k}) = \widetilde{\Phi}_s(0, \boldsymbol{k})$. In the limit we consider, the Rashba splitting $|\boldsymbol{g}|/v_F$ is much smaller than the size of the Brillouin zone and we can assume $m_{(j,\nu)} = m_{(j,-\nu)} \equiv m_j$. It follows that any Rashba even state will be topologically trivial and, in case of Rashba odd pairing, the invariant is given by

$$\nu_{\mathbb{Z}_2} = \prod_{j=1}^{N} (-1)^{m_j} = (-1)^{\sum_j m_j}. \tag{6.67}$$

The same also holds in 1D, where $m_j = 1$. Consequently, the total number of TRIM enclosed by Rashba pairs of Fermi surfaces must be necessarily odd for the interaction-induced superconductor to be topological.

To continue with 3D, we first note that the Fermi surface Chern numbers of Rashba partners must be equal in magnitude but opposite in sign, $C_{1(j,+)} = -C_{1(j,-)} \equiv C_{1j}$, which is just a manifestation of the fact that the spin-orientation of the eigenstates winds in opposite directions on Rashba partners (cf. Fig. 6.4) as dictated by Eq. (6.59). We refer to Appendix E.4 for an analytic proof of this statement. From Eq. (6.43) we then immediately see that any Rashba even state must again be trivial. For Rashba odd pairing, we get

$$\nu_{\mathbb{Z}} = \sum_j C_{1j} \operatorname{sign}\left(\widetilde{\Phi}_{(j,+)}(0,\Omega)\right). \tag{6.68}$$

Note that the right-hand side does not depend on Ω as the sign of the order parameter of a fully gapped superconductor cannot change on a given Fermi surface.

Irrespective of the dimensionality of the system, we have seen that Rashba odd pairing is required to make topologically nontrivial superconductivity possible. We expect this to be realized when the strongest nesting occurs between Rashba partners such that χ is dominated by momenta connecting the Rashba-split Fermi surfaces. An example for $N = 4$ is shown in Fig. 6.5(a) where a Rashba odd state is expected. On the other hand, if different Rashba pairs are most strongly nested, as in case of the Fermi surfaces of Fig. 6.5(b), a topologically trivial Rashba even state will arise.

More specifically, we can conclude that for just a single Rashba pair, $N = 2$, only Rashba odd pairing is possible. This simply follows from the fact that, in case of TRO fluctuations, the interaction is fully repulsive in the Cooper channel such that the superconducting state must have at least one sign change. Focusing on fully gapped superconductors (and neglecting sign changes as a function of frequency), this sign change must occur between the two Fermi surfaces. Irrespective of the dimensionality of the system, the superconductor will be automatically topological if the number of TRIM enclosed by the Rashba pair is odd. In 1D and 2D, this is directly seen from Eq. (6.67), whereas, for the 3D case, the relation $(-1)^{C_{1j}} = (-1)^{m_j}$ [280] implying $C_{1j} \neq 0$ for odd m_j has to be taken into account in Eq. (6.68).

6.2.5 More general fermion-boson couplings

Finally, let us generalize the previous analysis by considering more general forms of the fermion-boson coupling (6.47).

Momentum-dependent complex order parameter. To allow for the most general particle-hole order parameter we now investigate the coupling Hamiltonian

$$\hat{H}_{\text{int}} = \sum_{\boldsymbol{k},\boldsymbol{q}} \hat{c}^\dagger_{\boldsymbol{k}+\boldsymbol{q}\alpha} m^{(j)}_{\alpha\beta}(\boldsymbol{k}+\boldsymbol{q},\boldsymbol{k}) \hat{c}_{\boldsymbol{k}\beta}\, \hat{\varphi}_{\boldsymbol{q}j} + \text{H.c.}, \tag{6.69}$$

where $\hat{\varphi}_{\boldsymbol{q}j}$ are N'_B-component complex bosons ($\hat{\varphi}^\dagger_{\boldsymbol{q}j} \neq \hat{\varphi}_{-\boldsymbol{q}j}$) and $m^{(j)}(\boldsymbol{k}+\boldsymbol{q},\boldsymbol{k})$ are potentially momentum-dependent, generally non-Hermitian matrices. The momentum dependence is essential, e.g., when discussing current fluctuations, where $m(\boldsymbol{k}+\boldsymbol{q},\boldsymbol{k}) \propto (\boldsymbol{k}+\boldsymbol{q}/2)\sigma_0$ with σ_j being Pauli matrices in spin space. The generalization to non-Hermitian order parameters is relevant, e.g., in case of imaginary SDW ($m^{(j)} = i\sigma_j$) or imaginary CDW ($m = i\sigma_0$), which are discussed as competing instabilities in iron-based superconductors [351, 381, 382].

By decomposing both $\hat{\varphi}_{\boldsymbol{q}j}$ and the fermion bilinear into their Hermitian and Antihermitian parts, one can reduce Eq. (6.69) to the coupling to real bosons $\hat{\phi}_{\boldsymbol{q}j}$ with $N_B = 2N'_B$ components:

$$\hat{H}_{\text{int}} = \sum_{\boldsymbol{k},\boldsymbol{q}} \hat{c}^\dagger_{\boldsymbol{k}+\boldsymbol{q}\alpha} M^{(j)}_{\alpha\beta}(\boldsymbol{k}+\boldsymbol{q},\boldsymbol{k}) \hat{c}_{\boldsymbol{k}\beta}\, \hat{\phi}_{\boldsymbol{q}j}, \tag{6.70}$$

where $(M^{(j)}(\boldsymbol{k},\boldsymbol{k}'))^\dagger = M^{(j)}(\boldsymbol{k}',\boldsymbol{k})$. Let us for the moment again focus on either TRE or TRO fluctuations forcing $T\boldsymbol{M}^*(-\boldsymbol{k},-\boldsymbol{k}')T^\dagger = t\,\boldsymbol{M}(\boldsymbol{k},\boldsymbol{k}')$. Below we will comment on the situation of having both components at the same time.

Repeating the analysis presented above, one readily finds that Z must still satisfy all three properties in Eq. (6.32). In case of TRE fluctuations, spontaneous TRS breaking cannot occur with the resulting superconducting state being necessarily topologically trivial.

To derive the property (6.66) which is central for our analysis of superconductivity induced by TRO fluctuations, Eq. (6.60) with $\mathbf{\Lambda}_{ss'}(\boldsymbol{k},\boldsymbol{k}') = \psi^\dagger_{\boldsymbol{k}s}\boldsymbol{M}(\boldsymbol{k},\boldsymbol{k}')\psi_{\boldsymbol{k}'s'}$ must hold. Due to the additional momentum dependence of the order parameter, this is only the case (with t replaced by rt in Eq. (6.60)) if $\boldsymbol{M}(\boldsymbol{k},\boldsymbol{k}')$ changes little on the separation $|\boldsymbol{g}|/v_F$ of Rashba partners and if

$$\boldsymbol{M}(\boldsymbol{k},\boldsymbol{k}') = r\,\boldsymbol{M}(-\boldsymbol{k},-\boldsymbol{k}'), \quad r=\pm 1. \tag{6.71}$$

Note that Eq. (6.71) is satisfied by all examples discussed above. However, it can be violated when, e.g., current fluctuations and SDW fluctuations are simultaneously relevant.

Again assuming the presence of the unitary symmetry introduced in Eqs. (6.63) and (6.64), all constraints on the topological properties discussed in Sec. 6.2.4 also hold for momentum dependent, complex order parameters with coupling (6.69) as long as Eq. (6.71) is satisfied.

Frequency-dependent fermion-boson vertex. So far we have assumed that the fermion-boson interaction can be described by a Hamiltonian in the low-energy theory. If this interaction obtains significant frequency-dependent renormalization corrections resulting from processes at energies between Λ_t and Λ (see Fig. 6.3(a)), an action description,

$$S_{\text{int}} = \int_{k,q} \bar{c}_{k+q\alpha}\Gamma^{(j)}_{\alpha\beta}(k+q;k)c_{k\beta}\,\phi_{qj}, \tag{6.72}$$

is required. Here $\Gamma^{(j)}$ is the generally momentum- and frequency-dependent vertex function. Similar to our treatment of χ, the vertex will not be explicitly specified in the following. We will only take into account the exact relations resulting from TRS and Hermiticity (see Appendix E.1.3). To begin with the former symmetry, it holds

$$\Gamma^{(j)}_{\alpha\beta}(k;k') = t\,T_{\alpha\alpha'}\left[\Gamma^{(j)}_{\alpha'\beta'}(-k;-k')\right]^* T^\dagger_{\beta'\beta}, \tag{6.73}$$

which reduces to Eq. (6.48) for the coupling (6.47). The full effective electron-electron vertex is the same as in Eq. (6.51) with $\mathbf{\Lambda}_{s,s'}(\boldsymbol{k},\boldsymbol{k}')$ replaced by the renormalized $\mathbf{\Lambda}^\Gamma_{ss'}(k;k') = \psi^\dagger_{\boldsymbol{k}s}\mathbf{\Gamma}(k;k')\psi_{\boldsymbol{k}'s'}$ which now becomes frequency dependent. Due to the constraint (6.73), $\mathbf{\Lambda}^\Gamma$ satisfies the analogue of Eq. (6.53) such that we find the same structure as in Eq. (6.54a) with $\mathcal{V}$ being positive: As before, the interaction in the Cooper channel is either fully attractive or fully repulsive depending on whether the system is coupled to TRE or TRO fluctuations.

To analyze the forward-scattering channel defined in Fig. 6.2(b), we need to take into account the Hermiticity relation

$$\Gamma^{(j)}_{\alpha\beta}(i\omega_n,\boldsymbol{k};i\omega_{n'},\boldsymbol{k}') = \left[\Gamma^{(j)}_{\beta\alpha}(-i\omega_{n'},\boldsymbol{k}';-i\omega_n,\boldsymbol{k})\right]^*, \tag{6.74}$$

which reduces to $\boldsymbol{\lambda}^\dagger = \boldsymbol{\lambda}$ for the coupling (6.47). One can show that, despite the sign change of the frequencies on the right-hand side of Eq. (6.74), the resulting quasiparticle weight Z still satisfies Eq. (6.32). Furthermore, we find that, again, no TRS breaking is possible and $\delta > 0$ for TRE fluctuations.

To discuss the case of $t=-$, we have to take into account the implications for the vertex function resulting from the asymptotic symmetry introduced in Sec. 6.2.3. In Appendix E.1.3 it is shown that, as long as Eq. (6.71) is satisfied for the bare fermion-boson vertex, this imposes the constraint

$$\mathbf{\Lambda}^\Gamma_{ss'}(i\omega_n,\Omega;i\omega_{n'},\Omega') = r\,t\,e^{i(\gamma^{s'}_{\Omega'}-\gamma^s_\Omega)}\left[\mathbf{\Lambda}^\Gamma_{s_{\mathrm{R}}s'_{\mathrm{R}}}(-i\omega_n,\Omega;-i\omega_{n'},\Omega')\right]^* \tag{6.75}$$

on the fully renormalized vertex function, which constitutes the obvious generalization of relation (6.60).

Using the constraints resulting from the invariance of the system under $\hat{\mathcal{S}}$ defined in Eqs. (6.63) and (6.64) on the bosonic propagator, Eq. (6.65), as well as on the vertex function,

$$\mathbf{\Lambda}^{\Gamma}_{ss'}(i\omega_n, \Omega; i\omega_{n'}, \Omega') = \pm \mathbf{\Lambda}^{\Gamma}_{s_{\mathrm{K}} s'_{\mathrm{K}}}(i\omega_n, \Omega_{\mathrm{K}}; i\omega_{n'}, \Omega'_{\mathrm{K}}), \tag{6.76}$$

we recover the Rashba symmetry (6.62) of the Cooper channel. Similarly, one can show that $Z_s = Z_{s_{\mathrm{R}}}$ still holds. Consequently, the possible superconducting states can again be classified into Rashba even and Rashba odd according to Eq. (6.66). Assuming a finite gap and a TRS-preserving order parameter, we find exactly the same conclusions concerning the topology of the superconducting state as before.

We emphasize that starting with the generic vertex function in Eq. (6.72) and imposing exact symmetry constraints is *not* tantamount to solving the exact self-consistency equations of the Nambu Green's function beyond the Eliashberg approach. It is clear that, e.g., the last two diagrams in Fig. 6.2(c) containing anomalous vertex corrections cannot be captured with this approach.

General time-reversal properties. Finally, let us discuss the situation when the dominant fluctuations are neither fully TRE nor TRO, i.e., if the bosons coupling to the fermions according to Eq. (6.70) satisfy

$$\hat{\Theta}\hat{\phi}_{\boldsymbol{q}j}\hat{\Theta}^{\dagger} = t_j\, \hat{\phi}_{-\boldsymbol{q}j} \tag{6.77}$$

with $t_j = +$ and $t_j = -$ for the TRE and TRO components of the fluctuations, respectively.

From the analysis presented above, it is clear that the interaction cannot be generally repulsive or attractive in the Cooper channel. The constraint (6.50c) now assumes the generalized form

$$\chi_{jj'}(i\Omega_n, \boldsymbol{q}) = t_j t_{j'}\, \chi_{jj'}(-i\Omega_n, \boldsymbol{q}), \tag{6.78}$$

such that $\chi(q)$ is not Hermitian anymore. However, as long as we assume that all components $M^{(j)}$ in the bare coupling (6.70) satisfy Eq. (6.71), the properties (6.73) and (6.75) with t replaced by t_j are still valid and it can be shown that Eq. (6.62) as well as $Z_s = Z_{s_{\mathrm{R}}}$ hold. Consequently, the possible superconducting order parameters must obey Eq. (6.66) leading to the same conclusions as discussed in Sec. 6.2.4 as far as fully gapped, time-reversal symmetric superconducting phases are concerned.

6.3 Application to materials

In this section, we will apply the general results obtained above to two different physical systems, oxide heterostructures and single-layer FeSe on STO, where superconductivity has been observed experimentally [39, 40, 157] but not yet fully microscopically identified [36–38, 158, 159]. The purpose of this discussion is twofold: Firstly, it will illustrate the predictive power of the criteria derived in this chapter and, secondly, connect to and complement the symergetic arguments of Chap. 4 and the microscopic calculation of Chap. 5.

6.3.1 Oxide heterostructures

Let us begin with LAO/STO heterostructures which represent our prime example of systems where the weak-pairing approximation can be applied. As already discussed in Chap. 4.6.3, this is due to the combination of the small transition temperature [39, 40] of superconductivity and strong spin-orbit splitting [41–43] of the Fermi surfaces.

(001) orientation. In Chap. 5.1, we have derived a model for describing superconductivity in (001)-terminated LAO/STO heterostructures which takes into account the Ti $3d_{xz}$ and $3d_{yz}$ orbitals. From the resulting spectrum shown in Fig. 5.1(a), it can be seen that for the chemical potential being close to the bottom of the bands there are only two singly-degenerate Fermi surfaces. As the sweet spot of superconductivity is associated [344, 345] with the chemical potential entering the $3d_{xz}$ and $3d_{yz}$ bands, the RG calculation presented in Chap. 5 has been performed in this regime. We have shown that a microscopically repulsive interaction will drive the system close to a SDW instability with competing superconducting s^{+-} state ($\widetilde{\Delta}$ has opposite sign on the two Fermi surfaces) which is topologically nontrivial. If the electron-phonon coupling is dominant, the superconducting state will be the topologically trivial s^{++} state without sign changes – neither on a given nor between different Fermi surfaces.

All of these results of the explicit calculation are consistent with the analysis of this chapter which, on top of that, generalizes the absence of nontrivial topology in case of phonons beyond the weak-coupling limit since we have been using Eliashberg theory in this chapter. Furthermore, it is now also clear that the time-reversal properties of the competing SDW ($t = -1$) are key to induce a topologically nontrivial superconductor.

In addition, we know that when the energetically higher Rashba pair of bands (shown in gray in Fig. 5.1(a)) is populated, which can be induced via gate tuning [41, 42, 144, 145], the system necessarily becomes topologically trivial. This follows from the fact that the point group (C_{4v}) does not contain a threefold rotation symmetry such that the condensate must be time-reversal symmetric (see Chap. 4.4.1) but has a twofold rotation C_2^z perpendicular to the plane. Consequently, all prerequisites for applying Eq. (6.67) are satisfied which implies $\nu_{\mathbb{Z}_2} = (-1)^2 = 1$ (trivial). Note that although one might naively expect two pairs of counter-propagating Majorana modes at the boundary in this case, these modes can be gapped away [262] from the Fermi energy by surface perturbations mixing the two Rashba pairs of bands but breaking neither PHS nor TRS.

(110) orientation. Our general considerations in this chapter also readily allow for conclusions about the second orientation of the interface [142, 156] where superconductivity has been observed [40]. The point group of the (110) interface is C_{2v} and, hence, exactly as in case of the (001) termination, the prerequisites of Eq. (6.67) are fulfilled. Consequently, without taking into account further microscopic details, we know that if the chemical potential is gate tuned [43] to the lowest Rashba pair of bands, which again arises from the $3d_{xz}/3d_{yz}$ orbitals [383], we will have exactly the same correspondence between the mechanism and the topology of superconductivity as in the (001) interface: While phonons alone lead to a topologically trivial superconductor, TRO fluctuations will induce a superconducting state that, when fully gapped, must be topological. In this sense, also the (110) interface is a promising system for the realization of topological time-reversal symmetric superconductors. Naturally, the condensate will necessarily become trivial when the second lowest Rashba pair of bands [383] is populated.

6.3.2 Single-layer FeSe

As a second example, we will analyze the implications on single-layer FeSe on (001) STO. As we have discussed in Chap. 1.3.2, this is a fascinating system with many open questions [158, 159] and a remarkably high superconducting transition temperature much larger than the transition temperature of bulk FeSe [157]. Although the presence of the substrate manifestly breaks inversion symmetry, it is less obvious in this system whether the weak-pairing approximation can be applied as a consequence of the larger transition temperature. We will proceed as in Chap. 4.6.3: Although not *a priori* justifiable, we assume that the weak-pairing limit is indeed appropriate for deducing the superconducting

order parameter and discuss its consequences. Recalling that the point group is C_{4v}, we can, for the very same reason as in case of (001) oxide heterostructures, apply Eq. (6.67) and, hence, know that, irrespective of the unknown pairing mechanism, the condensate will be topologically trivial. The latter statement follows from the presence of two Rashba pairs of Fermi surfaces around the M point (Fig. 1.4(b) and its discussion in the main text in Chap. 1.3.2) leading to $\sum_j m_j = 2$ in Eq. (6.67). In the language of Chap. 4.6.3, the single topological order parameter configuration, with only one of the Fermi surfaces having a different sign, is neither Rashba even nor odd and, hence, inconsistent with the consequences of the Rashba symmetry (6.62). Note that this result does not contradict the recent proposal [173] of topological superconductivity in this system since the analysis of Ref. [173] has been performed in the opposite limit where inversion-symmetry breaking can be fully neglected for describing superconductivity.

6.4 Summary of Chapter 6

In summary, we have studied the connection between the mechanism leading to a superconducting phase and the time-reversal as well as the topological properties thereof. We have focused on noncentrosymmetric systems which can be described in the weak-pairing approximation justified as long as $E_{\mathrm{so}} \gtrsim T_c$ and defined by Eq. (6.21) on the level of Green's functions.

Firstly, our results complement the conditions for spontaneous TRS-breaking superconductivity of Chap. 4.4.1: We have shown that, irrespective of the point symmetries of the system, spontaneous TRS breaking can be ruled out for superconductivity resulting from electron-phonon coupling or from particle-hole fluctuations of an order parameter that is even under time-reversal ($t = +$ in Eq. (6.48)). Only when TRO particle-hole fluctuations ($t = -$) are relevant for the superconducting phase transition, TRS breaking can occur. In that case, we are left with the general condition of Chap. 4.4.1, formulated in terms of the point group of the system, to gain information about the time-reversal properties of the condensate without detailed microscopic information about the system.

Secondly, we have generalized the correspondence between the mechanism and the topology of superconductivity of Chap. 5 beyond the level of explicit model studies and the weak-coupling limit:

A proof has been provided that superconductivity arising from electron-phonon coupling alone will generically be fully gapped, neither break any point symmetry of the system nor be topologically nontrivial. This implies that one can generally use topological signatures to gain information about the microscopic pairing mechanism of superconductivity: The observation of topologically nontrivial properties, most importantly, the presence of MBSs at the edge of the sample, indicates that the mechanism cannot be conventional which means that other interaction channels have to be taken into account for understanding superconductivity. We have shown that exactly the same conclusions hold if superconductivity is induced by TRE particle-hole fluctuations. Note that the results of this chapter have been derived in the clean limit and, hence, only apply as long as disorder effects can be neglected for deducing the leading superconducting instability. In the next chapter, we will see that much of this carries over to the weakly disordered case due to Anderson's theorem [229–231] and its extensions [235–240]. Nonetheless, it will be shown (see Chap. 7.2) that magnetic disorder can render an electron-phonon superconductor topological.

The behavior is completely different in case of TRO particle-hole fluctuations where the Cooper channel of the interaction is fully repulsive within and between all different Fermi surfaces of the system. Consequently, the superconducting order parameter naturally has sign changes such that topologically nontrivial condensates become possible in the clean system.

In the limit where the spin-orbit splitting is much smaller than the bandwidth, $E_{\mathrm{so}} \ll \Lambda_t$, we have derived the asymptotic symmetry (6.62) of the interaction matrix elements from which follows that all possible superconducting order parameters can be grouped into Rashba even ($p = +$) and Rashba odd ($p = -$) as defined in Eq. (6.66). This classification of pairing states can be seen as the analogue of the well-known decomposition into even (singlet) and odd (triplet) order parameters in centrosymmetric superconductors (see Chap. 1.1.2).

For discussing topological aspects of superconductivity, we have focused on fully gapped, TRS-preserving states. It has been shown that only Rashba odd states can be topologically nontrivial which leads to constraints on the corresponding topological invariants. E.g., we have found that, for 1D and 2D systems, the total number of TRIM enclosed by Rashba pairs of Fermi surfaces must be necessarily odd for the superconductor to be topologically nontrivial. Furthermore, in case of just two singly-degenerate Fermi surfaces enclosing an odd number of TRIM, such as in case of LAO/STO heterostructures at low filling, the resulting superconductor, if fully gapped and induced by TRO fluctuations, will be automatically topological irrespective of the dimensionality of the system.

These necessary conditions for the emergence of nontrivial invariants, formulated in terms of Fermi surface topologies and the time-reversal properties of competing instabilities, are directly accessible experimentally and might, hence, serve as a guiding tool in the ongoing search for the realization of topological superconductivity. As for the structure of the Fermi surfaces which can be directly measured in photoemission experiments, we emphasize that one does not have to resolve the spin-orbit splitting as the criteria only refer to Rashba *pairs* of Fermi surfaces. E.g., for single-layer FeSe, the photoemission data of Ref. [167] shows that there are two Rashba pairs enclosing the M point. As long as the weak-pairing approximation applies in this system, the condensate must thus be topologically trivial.

According to our results, any system such as LAO/STO heterostructures that have the required Fermi surface topology [341–343, 383, 384] with respect to the TRIM and show a strong tendency towards magnetism [111, 148–155], which indicates the presence of sizable TRO particle-hole fluctuations, are promising candidates for realizing topological superconducting phases.

Chapter 7

7 Generalizations to weakly disordered systems

In the analysis presented in the preceding chapters of this thesis, the presence of imperfections in the crystal has been mostly neglected. As we have had a strong focus on exotic, non-BCS-like, superconducting states, a discussion of the impact of impurity scattering is crucial given that the protection of superconductivity against disorder according to the Anderson theorem [229–231] only refers to single-band s-wave superconductors (see Chap. 1.4.2). This chapter is concerned with supplementing various important aspects of Chaps. 4-6 with respect to the inclusion of weak disorder. In this context, "weak" means that the electronic states are still delocalized in the vicinity of the Fermi surface, which, as already mentioned in Chap. 1.4.2, requires $k_F l \gg 1$ with k_F and l denoting the Fermi wavelength and the mean-free path, respectively. In 2D, the localization length R_l must additionally satisfy $R_l \gg 1/\sqrt{T_c \rho_F}$ where T_c is the superconducting transition temperature and ρ_F the density of states at the Fermi level [227, 233].

In the first part of this chapter, Sec. 7.1, we will present an approach that allows for a compact understanding of the original Anderson theorem [229–231], i.e., the independence of T_c on weak nonmagnetic disorder (see also Chap. 1.4.2), and its various extensions found for multiband superconductors (see, e.g., [235–240]) which will be referred to as *generalized Anderson theorem* in the following. The generalized Anderson theorem will also provide intuitive qualitative understanding of the results of explicit calculations on impurity scattering in superconductors discussed in the remainder of the chapter.

In Sec. 7.2, we will analyze the impact of disorder on the correspondence between the mechanism and the topology of superconductivity established for noncentrosymmetric superconductors in Chap. 6. It will be shown explicitly that magnetic disorder can induce a transition from a conventional superconductor, that is necessarily topologically trivial in the clean limit, to a topological state that preserves TRS. Although the impurities break TRS, we show that residual unitary symmetries at edge of the system can still guarantee the presence of a Kramers pair of gapless counter-propagating Majorana modes. Furthermore, the design principles for spontaneous TRS-breaking Cooper instabilities [325, 326] derived in Chap. 4 is shown to carry over to the weakly disordered case irrespective of whether we consider magnetic or nonmagnetic impurities.

Finally, the sensitivity of the two candidate pairing states of (001) oxide heterostructures deduced in the microscopic calculation of Chap. 5 against both magnetic and nonmagnetic disorder will be discussed in Sec. 7.3.

This chapter is based on three different publications [239, 240, 367] and also contains unpublished

results. We refer to the relevant papers in the corresponding part of the text.

7.1 Generalized Anderson theorem

By investigating the impact of a given disorder realization on the gap of a superconducting mean-field Hamiltonian, we will derive a very general criterion for the stability of the transition temperature of a superconducting state against disorder in Sec. 7.1.1. This criterion is consistent with various explicit calculations on the impact of disorder on superconductors (see, e.g., Refs. [235–240] and Sec. 7.1.2). For the particularly relevant case of singly degenerate Fermi surfaces, we will explicitly reproduce the criterion diagrammatically in Sec. 7.1.3. A special case of this argument has been published in Ref. [239].

7.1.1 Algebraic criterion

As in Chap. 4, we start from a general d-dimensional superconducting mean-field Hamiltonian

$$\hat{H}_{\mathrm{MF}} = \sum_{\boldsymbol{k}} \hat{c}^\dagger_{\boldsymbol{k}\alpha} \left(h_{\boldsymbol{k}}\right)_{\alpha\alpha'} \hat{c}_{\boldsymbol{k}\alpha'} + \frac{1}{2}\sum_{\boldsymbol{k}} \left(\hat{c}^\dagger_{\boldsymbol{k}\alpha}\Delta_{\alpha\alpha'}(\boldsymbol{k})\hat{c}^\dagger_{-\boldsymbol{k}\alpha'} + \mathrm{H.c.}\right) \tag{7.1}$$

with normal state Hamiltonian $h_{\boldsymbol{k}}$, superconducting order parameter matrix $\Delta_{\alpha\alpha'}(\boldsymbol{k})$ and fermionic creation (annihilation) operator $\hat{c}^\dagger_{\boldsymbol{k}\alpha}$ ($\hat{c}_{\boldsymbol{k}\alpha}$) where α refers to all relevant degrees of freedom of the electron (spin, orbital, ...). Note that the final form of the generalized Anderson theorem will not make reference to an explicit single-particle basis and, hence, is readily applied, e.g., within the eigenbasis of a noncentrosymmetric normal state Hamiltonian as introduced in detail in Chap. 4.2 or within the pseudospin basis of a centrosymmetric system (see, e.g., Eq. (4.96)).

To understand the stability of a superconductor against impurities, it is very convenient to consider a given disorder realization [229, 385] which we describe by the most general, translation-symmetry-breaking quadratic perturbation to the Hamiltonian,

$$\hat{H}_{\mathrm{dis}} = \sum_{\boldsymbol{k},\boldsymbol{k}'} \hat{c}^\dagger_{\boldsymbol{k}\alpha} W_{\alpha\alpha'}(\boldsymbol{k},\boldsymbol{k}')\hat{c}_{\boldsymbol{k}\alpha'}, \tag{7.2}$$

where W is only constrained by Hermiticity, $W^\dagger(\boldsymbol{k},\boldsymbol{k}') = W(\boldsymbol{k}',\boldsymbol{k})$. As the time-reversal properties of the disorder potential play a crucial role for superconductivity [101, 229–231], let us split W into its TRE ($t_d = +$), also referred to as "nonmagnetic", and TRO ($t_d = -$), "magnetic", part according to

$$W = W^+ + W^-, \qquad W^{t_d}(\boldsymbol{k},\boldsymbol{k}') = t_d\,\Theta W^{t_d}(-\boldsymbol{k},-\boldsymbol{k}')\Theta^\dagger. \tag{7.3}$$

As before, $\Theta = T\mathcal{K}$ is the time-reversal operator with $\mathcal{K}$ denoting complex conjugation. Note that we will not have to specify whether $\Theta^2 = -\mathbb{1}$ or $\Theta^2 = \mathbb{1}$ and, hence, the following discussion holds both for spinfull as well as spinless fermions.

Guided by Anderson's original insights [229], we introducing Nambu spinors $\hat{\Phi}_{\boldsymbol{k}\alpha} = (\hat{c}_{\boldsymbol{k}\alpha}, T_{\alpha\alpha'}\hat{c}^\dagger_{-\boldsymbol{k}\alpha'})$ comprising Kramers partners. The full Hamiltonian can then be written in quadratic form $\hat{H}_{\mathrm{MF}}+\hat{H}_{\mathrm{dis}} = \frac{1}{2}\sum_{\boldsymbol{k},\boldsymbol{k}'}\hat{\Phi}^\dagger_{\boldsymbol{k}\alpha}\left(\check{h}^{\mathrm{BdG}}\right)_{\boldsymbol{k}\alpha,\boldsymbol{k}'\alpha'}\hat{\Phi}_{\boldsymbol{k}'\alpha'}$ with BdG Hamiltonian $\check{h}^{\mathrm{BdG}} = \check{h}^{\mathrm{BdG}}_n + \check{h}^{\mathrm{BdG}}_\Delta + \check{h}^{\mathrm{BdG}}_W$ where

$$\check{h}^{\mathrm{BdG}}_n = \begin{pmatrix} \check{h} & 0 \\ 0 & -\check{h} \end{pmatrix}, \qquad \check{h}^{\mathrm{BdG}}_\Delta = \begin{pmatrix} 0 & \check{\mathcal{D}} \\ \check{\mathcal{D}}^\dagger & 0 \end{pmatrix}, \qquad \check{h}^{\mathrm{BdG}}_W = \begin{pmatrix} \check{W}^+ + \check{W}^- & 0 \\ 0 & -\check{W}^+ + \check{W}^- \end{pmatrix}. \tag{7.4}$$

Here and in the following, the inverted hat is used to indicate that the quantities are matrices with respect to both $\boldsymbol{k}$ and α. We have introduced $(\check{h})_{\boldsymbol{k}\alpha,\boldsymbol{k}'\alpha'} = \delta_{\boldsymbol{k},\boldsymbol{k}'}(h_{\boldsymbol{k}})_{\alpha\alpha'}$ and $(\check{\mathcal{D}})_{\boldsymbol{k}\alpha,\boldsymbol{k}'\alpha'} = \delta_{\boldsymbol{k},\boldsymbol{k}'}(\Delta_{\boldsymbol{k}}T^\dagger)_{\alpha\alpha'}$ and taken advantage of Eq. (7.3) as well as the TRS of the normal state Hamiltonian.

As is readily shown (a proof can be found in Appendix F.1), if

$$\left\{\check{h}_n^{\mathrm{BdG}} + \check{h}_W^{\mathrm{BdG}},\, \check{h}_\Delta^{\mathrm{BdG}}\right\} = 0 \tag{7.5}$$

with $\{\cdot,\cdot\}$ denoting the anticommutator, the gap of the superconductor is not reduced by the presence of disorder which indicates the stability of the condensate against disorder configurations satisfying Eq. (7.5).

From the explicit form (7.4), it follows that the anticommutator of $\check{h}_n^{\mathrm{BdG}}$ and $\check{h}_\Delta^{\mathrm{BdG}}$ vanishes if $\check{h}$ and $\check{\mathcal{D}}$ commute, $[\check{h},\check{\mathcal{D}}] = 0$. Using the eigenstates $|\psi_{\boldsymbol{k}s}\rangle$ of $h_{\boldsymbol{k}}$, satisfying $h_{\boldsymbol{k}}\,|\psi_{\boldsymbol{k}s}\rangle = \epsilon_{\boldsymbol{k}s}\,|\psi_{\boldsymbol{k}s}\rangle$, as basis, the latter condition is equivalent to

$$(\epsilon_{\boldsymbol{k}s} - \epsilon_{\boldsymbol{k}s'})D_{ss'}(\boldsymbol{k}) = 0, \tag{7.6}$$

where $D_{ss'}(\boldsymbol{k}) = \langle\psi_{\boldsymbol{k}s}|\Delta(\boldsymbol{k})T^\dagger|\psi_{\boldsymbol{k}s'}\rangle$ as already introduced in Eq. (4.27). Eq. (7.6) constitutes a generalized form of the weak-pairing limit where all matrix elements $D_{ss'}(\boldsymbol{k})$ of the superconducting order parameter are neglected that couple single-particle states of nondegenerate bands $\epsilon_{\boldsymbol{k}s} \neq \epsilon_{\boldsymbol{k}s'}$. In the limit of singly degenerate bands, it reduces to Eq. (4.29).

If Eq. (7.6) holds, Eq. (7.5) will be equivalent to $\{\check{h}_W^{\mathrm{BdG}}, \check{h}_\Delta^{\mathrm{BdG}}\} = 0$. Inserting again Eq. (7.4), we find the very compact and general form of the *generalized Anderson theorem*: A superconductor with order parameter described by $\check{\mathcal{D}}$ will be protected against disorder with TRE and TRO components $\check{W}^+$ and $\check{W}^-$ if

$$\left[\check{W}^+,\, \check{\mathcal{D}}\right] + \left\{\check{W}^-,\, \check{\mathcal{D}}\right\} = 0. \tag{7.7}$$

In Eq. (7.7), the Anderson theorem assumes a purely algebraic form in the sense that it only refers to the commutation or anticommutation relations of the different components of the disorder potential and the superconducting order parameter without reference to a specific single-particle basis. We further note that the normal-state Hamiltonian $h_{\boldsymbol{k}}$ does not enter in Eq. (7.7) explicitly[1], i.e., the criterion is independent of the band structure of the high-temperature phase.

7.1.2 Special cases and applications

We will next focus on special cases of Eq. (7.7) and discuss basic consequences mainly for iron-based superconductors and oxide heterostructures as examples of centrosymmetric and noncentrosymmetric systems. These special cases will also allow us to compare Eq. (7.7) with the predictions of explicit diagrammatic calculations and, hence, to benchmark the to some extent phenomenological association "gap not reduced $\Leftrightarrow$ mean-field T_c unaffected" made above.

Spin-degenerate Fermi surfaces. Let us begin with the most frequently encountered case of doubly-degenerate Fermi surfaces which is relevant for any centrosymmetric system with spin-1/2 TRS (see Chap. 1.3). The wavefunctions of band j will be denoted by $|\psi_{\boldsymbol{k}j\sigma}\rangle$, where the label σ refers to the spin or pseudospin (see Appendix A.1) degree of freedom depending on the absence or presence of significant SOC, respectively. The generalized weak-pairing limit (7.6) means that all matrix elements of $\Delta(\boldsymbol{k})T^\dagger$ between states with $j \neq j'$ can be neglected and is applicable as long as different bands

[1] Of course, it enters indirectly via Eq. (7.6) and because the normal-state Hamiltonian affects the structure of the superconducting order parameter.

are energetically well separated (on the energy scales of the superconductor). We can then write $(\check{\mathcal{D}})_{\boldsymbol{k}j\sigma,\boldsymbol{k}'j'\sigma'} = \delta_{\boldsymbol{k},\boldsymbol{k}'}\delta_{j,j'}D^{(j)}_{\sigma\sigma'}(\boldsymbol{k})$ where $(\check{\mathcal{D}})_{\boldsymbol{k}j\sigma,\boldsymbol{k}'j'\sigma'} \equiv \delta_{\boldsymbol{k},\boldsymbol{k}'}\langle\psi_{\boldsymbol{k}j\sigma}|\Delta(\boldsymbol{k})T^\dagger|\psi_{\boldsymbol{k}j'\sigma'}\rangle$ is the band basis representation of the superconducting order parameter. In case of (pseudo)spin singlet or triplet, it holds $D^{(j)}_{\sigma\sigma'}(\boldsymbol{k}) = \delta_{\sigma\sigma'}\Delta^{S(j)}_{\boldsymbol{k}}$ or $D^{(j)}_{\sigma\sigma'}(\boldsymbol{k}) = \boldsymbol{d}^{(j)}_{\boldsymbol{k}}\cdot\boldsymbol{s}_{\sigma\sigma'}$, respectively. Transforming the disorder configuration to the band basis, $\check{W}_{\boldsymbol{k}j\sigma,\boldsymbol{k}'j'\sigma'} \equiv \langle\psi_{\boldsymbol{k}j\sigma}|W(\boldsymbol{k},\boldsymbol{k}')|\psi_{\boldsymbol{k}'j'\sigma'}\rangle$, and focusing for simplicity on either TRE ($t_d = +$) or TRO ($t_d = -$) disorder, the algebraic form of the Anderson theorem (7.7) becomes

$$\sum_{\sigma''} D^{(j)}_{\sigma\sigma''}(\boldsymbol{k})\check{W}_{\boldsymbol{k}j\sigma'',\boldsymbol{k}'j'\sigma'} = t_d\sum_{\sigma''}\check{W}_{\boldsymbol{k}j\sigma,\boldsymbol{k}'j'\sigma''}D^{(j')}_{\sigma''\sigma'}(\boldsymbol{k}'), \qquad \forall\,\boldsymbol{k},\boldsymbol{k}',j,j',\sigma,\sigma', \tag{7.8}$$

where summation over repeated indices is not implied. For a triplet state, the condition (7.8) will in general[2] not be satisfied since $\boldsymbol{d}^{(j)}_{\boldsymbol{k}}$ must be odd under $\boldsymbol{k}\to-\boldsymbol{k}$ and hence, cannot be constant on the Fermi surface[3]. This is the reason why triplet superconductivity is already prone to nonmagnetic disorder which is well-known theoretically and confirmed by experiments, e.g., for Sr_2RuO_4 [160]. We also see in Eq. (7.8) very directly that a triplet superconductor is sensitive to the (pseudo)spin structure of the impurities.

This changes in case of singlet pairing, $D^{(j)}_{\sigma\sigma'} = \delta_{\sigma,\sigma'}\Delta^{S(j)}_{\boldsymbol{k}}$, where Eq. (7.8) can be restated as (again no summation convention)

$$\left(\Delta^{S(j)}_{\boldsymbol{k}} - t_d\,\Delta^{S(j')}_{\boldsymbol{k}'}\right)\check{W}_{\boldsymbol{k}j\sigma,\boldsymbol{k}'j'\sigma'} = 0, \qquad \forall\,\boldsymbol{k},\boldsymbol{k}',j,j',\sigma,\sigma'. \tag{7.9}$$

It shows that, as expected, the stability of a singlet state against a specific impurity configuration does not depend on the (pseudo)spin structure of W. For a singlet state to be protected it only matters according to Eq. (7.9) that there is no impurity scattering process (with arbitrary spin index combinations σ,σ') connecting states $|\psi_{\boldsymbol{k}j\sigma}\rangle$ and $|\psi_{\boldsymbol{k}'j'\sigma'}\rangle$ with $\Delta^{S(j)}_{\boldsymbol{k}} \neq t_d\,\Delta^{S(j')}_{\boldsymbol{k}'}$.

It implies that an s-wave superconductor with the same value of the order parameter on all Fermi surfaces, $\Delta^{S(j)}_{\boldsymbol{k}} = \text{const.}$, is protected against nonmagnetic disorder ($t_d = +$) recovering the original Anderson theorem [229–231]. We further see that Eq. (7.9) is violated for a superconductor with $\Delta^{S(j)}_{\boldsymbol{k}} = \text{const.}$ in case of magnetic scattering ($t_d = -$) leading to the well-known [101] suppression of T_c with impurity concentration (see also Secs. 7.2.2 and 7.3).

In the presence of several bands, extensions of the Anderson theorem are possible [235–240] that are not only of purely academic interest and can be easily read off from Eq. (7.9): Let us consider for concreteness the simplest nontrivial case of two bands $j = 1,2$ and the singlet state with $\Delta^{S(j)}_{\boldsymbol{k}} = (-1)^j\Delta_0$ referred to as s^{+-} in the following. This pairing state is one of the most widely discussed candidates for the iron-based superconductors where the two bands correspond to the hole-like and electron-like bands[4] centered around the Γ and M point of the two-Fe Brillouin zone, respectively [26]. Eq. (7.9) directly implies that the s^{+-} state is protected against nonmagnetic intraband scattering as expected from the original Anderson theorem [229–231] while time-reversal symmetric interband processes will suppress its critical temperature T_c. More interestingly, we see that the s^{+-} state is unaffected by TRO interband scattering, i.e., enjoys an analogue of the original Anderson theorem for

[2] except for cases where both the superconducting order parameter as well as the disorder potential have special symmetry properties (see, e.g., Ref. [237])

[3] At least as long as the Fermi surface encloses TRIM.

[4] The presence of several hole and/or electron bands does not affect our discussion here as long as the order parameter is approximately constant in the vicinity of the Γ and M point.

magnetic impurities. This is fully consistent with explicit calculations considering both spin-magnetic [238] as well as orbital-magnetic [239] impurities.

Although it seems to be quite artificial at first sight to have a scattering potential with a purely interband magnetic component, it has been shown in Ref. [239] that such a situation might very naturally arise in the iron-based superconductors due to the complex phase competition in these systems: In model calculations, the s^{+-} state competes with a SDW and an imaginary and, hence, TRS-breaking, CDW phase in case of repulsive interband interactions [351, 381, 382]. In a system where superconductivity is the dominant bulk state, the competing particle-hole instabilities could nucleate in the vicinity of initially nonmagnetic impurities [386, 387]. For instance, in case of local imaginary CDW order this effectively corresponds to orbital magnetic impurities which can be shown [239] to lead to scattering potentials with vanishing intraband components. Since the s^{+-} state is protected against this type of scatterers as we have discussed above, the discrimination [241] between s^{+-} and its conventional counterpart s^{++} with $\Delta_{\boldsymbol{k}}^{S(j)} = \Delta_0$ on the basis of the response to initially nonmagnetic impurities becomes questionable. In particular, this might explain or, at least, yield an additional contribution to the unexpectedly weak suppression of the superconducting T_c with increasing concentration of (initially) nonmagnetic impurities seen in experiment [241].

We finally mention that the same algebraic approach can be used to analyze the stability of particle-hole phases. In this way, e.g., the SDW competing [351, 381, 382] with s^{+-} in iron-based superconductors can be shown to be protected against the imaginary CDW impurities discussed above. Note that the sensitivity of the SDW against disorder is also relevant for superconductivity as, e.g., the suppression of SDW order can enhance the superconducting T_c in a coexisting phase [388]. We refer to Ref. [239] for more details.

Nondegenerate Fermi surfaces. The conditions for the existence of a generalized Anderson theorem become even simpler for systems with singly degenerate bands. To discuss this case, we apply exactly the same notation as in Chap. 4.2: Using the eigenstates of the normal state Hamiltonian $|\psi_{\boldsymbol{k}s}\rangle$ as basis, we represent the superconducting order parameter as $(\check{\mathcal{D}})_{\boldsymbol{k}s,\boldsymbol{k}'s'} \equiv \delta_{\boldsymbol{k},\boldsymbol{k}'} \langle\psi_{\boldsymbol{k}s}|\Delta(\boldsymbol{k})T^\dagger|\psi_{\boldsymbol{k}s'}\rangle = \delta_{s,s'}\delta_{\boldsymbol{k},\boldsymbol{k}'}\widetilde{\Delta}_s(\boldsymbol{k})$, where the last equality corresponds to the weak-pairing limit. Similarly, disorder is represented by $\check{W}_{\boldsymbol{k}s,\boldsymbol{k}'s'} \equiv \langle\psi_{\boldsymbol{k}s}|W(\boldsymbol{k},\boldsymbol{k}')|\psi_{\boldsymbol{k}'s'}\rangle$ and Eq. (7.7) reads

$$\left(\widetilde{\Delta}_s(\boldsymbol{k}) - t_d\,\widetilde{\Delta}_{s'}(\boldsymbol{k}')\right)\check{W}_{\boldsymbol{k}s,\boldsymbol{k}'s'} = 0, \qquad \forall\,\boldsymbol{k},\boldsymbol{k}',s,s', \tag{7.10}$$

for either nonmagnetic ($t_d = +$) or magnetic scattering ($t_d = -$), where, again, no summation convention is implied. Note the similarity to the condition (7.9) for singlet superconductivity in a centrosymmetric system with doubly degenerate Fermi surfaces. Eq. (7.10) implies that a superconductor is protected against all nonmagnetic (magnetic) scattering processes between states $|\psi_{\boldsymbol{k}s}\rangle$ and $|\psi_{\boldsymbol{k}'s'}\rangle$ where $\widetilde{\Delta}_s(\boldsymbol{k}) = \widetilde{\Delta}_{s'}(\boldsymbol{k}')$ ($\widetilde{\Delta}_s(\boldsymbol{k}) = -\widetilde{\Delta}_{s'}(\boldsymbol{k}')$).

From this criterion, we already have a *qualitative* understanding of the stability of the two candidate pairing states of oxide heterostructures found in Chap. 5. For nonmagnetic scattering, the s^{++} superconductor characterized by $\widetilde{\Delta}_s(\boldsymbol{k}) = \Delta_0$ is protected as expected from the original Anderson theorem [229–231] while the s^{+-} state is prone to interband processes. In analogy to the discussion of the iron-based superconductors, the s^{+-} state is protected against magnetic interband scattering while the s^{++} is not. Therefore, the latter is more fragile in the presence of magnetic impurities which are expected to be particularly important for oxide heterostructures due the strong tendency of the system towards the formation of magnetic moments [111, 151–155]. Notwithstanding the generality of these arguments, in order to judge whether this is a relevant aspect for superconductivity in LAO/STO heterostructures,

one has to study the impact of scattering on the stability of the two pairing states *quantitatively* which will be the topic of Sec. 7.3.

Furthermore, Eq. (7.10) indicates that magnetic impurities, similarly to magnetic particle-hole fluctuations, favor a superconducting state with sign changes between different spin-orbit-split Fermi surfaces, i.e., a Rashba odd state, over a Rashba even state where the signs are identical on the Fermi surfaces (cf. Chap. 6.2). As only Rashba odd states can be topologically nontrivial, magnetic scattering is expected to be capable of inducing a transition from a trivial superconductor to a topological superconductor within class DIII. In Sec. 7.2, we will show explicitly that this, somewhat paradoxical expectation, is indeed true and discuss the implications for the resulting edge states.

Before, we will derive Eq. (7.10) by calculating the impact of disorder on the transition temperature of a general superconductor in the weak-pairing limit. This derivation will also introduce the basic conventions and assumptions of Secs. 7.2 and 7.3.

7.1.3 Diagrammatic approach

We follow Ref. [389] and calculate the disorder-averaged quadratic Ginzburg-Landau expansion in order to analyze the consequences of impurity scattering on the superconducting phase transition. The derivation of the general form of the kernel of the Ginzburg-Landau expansion (Eq. (7.20) below) has been published in Ref. [367].

Disorder ensemble. In this subsection, it will be more convenient to introduce disorder in a real-space representation

$$\hat{H}_{\text{dis}} = \int_{\boldsymbol{x},\boldsymbol{x}'} \hat{c}^\dagger_\alpha(\boldsymbol{x}) W_{\alpha\alpha'}(\boldsymbol{x},\boldsymbol{x}') \hat{c}_{\alpha'}(\boldsymbol{x}'), \qquad W^*_{\alpha'\alpha}(\boldsymbol{x}',\boldsymbol{x}) = W_{\alpha\alpha'}(\boldsymbol{x},\boldsymbol{x}') \tag{7.11}$$

with $\hat{c}^\dagger(\boldsymbol{x})$ and $\hat{c}(\boldsymbol{x})$ being the Fourier transforms of the microscopic creation and annihilation operators $\hat{c}^\dagger_{\boldsymbol{k}}$ and $\hat{c}_{\boldsymbol{k}}$ introduced in Eq. (7.1). We will make the same simplifying assumptions as in Chap. 1.4.1: Let the system be self-averaging allowing us to treat W as a Gaussian distributed real ($W^\dagger = W$) random field. We restrict the analysis to spatially local configurations, $\boldsymbol{x} = \boldsymbol{x}'$ in Eq. (7.11), with δ-correlated and homogeneous statistics and, hence, have

$$\langle W_{\alpha_1\alpha_1'}(\boldsymbol{x}_1,\boldsymbol{x}_1') W_{\alpha_2\alpha_2'}(\boldsymbol{x}_2,\boldsymbol{x}_2')\rangle_{\text{dis}} = \delta(\boldsymbol{x}_1-\boldsymbol{x}_1')\delta(\boldsymbol{x}_2-\boldsymbol{x}_2')\delta(\boldsymbol{x}_1-\boldsymbol{x}_2)\Gamma_{\alpha_1\alpha_1',\alpha_2\alpha_2'}, \tag{7.12}$$

where $\langle\ldots\rangle_{\text{dis}}$ represents the disorder average. Averaging over W produces an effective four-fermion interaction within replica theory [228] with bare vertex given by Γ (see Chap. 1.4.1).

The correlator Γ can always be expressed in terms of Hermitian basis matrices $\{w_\mu\}$,

$$\Gamma_{\alpha_1\alpha_1',\alpha_2\alpha_2'} = \sum_{\mu,\mu'} C_{\mu\mu'} (w_\mu)_{\alpha_1\alpha_1'} (w_{\mu'})_{\alpha_2\alpha_2'}, \qquad C = C^* = C^T, \tag{7.13}$$

where the constraints on the matrix C follow from Hermiticity of W and $\Gamma'_{\alpha_1\alpha_1',\alpha_2\alpha_2'} = \Gamma'_{\alpha_2\alpha_2',\alpha_1\alpha_1'}$. The expansion (7.13) will be very convenient when analyzing the restrictions resulting from the point symmetries of the clean system as we will see in Secs. 7.2 and 7.3. For the general purpose of proving Eq. (7.10) we will only consider the TRS properties of the disorder configurations. As before, we distinguish between TRE ("nonmagnetic") and TRO ("magnetic") disorder which is mathematically equivalent to restricting the expansion (7.13) to matrices satisfying

$$\Theta w_\mu \Theta^\dagger = t_d\, w_\mu \tag{7.14}$$

with $t_d = +$ and $t_d = -$, respectively.

Disordered Ginzburg-Landau expansion. As we have seen in previous chapters, the analysis of superconducting instabilities is most easily performed in the eigenbasis of the normal state Hamiltonian. We will assume that all bands (labeled by index s) are singly degenerate and that the weak-pairing description applies. Denoting, as before, the fermionic annihilation and creation operators in this basis by $\hat{f}_{\boldsymbol{k}s}$ and $\hat{f}^\dagger_{\boldsymbol{k}s}$, the Cooper channel of the interaction will be parameterized by

$$\hat{H}_{\mathrm{C}} = \sum_{\boldsymbol{k},\boldsymbol{k}'} e^{i(\varphi^s_{\boldsymbol{k}} - \varphi^{s'}_{\boldsymbol{k}'})} \mathcal{V}_{s's}(\boldsymbol{k}';\boldsymbol{k})\, \hat{f}^\dagger_{\boldsymbol{k}'s'} \hat{f}^\dagger_{-\boldsymbol{k}'s'_{\mathrm{K}}} \hat{f}_{-\boldsymbol{k}s_{\mathrm{K}}} \hat{f}_{\boldsymbol{k}s}, \tag{7.15}$$

where $\varphi^s_{\boldsymbol{k}}$ are the time-reversal phases of the eigenstates defined in Eq. (6.13) and s_{K} refers to the Kramers partner of Fermi surface s (see also Fig. 6.1(a)). Within this notation, an electron-phonon interaction necessarily leads to $\mathcal{V} \leq 0$ as has been shown in Chap. 6.1.1.

To solve for the dominant superconducting state in the presence of disorder, the interaction (7.15) will be treated within mean-field approximation. We introduce the order parameter

$$\widetilde{\Delta}_s(\boldsymbol{k}) = \sum_{\boldsymbol{k}',s'} \langle \hat{f}_{-\boldsymbol{k}'s'_{\mathrm{K}}} \hat{f}_{\boldsymbol{k}'s'} \rangle\, e^{i\varphi^{s'}_{\boldsymbol{k}'}} \mathcal{V}_{ss'}(\boldsymbol{k};\boldsymbol{k}') \tag{7.16}$$

such that the resulting mean-field Hamiltonian is of the form of Eq. (6.37) and the topological indices can be inferred from Eqs. (2.17) and (2.19) as long as the condensate preserves TRS ($\widetilde{\Delta}_s(\boldsymbol{k}) \in \mathbb{R}$).

The transition temperatures of the competing superconducting states are obtained by calculating the disorder-averaged free energy $\langle \mathcal{F} \rangle_{\mathrm{dis}}$ as a function of the order parameter [389]. Assuming that both $\widetilde{\Delta}_s(\boldsymbol{k})$ as well as the interaction matrix elements $\mathcal{V}_{s's}(\boldsymbol{k}';\boldsymbol{k})$ only depend on the Fermi surface index s and on the position on the Fermi surface (parameterized by Ω, see also Fig. 6.1(a)), but not on the momentum coordinate perpendicular to the Fermi surface, one finds

$$\langle \mathcal{F} \rangle_{\mathrm{dis}} \sim \sum_{s,s'} \int_s \mathrm{d}\Omega \int_{s'} \mathrm{d}\Omega'\, \widetilde{\Delta}^*_s(\Omega) \left(D_{\Omega s,\Omega' s'}(T) - \mathcal{V}^{-1}_{\Omega s,\Omega' s'} \right) \widetilde{\Delta}_{s'}(\Omega') \tag{7.17}$$

as $\widetilde{\Delta} \to 0$. Here, $\mathcal{V}^{-1}$ denotes the inverse of the interaction kernel $\mathcal{V}$ and the disorder averaged particle-particle bubble $D_{\Omega s,\Omega' s'}$ is represented diagrammatically in Fig. 7.1(a) in terms of the full Green's function (double line) and the dressed vertex (gray triangle). As discussed in Chap. 1.4.1, in the weak-disorder limit, where the mean-free path l is much larger than the inverse Fermi momentum $1/k_F$, all diagrams with crossed impurity lines, which are suppressed by a factor $(k_F l)^{-1}$, can be neglected (known as SCBA). The self-energy and vertex correction are thus simply given by the "rainbow diagrams" and "Cooperon ladder" as shown in Fig. 7.1(b) and (c), respectively [389].

In analogy to the Eliashberg approach of the previous chapter (see, in particular, Fig. 6.2(e)), the impurity line, which is just given by the transformation of the correlator (7.13) into the eigenbasis of the normal state Hamiltonian, only enters in the form of two distinct index combinations: The self-energy is determined by forward scattering,

$$\mathcal{S}^F_{\Omega s,\Omega' s'} := \quad \begin{array}{ccc} \Omega', s' & \longrightarrow & \Omega, s \\ & \vdots & \\ \Omega, s & \longrightarrow & \Omega', s' \end{array} \quad = \sum_{\mu,\mu'} \left(\psi^\dagger_{\Omega' s'} w_\mu \psi_{\Omega s} \right)^* C_{\mu\mu'}\, \psi^\dagger_{\Omega' s'} w_{\mu'} \psi_{\Omega s}, \tag{7.18}$$

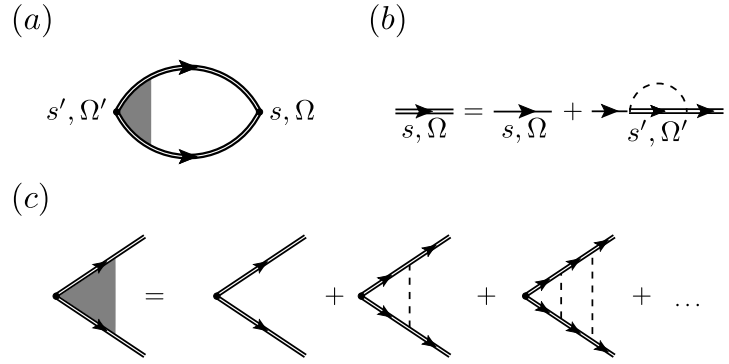

Figure 7.1: ***Disordered Ginzburg-Landau expansion.*** *An exact diagrammatic representation of the kernel D of the quadratic Ginzburg-Landau expansion is shown in (a) in terms of the full Greens function (double line) and renormalized vertex (gray triangle). Focusing on the limit $k_F l \gg 1$, the former and the latter only contain the noncrossing diagrams shown in (b) and (c), respectively. Here the impurity line (dashed) only enters in the combinations defined in Eqs. (7.18) and (7.19).*

which is real valued due to $C^\dagger = C$. The vertex-correction is determined by the Cooper scattering,

$$\mathcal{S}^C_{\Omega s,\Omega' s'} := \quad \begin{matrix} \Omega, s & \longrightarrow & \Omega', s' \\ \vdots & & \vdots \\ \Omega_{\rm K}, s_{\rm K} & \longrightarrow & \Omega'_{\rm K}, s'_{\rm K} \end{matrix} \quad = t_d\, e^{i(\varphi^s_\Omega - \varphi^{s'}_{\Omega'})} \mathcal{S}^F_{\Omega s,\Omega' s'}. \tag{7.19}$$

We use the same convention as in Chap. 6 and denote the Kramers partner of state (Ω, s) by $(\Omega_{\rm K}, s_{\rm K})$ (see Fig. 6.1(a)). To show the relation to $\mathcal{S}^F$ in Eq. (7.19), Eqs. (6.13) and (7.14) have been taken into account. The connection (7.19) between the Cooper and forward disorder scattering is the replica analogue of the relation for the electron-electron interaction in Eq. (6.54).

Summing up the diagrams in Fig. 7.1(b) and (c) using the matrix notation of Ref. [240] yields the general result [367]

$$D = -T \sum_{\omega_n} \Big(\mathcal{C}(\omega_n) - t_d\, \mathcal{S}^S \Big)^{-1} \tag{7.20}$$

with the symmetrized[5] scattering vertex $\mathcal{S}^S_{\Omega s,\Omega' s'} = \mathcal{S}^F_{\Omega s,\Omega' s'} + \mathcal{S}^F_{\Omega s,\Omega'_{\rm K} s'_{\rm K}}$ and the diagonal matrix

$$\mathcal{C}_{\Omega s,\Omega' s'}(i\omega_n) = \frac{\delta_{s,s'}\delta_{\Omega,\Omega'}}{\rho_s(\Omega)} \left(\frac{|\omega_n|}{\pi} + \sum_{\tilde{s}} \int_{\tilde{s}} \mathrm{d}\widetilde{\Omega}\, \rho_{\tilde{s}}(\widetilde{\Omega})\, \mathcal{S}^S_{\Omega s,\widetilde{\Omega}\tilde{s}} \right). \tag{7.21}$$

Note that the inverse in Eq. (7.20) refers to both s- and Ω-space and that the time-reversal phases in Eq. (7.19) have completely canceled out as required by gauge invariance. In Eq. (7.21), $\rho_s(\Omega)$ denotes the angle-resolved density of states on Fermi surface s (formally defined in Eq. (4.44)).

Proof of the generalized Anderson theorem. With the general form (7.20) of the kernel of the disordered Ginzburg-Landau expansion at hand, we are now in a position to derive Eq. (7.10) as a

[5] Since $\mathcal{S}^F_{\Omega s,\Omega' s'} = \mathcal{S}^F_{\Omega_{\rm K} s_{\rm K},\Omega'_{\rm K} s'_{\rm K}}$ both for nonmagnetic and magnetic disorder, $\mathcal{S}^S$ is automatically symmetrized in both indices, $\mathcal{S}^S_{\Omega s,\Omega' s'} = \mathcal{S}^S_{\Omega_{\rm K} s_{\rm K},\Omega' s'} = \mathcal{S}^S_{\Omega s,\Omega'_{\rm K} s'_{\rm K}}$.

sufficient condition for the protection of the superconducting state against disorder. As a first step, we note that $\check{W}_{\boldsymbol{k}s,\boldsymbol{k}'s'}$ should be replaced by $\psi^\dagger_{\Omega's'} w_\mu \psi_{\Omega s}$ in Eq. (7.10) within the disorder ensemble description we are currently using. As follows from Eq. (7.18), this means that the constraint Eq. (7.10) implies (again no summation convention)

$$\widetilde{\Delta}_s(\Omega)\mathcal{S}^S_{\Omega s,\Omega's'} = t_d\, \mathcal{S}^S_{\Omega s,\Omega's'}\widetilde{\Delta}_{s'}(\Omega'), \qquad \forall\, \Omega,\Omega',s,s', \tag{7.22}$$

for the impurity vertex. Secondly, assuming that Eq. (7.22) holds for the superconducting state of interest, the quadratic Ginzburg-Landau expansion becomes

$$\langle \mathcal{F}\rangle_{\mathrm{dis}} \sim \sum_{s,s'} \int_s \mathrm{d}\Omega \int_{s'} \mathrm{d}\Omega'\, \widetilde{\Delta}^*_s(\Omega)\left(d_{\Omega s}(T)\delta_{s,s'}\delta_{\Omega,\Omega'} - \mathcal{V}^{-1}_{\Omega s,\Omega's'}\right)\widetilde{\Delta}_{s'}(\Omega') \tag{7.23a}$$

as is shown in Appendix F.2 with

$$d_{\Omega s} = -T\sum_{\omega_n}\sum_{\tilde{s}}\int_{\tilde{s}} \mathrm{d}\widetilde{\Omega}\left[\left(\mathcal{C}(\omega_n) - \mathcal{S}^S\right)^{-1}\right]_{\tilde{s}\tilde{\Omega},s\Omega}. \tag{7.23b}$$

Note that apart from rendering the particle-particle bubble diagonal in both s and Ω, the factor t_d in Eq. (7.20) distinguishing between magnetic and nonmagnetic scattering has entirely left the stage. This means that sign changes of the order parameter will effectively cancel the factor t_d between $\mathcal{S}^C_{\Omega s,\Omega's'}$ and $\mathcal{S}^F_{\Omega s,\Omega's'}$ in Eq. (7.19) as long as Eq. (7.22) holds. Irrespective of the value of t_d, the Ginzburg-Landau expansion (7.23) looks as if we considered nonmagnetic impurities. Since D has become diagonal, all terms involving impurity scattering in Eq. (7.23a) are not sensitive to the sign of $\widetilde{\Delta}_s(\Omega)$ any more. From this point of view, it is not surprising that disorder will have no impact on Eq. (7.23). Indeed, it can be shown (see Appendix F.2) that the explicit dependence on $\mathcal{S}^S$ in Eq. (7.23b) resulting from the vertex corrections in Fig. 7.1(c) and the self-energy in Fig. 7.1(b) leading to the $\mathcal{S}^S$ dependence of $\mathcal{C}$ exactly cancel each other. This proves that both T_c as well as the superconducting order parameter are unaffected by impurities as long as Eq. (7.22) holds.

7.2 Topological superconductivity from phonons

In Chap. 6.1 we have shown under very general assumptions that electron-phonon coupling alone will in a clean system always lead to a time-reversal symmetric superconductor with trivial topological invariants. Besides additional Coulomb repulsion, also magnetic disorder could according to our discussion in Sec. 7.1.2 cause a transition into a topologically nontrivial superconducting state that will be necessarily subleading in the clean limit. In this section, which is based on Ref. [367], this expectation will be substantiated by a "proof-of-principle" model calculation (see Sec. 7.2.2) and a discussion of the impact of magnetic disorder on the Majorana edge modes (see Sec. 7.2.3). However, before approaching the model calculation, a few general comments on the time-reversal properties of superconducting states in systems with magnetic impurities are in order.

7.2.1 Selection rule for TRS breaking in the presence of disorder

Since the presence of magnetic impurities breaks TRS already in the normal state, one could naively expect that any resulting superconducting phase will automatically have a small TRS-breaking component and, hence, cannot be classified by a DIII invariant.

This is, however, not the case and physically based on the fact that TRS is restored on average. Within the analysis of this chapter, this is reflected by the fact that $\mathcal{S}^F$ and thus the entire kernel of the Ginzburg-Landau expansion (7.17) are both real and symmetric (see also Eq. (6.17)) such that all its eigenvectors can be chosen to be real.

Using the symmetry constraint (1.28) on the disorder correlator, that forces the point symmetries to be restored on average, it is straightforwardly shown that D and as a result the entire kernel of the Ginzburg-Landau expansion (7.17) are invariant under all operations of the point group. Therefore, the resulting superconducting order parameter must again transform under one of the IRs of the point group of the idealized clean system (see Chap. 1.1.1). As long as the order parameter transforms under a real one-dimensional IR, the superconducting state must be nondegenerate already on the quadratic level of the Ginzburg-Landau expansion and, hence, $\widetilde{\Delta}_s(\Omega)$ can always be chosen to be real, thus, preserving TRS.

From this discussion, it additionally follows that the selection rule for spontaneous TRS breaking [325, 326] discussed in Chap. 4.4.1 is readily generalized to the disordered case: In the absence of a threefold rotation symmetry perpendicular to the plane of a 2D system (and focusing on spinfull systems for simplicity), multidimensional or complex IRs are excluded by the Fermi-Dirac constraint (4.32) in the weak-pairing limit as argued in Chap. 4.4.1. This means that, irrespective of whether we consider magnetic or nonmagnetic disorder, the superconducting state of a 2D system must be necessarily time-reversal symmetric if there is no threefold rotation symmetry in the clean high-temperature phase.

7.2.2 Nontrivial topology induced by disorder

To show that disorder can drive an electron-phonon superconductor, that must be necessarily trivial in the clean limit, into a topological DIII state, let us focus for concreteness on 2D systems with C_{2v} point group. Note that, from the arguments presented above, it is already clear that the resulting superconducting state must be time-reversal symmetric due to the absence of a threefold rotation symmetry. Assuming that there are no additional orbital degrees of freedom, the normal-state Hamiltonian can be written as

$$h_{\boldsymbol{k}} = \epsilon_{\boldsymbol{k}}\sigma_0 + \boldsymbol{g}_{\boldsymbol{k}} \cdot \boldsymbol{\sigma}, \tag{7.24}$$

where σ_j are Pauli matrices in spin space. In addition, suppose the system has two singly degenerate Fermi surfaces enclosing only the Γ point and no other TRIM such as, e.g., in Fig. 6.4.

The basis matrices used to expand the disorder correlator in Eq. (7.13) can be chosen to be Pauli matrices, $w_\mu = \sigma_\mu$, $\mu = 0, 1, 2, 3$. The most general disorder correlator Γ in case of nonmagnetic disorder, i.e., with $t_d = +$ in Eq. (7.14), reads in the microscopic basis as

$$\Gamma_{\alpha_1\alpha_1',\alpha_2\alpha_2'} = \gamma_0(\sigma_0)_{\alpha_1\alpha_1'}(\sigma_0)_{\alpha_2\alpha_2'}, \tag{7.25}$$

whereas, in case of magnetic ($t_d = -$) impurities, we have

$$\Gamma_{\alpha_1\alpha_1',\alpha_2\alpha_2'} = \gamma_\parallel^{(1)}(\sigma_1)_{\alpha_1\alpha_1'}(\sigma_1)_{\alpha_2\alpha_2'} + \gamma_\parallel^{(2)}(\sigma_2)_{\alpha_1\alpha_1'}(\sigma_2)_{\alpha_2\alpha_2'} + \gamma_\perp(\sigma_3)_{\alpha_1\alpha_1'}(\sigma_3)_{\alpha_2\alpha_2'}. \tag{7.26}$$

Note that all terms coupling different Pauli matrices are ruled out by the fact that the C_{2v} point symmetry has to be restored on average (see Chap. 1.4.1). The terms proportional to $\gamma_\parallel^{(1,2)}$ and $\gamma_\perp$ describe spin-magnetic impurities which are aligned in the plane and perpendicular to the plane of the 2D system, respectively. It is straightforward to show, without further assumptions about the structure of the spin-orbit vector $\boldsymbol{g}_{\boldsymbol{k}}$, that $\mathcal{S}^S_{\Omega s,\Omega' s'} = \gamma_0$ in case of Γ given by Eq. (7.25) and $\mathcal{S}^S_{\Omega s,\Omega' s'} = \gamma_\parallel^{(1)} + \gamma_\parallel^{(2)} + \gamma_\perp =: \gamma_m$ for the correlator in Eq. (7.26).

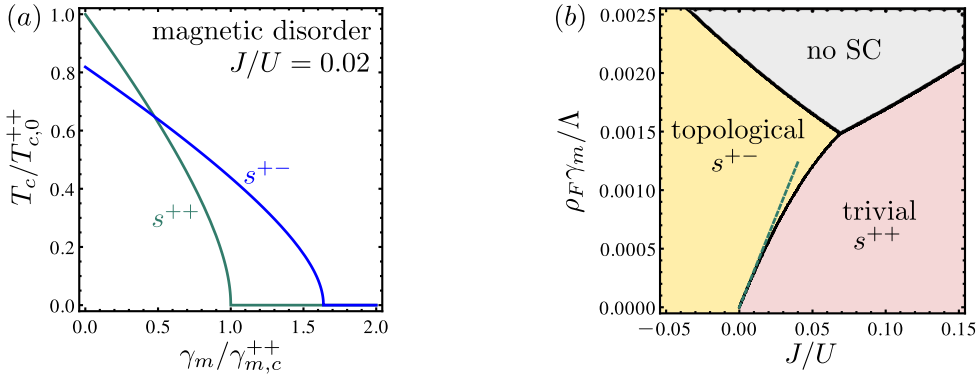

Figure 7.2: ***Scattering-inducing topology.*** *In (a), the transition temperatures of the s^{++} (green) and s^{+-} (blue) superconductors are shown as a function of the magnetic scattering strength γ_m assuming that the intraband (U) is much larger than the interband Cooper scattering (J). Here $\gamma_{m,c}^{++}$ and $T_{c,0}^{++}$ are the critical scattering rate of the s^{++} superconductor and its transition temperature in the absence of disorder, respectively. The full phase diagram together with the predictions of the asymptotic expression (7.28) for the critical scattering rate to enter the topological state (green line) are shown in (b). Here, "no SC" denotes the suppression of both superconducting states. In both plots, we have used $\rho_F U = -0.4$.*

Due to the simple form of the scattering matrix, it is possible to perform the inversion in Eq. (7.20) analytically (see Appendix F.3 for more details on the following analysis). To obtain a minimal phase diagram that captures the relevant physics, let us assume that $\rho_s(\Omega) \simeq$ const. and that the interaction matrix elements introduced in Eq. (7.15) can be parameterized as

$$\mathcal{V}_{\Omega s,\Omega' s'} \simeq \begin{pmatrix} U & J \\ J & U \end{pmatrix}_{s,s'}, \tag{7.27}$$

i.e., there is an intraband Cooper scattering (U) that is the same for both bands and an interband Cooper interaction (J) both of which are constant on the two Fermi surfaces.

By diagonalizing the associated kernel of the free energy expansion (7.17), one can deduce the transition temperatures of all possible superconducting order parameters and, hence, the dominant instability of the system as a function of the interaction parameters U, J as well as of the disorder strength parameterized by γ_0 and γ_m for nonmagnetic and magnetic disorder, respectively. As a consequence of the assumptions made above, the two competing candidate instabilities are the s^{++} and the s^{+-} phase characterized by $\widetilde{\Delta}_1(\Omega) = \widetilde{\Delta}_2(\Omega) =$ const. and $\widetilde{\Delta}_1(\Omega) = -\widetilde{\Delta}_2(\Omega) =$ const., respectively. As readily follows from Eq. (2.19), the former is topologically trivial while the latter is nontrivial.

In case of nonmagnetic disorder, the critical temperature of the s^{++} state is not affected by disorder in accordance with the original Anderson theorem [229–231]. As a consequence of the sign change between the Fermi surfaces, the transition temperature of the competing s^{+-} superconductor is reduced by disorder. As s^{++} dominates in the clean limit in case of electron-phonon pairing where $J < 0$, no transition to the topological s^{+-} state can be induced by nonmagnetic disorder.

This is different in case of magnetic impurities: Fig. 7.2(a) shows the transition temperatures of the s^{++} and s^{+-} superconductors as a function of the total amount of magnetic disorder γ_m. Despite being

dominant in the clean limit, the s^{++} state is more fragile against magnetic impurities since both inter- and intraband scattering act as pair breaking, while the s^{+-} superconductor is only prone to the latter type of scattering events as expected from the discussion in Sec. 7.1.2. This makes possible a finite range of impurity concentrations where the topological s^{+-} state is stabilized. For larger γ_m also the s^{+-} condensate is destroyed by disorder and no superconducting instability occurs at all.

The full phase diagram that shows the dependence on the ratio J/U of the interaction parameters for a fixed (negative) value of U can be found in Fig. 7.2(b). Here, $\rho_F := \sum_s \int \mathrm{d}\Omega \rho_s(\Omega)$ denotes the total density of states of the system and Λ is the energetic cutoff of the electron-phonon interaction. For completeness, we have also included positive values of J where s^{+-} is already dominant in the clean limit although $J > 0$ cannot be realized by pure electron-phonon coupling as has been shown in Sec. 6.1.1.

Since s^{++} and s^{+-} are degenerate for $J = 0$, the critical scattering rate $\rho_F \gamma_m^*$ for stabilizing a topological phase must go to zero as $J \to 0$. For small J/U, it varies linearly with J according to [cf. green line in Fig. 7.2(b)]

$$\rho_F \gamma_m^* \sim \frac{16}{\pi^2} \frac{J}{U} \frac{1}{\rho_F U} T_{c,0}^{++}, \tag{7.28}$$

where $T_{c,0}^{++}$ is the critical temperature of the s^{++} state in the clean limit.

If J is sufficiently strong, the critical temperatures of both s^{++} and s^{+-} will go to zero as a function of the magnetic scattering strength γ_m before a transition into the s^{+-} phase can occur. This gives rise to a critical ratio $(J/U)_c$ for the impurity-induced topological transition. One finds (for $U < 0$)

$$\big(J/U\big)_c = \frac{1}{\rho_F |U| \ln 2} \left(\sqrt{(\rho_F U \ln 2)^2 + 4} - 2 \right) \sim \frac{\ln 2}{4} \rho_F |U|, \qquad \rho_F |U| \ll 1, \tag{7.29}$$

showing that it scales linearly with U in the weak-coupling limit. Our mean-field approach predicts $(J/U)_c$ to approach 1 in the strong-coupling limit $\rho_F |U| \gg 1$.

Let us finally contrast the present discussion with Ref. [390], where magnetic scattering induces nontrivial topology with respect to a symmetry class with broken TRS: For the model considered in Ref. [390], a Zeeman field is required [391] to stabilize a topological superconductor. Our analysis shows that magnetic disorder can also drive the transition into a topological superconducting state that preserves TRS (class DIII). This means that while, locally, TRS is broken due to the presence of impurities it is restored globally in the sense that the resulting superconducting order parameter is time-reversal symmetric and that the impurities do not give rise to a net magnetic moment.

7.2.3 Protection of bound states

One major consequence of the topologically nontrivial DIII bulk invariant is the existence of gapless counter-propagating Kramers partners of Majorana modes at the interface of the superconductor to a topologically trivial phase such as the vacuum (see Chap. 2.2.3). The presence of these gapless modes is guaranteed by TRS. However, the magnetic impurities required to stabilize the bulk topology break TRS and might hence gap out the boundary states making them unobservable in experiments.

Let us first notice that, at least theoretically, there exists a parameter range where the disorder-induced gap in the surface spectrum is irrelevant. As can be seen in Eq. (7.28), the magnetic scattering rate required to induce a nontrivial bulk topology can be arbitrarily small as compared to the critical temperature and, hence, as compared to the gap of the superconductor at zero temperature. In this limit, the impact of the magnetic impurities on the Majorana modes can be neglected.

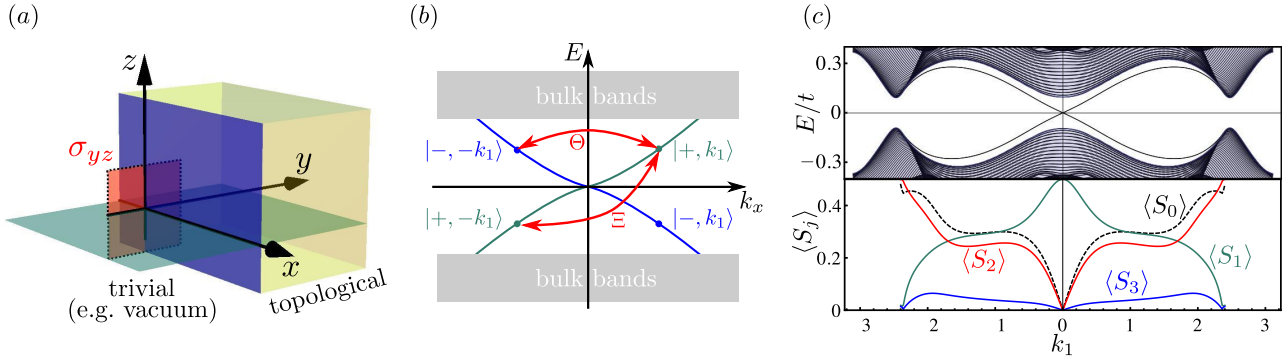

Figure 7.3: ***Protection of MBSs.*** *Point-symmetry protection of MBSs against magnetic impurities. In (a), the geometry of a boundary (blue plane) at $y = 0$ of two topologically distinct phases of a 2D system (xy plane) is shown. If both phases have point group C_{2v}, there will be a residual reflection symmetry (red plane). A schematic of the spectrum of the system with edge state dispersion shown in blue and green is presented in (b). Part (c) shows the spectrum (upper panel) of the model defined in the main text using open along the y and periodic boundary conditions along the x direction. Due to the protection resulting from TRS and the reflection symmetry at the boundary, the matrix elements (lower panel) of charge impurities ($\langle S_0\rangle$) and magnetic impurities polarized along y and z ($\langle S_2\rangle$ and $\langle S_3\rangle$) vanish at $k_1 = 0$. Here we use the same parameters as in Fig. 6.4, $\mu = -0.4t$, $\alpha = 0.25t$, for the normal-state Hamiltonian and choose $\Delta_t = 0.3t$, $\Delta_s = 0.1t$ for the superconducting order parameter.*

Secondly, unitary symmetries can protect the Kramers pair of MBSs even if TRS is broken. E.g., in the case of the 2D system with point group C_{2v}, the protection results from the residual reflection symmetry perpendicular to an interface along one of the crystallographic axes. To show this, let us assume that the system is located in the xy plane with a boundary to a trivial phase at $y = 0$ as illustrated in Fig. 7.3(a). The presence of two distinct phases breaks all symmetries of the point group except for the invariance under reflection σ_{yz} at the yz plane. Denoting the BdG Hamiltonian of the bulk system by $h^{\mathrm{BdG}}_{\boldsymbol{k}}$, the spectrum and wavefunctions of the edge modes are determined by

$$\widetilde{h}^{\mathrm{BdG}}_{k_1} |\pm, k_1\rangle = E_\pm(k_1) |\pm, k_1\rangle \,, \tag{7.30}$$

where $\widetilde{h}^{\mathrm{BdG}}_{k_1}$ follows from $h^{\mathrm{BdG}}_{\boldsymbol{k}}$ by replacing $k_2 \to -i\partial_y$ and introducing some y dependency to describe the boundary between the two topologically distinct phases. As illustrated in Fig. 7.3(b), PHS, $\Xi h^{\mathrm{BdG}}_{\boldsymbol{k}} \Xi^{-1} = -h^{\mathrm{BdG}}_{-\boldsymbol{k}}$ with antiunitary Ξ, and TRS of the BdG Hamiltonian lead to the constraints $E_\pm(k_1) = -E_\pm(-k_1)$ and $E_+(k_1) = E_-(-k_1)$ on the edge state spectrum, respectively (see also Chap. 2.1.1). Furthermore, PHS implies for the wavefunctions $\Xi |\pm, k_1\rangle = e^{i\alpha^\pm_{k_1}} |\pm, -k_1\rangle$ with some phases $\alpha^\pm_{k_1}$ and, in particular, $\Xi |\pm, 0\rangle = e^{i\alpha^\pm_0} |\pm, 0\rangle$ resulting from continuity in k_1. Denoting the spin operators in Nambu space by S_j, $j = 1, 2, 3$, and noting that $\Xi S_j \Xi^{-1} = -S_j$, we find

$$\langle \mu, 0|S_j|\mu', 0\rangle = -e^{i(\alpha^\mu_0 - \alpha^{\mu'}_0)} \langle \mu', 0|S_j|\mu, 0\rangle \tag{7.31}$$

with $\mu, \mu' = \pm$. From this, it already follows that the diagonal ($\mu = \mu'$) matrix elements of all spin operators S_j must vanish. To restrict the off-diagonal components ($\mu \neq \mu'$), the mirror symmetry has

to be taken into account. Under σ_{yz}, it holds $k_1 \to -k_1$ and $\mathcal{R}_{\sigma_{yz}} S_j \mathcal{R}_{\sigma_{yz}}^{-1} = p_j S_j$ with $p_1 = 1$ and $p_2 = p_3 = -1$ where $\mathcal{R}_{\sigma_{yz}} = \exp(-i\pi S_1)$ is the representation of σ_{yz} in Nambu space. It follows

$$\langle +, 0|S_j|-, 0\rangle = -p_j e^{-2i\alpha_0} \langle -, 0|S_j|+, 0\rangle , \tag{7.32}$$

where we have used $\mathcal{R}_{\sigma_{yz}} |+, k_1\rangle = e^{i\alpha_{k_1}} |-, -k_1\rangle$, $\alpha_{k_1} \in \mathbb{R}$, in the limit $k_1 \to 0$. The additional minus sign in Eq. (7.32) comes from $\mathcal{R}_{\sigma_{yz}}^2 = -\mathbb{1}$ which must hold for spin-1/2 fermions. Noting that $e^{2i\alpha_0} = e^{i(\alpha_0^- - \alpha_0^+)}$, which follows from $[\Xi, \mathcal{R}_{\sigma_{yz}}] = 0$, the combination of Eqs. (7.31) and (7.32) implies that

$$\langle \mu, 0|S_j|\mu', 0\rangle = 0 \tag{7.33}$$

for those component with $p_j = -1$, i.e., for $j = 2, 3$. This means that only impurities with finite spin polarization perpendicular to the mirror plane can open up a gap in the surface spectrum. This result is consistent with the numerical investigation of surface disorder in a model with C_{4v} symmetry in Ref. [392].

To further illustrate the protection of the MBSs resulting from the symmetries of the system, let us investigate the standard Rashba single-band model defined by $\epsilon_{\boldsymbol{k}} = -t(\cos k_1 + \cos k_2) - \mu$ and $\boldsymbol{g}_{\boldsymbol{k}} = \alpha(-\sin k_2, \sin k_1, 0)^T$ in Eq. (7.24) and Fermi surfaces as shown in Fig. 6.4. A natural Brillouin-zone regularization of the weak-pairing description of the s^{+-} superconductor is given by the mean-field pairing term in Eq. (7.1) with pure triplet component $\Delta_{\boldsymbol{k}} = \Delta_t \boldsymbol{g}_{\boldsymbol{k}} \cdot \boldsymbol{\sigma} i\sigma_2/\alpha$. In the upper panel of Fig. 7.3(c), we show the spectrum of the system with periodic boundary conditions along the x and open boundary condition along the y axis (100 sites), where, for the sake of generality, also a small singlet component $\Delta_t i\sigma_2$ has been added. The edge state dispersions (doubly degenerate corresponding to the two edges of the system) crossing the Fermi level are clearly visible. In the lower panel of Fig. 7.3(c), the maximum of the impurity matrix elements with respect to the subgap states at given k_1 is shown for both nonmagnetic, $\langle S_0\rangle$, as well as magnetic, $\langle S_j\rangle$, $j = 1, 2, 3$, scatterers localized at one of the boundaries. We see that $\langle S_0\rangle$ vanishes for $k_1 \to 0$ which is just a manifestation of the protection of the edge states resulting from TRS [262]. Furthermore, also $\langle S_2\rangle$ and $\langle S_3\rangle$ vanish, in accordance with our general symmetry discussion above, whereas $\langle S_1\rangle$ assumes a finite value at $k_1 = 0$.

Consequently, if the impurities are, e.g., mainly polarized perpendicular to the plane of 2D system, $\gamma_{\parallel}^{(1,2)} = 0$ in Eq. (7.26), a transition to a topological DIII superconductor can be induced by varying $\gamma_{\perp}$ without gapping the resulting boundary modes as long as the edges are along one of the crystallographic axes. Naturally, the same protection mechanism applies for all point groups C_{nv}, $n = 1, 2, 3, 4, 6$, as long as the boundary is oriented perpendicular to one of the mirror planes of the bulk system.

7.3 Disorder in LAO/STO heterostructures

As one of the central results of Chap. 5, two candidate pairing states for the (001) oxide heterostructures have been established: In case of a conventional mechanism, the order parameter is identical on the two spin-orbit-split Fermi surfaces (see Fig. 5.4), i.e., $\widetilde{\Delta}_s(\boldsymbol{k}) = \Delta_0$ denoted by s^{++}. In contrast, an unconventional mechanism leads to the s^{+-} state characterized by $\widetilde{\Delta}_s(\boldsymbol{k}) = (-1)^s \Delta_0$ [349]. From our discussion of the generalized Anderson theorem in Sec. 7.1, we have already obtained a qualitative understanding of the stability of these two superconducting phases against certain disorder configurations. In this section, which is based on Ref. [240], these expectations will be confirmed and supplemented quantitatively by an explicit microscopic analysis of the impact of impurity scattering on the two candidate pairing states.

Table 7.1: *Symmetry properties of the basis functions constructed from the Pauli matrices in spin and orbital space denoted by σ_j and τ_j, respectively. Here A_1, A_2, B_1, B_2 and E denote the IRs of C_{4v} (see Table 4.1), whereas TRE (TRO) indicates that the matrix is even (odd) under time-reversal.*

$\otimes$	σ_0	σ_1, σ_2	σ_3
τ_0	A_1/TRE	E/TRO	A_2/TRO
τ_1	B_2/TRE	E/TRO	B_1/TRO
τ_2	A_2/TRO	E/TRE	A_1/TRE
τ_3	B_1/TRE	E/TRO	B_2/TRO

7.3.1 Microscopic disorder configurations

Let us first discuss the possible microscopic disorder configurations by specifying the most general disorder correlator Γ in Eq. (7.12) within the two-orbital model of the Ti $3d_{xz}$ and $3d_{yz}$ states introduced in Chap. 5.1.1. Recall from Chap. 1.4.1 that, although a local defect can break any subset of the symmetries of the system, the symmetries must be restored on average forcing the disorder correlator to satisfy Eq. (1.28). We will represent the basis matrices $\{w_\mu\}$ in the expansion (7.13) of Γ as the 16 possible tensor products of the Pauli matrices σ_j and τ_j, $j = 0, 1, 2, 3$, referring to the spin and orbital degrees of freedom exactly as in, e.g., Eq. (5.3). Using Pauli matrices constitutes a particularly convenient choice since these basis matrices both transform under the IRs of the point group C_{4v} and are either even (TRE) or odd (TRO) under time-reversal as summarized in Table 7.1.

Nonmagnetic disorder. We start with nonmagnetic impurities characterized by basis matrices satisfying Eq. (7.14) with $t_d = +$. As readily follows from Table 7.1, the most general vertex reads in this case as

$$\begin{aligned}\Gamma_{\alpha_1\alpha_1',\alpha_2\alpha_2'} = {}& \gamma_{A_1}^{\mathrm{I}} \left(\tau_0\sigma_0\right)_{\alpha_1\alpha_1'} \left(\tau_0\sigma_0\right)_{\alpha_2\alpha_2'} + \gamma_{A_1}^{\mathrm{II}} \left(\tau_2\sigma_3\right)_{\alpha_1\alpha_1'} \left(\tau_2\sigma_3\right)_{\alpha_2\alpha_2'} \\ & + \frac{\gamma_{A_1}^{\mathrm{III}}}{2} \left[\left(\tau_0\sigma_0\right)_{\alpha_1\alpha_1'} \left(\tau_2\sigma_3\right)_{\alpha_2\alpha_2'} + \left(\tau_2\sigma_3\right)_{\alpha_1\alpha_1'} \left(\tau_0\sigma_0\right)_{\alpha_2\alpha_2'}\right] \\ & + \gamma_{B_1} \left(\tau_3\sigma_0\right)_{\alpha_1\alpha_1'} \left(\tau_3\sigma_0\right)_{\alpha_2\alpha_2'} + \gamma_{B_2} \left(\tau_1\sigma_0\right)_{\alpha_1\alpha_1'} \left(\tau_1\sigma_0\right)_{\alpha_2\alpha_2'} \\ & + \frac{\gamma_E}{2} \left[\left(\tau_2\sigma_1\right)_{\alpha_1\alpha_1'} \left(\tau_2\sigma_1\right)_{\alpha_2\alpha_2'} + \left(\tau_2\sigma_2\right)_{\alpha_1\alpha_1'} \left(\tau_2\sigma_2\right)_{\alpha_2\alpha_2'}\right].\end{aligned} \tag{7.34}$$

Similarly to the Rashba-Dresselhaus effect in Eq. (5.3), we see again that the combination of both orbital and spin degrees of freedom leads to a much richer structure of possible terms as in case of only spin (cf. Eq. (7.25)). To gain physical insight into Eq. (7.34), let us first discuss the meaning of the different terms and then analyze how they can emerge microscopically.

The contributions proportional to $\gamma_{A_1}^{\mathrm{I}}$, γ_{B_1} and γ_{B_2} correspond to spin-trivial disorder with orbital wavefunctions of different point symmetry: The different terms transform as A_1, B_1 and B_2 under C_{4v} which corresponds to s, $d_{x^2-y^2}$, and d_{xy} wave. Noting that τ_2 is the projection of the z-component of the orbital angular momentum operator on the subspace spanned by the $3d_{xz}$ and $3d_{yz}$ orbitals (see Appendix D.1.2), the terms with $\gamma_{A_1}^{\mathrm{II}}$ and γ_E represent (atomic) spin-orbit disorder with out-of-plane/longitudinal and in-plane/transversal orientation of the spin, respectively. The prefactors of the

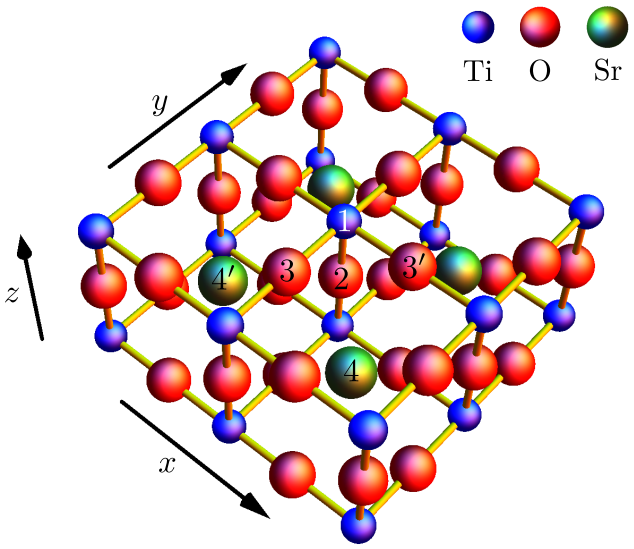

Figure 7.4: ***Ball-and-stick model of STO.*** *Four unit cells of the crystal structure of STO are shown. Different positions which are referred to in the main text are indicated by numbers.*

two terms in the last line of Eq. (7.34) must be identical in order to ensure C_4-rotation symmetry of the disorder distribution. Finally, the contribution proportional to $\gamma_{A_1}^{\mathrm{III}}$ describes the fact that the C_{4v} point group allows for an mixture of s-wave disorder and longitudinal spin-orbit disorder on the same site.

To understand how the different terms can be realized microscopically, let us investigate the schematic illustration of the crystal structure in Fig. 7.4. We begin with oxygen vacancies, which are discussed as one of the primary causes of disorder in the context of LAO/STO interfaces (see, e.g., Refs. [143, 153–155]). Assume that one oxygen at position 2, right below the central Ti at position 1, is vacant. In this case, the defect preserves the full C_{4v} point symmetry of the crystal such that only the first 3 terms in Eq. (7.34) can be present. The explicit values of $\gamma_{A_1}^{\mathrm{I}}$, $\gamma_{A_1}^{\mathrm{II}}$ and $\gamma_{A_1}^{\mathrm{III}}$ depend on microscopic details of the system, however, as will be seen below in Sec. 7.3.2, only the sum of these scattering rates enters the effective pair-breaking strength. If instead an oxygen adjacent to the central Ti, e.g., at position 3, is vacant, all point symmetries of the lattice are locally broken except for the mirror symmetry with respect to the yz plane. This symmetry constraint rules out the contribution proportional to γ_{B_2} and the first term in the last line of Eq. (7.34) as both $\tau_1\sigma_0$ and $\tau_2\sigma_1$ are odd under $(x, y) \to (-x, y)$. Correspondingly, if we consider oxygen vacancies at position $3'$, the second term in the last line of Eq. (7.34) and again the contribution with γ_{B_2} will be forbidden. Recalling that the prefactors of the two terms in the last line of Eq. (7.34) have to be equal by C_4 rotation symmetry, we see that, as expected, vacancies at position 3 and $3'$ have to be included with equal probability to restore the full point symmetry after averaging. In summary, single oxygen vacancies allow for all contributions in Eq. (7.34) except for the γ_{B_2} term.

To see how the latter can occur, let us now assume that a Sr atom is vacant, e.g., at position 4 in Fig. 7.4. Similarly as above, all point symmetries are broken save for the mirror reflection at the (110) plane. This now renders the γ_{B_2} term possible which is even under the reflection at (110). Assuming

that, with the same probability, a Sr atom is missing at position $4'$, one restores rotation symmetry. In this case, all terms in Eq. (7.34) are allowed except for the one proportional to γ_{B_1}. Finally, we note that the same is true for a local oxygen double vacancy where oxygen atoms are missing at position 3 and $3'$ at the same time.

We have thus provided examples of how all the terms in the most general nonmagnetic impurity vertex (7.34) can be realized.

Magnetic disorder. To proceed with magnetic disorder, i.e., focusing on $t_d = -$ in Eq. (7.14), Table 7.1 implies that there are three independent terms in Γ corresponding to in-plane magnetic moments,

$$\begin{aligned}\Gamma^{\parallel}_{\alpha_1\alpha_1',\alpha_2\alpha_2'} = &\frac{\gamma_E^{\mathrm{I}}}{2}\left[(\tau_0\sigma_1)_{\alpha_1\alpha_1'}(\tau_0\sigma_1)_{\alpha_2\alpha_2'} + (\tau_0\sigma_2)_{\alpha_1\alpha_1'}(\tau_0\sigma_2)_{\alpha_2\alpha_2'}\right]\\ &+\frac{\gamma_E^{\mathrm{II}}}{2}\left[(\tau_1\sigma_1)_{\alpha_1\alpha_1'}(\tau_1\sigma_1)_{\alpha_2\alpha_2'} + (\tau_1\sigma_2)_{\alpha_1\alpha_1'}(\tau_1\sigma_2)_{\alpha_2\alpha_2'}\right]\\ &+\frac{\gamma_E^{\mathrm{III}}}{2}\left[(\tau_3\sigma_1)_{\alpha_1\alpha_1'}(\tau_3\sigma_1)_{\alpha_2\alpha_2'} + (\tau_3\sigma_2)_{\alpha_1\alpha_1'}(\tau_3\sigma_2)_{\alpha_2\alpha_2'}\right],\end{aligned} \tag{7.35a}$$

and five terms,

$$\begin{aligned}\Gamma^{\perp}_{\alpha_1\alpha_1',\alpha_2\alpha_2'} = &\gamma_{A_2}^{\mathrm{I}}(\tau_0\sigma_3)_{\alpha_1\alpha_1'}(\tau_0\sigma_3)_{\alpha_2\alpha_2'} + \gamma_{B_1}(\tau_1\sigma_3)_{\alpha_1\alpha_1'}(\tau_1\sigma_3)_{\alpha_2\alpha_2'}\\ &+\gamma_{B_2}(\tau_3\sigma_3)_{\alpha_1\alpha_1'}(\tau_3\sigma_3)_{\alpha_2\alpha_2'} + \gamma_{A_2}^{\mathrm{II}}(\tau_2\sigma_0)_{\alpha_1\alpha_1'}(\tau_2\sigma_0)_{\alpha_2\alpha_2'}\\ &+\frac{\gamma_{A_2}^{\mathrm{III}}}{2}\left[(\tau_2\sigma_0)_{\alpha_1\alpha_1'}(\tau_0\sigma_3)_{\alpha_2\alpha_2'} + (\tau_0\sigma_3)_{\alpha_1\alpha_1'}(\tau_2\sigma_0)_{\alpha_2\alpha_2'}\right],\end{aligned} \tag{7.35b}$$

where the magnetic moment is oriented perpendicular to the plane.

Physically, the three terms γ_E^{I}, γ_E^{II} and γ_E^{III} in $\Gamma^{\parallel}$ correspond to impurities with in-plane spin magnetization and distinct orbital symmetry (s, d_{xy} and $d_{x^2-y^2}$ wave). Note that no orbital-magnetic disorder with in-plane orientation can occur in the two-orbital model as the projection of the x and y component of the orbital angular momentum operator onto the $3d_{xz}$ and $3d_{yz}$ subspace vanishes identically (see Appendix D.1.2). The analogous terms in $\Gamma^{\perp}$ with the same orbital symmetry but spin polarization along the z direction are proportional to $\gamma_{A_2}^{\mathrm{I}}$, γ_{B_1} and γ_{B_2}, respectively. Finally, $\gamma_{A_2}^{\mathrm{II}}$ corresponds to purely orbital magnetism along the z direction and $\gamma_{A_2}^{\mathrm{III}}$ shows that an arbitrary mixture of spin and orbital magnetism along the z direction is allowed by symmetry.

As in the nonmagnetic case, let us discuss some examples of how the terms in Eq. (7.35) can emerge microscopically. One can imagine that a Ti atom locally orders magnetically due to the proximity of the system to a competing magnetic instability [349] similarly to the discussion of imaginary CDW impurities in the context of iron-based superconductor in Sec. 7.1.2. Numerical calculations indicate [153, 155] that magnetic moments on Ti atoms can be induced by the presence of oxygen vacancies. Alternatively, we may think of Ti being replaced by a different magnetic atom. In all cases, the form of the resulting impurity potential crucially depends on the orbitals that host the magnetic moment and whether it is orbital or spin magnetism. Thus, in general, all terms in Eq. (7.35) are feasible. To be more specific, recalling that the observed magnetism at the interface is mainly due to the $3d_{xy}$ band [111, 151, 152, 346, 347], one may expect that, most likely, the spin degree of freedom of the Ti $3d_{xy}$ orbital orders locally. In that case, the impurity vertex would be described by the terms proportional γ_E^{II} and γ_{B_1} as the associated orbital structure, τ_1, transforms as xy under C_{4v}.

If, instead, a magnetic moment develops at a site that does not lie at a high symmetry point with respect to the Ti atoms, the symmetry constraints will be less restrictive. Assuming, e.g., a spin-magnetic moment along the z axis with s-wave orbital symmetry (i.e. $\tau_0\sigma_3$) at the oxygen site 3 ($3'$) in Fig. 7.4, the disorder potential is only restricted to be odd both under time-reversal and mirror reflection symmetry with respect to the yz plane (xz plane). The reduction of symmetry constraints simply follows from the fact that, irrespective of the symmetries of the local impurity, the presence of a perturbation at 3 ($3'$) already breaks all symmetries except for time-reversal and one mirror reflection. Under these two remaining symmetry operations, the resulting impurity potential in the effective model for the conducting Ti orbitals must have the same behavior as $\tau_0\sigma_3$ (in both cases being odd). From these criteria one finds that only the term proportional to γ_{B_1} can be excluded in Eq. (7.35).

7.3.2 Impact of disorder on transition temperatures

After having discussed the plethora of possible microscopic scattering processes, let us proceed by investigating the impact on the transition temperature of both the conventional s^{++} and the unconventional s^{+-} pairing state in oxide heterostructures.

For this purpose, we use the same low-energy approach as in Chap. 5.1.2 and only keep the fermionic modes belonging to the 16 nested patches of the Fermi surfaces highlighted in green and red in Fig. 7.5(a) as dynamical degrees of freedom (see also Fig. 5.1). The disorder correlator Γ given by Eqs. (7.34) and (7.35) in the microscopic basis for nonmagnetic and magnetic disorder, respectively, is transformed into the patch basis. To obtain results that only depend on the most relevant set of parameters, the wavefunctions are assumed to be constant within each patch and taken to have a spin orientation along one of the coordinate axis and to be either of $3d_{xz}$ or $3d_{yz}$ character. This constitutes a very good approximation as can be seen in Fig. 5.1(b) and (c). Apart from these assumptions, all possible impurity scattering processes between the patches are taken into account such that $\mathcal{S}^F$ and $\mathcal{S}^S$ in Eqs. (7.18) and (7.19) effectively become 16×16 matrices. To describe the superconducting instability, we focus on the pair hopping interaction in Fig. 5.2(d) or, put differently, set $\mathcal{V}_{12} = \mathcal{V}_{21} = J$ and $\mathcal{V}_{ss} = 0$ in Eq. (7.15). Furthermore, the density of states is taken to be the same on both Fermi surfaces. Similarly to Sec. 7.2.2, the superconducting phase competition can be analyzed in the presence of disorder by summing up the diagrams in Fig. 7.2. In the following, we just discuss the main results and refer to Ref. [240] for the details of the calculation.

Universality. Despite the complicated structure of the disorder correlator in Eqs. (7.34) and (7.35), the impurity distribution enters in the Ginzburg-Landau expansion only in form of the combined scattering rate

$$\gamma_0 = \gamma_{A_1}^{\mathrm{I}} + \gamma_{A_1}^{\mathrm{II}} + \gamma_{B_1} + \gamma_{B_2} + \gamma_E \tag{7.36a}$$

for nonmagnetic disorder and

$$\gamma_m = \gamma_E^{\mathrm{I}} + \gamma_E^{\mathrm{II}} + \gamma_E^{\mathrm{III}} + \gamma_{A_2}^{\mathrm{I}} + \gamma_{A_2}^{\mathrm{II}} + \gamma_{B_1} + \gamma_{B_2} \tag{7.36b}$$

in case of magnetic scattering. We see that all couplings in Eqs. (7.34) and (7.35) enter just as a sum except for the mixing terms $\gamma_{A_1}^{\mathrm{III}}$ and $\gamma_{A_2}^{\mathrm{III}}$ which do not enter at all. This means that the impact of disorder on superconductivity does not depend on the relative weight and on the symmetry-allowed mixing of the different scattering processes describe above and, hence, becomes widely independent of the microscopic details of the impurities considered. This "universality" of the impact of disorder is a consequence of our approximation of perfectly polarized wavefunctions in the nested patches of the

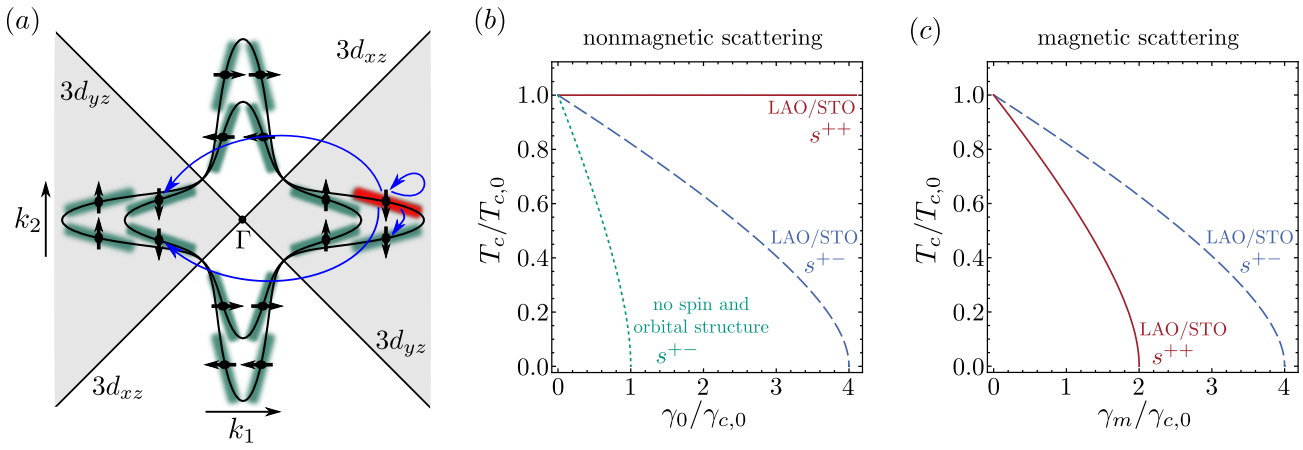

Figure 7.5: ***Patches and suppression of*** T_c***.*** *The 16 patches of the Fermi surfaces of the two-orbital model derived in Chap. 5.1.1 are illustrated schematically in (a) together with their orbital (shading) and spin (arrows) polarization. The blue arrows indicate the allowed scattering processes associated with* $\gamma^I_{A_1}$ *in Eq. (7.34) for an electron in the red patch. Part (b) and (c) show the suppression of the critical temperature* T_c *as a function of the nonmagnetic (*γ_0*) and magnetic (*γ_m*) scattering rate as calculated in Ref. [240].* $T_{c,0}$ *and* $\gamma_{c,0}$ *are the critical temperature of the clean system and the critical reference scattering strength defined in the main text.*

Fermi surface. In particular, the fact that $\gamma^{\mathrm{III}}_{A_1}$ in Eq. (7.34) does not enter is very easily seen from Eqs. (7.18) and (7.19) and the schematic illustration of the wavefunction polarization in Fig. 7.5(a): As the two scattered fermions either both switch or both keep their orbital character, either $\tau_0\sigma_0$ or $\tau_2\sigma_3$ yields zero in $\mathcal{S}^F$ and $\mathcal{S}^S$.

Nonmagnetic disorder. In case of nonmagnetic scattering, we find the behavior summarized in Fig. 7.5(b): The transition temperature of the s^{++} state, realized for attractive interactions ($J < 0$), is not affected by disorder as expected from the original Anderson theorem [229–231]. Due to the sign change of the order parameter between the Fermi surfaces, the s^{+-} superconductor ($J < 0$) is suppressed by disorder with the critical temperature T_c decaying according to $T_c/T_{c,0} = f(\gamma_0/\gamma_c)$ with increasing disorder strength γ_0 defined in Eq. (7.36a). Here $T_{c,0}$ is the critical temperature in the absence of disorder and f the functional dependence originally found by Abrikosov-Gorkov [101] for a BCS superconductor under the influence of spin-magnetic disorder normalized according to $f(0) = 1$ and $f(1) = 0$. Most importantly, the critical scattering rate γ_c is four times larger than the critical scattering rate $\gamma_{c,0}$ of a reference model where the patch wavefunctions are assumed to allow for electrons to scatter between all patches (without breaking TRS). In more physical terms, it corresponds to a model with the same band structure but without both spin and orbital degrees of freedom. The enhancement of the critical scattering rate by a factor of four can be readily understood by reexamination of the patch wavefunctions illustrated in Fig. 7.5(a). Assuming, for simplicity, s-wave impurities without spin structure described by the first term in Eq. (7.34), we see that an electron, e.g., in the red patch in Fig. 7.5(a), cannot scatter into a state belonging to the perpendicular lobes of the Fermi surface as a consequence of the orbital polarization. In addition, within the same lobe, only half of the possible patches can be reached as indicated by the arrows which results from the spin orientation of the

wavefunctions on the Fermi surfaces. This mechanism of protection against impurity scattering can in principle even rule out all pair-breaking scattering processes in a system as has been shown in Ref. [237].

Magnetic disorder. In full agreement with our discussion in Sec. 7.1.2 and Sec. 7.2.2, we find that both superconducting states are suppressed by disorder in case of magnetic impurities with s^{++} being prone to both intra- and interband scattering while the s^{+-} state is protected again interband processes. The explicit calculation of this section shows that this enhances the stability of s^{+-} by a factor of two compared to the s^{++} state as can be seen in Fig. 7.5(c). Note that this result does not depend on the relative weight of the different scattering channels in Eq. (7.35) since only their sum enters γ_m in Eq. (7.36b). The critical temperatures again follow the Abrikosov-Gorkov law [101].

Due to the aforementioned important role of magnetic disorder in oxide heterostructures [143, 153–155], the unconventional s^{+-} state cannot be ruled out by the presence of disorder, e.g., resulting from oxygen vacancies at the interface. If, indeed, magnetic scattering is the dominant source of disorder in the superconducting samples, the s^{+-} state will even be more stable and, hence, constitutes a more likely candidate than its conventional counterpart s^{++}.

7.4 Summary of Chapter 7

In this chapter, we have complemented our analysis of superconducting instabilities in Chaps. 4–6 with respect to the impact of weak disorder, i.e., disorder that does not cause localization in the vicinity of the Fermi surface (requires $k_F l \gg 1$ and $R_l \gg 1/\sqrt{T_c \rho_F}$ [227]).

From the criterion that the superconducting gap is not reduced by a given disorder realization, we have derived the compact form (7.7) of the generalized Anderson theorem. It states that a superconducting phase is protected against disorder if its order parameter $\Delta T^\dagger$ commutes with the TRE and anticommutes with the TRO component of the disorder potential. This condition is consistent with several explicit calculations [235–240].

As an example of a multiband system with doubly degenerate Fermi surfaces, we have discussed the iron-based superconductors [26]. Most interestingly, Eq. (7.7) implies that the unconventional s^{+-} state is protected against magnetic interband scattering which is confirmed by the calculations of Refs. [238, 239]. Magnetic impurities of purely interband character might be realized in iron-based superconductors by nucleation [386, 387] of a particle-hole instability competing [351, 381, 382] with s^{+-} in the vicinity of the a initially nonmagnetic defect [239]. As the conventional s^{++} state is prone to the resulting magnetic scatterers, this puts the connection [241] between the stability against seemingly nonmagnetic impurities and conventional pairing in question.

For the case of singly degenerate Fermi surfaces, which is particularly relevant for this thesis, we have also provided a diagrammatic proof of Eq. (7.7). In addition, we have shown that the necessary condition or "design principle" for TRS-breaking superconductivity in 2D systems [325, 326] discussed in Chap. 4.4.1 also holds in the presence of both nonmagnetic and magnetic impurities.

Furthermore, it has been shown by way of an explicit 2D example that magnetic disorder can drive a phase transition from a topologically trivial superconductor with TRS, e.g., resulting from electron-phonon coupling (see Chap. 6.1), to a time-reversal symmetric topological phase. It leads to the at first sight counterintuitive conclusion that magnetic impurities can stabilize a topological phase that is based on TRS (class DIII, see Chap. 2.1). The resulting MBSs are still necessarily gapless as long as the edge of the system is oriented perpendicular to one of the mirror planes of the point group of the bulk and the magnetic moments of the impurities are oriented perpendicular to the plane of the

system.

Finally, we have studied the stability against disorder of the two candidate pairing states of LAO/STO heterostructures – the conventional, topologically trivial s^{++} and the unconventional, nontrivial s^{+-} superconductor deduced microscopically in Ref. [349] (see Chap. 5). Within the two-orbital model of the Ti $3d_{xz}$ and $3d_{yz}$ states discussed in Chap. 5.1.1, there are various possible microscopic scattering channels as can be seen in the impurity vertices (7.34) and (7.35) for nonmagnetic and magnetic disorder, respectively. However, the different coupling constants just enter in form of the combined scattering rates (7.36) as a consequence of the strong orbital and spin polarization of the wavefunctions in the relevant parts of the Fermi surfaces (see Fig. 7.5(a)). The impact of nonmagnetic and magnetic scattering on the transition temperatures calculated in Ref. [240] is summarized in Fig. 7.5(b) and (c), respectively. Most importantly, it is found that the critical scattering rate of the unconventional s^{+-} superconductor is enhanced by a factor of four due to the orbital and spin polarization of the states at the Fermi surface. Furthermore, it is by a factor of two more stable against magnetic disorder than its conventional counterpart s^{++} resulting from its protection against magnetic interband scattering. Similarly to the discussion of TRS breaking at initially nonmagnetic impurities in iron-based superconductors [239], competing magnetic phases can occur at, e.g., oxygen vacancies due to the strong tendency of the system towards magnetism as has been shown numerically [153, 155]. From this it follows that, despite the inevitable presence of disorder at the interface, the unconventional topologically nontrivial s^{+-} phase remains a potential candidate pairing state.

Conclusion

In this thesis we have analyzed interaction- and disorder-induced phase transitions with a particular emphasis on the relation between the changes of *symmetry* as well as of *topology* and the *mechanism* responsible for the instability of the system. In this chapter, we will summarize the main results and briefly discuss related further research projects.

Chap. 3 was concerned with the "simulation" of topological insulator phases in cold-atom systems with the long-term goal of studying the impact of strong electronic repulsion on topological band structures and the experimental realization of exotic interacting topological phases such as the TMI (see Sec. 2.4.2). As a first step, we presented a noninteracting minimal model that can be implemented in cold-atom experiments [285, 286, 288] and allows realizing 2D time-reversal symmetric topological phases (QSH and trivially insulating) as well as its 3D analogues, the STI, the WTI and topologically trivial states. The crossover between 2D and 3D can be conveniently controlled by varying a single parameter in the Hamiltonian. In the second step, we have analyzed the impact of electron-electron interactions within slave-rotor theory [65–67] in the 3D limit of the system. As local Hubbard interactions turned out to lead to Mott phases with a gapless spinon spectrum, we had to study nonlocal interactions in order to find TMI states. We have discussed how these interactions can be realized experimentally. The main idea is to encode the pseudospin degree of freedom spatially. The resulting phase diagram (see Fig. 3.3(a) and (b)) contains both strong and weak TMI phases.

The central topic of Chap. 4 has been the derivation of general selection rules for superconducting instabilities in 2D and 3D systems with nondegenerate Fermi surfaces. The results are general in the sense that they only rely on the symmetries and the energetic splitting E_{so} of the Fermi surfaces of the high-temperature phase. The selection rules are valid as long as (1) the superconducting state is reached by a single phase transition from a time-reversal symmetric normal state, (2) no spontaneous translation symmetry breaking takes place at the superconducting phase transition and (3) the splitting E_{so} is larger than the zero-temperature gap or, equivalently, the transition temperature (times a factor of order 1).

The main results are the following: An order parameter transforming under a multidimensional or complex IR (see Chap. 1.1.1) of the point group of the high-temperature phase must necessarily break TRS. Consequently, if (1)–(3) are valid, the IR of the order parameter being multidimensional or complex is not only a necessary [81] but also a sufficient condition for TRS breaking. While this result indicates that the splitting of the Fermi surfaces enhances the tendency of the system towards the formation of a TRS-breaking condensate, there are additional strong restrictions on spontaneous TRS breaking for the special case of 2D systems. Geometrically, these constraints follow from the fact that inversion can be realized as a rotation in a 2D system. We have shown that the presence of a threefold rotation symmetry in the normal state is a necessary condition for spontaneous TRS breaking at a superconducting transition. It shows that TRS-breaking superconductivity is a particularly rare phenomenon in 2D given that inversion symmetry is very naturally broken in the experimental realization of 2D systems (see Chap. 1.3). At the same time, the result can be read as a "design principle" in the search for exotic 2D pairing states with broken TRS. Furthermore, we have seen that the triplet vector

will be necessarily aligned parallel to the plane of the 2D system, if the point group of the normal state contains a twofold rotation perpendicular to the plane.

We have illustrated these general results taking five different materials, Sr_2RuO_4, UPt_3, URu_2Si_2, LAO/STO heterostructures as well as FeSe on STO, as examples (see Chap. 1.3 for an introduction). Most notably, the results discussed above imply that TRS, which is broken [47, 51, 53] in the bulk superconducting state of Sr_2RuO_4, must be restored and its triplet vector, oriented along the [001] direction in the bulk [47, 51, 53, 188, 189], must rotate to lie in the (001) plane for a thin layer [68] of this material grown along the [001] direction. It has been argued that the same is expected to hold in the vicinity of (001) surfaces of Sr_2RuO_4. We have investigated all remaining possible pairing states of thin layers of Sr_2RuO_4 and concluded that it represents a promising system for the observation of Majorana modes. Note that the presence of TRS forces them to come in counter-propagating Kramers pairs. While the point group of thin layers of UPt_3 [69] contains a threefold rotation symmetry and, hence, TRS-breaking superconductivity cannot be excluded, we have shown how the selection rules can be used in order to reduce the number of 10 symmetry-allowed pairing states to only 3 energetically favorable candidates (see Table 4.4).

In case of LAO/STO heterostructures, which display conducting behavior [35, 142, 156] for the three different orientations (001), (110), and (111), the selection rules stated above directly imply that only in the latter orientation TRS-breaking superconductivity is possible. This motivates a closer experimental inspection of the less-studied (111) interface for which superconducting behavior has not yet been reported. In conjunction with the experimental observation [70] of the absence of nodes on the Fermi surfaces, we could fully determine the symmetry properties of the order parameter of the (001) interface, i.e., its relative phase on a given Fermi surface.

However, the selection rules neither yield information on the relative sign of the order parameter between the different Fermi surfaces nor on the mechanism driving the superconducting instability. For this purpose, we have performed a microscopic calculation for the (001) LAO/STO heterostructure which has been presented in Chap. 5. As a first step, an effective low-energy model for the electron liquid, that is motivated by various experimental observations (see Sec. 5.1), has been derived. In order to provide an unbiased analysis, all symmetry-allowed interaction processes are taken into account and the phase competition between all possible superconducting and density-wave instabilities of the effective model is analyzed using a Wilson-RG calculation. We find two possible pairing states as summarized in Fig. 5.4. In case of dominant electron-phonon coupling, i.e., a conventional mechanism, the s^{++} superconductor, where the order parameter has the same sign on the two spin-orbit-split Fermi surfaces, is realized. This phase has been shown to be topologically trivial. Assuming an unconventional mechanism, where the microscopically repulsive electron-electron interaction dominates, the s^{+-} state is the leading instability. The s^{+-} superconductor is characterized by a sign change between the two Fermi surfaces and is topologically nontrivial. This establishes a one-to-one correspondence between the mechanism and the topology of superconductivity in LAO/STO heterostructures. Experimental signatures (see Chap. 5.2.2) of Majorana modes, e.g., at the edge of the system, would represent an important result on its own. On top of that, it would also give direct hints on the unknown mechanism of superconductivity in this system.

In addition, we have seen that the competing density wave instabilities show very interesting spatial textures including vortex as well as Skyrmion lattices (see Fig. 5.6).

In Chap. 6, we have generalized the connection between the mechanism and topology of superconductivity found for LAO/STO heterostructures by investigating an arbitrary noncentrosymmetric system where the assumptions (1)–(3) defined above apply. The instabilities have been derived using Eliashberg theory [71, 72] and the topological classification has been performed using the full Green's function

which includes effects beyond the mean-field level (see Chap. 2.4.1). The main findings are the following. In case of a conventional pairing mechanism, i.e., superconductivity induced by electron-phonon coupling alone, the resulting superconducting state will generally be fully gapped, neither break any point group symmetry nor TRS and be topologically trivial. Consequently, the observation of topological signatures as well as spontaneous TRS breaking directly implies that the pairing mechanism must be unconventional. To describe unconventional pairing, we used the effective fluctuation approach of Refs. [31, 32] where the superconducting instability is driven by particle-hole fluctuations of a competing density-wave instability (see Chap. 6.2.1). We have shown that the time-reversal and topological properties of the resulting superconductor are crucially determined by the behavior of the order parameter of the competing instability under time-reversal. For an order parameter that is even under time-reversal, i.e., nonmagnetic such as a (real) CDW, exactly the same holds as in case of electron-phonon-induced pairing. Only for a competing instability with a magnetic (time-reversal-odd) order parameter, e.g., a (real) SDW, spontaneous point symmetry and TRS breaking as well as nontrivial topologies are possible.

To deduce guiding principles for the search of topologically nontrivial superconductors, we have derived an asymptotic symmetry of the Eliashberg equations that holds as long as the spin-orbit splitting is much smaller than the bandwidth. It follows that all superconducting order parameters can be classified into "Rashba even" and "Rashba odd" states in analogy to the classification into even and odd states of centrosymmetric systems (see Chap. 6.2.4 for a definition). It has been shown that only "Rashba odd" states can be topologically nontrivial which imposes necessary conditions for the emergence of nontrivial invariants. For instance, a 2D superconductor can only be topologically nontrivial if the total number of points in the Brillouin zone satisfying $\boldsymbol{k} = -\boldsymbol{k}$ enclosed by spin-orbit-split pairs of bands is odd. This criterion is readily accessible experimentally (e.g., via ARPES), in particular, since the spin-splitting does not have to be resolved.

We have illustrated the consequences of these general statements for LAO/STO heterostructures as well as for FeSe on STO. It confirms and complements the results of the calculation for the (001) oxide heterostructure presented in Chap. 5. For instance, it naturally explains why the topologically trivial (nontrivial) s^{++} (s^{+-}) superconductor mainly competes with a CDW (SDW) instability (see Fig. 5.5). Furthermore, also the (110)-oriented interface satisfies the necessary requirements for topological superconductivity and, hence, constitutes an interesting candidate system for the investigation of Majorana physics. The Fermi surface topology of FeSe (see Fig. 1.4(b)) represents an example where the necessary conditions for topological superconductivity are not satisfied.

The last chapter of the thesis, Chap. 7, was concerned with complementing the discussion of Chaps. 4–6 with respect to the inclusion of weak disorder, i.e., disorder that does not lead to localization [8]. We have first deduced a general condition for the independence of the mean-field transition temperature of a superconducting state on the presence of weak disorder. This "generalized Anderson theorem" [235–240] assumes a purely algebraic form (see Eq. (7.7)) and holds both for singly and doubly degenerate Fermi surfaces. It states that a superconducting phase is protected if its order parameter commutes with the nonmagnetic and anticommutes with the magnetic component of the disorder configuration. Special cases have been discussed, compared with explicit calculations [237–240] and shown to be relevant, e.g., to the iron-based superconductors [238, 239] and to LAO/STO heterostructures.

For the latter system, a detailed analysis of the possible microscopic impurity-scattering channels that are allowed by symmetry has been presented. We have studied quantitatively the sensitivity of the two candidate pairing states s^{++} and s^{+-} derived in Chap. 5 to both nonmagnetic and magnetic disorder. Most importantly, the critical scattering rates of both pairing states is crucially enhanced due to the spin and orbital polarizations of the wavefunctions on the Fermi surfaces. Furthermore,

the unconventional s^{+-} state is by a factor of two more stable than the s^{++} superconductor against magnetic disorder. Since even initially nonmagnetic impurities such as oxygen vacancies have been shown [153, 155] to induce local magnetic moments by spontaneous symmetry breaking, magnetic scattering is expected to be particularly relevant in oxide interfaces. It implies that the unconventional s^{+-} state cannot be ruled out due to the inevitable presence of disorder in the heterostructure.

In addition, we have shown that magnetic disorder can induce a transition from a time-reversal symmetric trivial superconductor, that, e.g., emerges due to electron-phonon coupling, to a topologically nontrivial, TRS-preserving superconducting condensate. Remarkably, the resulting Majorana edge modes can still be protected by the presence of additional crystal symmetries (see Fig. 7.3). This leads to the interesting conclusion that intentional magnetic doping can be used to stabilize time-reversal symmetric topological superconducting phases with gapless boundary modes.

Naturally, many aspects presented in this thesis deserve further investigations. Firstly, one of the central assumptions of our general analysis of superconducting instabilities in Chaps. 4, 6 and 7 has been that no additional translational symmetries are spontaneously broken at the phase transition. This was justified by the fact that many calculations [108–112] show that this is only to be expected to occur in the presence of a magnetic field. Nonetheless, it is interesting to ask whether one can derive general conditions for the exclusion of these types of states, at least in case of nondegenerate Fermi surfaces. Secondly, a detailed microscopic calculation of instabilities in thin layers of Sr_2RuO_4 should be performed which, similarly to the calculation in Ref. [198], takes into account all three bands but, on top of that, also the Dresselhaus-Rashba effect [333, 334]. This calculation could decide which out of the four remaining pairing states illustrated in Fig. 4.5(c)–(f) is expected to occur. Concerning the LAO/STO heterostructures, it would be interesting to perform a numerical RG calculation that does not restrict the theory to the nested regions of the Fermi surface. In addition, a detailed derivation of an effective low-energy model and a subsequent analysis of instabilities similarly to our discussion in Chap. 5 is required for the other two possible orientations of the interface.

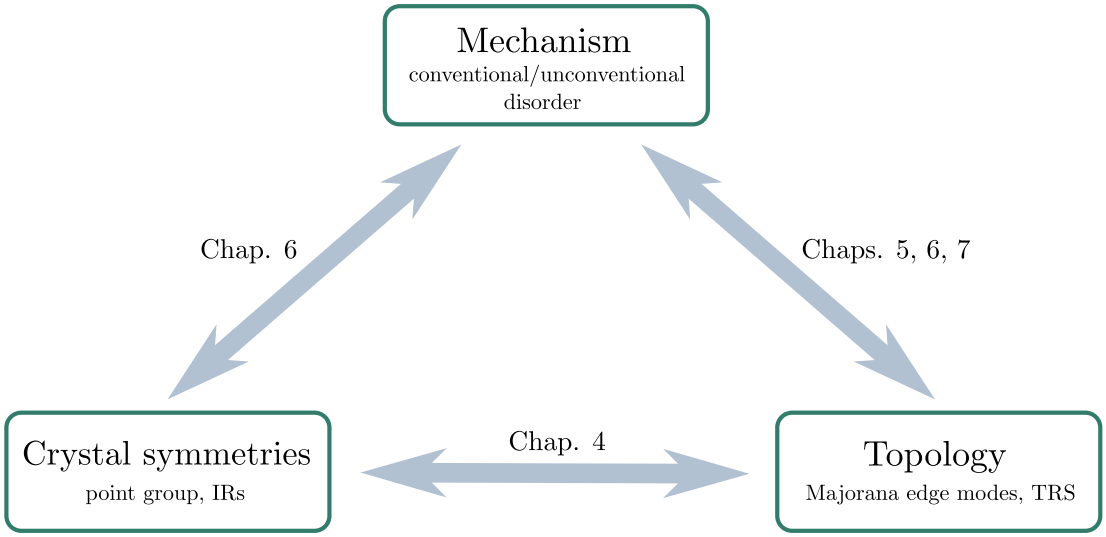

In conclusion, we have seen in this thesis that the three central aspects of phase transitions outlined in the introduction – mechanism, topology and symmetry – are inherently related, in particular, in noncentrosymmetric superconductors. As summarized schematically in the figure, the analysis of Chap. 4 showed that the crystal symmetries in combination with the energetic splitting of the Fermi surfaces have crucial implications for the time-reversal properties and, hence, for the topological classification of possible superconducting instabilities in the system. Furthermore, a proof has been provided in Chap. 6 that both electron-phonon coupling as well as fluctuations of a nonmagnetic density-wave order parameter will lead to a pairing state that preserves all point symmetries of the system. This relates the symmetry and mechanism of superconductivity. Finally, we have seen several times that there is also an inherent relation between the mechanism and the topology of superconductivity. While the microscopic analysis specifically for LAO/STO heterostructures presented in Chap. 5 revealed a one-to-one correspondence between these two aspects of superconductivity, the generalizations discussed in Chap. 6 and Chap. 7 showed that the presence of either magnetic particle-hole fluctuations or magnetic impurities is a necessary prerequisite for stabilizing a time-reversal invariant topological superconductor.

On top of the relevance from a fundamental scientific point of view, we have seen that these observations can both be used to pinpoint unknown order parameters as well as the pairing mechanism of superconductors and might serve as guiding principles in the search for exotic TRS-breaking states and topologically nontrivial superconductors.

On a more general level, the work presented in this thesis accomplishes the following main achievements. Conceptually, this thesis has shown that exact relations following from symmetries and general energetic arguments can be combined in order to derive physically relevant constraints on possible phase transitions beyond the level of explicit model studies. Examples are the design principle for spontaneous TRS breaking, the necessary conditions for topological superconductivity and the general form of the Anderson theorem. The crucial merits of this approach are tied to the fact that its results only depend on very generic properties of the system (such as symmetries) and hold irrespective of, e.g., the number and character of relevant orbitals or the detailed structure of the interaction vertices. This directly reveals the universality of the associated properties of materials. Furthermore, it also allows applying these results to many different systems without detailed knowledge about the dominant microscopic degrees of freedom. For instance, we did not have to take sides in the discussion [194–198] about which band is most relevant for superconductivity in Sr_2RuO_4 in order to deduce the behavior of the order parameter in the thin-layer limit. However, universality naturally comes at a price: The predictive power of our general arguments for a given system is limited compared to specific model studies as we have seen several times in this thesis. For this reason, we have also performed supplementary microscopic calculations in order to pinpoint the form of the order parameter, study the phase competition and analyze the quantitative impact of disorder. Taken together, this thesis shows that the combination of universal guiding principles based on general aspects of a system and explicit microscopic model studies constitutes an efficient way towards the experimental realization and theoretical understanding of exotic new states of matter.

Acknowledgments

First, I would like to express my deepest gratitude to Prof. Jörg Schmalian for giving me the opportunity to work in his group during the last three years and for supervising my doctorate. I am really thankful for his support, the plethora of interesting discussions we had, his useful advice (scientifically and beyond), the great freedom in choosing projects I was given, and for the very personal atmosphere. I really appreciated his "open-door philosophy". In addition, I would like to thank Prof. Alexander D. Mirlin for agreeing to be the co-referee of this thesis.

Special thanks also goes to my collaborators Peter P. Orth, Stephan Rachel, Mareike Hoyer, Sergey V. Syzranov, Chien-Lung Huang, Prof. v. Löhneysen, and, more recently, Prof. Agterberg. I learned so much during our discussions, enjoyed doing research together and am looking forward to potential future interactions.

I am also indebted to those proof reading my thesis: Matthias Bard, Patrik Hlobil, Mareike Hoyer, Nikolaos Kainaris, Janina Klier, Laura Künzel, Julia Link, Tim Ludwig, and Daniel Mendler. Thank you very much.

Furthermore, I am very grateful for the nice atmosphere in my office. I really enjoyed the time with my officemates Matthias Bard, Patrik Hlobil, Nikolaos Kainaris, Elio König, and Michael Schütt.

During my time at TKM, I could take the opportunity to participate in so many different "book seminars" that I will not list all of them here. Let me just emphasize the particularly important role played by Nikolaos Kainaris and Elio König who have been a crucial part of many seminars and also been very important in additional scientific discussions. A special thank also goes to Bhilahari Jeevanesan for sharing his passion about elegant mathematics.

I also want to thank Andreas Poenicke, Christian Seiler, and Michael Walz for technical support. Andreas Poenicke has been very important for my career as printer administrator.

Outside physics, I want to thank my father Michael and my fiancée Laura for their particularly important support.

Finally, a big "thank you" goes to all members of TKM for providing a nice atmosphere. I really enjoyed my time at the institute.

List of publications

In the following, a list of publications of the author of the thesis is presented.

1. *Damping of Plasmons of Closely Coupled Sphere Chains Due to Disordered Gaps*, M. S. Scheurer, M. D. Arnold, J. Setiadi, and M. J. Ford, J. Phys. Chem. C **116**, 1335-1343 (2012). Not cited in the thesis.

2. *Non-adiabatic processes in Majorana qubit systems*, M. S. Scheurer, Diploma thesis (2012). Ref. [292] in the bibliography.

3. *Nonadiabatic processes in Majorana qubit systems*, M. S. Scheurer and A. Shnirman, Phys. Rev. B **88**, 064515 (2013). Ref. [299] in the bibliography.

4. *Topological superconductivity and unconventional pairing in oxide interfaces*, M. S. Scheurer and J. Schmalian, Nat. Commun. **6**, 6005 (2015). Ref. [349] in the bibliography.

5. *Dimensional crossover and cold-atom realization of topological Mott insulators*, M. S. Scheurer, S. Rachel, and P. P. Orth, Sci. Rep. **5**, 8386 (2015). Ref. [317] in the bibliography.

6. *Pair breaking due to orbital magnetism in iron-based superconductors*, M. Hoyer, M. S. Scheurer, S. V. Syzranov, and J. Schmalian, Phys. Rev. B **91**, 054501 (2015). Ref. [239] in the bibliography.

7. *Anomalous quantum criticality in an itinerant ferromagnet*, C. L. Huang, D. Fuchs, M. Wissinger, R. Schneider, M. C. Ling, M. S. Scheurer, J. Schmalian, and H. v. Löhneysen, Nat. Commun. **6**, 8188 (2015). Not cited in the thesis.

8. *Design principles for time-reversal symmetry breaking superconductivity in interfaces and two-dimensional sheets*, M. S. Scheurer and J. Schmalian, arXiv:1503.03646 (preprint). Ref. [325] in the bibliography. To be published soon in extended form [326].

9. *Pair breaking in multiorbital superconductors: An application to oxide interfaces*, M. S. Scheurer, M. Hoyer, and J. Schmalian, Phys. Rev. B **92**, 014518 (2015). Ref. [240] in the bibliography.

10. *Mechanism, time-reversal symmetry and topology of superconductivity in noncentrosymmetric systems*, M. S. Scheurer, Phys. Rev. B **93**, 174509 (2016). Ref. [367] in the bibliography.

11. *Surface and Interface Superconductivity*, S. Gariglio, M. S. Scheurer, J. Schmalian, A. M. R. V. L. Monteiro, S. Goswami, and A. D. Caviglia, in *The Oxford Handbook of Small Superconductors* (Oxford University Press, Oxford, to be published). Ref. [38] in the bibliography.

Bibliography

[1] L. D. Landau. On the theory of phase transitions. *Zh. Eksp. Teor. Fiz.*, 7:19–32, 1937.
(Cited on pages vii, 1, 2, 4, 5, 6, and 55.)

[2] K. v. Klitzing, G. Dorda, and M. Pepper. New method for high-accuracy determination of the fine-structure constant based on quantized Hall resistance. *Phys. Rev. Lett.*, 45:494–497, Aug 1980.
(Cited on pages vii, 29, and 35.)

[3] D. J. Thouless, M. Kohmoto, M. P. Nightingale, and M. den Nijs. Quantized Hall conductance in a two-dimensional periodic potential. *Phys. Rev. Lett.*, 49:405–408, Aug 1982.
(Cited on pages vii and 35.)

[4] M. Z. Hasan and C. L. Kane. *Colloquium*: Topological insulators. *Rev. Mod. Phys.*, 82:3045, Nov 2010.
(Cited on pages vii, ix, 33, 35, and 36.)

[5] Xiao-Liang Qi and Shou-Cheng Zhang. Topological insulators and superconductors. *Rev. Mod. Phys.*, 83:1057–1110, Oct 2011.
(Cited on pages vii, ix, 29, 43, and 44.)

[6] Jason Alicea. New directions in the pursuit of Majorana fermions in solid state systems. *Reports on Progress in Physics*, 75(7):076501, 2012.
(Cited on pages vii, ix, 35, 36, 37, and 109.)

[7] Jan Carl Budich and Björn Trauzettel. From the adiabatic theorem of quantum mechanics to topological states of matter. *physica status solidi (RRL) – Rapid Research Letters*, 7(1-2):109–129, Jan 2013. ISSN 1862-6270.
(Cited on pages vii, 30, 31, and 43.)

[8] P. W. Anderson. Absence of diffusion in certain random lattices. *Phys. Rev.*, 109:1492–1505, Mar 1958.
(Cited on pages vii, ix, xi, 25, and 169.)

[9] Andreas P. Schnyder, Shinsei Ryu, Akira Furusaki, and Andreas W. W. Ludwig. Classification of topological insulators and superconductors in three spatial dimensions. *Phys. Rev. B*, 78:195125, Nov 2008.
(Cited on pages vii, 27, 29, 30, 34, and 53.)

[10] Andreas P. Schnyder, Shinsei Ryu, Akira Furusaki, and Andreas W. W. Ludwig. Classification of topological insulators and superconductors. *AIP Conference Proceedings*, 1134(1):10–21, 2009.
(Cited on pages vii, 27, 29, 34, and 53.)

[11] Felix Bloch. Über die Quantenmechanik der Elektronen in Kristallgittern. *Zeitschrift für Physik*, 52(7):555–600. ISSN 0044-3328.
(Cited on page vii.)

[12] D. C. Tsui, H. L. Stormer, and A. C. Gossard. Two-dimensional magnetotransport in the extreme quantum limit. *Phys. Rev. Lett.*, 48:1559–1562, May 1982.
(Cited on pages vii, x, and 43.)

[13] R. B. Laughlin. Anomalous quantum Hall effect: An incompressible quantum fluid with fractionally charged excitations. *Phys. Rev. Lett.*, 50:1395–1398, May 1983.
(Cited on pages vii, x, and 43.)

[14] F. London and H. London. The electromagnetic equations of the supraconductor. *Proceedings of the Royal Society of London A: Mathematical, Physical and Engineering Sciences*, 149(866): 71–88, 1935. ISSN 0080-4630.
(Cited on pages viii and 9.)

[15] V. L. Ginzburg and L. D. Landau. To the theory of superconductivity. *Zh. Eksp. Teor. Fiz.*, 20: 1064, 1950.
(Cited on pages viii, 1, 2, and 9.)

[16] H. K. Onnes. The resistance of pure mercury at helium temperatures. *Commun. Phys. Lab. Univ. Leiden*, 12:120, 1911.
(Cited on pages viii and 9.)

[17] J. Bardeen, L. N. Cooper, and J. R. Schrieffer. Microscopic theory of superconductivity. *Phys. Rev.*, 106:162–164, Apr 1957.
(Cited on pages viii and 9.)

[18] J. Bardeen, L. N. Cooper, and J. R. Schrieffer. Theory of superconductivity. *Phys. Rev.*, 108: 1175–1204, Dec 1957.
(Cited on pages viii and 9.)

[19] Emanuel Maxwell. Isotope effect in the superconductivity of mercury. *Phys. Rev.*, 78:477–477, May 1950.
(Cited on pages viii and 10.)

[20] C. A. Reynolds, B. Serin, W. H. Wright, and L. B. Nesbitt. Superconductivity of isotopes of mercury. *Phys. Rev.*, 78:487–487, May 1950.
(Cited on pages viii and 10.)

[21] F. Steglich, J. Aarts, C. D. Bredl, W. Lieke, D. Meschede, W. Franz, and H. Schäfer. Superconductivity in the presence of strong Pauli paramagnetism: $CeCu_2Si_2$. *Phys. Rev. Lett.*, 43: 1892–1896, Dec 1979.
(Cited on pages viii and 10.)

[22] H. R. Ott, H. Rudigier, Z. Fisk, and J. L. Smith. UBe_{13}: An unconventional actinide superconductor. *Phys. Rev. Lett.*, 50:1595–1598, May 1983.
(Cited on pages viii and 10.)

[23] G. R. Stewart, Z. Fisk, J. O. Willis, and J. L. Smith. Possibility of coexistence of bulk superconductivity and spin fluctuations in UPt_3. *Phys. Rev. Lett.*, 52:679–682, Feb 1984.
(Cited on pages viii, 10, 21, and 88.)

[24] J. G. Bednorz and K. A. Müller. Possible highTc superconductivity in the Ba−La−Cu−O system. *Zeitschrift für Physik B Condensed Matter*, 64(2):189–193. ISSN 1431-584X.
(Cited on pages viii and 10.)

[25] Karl-Heinz Bennemann and John B Ketterson. *The Physics of Superconductors: Vol II: Superconductivity in Nanostructures, High-Tc and Novel Superconductors, Organic Superconductors*, volume 2. Springer Science & Business Media, 2011.
(Cited on pages viii and 10.)

[26] Andrey V Chubukov and Peter J Hirschfeld. Fe-based superconductors: seven years later. *Physics Today*, 68:46, 2015.
(Cited on pages viii, 10, 148, and 164.)

[27] D. A. Wollman, D. J. Van Harlingen, W. C. Lee, D. M. Ginsberg, and A. J. Leggett. Experimental determination of the superconducting pairing state in YBCO from the phase coherence of YBCO-Pb dc SQUIDs. *Phys. Rev. Lett.*, 71:2134–2137, Sep 1993.
(Cited on pages viii, ix, and 97.)

[28] C. C. Tsuei, J. R. Kirtley, C. C. Chi, Lock See Yu-Jahnes, A. Gupta, T. Shaw, J. Z. Sun, and M. B. Ketchen. Pairing symmetry and flux quantization in a tricrystal superconducting ring of $YBa_2Cu_3O_{7-\delta}$. *Phys. Rev. Lett.*, 73:593–596, Jul 1994.
(Cited on pages viii, ix, and 97.)

[29] C. C. Tsuei and J. R. Kirtley. Pairing symmetry in cuprate superconductors. *Rev. Mod. Phys.*, 72:969–1016, Oct 2000.
(Cited on pages viii, ix, and 10.)

[30] P. Monthoux, A. V. Balatsky, and D. Pines. Toward a theory of high-temperature superconductivity in the antiferromagnetically correlated cuprate oxides. *Phys. Rev. Lett.*, 67:3448–3451, Dec 1991.
(Cited on pages viii, 10, and 116.)

[31] Ar. Abanov, Andrey V. Chubukov, and J. Schmalian. Quantum-critical theory of the spin-fermion model and its application to cuprates: Normal state analysis. *Advances in Physics*, 52(3):119–218, Sep 2003.
(Cited on pages viii, 10, 116, 130, 131, and 169.)

[32] A. V. Chubukov, D. Pines, and J. Schmalian. *The Physics of Superconductors: Vol. I. Conventional and High-T_c Superconductors*, chapter A Spin Fluctuation Model for d-Wave Superconductivity, pages 495–590. Springer Berlin Heidelberg, Berlin, Heidelberg, 2003. ISBN 978-3-642-55675-3.
(Cited on pages viii, 10, 116, 130, and 169.)

[33] G. Dresselhaus. Spin-orbit coupling effects in zinc blende structures. *Phys. Rev.*, 100:580–586, Oct 1955.
(Cited on pages viii, 14, and 99.)

[34] EI Rashba. Properties of semiconductors with an extremum loop. 1. cyclotron and combinational resonance in a magnetic field perpendicular to the plane of the loop. *Soviet Physics-Solid State*, 2(6):1109–1122, 1960.
(Cited on pages viii, 14, and 99.)

[35] A. Ohtomo and H. Y. Hwang. A high-mobility electron gas at the $LaAlO_3/SrTiO_3$ heterointerface. *Nature*, 427(6973):423–426, January 2004. ISSN 0028-0836. URL `http://dx.doi.org/10.1038/nature02308`.
(Cited on pages viii, 15, 17, 89, 96, and 168.)

[36] J. Mannhart and D. G. Schlom. Oxide interfaces—an opportunity for electronics. *Science*, 327 (5973):1607–1611, Mar 2010.
(Cited on pages viii, 15, 89, 97, and 140.)

[37] S. Gariglio, M. Gabay, J. Mannhart, and J.-M. Triscone. Interface superconductivity. *Physica C: Superconductivity and its Applications*, 514:189 – 198, Feb 2015. ISSN 0921-4534. Superconducting Materials: Conventional, Unconventional and Undetermined.
(Cited on pages viii, 15, 18, 55, 89, 97, and 140.)

[38] S. Gariglio, M. S. Scheurer, J. Schmalian, A. M. R. V. L. Monteiro, S. Goswami, and A. D. Caviglia. *The Oxford Handbook of Small Superconductors*, chapter Surface and Interface Superconductivity. Oxford University Press, 2017.
(Cited on pages viii, ix, 13, 15, 18, 55, 56, 89, 90, 97, 140, and 175.)

[39] N. Reyren, S. Thiel, A. D. Caviglia, L. Fitting Kourkoutis, G. Hammerl, C. Richter, C. W. Schneider, T. Kopp, A.-S. Rüetschi, D. Jaccard, M. Gabay, D. A. Muller, J.-M. Triscone, and J. Mannhart. Superconducting interfaces between insulating oxides. *Science*, 317(5842):1196–1199, 2007.
(Cited on pages viii, 15, 16, 55, 90, 98, 109, and 140.)

[40] Yin-Long Han, Sheng-Chun Shen, Jie You, Hai-Ou Li, Zhong-Zhong Luo, Cheng-Jian Li, Guo-Liang Qu, Chang-Min Xiong, Rui-Fen Dou, Lin He, Don Naugle, Guo-Ping Guo, and Jia-Cai Nie. Two-dimensional superconductivity at (110) $LaAlO_3/SrTiO_3$ interfaces. *Applied Physics Letters*, 105(19):192603, 2014.
(Cited on pages viii, 17, 55, 90, 97, 140, and 141.)

[41] A. D. Caviglia, M. Gabay, S. Gariglio, N. Reyren, C. Cancellieri, and J.-M. Triscone. Tunable rashba spin-orbit interaction at oxide interfaces. *Phys. Rev. Lett.*, 104:126803, Mar 2010.
(Cited on pages viii, 16, 90, 100, 103, 140, and 141.)

[42] M. Ben Shalom, M. Sachs, D. Rakhmilevitch, A. Palevski, and Y. Dagan. Tuning spin-orbit coupling and superconductivity at the $SrTiO_3/LaAlO_3$ interface: A magnetotransport study. *Phys. Rev. Lett.*, 104:126802, Mar 2010.
(Cited on pages viii, 16, 103, 140, and 141.)

[43] Kalon Gopinadhan, Anil Annadi, Younghyun Kim, Amar Srivastava, Brijesh Kumar, Jingsheng Chen, J. Michael D. Coey, Ariando, and Thirumalai Venkatesan. Gate tunable in- and out-of-plane spin-orbit coupling and spin-splitting anisotropy at $LaAlO_3/SrTiO_3$ (110) interface. *Advanced Electronic Materials*, 1(8), 2015.
(Cited on pages viii, 17, 140, and 141.)

[44] Ernst Bauer and Manfred Sigrist, editors. *Non-Centrosymmetric Superconductors: Introduction and Overview (Lecture Notes in Physics)*. Springer, 2012. ISBN 9783642246234.
(Cited on pages ix, 13, and 15.)

[45] F. Kneidinger, E. Bauer, I. Zeiringer, P. Rogl, C. Blaas-Schenner, D. Reith, and R. Podloucky. Superconductivity in non-centrosymmetric materials. *Physica C: Superconductivity and its Applications*, 514:388 – 398, 2015. ISSN 0921-4534. Superconducting Materials: Conventional, Unconventional and Undetermined.
(Cited on pages ix, 13, and 15.)

[46] Juan Pereiro, Alexander Petrovic, Christos Panagopoulos, and Ivan Bozović. Interface superconductivity: History, development and prospects. *Phys. Express*, 1:208, 2011.
(Cited on pages ix, 13, and 15.)

[47] Jing Xia, Yoshiteru Maeno, Peter T. Beyersdorf, M. M. Fejer, and Aharon Kapitulnik. High resolution polar kerr effect measurements of Sr_2RuO_4: Evidence for broken time-reversal symmetry in the superconducting state. *Phys. Rev. Lett.*, 97:167002, Oct 2006.
(Cited on pages ix, x, 18, 20, 55, 81, 126, and 168.)

[48] E. R. Schemm, W. J. Gannon, C. M. Wishne, W. P. Halperin, and A. Kapitulnik. Observation of broken time-reversal symmetry in the heavy-fermion superconductor UPt_3. *Science*, 345(6193): 190–193, 2014. ISSN 0036-8075. URL `http://science.sciencemag.org/content/345/6193/190`.
(Cited on pages ix, x, 18, 21, 22, 55, 87, 88, and 126.)

[49] E. R. Schemm, R. E. Baumbach, P. H. Tobash, F. Ronning, E. D. Bauer, and A. Kapitulnik. Evidence for broken time-reversal symmetry in the superconducting phase of URu_2Si_2. *Phys. Rev. B*, 91:140506, Apr 2015.
(Cited on pages ix, x, 18, 23, 55, 87, and 126.)

[50] Manfred Sigrist and Kazuo Ueda. Phenomenological theory of unconventional superconductivity. *Rev. Mod. Phys.*, 63:239–311, Apr 1991.
(Cited on pages ix, 4, 6, 10, 20, 55, 62, 94, and 129.)

[51] G. M. Luke, Y. Fudamoto, K. M. Kojima, M. I. Larkin, J. Merrin, B. Nachumi, Y. J. Uemura, Y. Maeno, Z. Q. Mao, Y. Mori, H. Nakamura, and M. Sigrist. Time-reversal symmetry-breaking superconductivity in Sr_2RuO_4. *Nature*, 394(6693):558–561, Aug 1998. ISSN 0028-0836.
(Cited on pages ix, x, 18, 20, 55, 81, 126, and 168.)

[52] Mihail Silaev, Julien Garaud, and Egor Babaev. Unconventional thermoelectric effect in superconductors that break time-reversal symmetry. *Phys. Rev. B*, 92:174510, Nov 2015.
(Cited on pages ix and 55.)

[53] Francoise Kidwingira, J. D. Strand, D. J. Van Harlingen, and Yoshiteru Maeno. Dynamical superconducting order parameter domains in Sr_2RuO_4. *Science*, 314(5803):1267–1271, 2006. ISSN 0036-8075.
(Cited on pages ix, x, 18, 20, 81, 126, and 168.)

[54] G. M. Luke, A. Keren, L. P. Le, W. D. Wu, Y. J. Uemura, D. A. Bonn, L. Taillefer, and J. D. Garrett. Muon spin relaxation in UPt_3. *Phys. Rev. Lett.*, 71:1466–1469, Aug 1993.
(Cited on pages ix, x, 18, 22, 87, 88, and 126.)

[55] A. D. Hillier, J. Quintanilla, and R. Cywinski. Evidence for time-reversal symmetry breaking in the noncentrosymmetric superconductor $LaNiC_2$. *Phys. Rev. Lett.*, 102:117007, Mar 2009.
(Cited on pages ix, 15, 95, and 126.)

[56] R. P. Singh, A. D. Hillier, B. Mazidian, J. Quintanilla, J. F. Annett, D. McK. Paul, G. Balakrishnan, and M. R. Lees. Detection of time-reversal symmetry breaking in the noncentrosymmetric superconductor Re_6Zr using muon-spin spectroscopy. *Phys. Rev. Lett.*, 112:107002, Mar 2014.
(Cited on pages ix, 15, 95, and 126.)

[57] Ettore Majorana. Teoria simmetrica dell'elettrone e del positrone. *Nuovo Cimento*, 14:171–184, 1937. ISSN 1827-6121.
(Cited on pages ix and 32.)

[58] D. A. Ivanov. Non-Abelian statistics of half-quantum vortices in p-wave superconductors. *Phys. Rev. Lett.*, 86:268–271, Jan 2001.
(Cited on pages ix, 37, and 40.)

[59] Chetan Nayak, Steven H. Simon, Ady Stern, Michael Freedman, and Sankar Das Sarma. Non-Abelian anyons and topological quantum computation. *Rev. Mod. Phys.*, 80:1083–1159, Sep 2008.
(Cited on pages ix, 39, 40, and 42.)

[60] V. Mourik, K. Zuo, S. M. Frolov, S. R. Plissard, E. P. A. M. Bakkers, and L. P. Kouwenhoven. Signatures of Majorana fermions in hybrid superconductor-semiconductor nanowire devices. *Science*, 336(6084):1003–1007, 2012.
(Cited on pages x, 36, 109, and 114.)

[61] Stevan Nadj-Perge, Ilya K. Drozdov, Jian Li, Hua Chen, Sangjun Jeon, Jungpil Seo, Allan H. MacDonald, B. Andrei Bernevig, and Ali Yazdani. Observation of Majorana fermions in ferromagnetic atomic chains on a superconductor. *Science*, 346(6209):602–607, Oct 2014. ISSN 0036-8075.
(Cited on pages x, 36, 109, and 114.)

[62] Maciej Lewenstein, Anna Sanpera, Veronica Ahufinger, Bogdan Damski, Aditi Sen(De), and Ujjwal Sen. Ultracold atomic gases in optical lattices: mimicking condensed matter physics and beyond. *Advances in Physics*, 56(2):243–379, 2007.
(Cited on pages x, 39, and 45.)

[63] Immanuel Bloch, Jean Dalibard, and Sylvain Nascimbène. Quantum simulations with ultracold quantum gases. *Nat. Phys.*, 8(4):267–276, April 2012. ISSN 1745-2473.
(Cited on pages x, 39, and 45.)

[64] D. A. Pesin and L. Balents. Mott physics and band topology in materials with strong spin-orbit interaction. *Nature Phys.*, 6:376, Mar 2010.
(Cited on pages x, 43, 44, 49, 50, 51, and 53.)

[65] Serge Florens and Antoine Georges. Quantum impurity solvers using a slave-rotor representation. *Phys. Rev. B*, 66:165111, 2002.
(Cited on pages x, 44, 45, 50, 51, 53, 167, 226, and 227.)

[66] Serge Florens and Antoine Georges. Slave-rotor mean-field theories of strongly correlated systems and the Mott transition in finite dimensions. *Phys. Rev. B*, 70:035114, 2004.
(Cited on pages x, 44, 45, 50, 53, 167, and 226.)

[67] E. Zhao and A. Paramekanti. Self-consistent slave rotor mean-field theory for strongly correlated systems. *Phys. Rev. B*, 76:195101, 2007.
(Cited on pages x, 44, 45, 50, 53, 167, and 226.)

[68] Y. Krockenberger, M. Uchida, K. S. Takahashi, M. Nakamura, M. Kawasaki, and Y. Tokura. Growth of superconducting Sr_2RuO_4 thin films. *Applied Physics Letters*, 97(8):082502, Aug 2010.
(Cited on pages x, 18, 21, 82, 96, and 168.)

[69] M Huth, S Reber, C Heske, P Schicketanz, J Hessert, P Gegenwart, and H Adrian. Growth characteristics of sputter-deposited UPt_3 thin films. *Journal of Physics: Condensed Matter*, 8 (45):8777, Aug 1996.
(Cited on pages x, 18, 22, 88, 96, and 168.)

[70] C. Richter, H. Boschker, W. Dietsche, E. Fillis-Tsirakis, R. Jany, F. Loder, L. F. Kourkoutis, D. A. Muller, J. R. Kirtley, C. W. Schneider, and J. Mannhart. Interface superconductor with gap behaviour like a high-temperature superconductor. *Nature*, 502(7472):528–531, Oct 2013. ISSN 0028-0836. URL `http://dx.doi.org/10.1038/nature12494`.
(Cited on pages x, 16, 17, 90, 100, 107, 109, 114, and 168.)

[71] G. M. Eliashberg. Interactions between electrons and lattice vibrations in a superconductor. *Sov. Phys. JETP*, 11:696, Sep 1960.
(Cited on pages xi, 115, 119, 120, 122, and 168.)

[72] G. M. Eliashberg. Temperature green's function for electrons in a superconductor. *Sov. Phys. JETP*, 12:1000, May 1961.
(Cited on pages xi, 115, 119, 120, 122, and 168.)

[73] L. D. Landau. *Physikalische Zeitschrift der Sowjetunion*, 4:43, 1933.
(Cited on pages 1 and 3.)

[74] Jörg Schmalian. Failed theories of superconductivity. *Modern Physics Letters B*, 24(27):2679–2691, Oct 2010.
(Cited on pages 1 and 9.)

[75] LD Landau. A possible explanation of the field dependence of the susceptibility at low temperatures. *Phys. Z. Sowjet*, 4:675, 1933.
(Cited on page 2.)

[76] Norman E. Phillips. Heat capacity of aluminum between 0.1°K and 4.0°K. *Phys. Rev.*, 114: 676–685, May 1959.
(Cited on page 3.)

[77] Gerd Czycholl. *Theoretische Festkörperphysik: Von den klassischen Modellen zu modernen Forschungsthemen*. Springer, 3. edition, Nov 2007. ISBN 9783540747895.
(Cited on pages 3 and 9.)

[78] Dieter Vollhardt and Peter Wölfle. *The Superfluid Phases of Helium 3 (Dover Books on Physics)*. Dover Publications, reprint edition, Oct 2013. ISBN 9780486486314.
(Cited on pages 4, 6, 13, 22, 38, and 55.)

[79] G. E. Volovik and L. P. Gorkov. Superconducting classes in heavy-fermions systems. *Sov. Phys. JETP*, 61(4):843–853, Apr 1985.
(Cited on pages 4, 55, 68, and 71.)

[80] E. I. Blount. Symmetry properties of triplet superconductors. *Phys. Rev. B*, 32:2935–2944, Sep 1985.
(Cited on pages 4 and 55.)

[81] Sungkit Yip and Anupam Garg. Superconducting states of reduced symmetry: General order parameters and physical implications. *Phys. Rev. B*, 48:3304–3308, Aug 1993.
(Cited on pages 4, 55, 56, 59, 167, and 229.)

[82] M. Sigrist and T. M. Rice. Symmetry classification of states in high temperature superconductors. *Zeitschrift für Physik B Condensed Matter*, 68(1):9–14. ISSN 1431-584X.
(Cited on pages 4 and 55.)

[83] James F. Annett. Symmetry of the order parameter for high-temperature superconductivity. *Advances in Physics*, 39(2):83–126, 1990.
(Cited on pages 4, 6, and 55.)

[84] Jorge Quintanilla, Adrian D. Hillier, James F. Annett, and R. Cywinski. Relativistic analysis of the pairing symmetry of the noncentrosymmetric superconductor $LaNiC_2$. *Phys. Rev. B*, 82: 174511, Nov 2010.
(Cited on pages 4, 6, 8, 13, and 55.)

[85] Melvin Lax. *Symmetry Principles in Solid State and Molecular Physics*. John Wiley & Sons Inc, first printing edition, 11 1974. ISBN 9780471519041.
(Cited on pages 5, 7, 18, 28, 222, and 223.)

[86] John David Jackson. *Klassische Elektrodynamik*. Walter de Gruyter, 4 edition, Jul 2006. ISBN 9783110189704.
(Cited on pages 7 and 16.)

[87] Roland Winkler. *Spin-orbit Coupling Effects in Two-Dimensional Electron and Hole Systems (Springer Tracts in Modern Physics)*. Springer, Dec 2003. ISBN 9783540011873.
(Cited on pages 7, 14, and 48.)

[88] Liang Fu. Parity-breaking phases of spin-orbit-coupled metals with gyrotropic, ferroelectric, and multipolar orders. *Phys. Rev. Lett.*, 115:026401, Jul 2015.
(Cited on pages 8 and 78.)

[89] P. M. R. Brydon, S. Das Sarma, Hoi-Yin Hui, and Jay D. Sau. Odd-parity superconductivity from phonon-mediated pairing: Application to $Cu_xBi_2Se_3$. *Phys. Rev. B*, 90:184512, Nov 2014.
(Cited on pages 8, 78, and 129.)

[90] Lev P. Gor'kov and Emmanuel I. Rashba. Superconducting 2D system with lifted spin degeneracy: Mixed singlet-triplet state. *Phys. Rev. Lett.*, 87:037004, Jul 2001.
(Cited on pages 8 and 13.)

[91] George F. Koster, John O. Dimmock, Robert G. Wheeler, and Hermann Statz. *The Properties of the Thirty-Two Point Groups (Research Monograph)*. The MIT Press, Dec 1963. ISBN 9780262110105.
(Cited on pages 8, 58, and 223.)

[92] Leon N. Cooper. Bound electron pairs in a degenerate fermi gas. *Phys. Rev.*, 104:1189–1190, Nov 1956.
(Cited on page 9.)

[93] Albert Messiah. *Quantenmechanik 2, 3rd Edition (German Edition)*. de Gruyter, 3rd edition, Nov 1990. ISBN 9783110126693.
(Cited on pages 9, 13, 28, and 57.)

[94] Henrik Bruus and Karsten Flensberg. *Many-Body Quantum Theory in Condensed Matter Physics: An Introduction*. Oxford University Press, Nov 2004. ISBN 9780198566335.
(Cited on pages 9, 23, 24, 253, and 255.)

[95] Lev Petrovich Gorkov. Microscopic derivation of the Ginzburg-Landau equations in the theory of superconductivity. *Sov. Phys. JETP*, 9(6):1364–1367, 1959.
(Cited on page 9.)

[96] H. Fröhlich. Theory of the superconducting state. I. the ground state at the absolute zero of temperature. *Phys. Rev.*, 79:845–856, Sep 1950.
(Cited on page 9.)

[97] John Bardeen and David Pines. Electron-phonon interaction in metals. *Phys. Rev.*, 99:1140–1150, Aug 1955.
(Cited on pages 10 and 129.)

[98] P. Morel and P. W. Anderson. Calculation of the superconducting state parameters with retarded electron-phonon interaction. *Phys. Rev.*, 125:1263–1271, Feb 1962.
(Cited on pages 10 and 129.)

[99] R. Shankar. Renormalization-group approach to interacting fermions. *Rev. Mod. Phys.*, 66:129–192, Jan 1994.
(Cited on pages 10, 104, and 129.)

[100] W. L. McMillan. Transition temperature of strong-coupled superconductors. *Phys. Rev.*, 167: 331–344, Mar 1968.
(Cited on pages 10 and 129.)

[101] A. A. Abrikosov and L. P. Gorkov. Contribution to the theory of superconducting alloys with paramagnetic impurities. *Zh. Eksp. Teor. Fiz.*, 39:1781, 1961.
(Cited on pages 10, 25, 146, 148, 163, and 164.)

[102] H. R. Ott, H. Rudigier, T. M. Rice, K. Ueda, Z. Fisk, and J. L. Smith. p-wave superconductivity in UBe_{13}. *Phys. Rev. Lett.*, 52:1915–1918, May 1984.
(Cited on page 10.)

[103] D Jerome, A Mazaud, M Ribault, and K Bechgaard. Superconductivity in a synthetic organic conductor (TMTSF) 2PF 6. *Journal de Physique Lettres*, 41(4):95–98, 1980.
(Cited on page 10.)

[104] Yoichi Kamihara, Hidenori Hiramatsu, Masahiro Hirano, Ryuto Kawamura, Hiroshi Yanagi, Toshio Kamiya, and Hideo Hosono. Iron-based layered superconductor: LaOFeP. *Journal of the American Chemical Society*, 128(31):10012–10013, 2006. PMID: 16881620.
(Cited on page 10.)

[105] Peter Fulde and Richard A. Ferrell. Superconductivity in a strong spin-exchange field. *Phys. Rev.*, 135:A550–A563, Aug 1964.
(Cited on pages 10, 95, and 122.)

[106] A. I. Larkin and Y. N. Ovchinnikov. Inhomogeneous state of superconductors. *Sov. Phys. JETP*, 20:762–769, 1965.
(Cited on pages 10, 95, and 122.)

[107] Yuji Matsuda and Hiroshi Shimahara. Fulde–Ferrell–Larkin–Ovchinnikov state in heavy fermion superconductors. *Journal of the Physical Society of Japan*, 76(5):051005, May 2007.
(Cited on pages 10 and 11.)

[108] Victor Barzykin and Lev P. Gor'kov. Inhomogeneous stripe phase revisited for surface superconductivity. *Phys. Rev. Lett.*, 89:227002, Nov 2002.
(Cited on pages 11, 91, and 170.)

[109] R. P. Kaur, D. F. Agterberg, and M. Sigrist. Helical vortex phase in the noncentrosymmetric $CePt_3Si$. *Phys. Rev. Lett.*, 94:137002, Apr 2005.
(Cited on pages 11 and 170.)

[110] Ol'ga Dimitrova and M. V. Feigel'man. Theory of a two-dimensional superconductor with broken inversion symmetry. *Phys. Rev. B*, 76:014522, Jul 2007.
(Cited on pages 11, 91, and 170.)

[111] Karen Michaeli, Andrew C. Potter, and Patrick A. Lee. Superconducting and ferromagnetic phases in $LaAlO_3/SrTiO_3$ oxide interface structures: Possibility of finite momentum pairing. *Phys. Rev. Lett.*, 108:117003, Mar 2012.
(Cited on pages 11, 16, 91, 98, 113, 143, 149, 161, and 170.)

[112] Florian Loder, Arno P Kampf, and Thilo Kopp. Superconductivity with rashba spin–orbit coupling and magnetic field. *Journal of Physics: Condensed Matter*, 25(36):362201, 2013.
(Cited on pages 11, 91, and 170.)

[113] R. Beyer and J. Wosnitza. Emerging evidence for FFLO states in layered organic superconductors (review article). *Low Temperature Physics*, 39(3):225–231, 2013.
(Cited on page 11.)

[114] Alexander Altland and Ben D. Simons. *Condensed Matter Field Theory.* Cambridge University Press, 2. edition, Apr 2010. ISBN 9780521769754.
(Cited on pages 11, 12, 23, 24, 25, 100, 117, and 232.)

[115] Jean Zinn-Justin. *Quantum Field Theory and Critical Phenomena (International Series of Monographs on Physics).* Clarendon Press, 4. edition, Aug 2002. ISBN 9780198509233.
(Cited on pages 11, 12, 100, 117, and 232.)

[116] Yoichiro Nambu. Quasi-particles and gauge invariance in the theory of superconductivity. *Phys. Rev.*, 117:648–663, Feb 1960.
(Cited on page 11.)

[117] J. Goldstone. Field theories with « superconductor » solutions. *Il Nuovo Cimento (1955-1965)*, 19(1):154–164, Jan 1961. ISSN 1827-6121.
(Cited on page 11.)

[118] Jeffrey Goldstone, Abdus Salam, and Steven Weinberg. Broken symmetries. *Phys. Rev.*, 127: 965–970, Aug 1962.
(Cited on page 11.)

[119] N. D. Mermin and H. Wagner. Absence of ferromagnetism or antiferromagnetism in one- or two-dimensional isotropic Heisenberg models. *Phys. Rev. Lett.*, 17:1133–1136, Nov 1966.
(Cited on page 12.)

[120] P. C. Hohenberg. Existence of long-range order in one and two dimensions. *Phys. Rev.*, 158: 383–386, Jun 1967.
(Cited on page 12.)

[121] Sidney Coleman. There are no Goldstone bosons in two dimensions. *Communications in Mathematical Physics*, 31(4):259–264. ISSN 1432-0916.
(Cited on page 12.)

[122] V. L. Berezinskii. Destruction of long-range order in one-dimensional and two-dimensional systems having a continuous symmetry group I. classical systems. *Soviet Journal of Experimental and Theoretical Physics*, 32:493, 1971.
(Cited on pages 12, 67, and 95.)

[123] J M Kosterlitz and D J Thouless. Ordering, metastability and phase transitions in two-dimensional systems. *Journal of Physics C: Solid State Physics*, 6(7):1181, 1973.
(Cited on pages 12, 67, and 95.)

[124] Jorge V. José, Leo P. Kadanoff, Scott Kirkpatrick, and David R. Nelson. Renormalization, vortices, and symmetry-breaking perturbations in the two-dimensional planar model. *Phys. Rev. B*, 16:1217–1241, Aug 1977.
(Cited on pages 12 and 67.)

[125] Martin Greiter. Is electromagnetic gauge invariance spontaneously violated in superconductors? *Annals of Physics*, 319(1):217 – 249, May 2005. ISSN 0003-4916.
(Cited on page 13.)

[126] J. Pearl. Current distribution in superconducting films carrying quantized fluxoids. *Applied Physics Letters*, 5(4):65–66, 1964.
(Cited on pages 13 and 95.)

[127] V. G. Kogan. Interaction of vortices in thin superconducting films and the Berezinskii-Kosterlitz-Thouless transition. *Phys. Rev. B*, 75:064514, Feb 2007.
(Cited on pages 13 and 95.)

[128] B. I. Halperin, T. C. Lubensky, and Shang-keng Ma. First-order phase transitions in superconductors and smectic-A liquid crystals. *Phys. Rev. Lett.*, 32:292–295, Feb 1974.
(Cited on pages 13, 67, and 95.)

[129] C. Dasgupta and B. I. Halperin. Phase transition in a lattice model of superconductivity. *Phys. Rev. Lett.*, 47:1556–1560, Nov 1981.
(Cited on page 13.)

[130] L. Petersen and P. Hedegård. A simple tight-binding model of spin–orbit splitting of sp-derived surface states. *Surface Science*, 459(1–2):49 – 56, 2000. ISSN 0039-6028.
(Cited on pages 14 and 100.)

[131] E. Bauer, G. Hilscher, H. Michor, Ch. Paul, E. W. Scheidt, A. Gribanov, Yu. Seropegin, H. Noël, M. Sigrist, and P. Rogl. Heavy fermion superconductivity and magnetic order in noncentrosymmetric $CePt_3Si$. *Phys. Rev. Lett.*, 92:027003, Jan 2004.
(Cited on page 14.)

[132] P. W. Anderson. Structure of "triplet" superconducting energy gaps. *Phys. Rev. B*, 30:4000–4002, Oct 1984.
(Cited on page 14.)

[133] P. A. Frigeri, D. F. Agterberg, A. Koga, and M. Sigrist. Superconductivity without inversion symmetry: MnSi versus $CePt_3Si$. *Phys. Rev. Lett.*, 92:097001, Mar 2004.
(Cited on pages 15 and 81.)

[134] V.L. Ginzburg. On surface superconductivity. *Physics Letters*, 13(2):101 – 102, 1964. ISSN 0031-9163.
(Cited on page 15.)

[135] S. Reich and Y. Tsabba. Possible nucleation of a 2d superconducting phase on WO single crystals surface doped with Na. *The European Physical Journal B - Condensed Matter and Complex Systems*, 9(1):1–4. ISSN 1434-6036.
(Cited on page 15.)

[136] Kostya S Novoselov, Andre K Geim, SV Morozov, D Jiang, Y Zhang, SV Dubonos, , IV Grigorieva, and AA Firsov. Electric field effect in atomically thin carbon films. *Science*, 306(5696): 666–669, Oct 2004.
(Cited on page 15.)

[137] I. Bozovic, G. Logvenov, I. Belca, B. Narimbetov, and I. Sveklo. Epitaxial strain and superconductivity in $La_{2-x}Sr_xCuO_4$ thin films. *Phys. Rev. Lett.*, 89:107001, Aug 2002.
(Cited on page 15.)

[138] A. Gozar, G. Logvenov, L. Fitting Kourkoutis, A. T. Bollinger, L. A. Giannuzzi, D. A. Muller, and I. Bozovic. High-temperature interface superconductivity between metallic and insulating copper oxides. *Nature*, 455(7214):782–785, Oct 2008. ISSN 0028-0836.
(Cited on page 15.)

[139] Naoyuki Nakagawa, Harold Y. Hwang, and David A. Muller. Why some interfaces cannot be sharp. *Nat Mater*, 5(3):204–209, Mar 2006. ISSN 1476-1122.
(Cited on pages 15, 16, and 98.)

[140] Zoran S. Popović, Sashi Satpathy, and Richard M. Martin. Origin of the two-dimensional electron gas carrier density at the $LaAlO_3$ on $SrTiO_3$ interface. *Phys. Rev. Lett.*, 101:256801, Dec 2008.
(Cited on pages 15 and 16.)

[141] S. Thiel, G. Hammerl, A. Schmehl, C. W. Schneider, and J. Mannhart. Tunable quasi-two-dimensional electron gases in oxide heterostructures. *Science*, 313(5795):1942–1945, 2006. ISSN 0036-8075.
(Cited on page 16.)

[142] G. Herranz, F. Sánchez, N. Dix, M. Scigaj, and J. Fontcuberta. High mobility conduction at (110) and (111) $LaAlO_3/SrTiO_3$ interfaces. *Sci. Rep.*, 2:758, October 2012.
(Cited on pages 16, 17, 89, 96, 141, and 168.)

[143] Z. Q. Liu, C. J. Li, W. M. Lü, X. H. Huang, Z. Huang, S. W. Zeng, X. P. Qiu, L. S. Huang, A. Annadi, J. S. Chen, J. M. D. Coey, T. Venkatesan, and Ariando. Origin of the two-dimensional electron gas at $LaAlO_3/SrTiO_3$ interfaces: The role of oxygen vacancies and electronic reconstruction. *Phys. Rev. X*, 3:021010, May 2013.
(Cited on pages 16, 160, and 164.)

[144] A. D. Caviglia, S. Gariglio, N. Reyren, D. Jaccard, T. Schneider, M. Gabay, S. Thiel, G. Hammerl, J. Mannhart, and J.-M. Triscone. Electric field control of the $LaAlO_3/SrTiO_3$ interface ground state. *Nature*, 456(7222):624–627, December 2008. ISSN 0028-0836.
(Cited on pages 16 and 141.)

[145] Julie A. Bert, Katja C. Nowack, Beena Kalisky, Hilary Noad, John R. Kirtley, Chris Bell, Hiroki K. Sato, Masayuki Hosoda, Yasayuki Hikita, Harold Y. Hwang, and Kathryn A. Moler. Gate-tuned superfluid density at the superconducting $LaAlO_3/SrTiO_3$ interface. *Phys. Rev. B*, 86:060503, Aug 2012.
(Cited on pages 16 and 141.)

[146] Christof W Schneider, S Thiel, G Hammerl, Christoph Richter, and J Mannhart. Microlithography of electron gases formed at interfaces in oxide heterostructures. *Applied physics letters*, 89 (12):122101–122101, Sep 2006.
(Cited on pages 16 and 109.)

[147] C. Cen, S. Thiel, G. Hammerl, C. W. Schneider, K. E. Andersen, C. S. Hellberg, J. Mannhart, and J. Levy. Nanoscale control of an interfacial metal-insulator transition at room temperature. *Nat Mater*, 7(4):298–302, Apr 2008. ISSN 1476-1122.
(Cited on pages 16 and 109.)

[148] A. Brinkman, M. Huijben, M. van Zalk, J. Huijben, U. Zeitler, J. C. Maan, W. G. van der Wiel, G. Rijnders, D. H. A. Blank, and H. Hilgenkamp. Magnetic effects at the interface between non-magnetic oxides. *Nat Mater*, 6(7):493–496, July 2007. ISSN 1476-1122.
(Cited on pages 16, 91, and 143.)

[149] Julie A. Bert, Beena Kalisky, Christopher Bell, Minu Kim, Yasuyuki Hikita, Harold Y. Hwang, and Kathryn A. Moler. Direct imaging of the coexistence of ferromagnetism and superconductivity at the $LaAlO_3/SrTiO_3$ interface. *Nat Phys*, 7(10):767–771, Oct 2011. ISSN 1745-2473.
(Cited on pages 16, 91, 92, 98, 113, and 143.)

[150] Lu Li, C. Richter, J. Mannhart, and R. C. Ashoori. Coexistence of magnetic order and two-dimensional superconductivity at $LaAlO_3/SrTiO_3$ interfaces. *Nat Phys*, 7(10):762–766, Oct 2011. ISSN 1745-2473.
(Cited on pages 16, 91, and 143.)

[151] Rossitza Pentcheva and Warren E. Pickett. Correlation-driven charge order at the interface between a mott and a band insulator. *Phys. Rev. Lett.*, 99:016802, Jul 2007.
(Cited on pages 16, 91, 98, 113, 143, 149, and 161.)

[152] Rossitza Pentcheva and Warren E. Pickett. Ionic relaxation contribution to the electronic reconstruction at the n-type $LaAlO_3/SrTiO_3$ interface. *Phys. Rev. B*, 78:205106, Nov 2008.
(Cited on pages 16, 91, 98, 113, 143, 149, and 161.)

[153] N. Pavlenko, T. Kopp, E. Y. Tsymbal, G. A. Sawatzky, and J. Mannhart. Magnetic and superconducting phases at the $LaAlO_3/SrTiO_3$ interface: The role of interfacial Ti $3d$ electrons. *Phys. Rev. B*, 85:020407(R), Jan 2012.
(Cited on pages 16, 98, 143, 149, 160, 161, 164, 165, and 170.)

[154] M. Salluzzo, S. Gariglio, D. Stornaiuolo, V. Sessi, S. Rusponi, C. Piamonteze, G. M. De Luca, M. Minola, D. Marré, A. Gadaleta, H. Brune, F. Nolting, N. B. Brookes, and G. Ghiringhelli. Origin of interface magnetism in $BiMnO_3/SrTiO_3$ and $LaAlO_3/SrTiO_3$ heterostructures. *Phys. Rev. Lett.*, 111:087204, Aug 2013.
(Cited on pages 16, 98, 143, 149, 160, and 164.)

[155] N. Pavlenko, T. Kopp, and J. Mannhart. Emerging magnetism and electronic phase separation at titanate interfaces. *Phys. Rev. B*, 88:201104(R), Nov 2013.
(Cited on pages 16, 98, 143, 149, 160, 161, 164, 165, and 170.)

[156] A. Annadi, Q. Zhang, X. Renshaw Wang, N. Tuzla, K. Gopinadhan, W. M. Lü, A. Roy Barman, Z. Q. Liu, A. Srivastava, S. Saha, Y. L. Zhao, S. W. Zeng, S. Dhar, E. Olsson, B. Gu, S. Yunoki, S. Maekawa, H. Hilgenkamp, T. Venkatesan, and Ariando. Anisotropic two-dimensional electron gas at the $LaAlO_3/SrTiO_3$ (110) interface. *Nat Commun*, 4:1838–, May 2013.
(Cited on pages 17, 89, 96, 141, and 168.)

[157] Wang Qing-Yan, Li Zhi, Zhang Wen-Hao, Zhang Zuo-Cheng, Zhang Jin-Song, Li Wei, Ding Hao, Ou Yun-Bo, Deng Peng, Chang Kai, Wen Jing, Song Can-Li, He Ke, Jia Jin-Feng, Ji Shuai-Hua, Wang Ya-Yu, Wang Li-Li, Chen Xi, Ma Xu-Cun, and Xue Qi-Kun. Interface-induced high-temperature superconductivity in single unit-cell FeSe films on $SrTiO_3$. *Chinese Physics Letters*, 29(3):037402, 2012.
(Cited on pages 18, 55, 92, 140, and 141.)

[158] Ivan Bozovic and Charles Ahn. A new frontier for superconductivity. *Nat Phys*, 10(12):892–895, Dec 2014. ISSN 1745-2473.
(Cited on pages 18, 19, 89, 140, and 141.)

[159] Dung-Hai Lee. What makes the T_c of $FeSe/SrTiO_3$ so high? *Chinese Physics B*, 24(11):117405, Oct 2015.
(Cited on pages 18, 19, 55, 89, 140, and 141.)

[160] Andrew Peter Mackenzie and Yoshiteru Maeno. The superconductivity of Sr_2RuO_4 and the physics of spin-triplet pairing. *Rev. Mod. Phys.*, 75:657–712, May 2003.
(Cited on pages 18, 20, 26, 55, 84, 86, and 148.)

[161] Yoshiteru Maeno, Shunichiro Kittaka, Takuji Nomura, Shingo Yonezawa, and Kenji Ishida. Evaluation of spin-triplet superconductivity in Sr_2RuO_4. *Journal of the Physical Society of Japan*, 81 (1):011009, Dec 2012.
(Cited on pages 18, 20, and 55.)

[162] Ying Liu and Zhi-Qiang Mao. Unconventional superconductivity in Sr_2RuO_4. *Physica C: Superconductivity and its Applications*, 514:339 – 353, Mar 2015. ISSN 0921-4534. Superconducting Materials: Conventional, Unconventional and Undetermined.
(Cited on pages 18, 20, and 55.)

[163] Robert Joynt and Louis Taillefer. The superconducting phases of UPt_3. *Rev. Mod. Phys.*, 74: 235–294, Mar 2002.
(Cited on pages 18, 21, 22, 55, and 88.)

[164] H.v. Löhneysen. The superconducting phases of UPt_3. *Physica B: Condensed Matter*, 197(1):551 – 562, 1994. ISSN 0921-4526.
(Cited on pages 18, 21, 22, and 55.)

[165] J. A. Mydosh and P. M. Oppeneer. *Colloquium* : Hidden order, superconductivity, and magnetism: The unsolved case of URu_2Si_2. *Rev. Mod. Phys.*, 83:1301–1322, Nov 2011.
(Cited on pages 18, 22, 23, 55, 87, and 88.)

[166] Kai Liu, Zhong-Yi Lu, and Tao Xiang. Atomic and electronic structures of FeSe monolayer and bilayer thin films on $SrTiO_3$ (001): First-principles study. *Phys. Rev. B*, 85:235123, Jun 2012. URL `http://dx.doi.org/10.1103/PhysRevB.85.235123`.
(Cited on page 19.)

[167] Defa Liu, Wenhao Zhang, Daixiang Mou, Junfeng He, Yun-Bo Ou, Qing-Yan Wang, Zhi Li, Lili Wang, Lin Zhao, Shaolong He, Yingying Peng, Xu Liu, Chaoyu Chen, Li Yu, Guodong Liu, Xiaoli Dong, Jun Zhang, Chuangtian Chen, Zuyan Xu, Jiangping Hu, Xi Chen, Xucun Ma, Qikun

Xue, and X.J. Zhou. Electronic origin of high-temperature superconductivity in single-layer FeSe superconductor. *Nat Commun*, 3:931, Jul 2012. URL http://dx.doi.org/10.1038/ncomms1946. (Cited on pages 18, 19, 92, and 143.)

[168] Shaolong He, Junfeng He, Wenhao Zhang, Lin Zhao, Defa Liu, Xu Liu, Daixiang Mou, Yun-Bo Ou, Qing-Yan Wang, Zhi Li, Lili Wang, Yingying Peng, Yan Liu, Chaoyu Chen, Li Yu, Guodong Liu, Xiaoli Dong, Jun Zhang, Chuangtian Chen, Zuyan Xu, Xi Chen, Xucun Ma, Qikun Xue, and X. J. Zhou. Phase diagram and electronic indication of high-temperature superconductivity at 65 K in single-layer FeSe films. *Nat Mater*, 12(7):605–610, Jul 2013. ISSN 1476-1122. (Cited on page 18.)

[169] Jian-Feng Ge, Zhi-Long Liu, Canhua Liu, Chun-Lei Gao, Dong Qian, Qi-Kun Xue, Ying Liu, and Jin-Feng Jia. Superconductivity above 100 K in single-layer FeSe films on doped $SrTiO_3$. *Nat Mater*, 14(3):285–289, March 2015. ISSN 1476-1122. (Cited on page 18.)

[170] Jang Song Yoo, Beom Hong Jong, Hun Min Byeong, Seung Kwon Yong, Jun Lee Kyu, Hwa Jung Myung, and Rhyee Jong-Soo. Superconducting properties of a stoichiometric FeSe compound and two anomalous features in the normal state. *Journal of Korean Physical Society*, 59:312, 2011. (Cited on page 18.)

[171] G Wu, Y L Xie, H Chen, M Zhong, R H Liu, B C Shi, Q J Li, X F Wang, T Wu, Y J Yan, J J Ying, and X H Chen. Superconductivity at 56 K in samarium-doped SrFeAsF. *Journal of Physics: Condensed Matter*, 21(14):142203, Mar 2009. (Cited on page 18.)

[172] Vladimir Cvetkovic and Oskar Vafek. Space group symmetry, spin-orbit coupling, and the low-energy effective hamiltonian for iron-based superconductors. *Phys. Rev. B*, 88:134510, Oct 2013. (Cited on page 18.)

[173] Ningning Hao and Shun-Qing Shen. Topological superconducting states in monolayer FeSe/$SrTiO_3$. *Phys. Rev. B*, 92:165104, Oct 2015. (Cited on pages 18 and 142.)

[174] Ningning Hao and Jiangping Hu. Topological phases in the single-layer FeSe. *Phys. Rev. X*, 4: 031053, Sep 2014. (Cited on page 18.)

[175] J. J. Lee, F. T. Schmitt, R. G. Moore, S. Johnston, Y.-T. Cui, W. Li, M. Yi, Z. K. Liu, M. Hashimoto, Y. Zhang, D. H. Lu, T. P. Devereaux, D.-H. Lee, and Z.-X. Shen. Interfacial mode coupling as the origin of the enhancement of T_c in FeSe films on $SrTiO_3$. *Nature*, 515 (7526):245–248, Nov 2014. ISSN 0028-0836. (Cited on page 19.)

[176] Liu Kai, Gao Miao, Lu Zhong-Yi, and Xiang Tao. First-principles study of FeSe epitaxial films on $SrTiO_3$. *Chinese Physics B*, 24(11):117402, 2015. (Cited on page 19.)

[177] Shiyong Tan, Yan Zhang, Miao Xia, Zirong Ye, Fei Chen, Xin Xie, Rui Peng, Difei Xu, Qin Fan, Haichao Xu, Juan Jiang, Tong Zhang, Xinchun Lai, Tao Xiang, Jiangping Hu, Binping Xie, and Donglai Feng. Interface-induced superconductivity and strain-dependent spin density waves in FeSe/$SrTiO_3$ thin films. *Nat Mater*, 12(7):634–640, July 2013. ISSN 1476-1122.
(Cited on pages 19 and 92.)

[178] PK Biswas, Z Salman, Q Song, R Peng, J Zhang, L Shu, DL Feng, T Prokscha, A Suter, and E Morenzoni. Direct evidence of nodeless clean superconductivity and determination of the superfluid density in single-layer FeSe grown on $SrTiO_3$. *arXiv:1602.02580*, Feb 2016.
(Cited on pages 19 and 92.)

[179] Y. Maeno, H. Hashimoto, K. Yoshida, S. Nishizaki, T. Fujita, J. G. Bednorz, and F. Lichtenberg. Superconductivity in a layered perovskite without copper. *Nature*, 372(6506):532–534, December 1994. URL `http://dx.doi.org/10.1038/372532a0`.
(Cited on pages 20, 21, and 81.)

[180] Tamio Oguchi. Electronic band structure of the superconductor Sr_2RuO_4. *Phys. Rev. B*, 51: 1385–1388, Jan 1995.
(Cited on page 20.)

[181] A. P. Mackenzie, S. R. Julian, A. J. Diver, G. J. McMullan, M. P. Ray, G. G. Lonzarich, Y. Maeno, S. Nishizaki, and T. Fujita. Quantum oscillations in the layered perovskite superconductor Sr_2RuO_4. *Phys. Rev. Lett.*, 76:3786–3789, May 1996.
(Cited on pages 20, 81, and 84.)

[182] C. Bergemann, S. R. Julian, A. P. Mackenzie, S. NishiZaki, and Y. Maeno. Detailed topography of the fermi surface of sr_2ruo_4. *Phys. Rev. Lett.*, 84:2662–2665, Mar 2000.
(Cited on page 20.)

[183] T M Rice and M Sigrist. Sr_2RuO_4: an electronic analogue of ^{3}He? *Journal of Physics: Condensed Matter*, 7(47):L643, 1995.
(Cited on pages 20, 81, 82, and 94.)

[184] G Baskaran. Why is Sr_2RuO_4 not a high Tc superconductor? electron correlation, hund's coupling and p-wave instability. *Physica B: Condensed Matter*, 223–224:490 – 495, Jun 1996. ISSN 0921-4526. Proceedings of the International Conference on Strongly Correlated Electron Systems.
(Cited on page 20.)

[185] K. Ishida, H. Mukuda, Y. Kitaoka, K. Asayama, Z. Q. Mao, Y. Mori, and Y. Maeno. Spin-triplet superconductivity in Sr_2RuO_4 identified by 17O knight shift. *Nature*, 396(6712):658–660, December 1998. ISSN 0028-0836.
(Cited on pages 20 and 81.)

[186] J. A. Duffy, S. M. Hayden, Y. Maeno, Z. Mao, J. Kulda, and G. J. McIntyre. Polarized-neutron scattering study of the cooper-pair moment in Sr_2RuO_4. *Phys. Rev. Lett.*, 85:5412–5415, Dec 2000.
(Cited on pages 20 and 81.)

[187] K. D. Nelson, Z. Q. Mao, Y. Maeno, and Y. Liu. Odd-parity superconductivity in Sr_2RuO_4. *Science*, 306(5699):1151–1154, Nov 2004. ISSN 0036-8075.
(Cited on pages 20 and 81.)

[188] P. G. Kealey, T. M. Riseman, E. M. Forgan, L. M. Galvin, A. P. Mackenzie, S. L. Lee, D. McK. Paul, R. Cubitt, D. F. Agterberg, R. Heeb, Z. Q. Mao, and Y. Maeno. Reconstruction from small-angle neutron scattering measurements of the real space magnetic field distribution in the mixed state of Sr_2RuO_4. *Phys. Rev. Lett.*, 84:6094–6097, Jun 2000.
(Cited on pages 20, 81, and 168.)

[189] M. S. Anwar, Taketomo Nakamura, S. Yonezawa, M. Yakabe, R. Ishiguro, H. Takayanagi, and Y. Maeno. Anomalous switching in $Nb/Ru/Sr_2RuO_4$ topological junctions by chiral domain wall motion. *Scientific Reports*, 3:2480–, Aug 2013.
(Cited on pages 20, 81, and 168.)

[190] Michael Stone and Rahul Roy. Edge modes, edge currents, and gauge invariance in p_x+ip_y superfluids and superconductors. *Phys. Rev. B*, 69:184511, May 2004.
(Cited on pages 20, 37, and 94.)

[191] J. R. Kirtley, C. Kallin, C. W. Hicks, E.-A. Kim, Y. Liu, K. A. Moler, Y. Maeno, and K. D. Nelson. Upper limit on spontaneous supercurrents in Sr_2RuO_4. *Phys. Rev. B*, 76:014526, Jul 2007.
(Cited on pages 20, 37, and 94.)

[192] Clifford W. Hicks, John R. Kirtley, Thomas M. Lippman, Nicholas C. Koshnick, Martin E. Huber, Yoshiteru Maeno, William M. Yuhasz, M. Brian Maple, and Kathryn A. Moler. Limits on superconductivity-related magnetization in Sr_2RuO_4 and $PrOs_4Sb_{12}$ from scanning SQUID microscopy. *Phys. Rev. B*, 81:214501, Jun 2010.
(Cited on pages 20, 37, and 94.)

[193] K. Deguchi, Z. Q. Mao, H. Yaguchi, and Y. Maeno. Gap structure of the spin-triplet superconductor Sr_2RuO_4 determined from the field-orientation dependence of the specific heat. *Phys. Rev. Lett.*, 92:047002, Jan 2004.
(Cited on page 20.)

[194] Takuji Nomura and Kosaku Yamada. Perturbation theory of spin-triplet superconductivity for Sr_2RuO_4. *Journal of the Physical Society of Japan*, 69(11):3678–3688, Nov 2000.
(Cited on pages 20 and 171.)

[195] Youichi Yanase and Masao Ogata. Microscopic identification of the d-vector in triplet superconductor Sr_2RuO_4. *Journal of the Physical Society of Japan*, 72(3):673–687, 2003.
(Cited on pages 20, 81, 82, 94, and 171.)

[196] D. F. Agterberg, T. M. Rice, and M. Sigrist. Orbital dependent superconductivity in Sr_2RuO_4. *Phys. Rev. Lett.*, 78:3374–3377, Apr 1997.
(Cited on pages 20 and 171.)

[197] S. Raghu, A. Kapitulnik, and S. A. Kivelson. Hidden quasi-one-dimensional superconductivity in Sr_2RuO_4. *Phys. Rev. Lett.*, 105:136401, Sep 2010.
(Cited on pages 20, 82, and 171.)

[198] Thomas Scaffidi, Jesper C. Romers, and Steven H. Simon. Pairing symmetry and dominant band in Sr_2RuO_4. *Phys. Rev. B*, 89:220510, Jun 2014.
(Cited on pages 20, 84, 85, 86, 170, and 171.)

[199] Mark A. Zurbuchen, Yunfa Jia, Stacy Knapp, Altaf H. Carim, Darrell G. Schlom, Ling-Nian Zou, and Ying Liu. Suppression of superconductivity by crystallographic defects in epitaxial Sr_2RuO_4 films. *Applied Physics Letters*, 78(16):2351–2353, 2001.
(Cited on page 21.)

[200] Mark A. Zurbuchen, Yunfa Jia, Stacy Knapp, Altaf H. Carim, Darrell G. Schlom, and X. Q. Pan. Defect generation by preferred nucleation in epitaxial $Sr_2RuO_4/LaAlO_3$. *Applied Physics Letters*, 83(19):3891–3893, 2003.
(Cited on page 21.)

[201] S. Adenwalla, S. W. Lin, Q. Z. Ran, Z. Zhao, J. B. Ketterson, J. A. Sauls, L. Taillefer, D. G. Hinks, M. Levy, and Bimal K. Sarma. Phase diagram of UPt_3 from ultrasonic velocity measurements. *Phys. Rev. Lett.*, 65:2298–2301, Oct 1990.
(Cited on pages 21 and 22.)

[202] Y Kasahara, H Shishido, T Shibauchi, Y Haga, T D Matsuda, Y Onuki, and Y Matsuda. Superconducting gap structure of heavy-fermion compound URu_2Si_2 determined by angle-resolved thermal conductivity. *New Journal of Physics*, 11(5):055061, May 2009. doi: 10.1088/1367-2630/11/5/055061. URL `http://stacks.iop.org/1367-2630/11/i=5/a=055061`.
(Cited on pages 21, 23, and 87.)

[203] C. S. Wang, M. R. Norman, R. C. Albers, A. M. Boring, W. E. Pickett, H. Krakauer, and N. E. Christensen. Fermi surface of UPt_3 within the local-density approximation. *Phys. Rev. B*, 35: 7260–7263, May 1987.
(Cited on pages 21 and 88.)

[204] R. A. Fisher, S. Kim, B. F. Woodfield, N. E. Phillips, L. Taillefer, K. Hasselbach, J. Flouquet, A. L. Giorgi, and J. L. Smith. Specific heat of UPt_3: Evidence for unconventional superconductivity. *Phys. Rev. Lett.*, 62:1411–1414, Mar 1989.
(Cited on page 21.)

[205] K. Hasselbach, L. Taillefer, and J. Flouquet. Critical point in the superconducting phase diagram of UPt_3. *Phys. Rev. Lett.*, 63:93–96, Jul 1989.
(Cited on page 21.)

[206] Benoit Lussier, Brett Ellman, and Louis Taillefer. Determination of the gap structure in UPt_3 by thermal conductivity. *Phys. Rev. B*, 53:5145–5148, Mar 1996.
(Cited on pages 22 and 88.)

[207] J. D. Strand, D. J. Van Harlingen, J. B. Kycia, and W. P. Halperin. Evidence for complex superconducting order parameter symmetry in the low-temperature phase of UPt_3 from josephson interferometry. *Phys. Rev. Lett.*, 103:197002, Nov 2009.
(Cited on pages 22 and 88.)

[208] C. H. Choi and J. A. Sauls. Identification of odd-parity superconductivity in UPt_3 from paramagnetic effects on the upper critical field. *Phys. Rev. Lett.*, 66:484–487, Jan 1991.
(Cited on pages 22, 88, and 89.)

[209] R. H. Heffner, D. W. Cooke, A. L. Giorgi, R. L. Hutson, M. E. Schillaci, H. D. Rempp, J. L. Smith, J. O. Willis, D. E. MacLaughlin, C. Boekema, R. L. Lichti, J. Oostens, and A. B. Denison. Muon spin rotation in the magnetic and superconducting ground states of $(U, Th)Be_{13}$ and $(U, Th)Pt_3$. *Phys. Rev. B*, 39:11345–11357, Jun 1989.
(Cited on pages 22, 88, and 89.)

[210] G. Aeppli, E. Bucher, C. Broholm, J. K. Kjems, J. Baumann, and J. Hufnagl. Magnetic order and fluctuations in superconducting UPt_3. *Phys. Rev. Lett.*, 60:615–618, Feb 1988.
(Cited on pages 22, 88, and 89.)

[211] T. Trappmann, H. v. Löhneysen, and L. Taillefer. Pressure dependence of the superconducting phases in UPt_3. *Phys. Rev. B*, 43:13714–13716, Jun 1991.
(Cited on pages 22 and 88.)

[212] S. M. Hayden, L. Taillefer, C. Vettier, and J. Flouquet. Antiferromagnetic order in UPt_3 under pressure: Evidence for a direct coupling to superconductivity. *Phys. Rev. B*, 46:8675–8678, Oct 1992.
(Cited on pages 22 and 88.)

[213] Robert Joynt. Superconducting UPt_3 under pressure. *Phys. Rev. Lett.*, 71:3015–3018, Nov 1993.
(Cited on pages 22, 74, 88, and 89.)

[214] JA Sauls. The order parameter for the superconducting phases of UPt_3. *Advances in Physics*, 43 (1):113–141, 1994.
(Cited on pages 22, 74, 88, and 89.)

[215] John A Mydosh and Peter M Oppeneer. Hidden order behaviour in URu_2Si_2 (a critical review of the status of hidden order in 2014). *Philosophical Magazine*, 94(32-33):3642–3662, 2014.
(Cited on pages 22 and 88.)

[216] T. T. M. Palstra, A. A. Menovsky, J. van den Berg, A. J. Dirkmaat, P. H. Kes, G. J. Nieuwenhuys, and J. A. Mydosh. Superconducting and magnetic transitions in the heavy-fermion system URu_2Si_2. *Phys. Rev. Lett.*, 55:2727–2730, Dec 1985.
(Cited on pages 22 and 87.)

[217] M. B. Maple, J. W. Chen, Y. Dalichaouch, T. Kohara, C. Rossel, M. S. Torikachvili, M. W. McElfresh, and J. D. Thompson. Partially gapped fermi surface in the heavy-electron superconductor URu_2Si_2. *Phys. Rev. Lett.*, 56:185–188, Jan 1986.
(Cited on pages 22 and 87.)

[218] W. Schlabitz, J. Baumann, B. Pollit, U. Rauchschwalbe, H. M. Mayer, U. Ahlheim, and C. D. Bredl. Superconductivity and magnetic order in a strongly interacting fermi-system: URu_2Si_2. *Zeitschrift für Physik B Condensed Matter*, 62(2):171–177. ISSN 1431-584X.
(Cited on pages 22 and 87.)

[219] C. Broholm, J. K. Kjems, W. J. L. Buyers, P. Matthews, T. T. M. Palstra, A. A. Menovsky, and J. A. Mydosh. Magnetic excitations and ordering in the heavy-electron superconductor URu_2Si_2. *Phys. Rev. Lett.*, 58:1467–1470, Apr 1987.
(Cited on pages 22 and 87.)

[220] K. Behnia, R. Bel, Y. Kasahara, Y. Nakajima, H. Jin, H. Aubin, K. Izawa, Y. Matsuda, J. Flouquet, Y. Haga, Y. Ōnuki, and P. Lejay. Thermal transport in the hidden-order state of URu_2Si_2. *Phys. Rev. Lett.*, 94:156405, Apr 2005.
(Cited on page 22.)

[221] Y. Kasahara, T. Iwasawa, H. Shishido, T. Shibauchi, K. Behnia, Y. Haga, T. D. Matsuda, Y. Onuki, M. Sigrist, and Y. Matsuda. Exotic superconducting properties in the electron-hole-compensated heavy-fermion "semimetal" URu_2Si_2. *Phys. Rev. Lett.*, 99:116402, Sep 2007.
(Cited on pages 23 and 87.)

[222] K. Yano, T. Sakakibara, T. Tayama, M. Yokoyama, H. Amitsuka, Y. Homma, P. Miranović, M. Ichioka, Y. Tsutsumi, and K. Machida. Field-angle-dependent specific heat measurements and gap determination of a heavy fermion superconductor URu_2Si_2. *Phys. Rev. Lett.*, 100:017004, Jan 2008.
(Cited on pages 23 and 87.)

[223] Shunichiro Kittaka, Yusei Shimizu, Toshiro Sakakibara, Yoshinori Haga, Etsuji Yamamoto, Yoshichika Onuki, Yasumasa Tsutsumi, Takuya Nomoto, Hiroaki Ikeda, and Kazushige Machida. Evidence for chiral d-wave superconductivity in URu_2Si_2 from the field-angle variation of its specific heat. *J. Phys. Soc. Jpn.*, 85(3):033704, February 2016. ISSN 0031-9015.
(Cited on pages 23 and 87.)

[224] A. A. Abrikosov, L. P. Gorkov, and I. E. Dzyaloshinski. *Methods of Quantum Field Theory in Statistical Physics*. Dover Publications, revised english edition, 1975.
(Cited on pages 23 and 24.)

[225] A. V. Balatsky, I. Vekhter, and Jian-Xin Zhu. Impurity-induced states in conventional and unconventional superconductors. *Rev. Mod. Phys.*, 78:373–433, May 2006.
(Cited on pages 23 and 26.)

[226] A.M. Finkel'stein. Suppression of superconductivity in homogeneously disordered systems. *Physica B: Condensed Matter*, 197(1):636 – 648, 1994. ISSN 0921-4526.
(Cited on pages 23 and 25.)

[227] Michael V Sadovskii. Superconductivity and localization. *Physics Reports*, 282(5–6):225 – 348, 1997. ISSN 0370-1573.
(Cited on pages 23, 26, 145, and 164.)

[228] S. F. Edwards and P. W. Anderson. Theory of spin glasses. *Journal of Physics F: Metal Physics*, 5(5):965, 1975.
(Cited on pages 24 and 150.)

[229] P.W. Anderson. Theory of dirty superconductors. *Journal of Physics and Chemistry of Solids*, 11(1–2):26, Sep 1959. ISSN 0022-3697.
(Cited on pages 25, 142, 145, 146, 148, 149, 155, 163, and 263.)

[230] A. A. Abrikosov and L. P. Gorkov. On the theory of superconducting alloys I. The electrodynamics of alloys at absolute zero. *Zh. Eksp. Teor. Fiz.*, 35:1558, 1958.
(Cited on pages 25, 142, 145, 146, 148, 149, 155, 163, and 263.)

[231] A. A. Abrikosov and L. P. Gorkov. Superconducting alloys at finite temperatures. *Zh. Eksp. Teor. Fiz.*, 36:319, 1959.
(Cited on pages 25, 142, 145, 146, 148, 149, 155, 163, and 263.)

[232] I. S. Burmistrov, I. V. Gornyi, and A. D. Mirlin. Enhancement of the critical temperature of superconductors by anderson localization. *Phys. Rev. Lett.*, 108:017002, Jan 2012.
(Cited on page 25.)

[233] L. N. Bulaevskii and M. V. Sadovskii. Localization and superconductivity. *JETP Lett.*, 39:640, Jun 1984.
(Cited on pages 26 and 145.)

[234] R. Balian and N. R. Werthamer. Superconductivity with pairs in a relative p wave. *Phys. Rev.*, 131:1553–1564, Aug 1963.
(Cited on pages 26 and 38.)

[235] A. A. Golubov and I. I. Mazin. Effect of magnetic and nonmagnetic impurities on highly anisotropic superconductivity. *Phys. Rev. B*, 55:15146–15152, Jun 1997.
(Cited on pages 26, 142, 145, 146, 148, 164, and 169.)

[236] D. V. Efremov, M. M. Korshunov, O. V. Dolgov, A. A. Golubov, and P. J. Hirschfeld. Disorder-induced transition between $s_{\pm}$ and s_{++} states in two-band superconductors. *Phys. Rev. B*, 84: 180512, Nov 2011.
(Cited on pages 26, 142, 145, 146, 148, 164, and 169.)

[237] Karen Michaeli and Liang Fu. Spin-orbit locking as a protection mechanism of the odd-parity superconducting state against disorder. *Phys. Rev. Lett.*, 109:187003, Oct 2012.
(Cited on pages 26, 142, 145, 146, 148, 164, and 169.)

[238] M. M. Korshunov, D. V. Efremov, A. A. Golubov, and O. V. Dolgov. Unexpected impact of magnetic disorder on multiband superconductivity. *Phys. Rev. B*, 90:134517, Oct 2014.
(Cited on pages 26, 142, 145, 146, 148, 149, 164, and 169.)

[239] M. Hoyer, M. S. Scheurer, S. V. Syzranov, and J. Schmalian. Pair breaking due to orbital magnetism in iron-based superconductors. *Phys. Rev. B*, 91:054501, Feb 2015.
(Cited on pages 26, 142, 145, 146, 148, 149, 164, 165, 169, 175, and 261.)

[240] M. S. Scheurer, M. Hoyer, and J. Schmalian. Pair breaking in multiorbital superconductors: An application to oxide interfaces. *Phys. Rev. B*, 92:014518, Jul 2015.
(Cited on pages 26, 142, 145, 146, 148, 152, 158, 162, 163, 164, 165, 169, and 175.)

[241] Jun Li, Yanfeng Guo, Shoubao Zhang, Shan Yu, Yoshihiro Tsujimoto, Hiroshi Kontani, Kazunari Yamaura, and Eiji Takayama-Muromachi. Linear decrease of critical temperature with increasing Zn substitution in the iron-based superconductor $BaFe_{1.89-2x}Zn_{2x}Co_{0.11}As_2$. *Phys. Rev. B*, 84: 020513, Jul 2011.
(Cited on pages 26, 149, and 164.)

[242] M. A. Armstrong. *Basic topology*. McGraw-Hill Book Company, 1979.
(Cited on page 27.)

[243] J. Bellissard, A. van Elst, and H. Schulz-Baldes. The noncommutative geometry of the quantum Hall effect. *Journal of Mathematical Physics*, 35(10):5373–5451, 1994.
(Cited on page 27.)

[244] Jian Li, Rui-Lin Chu, J. K. Jain, and Shun-Qing Shen. Topological anderson insulator. *Phys. Rev. Lett.*, 102:136806, Apr 2009.
(Cited on page 27.)

[245] Liang Fu. Topological crystalline insulators. *Phys. Rev. Lett.*, 106:106802, Mar 2011.
(Cited on page 28.)

[246] Yoichi Ando and Liang Fu. Topological crystalline insulators and topological superconductors: From concepts to materials. *Annual Review of Condensed Matter Physics*, 6(1):361–381, 2015.
(Cited on pages 28 and 38.)

[247] Shinsei Ryu, Andreas P Schnyder, Akira Furusaki, and Andreas W W Ludwig. Topological insulators and superconductors: tenfold way and dimensional hierarchy. *New Journal of Physics*, 12(6):065010, 2010.
(Cited on pages 28, 29, 30, 32, 34, 35, 37, and 86.)

[248] Martin R. Zirnbauer. Riemannian symmetric superspaces and their origin in random-matrix theory. *Journal of Mathematical Physics*, 37(10):4986–5018, 1996.
(Cited on page 28.)

[249] Alexander Altland and Martin R. Zirnbauer. Nonstandard symmetry classes in mesoscopic normal-superconducting hybrid structures. *Phys. Rev. B*, 55:1142–1161, Jan 1997.
(Cited on pages 28, 45, 46, 53, and 127.)

[250] C. W. J. Beenakker. Random-matrix theory of quantum transport. *Rev. Mod. Phys.*, 69:731–808, Jul 1997.
(Cited on page 28.)

[251] Élie Cartan. Sur une classe remarquable d'espaces de riemann, I. *Bulletin de la Société Mathématique de France*, 54:214–216, 1926.
(Cited on pages 28, 45, 46, 53, and 127.)

[252] B. A. Bernevig, T. L. Hughes, and S.-C. Zhang. Quantum spin Hall effect and topological phase transition in HgTe quantum wells. *Science*, 314:1757, 2006.
(Cited on pages 29, 35, and 48.)

[253] Liang Fu, C. L. Kane, and E. J. Mele. Topological insulators in three dimensions. *Phys. Rev. Lett.*, 98:106803, Mar 2007.
(Cited on pages 29, 34, 36, and 48.)

[254] J. E. Moore and L. Balents. Topological invariants of time-reversal-invariant band structures. *Phys. Rev. B*, 75:121306(R), Mar 2007.
(Cited on pages 29, 34, 36, and 48.)

[255] Rahul Roy. Topological phases and the quantum spin Hall effect in three dimensions. *Phys. Rev. B*, 79:195322, May 2009.
(Cited on pages 29, 34, 36, and 48.)

[256] Xiao-Liang Qi, Taylor L. Hughes, and Shou-Cheng Zhang. Topological field theory of time-reversal invariant insulators. *Phys. Rev. B*, 78:195424, Nov 2008.
(Cited on pages 29, 32, 37, 38, 43, and 44.)

[257] Alexei Kitaev. Periodic table for topological insulators and superconductors. *AIP Conference Proceedings*, 1134(1):22–30, 2009.
(Cited on pages 30 and 34.)

[258] A Yu Kitaev. Unpaired majorana fermions in quantum wires. *Physics-Uspekhi*, 44(10S):131, 2001.
(Cited on pages 30, 32, and 33.)

[259] T. Kaluza. Sitzungsber. Preuss. Akad. Wiss. Berlin (Math. Phys.). *Z. Phys*, 37:895, 1921.
(Cited on page 32.)

[260] Oskar Klein. Quantentheorie und fünfdimensionale relativitätstheorie. *Zeitschrift für Physik*, 37 (12):895–906, Dec . ISSN 0044-3328.
(Cited on page 32.)

[261] Meng Cheng, Roman M. Lutchyn, Victor Galitski, and S. Das Sarma. Splitting of Majorana-fermion modes due to intervortex tunneling in a $p_x + ip_y$ superconductor. *Phys. Rev. Lett.*, 103: 107001, Aug 2009.
(Cited on page 33.)

[262] B. Andrei Bernevig. *Topological Insulators and Topological Superconductors*. Princeton University Press, Apr 2013. ISBN 9780691151755.
(Cited on pages 33, 34, 35, 36, 37, 42, 43, 109, 141, and 158.)

[263] Constantine Callias. Axial anomalies and index theorems on open spaces. *Communications in Mathematical Physics*, 62(3):213–234, 1978. ISSN 1432-0916.
(Cited on page 34.)

[264] R. Bott and R. Seeley. Some remarks on the paper of Callias. *Communications in Mathematical Physics*, 62(3):235–245, 1978. ISSN 1432-0916.
(Cited on page 34.)

[265] Takahiro Fukui and Takanori Fujiwara. Topological stability of Majorana zero modes in superconductor–topological insulator systems. *Journal of the Physical Society of Japan*, 79(3):033701, Feb 2010.
(Cited on page 34.)

[266] Rahul Roy. Topological Majorana and Dirac zero modes in superconducting vortex cores. *Phys. Rev. Lett.*, 105:186401, Oct 2010.
(Cited on pages 34 and 42.)

[267] Takahiro Fukui and Takanori Fujiwara. Z_2 index theorem for Majorana zero modes in a class D topological superconductor. *Phys. Rev. B*, 82:184536, Nov 2010.
(Cited on pages 34 and 37.)

[268] Ying Ran, Yi Zhang, and Ashvin Vishwanath. One-dimensional topologically protected modes in topological insulators with lattice dislocations. *Nat Phys*, 5(4):298–303, Apr 2009. ISSN 1745-2473.
(Cited on page 34.)

[269] Jeffrey C. Y. Teo and C. L. Kane. Topological defects and gapless modes in insulators and superconductors. *Phys. Rev. B*, 82:115120, Sep 2010.
(Cited on pages 34, 35, 37, 42, and 86.)

[270] Suk Bum Chung, Cheung Chan, and Hong Yao. Dislocation Majorana zero modes in perovskite oxide 2DEG. *arXiv:1505.00790*, May 2015.
(Cited on pages 35 and 86.)

[271] C. L. Kane and E. J. Mele. Z_2 topological order and the quantum spin Hall effect. *Phys. Rev. Lett.*, 95:146802, 2005.
(Cited on pages 35 and 46.)

[272] C. L. Kane and E. J. Mele. Quantum spin Hall effect in graphene. *Phys. Rev. Lett.*, 95:226801, 2005.
(Cited on pages 35 and 46.)

[273] Markus König, Steffen Wiedmann, Christoph Brüne, Andreas Roth, Hartmut Buhmann, Laurens W. Molenkamp, Xiao-Liang Qi, and Shou-Cheng Zhang. Quantum spin Hall insulator state in HgTe quantum wells. *Science*, 318(5851):766–770, November 2007.
(Cited on page 35.)

[274] Yuval Oreg, Gil Refael, and Felix von Oppen. Helical liquids and Majorana bound states in quantum wires. *Phys. Rev. Lett.*, 105:177002, Oct 2010.
(Cited on pages 36 and 109.)

[275] Roman M. Lutchyn, Jay D. Sau, and S. Das Sarma. Majorana fermions and a topological phase transition in semiconductor-superconductor heterostructures. *Phys. Rev. Lett.*, 105:077001, Aug 2010.
(Cited on pages 36 and 109.)

[276] Sumanta Tewari and Jay D. Sau. Topological invariants for spin-orbit coupled superconductor nanowires. *Phys. Rev. Lett.*, 109:150408, Oct 2012.
(Cited on page 36.)

[277] V. Gurarie and L. Radzihovsky. Zero modes of two-dimensional chiral p-wave superconductors. *Phys. Rev. B*, 75:212509, Jun 2007.
(Cited on page 37.)

[278] Rahul Roy. Topological superfluids with time reversal symmetry. *arXiv:0803.2868*, Mar 2008.
(Cited on pages 37 and 42.)

[279] Xiao-Liang Qi, Taylor L. Hughes, S. Raghu, and Shou-Cheng Zhang. Time-reversal-invariant topological superconductors and superfluids in two and three dimensions. *Phys. Rev. Lett.*, 102: 187001, May 2009.
(Cited on pages 37 and 42.)

[280] Xiao-Liang Qi, Taylor L. Hughes, and Shou-Cheng Zhang. Topological invariants for the Fermi surface of a time-reversal-invariant superconductor. *Phys. Rev. B*, 81:134508, Apr 2010.
(Cited on pages 37, 38, 83, 128, 138, and 260.)

[281] Satoshi Murakawa, Yuichiro Wada, Yuta Tamura, Masahiro Wasai, Masamichi Saitoh, Yuki Aoki, Ryuji Nomura, Yuichi Okuda, Yasushi Nagato, Mikio Yamamoto, Seiji Higashitani, and Katsuhiko Nagai. Surface Majorana cone of the superfluid ^{3}He B phase. *Journal of the Physical Society of Japan*, 80(1):013602, Dec 2011.
(Cited on page 38.)

[282] Liang Fu and Erez Berg. Odd-parity topological superconductors: Theory and application to $Cu_xBi_2Se_3$. *Phys. Rev. Lett.*, 105:097001, Aug 2010.
(Cited on pages 38 and 129.)

[283] Masatoshi Sato. Topological odd-parity superconductors. *Phys. Rev. B*, 81:220504, Jun 2010.
(Cited on page 38.)

[284] Y. S. Hor, A. J. Williams, J. G. Checkelsky, P. Roushan, J. Seo, Q. Xu, H. W. Zandbergen, A. Yazdani, N. P. Ong, and R. J. Cava. Superconductivity in $Cu_xBi_2Se_3$ and its implications for pairing in the undoped topological insulator. *Phys. Rev. Lett.*, 104:057001, Feb 2010.
(Cited on page 38.)

[285] N. Goldman, I. Satija, P. Nikolic, A. Bermudez, M. A. Martin-Delgado, M. Lewenstein, and I. B. Spielman. Realistic time-reversal invariant topological insulators with neutral atoms. *Phys. Rev. Lett.*, 105:255302, 2010.
(Cited on pages 39, 45, 46, 53, and 167.)

[286] Fabrice Gerbier and Jean Dalibard. Gauge fields for ultracold atoms in optical superlattices. *New J. Phys.*, 12(3):033007, 2010. ISSN 1367-2630.
(Cited on pages 39, 45, 46, 53, and 167.)

[287] Daniel Cocks, Peter P. Orth, Stephan Rachel, Michael Buchhold, Karyn Le Hur, and Walter Hofstetter. Time-reversal-invariant Hofstadter-Hubbard model with ultracold fermions. *Phys. Rev. Lett.*, 109:205303, 2012.
(Cited on pages 39, 45, and 46.)

[288] N Goldman, F Gerbier, and M Lewenstein. Realizing non-Abelian gauge potentials in optical square lattices: an application to atomic chern insulators. *J. Phys. B*, 46(13):134010, 2013.
(Cited on pages 39, 45, 46, 53, and 167.)

[289] M. Aidelsburger, M. Atala, M. Lohse, J. T. Barreiro, B. Paredes, and I. Bloch. Realization of the hofstadter hamiltonian with ultracold atoms in optical lattices. *Phys. Rev. Lett.*, 111:185301, Oct 2013.
(Cited on page 39.)

[290] Gregor Jotzu, Michael Messer, Remi Desbuquois, Martin Lebrat, Thomas Uehlinger, Daniel Greif, and Tilman Esslinger. Experimental realization of the topological Haldane model with ultracold fermions. *Nature*, 515(7526):237–240, November 2014. ISSN 0028-0836.
(Cited on page 39.)

[291] Jean Dalibard, Fabrice Gerbier, Gediminas Juzeliūnas, and Patrik Öhberg. *Colloquium* : Artificial gauge potentials for neutral atoms. *Rev. Mod. Phys.*, 83:1523–1543, Nov 2011.
(Cited on page 39.)

[292] Mathias S. Scheurer. Non-adiabatic processes in Majorana qubit systems. Master's thesis, Karlsruher Institute of Technology, Department of Physics, Institut für Theorie der Kondensierten Materie, 2012.
(Cited on pages 39, 42, and 175.)

[293] Ady Stern, Felix von Oppen, and Eros Mariani. Geometric phases and quantum entanglement as building blocks for non-Abelian quasiparticle statistics. *Phys. Rev. B*, 70:205338, Nov 2004.
(Cited on page 40.)

[294] Michael Stone and Suk-Bum Chung. Fusion rules and vortices in $p_x + ip_y$ superconductors. *Phys. Rev. B*, 73:014505, Jan 2006.
(Cited on page 40.)

[295] Michael A. Nielsen and Isaac L. Chuang. *Quantum Computation and Quantum Information*. Cambridge University Press, 2000. ISBN 9780521635035.
(Cited on page 41.)

[296] Meng Cheng, Victor Galitski, and S. Das Sarma. Nonadiabatic effects in the braiding of non-Abelian anyons in topological superconductors. *Phys. Rev. B*, 84:104529, Sep 2011.
(Cited on page 42.)

[297] G. Goldstein and C. Chamon. Decay rates for topological memories encoded with Majorana fermions. *Phys. Rev. B*, 84:205109, Nov 2011.
(Cited on page 42.)

[298] E. Perfetto. Dynamical formation and manipulation of Majorana fermions in driven quantum wires in contact with a superconductor. *Phys. Rev. Lett.*, 110:087001, Feb 2013.
(Cited on page 42.)

[299] M. S. Scheurer and A. Shnirman. Nonadiabatic processes in Majorana qubit systems. *Phys. Rev. B*, 88:064515, Aug 2013.
(Cited on pages 42 and 175.)

[300] Torsten Karzig, Gil Refael, and Felix von Oppen. Boosting Majorana zero modes. *Phys. Rev. X*, 3:041017, Nov 2013.
(Cited on page 42.)

[301] Diego Rainis and Daniel Loss. Majorana qubit decoherence by quasiparticle poisoning. *Phys. Rev. B*, 85:174533, May 2012.
(Cited on page 42.)

[302] Jay D. Sau, Sumanta Tewari, and S. Das Sarma. Universal quantum computation in a semiconductor quantum wire network. *Phys. Rev. A*, 82:052322, Nov 2010.
(Cited on page 42.)

[303] Karsten Flensberg. Non-Abelian operations on Majorana fermions via single-charge control. *Phys. Rev. Lett.*, 106:090503, Mar 2011.
(Cited on page 42.)

[304] Lukasz Fidkowski and Alexei Kitaev. Effects of interactions on the topological classification of free fermion systems. *Phys. Rev. B*, 81:134509, Apr 2010.
(Cited on pages 42 and 43.)

[305] Zhong Wang, Xiao-Liang Qi, and Shou-Cheng Zhang. Topological order parameters for interacting topological insulators. *Phys. Rev. Lett.*, 105:256803, Dec 2010.
(Cited on page 43.)

[306] Maarten F.L. Golterman, Karl Jansen, and David B. Kaplan. Chern-Simons currents and chiral fermions on the lattice. *Physics Letters B*, 301(2–3):219 – 223, 1993. ISSN 0370-2693.
(Cited on page 43.)

[307] V. Gurarie. Single-particle Green's functions and interacting topological insulators. *Phys. Rev. B*, 83:085426, Feb 2011.
(Cited on pages 43 and 44.)

[308] Lei Wang, Hua Jiang, Xi Dai, and X. C. Xie. Pole expansion of self-energy and interaction effect for topological insulators. *Phys. Rev. B*, 85:235135, Jun 2012.
(Cited on pages 43 and 128.)

[309] Zhong Wang and Shou-Cheng Zhang. Simplified topological invariants for interacting insulators. *Phys. Rev. X*, 2:031008, Aug 2012.
(Cited on pages 43, 44, and 128.)

[310] Zhong Wang and Shou-Cheng Zhang. Strongly correlated topological superconductors and topological phase transitions via Green's function. *Phys. Rev. B*, 86:165116, Oct 2012.
(Cited on pages 43, 44, 128, and 255.)

[311] Zhong Wang and Binghai Yan. Topological Hamiltonian as an exact tool for topological invariants. *Journal of Physics: Condensed Matter*, 25(15s):155601, Mar 2013.
(Cited on page 44.)

[312] S. Raghu, X.-L. Qi, C. Honerkamp, and S.-C. Zhang. Topological Mott insulators. *Phys. Rev. Lett.*, 100:156401, 2008.
(Cited on page 44.)

[313] P.W. Anderson. Resonating valence bonds: A new kind of insulator? *Materials Research Bulletin*, 8(2):153 – 160, 1973. ISSN 0025-5408.
(Cited on page 44.)

[314] Stephan Rachel and Karyn Le Hur. Topological insulators and Mott physics from the Hubbard interaction. *Phys. Rev. B*, 82:075106, Aug 2010.
(Cited on pages 44 and 49.)

[315] A.M. Polyakov. Compact gauge fields and the infrared catastrophe. *Physics Letters B*, 59(1):82 – 84, 1975. ISSN 0370-2693.
(Cited on page 44.)

[316] Michael W. Young, Sung-Sik Lee, and Catherine Kallin. Fractionalized quantum spin Hall effect. *Phys. Rev. B*, 78:125316, Sep 2008.
(Cited on page 44.)

[317] Mathias S. Scheurer, Stephan Rachel, and Peter P. Orth. Dimensional crossover and cold-atom realization of topological Mott insulators. *Scientific Reports*, 5:8386, February 2015.
(Cited on pages 45, 175, and 225.)

[318] Douglas R. Hofstadter. Energy levels and wave functions of Bloch electrons in rational and irrational magnetic fields. *Phys. Rev. B*, 14:2239–2249, Sep 1976.
(Cited on page 46.)

[319] Chao-Xing Liu, HaiJun Zhang, Binghai Yan, Xiao-Liang Qi, Thomas Frauenheim, Xi Dai, Zhong Fang, and Shou-Cheng Zhang. Oscillatory crossover from two-dimensional to three-dimensional topological insulators. *Phys. Rev. B*, 81:041307(R), Jan 2010.
(Cited on page 46.)

[320] Takahiro Fukui and Yasuhiro Hatsugai. Topological aspects of the quantum spin-Hall effect in graphene: Z_2 topological order and spin Chern number. *Phys. Rev. B*, 75(12):121403, Mar 2007.
(Cited on pages 49 and 228.)

[321] Jan Carl Budich, Ronny Thomale, Gang Li, Manuel Laubach, and Shou-Cheng Zhang. Fluctuation-induced topological quantum phase transitions in quantum spin-Hall and anomalous-Hall insulators. *Phys. Rev. B*, 86:201407, Nov 2012.
(Cited on page 49.)

[322] Xibo Zhang, Chen-Lung Hung, Shih-Kuang Tung, and Cheng Chin. Observation of quantum criticality with ultracold atoms in optical lattices. *Science*, 335(6072):1070–1072, 2012.
(Cited on page 53.)

[323] Eric L. Hazlett, Li-Chung Ha, and Cheng Chin. Anomalous thermoelectric transport in two-dimensional bose gas. *arXiv:1306.4018*, 2013.
(Cited on page 53.)

[324] William Witczak-Krempa, Ting Pong Choy, and Yong Baek Kim. Gauge field fluctuations in three-dimensional topological Mott insulators. *Phys. Rev. B*, 82:165122, Oct 2010.
(Cited on page 53.)

[325] Mathias S. Scheurer and Jörg Schmalian. Design principles for time-reversal symmetry breaking superconductivity in interfaces and two-dimensional sheets. *arXiv:1503.03646*, 2015.
(Cited on pages 56, 63, 76, 79, 90, 92, 93, 145, 154, 164, 175, and 229.)

[326] Mathias S. Scheurer, Daniel F. Agterberg, and Jörg Schmalian. Selection rules for cooper pairing in two-dimensional interfaces and sheets. *arXiv:1503.03646v2*, 2016.
(Cited on pages 56, 76, 77, 93, 145, 154, 164, 175, and 229.)

[327] I. A. Sergienko and S. H. Curnoe. Order parameter in superconductors with nondegenerate bands. *Phys. Rev. B*, 70:214510, Dec 2004.
(Cited on pages 61 and 63.)

[328] Michael Tinkham. *Introduction to Superconductivity: Second Edition (Dover Books on Physics) (Vol i)*. Dover Publications, second edition edition, 6 2004. ISBN 9780486435039.
(Cited on page 67.)

[329] M. Gomes da Silva, F. Dinóla Neto, I.T. Padilha, J. Ricardo de Sousa, and M.A. Continentino. First-order superconducting transition in the inter-band model. *Physics Letters A*, 378(20):1396 – 1401, 2014. ISSN 0375-9601.
(Cited on page 67.)

[330] K. V. Samokhin. Symmetry and topology of two-dimensional noncentrosymmetric superconductors. *Phys. Rev. B*, 92:174517, Nov 2015.
(Cited on page 75.)

[331] H. Murakawa, K. Ishida, K. Kitagawa, Z. Q. Mao, and Y. Maeno. Measurement of the ^{101}Ru-Knight shift of superconducting Sr_2RuO_4 in a parallel magnetic field. *Phys. Rev. Lett.*, 93:167004, Oct 2004.
(Cited on pages 81 and 94.)

[332] H. Murakawa, K. Ishida, K. Kitagawa, H. Ikeda, Z. Q. Mao, and Y. Maeno. 101Ru knight shift measurement of superconducting Sr_2RuO_4 under small magnetic fields parallel to the RuO_2 plane. *Journal of the Physical Society of Japan*, 76(2):024716, 2007.
(Cited on pages 81 and 94.)

[333] Y Tada, N Kawakami, and S Fujimoto. Pairing state at an interface of Sr_2RuO_4: parity-mixing, restored time-reversal symmetry and topological superconductivity. *New Journal of Physics*, 11 (5):055070, 2009.
(Cited on pages 82, 94, and 170.)

[334] Youichi Yanase. Electronic structure and noncentrosymmetric superconductivitity in three-orbital t_{2g} model with spin–orbit coupling: Sr_2RuO_4 near [001] surface/interface. *Journal of the Physical Society of Japan*, 82(4):044711, Mar 2013.
(Cited on pages 82, 94, and 170.)

[335] H. Kontani, T. Tanaka, D. S. Hirashima, K. Yamada, and J. Inoue. Giant intrinsic spin and orbital hall effects in Sr_2MO_4 ($M = Ru, Rh, Mo$). *Phys. Rev. Lett.*, 100:096601, Mar 2008.
(Cited on page 84.)

[336] K. K. Ng and M. Sigrist. The role of spin-orbit coupling for the superconducting state in Sr_2RuO_4. *EPL (Europhysics Letters)*, 49(4):473, Feb 2000.
(Cited on page 84.)

[337] Howard Georgi. *Lie Algebras In Particle Physics: from Isospin To Unified Theories (Frontiers in Physics)*. Westview Press, 2 edition, Oct 1999. ISBN 9780738202334.
(Cited on pages 84 and 246.)

[338] R Okazaki, T Shibauchi, HJ Shi, Y Haga, TD Matsuda, E Yamamoto, Y Onuki, H Ikeda, and Y Matsuda. Rotational symmetry breaking in the hidden-order phase of URu_2Si_2. *Science*, 331 (6016):439–442, 2011.
(Cited on page 87.)

[339] H. Amitsuka, K. Matsuda, I. Kawasaki, K. Tenya, M. Yokoyama, C. Sekine, N. Tateiwa, T.C. Kobayashi, S. Kawarazaki, and H. Yoshizawa. Pressure–temperature phase diagram of the heavy-electron superconductor. *Journal of Magnetism and Magnetic Materials*, 310(2, Part 1):214 – 220, Oct 2007. ISSN 0304-8853. Proceedings of the 17th International Conference on MagnetismThe International Conference on Magnetism.
(Cited on page 87.)

[340] J. Schmalian and W. Hübner. Nonlinear magneto-optical response of s - and d -wave superconductors. *Phys. Rev. B*, 53:11860–11867, May 1996.
(Cited on page 87.)

[341] A. F. Santander-Syro, O. Copie, T. Kondo, F. Fortuna, S. Pailhes, R. Weht, X. G. Qiu, F. Bertran, A. Nicolaou, A. Taleb-Ibrahimi, P. Le Fevre, G. Herranz, M. Bibes, N. Reyren, Y. Apertet, P. Lecoeur, A. Barthelemy, and M. J. Rozenberg. Two-dimensional electron gas with universal subbands at the surface of $SrTiO_3$. *Nature*, 469(7329):189–193, Jan 2011. ISSN 0028-0836.
(Cited on pages 90, 98, 99, 100, 114, and 143.)

[342] PDC King, S McKeown Walker, Anna Tamai, Alberto De La Torre, T Eknapakul, P Buaphet, S-K Mo, W Meevasana, MS Bahramy, and Félix Baumberger. Quasiparticle dynamics and spin–orbital texture of the $SrTiO_3$ two-dimensional electron gas. *Nature communications*, 5, Feb 2014.
(Cited on pages 90, 98, 100, 113, 114, and 143.)

[343] G. Berner, M. Sing, H. Fujiwara, A. Yasui, Y. Saitoh, A. Yamasaki, Y. Nishitani, A. Sekiyama, N. Pavlenko, T. Kopp, C. Richter, J. Mannhart, S. Suga, and R. Claessen. Direct k-space mapping of the electronic structure in an oxide-oxide interface. *Phys. Rev. Lett.*, 110:247601, Jun 2013.
(Cited on pages 90, 98, 100, 113, 114, and 143.)

[344] Arjun Joshua, S. Pecker, J. Ruhman, E. Altman, and S. Ilani. A universal critical density underlying the physics of electrons at the $LaAlO_3/SrTiO_3$ interface. *Nat Commun*, 3:1129, October 2012.
(Cited on pages 91, 98, 100, 113, and 141.)

[345] A. Fête, S. Gariglio, A. D. Caviglia, J.-M. Triscone, and M. Gabay. Rashba induced magnetoconductance oscillations in the $LaAlO_3$-$SrTiO_3$ heterostructure. *Phys. Rev. B*, 86:201105(R), Nov 2012.
(Cited on pages 91, 98, 100, 113, and 141.)

[346] J.-S. Lee, Y. W. Xie, H. K. Sato, C. Bell, Y. Hikita, H. Y. Hwang, and C.-C. Kao. Titanium d_{xy} ferromagnetism at the $LaAlO_3/SrTiO_3$ interface. *Nat Mater*, 12(8):703–706, Aug 2013. ISSN 1476-1122.
(Cited on pages 91, 98, 113, and 161.)

[347] A. F. Santander-Syro, F. Fortuna, C. Bareille, T. C. Rödel, G. Landolt, N. C. Plumb, J. H. Dil, and M. Radović. Giant spin splitting of the two-dimensional electron gas at the surface of $SrTiO_3$.

Nat Mater, 13(12):1085–1090, Dec 2014. ISSN 1476-1122.
(Cited on pages 91, 98, 113, and 161.)

[348] V. Ambegaokar, P. G. deGennes, and D. Rainer. Landau-Ginsburg equations for an anisotropic superfluid. *Phys. Rev. A*, 9:2676–2685, Jun 1974.
(Cited on page 94.)

[349] Mathias S. Scheurer and Jörg Schmalian. Topological superconductivity and unconventional pairing in oxide interfaces. *Nat Commun*, 6:6005, Jan 2015.
(Cited on pages 97, 103, 158, 161, 165, 175, and 245.)

[350] Zhicheng Zhong, Anna Tóth, and Karsten Held. Theory of spin-orbit coupling at $LaAlO_3/SrTiO_3$ interfaces and $SrTiO_3$ surfaces. *Phys. Rev. B*, 87:161102, Apr 2013.
(Cited on pages 98 and 100.)

[351] A. V. Chubukov, D. V. Efremov, and I. Eremin. Magnetism, superconductivity, and pairing symmetry in iron-based superconductors. *Phys. Rev. B*, 78:134512, Oct 2008.
(Cited on pages 104, 105, 138, 149, 164, and 248.)

[352] Vladimir Cvetkovic, Robert E. Throckmorton, and Oskar Vafek. Electronic multicriticality in bilayer graphene. *Phys. Rev. B*, 86:075467, Aug 2012.
(Cited on pages 104, 105, and 248.)

[353] Igor Solovyev, Noriaki Hamada, and Kiyoyuki Terakura. t_{2g} versus all 3 d localization in LaMO$_3$ perovskites (M =Ti–Cu): First-principles study. *Phys. Rev. B*, 53:7158–7170, Mar 1996.
(Cited on page 106.)

[354] Hans Boschker, Christoph Richter, Evangelos Fillis-Tsirakis, Christof W. Schneider, and Jochen Mannhart. Electron-phonon coupling and the superconducting phase diagram of the $LaAlO_3$-$SrTiO_3$ interface. *Scientific Reports*, 5:12309–, July 2015.
(Cited on page 107.)

[355] S. N. Klimin, J. Tempere, J. T. Devreese, and D. van der Marel. Interface superconductivity in $LaAlO_3 - SrTiO_3$ heterostructures. *Phys. Rev. B*, 89:184514, May 2014.
(Cited on page 107.)

[356] Lukasz Fidkowski, Roman M. Lutchyn, Chetan Nayak, and Matthew P. A. Fisher. Majorana zero modes in one-dimensional quantum wires without long-ranged superconducting order. *Phys. Rev. B*, 84:195436, Nov 2011.
(Cited on page 109.)

[357] Lukasz Fidkowski, Hong-Chen Jiang, Roman M. Lutchyn, and Chetan Nayak. Magnetic and superconducting ordering in one-dimensional nanostructures at the $LaAlO_3/SrTiO_3$ interface. *Phys. Rev. B*, 87:014436, Jan 2013.
(Cited on page 109.)

[358] N. Mohanta and A. Taraphder. Topological superconductivity and Majorana bound states at the $LaAlO_3/SrTiO_3$ interface. *EPL (Europhysics Letters)*, 108(6):60001, 2014.
(Cited on page 109.)

[359] T. Senthil and Matthew P. A. Fisher. Quasiparticle localization in superconductors with spin-orbit scattering. *Phys. Rev. B*, 61:9690–9698, Apr 2000.
(Cited on pages 109 and 114.)

[360] N. Read and Dmitry Green. Paired states of fermions in two dimensions with breaking of parity and time-reversal symmetries and the fractional quantum Hall effect. *Phys. Rev. B*, 61:10267–10297, Apr 2000.
(Cited on pages 109 and 114.)

[361] A. Milsted, L. Seabra, I. C. Fulga, C. W. J. Beenakker, and E. Cobanera. Statistical translation invariance protects a topological insulator from interactions. *Phys. Rev. B*, 92:085139, Aug 2015.
(Cited on pages 109 and 114.)

[362] Suk Bum Chung, Joshua Horowitz, and Xiao-Liang Qi. Time-reversal anomaly and Josephson effect in time-reversal-invariant topological superconductors. *Phys. Rev. B*, 88:214514, Dec 2013.
(Cited on pages 109 and 114.)

[363] Srijit Goswami, Emre Mulazimoglu, Ana MRVL Monteiro, Roman Wölbing, Dieter Koelle, Reinhold Kleiner, Ya M Blanter, Lieven MK Vandersypen, and Andrea D Caviglia. Quantum interference in an interfacial superconductor. *arXiv preprint arXiv:1512.04290*, Dec 2015.
(Cited on page 109.)

[364] Xiaopeng Li, W. Vincent Liu, and Leon Balents. Spirals and Skyrmions in two dimensional oxide heterostructures. *Phys. Rev. Lett.*, 112:067202, Feb 2014.
(Cited on page 111.)

[365] Daniel F. Agterberg, Egor Babaev, and Julien Garaud. Microscopic prediction of skyrmion lattice state in clean interface superconductors. *Phys. Rev. B*, 90:064509, Aug 2014.
(Cited on page 111.)

[366] A. B. Migdal. Interactions between electrons and lattice vibrations in a normal metal. *Sov. Phys. JETP*, 7:996, Dec 1958.
(Cited on pages 115, 120, 121, and 122.)

[367] M. S. Scheurer. Mechanism, time-reversal symmetry, and topology of superconductivity in non-centrosymmetric systems. *Phys. Rev. B*, 93:174509, May 2016.
(Cited on pages 116, 145, 150, 152, 153, 175, 222, 253, and 262.)

[368] Gerald D. Mahan. *Many-Particle Physics (Physics of Solids and Liquids)*. Springer, 3. edition, Oct 2000. ISBN 9780306463389.
(Cited on pages 116 and 120.)

[369] J. P. Carbotte. Properties of boson-exchange superconductors. *Rev. Mod. Phys.*, 62:1027–1157, Oct 1990.
(Cited on pages 120 and 122.)

[370] J. C. Swihart, D. J. Scalapino, and Y. Wada. Solution of the gap equation for Pb, Hg, and Al. *Phys. Rev. Lett.*, 14:106–108, Jan 1965.
(Cited on page 120.)

[371] M. Born and R. Oppenheimer. Zur quantentheorie der molekeln. *Annalen der Physik*, 389(20): 457–484, 1927. ISSN 1521-3889.
(Cited on page 120.)

[372] Oskar Perron. Zur theorie der matrices. *Mathematische Annalen*, 64(2):248–263, 1907.
(Cited on pages 125 and 258.)

[373] Georg Frobenius. Ueber matrizen aus nicht negativen elementen. *Sitzungsber. Königl. Preuss. Akad. Wiss.*, pages 456–477, 1912.
(Cited on pages 125 and 258.)

[374] Carl D. Meyer. *Matrix Analysis and Applied Linear Algebra Book and Solutions Manual*. SIAM: Society for Industrial and Applied Mathematics, Feb 2001. ISBN 9780898714548.
(Cited on pages 125, 257, 258, and 259.)

[375] I. F. Foulkes and B. L. Gyorffy. p-wave pairing in metals. *Phys. Rev. B*, 15:1395–1398, Feb 1977.
(Cited on page 129.)

[376] I. Schnell, I. I. Mazin, and Amy Y. Liu. Unconventional superconducting pairing symmetry induced by phonons. *Phys. Rev. B*, 74:184503, Nov 2006.
(Cited on page 129.)

[377] A. S. Alexandrov. Unconventional pairing symmetry of layered superconductors caused by acoustic phonons. *Phys. Rev. B*, 77:094502, Mar 2008.
(Cited on page 129.)

[378] Andrey V. Chubukov and Jörg Schmalian. Superconductivity due to massless boson exchange in the strong-coupling limit. *Phys. Rev. B*, 72:174520, Nov 2005.
(Cited on pages 132 and 133.)

[379] Sung-Sik Lee. Low-energy effective theory of fermi surface coupled with U(1) gauge field in $2+1$ dimensions. *Phys. Rev. B*, 80:165102, Oct 2009.
(Cited on page 133.)

[380] David F. Mross, John McGreevy, Hong Liu, and T. Senthil. Controlled expansion for certain non-fermi-liquid metals. *Phys. Rev. B*, 82:045121, Jul 2010.
(Cited on page 133.)

[381] D. Podolsky, H.-Y. Kee, and Y. B. Kim. Collective modes and emergent symmetry of superconductivity and magnetism in the iron pnictides. *EPL (Europhysics Letters)*, 88(1):17004, Oct 2009.
(Cited on pages 138, 149, and 164.)

[382] Jian Kang and Zlatko Tešanović. Theory of the valley-density wave and hidden order in iron pnictides. *Phys. Rev. B*, 83:020505, Jan 2011.
(Cited on pages 138, 149, and 164.)

[383] Zhiming Wang, Zhicheng Zhong, Xianfeng Hao, Stefan Gerhold, Bernhard Stöger, Michael Schmid, Jaime Sánchez-Barriga, Andrei Varykhalov, Cesare Franchini, Karsten Held, and Ulrike Diebold. Anisotropic two-dimensional electron gas at $SrTiO_3$(110). *Proceedings of the National*

Academy of Sciences, 111(11):3933–3937, 2014.
(Cited on pages 141 and 143.)

[384] T. C. Rödel, C. Bareille, F. Fortuna, C. Baumier, F. Bertran, P. Le Fèvre, M. Gabay, O. Hijano Cubelos, M. J. Rozenberg, T. Maroutian, P. Lecoeur, and A. F. Santander-Syro. Orientational tuning of the fermi sea of confined electrons at the $SrTiO_3$ (110) and (111) surfaces. *Phys. Rev. Applied*, 1:051002, Jun 2014.
(Cited on page 143.)

[385] Andrew C. Potter and Patrick A. Lee. Engineering a $p + ip$ superconductor: Comparison of topological insulator and Rashba spin-orbit-coupled materials. *Phys. Rev. B*, 83:184520, May 2011.
(Cited on page 146.)

[386] A. J. Millis, D. K. Morr, and J. Schmalian. Local defect in metallic quantum critical systems. *Phys. Rev. Lett.*, 87:167202, Oct 2001.
(Cited on pages 149 and 164.)

[387] Maria N. Gastiasoro and Brian M. Andersen. Impurity bound states and disorder-induced orbital and magnetic order in the s^{+-} state of Fe-based superconductors. *Journal of Superconductivity and Novel Magnetism*, 26(8):2651–2655, 2013. ISSN 1557-1947.
(Cited on pages 149 and 164.)

[388] R. M. Fernandes, M. G. Vavilov, and A. V. Chubukov. Enhancement of T_c by disorder in underdoped iron pnictide superconductors. *Phys. Rev. B*, 85:140512, Apr 2012.
(Cited on page 149.)

[389] M. Hoyer, S. V. Syzranov, and J. Schmalian. Effect of weak disorder on the phase competition in iron pnictides. *Phys. Rev. B*, 89:214504, Jun 2014.
(Cited on pages 150 and 151.)

[390] Wei Qin, Di Xiao, Kai Chang, Shun-Qing Shen, and Zhenyu Zhang. Converting a topologically trivial superconductor into a topological superconductor via magnetic doping. *arXiv:1509.01666*, 2015.
(Cited on page 156.)

[391] Jay D. Sau, Roman M. Lutchyn, Sumanta Tewari, and S. Das Sarma. Generic new platform for topological quantum computation using semiconductor heterostructures. *Phys. Rev. Lett.*, 104: 040502, Jan 2010.
(Cited on page 156.)

[392] Raquel Queiroz and Andreas P. Schnyder. Helical majorana surface states of strongly disordered topological superconductors with time-reversal symmetry. *Phys. Rev. B*, 91:014202, Jan 2015.
(Cited on page 158.)

List of Figures

Acronyms

1D one-dimensional. 20, 30, 34, 35, 37, 38, 42, 43, 49, 52, 61, 84, 86, 109, 127, 128, 137, 138, 143, 223

2D two-dimensional. ix, x, 10, 12–17, 20, 22, 23, 25, 29, 34–39, 44–49, 53, 55, 56, 61, 63, 65, 67, 70, 72–78, 83, 87–90, 93–96, 98, 108, 109, 115, 119, 127–129, 133, 134, 136–138, 143, 145, 154, 157, 158, 164, 167–169, 221–224, 238, 240

3D three-dimensional. ix, x, 7, 13–15, 26, 29, 34–39, 41, 44–48, 51, 53, 55, 56, 65, 67, 70, 73, 74, 76, 81, 95, 111, 119, 120, 127, 128, 136–138, 167, 222–224, 238, 240

ARPES angle-resolved photoemission spectroscopy. 18, 19, 100, 169

BCS Bardeen-Cooper-Schrieffer. viii, 9, 10, 25, 26, 57, 108, 109, 120, 124, 128, 137, 145, 163

BdG Bogoliubov-de Gennes. 29, 31, 33, 36, 37, 40, 62, 126, 127, 129, 146, 157, 241

BHZ Bernevig-Hughes-Zhang. 35, 36, 48, 53

BKT Berezinskii-Kosterlitz-Thouless. 12, 13, 16, 67

CDW charge-density wave. 110, 114, 131, 138, 149, 161, 169

FFLO Fulde-Ferrell-Larkin-Ovchinnikov. 10, 11, 91, 92, 95, 106, 113, 122, 252

IR irreducible representation. 5–8, 22, 55, 56, 58–60, 64, 65, 67, 70–78, 80–83, 87–95, 107, 110, 154, 159, 167, 222, 223, 229, 232, 236, 238–241, 245–247

LAO $LaAlO_3$. viii, x, xi, 15–17, 26, 77, 89, 91, 97, 98, 100, 103, 107, 109, 113, 114, 130, 140, 141, 143, 149, 158, 160, 165, 168–171

MBS Majorana bound state. 32–37, 39, 40, 42, 86, 87, 96, 109, 114, 142, 157, 158, 164

NI normal insulator. 46, 48, 49, 53

NMR nuclear magnetic resonance. 131

PHS particle-hole symmetry. 28–30, 33, 34, 86, 126, 141, 157, 241

PKE polar Kerr effect. ix, 20, 22, 23, 55

PLD pulsed laser deposition. 21

QSH quantum spin Hall. 35, 37, 45, 46, 48, 49, 53, 167

RG renormalization group. x, 10, 12, 86, 96, 102, 104–107, 110, 111, 114, 129, 130, 141, 168, 170, 248, 251, 252

SCBA self-consistent Born approximation. 25, 122, 151

SDW spin-density wave. 19, 59, 92, 110, 111, 114, 130, 131, 138, 139, 141, 149, 169, 229, 230

SOC spin-orbit coupling. viii, 6–8, 11, 13, 14, 36, 39, 55, 61, 77, 78, 81, 82, 84, 87, 88, 91–93, 99, 100, 118, 134, 147, 246

SQUID superconducting quantum interference devise. 16, 20, 109

STI strong topological insulator. 34, 45, 46, 48, 49, 53, 167

STM scanning tunneling microscope. 18, 19

STMI strong topological Mott insulator. 44, 45, 51–53

STO $SrTiO_3$. viii, x, xi, 15–19, 22, 26, 55, 77, 89, 91, 92, 96–98, 100, 103, 107, 109, 113, 114, 116, 130, 140, 141, 143, 149, 158, 160, 165, 168–171

TMI topological Mott insulator. x, 44, 45, 49–51, 53, 167

TRE time-reversal even. 131–133, 138–140, 142, 146–148, 150, 159, 164, 257, 259

TRIM time-reversal invariant momenta. 38, 49, 83–85, 108, 119, 128, 137, 138, 143, 148, 154

TRO time-reversal odd. 131–133, 138–143, 146–148, 150, 159, 164, 257, 259

TRS time-reversal symmetry. vii, ix–xi, 4, 11, 13, 15, 18, 20, 22, 23, 25, 28–30, 34, 36–39, 42, 46, 48, 55–64, 67, 68, 70, 73–76, 78, 80–83, 86–96, 99, 101–103, 107–109, 114–118, 126–129, 131–136, 138–143, 145, 147, 149–151, 153, 154, 156–158, 163–165, 167–171, 221, 225, 229, 231, 238, 240, 241, 245–247, 254, 256

WTI weak topological insulator. 34, 45, 46, 48, 49, 53, 167

WTMI weak topological Mott insulator. 44, 45, 51–53

Notation and conventions

The following list summarizes the conventions used throughout the thesis:

1. We set $\hbar = k_B = 1$ where $\hbar$ and k_B denote the reduced Planck and Boltzmann constant.

2. Unless stated otherwise, indices appearing twice are assumed to be summed over (Einstein summation convention).

3. The compact notation $k \equiv (i\omega_n, \boldsymbol{k})$ and $q \equiv (i\Omega_n, \boldsymbol{q})$ for fermionic and bosonic momenta is used. The symbol $\int_k$ comprises both momentum and Matsubara summation,

$$\int_k \cdots = T \sum_{\omega_n} \sum_{\boldsymbol{k}} \cdots ,$$

   and similarly in the bosonic case.

4. In order to distinguish between operators acting in Fock and single-particle space, the former have hats whereas the latter not (see, e.g., $\hat{c}_{\boldsymbol{k}\alpha}$ and $h_{\boldsymbol{k}}$ in Eq. (4.2)).

5. The Grassmann variable corresponding to a fermionic operator has the same symbol without the hat, e.g., $c_{k\alpha}$ is the Grassmann analogue $\hat{c}_{\boldsymbol{k}\alpha}$. The same holds for bosons (ϕ_{qj} represents $\hat{\phi}_{\boldsymbol{q}j}$ in the field integral description).

6. Pauli matrices are defined as usual,

$$\sigma_0 = \tau_0 = s_0 = \begin{pmatrix} 1 & 0 \\ 0 & 1 \end{pmatrix}, \qquad \sigma_1 = \tau_1 = s_1 = \begin{pmatrix} 0 & 1 \\ 1 & 0 \end{pmatrix},$$
$$\sigma_2 = \tau_2 = s_2 = \begin{pmatrix} 0 & -i \\ i & 0 \end{pmatrix}, \qquad \sigma_3 = \tau_3 = s_3 = \begin{pmatrix} 1 & 0 \\ 0 & -1 \end{pmatrix},$$

   but three different symbols are used in order to emphasize whether it refers to the microscopic spin of the electron (σ_j), a general abstract isospin (τ_j) or pseudospin (s_j) in the sense of Appendix A.1.

7. The commutator $[\cdot, \cdot]$ and anticommutator $\{\cdot, \cdot\}$ are defined as

$$[A, B] := AB - BA, \qquad \{A, B\} := AB + BA$$

   for two operators A and B.

8. In all symmetry arguments presented in this thesis, we neglect the possibility of accidental degeneracies as they require fine-tuning.

9. Throughout the thesis we define Fermi surfaces as connected sets of momenta and assume that all Fermi surfaces have dimension $d-1$ in case of a d-dimensional system.

10. A "Rashba pair" of Fermi surfaces is defined as a pair of nondegenerate Fermi surfaces that merge into one doubly degenerate Fermi surface upon hypothetically switching off all terms in the Hamiltonian that break inversion-symmetry.

11. Although different conventions exist in the literature, we will use the term "conventional" in the context of superconductivity to refer to superconductors that arise mainly due to electron-phonon interactions in the sense that (the symmetry, topology and nodal structure of) the order parameter would be unchanged when hypothetically switching off all other microscopic interaction channels in the material. All other superconductors are referred to as "unconventional". Note that, according to this definition, an unconventional superconductor does not have to break symmetries (as, e.g., the s^{+-} state of Chap. 5).

We next present the basic notation of this thesis:

e	elementary charge
μ_B	Bohr magneton
d	dimensionality of the system
$\boldsymbol{k}$, $\boldsymbol{q}$	crystal momenta
$\boldsymbol{x}$	real space coordinate (Fourier conjugate to $\boldsymbol{k}$, $\boldsymbol{q}$)
$\epsilon_{\boldsymbol{k}s}$	spectrum of band s, eigenvalue of the noninteracting Bloch-Hamiltonian $h_{\boldsymbol{k}}$
$\psi_{\boldsymbol{k}s}$	Bloch wavefunctions, i.e., $h_{\boldsymbol{k}}\psi_{\boldsymbol{k}s} = \epsilon_{\boldsymbol{k}s}\psi_{\boldsymbol{k}s}$
$\varphi^s_{\boldsymbol{k}}$	time-reversal phases defined in Eq. (4.24)
Ω	set of angular variables parameterizing the Fermi surfaces
$\rho_s(\Omega)$	angle-resolved density of states on Fermi surface s
E_F	Fermi energy
ρ_F	total density of states of the system $\rho_F := \sum_s \int_s \mathrm{d}\Omega \rho_s(\Omega)$
v_F	Fermi velocity
k_F	Fermi momentum
E_{so}	spin-orbit splitting
Λ_t	bandwidth
$\omega_{\boldsymbol{q}l}$	phonon spectrum of branch l
ω_D	Debye frequency, i.e., scale for upper bound of $\omega_{\boldsymbol{q}l}$
β	inverse of temperature (T), $\beta := 1/T$
T_c	transition temperature

ω_n	fermionic Matsubara frequencies, $\omega_n = \pi T(2n+1)$, $n \in \mathbb{Z}$
Ω_n	bosonic Matsubara frequencies, $\omega_n = 2\pi T n$, $n \in \mathbb{Z}$
$\hat{c}_{\boldsymbol{k}\alpha}$ ($\hat{c}^\dagger_{\boldsymbol{k}\alpha}$)	electronic annihilation (creation) operator in microscopic basis; α refers to all relevant microscopic degrees of freedom (spin, orbitals, ...)
$\hat{f}_{\boldsymbol{k}s}$ ($\hat{f}^\dagger_{\boldsymbol{k}s}$)	electronic annihilation (creation) operator in band basis (Fermi surface s, see Fig. 4.1)
$\hat{d}_{\boldsymbol{j}\mu}$ ($\hat{d}^\dagger_{\boldsymbol{j}\mu}$)	fermionic annihilation (creation) operator for the new lattice introduced in Chap. 3
$\hat{s}_{\boldsymbol{j}\mu}$ ($\hat{s}^\dagger_{\boldsymbol{j}\mu}$)	spinon annihilation (creation) operator introduced in Eq. (3.8)
$\hat{b}_{\boldsymbol{q}l}$ ($\hat{b}^\dagger_{\boldsymbol{q}l}$)	creation (annihilation) operator of phonons of branch l
$\hat{\phi}_{\boldsymbol{q}j}$	Hermitian ($\hat{\phi}^\dagger_{\boldsymbol{q}j} = \hat{\phi}_{-\boldsymbol{q}j}$) collective bosonic mode ($j = 1, 2, ..., N_B$)
$\mathcal{G}_p$	point group of the system
$\propto$	proportional to
T_τ	time-ordering operator in imaginary time τ
$\Delta^S_{\boldsymbol{k}}$	singlet component of superconducting order parameter defined in Eq. (1.17)
$\boldsymbol{d}_{\boldsymbol{k}}$	triplet vector (see Eq. (1.17))
$\Delta(\boldsymbol{k})$	microscopic superconducting order parameter (see Eq. (4.2))
$D_{ss'}(\boldsymbol{k})$	order parameter in basis of normal state Hamiltonian (see Eq. (4.27))
$\widetilde{\Delta}_s(\boldsymbol{k})$	its diagonal elements, $\widetilde{\Delta}_s(\boldsymbol{k}) := D_{ss}(\boldsymbol{k})$
$\boldsymbol{g}_{\boldsymbol{k}}$	spin-orbit vector
$\mathcal{F}$	free energy of the system
$\sim$	asymptotic to
$\mathcal{O}(x)$	Landau symbol
$\boldsymbol{\nabla}$	Nabla operator $\boldsymbol{\nabla} = (\partial_x, \partial_y, \dots)^T$
$\boldsymbol{A}$	Vector potential (maybe remove again)
ξ	superconducting coherence length
λ	penetration depth
R_l	localization length
l	mean-free path
I	inversion operator
O(N)	orthogonal group
U(N)	unitary group
SO(N)	special orthogonal group
SU(N)	special unitary group

E	identity element of a group
$\cong$	isomorphic
$\mathbb{T}_d$	d-dimensional torus
$\mathbb{S}_d$	d-dimensional hypersphere
π_d	d-th homotopy group
$\mathbb{1}$	unity matrix
$\mathrm{tr}\,\ldots$	trace of a matrix
$\mathrm{diag}(a_1, a_2, \ldots)$	diagonal matrix with a_1, a_2 etc. on its diagonals
$\delta_{i,j}$	Kronecker delta
$\delta(\boldsymbol{x})$	(multidimensional) delta function
$\mathrm{sign}(x)$	sign function, $\mathrm{sign}(x) = 1$ for $x > 0$, $\mathrm{sign}(x) = -1$ for $x < 0$
$\boldsymbol{e}_j$	unit vector, $(\boldsymbol{e}_j)_i = \delta_{i,j}$
(hkl), $[hkl]$	Miller indices describing planes and directions
$\zeta(s) = \sum_{n=1}^{\infty} n^{-s}$	Riemann zeta function
$\psi(x)$	digamma function
γ	Euler-Mascheroni constant ($\gamma \simeq 0.577$)
$\binom{n}{k}$	binomial coefficient
c.c.	complex conjugate
H.c.	Hermitian conjugate

A Appendix A

Basic calculations and results

In this first appendix, we present additional basic discussions that will be useful several times in this thesis.

A.1 Pseudospin basis

Here we provide a proof by construction that it is always possible to find a pseudospin basis $\{|-,\boldsymbol{k}\rangle, |+,\boldsymbol{k}\rangle\}$ of the Hamiltonian $h_{\boldsymbol{k}}$ in the presence of inversion symmetry (I) and spin-1/2 TRS (Θ with $\Theta^2 = -\mathbb{1}$),

$$\mathcal{R}_\Psi(I) h_{\boldsymbol{k}} \mathcal{R}_\Psi^\dagger(I) = h_{-\boldsymbol{k}}, \tag{A.1a}$$

$$\Theta h_{\boldsymbol{k}} \Theta^\dagger = h_{-\boldsymbol{k}}, \tag{A.1b}$$

that transforms under these operations exactly in the same way as the physical spin. Mathematically, this means that

$$\mathcal{R}_\Psi(I) |\pm,\boldsymbol{k}\rangle = |\pm,-\boldsymbol{k}\rangle, \tag{A.2a}$$

$$\Theta |\pm,\boldsymbol{k}\rangle = \pm |\mp,-\boldsymbol{k}\rangle. \tag{A.2b}$$

Take an arbitrary, but fixed $\boldsymbol{k}$ and choose an eigenstate $|\boldsymbol{k}\rangle$ of the Hamiltonian, $h_{\boldsymbol{k}}|\boldsymbol{k}\rangle = \epsilon_{\boldsymbol{k}}|\boldsymbol{k}\rangle$, belonging to the low-energy subspace of interest. We set $|+,\boldsymbol{k}\rangle := |\boldsymbol{k}\rangle$ and define

$$|+,-\boldsymbol{k}\rangle := \mathcal{R}_\Psi(I)|+,\boldsymbol{k}\rangle, \tag{A.3a}$$

$$|-,-\boldsymbol{k}\rangle := \Theta|+,\boldsymbol{k}\rangle, \tag{A.3b}$$

$$|-,\boldsymbol{k}\rangle := \mathcal{R}_\Psi(I)|-,-\boldsymbol{k}\rangle. \tag{A.3c}$$

It is now only left to show, that these states indeed form a basis of eigenstates that have the correct transformation behavior.

Firstly, they are indeed eigenstates, $h_{s\boldsymbol{k}}|\pm,s\boldsymbol{k}\rangle = \epsilon_{\boldsymbol{k}}|\pm,s\boldsymbol{k}\rangle$, $s = \pm$, as readily follows from the symmetries (A.1) of the Hamiltonian.

Secondly, in order to form a complete basis of the 2D low-energy Hilbert space, $|+,s\boldsymbol{k}\rangle$ and $|-,s\boldsymbol{k}\rangle$ have to be linearly independent both for $s = +$ and $s = -$. To show this, consider

$$\langle -,\boldsymbol{k}|+,\boldsymbol{k}\rangle \overset{(A.3c)}{=} \langle -,-\boldsymbol{k}|\mathcal{R}_\Psi^\dagger(I)|+,\boldsymbol{k}\rangle \overset{(A.3b)}{=} -\langle -,-\boldsymbol{k}|\mathcal{R}_\Psi^\dagger(I)\Theta|-,-\boldsymbol{k}\rangle = \langle -,-\boldsymbol{k}|\mathcal{R}_\Psi^\dagger(I)\Theta|-,-\boldsymbol{k}\rangle = 0, \tag{A.4}$$

where we have used $[\Theta, \mathcal{R}_\Psi(I)] = 0$ as well as $\Theta = -\Theta^\dagger$ and $\mathcal{R}_\Psi(I) = \mathcal{R}_\Psi^\dagger(I)$ following from $\Theta^2 = -\mathbb{1}$ and $\mathcal{R}_\Psi^2(I) = \mathbb{1}$. Similarly, one can show that $\langle -, -\boldsymbol{k}|+, -\boldsymbol{k}\rangle = 0$ which completes the proof of completeness of the set $\{|-, s\boldsymbol{k}\rangle, |+, s\boldsymbol{k}\rangle\}$ with respect to the low-energy theory.

Thirdly, we have to show that the required transformation behavior (A.2) holds. Eqs. (A.2a) and (A.2b) with + hold by design due to Eqs. (A.3a) and (A.3b). Multiplying Eq. (A.3c) by $\mathcal{R}_\Psi^\dagger(I) = \mathcal{R}_\Psi(I)$ reproduces Eq. (A.2a) with −. Similarly, Eq. (A.2b) with − can be readily shown.

This completes the proof of the existence of the pseudospin basis and its explicit construction recipe (A.3). We finally mention without presenting a proof that $|\boldsymbol{k}\rangle$ can always be chosen such that the pseudospin basis constructed according to Eq. (A.3) also transforms as spin-up and spin-down under a twofold rotation C_2^z if the latter belongs to the point group of the system.

A.2 Consequences of a two-fold rotation and inversion for IRs

Here it is shown that a two-fold rotation C_2^z perpendicular to the plane of a 2D system, exactly as inversion I for any centrosymmetric point group, forces all IRs and, hence, all possible order parameters to be either even or odd under under this operation. This appendix is particularly important for the analysis of Chaps. 4 and 6 and has, in its main part, been published in Ref. [367].

As a first step, we have to show that I and C_2^z commutes with all symmetry operations of the point group $\mathcal{G}_p$. In case of inversion this is trivial as its coordinate representation is simply given by $-\mathbb{1}_d$, where d is the dimensionality of the system. To study C_2^z, we first have to notice that, by design, all symmetry operations of a 2D system cannot mix in-plane (x, y) and out-of-plane (z) coordinates such that the coordinate representation of any $g \in \mathcal{G}_p$ must have the form

$$M(g) = \begin{pmatrix} & & 0 \\ & m(g) & 0 \\ & & \\ 0 & 0 & c(g) \end{pmatrix} \tag{A.5}$$

in the basis $\{x, y, z\}$, where $m(g)$ is a real 2×2 matrix and $c(g) \in \mathbb{R}$. Obviously, $M(g)$ commutes with $M(C_2^z) = \mathrm{diag}(-1, -1, 1)$ and, hence, $[C_2^z, g] = 0$.

Therefore, it holds for any representation ρ

$$[\rho(C_2^z), \rho(h)] = 0 \quad \forall g \in \mathcal{G}_p. \tag{A.6}$$

If ρ is irreducible, Schur's lemma [85] implies $\rho(C_2^z) = C\mathbb{1}_{d_\rho}$ with $C \in \mathbb{C}$. Due to $(C_2^z)^2 = E$, where E is the identity operation, we have $C \in \{+1, -1\}$.

Assuming a second order phase transition, the competing order parameter must transform under one of the IRs of the point group and, hence, can only be either even or odd under I if $I \in \mathcal{G}_p$ (under C_2^z if $d = 2$ and $C_2^z \in \mathcal{G}_p$). We emphasize that this generally only holds for bosonic order parameters such as the superconducting order parameter ($\langle \hat{c}^\dagger \hat{c}^\dagger \rangle$) and particle-hole order parameters ($\langle \hat{c}^\dagger \hat{c} \rangle$) where we do not have to consider the IRs of the double group associated with $\mathcal{G}_p$ (see the discussion at the end of Chap. 1.1.1).

A.3 Overview: Point groups of 2D and 3D crystalline systems

Here we summarize the possible point groups of 2D and 3D systems together with the properties of their IRs that are important for this thesis. In particular in Chap. 4, extensive use will be made of the

information presented in this appendix. For a full listing of all IRs we refer to Ref. [91].

We focus entirely on crystalline systems, i.e., on systems with a Bravais lattice, which crucially limits the possible rotation symmetries to be only two-, three-, four- or sixfold [85]. In 3D, this leads to 32 point groups as summarized below:

1. Nonaxial groups: $C_1 = \{E\}$, $C_i = \{E, I\}$, $C_s = \{E, \sigma_h\}$, where I and σ_h denote inversion and reflection at a plane. All are Abelian and there are only real 1D IRs. Only C_i is centrosymmetric.

2. Cyclic groups: C_n, $n = 2, 3, 4, 6$. Generated by n-fold rotation C_n. All are Abelian and, hence, only have 1D IRs. Except for C_2 all have complex IRs. All are noncentrosymmetric.

3. Reflection groups: C_{nh}, $n = 2, 3, 4, 6$. Characterized by n-fold rotation C_n and mirror plane (σ_h) normal to the rotation axis. Again all are Abelian and only have 1D IRs. Only C_{2h} has entirely real IRs. Only $C_{3h} \cong C_6$ is noncentrosymmetric.

4. Pyramidal groups: C_{nv}, $n = 2, 3, 4, 6$. Generated by n-fold rotation C_n and a mirror plane (σ_v) containing the rotation axis. Except for C_{2v} all are non-Abelian and have real IRs of dimension one and two. C_{2v} only has real 1D IRs. All are noncentrosymmetric.

5. Improper rotation groups: $S_n \cong C_n$, $n = 4, 6$. Generated by n-fold improper rotation S_n (rotation followed by reflection at plane normal to axis). Both are Abelian and only have 1D IRs. Both have complex IRs. Only S_4 is noncentrosymmetric.

6. Dihedral groups: D_n, $n = 2, 3, 4, 6$. Generated by n-fold rotation C_n and a perpendicular twofold rotation C_2'. As $D_n \cong C_{nv}$, the IRs have the same properties as that of C_{nv} above. All are noncentrosymmetric.

7. Prismatic groups: D_{nh}, $n = 2, 3, 4, 6$. Characterized by n-fold rotation C_n, n twofold rotations normal to C_n and a mirror plane (σ_h) containing the twofold rotations. All only have real IRs. Except for the Abelian member D_{2h} all also have 2D IRs. Only $D_{3h} \cong C_{6v}$ is noncentrosymmetric.

8. Antiprismatic groups: $D_{2d} \cong C_{4v}$ and $D_{3d} \cong C_{6v}$. Generated by a $2n$-fold improper rotation axis S_{2n} and a perpendicular twofold rotation C_2'. Only D_{2d} is noncentrosymmetric.

9. Cubic groups: T, T_d, T_h, O and O_h. T is generated by one of its threefold and one of its twofold rotation axes. T_d is generated by one of its fourfold improper and one of its threefold proper rotation axes. O is generated by two distinct fourfold rotation axes. The generation of the remaining two centrosymmetric point groups follow from $T_h = T \times C_i$ and $O_h = O \times C_i$. None of these groups is Abelian. The analysis of IRs is simplified by noting that $T_d \cong O$. All have multidimensional real IRs while only T and T_h also have complex IRs.

2D systems should in general be thought of as being embedded in 3D-space: While crystal momenta $\boldsymbol{k}$ become two-component in-plane (xy-plane) vectors, there is no generic reason to neglect the z-component of the spin or orbital angular momentum operator.

By design, one has to focus on symmetry groups that do not mix in-plane and out-of-plane momenta. This rules out the five cubic point groups such that only 27 of the 32 crystal classes are of interest for describing 2D systems. As already mentioned in Chap. 1.3, it makes sense to distinguish between:

1. Interfaces/surfaces/thin layers on substrate: No symmetry operation relating z and $-z$ is possible since the conducting system is embedded in an asymmetric environment as shown in Fig. 1.2(a) and (b). This restricts the possible point groups to C_n, C_{nv}, $n = 1, 2, 3, 4, 6$ (all of which are necessarily non-centrosymmetric).

2. 2D sheets in symmetric environment: As illustrated in Fig. 1.2(c), the conducting sheet can have a symmetric environment with A either being vacuum or some dielectric substrate. In this case, the system can have point symmetries relating z and $-z$. Consequently, the following additional point groups have to be considered:
   a) Non-centrosymmetric: C_s, C_{3h}, S_4, D_n, $n = 1, 2, 3, 4, 6$, D_{3h}, D_{2d}
   b) Centrosymmetric: C_i, C_{nh}, S_6, D_{nh}, D_{3d} with $n = 2, 4, 6$

To retain the expected number (27) of allowed point groups, we note that, in 3D, $C_s \equiv C_{1v}$ and $D_1 \equiv C_2$. In 2D, this identification does not hold when forcing the principal axes to be perpendicular to the plane and, hence, the list above contains 29 point groups.

B Appendix B

Cold-atom realization of topological Mott insulators

This appendix provides additional information on Chap. 3 of the main text. More specifically, we first discuss in more detail how the nonlocal Hubbard interaction (3.7) can be effectively realized (see Sec. B.1) and then present the slave-rotor approach we use to deduce the interacting phase diagrams in Fig. 3.3 (see Sec. B.2). Exactly as Chap. 3, this appendix is based on Ref. [317].

B.1 Twisting the Hubbard interaction

In the following we present more details about how the nonlocal interaction term

$$\hat{H}'_U = \frac{U}{2} \sum_{\boldsymbol{j},\sigma=\uparrow,\downarrow} (\hat{n}_{2j_x j_y j_z \sigma} + \hat{n}_{(2j_x+1) j_y j_z \sigma} - 1)^2, \qquad \hat{n}_{\boldsymbol{j}\sigma} = \hat{c}^\dagger_{\boldsymbol{j}\sigma} \hat{c}_{\boldsymbol{j}\sigma}, \tag{B.1}$$

can be implemented in a cold-atom setup. The procedure we propose is based on interchanging degrees of freedom: As illustrated in Fig. B.1, the spin degree of freedom σ of the original fermions $\hat{c}_{\boldsymbol{j}\sigma}$ will be encoded by the evenness and oddness of j_x of the new fermions $\hat{d}_{\boldsymbol{j}\mu}$, whereas the parity $(-1)^{j_x}$ of j_x in the original basis is represented by the internal on-site degree of freedom $\mu = \pm$ of the new fermions. By construction, the nonlocal interaction term in Eq. (B.1) assumes the form of the usual Hubbard on-site interaction in terms of the transformed fermions $\hat{d}_{\boldsymbol{j}\mu}$. Keeping the noninteracting part of the theory $\hat{H}_{\mathrm{2D}} + \hat{H}_z$ fixed, the full Hamiltonian reads in the new basis as

$$\hat{H} = -\sum_{\boldsymbol{j},\boldsymbol{j}'} \sum_{\mu,\mu'} \left(\hat{d}^\dagger_{\boldsymbol{j}\mu} \mathcal{A}_{\mu\mu'}(\boldsymbol{j},\boldsymbol{j}') \hat{d}_{\boldsymbol{j}'\mu'} + \mathrm{H.c.} \right) + \lambda \sum_{\boldsymbol{j}} \sum_{\mu,\mu'} \hat{d}^\dagger_{\boldsymbol{j}\mu} \left(\sigma_3\right)_{\mu\mu'} \hat{d}_{\boldsymbol{j}\mu'} + \frac{U}{2} \sum_{\boldsymbol{j}} \left(\sum_{\mu} \hat{d}^\dagger_{\boldsymbol{j}\mu} \hat{d}_{\boldsymbol{j}\mu} - 1 \right)^2, \tag{B.2}$$

where $\mathcal{A}_{\mu\mu'}(\boldsymbol{j},\boldsymbol{j}')$ are the transformed hopping amplitudes of $\hat{H}_{\mathrm{2D}} + \hat{H}_z$ as illustrated in Fig. B.1 for all three spatial directions. Redistributing the original spin degree of freedom in the way we propose, the system only contains nearest and next-nearest neighbor hopping elements. It is very important to note that, although the staggered hopping now has the form of a Zeeman term, Eq. (B.2) is mathematically equivalent to $\hat{H}_{\mathrm{2D}} + \hat{H}_z + \hat{H}'_U$ and, consequently, respects TRS.

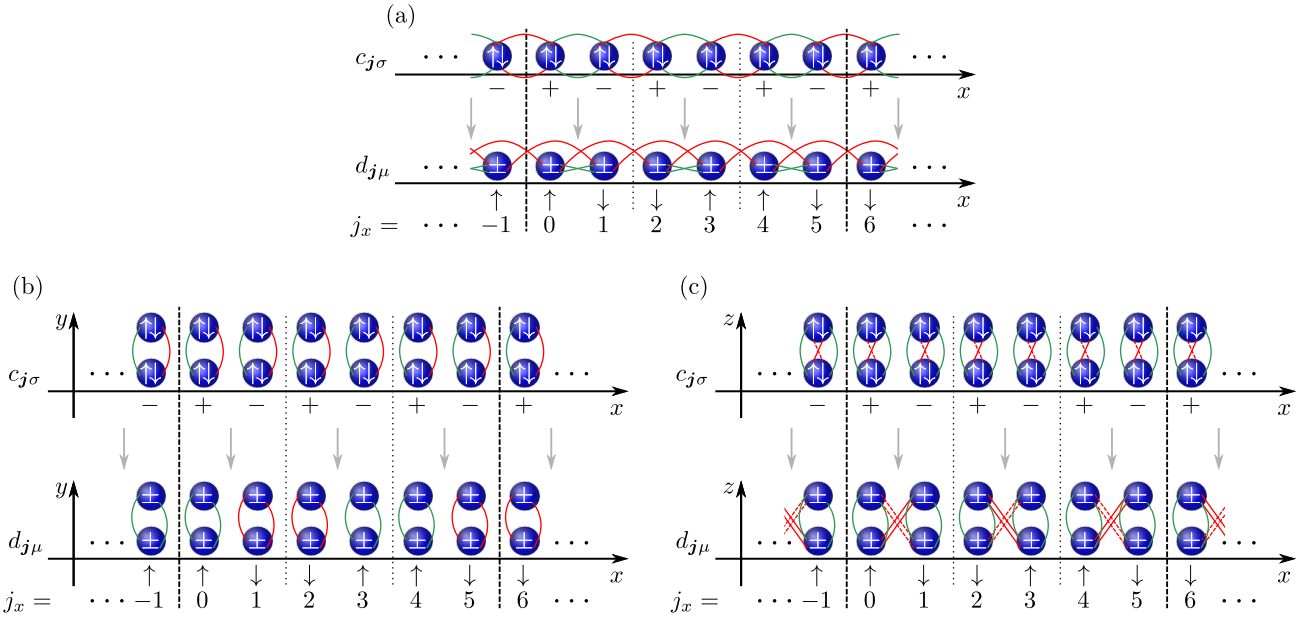

Figure B.1: ***Transformation to the new lattice and required hopping matrix elements along the three spatial directions.*** *Panels (a), (b) and (c) show the hopping elements along the x, y, and z directions, respectively. The upper part of the respective panels refers to the hopping elements of the $\hat{c}_{j\sigma}$ fermions in the Hamiltonian $\hat{H}_{2D}+\hat{H}_z$ defined in Eqs. (3.1) and (3.2) of the main text. The lower part of the panels shows the required hopping elements of the $\hat{d}_{j\mu}$ fermions that have to be implemented in order to obtain the identical Hamiltonian in terms of the $\hat{c}_{j\sigma}$ fermions if the spin σ is encoded spatially (as even and odd sites) and the site parity along x, $\mu = \pm$, as the internal hyperfine degree of the freedom.*

B.2 Slave rotor theory

To derive the interacting phase diagrams reported in the main part of the paper, we apply slave-rotor theory [65–67] to the Hamiltonian $\hat{H}_{2D} + \hat{H}_z + \hat{H}'_U$ restated in the new basis ($\hat{d}_{j\mu}$ fermions) where the interaction is an on-site Hubbard term. As already mentioned in the main text, one introduces phases θ_j conjugate to the total number of fermions on one site of the lattice and auxiliary fermionic operators $\hat{s}_{j\mu}$ via

$$\hat{d}_{j\mu} = e^{i\theta_j}\hat{s}_{j\mu}, \qquad \hat{d}^\dagger_{j\mu} = e^{-i\theta_j}\hat{s}^\dagger_{j\mu}. \tag{B.3}$$

To restrict the theory to the physical part of the Hilbert space, we have to impose the constraint

$$\hat{L}_j + \sum_{\mu=\pm} \hat{s}^\dagger_{j\mu}\hat{s}_{j\mu} = \hat{\mathbb{1}}, \qquad \hat{L}_j := -i\partial_{\theta_j}. \tag{B.4}$$

This condition will be treated on average and accounted for by introducing Lagrange multipliers $h_{\boldsymbol{j}}$. Passing to a path-integral description, the associated action is given by

$$\begin{aligned} S_{\mathrm{SR}} = \int_0^\beta \mathrm{d}\tau \Bigg[& \frac{1}{2U} \sum_{\boldsymbol{j}} \left(\partial_\tau \theta_{\boldsymbol{j}} - i h_{\boldsymbol{j}} \right)^2 + \sum_{\boldsymbol{j}} \bar{s}_{\boldsymbol{j}\mu} \left(\partial_\tau - h_{\boldsymbol{j}} \right) s_{\boldsymbol{j}\mu} \\ & - \sum_{\boldsymbol{j},\boldsymbol{j}'} \left(\bar{s}_{\boldsymbol{j}\mu} \mathcal{A}_{\mu\mu'}(\boldsymbol{j},\boldsymbol{j}') e^{i(\theta_{\boldsymbol{j}'} - \theta_{\boldsymbol{j}})} s_{\boldsymbol{j}'\mu'} + \mathrm{G.c.} \right) + \lambda \sum_{\boldsymbol{j}} \bar{s}_{\boldsymbol{j}\mu} \left(\sigma_3 \right)_{\mu\mu'} s_{\boldsymbol{j}\mu'} \Bigg], \end{aligned} \tag{B.5}$$

where $s_{\boldsymbol{j}\mu}$, $\bar{s}_{\boldsymbol{j}\mu}$ denote Grassmann variables and $\mathcal{A}_{\mu\mu'}(\boldsymbol{j},\boldsymbol{j}')$ represent the hopping matrix elements in the new lattice (see Sec. B.1).

We use the sigma-model description of Ref. [65], where the phase degrees of freedom are represented by complex bosonic fields

$$X_{\boldsymbol{j}}(\tau) := e^{i\theta_{\boldsymbol{j}}(\tau)} \tag{B.6}$$

with the nonlinear constraint

$$|X_{\boldsymbol{j}}(\tau)|^2 = 1. \tag{B.7}$$

The latter will be ensured on average via additonal Lagrange multipliers $\rho_{\boldsymbol{j}}$. Applying a mean-field approximation to the hopping terms in Eq. (B.5), we arrive at the bosonic and fermionic actions

$$S_X = \int_0^\beta \mathrm{d}\tau \left[\sum_{\boldsymbol{j}} X^*_{\boldsymbol{j}}(\tau) \left(\frac{1}{2U} \overleftarrow{\partial_\tau} \overrightarrow{\partial_\tau} + \rho_{\boldsymbol{j}} \right) X_{\boldsymbol{j}}(\tau) - \sum_{\boldsymbol{j},\boldsymbol{j}'} \left(X^*_{\boldsymbol{j}}(\tau) \mathcal{Q}(\boldsymbol{j},\boldsymbol{j}') X_{\boldsymbol{j}'}(\tau) + \mathrm{c.c.} \right) \right] \tag{B.8}$$

and

$$S_s = \int_0^\beta \mathrm{d}\tau \left[\sum_{\boldsymbol{j}} \bar{s}_{\boldsymbol{j}}(\tau) \left(\partial_\tau + \lambda \sigma_3 \right) s_{\boldsymbol{j}}(\tau) - \sum_{\boldsymbol{j},\boldsymbol{j}'} \left(\bar{s}_{\boldsymbol{j}\mu}(\tau) Z(\boldsymbol{j},\boldsymbol{j}') \mathcal{A}_{\mu\mu'}(\boldsymbol{j},\boldsymbol{j}') s_{\boldsymbol{j}'\mu'}(\tau) + \mathrm{G.c.} \right) \right], \tag{B.9}$$

where G.c. stands for Grassmann conjugate, i.e., Hermitian conjugate in the associated Hamiltonian description. These actions are coupled via the self-consistency equations

$$\mathcal{Q}(\boldsymbol{j},\boldsymbol{j}') = \sum_{\mu,\mu'} \langle \bar{s}_{\boldsymbol{j}\mu}(\tau) \mathcal{A}_{\mu\mu'}(\boldsymbol{j},\boldsymbol{j}') s_{\boldsymbol{j}'\mu'}(\tau) \rangle \,, \tag{B.10a}$$

$$Z(\boldsymbol{j},\boldsymbol{j}') = \langle X^*_{\boldsymbol{j}}(\tau) X_{\boldsymbol{j}'}(\tau) \rangle \,. \tag{B.10b}$$

Here we have already taken into account that, at half filling, the constraint (B.4) is satisfied on average by choosing $h_{\boldsymbol{j}} = 0$. Note that only three of the Lagrange multipliers $\rho_{\boldsymbol{j}}$, e.g. $\rho_{0,0,0}$, $\rho_{2,0,0}$ and $\rho_{4,0,0}$, are independent which is due to the combination of translation symmetry and time-reversal invariance.

For any given U one has to solve the set of equations (B.10) and find the correct Lagrange multipliers $\rho_{0,0,0}$, $\rho_{2,0,0}$, $\rho_{4,0,0}$ yielding the renormalization factors $Z(\boldsymbol{j},\boldsymbol{j}')$ of the auxiliary fermions $s_{\boldsymbol{j}\mu}$. The band structure resulting from Eq. (B.9) can again be classified exactly as for noninteracting fermions leading to the variety of different correlated topologically trivial and nontrivial phases discussed in the main part. The transition into the Mott phase, where the local number degree of freedom is frozen out, occurs when the gap of the bosons in Eq. (B.8) closes. This point marks the transition from a ferromagnetic to a paramagnetic state of the rotors $X_{\boldsymbol{j}}$. Even in the paramagnetic state there exist short range

correlations between the rotors which implies that the renormalization factors $Z(\boldsymbol{j}, \boldsymbol{j}')$ are nonzero. A topologically nontrivial spinon band structure while having paramagnetic rotors defines the weak and strong topological Mott insulator phases.

To obtain the phase diagram in Fig. 3.3(b), we have calculated the renormalization factors (B.10b) right at the Mott transition ($U = U_c$) and determined the topological invariant of the auxiliary fermions $s_{\boldsymbol{j}\mu}$ using the numerical approach of Ref. [320]. The phase boundaries for $0 < U < U_c$, shown in Fig. 3.3(a) in the main text, have been obtained via linear interpolation of the renormalization factors,

$$Z(\boldsymbol{j}, \boldsymbol{j}')\Big|_U = 1 + \left(Z(\boldsymbol{j}, \boldsymbol{j}')\Big|_{U_c} - 1 \right) U/U_c. \tag{B.11}$$

C Appendix C

Combining symmetry and energetic arguments

In this appendix, which is based on Refs. [325, 326], we present supplementary material to Chap. 4.

C.1 Time-reversal constraint on basis functions

In this section we proof the property Eq. (4.16) of the basis functions $\{\chi_\mu^n\}$ used to express the superconducting order parameter according to

$$\Delta(\boldsymbol{k}) = \sum_n \sum_{\mu=1}^{d_n} \eta_\mu^n \widetilde{\chi}_\mu^n(\boldsymbol{k}) T. \tag{C.1}$$

The arguments presented generalize the proof of Ref. [81] to allow for complex IRs as well as for the presence of SDW and magnetic impurities where TRS is only restored on average.

As a first step we generalize the parameterization (C.1) we have been using so far to

$$\Delta(\boldsymbol{k}) = \sum_n \sum_{\mu=1}^{d_n} \eta_\mu^n \Xi_\mu^n(\boldsymbol{k}; h_1^n, h_2^n) T, \qquad \Xi_\mu^n(\boldsymbol{k}; h_1^n, h_2^n) = h_1^n \widetilde{\chi}_\mu^n(\boldsymbol{k}) + h_2^n \left(\widetilde{\chi}_\mu^{\bar{n}}(\boldsymbol{k})\right)^\dagger, \qquad \eta_\mu^n, h_1^n, h_2^n \in \mathbb{C}, \tag{C.2}$$

where $\widetilde{\chi}_\mu^n(\boldsymbol{k})$ satisfies Eq. (4.14) and the same holds for $\left(\widetilde{\chi}_\mu^{\bar{n}}(\boldsymbol{k})\right)^\dagger$. Consequently, irrespective of h_1 and h_2, the transformation behavior of $\Xi_\mu^n(\boldsymbol{k}; h_1^n, h_2^n)$ and $\widetilde{\chi}_\mu^n(\boldsymbol{k})$ is identical for all $g \in \mathcal{G}_0$. Eq. (C.2) reduces to Eq. (C.1) for $(h_1, h_2) = (1, 0)$ and, hence, can describe any order parameter possible. Finally, note that the generalized parameterization (C.2) also automatically satisfies the Fermi-Dirac constraint (4.3) if this holds for Eq. (C.1) which can be straightforwardly shown.

To study time-reversal symmetry, let us rewrite our parameterization according to

$$\Delta(\boldsymbol{k}) = \sum_n \sum_{\mu=1}^{d_n} \eta_\mu^n \left(\frac{h_1^n + h_2^n}{2} \left(\widetilde{\chi}_\mu^n(\boldsymbol{k}) + \left(\widetilde{\chi}_\mu^{\bar{n}}(\boldsymbol{k})\right)^\dagger \right) + \frac{h_1^n - h_2^n}{2i} \left(\widetilde{\chi}_\mu^n(\boldsymbol{k}) - \left(\widetilde{\chi}_\mu^{\bar{n}}(\boldsymbol{k})\right)^\dagger \right) \right) T \tag{C.3}$$

$$\equiv \sum_n \sum_{\mu=1}^{d_n} \eta_\mu^n \widetilde{\Xi}_\mu^n(\boldsymbol{k}; H_1^n, H_2^n) T \tag{C.4}$$

with $H_1^n = \frac{1}{2}(h_1^n + h_2^n)$ and $H_2^n = \frac{1}{2i}(h_1^n - h_2^n)$. Note that it holds

$$\left(\widetilde{\Xi}_\mu^n(\boldsymbol{k}; H_1^n, H_2^n)\right)^\dagger = \widetilde{\Xi}_\mu^{\bar{n}}(\boldsymbol{k}; (H_1^n)^*, (H_2^n)^*) \tag{C.5}$$

by construction.

Repeating the expansion of the free energy described in Chap. 1.1.1 for arbitrary H_1^n and H_2^n yields (cf. Eq. (1.11))

$$\mathcal{F}\left(\eta_\mu^n, (\eta_\mu^n)^*\right) = \mathcal{F}(0,0) + \sum_n \sum_{\mu=1}^{d_n} a_n(T, \boldsymbol{M}; H_1^n, H_2^n) \left|\eta_\mu^n\right|^2 + \mathcal{O}\left(|\eta|^4\right). \tag{C.6}$$

For the sake of generality, we will also discuss the potential presence of SDW order, such as antiferromagnetism, described by the order parameter vector $\boldsymbol{M}$ in Eq. (C.6). Assuming that the SDW can be approximated to be commensurate[1], there is a translation by the Bravais lattice vector $\boldsymbol{R}_0$ under which $\boldsymbol{M}$ goes to $-\boldsymbol{M}$.

With our ansatz (C.1) we assume that superconductivity is invariant under all translation operations of the lattice. Therefore, translation by $\boldsymbol{R}_0$ is represented by

$$(\eta_\mu, H_1^n, H_2^n, \boldsymbol{M}) \longrightarrow (\eta_\mu, H_1^n, H_2^n, -\boldsymbol{M}) \tag{C.7}$$

on the order parameters. Invariance of the free energy thus leads to

$$a_n(T, \boldsymbol{M}; H_1^n, H_2^n) = a_n(T, -\boldsymbol{M}; H_1^n, H_2^n). \tag{C.8}$$

Let us next discuss invariance under time-reversal: Recalling Eq. (4.10) and taking into account Fermi Dirac statistics (4.3), we have

$$\Delta(\boldsymbol{k}) \longrightarrow T\Delta(-\boldsymbol{k})^* T^T = (-1)^{2S+1} T\Delta^\dagger(\boldsymbol{k}) T = (-1)^{2S+1} \sum_n \sum_{\mu=1}^{d_n} \left(\eta_\mu^n\right)^* \left(\widetilde{\Xi}_\mu^n(\boldsymbol{k}; H_1^n, H_2^n)\right)^\dagger T, \tag{C.9}$$

or, put differently,

$$\left(\eta_\mu^n, \widetilde{\Xi}_\mu^n(\boldsymbol{k}; H_1^n, H_2^n)\right) \longrightarrow \left((-1)^{2S+1}(\eta_\mu^n)^*, \widetilde{\Xi}_\mu^{\bar{n}}(\boldsymbol{k}; (H_1^n)^*, (H_2^n)^*)\right) \tag{C.10}$$

using Eq. (C.5). Alternatively, this can be represented by

$$(\eta_\mu^n, H_1^n, H_2^n) \longrightarrow \left((-1)^{2S+1}(\eta_\mu^{\bar{n}})^*, (H_1^{\bar{n}})^*, (H_2^{\bar{n}})^*\right), \tag{C.11}$$

which constraints the Ginzburg Landau expansion in Eq. (C.6):

$$a_n(T, \boldsymbol{M}; H_1^n, H_2^n) = a_{\bar{n}}(T, -\boldsymbol{M}; (H_1^n)^*, (H_2^n)^*). \tag{C.12}$$

Noting that the free energy should be invariant under

$$(H_1^n, H_2^n) \longrightarrow e^{i\varphi}(H_1^n, H_2^n), \qquad \varphi \in \mathbb{R}, \tag{C.13}$$

[1] In the present context this simply means that $|\boldsymbol{R}_0|$ must be much smaller than the linear system size.

and

$$(\eta_\mu^n, H_1^n, H_2^n) \longrightarrow (\eta_\mu^n/\lambda, \lambda H_1^n, \lambda H_2^n), \qquad \lambda \in \mathbb{R}^+, \tag{C.14}$$

implies that

$$a_n(T, \boldsymbol{M}; H_1^n, H_2^n) = \sum_{j,j'=1}^{2} C_{jj'}^{(n)}(T, \boldsymbol{M})(H_j^n)^* H_{j'}^n. \tag{C.15}$$

Reality of the free energy, $\mathcal{F}[\eta_\mu^n] \in \mathbb{R}$, and the combination of the translation, Eq. (C.8), and the TRS, Eq. (C.12), constraints lead to

$$\left(C^{(n)}(T, \boldsymbol{M})\right)^\dagger = C^{(n)}(T, \boldsymbol{M}), \tag{C.16a}$$

$$\left(C^{(\bar{n})}(T, \boldsymbol{M})\right)^T = C^{(n)}(T, \boldsymbol{M}), \tag{C.16b}$$

respectively. Since the matrices $C^{(n)}$ are Hermitian, they can be diagonalized and have real eigenvalues $\{\lambda_<^{(n)}, \lambda_>^{(n)}\}$ chosen such that $\lambda_<^{(n)} < \lambda_>^{(n)}$ with associated eigenvectors $\boldsymbol{v}_<^{(n)}$ and $\boldsymbol{v}_>^{(n)}$. To minimize the free energy, we set $\boldsymbol{H} = \boldsymbol{v}_<^{(n)}$ and the free energy assumes the form

$$\mathcal{F}\left(\eta_\mu^n, (\eta_\mu^n)^*\right) = \mathcal{F}(0,0) + \sum_n \lambda_<^{(n)}(T, \boldsymbol{M}) \sum_{\mu=1}^{d_n} \left|\eta_\mu^n\right|^2 + \mathcal{O}\left(|\eta|^4\right). \tag{C.17}$$

Eq. (C.16) implies $\left(C^{(n)}(T, \boldsymbol{M})\right)^* = C^{(\bar{n})}(T, \boldsymbol{M})$ such that $\lambda_<^{(n)} = \lambda_<^{(\bar{n})}$ and we can choose $(\boldsymbol{v}_<^{(n)})^* = \boldsymbol{v}_<^{(\bar{n})}$ without loss of generality. Recalling Eq. (C.5), the latter directly implies that $\widetilde{\chi}_\mu^n = \widetilde{\Xi}_\mu^n$ with $\boldsymbol{H}^n = \boldsymbol{v}_<^{(n)}$, as enforced by minimizing the free energy, satisfy Eq. (4.16).

Finally, let us extend this result to the presence of magnetic impurities. For a given disorder realization, the free energy is again of the form (C.6) where $\boldsymbol{M}$ has to be understood as a thermodynamically large vector encoding the magnetic moments in all unit cells of the system. Assuming that the system is self-averaging, the superconducting properties can be calculated from the averaged free energy

$$\mathcal{F}\left(\eta_\mu^n, (\eta_\mu^n)^*\right) = \mathcal{F}(0,0) + \sum_n \sum_{\mu=1}^{d_n} \langle a_n(T, \boldsymbol{M}; H_1^n, H_2^n)\rangle_{\text{dis}} \left|\eta_\mu^n\right|^2 + \mathcal{O}\left(|\eta|^4\right), \tag{C.18}$$

$$\langle a_n(T, \boldsymbol{M}; H_1^n, H_2^n)\rangle_{\text{dis}} \equiv \int \mathrm{d}\boldsymbol{M}\, p(\boldsymbol{M})\, a_n(T, \boldsymbol{M}; H_1^n, H_2^n), \tag{C.19}$$

where $p(\boldsymbol{M})$ is the probability distribution of magnetic moments and $\int \mathrm{d}\boldsymbol{M}$ denotes the integration over all microscopic disorder realizations. Naturally, Eq. (C.12) still holds. This, together with $p(\boldsymbol{M}) = p(-\boldsymbol{M})$, which is required for TRS to be restored on average, implies

$$\langle a_n(T, \boldsymbol{M}; H_1^n, H_2^n)\rangle_{\text{dis}} = \langle a_{\bar{n}}(T, \boldsymbol{M}; (H_1^n)^*, (H_2^n)^*)\rangle_{\text{dis}}\,. \tag{C.20}$$

This directly implies that Eq. (C.16) has to hold after averaging over disorder and, following the same logic as above, proves Eq. (4.16).

C.2 Ginzburg-Landau expansion from microscopic theory

In this appendix, the Ginzburg-Landau expansion is calculated up to infinite order in the weak-coupling limit (Sec. C.2.1) and up to quadratic order also taking into account Fermi-surface-off-diagonal matrix elements (Sec. C.2.2).

C.2.1 In the weak-pairing limit

To derive the Ginzburg-Landau expansion (4.41), we will first restate the interacting Hamiltonian (4.40) in the action description [114, 115]:

$$S = \int_k \bar{c}_k \left(-i\omega_n + h_{\boldsymbol{k}}\right) c_k - T g_{n_0} \sum_{\mu=1}^{d_{n_0}} \left[\int_k \bar{c}_k \chi_\mu^{n_0}(\boldsymbol{k}) \bar{c}_{-k}^T\right] \left[\int_{k'} c_{-k'}^T \left(\chi_\mu^{n_0}(\boldsymbol{k}')\right)^\dagger c_{k'}\right], \tag{C.21}$$

where c and $\bar{c}$ are the Grassmann analogues of the microscopic creation and annihilation operators $\hat{c}$ and $\hat{c}^\dagger$. As usual, $k \equiv (\omega_n, \boldsymbol{k})$ and $\int_k \cdots = T\sum_{\omega_n}\sum_{\boldsymbol{k}}\ldots$ comprises both momentum, $\boldsymbol{k}$, and (fermionic) Matsubara frequency, $\omega_n = \pi T(2n+1)$, summation.

To proceed, we perform a Hubbard-Stratonovich transformation[2]: Introducing the complex bosonic fields $\eta_\mu^{n_0}$, $\overline{\eta}_\mu^{n_0}$, the interaction can be decoupled with corresponding action

$$S_{\mathrm{HS}} = \int_k \bar{c}_k \left(-i\omega_n + h(\boldsymbol{k})\right) c_k + \sum_\mu \left(\overline{\eta}_\mu^{n_0} \int_k c_{-k}^T \left(\chi_\mu^{n_0}(\boldsymbol{k})\right)^\dagger c_k + \int_k \bar{c}_k \chi_\mu^{n_0}(\boldsymbol{k}) \bar{c}_{-k}^T \eta_\mu^{n_0} + \frac{1}{g_{n_0} T} \overline{\eta}_\mu^{n_0} \eta_\mu^{n_0}\right). \tag{C.22}$$

In direct analogy to Eq. (4.23) we transform into the eigenbasis of the normal state Hamiltonian $h_{\boldsymbol{k}}$ by introducing the new field operators f and $\bar{f}$ with

$$c_{k\alpha} = \sum_s \left(\psi_{\boldsymbol{k}s}\right)_\alpha f_{ks}, \qquad \bar{c}_{k\alpha} = \sum_s \bar{f}_{ks} \left(\psi_{\boldsymbol{k}s}^*\right)_\alpha. \tag{C.23}$$

In the weak-pairing limit (4.29), the action can then be restated as

$$S_{\mathrm{HS}} = -\frac{1}{2}\int_k \Psi_{-ks}^T \tau_x \mathcal{G}_{ss'}^{-1}(k) \Psi_{ks'} + \frac{1}{g_{n_0} T} \sum_\mu \overline{\eta}_\mu^{n_0} \eta_\mu^{n_0} \tag{C.24}$$

with Nambu spinor $\Psi_{ks} = (f_{ks}, \bar{f}_{-ks_{\mathrm{K}}})^T$ and Nambu Green's function

$$\mathcal{G}_{ss'}^{-1}(k) = \delta_{ss'} \begin{pmatrix} G_s^{-1}(k) & -2\widetilde{m}_{ss}(\boldsymbol{k}) \\ -2\widetilde{m}_{ss}^*(\boldsymbol{k}) & -G_{s_K}^{-1}(-k) \end{pmatrix}, \quad G_s^{-1}(k) = i\omega_n - \epsilon_{\boldsymbol{k}s}. \tag{C.25}$$

In Eq. (C.25), we have introduced the matrix elements

$$\widetilde{m}_{ss}(\boldsymbol{k}) := \sum_\mu \eta_\mu^{n_0} \psi_{\boldsymbol{k}s}^\dagger \chi_\mu^{n_0}(\boldsymbol{k}) \psi_{-\boldsymbol{k}s_{\mathrm{K}}}^* = \sum_\mu \eta_\mu^{n_0} \varphi_\mu^{n_0}(\boldsymbol{k}, \alpha) e^{-i\varphi_{\boldsymbol{k}}^\alpha} = \widetilde{\Delta}_s(\boldsymbol{k}) e^{-i\varphi_{\boldsymbol{k}}^\alpha} \tag{C.26}$$

with $\widetilde{\Delta}_s(\boldsymbol{k})$ as given in Eq. (4.33) restricted to the IR n_0. In the second equality of Eq. (C.26), use has been made of Eq. (4.24) and the definition (4.34) of the basis functions $\{\varphi_\mu^{n_0}\}$ has been inserted. The main advantage of this representation is that the entire relative complexity of different components $\mu = 1, 2, \ldots, d_{n_0}$ entering the matrix elements $\widetilde{m}$ is, in case of a real representation n, manifestly contained in the coefficients $\eta_\mu^{n_0}$ as $\varphi_\mu^{n_0}(\boldsymbol{k}, s) \in \mathbb{R}$.

[2] See, e.g., Ref. [114] for a pedagogical introduction to the method.

Integrating out the fermions, we obtain the exact free energy

$$\mathcal{F}(\eta_\mu^{n_0}) = \frac{1}{g_{n_0}} \sum_\mu |\eta_\mu^{n_0}|^2 - \frac{T}{2} \mathrm{tr} \ln \left(\mathcal{G}^{-1} \right), \tag{C.27}$$

where the trace involves Matsubara, momentum, particle-hole space as well as Fermi-surface summation. To perform an expansion in terms of the superconducting order parameter, let us split

$$\mathcal{G}_{ss'}^{-1}(k) = \delta_{s,s'} \left(\mathcal{G}_{0s}^{-1}(k) - \Sigma_s(k) \right) \tag{C.28}$$

with

$$\mathcal{G}_{0s}^{-1}(k) = \begin{pmatrix} G_s^{-1}(k) & 0 \\ 0 & -G_s^{-1}(-k) \end{pmatrix}, \qquad \Sigma_s(k) = \begin{pmatrix} 0 & 2\widetilde{m}_{ss}(\boldsymbol{k}) \\ 2\widetilde{m}_{ss}^*(\boldsymbol{k}) & 0 \end{pmatrix} \tag{C.29}$$

and write

$$\frac{T}{2} \mathrm{tr} \ln \left(\mathcal{G}^{-1} \right) = \frac{T}{2} \mathrm{tr} \ln \left(\mathcal{G}_0^{-1} \left(\mathbb{1} - \mathcal{G}_0 \Sigma \right) \right) \tag{C.30}$$

$$= -\mathcal{F}(0) - \frac{T}{2} \sum_{l=1}^{\infty} \frac{1}{l} \mathrm{tr} \left(\left(\mathcal{G}_0 \Sigma \right)^l \right) \tag{C.31}$$

within the radius of convergence of the series. Taking into account that only even l will contribute, we have the following still very formal Ginzburg-Landau expansion

$$\mathcal{F}(\eta_\mu^{n_0}) = \mathcal{F}(0) + \frac{1}{g_{n_0}} \sum_\mu |\eta_\mu^{n_0}|^2 + \frac{T}{2} \sum_{l=1}^{\infty} \frac{1}{2l} \mathrm{tr} \left(\left(\mathcal{G}_0 \Sigma \right)^{2l} \right). \tag{C.32}$$

Taking advantage of the fact that $\mathcal{G}_0$ and Σ are diagonal with respect to both frequency/momentum k as well as Fermi surfaces s, the trace simply becomes

$$\mathrm{tr} \left(\left(\mathcal{G}_0 \Sigma \right)^{2l} \right) = \sum_k \sum_s \mathrm{tr}^{\mathrm{ph}} \left[\left(\mathcal{G}_{0,s}(k) \Sigma_s(k) \right)^{2l} \right] \tag{C.33}$$

$$= \sum_k \sum_s \mathrm{tr}^{\mathrm{ph}} \left[\begin{pmatrix} 0 & 2G_s(k)\widetilde{m}_{ss}(\boldsymbol{k}) \\ -2G_{s_\mathrm{K}}(-k)\widetilde{m}_{ss}^*(\boldsymbol{k}) & 0 \end{pmatrix}^{2l} \right] \tag{C.34}$$

$$= (-1)^l 2^{2l+1} \sum_k \sum_s \left(G_s(k) G_{s_\mathrm{K}}(-k) \right)^l |\widetilde{m}_{ss}(\boldsymbol{k})|^{2l}, \tag{C.35}$$

where $\mathrm{tr}^{\mathrm{ph}}(\dots)$ denotes the trace over the particle-hole degrees of freedom only. Inserting this into Eq. (C.32), we get

$$\mathcal{F}(\eta_\mu^{n_0}) = \mathcal{F}(0) + \frac{1}{g_{n_0}} \sum_\mu |\eta_\mu^{n_0}|^2 + \sum_{l=1}^{\infty} \frac{(-1)^l}{l} 2^{2l-1} T \sum_s \sum_k \left(G_s(k) G_{s_\mathrm{K}}(-k) \right)^l \left| \sum_\mu \eta_\mu^{n_0} \varphi_\mu^{n_0}(\boldsymbol{k}, s) \right|^{2l}. \tag{C.36}$$

Note that the time-reversal phases in Eq. (C.26) have canceled out.

To simplify Eq. (C.36) further, let us rewrite the momentum sums according to

$$\sum_s \sum_{\boldsymbol{k}}^{s;\Lambda} \ldots \sim \sum_s \int_s \mathrm{d}\Omega\, \rho_s(\Omega) \int_{-\Lambda}^{\Lambda} \mathrm{d}\epsilon \ldots , \tag{C.37}$$

where we have introduced the angle-resolved and generally also Fermi-surface-dependent density of states $\rho_s(\Omega)$. With this we can write

$$\begin{aligned} T \sum_s \sum_k \Big(G_s(k) G_{s_\mathrm{K}}(-k) \Big)^l \left| \sum_\mu \eta_\mu^{n_0} \varphi_\mu^{n_0}(\boldsymbol{k}, s) \right|^{2l} \\ \sim T \sum_{\omega_n} \sum_s \int_s \mathrm{d}\Omega\, \rho_s(\Omega) \left| \sum_\mu \eta_\mu^{n_0} \varphi_\mu^{n_0}(\Omega, s) \right|^{2l} \int_{-\Lambda}^{\Lambda} \mathrm{d}\epsilon\, \frac{1}{(\omega_n^2 + \epsilon^2)^l} \end{aligned} \tag{C.38}$$

where we have assumed that, within the low-energy theory, the basis functions $\varphi_\mu^{n_0}(\boldsymbol{k}, s)$ only weakly depend on the momentum coordinate perpendicular to the Fermi surface, i.e., on the single-particle energy ϵ. Defining the Fermi surface average

$$\langle F(\Omega) \rangle_s := \rho_F^{-1} \int_s \mathrm{d}\Omega\, \rho_s(\Omega) F(\Omega), \qquad \rho_F := \sum_s \int_s \mathrm{d}\Omega\, \rho_s(\Omega), \tag{C.39}$$

for any function $F(\Omega)$ as well as

$$I_l(\Lambda, T) := \rho_F \int_{-\Lambda}^{\Lambda} \mathrm{d}\epsilon\, T \sum_{\omega_n} \frac{1}{(\omega_n^2 + \epsilon^2)^l}, \tag{C.40}$$

we obtain the form (4.41) of the Ginzburg-Landau expansion stated in the main text.

C.2.2 For weak inversion symmetry breaking

Here we deduce an expression for the Ginzburg-Landau expansion in the complementary limit of weak spin-orbit splitting $E_\mathrm{so} \ll T_c$. From this, we derive the central relation (4.102) of the analysis in Chap. 4.5.2.

Proceeding similarly to Sec. C.2.1, but keeping the Fermi-surface-off-diagonal matrix elements of the order parameter, we obtain for the free energy

$$\mathcal{F}(\Delta_n) = \sum_n |\Delta_n|^2 \left[\frac{1}{g_n} - 2 \sum_{s,s'} \int_k |m_{ss'}(\boldsymbol{k}, n)|^2 G_s(k) G_{s_\mathrm{K}}(-k) \right] + \mathcal{O}\left(|\Delta_n|^4 \right) \tag{C.41}$$

associated with the Hamiltonian (4.101), where

$$|m_{ss'}(\boldsymbol{k}, n)| := \frac{1}{\Delta_n} \left| \sum_\mu \eta_\mu^n \langle \psi_{\boldsymbol{k}s} | \widetilde{\chi}_\mu^n(\boldsymbol{k}) | \psi_{\boldsymbol{k}s'} \rangle \right|, \qquad \Delta_n := \sqrt{\sum_\mu |\eta_\mu^n|^2}. \tag{C.42}$$

Let us write Eq. (C.41) in a more explicit and convenient way: In the absence of inversion-symmetry breaking, all Fermi surfaces are doubly degenerate. This degeneracy will be lifted for $E_\mathrm{so} \neq 0$ such that

any Fermi surface will be split into two which we call a "Rashba pair" of Fermi surfaces (extensively used in Chap. 6). As mentioned in the main text, we will assume here that the energetic separation between different Rashba pairs is sufficiently large to neglect the coupling terms between them in Eq. (C.41). Then we can replace

$$\sum_{s,s'}\int_k \cdots = T\sum_{\omega_n}\sum_{s,s'}\sum_{\boldsymbol{k}}^{s,s';\Lambda}\cdots \to T\sum_{\omega_n}\sum_{j,j'=1,2}\sum_{\boldsymbol{k}}^{\Lambda}\ldots, \tag{C.43}$$

where j, j' refer to the two members of Rashba pairs, $\sum_{\boldsymbol{k}}^{s,s';\Lambda}$ is the sum over momenta with $|\epsilon_{\boldsymbol{k}s}|, |\epsilon_{\boldsymbol{k}s'}| < \Lambda$, whereas $\sum_{\boldsymbol{k}}^{\Lambda}$ just indicates the summation over all momenta in the energetic vicinity (cutoff Λ) of the Fermi surfaces. Then Eq. (C.41) becomes

$$\mathcal{F}[\Delta_n] \sim \sum_n |\Delta_n|^2 \left[\frac{1}{g_n} - 2T\sum_{\omega_n}\sum_{j,j'=1,2}\sum_{\boldsymbol{k}}^{\Lambda}|m_{jj'}(\boldsymbol{k},n)|^2 G_j(k)G_{j'}(-k)\right]. \tag{C.44}$$

Note that the identification $G_j(k) \leftrightarrow G_s(k)$ and $m_{jj'}(\boldsymbol{k},n) \leftrightarrow m_{ss'}(\boldsymbol{k},n)$ is unique since we assume the sets of momenta involved in the low-energy theory of different Rashba pairs to be disjoint.

To evaluate the right-hand side of Eq. (C.44), we assume that the matrix elements $|m_{jj}(\boldsymbol{k},n)|$ and $E_{\mathrm{so}}(\boldsymbol{k})$ do, within the cutoff, not significantly depend on the momentum perpendicular to the Fermi surface ($m_{jj}(\boldsymbol{k},n) \to m_{jj}(\Omega,n)$, $E_{\mathrm{so}}(\boldsymbol{k}) \to E_{\mathrm{so}}(\Omega)$, see Chap. 4.3 and Fig. 4.1(a) for the definition of Ω), introduce the angle-resolved density of states $\rho(\Omega)$ via rewriting

$$\sum_{\boldsymbol{k}}^{\Lambda}\ldots \sim \int \mathrm{d}\Omega\,\rho(\Omega)\int_{-\Lambda}^{\Lambda}\mathrm{d}\epsilon\ldots \tag{C.45}$$

and find

$$\mathcal{F}[\Delta_n] \sim \sum_n |\Delta_n|^2\left[\frac{1}{g_n} - 2\rho_F C_n^d \ln\left(\frac{2e^\gamma}{\pi}\frac{\Lambda}{T}\right) - 2\rho_F C_n^o\left(\ln\left(\frac{2e^\gamma}{\pi}\frac{\Lambda}{T}\right) - \frac{7}{16\pi^2}\zeta(3)\frac{\langle E_{\mathrm{so}}^2\rangle_{\mathrm{FS}}^n}{T^2}\right)\right] \tag{C.46}$$

with γ and $\zeta(s)$ denoting the Euler-Mascheroni constant and the Riemann zeta function, the average Fermi-surface diagonal and off-diagonal matrix elements

$$C_n^d := \sum_{j=1,2}\langle|m_{jj}(\Omega,n)|^2\rangle, \qquad C_n^o := 2\langle|m_{12}(\Omega,n)|^2\rangle, \tag{C.47}$$

where

$$\langle|m_{12}(\Omega,n)|^2\rangle := \rho_F^{-1}\int \mathrm{d}\Omega\,\rho(\Omega)|m_{12}(\Omega,n)|^2, \tag{C.48}$$

and

$$\langle E_{\mathrm{so}}^2\rangle_n := \rho_F^{-1}\int \mathrm{d}\Omega\,\rho(\Omega)\frac{|m_{12}(\Omega,n)|^2}{\langle|m_{12}(\Omega,n)|^2\rangle}E_{\mathrm{so}}^2(\Omega). \tag{C.49}$$

Writing

$$\langle E_{\mathrm{so}}^2\rangle_n = S_n\widehat{E}_{\mathrm{so}}^2, \qquad S_n := \langle E_{\mathrm{so}}^2/\widehat{E}_{\mathrm{so}}^2\rangle_n, \qquad \widehat{E}_{\mathrm{so}} := \max_{\boldsymbol{k}}|E_{\mathrm{so}}(\boldsymbol{k})|, \tag{C.50}$$

the equation determining the transition temperature T_c^n of the superconducting state transforming under the IR n reads

$$\frac{1}{2\rho_F g_n} = C_n^d \ln\left(\frac{2e^\gamma}{\pi}\frac{\Lambda}{T_c^n}\right) + C_n^o\left(\ln\left(\frac{2e^\gamma}{\pi}\frac{\Lambda}{T_c^n}\right) - \frac{7}{16\pi^2}\zeta(3)S_n\frac{\widehat{E}_{\rm so}^2}{(T_c^n)^2}\right). \tag{C.51}$$

Denoting the transition temperature in the absence of inversion-symmetry breaking by $T_{c,0}^n$, we can write more compactly

$$\frac{7}{16\pi^2}\zeta(3)\frac{S_n C_n^o}{C_n^o + C_n^d}\frac{\widehat{E}_{\rm so}^2}{(T_c^n)^2} = \ln\left(\frac{T_{c,0}^n}{T_c^n}\right). \tag{C.52}$$

Now let us consider the situation outline in the main text: For vanishing spin-orbit splitting the leading instability transforms under a representation $n = n_1$ that is even under a twofold rotation perpendicular to the plane such that $C_{n_1}^d = 0$ is enforced by symmetry. Furthermore, this state is nearly degenerate with another phase transforming under a different representation $n = n_2$, i.e., $T_{c,0}^{n_1} > T_{c,0}^{n_2}$ with $T_{c,0}^{n_1} - T_{c,0}^{n_2} \ll T_{c,0}^{n_1}$. From Eq. (C.52), we find that the critical value $\widehat{E}_{\rm so}^c$ of the spin-orbit splitting strength for having $T_{n_1} = T_{n_2}$ is given by

$$\widehat{E}_{\rm so}^c \sim \frac{4\pi}{\sqrt{7\zeta(3)}}\sqrt{\frac{C_{n_2}^o + C_{n_2}^d}{C_{n_2}^o(S_{n_1} - S_{n_2}) + C_{n_2}^d S_{n_1}}}T_{c,0}^{n_1}\sqrt{\frac{T_{c,0}^{n_1} - T_{c,0}^{n_2}}{T_{c,0}^{n_1}}} \tag{C.53}$$

as $(T_{c,0}^{n_1} - T_{c,0}^{n_2})/T_{c,0}^{n_1} \to 0$. To restate this result in simpler form, let us assume $S_{n_1} = S_{n_2}$ such that $\langle E_{\rm so}^2\rangle_{n_1} = \langle E_{\rm so}^2\rangle_{n_2} \equiv \langle E_{\rm so}^2\rangle$. Its critical value $\langle E_{\rm so}^2\rangle^c$ is then given by Eq. (4.102) of the main text.

C.3 Resummation of the Ginzburg-Landau expansion

Here we present additional information on how we come to the conclusion in Chap. 4.3.1 that a first order mean-field transition can be ruled out in the weak-pairing limit.

In the limit $\Lambda \to \infty$, the integrals I_l with $l \geq 2$ are finite and readily evaluated

$$I_l(\infty, T) \equiv T\sum_{\omega_n}\rho_F\int_{-\infty}^{\infty}{\rm d}\epsilon\frac{1}{(\omega_n^2 + \epsilon^2)^l} = 2(2\pi)^{2-2l}\binom{2l-2}{l-1}\rho_F T^{2-2l}(1 - 2^{1-2l})\zeta(2l-1), \tag{C.54}$$

where $\zeta(s)$ is the Riemann zeta function and $\binom{n}{k}$ the binomial coefficient. Using this in Eq. (4.45), one finds Eq. (4.46) within the radius of convergence of the power series

$$f_{\geq 4}(x) = \sum_{l=2}^{\infty}(-1)^l c_l\, x^l, \qquad c_l = \frac{4\pi^{2-2l}}{l}\binom{2l-2}{l-1}(1 - 2^{1-2l})\zeta(2l-1). \tag{C.55}$$

To show positivity, we use associativity of the infinite sum (holds since the sum converges for $|x| < \pi^2/4$) allowing us to write

$$f_{\geq 4}(x) = \frac{c_2}{2}x^2 + \sum_{n=1}^{\infty}x^{2n}C_n(x), \qquad C_n(x) = \frac{c_{2n}}{2} - c_{2n+1}x + \frac{c_{2n+2}}{2}x^2. \tag{C.56}$$

One readily finds

$$C_n(x) \geq C_n(c_{2n+1}/c_{2n+2}) = \left(c_{2n} - c_{2n+1}^2/c_{2n+2}\right)/2 \tag{C.57}$$

such that all $C_n(x)$ and, hence, the entire series is positive if

$$c_{2n}c_{2n+2} > c_{2n+1}^2. \tag{C.58}$$

It is straightforward to show that, indeed, the coefficients c_l defined in Eq. (C.55) satisfy this inequality rendering the power series positive in accordance with Fig. 4.2.

For the purpose of analytic continuation of $f_{\geq 4}(x)$ in Eq. (C.55), it is very convenient to start again from Eq. (4.45) and rewrite the expression as

$$\mathcal{F}_{\geq 4}[\eta_\mu^{n_0}] = \sum_s \int_s \mathrm{d}\Omega\, \rho_s(\Omega) T \int_{-\Lambda}^{\Lambda} \mathrm{d}\epsilon \sum_{\omega_n} \sum_{l=2}^{\infty} \frac{2^{2l-1}}{l} (-1)^l \left(\frac{\left| \sum_{\mu=1}^{d_{n_0}} \eta_\mu^{n_0} \varphi_\mu^{n_0}(\Omega, s) \right|^2}{\omega_n^2 + \epsilon^2} \right)^l, \tag{C.59}$$

which is allowed within the radius of convergence $1/4$ of the power series, i.e., as long as

$$\frac{\left| \sum_{\mu=1}^{d_{n_0}} \eta_\mu^{n_0} \varphi_\mu^{n_0}(\Omega, s) \right|^2}{\omega_n^2 + \epsilon^2} < 1/4 \quad \Leftrightarrow \quad \frac{\left| \sum_{\mu=1}^{d_{n_0}} \eta_\mu^{n_0} \varphi_\mu^{n_0}(\Omega, s) \right|}{T} < \frac{\pi}{2}. \tag{C.60}$$

This means that

$$f_{\geq 4}(x) = T^{-1} \int_{-\Lambda}^{\Lambda} \mathrm{d}\epsilon \sum_{\omega_n} g_{\geq 4}\left(\frac{x\, T^2}{\omega_n^2 + \epsilon^2} \right) \tag{C.61}$$

with

$$g_{\geq 4}(y) = \sum_{l=2}^{\infty} \frac{2^{2l-1}}{l} (-1)^l y^l = \frac{1}{2} \left(4y - \ln(1+4y) \right) \tag{C.62}$$

coincides (for $\Lambda \to \infty$) with the power series representation (C.55) within the radius of convergence of the latter, i.e., for $|x| < \pi^2/4$. Furthermore, Eq. (C.61) defines an analytic continuation on $\mathbb{R}^+$. To see this note that the summation and integration in Eq. (C.61) converges absolutely (the same holds for all its derivatives with respect to x) since

$$g_{\geq 4}(y) \sim 4y^2, \qquad y \to 0 \tag{C.63}$$

and that $g_{\geq 4}(y)$ is analytic for $\mathrm{Re}(y) > -1/4$. Due to the uniqueness of analytic continuation, Eq. (C.61) must hold for all $x \geq 0$. Since $g_{\geq 4} > 0$ on $\mathbb{R}^+$, we find that

$$f_{\geq 4}(x) > 0 \qquad \forall x > 0. \tag{C.64}$$

As opposed to the analysis using a power series representation, we here even did not have to set $\Lambda \to \infty$ in order to come to this conclusion.

For completeness we have also performed the energy integration in Eq. (C.61) explicitly (in the limit $\Lambda \to \infty$) yielding the compact representation (4.47) stated in the main text. Since the terms in the sum in Eq. (4.47) behave as $\sim x^2/(2\pi^3 n^3) + \mathcal{O}(n^{-4})$ for large n, the sum and all its derivatives with respect to x exist.

C.4 Sufficient condition for TRS-breaking superconductivity

In this section, we will show that invariance of the free energy under Eq. (4.57) and Eq. (4.58) are satisfied for any real IR as well as for most complex IRs of the point groups of crystalline 2D and 3D systems.

To streamline the following discussion, we first notice that it will be sufficient to analyze the noncentrosymmetric point groups as any centrosymmetric point group $\mathcal{G}_p$ can be written as $\mathcal{G}_p = \widetilde{\mathcal{G}_p} \times C_i$, where $C_i = \{E, I\}$ and $I \notin \widetilde{\mathcal{G}_p}$. All IRs of $\mathcal{G}_p$ can then be constructed by taking an IR n of the corresponding noncentrosymmetric point group $\widetilde{\mathcal{G}_p}$ and setting

$$\mathcal{R}_\chi^{n\pm}(g) = \mathcal{R}_\chi^n(g), \qquad \mathcal{R}_\chi^{n\pm}(gI) = \pm\mathcal{R}_\chi^n(g), \qquad \forall g \in \widetilde{\mathcal{G}_p}, \tag{C.65}$$

where $+$ $(-)$ corresponds to a gerade (ungerade) IR of $\mathcal{G}_p$ (see also Appendix A.2). The additional constraints coming from the symmetry transformations $g \notin \widetilde{\mathcal{G}_p}$ therefore effectively only require the free energy to be invariant under a simultaneous sign change of all η_μ which is just a global U(1)-gauge transformation and, hence, do not have to be considered in the following.

C.4.1 Real multidimensional representations

In case of real IRs, the discussion of Chap. 4.3.2 is only relevant when the representation is multidimensional. Investigating the list of crystalline point groups provided in Appendix A.3, we see that we thus do not have to consider the nonaxial, cyclic, reflection and improper rotation groups as well as $C_{2v} \cong D_2$. Only $C_{nv} \cong D_n$ with $n = 3, 4, 6$ and the remaining noncentrosymmetric groups D_{3h}, D_{2d} and T, T_d, O need to be analyzed. Due to the additional isomorphisms $D_{3h} \cong C_{6v}$, $D_{2d} \cong C_{4v}$ and $T_d \cong O$ it will be sufficient to focus on the point groups

$$C_{3v}, \qquad C_{4v}, \qquad C_{6v}, \qquad T, \qquad O \tag{C.66}$$

in the following.

Pyramidal groups. In case of the groups C_{nv} it is sufficient to focus on $n = 3, 6$ as C_{4v} has already been discussed in detail in the main text. C_{3v} (C_{6v}) is generated by the reflection σ_{xz} at the xz-plane and the threefold rotation C_3^z (sixfold rotation C_6^z) along the z-axis. To begin with the constraints following from the reflection symmetry, we note that

$$\sigma_{xz}: \quad (\eta_1, \eta_2) \longrightarrow (\eta_1, -\eta_2), \tag{C.67}$$

for both two-dimensional IRs E_1 and E_2 of C_{6v} as well as for E of C_{3v}. Exactly as Eq. (4.54a), it forces the free energy to be invariant under Eq. (4.57) which is already the first requirement for our general proof presented in Chap. 4.3.2.

To approach the second requirement (4.58) we consider the second generator of C_{3v} and C_{6v}, the rotation symmetries C_3^z and C_6^z represented by

$$\mathcal{R}_\chi^{E_1}(C_6^z) = \frac{1}{2}\begin{pmatrix} 1 & -\sqrt{3} \\ \sqrt{3} & 1 \end{pmatrix}, \qquad \mathcal{R}_\chi^{E_2}(C_6^z) = \mathcal{R}_\chi^{E}(C_3^z) = \frac{1}{2}\begin{pmatrix} -1 & -\sqrt{3} \\ \sqrt{3} & -1 \end{pmatrix}. \tag{C.68}$$

Demanding invariance of Eq. (4.52) (with $\gamma_{12} = \gamma_{21} = 0$ due to Eq. (C.67)) under Eq. (C.68) leads in all cases to $\alpha_1 = \alpha_2$ as required.

Chiral tetrahedral group. To continue with the (chiral) tetrahedral group T which can be generated by any one of its threefold rotation symmetries C_3 together with one of its twofold rotation symmetries C_2. We choose the coordinate system such that the generating C_3 and C_2 are along $\boldsymbol{e}_x + \boldsymbol{e}_y + \boldsymbol{e}_z$ and $\boldsymbol{e}_z$, respectively. This group has one multidimensional IR, following the standard conventions denoted by T, which is three dimensional. Its three components (η_1, η_2, η_3) transform as (x, y, z) such that

$$\mathcal{R}_\chi^T(C_3) = \begin{pmatrix} 0 & 0 & 1 \\ 1 & 0 & 0 \\ 0 & 1 & 0 \end{pmatrix}, \qquad \mathcal{R}_\chi^T(C_2) = \mathrm{diag}(1, -1, -1). \tag{C.69}$$

Combining the two-fold rotation with a gauge transformation $\eta_\mu \to -\eta_\mu$, we see that the free energy must be invariant under $(\eta_1, \eta_2, \eta_3) \to (-\eta_1, \eta_2, \eta_3)$. Since $\mathcal{R}_\chi^T(C_3)$ is a cyclic permutation matrix, the free energy must automatically also be even in η_2 and η_3 which proves invariance under (4.57).

As for Eq. (4.58), we first note that, generally for any $\mathcal{G}_0$ and n,

$$\alpha_\mu \equiv \left\langle \left(\varphi_\mu^n(\Omega, s)\right)^4 \right\rangle_s \equiv \int_s \mathrm{d}\Omega\, \rho_s(\Omega) \left(\varphi_\mu^n(\Omega, s)\right)^4 = \left(\mathcal{R}_\chi^n(g)\right)_{\mu\nu}^4 \alpha_\nu \tag{C.70}$$

as long as $\mathcal{R}_\chi^n(g)$ is a permutation. Eq. (C.70) readily follows from the transformation property (4.37) of the basis functions and the invariance of $\rho_s(\Omega)$ under all symmetry operations of $\mathcal{G}_0$.

Using $\mathcal{R}_\chi^T(C_3)$ in Eq. (C.70) directly yields $\alpha_1 = \alpha_2 = \alpha_3$.

Chiral octahedral group. Let us continue with the chiral octahedral group O which has three different multidimensional IRs, T_1, T_2 and E with $\dim(T_1) = \dim(T_2) = 3$ and $\dim(E) = 2$. This group can be generated by two distinct C_4-rotation axes, which we choose to be aligned along $\boldsymbol{e}_x$ and $\boldsymbol{e}_z$ (denoted by C_4^x and C_4^z).

In case of the IR T_1, the components (η_1, η_2, η_3) transform as (x, y, z) and, hence,

$$\mathcal{R}_\chi^{T_1}(C_4^x) = \begin{pmatrix} 1 & 0 & 0 \\ 0 & 0 & -1 \\ 0 & 1 & 0 \end{pmatrix}, \qquad \mathcal{R}_\chi^{T_1}(C_4^y) = \begin{pmatrix} 0 & 0 & 1 \\ 0 & 1 & 0 \\ -1 & 0 & 0 \end{pmatrix}, \qquad \mathcal{R}_\chi^{T_1}(C_4^z) = \begin{pmatrix} 0 & -1 & 0 \\ 1 & 0 & 0 \\ 0 & 0 & 1 \end{pmatrix}. \tag{C.71}$$

Although redundant, we have also added the representation of C_4^y for future reference. Recalling Eq. (C.70), C_4^x and C_4^z imply $\alpha_2 = \alpha_3$ and $\alpha_1 = \alpha_2$, respectively, proofing that Eq. (4.58) holds. Since

$$\left[- \left(\mathcal{R}_\chi^{T_1}(C_4^{\mu_0})\right)^2 \right]_{\mu\nu} = \delta_{\mu,\nu} \begin{cases} -1 & \mu = \mu_0 \\ 1 & \mu \neq \mu_0 \end{cases}, \qquad \mu_0 = x, y, z, \tag{C.72}$$

invariance under Eq. (4.57) is guaranteed as a consequence of rotational and gauge invariance.

In case of the irreducible representation T_2, we choose the components (η_1, η_2, η_3) to transform as (yz, xz, xy). It then holds $\mathcal{R}_\chi^{T_2}(C_4^{\mu_0}) = -\mathcal{R}_\chi^{T_1}(C_4^{\mu_0})$ as is readily verified from Eq. (C.71). We can thus directly conclude that Eq. (4.58) and invariance under (4.57) must hold also for T_2.

Table C.1: *Summary of the transformation behavior under the complex IRs of the crystalline point groups together with the restrictions on the coupling constants in the free energy (4.52).*

Point groups	IR n	g	$c(g)$	$\widetilde{\mathcal{R}}^n_\chi(g)$	Coefficients in Eq. (4.52)
C_3	E	C_3	$e^{\frac{2\pi i}{3}}$	$\frac{1}{2}\begin{pmatrix} -1 & -\sqrt{3} \\ \sqrt{3} & -1 \end{pmatrix}$	$\alpha_1 = \alpha_2 = 3\beta$, $\gamma_{12} = \gamma_{21} = 0$
$C_6 \simeq C_{3h}$	E_1	C_6	$e^{\frac{2\pi i}{6}}$	$\frac{1}{2}\begin{pmatrix} 1 & -\sqrt{3} \\ \sqrt{3} & 1 \end{pmatrix}$	——— " ———
	E_2	C_6	$-e^{-\frac{2\pi i}{6}}$	$\frac{1}{2}\begin{pmatrix} -1 & -\sqrt{3} \\ \sqrt{3} & -1 \end{pmatrix}$	——— " ———
T	E	C_3	$e^{\frac{2\pi i}{3}}$	$\frac{1}{2}\begin{pmatrix} -1 & -\sqrt{3} \\ \sqrt{3} & -1 \end{pmatrix}$	——— " ———
		C_2	1	σ_0	
$C_4 \simeq S_4$	E	C_4	i	$-i\sigma_y$	$\alpha_1 = \alpha_2$, $\gamma_{12} = -\gamma_{21}$

Finally, it is only left to discuss the irreducible representation E, where the components (η_1, η_2) transform as $(2z^2 - x^2 - y^2, \sqrt{3}(x^2 - y^2))$. From this, it follows

$$\mathcal{R}^E_\chi(C_4^z) = \sigma_3, \qquad \mathcal{R}^E_\chi(C_4^x) = \frac{1}{2}\begin{pmatrix} -1 & -\sqrt{3} \\ -\sqrt{3} & 1 \end{pmatrix}. \tag{C.73}$$

Noting that $\mathcal{R}^E_\chi(C_4^z) = \mathcal{R}^{E_2}_\chi(\sigma_{xz})$ and $\mathcal{R}^E_\chi(C_4^z)\mathcal{R}^E_\chi(C_4^x) = \mathcal{R}^{E_2}_\chi(C_6^z)$ for the irreducible representation E_2 of C_{6v} (see Eq. (C.68)), we know, without further analysis, that the requirements for the validity general proof of the main text are also given in case of the IR E of the chiral octahedral group O.

C.4.2 Complex representations

Let us also analyze complex IRs as they offer an additional possibility to break TRS. As we have discussed in detail seen in Chap. 4.1.2, any complex representation n should always be analyzed together with its conjugate representation $\bar{n}$ since these two are degenerate at the quadratic level of the Ginzburg-Landau expansion due to TRS. It is very convenient to introduce a new basis, $\{\widetilde{\chi}^{n_0}_\mu, \widetilde{\chi}^{\bar{n}_0}_\mu\} \to \{\widetilde{\chi}^{\widetilde{n}_0}_\mu\}$, and $\{\eta^n_\mu, \eta^{\bar{n}}_\mu\} \to \{\eta^{\widetilde{n}}_\mu\}$ as defined in Eqs. (4.21) and (4.22), such that $\{\widetilde{\chi}^{\widetilde{n}_0}_\mu\}$ and $\{\eta^{\widetilde{n}}_\mu\}$ transform under a real reducible representation $\widetilde{n}$ of dimension $2d_n$.

All complex representations of point groups of 2D and 3D crystalline systems are one-dimensional. From the form (4.21) of the unitary transformation, we easily find that if

$$(\eta^n, \eta^{\bar{n}}) \xrightarrow{g} (c(g)\,\eta^n, c^*(g)\,\eta^{\bar{n}}), \qquad |c(g)| = 1, \tag{C.74}$$

for an arbitrary symmetry operation $g \in \mathcal{G}_p$, the transformation behavior in the new basis is given by

$$\left(\eta_1^{\widetilde{n}}, \eta_2^{\widetilde{n}}\right) \xrightarrow{g} \left(\eta_1^{\widetilde{n}}, \eta_2^{\widetilde{n}}\right) \widetilde{\mathcal{R}}_\chi^{\widetilde{n}}(g), \qquad \widetilde{\mathcal{R}}_\chi^{\widetilde{n}}(g) = \begin{pmatrix} \mathrm{Re}\, c(g) & -\mathrm{Im}\, c(g) \\ \mathrm{Im}\, c(g) & \mathrm{Re}\, c(g) \end{pmatrix}. \tag{C.75}$$

Recalling that, as discussed above, it is sufficient to focus on the noncentrosymmetric point groups, only the point groups C_3, C_4, C_6, C_{3h}, S_4 and T of the list given in Appendix A.3 have to be considered here. The transformation matrices in Eq. (C.75) for the associated complex IRs are summarized in Table C.1 together with the resulting constraints on the coefficients in the fourth-order term (4.52) of the Ginzburg-Landau expansion.

We can directly read off that in all cases, except for $C_4 \simeq S_4$ and the associated centrosymmetric point group $C_{4h} = C_4 \times C_i$, the symmetries force $\alpha_1 = \alpha_2$ and $\gamma_1 = \gamma_1 = 0$. Consequently, the free energy is again invariant under (4.57) and Eq. (4.58) holds. Therefore, based on the general proof by contradiction given above, we can already conclude that the superconducting order parameter must necessarily break TRS when transforming under one of these complex representations.

C.5 Superconductivity suppressed by spin-orbit splitting

In this appendix, we will provide more details on the analysis in Chap. 4.5.1 concerning the condensation energy of a superconducting state with vanishing Fermi-surface-diagonal matrix elements.

C.5.1 Expression for the condensation energy

As a first step, we transform the full mean-field Hamiltonian

$$\hat{H}_{\mathrm{MF}} = \sum_{\boldsymbol{k}} \hat{c}^\dagger_{\boldsymbol{k}\alpha} \left(h_{\boldsymbol{k}}\right)_{\alpha\beta} \hat{c}_{\boldsymbol{k}\beta} + \hat{H}^{\mathrm{MF}}_{\mathrm{int}} \tag{C.76}$$

with $\hat{H}^{\mathrm{MF}}_{\mathrm{int}}$ as given in Eq. (4.98) into the eigenbasis of $h_{\boldsymbol{k}}$ according to Eq. (4.23).

Writing the Hamiltonian in quadratic form by means of Nambu spinors, diagonalizing the resulting BdG Hamiltonian with eigenvalues $E_{\boldsymbol{k}s}(\Delta_0)$ and associated Bogoliubov-quasiparticle operators $\hat{\alpha}_{\boldsymbol{k}s}$ leads to

$$\hat{H}_{\mathrm{MF}} = \sum_s \sum_{\boldsymbol{k}} E_{\boldsymbol{k}s}(\Delta_0) \hat{\alpha}^\dagger_{\boldsymbol{k}s} \hat{\alpha}_{\boldsymbol{k}s} + \frac{1}{2} \sum_s \sum_{\boldsymbol{k}} \left(\epsilon_{\boldsymbol{k}s} - E_{\boldsymbol{k}s}(\Delta_0)\right) + \frac{\Delta_0^2}{g_{n_0}}, \tag{C.77}$$

where we have already made use of the Majorana/PHS-symmetry of the Nambu spinors such that all operators $\hat{\alpha}_{\boldsymbol{k}s}$ appearing in Eq. (C.77) are independent. From this, we immediately get the $T = 0$ condensation energy

$$E_c(\Delta_0) := E_{\mathrm{GS}}(0) - E_{\mathrm{GS}}(\Delta_0) = \frac{1}{2} \sum_s \sum_{\boldsymbol{k}} \left(|E_{\boldsymbol{k}s}(\Delta_0)| - |\epsilon_{\boldsymbol{k}s}|\right) - \frac{\Delta_0^2}{g_{n_0}}, \tag{C.78}$$

where $E_{\mathrm{GS}}(\Delta_0)$ denotes the ground states energy at given Δ_0. By design, a positive value of $E_c(\Delta_0)$ for some $\Delta_0 \neq 0$ is required for the superconducting state to occur.

As discussed in the main text, we focus for simplicity on the situation where, for each $\boldsymbol{k}$, only two bands have to be considered, i.e., the bands can be relabeled such that s only assumes the two values

$s = 1, 2$ in Eq. (C.78). Recalling that all diagonal matrix elements of the order parameter vanish, one finds

$$E_c(\Delta_0) = \frac{1}{2}\sum_{\boldsymbol{k}}\left(\frac{1}{2}\sum_{p=\pm}\left|\epsilon_{\boldsymbol{k}2} - \epsilon_{\boldsymbol{k}1} + p\sqrt{\left(\epsilon_{\boldsymbol{k}1}+\epsilon_{\boldsymbol{k}2}\right)^2 + 16\Delta_0^2|m_{21}(\boldsymbol{k})|^2}\right| - \left|\epsilon_{\boldsymbol{k}1}\right| - \left|\epsilon_{\boldsymbol{k}2}\right|\right) - \frac{\Delta_0^2}{g_{n_0}}, \quad \text{(C.79)}$$

where we have introduced $m_{ss'}(\boldsymbol{k}) = D_{ss'}(\boldsymbol{k})/\Delta_0$.

C.5.2 Derivation of a general inequality

The expression (C.79) is most easily evaluated by first noting that there are only contributions for $\boldsymbol{k}$ with $m_{12}(\boldsymbol{k}) \neq 0$ ($\boldsymbol{k} \in \mathrm{supp}(m_{21})$) and splitting the remaining $\boldsymbol{k}$-sum intro three disjoint regions:

1. $R_1 := \left\{\boldsymbol{k} \in \mathrm{supp}(m_{21}) \middle| \sqrt{\left(\epsilon_{\boldsymbol{k}1}+\epsilon_{\boldsymbol{k}2}\right)^2 + 16\Delta^2|m_{21}(\boldsymbol{k})|^2} < E_{\mathrm{so}}(\boldsymbol{k})\right\}$, where we have introduced $E_{\mathrm{so}}(\boldsymbol{k}) := \epsilon_{\boldsymbol{k}2} - \epsilon_{\boldsymbol{k}1} > 0$,
2. $R_2 := \left\{\boldsymbol{k} \in \mathrm{supp}(m_{21}) \middle| |\epsilon_{\boldsymbol{k}1}+\epsilon_{\boldsymbol{k}2}| < E_{\mathrm{so}}(\boldsymbol{k}) < \sqrt{\left(\epsilon_{\boldsymbol{k}1}+\epsilon_{\boldsymbol{k}2}\right)^2 + 16\Delta^2|m_{21}(\boldsymbol{k})|^2}\right\}$ and
3. $R_3 := \left\{\boldsymbol{k} \in \mathrm{supp}(m_{21}) \middle| E_{\mathrm{so}}(\boldsymbol{k}) < |\epsilon_{\boldsymbol{k}1}+\epsilon_{\boldsymbol{k}2}|\right\}$.

Analyzing every region separately, replacing $m_{21}(\boldsymbol{k}) \to m := \max_{\boldsymbol{k}}|m_{21}(\boldsymbol{k})|$, which can be rigorously shown to increase the value of $E_c(\Delta_0)$ for every Δ_0, approximating $E_{\mathrm{so}}(\boldsymbol{k}) \simeq E_{\mathrm{so}}$ to be a constant on the Fermi surface and introducing the "joint density of states" according to

$$\sum_{\boldsymbol{k}\in\mathrm{supp}(m_{21})} f\left(\frac{\epsilon_{\boldsymbol{k}1}+\epsilon_{\boldsymbol{k}2}}{2}\right) \sim \rho_F \int_{-\Lambda}^{\Lambda} \mathrm{d}\epsilon\, f(\epsilon) \quad \text{(C.80)}$$

yields:

$$E_c(\Delta_0) < E_c^{\max}(\Delta_0) = \begin{cases} E^{\max}_{c,\Delta_0,\Lambda}(\Delta_0), & \hat{\Delta}_0 > E_{\mathrm{so}}/2,\ \Lambda > E_{\mathrm{so}}/2 \\ E^{\max}_{c,E_{\mathrm{so}},\Lambda}(\Delta_0), & \hat{\Delta}_0 < E_{\mathrm{so}}/2,\ \Lambda > E_{\mathrm{so}}/2, \\ E^{\max}_{c,\Delta_0,E_{\mathrm{so}}}(\Delta_0), & \hat{\Delta}_0 > E_{\mathrm{so}}/2,\ \Lambda < E_{\mathrm{so}}/2, \\ E^{\max}_{c,E_{\mathrm{so}},E_{\mathrm{so}}}(\Delta_0), & \hat{\Delta}_0 < E_{\mathrm{so}}/2,\ \Lambda < E_{\mathrm{so}}/2 < \sqrt{\Lambda^2+\hat{\Delta}_0^2} \\ -\frac{\Delta_0^2}{g_{n_0}}, & \text{otherwise,} \end{cases} \quad \text{(C.81)}$$

where we have introduced $\hat{\Delta}_0 = 2m\Delta_0$,

$$\begin{aligned} E^{\max}_{c,E_{\mathrm{so}},\Lambda}(\Delta_0) =& \rho_F\left[\Lambda\left(\sqrt{\Lambda^2+\hat{\Delta}_0^2}-\Lambda\right) - \frac{1}{4}E_{\mathrm{so}}\left(E_{\mathrm{so}} - \sqrt{E_{\mathrm{so}}^2 - 4\hat{\Delta}_0^2}\right)\right. \\ &\left. + \hat{\Delta}_0^2 \ln\left(\frac{2\left(\Lambda+\sqrt{\Lambda^2+\hat{\Delta}_0^2}\right)}{E_{\mathrm{so}}+\sqrt{E_{\mathrm{so}}^2-4\hat{\Delta}_0^2}}\right)\right] - \frac{\Delta_0^2}{g_{n_0}} \end{aligned} \quad \text{(C.82)}$$

and

$$E^{\max}_{c,\Delta_0,\Lambda}(\Delta_0) = \rho_F \left[\Lambda \left(\sqrt{\Lambda^2 + \hat{\Delta}_0^2} - \Lambda \right) - \frac{1}{4} E_{\mathrm{so}}^2 + \hat{\Delta}_0^2 \ln \left(\frac{\Lambda + \sqrt{\Lambda^2 + \hat{\Delta}_0^2}}{\hat{\Delta}_0} \right) \right] - \frac{\Delta_0^2}{g_{n_0}}. \tag{C.83}$$

as well as

$$\begin{aligned} E^{\max}_{c,\Delta_0,E_{\mathrm{so}}}(\Delta_0) &= E^{\max}_{c,\Delta_0,\Lambda}(\Delta_0) + \frac{\rho_F}{2} \left(E_{\mathrm{so}} - 2\Lambda \right)^2, \\ E^{\max}_{c,E_{\mathrm{so}},E_{\mathrm{so}}}(\Delta_0) &= E^{\max}_{c,E_{\mathrm{so}},\Lambda}(\Delta_0) + \frac{\rho_F}{2} \left(E_{\mathrm{so}} - 2\Lambda \right)^2. \end{aligned} \tag{C.84}$$

A careful functional analysis of $E_c^{\max}(\Delta_0)$ shows that a superconductor with $D_{ss} = 0$ is only possible when

$$E_{\mathrm{so}} < E_{\mathrm{so}}^{\max}(\lambda, \Lambda, E_{\mathrm{so}}) \tag{C.85}$$

with

$$E_{\mathrm{so}}^{\max}(\lambda, \Lambda, E_{\mathrm{so}}) = \begin{cases} 2\Lambda \sqrt{\frac{e^{-1/\lambda}}{\sinh(1/\lambda)}}, & E_{\mathrm{so}} < 2\Lambda, \\ \frac{\Lambda}{\tanh(1/\lambda)}, & E_{\mathrm{so}} > 2\Lambda, \end{cases} \tag{C.86}$$

where $\lambda := 4m^2 \rho_F g_{n_0}$.

In order to avoid distinguishing between $E_{\mathrm{so}} < 2\Lambda$ and $E_{\mathrm{so}} > 2\Lambda$, one can replace Eq. (C.86) by the weaker necessary constraint

$$E_{\mathrm{so}} < \frac{2\Lambda}{\sinh(1/\lambda)}, \tag{C.87}$$

which has been stated in the main text.

Finally, if Eq. (C.85) holds, one finds that $E_c^{\max}(\Delta_0)$ is maximized by

$$m\Delta_0 = \frac{\Lambda}{2\sinh(1/\lambda)} > E_{\mathrm{so}}/4. \tag{C.88}$$

D Appendix D

Microscopic analysis of oxide heterostructures

This appendix contains supplementary information for Chap. 5 of the main text. Exactly as the latter, this appendix is based on Ref. [349].

D.1 Symmetry analysis of noninteracting Hamiltonian

In the first section, we will provide more details on the noninteracting models discussed in Chap. 5.1.1.

D.1.1 Symmetry analysis for the two-band model

To see how the form of Eqs. (5.2) and (5.3) result from the constraints of TRS and the C_{4v} point group, we first note that the spin and orbital (basis $\{3d_{xz}, 3d_{yz}\}$) Pauli matrices σ_j and τ_j transform under the IRs of C_{4v} as summarized in Table D.1.

To begin with the spin-independent part $h^{\mathrm{m}}_{\boldsymbol{k}}$, we directly see that TRS generally only allows for terms $\propto \tau_0, \tau_1, \tau_3$. The diagonal components of Eq. (5.2) are simply a linear combinations of $\tau_0(k_1^2+k_2^2+\text{const.})$ and $\tau_3(k_1^2 - k_2^2)$ while the off-diagonal is $\eta k_1 k_2 \tau_1$.

Table D.1: *Transformation behavior of the spin- (σ_j) and orbital (τ_j) Pauli matrices under C_{4v}.*

	IR	Leading basis functions
(σ_1, σ_2)	E	$(k_2, -k_1)$
σ_3	A_2	$k_1 k_2 (k_1^2 - k_2^2)$
τ_0	A_1	$1,\ k_1^2 + k_2^2$
τ_1	B_2	$k_1 k_2$
τ_2	A_2	$k_1 k_2 (k_1^2 - k_2^2)$
τ_3	B_1	$k_1^2 - k_2^2$

Table D.2: *Transformation of different combinations of momentum and spin under C_{4v}.*

	E	$2C_4$	C_2	$2\sigma_v$	$2\sigma_d$	IR
$k_1\sigma_1 + k_2\sigma_2$	1	1	1	-1	-1	A_2
$k_1\sigma_1 - k_2\sigma_2$	1	-1	1	-1	1	B_2
$k_1\sigma_2 + k_2\sigma_1$	1	-1	1	1	-1	B_1
$k_1\sigma_2 - k_2\sigma_1$	1	1	1	1	1	A_1

To obtain the most general expression for $h^{\mathrm{so}}_{\boldsymbol{k}}$ up to linear order in momentum, we have to take into account combinations of τ_j and σ_j. Combining (σ_1, σ_2) and $(k_y, -k_x)$ that transform under the same representation yields the usual Rashba term

$$\alpha_0\tau_0(k_1\sigma_2 - k_2\sigma_1). \tag{D.1}$$

To discuss the most general term, we use $E \otimes E = A_1 \oplus A_2 \oplus B_1 \oplus B_2$ (see Table D.2) yielding the additional contributions

$$\alpha_1\tau_1(k_1\sigma_1 - k_2\sigma_2), \qquad \alpha_3\tau_3(k_1\sigma_2 + k_2\sigma_1). \tag{D.2}$$

Here we have already taken into account that the term $\propto \tau_2(k_1\sigma_1 + k_2\sigma_2)$ is ruled out by TRS as τ_1 is odd under time-reversal. For the very same reason τ_1 can be combined with the Pauli matrix σ_3 that transforms under the same IR to get the atomic SOC $\sigma_3\tau_2$.

D.1.2 Three-orbital model

In this subsection, we derive the most general form of the spin-independent part $\widetilde{h}^{\mathrm{m}}_{\boldsymbol{k}}$ of the three-orbital model for (001) oxide heterostructures. Since the symmetry of the involved orbitals and the point group is identical, the following discussion also applies to the model of single layer Sr_2RuO_4 used in Sec. 4.6.1.

To proceed systematically, we expand $\widetilde{h}^{\mathrm{m}}_{\boldsymbol{k}}$ in terms of Gell-Mann matrices [337]

$$\widetilde{h}^{\mathrm{m}}_{\boldsymbol{k}} = \sum_{j=0}^{8} f_j(\boldsymbol{k})\lambda_j \tag{D.3}$$

using, exactly as in the main text, the basis $\{d_{xy}, d_{xz}, d_{yz}\}$. Here $f_j(\boldsymbol{k}) \in \mathbb{R}$ due to Hermiticity and

$$\lambda_0 = \sqrt{\frac{2}{3}}\,\mathbb{1}_3, \qquad \lambda_1 = \begin{pmatrix} 0 & 1 & 0 \\ 1 & 0 & 0 \\ 0 & 0 & 0 \end{pmatrix}, \qquad \lambda_2 = L_1 = \begin{pmatrix} 0 & -i & 0 \\ i & 0 & 0 \\ 0 & 0 & 0 \end{pmatrix}, \tag{D.4a}$$

$$\lambda_3 = \begin{pmatrix} 1 & 0 & 0 \\ 0 & -1 & 0 \\ 0 & 0 & 0 \end{pmatrix}, \qquad \lambda_4 = \begin{pmatrix} 0 & 0 & 1 \\ 0 & 0 & 0 \\ 1 & 0 & 0 \end{pmatrix}, \qquad \lambda_5 = -L_2 = \begin{pmatrix} 0 & 0 & -i \\ 0 & 0 & 0 \\ i & 0 & 0 \end{pmatrix}, \tag{D.4b}$$

Table D.3: *Transformation behavior of the Gell-Mann matrices $\{\lambda_j\}$ under C_{4v}.*

	E	$2C_4$	C_2	$2\sigma_v$	$2\sigma_d$	IR	Leading basis functions
(l_1, l_2)	2	0	-2	0	0	E	$(k_2, -k_1)$
l_3	1	1	1	-1	-1	A_2	$k_1k_2(k_1^2 - k_2^2)$
(λ_1, λ_4)	2	0	-2	0	0	E	(k_2, k_1)
λ_6	1	-1	1	-1	1	B_2	k_1k_2
$\left(\sqrt{3}\lambda_8 - \lambda_3\right)/2$	1	-1	1	1	-1	B_1	$k_1^2 - k_2^2$
$\left(\sqrt{3}\lambda_3 + \lambda_8\right)/2$	1	1	1	1	1	A_1	$1,\ k_1^2 + k_2^2$

$$\lambda_6 = \begin{pmatrix} 0 & 0 & 0 \\ 0 & 0 & 1 \\ 0 & 1 & 0 \end{pmatrix}, \qquad \lambda_7 = L_3 = \begin{pmatrix} 0 & 0 & 0 \\ 0 & 0 & -i \\ 0 & i & 0 \end{pmatrix}, \qquad \lambda_8 = \frac{1}{\sqrt{3}} \begin{pmatrix} 1 & 0 & 0 \\ 0 & 1 & 0 \\ 0 & 0 & -2 \end{pmatrix}, \tag{D.4c}$$

where L_j, $j = 1, 2, 3$, denote the projections of the angular momentum operators onto the t_{2g} manifold.

As all relevant orbitals are real, TRS forces $f_j(\boldsymbol{k})$ to be even for all real and odd for all purely imaginary Gell-Mann matrices. As d orbitals are even under inversion, this proves that the terms in Eq. (D.3) that are antisymmetric (symmetric) under inversion can only (cannot) involve the angular momentum operators L_1, L_2 and L_3.

To take into account the constraints from the C_{4v} point group, it is convenient to find the linear combinations of the Gell-Mann matrices that transform under the IRs of C_{4v}. The result is summarized in Table D.3 where also show the leading basis functions in a small $\boldsymbol{k}$-expansion around the Γ point.

To begin with the inversion symmetry breaking *odd parity* terms, we see that the leading contribution reads

$$\delta\left(L_1k_2 - L_2k_1\right) = \delta \begin{pmatrix} 0 & -ik_2 & -ik_1 \\ ik_2 & 0 & 0 \\ ik_1 & 0 & 0 \end{pmatrix}. \tag{D.5}$$

Note that there cannot be any term of the form $f_7(\boldsymbol{k})L_3$ as time-reversal and C_2 rotation symmetry require $f_7(\boldsymbol{k}) = -f_7(-\boldsymbol{k})$ and $f_7(\boldsymbol{k}) = f_7(-\boldsymbol{k})$, respectively, which implies $f_7 = 0$. Consequently, the impact of the broken inversion symmetry can be described by the single parameter δ. The periodicity of the Brillouin zone is easily restored by replacing $k_j \to \sin(k_j)$ recovering Eq. (4.108).

To continue with the *inversion symmetric* terms, we first note that (λ_1, λ_4) cannot enter the Hamiltonian for the same reason: Due to the C_2 rotation symmetry, we know that $f_j(\boldsymbol{k}) = -f_j(-\boldsymbol{k})$, $j = 1, 4$. Time-reversal symmetry, on the other hand, implies $f_j(\boldsymbol{k}) = f_j(-\boldsymbol{k})$, $j = 1, 4$ such that $f_1 = f_4 = 0$.

From λ_6, we get the interorbital second nearest neighbor hopping term $\eta k_x k_y \lambda_6$ as leading contribution. The remaining Gell-Mann matrices, can be used to construct the splitting term between the d_{xy}- and d_{xz}/d_{yz} orbitals as well as the anisotropic masses as a linear combination of $\mathbb{1}_3$, $\sqrt{3}\lambda_3 + \lambda_8$ and $\sqrt{3}\lambda_8 - \lambda_3$ multiplied with the respective leading basis functions in Table D.3 (5 independent parameters corresponding to m_{xy}, μ, $\delta\epsilon_{xy}$, $\widetilde{m}_\mathrm{l}$ and $\widetilde{m}_\mathrm{h}$ in Eq. (5.4)).

D.2 Identification of the nature of the instability

Here we present the basic steps on how the leading and subleading ("competing") instabilities are derived from the RG flow. As in Refs. [351, 352], we calculate the transition temperatures of all possible particle-particle (superconducting) and particle-hole (density wave) order parameters introduced in Eq. (5.18) using mean-field theory with renormalized coupling constants.

As we are only interested in the transition temperature, it suffices to consider the linearized mean-field equations which read

$$\Delta^{\mathrm{DW}}_{\tau_1\tau_2} \sim \int_k^{\Lambda_\perp,\Lambda_\parallel} G_{\tau_1}(k)\,\delta_{\tau_1,\tau_2} + 2\Delta^{\mathrm{DW}}_{\tau\tau'}\mathcal{W}^{\tau\tau_2}_{\tau_1\tau'}\int_k^{\Lambda_\perp,\Lambda_\parallel} G_{\tau_1}(k)G_{\tau_2}(k) \tag{D.6a}$$

and

$$\overline{\Delta}^{\mathrm{SC}}_{\tau_1\tau_2} \sim 2\mathcal{W}^{\tau\tau'}_{\tau_1\tau_2}\overline{\Delta}^{\mathrm{SC}}_{\tau'\tau}\int_k^{\Lambda_\perp,\Lambda_\parallel} G_{\tau_1}(k)G_{\tau_2}(k) \tag{D.6b}$$

for the density wave and superconducting order parameters, respectively. Here $G_{(\sigma,s)}(k) = (i\omega - \sigma v_s k_\perp)^{-1}$ denotes the noninteracting Green's function.

To write down the mean-field equations in more explicit form, we expand the density wave order parameters,

$$\Delta^{\mathrm{DW}}_{(\sigma,s)(\sigma',s')} = \sum_{j,j'=0}^{3} c_{jj'}\left(\widetilde{\tau}_j\right)_{\sigma\sigma'}\left(\tau_{j'}\right)_{ss'}, \quad c_{jj'}\in\mathbb{R}, \tag{D.7a}$$

and the anomalous expectation values,

$$\overline{\Delta}^{\mathrm{SC}}_{(-,s)(+,s')} = \sum_{j=0}^{3}\tilde{c}_j\left(\tau_j\right)_{ss'}, \quad \tilde{c}_j\in\mathbb{C}, \tag{D.7b}$$

in Pauli matrices. In Eq. (D.7b), we have already anticipated that the anomalous expectation values with $\sigma=\sigma'$ will always be subdominant in the weak-coupling limit and taken into account the antisymmetry of $\overline{\Delta}^{\mathrm{SC}}_{\tau\tau'}$ making it sufficient to focus on $(\sigma,\sigma')=(-,+)$ for uniquely defining the superconducting order parameter.

D.2.1 Identical Fermi velocities

We begin with the limit of equal Fermi velocities $v_1 = v_2 \equiv v$. As we are interested in the weak-coupling limit where $T_c \ll v\Lambda_\perp$, we only keep the leading terms in the mean-field equations that asymptotically diverge as $L_T := \log(v\Lambda_\perp/T)$. Inserting Eq. (D.7) into Eq. (D.6) yields the mean-field equations summarized in Table D.4.

To discuss the *leading instability*, let us first assume that the couplings diverge before the RG flow is cut off due to the finite curvature of the Fermi surfaces. In regime (II) of Fig. 5.3(d), the couplings behave asymptotically as $g_{11} \sim -g_{33} \to \infty$, whereas g_{00} and g_{30} stay finite since they do not flow at all. As is easily seen from Table D.4, the leading instability is, in this case, characterized by $\overline{\Delta}^{\mathrm{SC}}_{(-,s),(+,s')} \propto (\tau_3)_{ss'}$ (the s^{+-} state). Correspondingly, in regime (III), we have $g_{11} \sim g_{33} \to -\infty$ and hence $\overline{\Delta}^{\mathrm{SC}}_{(-,s),(+,s')} \propto (\tau_0)_{ss'}$ (the s^{++} state).

To derive the *subleading instabilities*, we have investigated the flow of all mean-field equations in Table D.4 according to Eq. (5.17) and analyzed which of the order parameters is dominant before

Table D.4: *Mean-field equations for the density wave, Eq. (D.7a), and superconducting order parameters, Eq. (D.7b), in case of identical velocities. The plus (minus) sign in the column of C_2^z and Θ means that the corresponding order parameter is symmetric (antisymmetric) under π-rotation and time-reversal, respectively.*

Mean-field equations ($j = 1, 2$)	Order parameter	C_2^z	Θ	Phase
$L_T \begin{pmatrix} g_{00}+g_{33} & 2g_{30} \\ 2g_{30} & g_{00}+g_{33} \end{pmatrix} \begin{pmatrix} c_{j0} \\ c_{j3} \end{pmatrix} = \begin{pmatrix} c_{j0} \\ c_{j3} \end{pmatrix}$	$\begin{pmatrix} \widetilde{\tau}_1\tau_0 \\ \widetilde{\tau}_1\tau_3 \end{pmatrix}, \begin{pmatrix} \widetilde{\tau}_2\tau_0 \\ \widetilde{\tau}_2\tau_3 \end{pmatrix}$	$-, +$	$-, -$	$SDW^{11}(g_{30} > 0)/$ $SDW^{22}(g_{30} < 0)$
$L_T \left(g_{00} + 2g_{11} - g_{33}\right) c_{j1} = c_{j1}$	$\widetilde{\tau}_1\tau_1,\, \widetilde{\tau}_2\tau_1$	$-, +$	$-, -$	SDW^{12}
$L_T \left(g_{00} - 2g_{11} - g_{33}\right) c_{j2} = c_{j2}$	$\widetilde{\tau}_1\tau_2,\, \widetilde{\tau}_2\tau_2$	$-, +$	$+, +$	CDW^{12}
$-2L_T \begin{pmatrix} g_{00}+2g_{11}+g_{33} & 2g_{30} \\ 2g_{30} & g_{00}-2g_{11}+g_{33} \end{pmatrix} \begin{pmatrix} \tilde{c}_0 \\ \tilde{c}_3 \end{pmatrix} = \begin{pmatrix} \tilde{c}_0 \\ \tilde{c}_3 \end{pmatrix}$	$\begin{pmatrix} \tau_0 \\ \tau_3 \end{pmatrix}$	$+$	$+$	s^{++}/s^{+-}
$2L_T \left(g_{33} - g_{00}\right) \tilde{c}_j = \tilde{c}_j$	$\tau_1,\, \tau_2$	$+, -$	$+, +$	s^{12}

superconductivity eventually wins. Since, at that point, g_{11} and g_{33} are still finite, the result also depends on the value of the non-flowing coupling constants. The associated instabilities, that compete with s^{+-} and s^{++} superconductivity, are shown in Fig. 5.5(b) and (c) of the main text.

D.2.2 Mean-field equations for significantly different Fermi velocities

Similarly, the phase competition can be studied for different Fermi velocities. Since the two Fermi surfaces can be relabeled, we can choose $v_1 > v_2$ without loss of generality. Again only the leading logarithm, in this case $L_T = \log(v_1\Lambda_\perp/T)$, is kept yielding the mean-field equations presented in Table D.5.

We see that, as a consequence of the asymmetry between the fermions from the inner and outer Fermi surfaces, e.g. the instability s^{11} dominates over s^{22} (and similarly for SDW^{jj}). Note that also taking into account the subleading logarithm $\log(v_2\Lambda_\perp/T)$, one would find a continuous transition as a function of v_2/v_1 between having anomalous expectation values of equal magnitude on the two Fermi surfaces and the situation where the anomalous expectation value is only finite on one Fermi surface. The associated scale of the crossover depends on the cutoff of the theory as both $\log(v_1\Lambda_\perp/T_c)$ and $\log(v_2\Lambda_\perp/T_c)$ appear in the mean-field equations. In Table D.5, this continuous crossover is not seen as we focus on the case of "significantly" different Fermi velocities in the sense that

$$\log(v_1\Lambda_\perp/T_c) \gg \log(v_2\Lambda_\perp/T_c) \tag{D.8}$$

such that it is sufficient to keep only the leading logarithm. Of course, for sufficiently large $v_1\Lambda_\perp/T_c$, Eq. (D.8) is already satisfied for v_2/v_1 slightly below one.

Table D.5: *Mean-field equations for different velocities ($v_1 > v_2$). The notation is similar to Table D.4 with $L_T := \log(v_1\Lambda_\perp/T)$.*

Mean-field equations ($j = 1, 2$)	Order parameter	C_2^z	Θ	Phase
$L_T\left(g_{00} + 2g_{30} + g_{33}\right) c_{j0} = c_{j0}, \quad c_{j0} = c_{j3}$	$\widetilde{\tau}_1(\tau_0 + \tau_1)$, $\widetilde{\tau}_2(\tau_0 + \tau_1)$	$-, +$	$-, -$	SDW^{11}
$\frac{v_1 L_T}{v_1+v_2}\left(g_{00} + 2g_{11} - g_{33}\right) c_{j1} = c_{j1}$	$\widetilde{\tau}_1\tau_1$, $\widetilde{\tau}_2\tau_1$	$-, +$	$-, -$	SDW^{12}
$\frac{v_1 L_T}{v_1+v_2}\left(g_{00} - 2g_{11} - g_{33}\right) c_{j2} = c_{j2}$	$\widetilde{\tau}_1\tau_2$, $\widetilde{\tau}_2\tau_2$	$-, +$	$+, +$	CDW^{12}
$-2L_T(g_{00} + 2g_{30} + g_{33})\tilde{c}_0 = \tilde{c}_0, \quad \tilde{c}_0 = \tilde{c}_3$	$\tau_0 + \tau_3$	$+$	$+$	s^{11}
$\frac{2v_1 L_T}{v_1+v_2}\left(g_{33} - g_{00}\right) \tilde{c}_j = \tilde{c}_j$	τ_1, τ_2	$+, -$	$+, +$	s^{12}

D.3 Textures of competing density wave instabilities

In this section, more details are given on how to obtain the density wave profiles presented in Fig. 5.6 of the main text. The charge, $j = 0$, and spin, $j = 1, 2, 3$, expectation values read

$$\mathcal{S}_j(\boldsymbol{x}, \tau) = \int_q \widetilde{\mathcal{S}}_j(q) e^{i(\boldsymbol{q}\cdot\boldsymbol{x} - \omega_n\tau)}, \qquad \widetilde{\mathcal{S}}_j(q) = \int_k \langle \bar{c}_k \sigma_j c_{k+q} \rangle \,, \tag{D.9a}$$

where τ denotes (imaginary) time, c are the four-component Grassmann analogues of the field operators $\hat{c}$ introduced in Eq. (5.1) and σ_j are Pauli matrices acting in spin space. Transforming to the eigenbasis of the high-temperature Hamiltonian yields

$$\hat{\mathcal{S}}_j(q) = \int_k \psi^\dagger_{\boldsymbol{k}\tau} \sigma_j \psi_{\boldsymbol{k}+\boldsymbol{q}\tau'} \langle \bar{f}_{k\tau} f_{k+q\tau'} \rangle \,. \tag{D.10}$$

We assume that the mass anisotropy is sufficiently large such that the contribution to $\mathcal{S}_j$ from the strongly curved segments of the Fermi surface is negligible. Recall from Fig. 5.1(b) and (c) that the orbital part of the wave functions is strongly polarized to either $3d_{xz}$ or $3d_{yz}$ in the remaining nearly straight segments of the Fermi surface. For this reason, the orbital momentum L_j cannot contribute to the magnetization of the sample as the matrix elements $\langle 3d_{xz}|L_j|3d_{xz}\rangle$ and $\langle 3d_{yz}|L_j|3d_{yz}\rangle$ vanish for all components $j = 1, 2, 3$ (see Eq. (D.4)).

Let us first discuss the SDW^{12} state, which is characterized by $\Delta^{\mathrm{DW}} = c\,\widetilde{\tau}_1\tau_1$ or $\Delta^{\mathrm{DW}} = c\,\widetilde{\tau}_2\tau_1$, $c \in \mathbb{R}$. As mentioned in the main text, we focus, for concreteness, on the latter choice as it does not break C_2^z rotation symmetry. However, using the procedure presented in this section, it is straightforward to derive the spatial texture when some of the point symmetries are broken spontaneously.

The contribution of the red parts in Fig. 5.1(a) is then readily found from Eq. (D.10),

$$\mathcal{S}_j(\boldsymbol{x}, \tau) = ic\, e^{i\boldsymbol{Q}_{12}^{(1)}\cdot\boldsymbol{x}} \left[\psi^\dagger_{-\boldsymbol{k}_1 1}\sigma_j\psi_{\boldsymbol{k}_2 2} + \psi^\dagger_{-\boldsymbol{k}_2 2}\sigma_j\psi_{\boldsymbol{k}_1 1}\right] + \text{c.c.} + \ldots, \tag{D.11}$$

where we have introduced the corresponding nesting vector $\boldsymbol{Q}_{12}^{(1)} = \boldsymbol{k}_1 + \boldsymbol{k}_2$ with $\boldsymbol{k}_s$ parameterizing the centers of the nested subspaces (see Fig. 5.1(a)). Using the phase conventions (5.8) and (5.9), one can

show that $\mathcal{S}_0 = 0$, as required since the order parameter of SDW^{12} is odd under time-reversal, and simplify Eq. (D.11) to

$$\boldsymbol{\mathcal{S}}(\boldsymbol{x},\tau) = 2ic\, e^{i\boldsymbol{Q}_{12}^{(1)}\cdot\boldsymbol{x}} \psi_{\boldsymbol{k}_1 1}^{\dagger} \left(-\sigma_2, \sigma_1, i\sigma_0\right)^T \psi_{\boldsymbol{k}_2 2} + \text{c.c.} + \dots \,. \tag{D.12}$$

From Fig. 5.1(b) and (c), it is easily seen that the wave functions are strongly spin-polarized such that $\sigma_2 \psi_{\boldsymbol{k}_1 1} \simeq -\psi_{\boldsymbol{k}_1 1}$ and $\sigma_2 \psi_{\boldsymbol{k}_2 2} \simeq \psi_{\boldsymbol{k}_2 2}$. Within this approximation and, again, using Eq. (5.9), we find

$$\boldsymbol{\mathcal{S}}(\boldsymbol{x},\tau) \propto \left(0, \sin\left(\boldsymbol{Q}_{12}^{(1)}\cdot\boldsymbol{x}\right), 0\right)^T + \dots \,. \tag{D.13}$$

Assuming that none of the additional point symmetries are broken spontaneously, we can directly infer the contributions of the other three nested subspaces (blue regions in Fig. 5.1(a)). Demanding that $\boldsymbol{\mathcal{S}}$ transform as a pseudovector under reflection at the xz-plane and under C_2^z rotation around the z-axis, one finds

$$\boldsymbol{\mathcal{S}}(\boldsymbol{x},\tau) \propto \begin{pmatrix} \sin\left(\boldsymbol{Q}_{12}^{(3)}\cdot\boldsymbol{x}\right) + \sin\left(\boldsymbol{Q}_{12}^{(4)}\cdot\boldsymbol{x}\right) \\ \sin\left(\boldsymbol{Q}_{12}^{(1)}\cdot\boldsymbol{x}\right) + \sin\left(\boldsymbol{Q}_{12}^{(2)}\cdot\boldsymbol{x}\right) \\ 0 \end{pmatrix}, \tag{D.14}$$

where the reflected and rotated nesting vectors

$$\boldsymbol{Q}_{12}^{(2)} = \left(Q_{12,x}^{(1)}, -Q_{12,y}^{(1)}\right)^T, \quad \boldsymbol{Q}_{12}^{(3)} = \left(Q_{12,y}^{(1)}, -Q_{12,x}^{(1)}\right)^T, \quad \boldsymbol{Q}_{12}^{(4)} = \left(-Q_{12,y}^{(1)}, -Q_{12,x}^{(1)}\right)^T \tag{D.15}$$

have been defined. Eq. (D.14) has been plotted in Fig. 5.6(b) for a specific choice of $\boldsymbol{Q}_{12}^{(1)}$.

In the same way, one obtains

$$\mathcal{S}_0(\boldsymbol{x},\tau) \propto \sum_{j=1}^{4} \cos\left(\boldsymbol{Q}_{12}^{(j)}\cdot\boldsymbol{x}\right) \tag{D.16}$$

for the CDW^{12} and $(s = 1, 2)$

$$\boldsymbol{\mathcal{S}}(\boldsymbol{x},\tau) \propto \begin{pmatrix} \sin\left(\boldsymbol{Q}_{ss}^{(1)}\cdot\boldsymbol{x}\right) - \sin\left(\boldsymbol{Q}_{ss}^{(2)}\cdot\boldsymbol{x}\right) \\ \sin\left(\boldsymbol{Q}_{ss}^{(4)}\cdot\boldsymbol{x}\right) - \sin\left(\boldsymbol{Q}_{ss}^{(3)}\cdot\boldsymbol{x}\right) \\ (-1)^{s+1} \sum\limits_{j=1,2} \left[\cos\left(\boldsymbol{Q}_{ss}^{(2j-1)}\cdot\boldsymbol{x}\right) - \cos\left(\boldsymbol{Q}_{ss}^{(2j)}\cdot\boldsymbol{x}\right)\right] \end{pmatrix} \tag{D.17}$$

in case of the SDW^{ss} phase, where $\boldsymbol{Q}_{ss}^{(1)} = 2\boldsymbol{k}_s$ and $\boldsymbol{Q}_{ss}^{(p)}$, $p = 2, 3, 4$, as defined similarly to Eq. (D.15).

D.4 Different Fermi velocities

Finally, we also discuss the phase competition for different Fermi velocities $v_1 \neq v_2$. In this case all four backscattering coupling constants flow according to the RG equations

$$\frac{\mathrm{d}g_{00}}{\mathrm{d}l} = -g_{11}^2 \frac{(v_1 - v_2)^2}{2v_2\,(v_1 + v_2)}, \tag{D.18a}$$

$$\frac{\mathrm{d}g_{30}}{\mathrm{d}l} = -g_{11}^2 \frac{v_1 - v_2}{2v_2}, \tag{D.18b}$$

$$\frac{\mathrm{d}g_{11}}{\mathrm{d}l} = -\frac{g_{11}}{2v_2\,(v_1+v_2)}\Big[g_{33}(v_1^2+v_2^2+6v_1v_2) + g_{00}(v_1-v_2)^2 - 2g_{30}\left(v_1^2-v_2^2\right)\Big], \tag{D.18c}$$

$$\frac{\mathrm{d}g_{33}}{\mathrm{d}l} = -g_{11}^2 \frac{v_1^2+v_2^2+6v_1v_2}{2v_2\,(v_1+v_2)}. \tag{D.18d}$$

As required by consistency, this reduces to Eq. (5.17) in the limit $v_1 \to v_2$. A projection of the flow described by Eq. (D.18) is shown in Fig. 5.7. Since g_{00}, g_{30} and g_{33} can only diverge if g_{11} diverges as well, which readily follows from Eq. (D.18), all coupling constants stay finite in region (I).

The leading and subleading instabilities in regions (II) and (III) are obtained similarly to our discussion in Sec. D.2.1 of the $v_1 = v_2$ case: We now analyze the flow of the mean-field equations of Sec. D.2.2, as summarized in Table D.5, under the RG determined by Eq. (D.18).

It turns out that superconductivity will still be the leading instability unless the flow is not cut off before the backscattering coupling constants diverge. The difference, compared to the situation with identical velocities, is that the anomalous expectation value of the resulting superconductor (s^{11}) is given by ($v_1 > v_2$ has been assumed without loss of generality)

$$\overline{\Delta}^{\mathrm{SC}}_{(-,s)(+,s')} \propto \delta_{s,1}\delta_{s',1}, \tag{D.19}$$

both for the conventional and for the unconventional pairing scenario. However, the resulting mean-field theories at the associated strong-coupling fixed points are not identical since the couplings are different.

We will next show that the superconductors even differ in their topology. Performing a mean-field decoupling of the interaction (5.10) using Eq. (D.19) one finds $\gamma_0 = g_{00} + 2g_{11} + g_{33} + 2g_{30}$ and $\gamma_3 = g_{00} - 2g_{11} + g_{33} + 2g_{30}$ using the parameterization $\widetilde{m} = 4(\gamma_0\tau_0 + \gamma_3\tau_3)\Delta_0^*$ in Eq. (5.21). The condition $|\gamma_0| < |\gamma_3|$ for having a topologically nontrivial superconductor then becomes

$$|g_{00} + 2g_{11} + g_{33} + 2g_{30}| < |g_{00} - 2g_{11} + g_{33} + 2g_{30}|. \tag{D.20}$$

From the flow equations (D.18) it follows that g_{00}, g_{33} and g_{30} can only diverge to $-\infty$, whereas $g_{11} \to \infty$ in case of unconventional pairing (regime (II) in Fig. 5.7) and $g_{11} \to -\infty$ for the conventional superconductor (regime (III)). Hence, we can directly see from Eq. (D.20), that, exactly as for $v_1 = v_2$, the conventional superconductor (with $\widetilde{m}_{11}\widetilde{m}_{22} > 0$, i.e., s^{++}-like mean-field Hamiltonian) is trivial and the unconventionally paired state ($\widetilde{m}_{11}\widetilde{m}_{22} < 0$ and, hence, of s^{+-} type) is topological.

The phase diagrams of subleading instabilities analogous to Fig. 5.5 are straightforwardly derived. Most interestingly, the unconventional superconductor competes (among others) with the FFLO-like s^{12} superconductor (see Table D.5). However, the latter can only be stabilized for $g_{00}g_{33} < 0$ which is far away from the expected properties (5.20) of the coupling constants.

Appendix E

E General properties of leading superconducting instabilities

In this appendix, we present supplementary material to Chap. 6. We will first derive various exact relations of different many-body correlation functions following from symmetries. In Appendix E.2, it will then be shown that, exactly as in mean-field theory, the leading superconductivity instability is determined by the largest eigenvalue of the kernel tv of the Eliashberg equation. We finally proof that positivity of the anomalous self-energy $\widetilde{\Phi}$ implies the absence of point-symmetry breaking (Appendix E.3) and that Chern numbers of Rashba partners have opposite sign (Appendix E.4). Exactly as in case of Chap. 6 of the main text, also the analysis presented in this appendix has been published in Ref. [367].

E.1 Exact relations following from the spectral representation

In this section of the appendix, properties of the bosonic propagator, the Nambu Green's function, and the fermion-boson vertex function, which are consequences of certain unitary or antiunitary symmetries, are derived. These relations are most easily seen from the spectral representation (also known as Lehmann representation) [94] of the corresponding n-point functions.

E.1.1 Identities for the order-parameter susceptibility

We begin with the bosonic propagator

$$\chi_{jj'}(i\Omega_n, \boldsymbol{q}) := \frac{1}{2}\int_0^\beta \mathrm{d}\tau e^{i\Omega_n\tau}\,\langle T_\tau \hat{\phi}_{\boldsymbol{q}j'}(\tau)\hat{\phi}_{-\boldsymbol{q}j}(0)\rangle \tag{E.1}$$

as the discussion is most transparent in this case. In Eq. (E.1), T_τ denotes the time-ordering operator. The spectral representation reads

$$\chi_{jj'}(i\Omega_n, \boldsymbol{q}) = \frac{1}{2}\sum_{n_1,n_2}\frac{\langle n_1|\hat{\phi}_{\boldsymbol{q}j'}|n_2\rangle\,\langle n_2|\hat{\phi}_{-\boldsymbol{q}j}|n_1\rangle}{i\Omega_n - (E_{n_2}-E_{n_1})} I^+_{n_1n_2}, \tag{E.2}$$

where $\{|n\rangle\}$ is a basis of exact eigenstates of the full many-body Hamiltonian with respective energies E_n and

$$I^\zeta_{n_1n_2} := \frac{1}{Z}\left(e^{-\beta E_{n_2}} - \zeta\, e^{-\beta E_{n_1}}\right) \tag{E.3}$$

has been introduced with Z denoting the partition function. Upon relabeling $n_1 \leftrightarrow n_2$ in Eq. (E.2), one readily finds that $\chi_{jj'}(q) = \chi_{j'j}(-q)$ which is already the first property in Eq. (6.50).

Using Hermiticity, $\hat{\phi}^\dagger_{\boldsymbol{q}j} = \hat{\phi}_{-\boldsymbol{q}j}$, we can rewrite the spectral representation (E.2) as

$$\chi_{jj'}(i\Omega_n, \boldsymbol{q}) = \frac{1}{2}\sum_{n_1,n_2} \frac{\langle n_1|\hat{\phi}_{\boldsymbol{q}j'}|n_2\rangle \left(\langle n_1|\hat{\phi}_{\boldsymbol{q}j}|n_2\rangle\right)^*}{i\Omega_n - (E_{n_2} - E_{n_1})} I^+_{n_1 n_2}, \tag{E.4}$$

from which $\chi_{jj'}(i\Omega_n, \boldsymbol{q}) = \chi^*_{j'j}(-i\Omega_n, \boldsymbol{q})$, i.e., the second property (6.50b), can be read off.

To derive the constraint following from TRS, we rearrange the summation in Eq. (E.4) by replacing $|n_{1,2}\rangle \to \hat{\Theta}\,|n_{1,2}\rangle$. Noting that $|n\rangle$ and $\hat{\Theta}\,|n\rangle$ have the same energy together with

$$\langle \hat{\Theta} n_1|\hat{\phi}_{\boldsymbol{q}j}|\hat{\Theta} n_2\rangle = \langle n_1|\hat{\Theta}^\dagger \hat{\phi}_{\boldsymbol{q}j}\hat{\Theta}|n_2\rangle^* = t\,\langle n_1|\hat{\phi}_{-\boldsymbol{q}j}|n_2\rangle^*, \tag{E.5}$$

where we used Eq. (6.46) in the second equality, yields $\chi(i\Omega_n, \boldsymbol{q}) = \chi^T(i\Omega_n, -\boldsymbol{q})$. Applying Eq. (6.50a), we arrive at the relation (6.50c) stated in the main text.

Finally, the proof of Eq. (6.65) proceeds very similarly to the discussion of TRS above: We rearrange the sums in the spectral representation (E.4) such that $|n_{1,2}\rangle$ is replaced by $\hat{S}\,|n_{1,2}\rangle$, take advantage of the fact that the energies of $|n\rangle$ and $\hat{S}\,|n\rangle$ are identical and then write

$$\langle \hat{S} n_1|\hat{\phi}_{\boldsymbol{q}j}|\hat{S} n_2\rangle = \pm\,\langle n_1|\hat{\phi}_{-\boldsymbol{q}j}|n_2\rangle \tag{E.6}$$

where Eq. (6.64) has been applied. This directly leads to Eq. (6.65).

E.1.2 Identities for the Nambu Green's function

Let us begin with the derivation of the TRS constraint (6.35) of the Nambu Green's function. For this purpose, it is convenient to first work in the microscopic basis and define

$$\mathcal{G}^m_{\alpha\beta}(i\omega_n, \boldsymbol{k}) := -\int_0^\beta \mathrm{d}\tau e^{i\omega_n\tau} \begin{pmatrix} \langle T_\tau \hat{c}_{\boldsymbol{k}\alpha}(\tau)\hat{c}^\dagger_{\boldsymbol{k}\beta}(0)\rangle & \langle T_\tau \hat{c}_{\boldsymbol{k}\alpha}(\tau)\hat{c}_{-\boldsymbol{k}\beta}(0)\rangle \\ \langle T_\tau \hat{c}^\dagger_{-\boldsymbol{k}\alpha}(\tau)\hat{c}^\dagger_{\boldsymbol{k}\beta}(0)\rangle & \langle T_\tau \hat{c}^\dagger_{-\boldsymbol{k}\alpha}(\tau)\hat{c}_{-\boldsymbol{k}\beta}(0)\rangle \end{pmatrix}. \tag{E.7}$$

Consider, e.g., the upper left component with spectral representation

$$\left(\mathcal{G}^m_{\alpha\beta}(k)\right)_{11} = \sum_{n_1,n_2} \frac{\langle n_1|\hat{c}_{\boldsymbol{k}\alpha}|n_2\rangle\,\langle n_2|\hat{c}^\dagger_{\boldsymbol{k}\beta}|n_1\rangle}{i\omega_n - (E_{n_2} - E_{n_1})} I^-_{n_1 n_2}. \tag{E.8}$$

Exactly as in case of the bosons, we rewrite the summation and then use

$$\langle \hat{\Theta} n_1|\hat{c}_{\boldsymbol{k}\alpha}|\hat{\Theta} n_2\rangle = T_{\alpha\alpha'}\,\langle n_1|\hat{c}_{-\boldsymbol{k}\alpha'}|n_2\rangle^* \tag{E.9}$$

based on Eq. (4.7). This yields

$$T_{\alpha\alpha'}\left(\mathcal{G}^m_{\alpha'\beta'}(-k)\right)^*_{11} T^\dagger_{\beta'\beta} = \left(\mathcal{G}^m_{\alpha\beta}(k)\right)_{11}. \tag{E.10}$$

Collecting the resulting behavior of all four components, one finds

$$\mathcal{T}_{\alpha\alpha'}\left(\mathcal{G}^m_{\alpha'\beta'}(-k)\right)^* \mathcal{T}^\dagger_{\beta'\beta} = \mathcal{G}^m_{\alpha\beta}(k), \quad \mathcal{T}_{\alpha\beta} = \begin{pmatrix} T_{\alpha\beta} & \\ & T^*_{\alpha\beta} \end{pmatrix} \tag{E.11}$$

in accordance with the relations derived in Ref. [310]. Note that Eq. (E.11) holds both for $T^T = -T$ (spin-1/2 electrons) and $T^T = T$ (spinless electrons).

To arrive at the constraint (6.35), we have to transform Eq. (E.11) into the eigenbasis of the normal state Hamiltonian. Using Eq. (6.8) in, e.g., the upper left component of the Nambu Green's function yields

$$\left(\mathcal{G}^m_{\alpha\beta}(k)\right)_{11} = \left(\psi_{\boldsymbol{k}s}\right)_\alpha \left(\mathcal{G}_{ss'}(k)\right)_{11} \left(\psi^*_{\boldsymbol{k}s'}\right)_\beta \tag{E.12}$$

with $\mathcal{G}_{ss'}$ as defined in Eq. (6.20). Inserting this into Eq. (E.11), using the property (6.13) of the wavefunctions and proceeding analogously for all four components, one finds that Eq. (E.11) is, within the weak-pairing approximation (6.21), equivalent to

$$e^{-i\varphi^s_{\boldsymbol{k}}\tau_3}\tau_3\mathcal{G}^*_{s_\mathrm{K}}(-k)\tau_3 e^{i\varphi^s_{\boldsymbol{k}}\tau_3} = \mathcal{G}_s(k) \tag{E.13}$$

as stated in the main text.

The derivation of the charge-conjugation symmetry (6.34) of the Green's function proceeds in two steps: Firstly, one can directly read off from the path integral definition (6.20) that

$$\tau_1\mathcal{G}_{ss'}(k)\tau_1 = -\left(\mathcal{G}_{s'_\mathrm{K}s_\mathrm{K}}\right)^T(-k), \tag{E.14}$$

where T (transposition) only refers to particle-hole space. Secondly, applying the well-known relation (see, e.g., Ref. [310])

$$\mathcal{G}(i\omega_n, \boldsymbol{k}) = \mathcal{G}^\dagger(-i\omega_n, \boldsymbol{k}), \tag{E.15}$$

which can also be shown from the spectral representation (using Hermiticity, $\langle n|\hat{f}|n'\rangle^* = \langle n'|\hat{f}^\dagger|n\rangle$), we find

$$\tau_1\mathcal{G}_{ss'}(i\omega_n, \boldsymbol{k})\tau_1 = -\mathcal{G}^*_{s_\mathrm{K}s'_\mathrm{K}}(i\omega_n, -\boldsymbol{k}). \tag{E.16}$$

In the weak-pairing approximation, this reduces to Eq. (6.34).

E.1.3 Identities for the fermion-boson vertex

Let us now discuss exact relations of the renormalized fermion-boson vertex $\Gamma^{(j)}$ in Eq. (6.72). To this end, we start by analyzing the associated three-point function

$$C^{(j)}_{\alpha\beta}(k;k') = \int_0^\beta \mathrm{d}\tau \int_0^\beta \mathrm{d}\tau' e^{i(\omega_{n'}\tau' - \omega_n\tau)} \left\langle T_\tau \hat{c}^\dagger_{\boldsymbol{k}\alpha}(\tau)\hat{c}_{\boldsymbol{k}'\beta}(\tau')\hat{\phi}_{\boldsymbol{k}-\boldsymbol{k}'j}(0)\right\rangle. \tag{E.17}$$

Performing the standard steps to derive spectral representations [94], it is straightforwardly shown that

$$\begin{aligned} C^{(j)}_{\alpha\beta}(k;k') = \sum_{n_1,n_2,n_3} \Big(& \langle n_1|\hat{c}^\dagger_{\boldsymbol{k}\alpha}|n_2\rangle \langle n_2|\hat{c}_{\boldsymbol{k}'\beta}|n_3\rangle \langle n_3|\hat{\phi}_{\boldsymbol{k}-\boldsymbol{k}'j}|n_1\rangle \; I_{n_1n_2n_3}(\omega_n, \omega_{n'}) \\ & - \langle n_1|\hat{c}_{\boldsymbol{k}'\beta}|n_2\rangle \langle n_2|\hat{c}^\dagger_{\boldsymbol{k}\alpha}|n_3\rangle \langle n_3|\hat{\phi}_{\boldsymbol{k}-\boldsymbol{k}'j}|n_1\rangle \; I_{n_1n_2n_3}(-\omega_{n'}, -\omega_n)\Big), \end{aligned} \tag{E.18}$$

where we have introduced

$$I_{n_1n_2n_3}(\omega,\omega') = \frac{1}{Z}\frac{e^{-\beta E_{n_3}}(\Delta_{21}+i\omega)+e^{-\beta E_{n_2}}(\Delta_{31}+i(\omega-\omega'))+e^{-\beta E_{n_1}}(\Delta_{32}-i\omega')}{(\Delta_{21}+i\omega)(\Delta_{31}+i(\omega-\omega'))(\Delta_{32}-i\omega')} \tag{E.19}$$

using the shortcut notation $\Delta_{ij} := E_{n_i} - E_{n_j}$.

Hermiticity. Complex conjugation of Eq. (E.18), relabeling $n_1 \leftrightarrow n_3$ and using that

$$I^*_{n_1n_2n_3}(\omega,\omega') = I_{n_1n_2n_3}(-\omega,-\omega'), \tag{E.20}$$
$$I_{n_3n_2n_1}(\omega,\omega') = I_{n_1n_2n_3}(\omega',\omega), \tag{E.21}$$

one finds

$$C^{(j)}_{\alpha\beta}(i\omega_n,\boldsymbol{k};i\omega_{n'},\boldsymbol{k}') = \left[C^{(j)}_{\beta\alpha}(-i\omega_{n'},\boldsymbol{k}';-i\omega_n,\boldsymbol{k})\right]^*. \tag{E.22}$$

The vertex function $\Gamma^{(j)}$ is related to $C^{(j)}$ according to

$$C^{(j)}_{\beta\alpha}(k_2;k_1) = \left(\mathcal{G}^m_{\alpha\alpha'}(k_1)\right)_{11}\Gamma^{(j')}_{\alpha'\beta'}(k_1;k_2)\left(\mathcal{G}^m_{\beta'\beta}(k_2)\right)_{11}\chi^{j'j}(k_1-k_2). \tag{E.23}$$

Inserting this in Eq. (E.22) and using $\chi^*(i\Omega,\boldsymbol{q}) = \chi(i\Omega,-\boldsymbol{q})$ (see Eq. (6.50)) as well as $\left(\mathcal{G}^m_{\alpha\beta}(i\omega_n,\boldsymbol{k})\right)^*_{11} = \left(\mathcal{G}^m_{\beta\alpha}(-i\omega_n,\boldsymbol{k})\right)_{11}$, which is readily shown from Eq. (E.8) (and constitutes a special case of Eq. (E.15)), we arrive at the property (6.74) stated in the main text.

TRS. Using the same steps as in Appendix E.1.1 and E.1.2, one can analyze the consequences of TRS in the spectral representation (E.18) yielding

$$C^{(j)}_{\alpha\beta}(k;k') = t\,T^\dagger_{\alpha\alpha'}\left[C^{(j)}_{\alpha'\beta'}(-k;-k')\right]^* T_{\beta'\beta}. \tag{E.24}$$

Taking into account the properties of the fermionic and bosonic propagator in Eqs. (E.10) and (6.50), one finds the required identity (6.73).

Symmetry between Rashba partners. Finally, we show that the asymptotic symmetry introduced in Chap. 6.2.3 leads to the constraint (6.75) for the vertex function. For this purpose, it is most convenient to work directly in the eigenbasis of the noninteracting fermionic Hamiltonian. Denoting the fermionic creation and annihilation operators in this basis by $\hat{f}^\dagger_{\Omega s}$ and $\hat{f}_{\Omega s}$ (cf. Eq. (4.23)), we introduce the antiunitary Fock operator $\hat{R}$ via

$$\hat{R}\hat{f}_{\Omega s}\hat{R}^\dagger = e^{i\gamma^s_\Omega}\hat{f}_{\Omega s_{\mathrm{R}}}, \quad \hat{R}\hat{\phi}_{\boldsymbol{q}j}\hat{R}^\dagger = r\,t\,\hat{\phi}_{\boldsymbol{q}j}. \tag{E.25}$$

In the asymptotic limit discussed in detail in Chap. 6.2.3, the entire Hamiltonian commutes with $\hat{R}$: The quadratic fermionic Hamiltonian is invariant since the Fermi velocities of Rashba partners are asymptotically identical. The bare fermion-boson interaction (6.70) commutes with $\hat{R}$ as long as Eq. (6.60) with $\boldsymbol{\Lambda}_{ss'}(\boldsymbol{k},\boldsymbol{k}') = \psi^\dagger_{\boldsymbol{k}s}\boldsymbol{M}(\boldsymbol{k},\boldsymbol{k}')\psi_{\boldsymbol{k}'s'}$ as well as $t \to rt$ holds (which is guaranteed by assuming Eq. (6.71)) and the bosons vary slowly on the scale $|\boldsymbol{g}|/v_F$. Any bosonic Hamiltonian quadratic in $\hat{\phi}$ must be invariant if, as required already before, the symmetry defined by Eqs. (6.63) and (6.64) holds. This readily follows from the fact that $\hat{C}\hat{\phi}_{\boldsymbol{q}j}\hat{C}^\dagger = \pm r\,\hat{\phi}_{\boldsymbol{q}j}$ for the combined linear operator $\hat{C} = \hat{R}\hat{S}\hat{\Theta}$.

Consequently, $\hat{C}$ is a symmetry of any bosonic Hamiltonian that is even in $\hat{\phi}$. If $\hat{C}$, $\hat{\Theta}$ and $\hat{S}$ are symmetries of the bosonic Hamiltonian, the same will hold for $\hat{R}$.

The analysis of the consequences of the invariance under $\hat{R}$ is completely analogous to $\hat{\Theta}$ as both are antiunitary symmetries of the many-body Hamiltonian: Using the spectral representation of the normal component of the weak-pairing Green's function $\mathcal{G}_s$,

$$\big(\mathcal{G}_s(i\omega_n,\Omega)\big)_{11} = \sum_{n_1,n_2} \frac{\langle n_1|\hat{f}_{\Omega s}|n_2\rangle\,\langle n_2|\hat{f}^\dagger_{\Omega s}|n_1\rangle}{i\omega_n - (E_{n_2}-E_{n_1})} I^-_{n_1 n_2}, \tag{E.26}$$

we find

$$\big(\mathcal{G}_s(i\omega_n,\Omega)\big)_{11} = \Big(\mathcal{G}_{s_{\mathrm{R}}}(-i\omega_n,\Omega)\Big)^*_{11}. \tag{E.27}$$

In the same way, the spectral representation of the three-point function $\widetilde{C}^{(j)}_{ss'}(k,k')$ in the eigenbasis of the normal state Hamiltonian can be used to proof the consequence

$$\widetilde{C}^{(j)}_{ss'}(i\omega_n,\Omega;i\omega_{n'},\Omega') = r\,t\,e^{i(\gamma^s_\Omega-\gamma^{s'}_{\Omega'})}\left[\widetilde{C}^{(j)}_{s_{\mathrm{R}}s'_{\mathrm{R}}}(-i\omega_n,\Omega;-i\omega_{n'},\Omega')\right]^* \tag{E.28}$$

of the symmetry under $\hat{R}$. The combination of Eqs. (E.27) and (E.28) then leads to the symmetry constraint (6.75) of the main text.

By rearranging the sums in the spectral representations such that $|n_j\rangle$ is effectively replaced by $\hat{\mathcal{S}}\,|n_j\rangle$, one can proof Eq. (6.76) straightforwardly.

E.2 The leading superconducting instability

In this section, we show that the leading superconducting instability, i.e., the first nontrivial solution $\delta \neq 0$ of the Eliashberg equations when the temperature is decreased, is, in case of phonons and TRE particle-hole fluctuations, determined by the largest eigenvalue (the so-called Perron root [374]) of the positive matrix v defined in Eq. (6.30) and for TRO fluctuations by its eigenspace with smallest eigenvalue. As a first step, let us formally diagonalize v,

$$\sum_{n'}\sum_{s'}\int_{s'} \mathrm{d}\Omega' v_{s,s'}(i\omega_n,\Omega;i\omega_{n'},\Omega')a^j_{s'}(i\omega_{n'},\Omega') = \lambda^j(\beta)a^j_s(i\omega_n,\Omega). \tag{E.29}$$

Due to v being symmetric and real, this is always possible, all eigenvalues $\lambda^j(\beta) \in \mathbb{R}$ and the eigenvectors $\{a^j\}_j$ form an orthonormal basis such that Eq. (6.27b) assumes the simple form $\lambda^j(\beta) = 1$. The set of degenerate eigenvalues that, upon lowering the temperature, first become 1 determines the critical temperature and the order parameter δ must then be a superposition of the associated eigenvectors. So far, this is completely analogous to mean-field theory. However, due to the more indirect way the temperature enters in the Eliashberg equations, it is not clear whether the largest eigenvalue first becomes 1. E.g., a finite subset of the eigenvalues could be larger than 1 for all temperatures. In other words, we still have to show that all eigenvalues are smaller than 1 in the limit of high temperatures $\beta \to 0$.

E.2.1 Electron-phonon coupling

Let us first focus on the effective electron-electron interaction resulting from electron-phonon coupling. In the high temperature limit, the interaction matrix elements (6.17) assume the form

$$\mathcal{V}_{ss'}(k;k') \overset{\beta\to 0}{\longrightarrow} -\delta_{n,n'} \sum_l \frac{1}{\omega_{\boldsymbol{k}-\boldsymbol{k}'l}} \left| \mathcal{G}^{(l)}_{ss'}(\boldsymbol{k},\boldsymbol{k}') \right|^2 . \tag{E.30}$$

Using this in Eq. (6.27a), the quasiparticle residue becomes

$$Z_s(i\omega_n,\Omega) \overset{\beta\to 0}{\longrightarrow} 1 + \frac{2}{|2n+1|} \sum_{s'} \int_{s'} \mathrm{d}\Omega' \rho_{s'}(\Omega') f_{s,\Omega;s',\Omega'}, \tag{E.31}$$

where, for notational convenience, we have introduced

$$f_{s,\Omega;s',\Omega'} = \sum_l \frac{1}{\omega_{\boldsymbol{k}-\boldsymbol{k}'l}} \left| \mathcal{G}^{(l)}_{ss'}(\boldsymbol{k},\boldsymbol{k}') \right|^2 . \tag{E.32}$$

Here, $\boldsymbol{k}$ and $\boldsymbol{k}'$ denote the momenta associated with (s,Ω) and (s',Ω'), respectively. The interaction kernel then behaves asymptotically according to

$$v_{s,s'}(i\omega_n,\Omega;i\omega_{n'},\Omega') \overset{\beta\to 0}{\longrightarrow} 2\delta_{n,n'} \theta_{s,n,\Omega}\, f_{s,\Omega;s',\Omega'}\, \theta_{s',n',\Omega'} \tag{E.33}$$

with

$$\theta_{s,n,\Omega} = \frac{\sqrt{\rho_s(\Omega)}}{\sqrt{|2n+1| + 2\sum_{\tilde{s}} \int_{\tilde{s}} \mathrm{d}\tilde{\Omega}\, \rho_{\tilde{s}}(\tilde{\Omega}) f_{s,\Omega;\tilde{s},\tilde{\Omega}}}}. \tag{E.34}$$

We thus see that, in the high-temperature limit, the eigenvalue problem (E.29) splits into the different sectors characterized by a given Matsubara frequency. Since the right-hand side of Eq. (E.33) decays monotonically as a function of $|2n+1|$, we know from the Perron-Frobenius theorem [372–374] that the Perron root of $\lim_{\beta\to 0} v$ equals the Perron root of

$$m_{s,\Omega;s',\Omega'} = \lim_{\beta\to 0} v_{s,s'}(i\omega_0,\Omega;i\omega_0,\Omega'), \tag{E.35}$$

which is a matrix only with respect to s and Ω.

We will show in the following that $m_{s,\Omega;s',\Omega'}$, as any matrix of the more general form

$$M_{\mu\mu'} = \frac{\sqrt{\rho_\mu} f_{\mu\mu'} \sqrt{\rho_{\mu'}}}{\left(c + \sum_{\tilde{\mu}} f_{\mu\tilde{\mu}} \rho_{\tilde{\mu}}\right)^{1/2} \left(c + \sum_{\tilde{\mu}} f_{\mu'\tilde{\mu}} \rho_{\tilde{\mu}}\right)^{1/2}} \tag{E.36}$$

with $\rho_\mu, f_{\mu\mu'}, c \in \mathbb{R}^+$, has a Perron root r_M smaller than 1 (f does not have to symmetric for this to be true). For this purpose, let us rewrite $M = D_1 D_2 f D_2 D_1$ where the diagonal matrices are defined according to

$$\left(D_1\right)_{\mu\mu'} := \delta_{\mu,\mu'} \frac{1}{\left(c + \sum_{\tilde{\mu}} f_{\mu\tilde{\mu}} \rho_{\tilde{\mu}}\right)^{1/2}}, \tag{E.37}$$

$$\left(D_2\right)_{\mu\mu'} := \delta_{\mu,\mu'} \sqrt{\rho_\mu}. \tag{E.38}$$

Being similar, the two matrices $\widetilde{M} = D_1^2 f D_2^2$ and M have the same spectrum and, in particular, the same Perron root. We thus know that [374]

$$r_M \leq \max_{\mu} \sum_{\mu'} \left| \widetilde{M}_{\mu\mu'} \right| = \max_{\mu} \frac{\sum_{\mu'} f_{\mu\mu'} \rho_{\mu'}}{c + \sum_{\tilde{\mu}} f_{\mu\tilde{\mu}} \rho_{\tilde{\mu}}} < 1. \tag{E.39}$$

Consequently, the eigenvalues of m and, hence, of $\lim_{\beta\to 0} v$ are all smaller than 1. Since all $\lambda^j(\beta)$ are continuous functions of β, the eigenvalue that first becomes 1 must necessarily be the largest eigenvalue of v.

E.2.2 Unconventional mechanism

The main question in case of unconventional pairing concerns the high-temperature limit of the interaction matrix element $\mathcal{V}$ given by Eq. (6.55). To analyze this limit, we first note that $\chi(i\Omega_n, \boldsymbol{q}) \to 0$ for $\Omega_n \to \infty$ is very reasonable to assume since the same must hold on the real axis in the limit of large energies. As before, the interaction becomes diagonal in Matsubara indices and the analysis is the same as in Sec. E.2.1 above. The sole difference is that v is replaced by tv in the gap equation (6.27b) such that the order parameter δ of the leading instability belongs to the eigenspace of the positive matrix v with largest or smallest eigenvalue depending on whether the driving fluctuations are TRE or TRO.

E.3 Absence of point-symmetry breaking

Here, we show that the absence of sign changes of the order parameter, $\widetilde{\Phi}_s(i\omega_n, \boldsymbol{k}) > 0$, implies that the condensate does not break any point symmetry of the normal state.

As we have discussed in Chap. 1.1, the order parameter of a second order phase transition must transform under one of the irreducible representations of the point group of the high-temperature phase. Denoting this irreducible representation and its dimension by n_0 and d_{n_0}, respectively, it holds for the order parameter in the weak-pairing description

$$\widetilde{\Phi}_s(i\omega_n, \boldsymbol{k}) = \sum_{\mu=1}^{d_{n_0}} \eta_\mu \varphi^{\mu n_0}_{\boldsymbol{k}s}(i\omega_n), \tag{E.40}$$

where $\varphi^{\mu n_0}$ denote scalar basis functions transforming under n_0 with respect to $\boldsymbol{k}$ and s (exactly as in Eq. (4.37) except for the additional ω_n dependence). Note that Eq. (E.40) is the generalization of Eq. (4.38) beyond mean-field.

The grand orthogonality theorem (1.10) of group theory implies that two sets of basis functions, $\{|\varphi^{\mu n}\rangle\}$ and $\{|\widetilde{\varphi}^{\mu n}\rangle\}$, satisfy $\langle \widetilde{\varphi}^{\mu' n'} | \varphi^{\mu n} \rangle \propto \delta_{n,n'} \delta_{\mu,\mu'}$. Let us take $\widetilde{\varphi}_{\boldsymbol{k}s}(i\omega_n) = 1$, which transforms under the trivial representation, and assume that n_0 is a nontrivial representation. It then follows

$$\sum_{s,\boldsymbol{k}} \widetilde{\Phi}_s(i\omega_n, \boldsymbol{k}) = \sum_{\mu=1}^{d_{n_0}} \eta_\mu \, \langle \widetilde{\varphi}(i\omega_n) | \varphi^{\mu n_0}(i\omega_n) \rangle = 0 \tag{E.41}$$

conflicting with $\widetilde{\Phi}_s(i\omega_n, \boldsymbol{k}) > 0$. The superconductor must thus transform under the trivial representation of the point group of the normal state and, hence, cannot break any point symmetry.

E.4 Relation between Chern numbers of Rashba partners

Finally, we proof that the symmetry (6.59) forces the Fermi surface Chern numbers defined by [280]

$$C_{1s} := \frac{i}{2\pi}\int_s \mathrm{d}\omega^{jj'}\left(\partial_{k_{j'}}\psi^\dagger_{\boldsymbol{k}s}\partial_{k_j}\psi_{\boldsymbol{k}s} - (j \leftrightarrow j')\right) \tag{E.42}$$

to satisfy $C_{1s} = -C_{1s_\mathrm{R}}$. In Eq. (E.42), $\mathrm{d}\omega^{jj'}$ are the surface element two forms of the Fermi surface s.

Using the notation $\psi_{\boldsymbol{k}s} \simeq \psi_{\Omega s}$, we rewrite the integrand according to

$$\begin{aligned}
&\left(\partial_{k_{j'}}\psi^\dagger_{\Omega s}\right)\partial_{k_j}\psi_{\Omega s} - (j \leftrightarrow j') \\
&= \left(\partial_{k_{j'}} e^{-i\gamma^s_\Omega}\psi^T_{\Omega s_\mathrm{R}} T^\dagger\right)\left(\partial_{k_j} e^{i\gamma^s_\Omega} T\psi^*_{\Omega s_\mathrm{R}}\right) - (j \leftrightarrow j') \\
&= -\left[\left(\partial_{k_{j'}}\psi^\dagger_{\Omega s_\mathrm{R}}\right)\partial_{k_j}\psi_{\Omega s_\mathrm{R}} - (j \leftrightarrow j')\right].
\end{aligned} \tag{E.43}$$

Here we have applied the symmetry (6.59) in the second line and used $(\partial_{k_j}\psi^\dagger)\psi = -\psi^\dagger\partial_{k_j}\psi$ in the last line to show that all contributions involving derivatives of the phases γ^s_Ω vanish due to the anti-symmetrization in j and j'. Inserting this back into the integral of Eq. (E.42), we readily obtain the required property.

Appendix F

Weak disorder

The aim of this appendix is to provide supplementary information for Chap. 7.

F.1 Proof of stability of superconducting gap

Here we will show that Eq. (7.5) is a sufficient condition for the superconducting gap to be stable against the disorder configuration described by $\check{h}_W^{\mathrm{BdG}}$. The analogous discussion for the stability of a density wave gap has been published in Ref. [239].

As a first step, consider two Hermitian matrices A and B with real eigenvalues denoted by $\{\lambda_A^{(i)}\}$ and $\{\lambda_B^{(i)}\}$. If A and B anticommute, it will hold

$$(A+B)^2 = A^2 + B^2 + \{A,B\} = A^2 + B^2. \tag{F.1}$$

Furthermore, it implies that A^2 and B^2 commute and can, hence, be diagonalized simultaneously. Denoting the eigenvalues of $A+B$ by $\{\lambda_{A+B}^{(i)}\}$, we have

$$\left(\lambda_{A+B}^{(i)}\right)^2 = \left(\lambda_A^{(i)}\right)^2 + \left(\lambda_B^{(i)}\right)^2 \quad \Rightarrow \quad \left|\lambda_{A+B}^{(i)}\right| \geq \left|\lambda_A^{(i)}\right|, \left|\lambda_B^{(i)}\right| \tag{F.2}$$

upon properly choosing the labeling of the eigenvalues.

Choosing $A = \check{h}_n^{\mathrm{BdG}} + \check{h}_W^{\mathrm{BdG}}$ and $B = \check{h}_\Delta^{\mathrm{BdG}}$, Eqs. (7.5) and (F.2) imply that the modulus of the eigenvalues of $\check{h}^{\mathrm{BdG}} = A + B$ is bounded from below by the modulus of the eigenvalues of $B = \check{h}_\Delta^{\mathrm{BdG}}$. This shows that the gap is not reduced due to the presence of disorder (assuming, as usual, that the superconducting order parameter does not depend on the coordinate perpendicular to the Fermi surface within the low-energy theory).

F.2 Diagrammatic proof of the generalized Anderson theorem

In this appendix, additional information is presented on the diagrammatic proof of the Anderson theorem for superconductors with singly degenerate Fermi surfaces in the normal state. As Ω and s always occur simultaneously, we introduce the composite index $\tau \equiv (\Omega, s)$ and use a discretized description of the angular coordinate Ω. This allows us to write all expressions conveniently in matrix form. Note that no summation convention is implied throughout this section.

Firstly, we will derive Eq. (7.23). Using Eq. (7.20) in the Ginzburg-Landau expansion (7.17), we have

$$\langle \mathcal{F} \rangle_{\text{dis}} \sim \sum_{\tau,\tau'} \widetilde{\Delta}^*_\tau \left[-T \sum_{\omega_n} \left(\mathcal{C}(\omega_n) - t_d \, \mathcal{S}^S \right)^{-1} - \mathcal{V}^{-1} \right]_{\tau\tau'} \widetilde{\Delta}_{\tau'}. \tag{F.3}$$

The first term is straightforwardly rewritten using

$$\sum_{\tau,\tau'} \widetilde{\Delta}^*_\tau \left[\mathcal{C} - t_d \, \mathcal{S}^S \right]^{-1}_{\tau\tau'} \widetilde{\Delta}_{\tau'} = \sum_{\tau,\tau'} \widetilde{\Delta}^*_\tau \left[\sum_{n=0}^{\infty} \left(t_d \, \mathcal{C}^{-1} \mathcal{S}^S \right)^n \mathcal{C}^{-1} \right]_{\tau\tau'} \widetilde{\Delta}_{\tau'} \tag{F.4}$$

$$= \sum_{\tau,\tau'} \left[\sum_{n=0}^{\infty} \left(\mathcal{C}^{-1} \mathcal{S}^S \right)^n \mathcal{C}^{-1} \right]_{\tau\tau'} \left| \widetilde{\Delta}_{\tau'} \right|^2, \tag{F.5}$$

where, in the second line, $\widetilde{\Delta}^*_\tau (\mathcal{C}^{-1})_{\tau\tau'} = (\mathcal{C}^{-1})_{\tau\tau'} \widetilde{\Delta}^*_{\tau'}$ and $\widetilde{\Delta}^*_\tau \mathcal{S}^S_{\tau\tau'} = t_d \, \mathcal{S}^S_{\tau\tau'} \widetilde{\Delta}^*_{\tau'}$, following from $\mathcal{C}$ being diagonal and Eq. (7.22), have been applied iteratively. Summing the series leads directly to Eq. (7.23) stated in the main text.

Secondly, we will show how the self-energy and vertex corrections cancel each other in Eq. (7.23b). For this purpose, we split the clean and purely disorder-induced contributions to d by writing $\mathcal{C}(\omega_n) - \mathcal{S}^S = \frac{|\omega_n|}{\pi} \underline{\rho}^{-1} - \mathcal{M}$ where

$$\underline{\rho}_{\tau\tau'} = \delta_{\tau,\tau'} \rho_\tau, \qquad \mathcal{M}_{\tau\tau'} = \mathcal{S}^S_{\tau\tau'} - \delta_{\tau,\tau'} \frac{1}{\rho_\tau} \sum_{\tilde{\tau}} \mathcal{S}^S_{\tau\tilde{\tau}} \rho_{\tilde{\tau}}. \tag{F.6}$$

Note that the first and the second term in $\mathcal{M}$ correspond to the vertex correction and self-energy, respectively. Using this parameterization, we can rewrite Eq. (7.23b) as

$$d_\tau = -T \sum_{\omega_n} \sum_{\tilde{\tau}} \left[\left(\frac{|\omega_n|}{\pi} \underline{\rho}^{-1} - \mathcal{M} \right)^{-1} \right]_{\tilde{\tau}\tau} \tag{F.7}$$

$$= -T \rho_\tau \sum_{\omega_n} \frac{\pi}{|\omega_n|} - T \sum_{\omega_n} \sum_{n=1}^{\infty} \left(\frac{\pi}{|\omega_n|} \right)^{n+1} \sum_{\tilde{\tau}} \left[\left(\underline{\rho} \mathcal{M} \right)^n \right]_{\tilde{\tau}\tau}. \tag{F.8}$$

The second term in Eq. (F.8) vanishes due to the summation over $\tilde{\tau}$ as follows from

$$\sum_{\tilde{\tau}} \left(\underline{\rho} \mathcal{M} \right)_{\tilde{\tau}\tau} = \sum_{\tilde{\tau}} \left(\mathcal{S}^S_{\tilde{\tau}\tau} - \mathcal{S}^S_{\tau\tilde{\tau}} \right) \rho_{\tilde{\tau}} = 0, \tag{F.9}$$

where we have used that $\mathcal{S}^S$ is symmetric. We thus have $d_\tau = -T \rho_\tau \sum_{\omega_n} \frac{\pi}{|\omega_n|}$ exactly as in the clean case.

F.3 Disorder-induced topology

Here we present more details on the calculation of the impact of disorder on the superconducting instabilities discussed in Chap. 7.2.2. Exactly as Chap. 7.2 of the main text, this appendix is based on Ref. [367].

In the simple case $\mathcal{S}^S_{\Omega s,\Omega' s'} = \gamma$ which is realized in the example discussed in the main text, one can invert $\mathcal{C} - t_d \mathcal{S}^S$ analytically. Defining $\rho_F := \sum_s \int \mathrm{d}\Omega \rho_s(\Omega)$, Eq. (7.20) becomes

$$D_{\Omega s,\Omega' s'} = -T \sum_{\omega_n} \frac{\rho_s(\Omega)}{\frac{|\omega_n|}{\pi} + \rho_F \gamma} \left(\delta_{s,s'} \delta_{\Omega,\Omega'} + \frac{t_d \rho_{s'}(\Omega') \gamma}{\frac{|\omega_n|}{\pi} + \rho_F \gamma (1 - t_d)} \right). \tag{F.10}$$

With the assumptions stated in the main text, $\rho_s(\Omega) \simeq$ const. and Eq. (7.27), we have $\widetilde{\Delta}_s(\Omega) = \widetilde{\Delta}_s$ and the kernel of the free energy expansion (7.17) effectively becomes a 2×2 matrix. Its eigenvalues λ^{++} and λ^{+-} corresponding to the s^{++} ($\widetilde{\Delta}_1 = \widetilde{\Delta}_2$) and s^{+-} ($\widetilde{\Delta}_1 = -\widetilde{\Delta}_2$) state, the zeros of which determine the associated transition temperatures, read

$$\lambda^{++} = -\frac{1}{U+J} - \frac{\rho}{2} \ln\left(\frac{2e^\gamma \Lambda}{\pi T} \right), \tag{F.11a}$$

$$\lambda^{+-} = -\frac{1}{U-J} - \frac{\rho}{2} \left[\ln\left(\frac{\Lambda}{2\pi T} \right) - \psi\left(\frac{1}{2} + \frac{\gamma}{2T} \right) \right] \tag{F.11b}$$

for nonmagnetic ($t_d = +1$) disorder. Here ψ denotes the digamma function. We see that the transition temperature T_c^{++} of the s^{++} state is unaffected by disorder as required by the Anderson theorem [229–231]. In contrast, the critical temperature T_c^{+-} of the s^{+-} phase is reduced as can be seen in Eq. (F.11b) by noting that $\psi(x)$ is monotonically increasing for $x > 0$. As long as $J < 0$, it holds $T_c^{+-} < T_c^{++}$ irrespective of the disorder strength.

In case of magnetic ($t_d = -1$) scattering, we have

$$\lambda^{++} = -\frac{1}{U+J} - \frac{\rho}{2} \left[\ln\left(\frac{\Lambda}{2\pi T} \right) - \psi\left(\frac{1}{2} + \frac{2\gamma}{2T} \right) \right], \tag{F.12a}$$

$$\lambda^{+-} = -\frac{1}{U-J} - \frac{\rho}{2} \left[\ln\left(\frac{\Lambda}{2\pi T} \right) - \psi\left(\frac{1}{2} + \frac{\gamma}{2T} \right) \right]. \tag{F.12b}$$

In this case, both T_c^{++} and T_c^{+-} are reduced by disorder. However, T_c^{++} is more strongly affected due to the additional factor of 2 in front of γ in Eq. (F.12a). Physically, 2γ has to be seen as the sum of intra- and interband scattering strengths which happen to be identical in the example considered, whereas γ in Eq. (F.12b) is just the intraband contribution.

Eqs. (7.28) and (7.29) are straightforwardly obtained by analyzing Eq. (F.12) in the associated asymptotic limits $J/U \to 0$ and $T \to 0$, respectively.